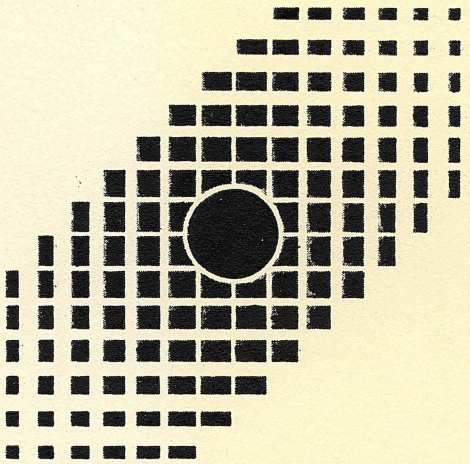
SCHOOL OF ENGINEERING
DUKE UNIVERSITY
DURHAM, NC 27706

CENTER FOR SOLID-STATE POWER CONDITIONING AND CONTROL



Modeling Multiwinding Transformers for High-Frequency Applications

Part I: Analysis

Van A. Niemela, Glenn R. Skutt, Audrey M. Urling
Thomas G. Wilson, Ronald C. Wong

Prepared for Digital Equipment Corporation
Maynard, Massachusetts

July 7, 1989

Vesic
621.314
M689
1989
pt. 1

Contents

Table of Contents i

Glossary of Symbols vii

Acknowledgements xvii

1 Introduction 1
- 1.1 OVERVIEW OF THE REPORT 2
  - 1.1.1 Overview of Part I of the Report 3
  - 1.1.2 Goals and Assumptions of Part I 3
- 1.2 OUTLINE OF ANALYTICAL STEPS PRESENTED IN PART I 5
- 1.3 NOTATIONAL CONVENTIONS USED IN THE REPORT 7

2 Deriving a Model Transformer Structure From An Actual Transformer Winding Arrangement 11
- 2.1 EXAMPLE WINDING STRUCTURES 11
  - 2.1.1 Transformer Configuration of Interest 12
  - 2.1.2 Dimension Directions 13
  - 2.1.3 Definition of Winding Geometry Terms 15
- 2.2 GEOMETRICAL WINDING STRUCTURES 18
  - 2.2.1 Converting Real Windings to Model Windings 18
  - 2.2.2 Admonitions Concerning the Use of Layer Porosity η 22
- 2.3 DIFFERENT COMPONENTS OF LEAKAGE FLUX 23

3 Magnetic-Field Distribution in the Winding Space of a Transformer 29
- 3.1 INFINITE-SOLENOID MODEL OF A TRANSFORMER 30
  - 3.1.1 The Magnetic Field Outside an Infinite Solenoid 32
  - 3.1.2 Field Distribution with DC Current 34
  - 3.1.3 Field Distribution with AC Current 44
- 3.2 EDDY-CURRENT EFFECTS IN INFINITE SOLENOIDS 44
  - 3.2.1 Skin Effect 44
  - 3.2.2 Proximity Effect 46

3.2.3 Combined Frequency Effects 48
3.2.4 The Effect of the Field Distribution on Impedance Values 52
3.3 CURRENT-SHEET APPROXIMATION OF A WINDING LAYER . . . 53
3.3.1 Modeling an Infinite Cylindrical Layer as an Infinite Current Sheet 53
3.3.2 Power and Magnetic-Energy Density in a Region of Space 56

4 Field Solution for an Infinite Current Sheet 57
4.1 APPLICATION OF MAXWELL'S EQUATIONS TO THE INFINITE CURRENT SHEET 57
4.1.1 Description of Problem 57
4.1.2 Derivation of the Diffusion Equations 58
4.1.3 Form of Solution of the Boundary Value Problem 60
4.1.4 Differential Relationships between $\underline{H_z}(x)$ and $\underline{J_y}(x)$ in the Current Sheet 63
4.2 SOLUTION TO FIELD EQUATIONS FOR $\underline{H_z}(x)$ AND $\underline{J_y}(x)$ FOR AN INFINITE CURRENT SHEET 64
4.3 GRAPHICAL ILLUSTRATIONS OF $\underline{H_z}(x)$ AND $\underline{J_y}(x)$ IN AN INFINITE CURRENT SHEET 68
4.3.1 Plots of Phasor Magnitudes for a Single-Layer Example 69
4.3.2 Plots of Phasors for a Single-Layer Example 69
4.4 GRAPHICAL ILLUSTRATIONS OF $\underline{H_z}(x)$ AND $\underline{J_y}(x)$ IN AN IDEALIZED TRANSFORMER 91
4.4.1 Plots of Phasor Magnitudes Across Four Layers 91
4.4.2 Plots of Phasors Across Four Layers 95
4.5 COMPUTATION OF POWER DISSIPATION AND ENERGY-STORAGE IN WINDING LAYERS FROM THE FIELD SOLUTIONS 111
4.5.1 Overview 111
4.5.2 Average Power Dissipation Per Square Meter of an Infinite Current Sheet 115
4.5.3 Average Energy Storage Per Square Meter of an Infinite Current Sheet 121
4.6 SUMMARY OF THE FIELD SOLUTION FOR AN INFINITE CURRENT SHEET 125
4.6.1 Introduction of Layer Porosity η Into the Equations 125
4.6.2 Restatement of Significant Equations 126

5 Derivation of Short-Circuit Impedances from Field Solutions 129
5.1 IMPEDANCE MEASUREMENTS OF TRANSFORMER WINDINGS . . 129
5.1.1 Two-Winding Transformer Measurements 130
5.1.2 Multiwinding Transformer Measurements 132
5.2 DETERMINATION OF THE SHORT-CIRCUIT IMPEDANCE FORMULAE 133
5.2.1 Short-Circuit Conditions 133

5.2.2 Deriving the Magnetic-Field-Intensity Boundary Conditions for a Winding Layer . . . 135
5.2.3 Normalized Values of Field Intensity and MMF . . . 136
5.2.4 Calculation of Resistance Values . . . 139
5.2.5 Winding-Inductance Calculations . . . 143
5.2.6 Short-Circuit Impedance Formula . . . 149
5.2.7 Relating Field Solutions to Winding Layout . . . 150

6 Calculation and Verification of Short-Circuit Impedances 153
6.1 STEP-BY-STEP NUMERICAL EXAMPLE OF DETERMINING $R_{(jk)}$ AND $L_{(jk)}$ . . . 153
6.1.1 Step 1—Collect Known Quantities . . . 154
6.1.2 Step 2—Determine the Related Mechanical Properties . . . 157
6.1.3 Step 3—Determine the Electrical and Magnetic Properties . . . 164
6.1.4 Step 4—Determine Short-Circuit Resistance and Inductance . . . 167
6.2 PLOTS OF SHORT-CIRCUIT RESISTANCES AND INDUCTANCES VERSUS FREQUENCY . . . 171
6.3 MEASURED IMPEDANCE VALUES . . . 176
6.3.1 Laboratory Equipment Setup and Methods . . . 177
6.3.2 Laboratory Results . . . 180
6.3.3 Sources of Disagreement Between Measured and Calculated Data . 186

7 Admittance-Link Equivalent Circuit 189
7.1 GENERAL TRANSFORMER EQUIVALENT CIRCUITS . . . 190
7.2 DERIVATION OF THE ADMITTANCE-LINK EQUIVALENT CIRCUIT 193
7.2.1 4-Port Network . . . 194
7.2.2 5-Terminal Circuit . . . 197
7.2.3 4-Terminal Circuit . . . 198
7.2.4 3-Port Network . . . 202
7.2.5 Admittance-Link Equivalent Circuit . . . 202
7.3 CALCULATION OF ADMITTANCE-LINK VALUES FROM SHORT-CIRCUIT IMPEDANCES . . . 209
7.3.1 Obtaining the Reduced Impedance Martix from the Short-Circuit Impedances . . . 209
7.3.2 Inverting the Reduced Impedance Matrix . . . 215
7.3.3 Obtaining the Admittance-Link Values from the Reduced Admittance Matrix . . . 216
7.3.4 Summary of Equations . . . 217
7.3.5 Calculation Example . . . 218
7.4 APPLICATION OF THE ADMITTANCE-LINK MODEL . . . 222

8 Coupled-Secondaries Equivalent Circuit 225
8.1 CIRCUIT DESCRIPTIONS 225
8.2 DETERMINING THE TERMS OF THE IMPEDANCE MATRIX 231
8.2.1 Self-Impedance Terms 231
8.2.2 Mutual Impedance Terms 232
8.3 COMPARISON OF THE COUPLED-SECONDARIES AND ADMITTANCE-LINK MODELS 235
8.3.1 Relationship Between the Three-Port Networks 235
8.3.2 Merits of Each Model 239

9 CONCLUSIONS 243
9.1 BACKGROUND AND REVIEW 243
9.2 REVIEW OF THE ASSUMPTIONS 245
9.3 FUTURE WORK 246

Appendices

A Derivation of Diffusion Equation (4.1) in Terms of E from Maxwell's Equations A–1

B Derivation of Diffusion Equation (4.9) in Terms of H from Maxwell's Equations B–1

C Derivation of Equation (4.27) from (4.21) and of Equation (4.28) from (4.26) C–1

D Physical Basis for the Distributions of $\underline{H}_z(x)$ and $\underline{J}_y(x)$ D–1

E Expansion of $\underline{J}_y(\chi)\,\underline{J}_y^*(\chi)$ E–1

F Expansion of $\underline{H}_z(\chi)\,\underline{H}_z^*(\chi)$ F–1

G Integration of $\underline{J}_y(\chi)\,\underline{J}_y^*(\chi)$ with respect to χ G–1

H Integration of $\underline{H}_z(\chi)\,\underline{H}_z^*(\chi)$ with respect to χ H–1

I Description of Pot-Core Transformer Tested in Section 6.3 I–1

J Calculating the Short-Circuit Impedances of a Multiwinding Transformer from its Geometry J–1

K Magnetic-Field-Intensity and Current-Density Distributions in Transformer Windings K–1

Bibliography 1101

Appendices

A Derivation of Diffusion Equation (4.1) in Terms of E from Maxwell's Equations A–1

B Derivation of Diffusion Equation (4.9) in Terms of H from Maxwell's Equations B–1

C Derivation of Equation (4.27) from (4.21) and of Equation (4.28) from (4.26) C–1

D Physical Basis for the Distributions of $\underline{H}_z(x)$ and $\underline{J}_y(x)$ D–1

E Expansion of $\underline{J}_y(\chi)\,\underline{J}_y^*(\chi)$ E–1

F Expansion of $\underline{H}_z(\chi)\,\underline{H}_z^*(\chi)$ F–1

G Integration of $\underline{J}_y(\chi)\,\underline{J}_y^*(\chi)$ with respect to χ G–1

H Integration of $\underline{H}_z(\chi)\,\underline{H}_z^*(\chi)$ with respect to χ H–1

I Description of Pot-Core Transformer Tested in Section 6.3 I–1

J Calculating the Short-Circuit Impedances of a Multiwinding Transformer from its Geometry J–1

K Magnetic-Field-Intensity and Current-Density Distributions in Transformer Windings K–1

Bibliography 1101

Glossary of Symbols

The common set of symbols used throughout this report is listed in this glossary. Appearing with each symbol is its name and the page number where it is defined, discussed, or first used.

Some of these symbols appear in the text of the report in several different forms, e.g., in boldface or italic type, in upper or lower case, with or without an underline, or possibly subscripted in different ways. The form of a symbol usually conveys additional meaning beyond the basic meaning given in the table below. This additional meaning is explained in Section 1.3 or in the text where a particular form is used. As an additional aid to understanding some of the more complicated notation, examples of the different forms used with vector phasors and ratios of phasors are reviewed below.

Vector phasors such as $\underline{\mathbf{B}}$, $\underline{\mathbf{D}}$, $\underline{\mathbf{E}}$, $\underline{\mathbf{H}}$, and $\underline{\mathbf{J}}$ are directed quantities which vary in space and time as described in Section 1.3. The notational conventions associated with vector phasors are shown below for the symbol $\underline{\mathbf{E}}$, defined in the table of symbols as "electric field intensity." In Section 1.3, several different forms of this symbol are described with reference to a three-dimensional space. To understand the notation, it is helpful to keep in mind that boldface type signifies a vector with three spatial components, and an underline means "complex."

- $\underline{\mathbf{E}}$ electric-field-intensity vector phasor consisting of a phasor (complex number) in each of the three spatial coordinate directions
- $\underline{E}_y$ (complex number) phasor that is the y-directed component of the electric-field-intensity vector phasor
- $\mathbf{E}$ electric-field-intensity vector at some instant in time, consisting of three time-varying quantities, one in each of the spatial coordinate directions
- E_y (real number) y-directed component of the electric-field-intensity vector at some instant in time
- $|\underline{E}_y(x)|$ (real number) rms magnitude of the phasor that is the y-directed component of the electric-field-intensity vector phasor, as a function of x
- $\mathrm{Re}(\underline{E}_y)$ (real number) real part of the phasor that is the y-directed component of the electric-field-intensity vector phasor

Another set of notational conventions applies to ratios of phasors such as the impedance $\underline{Z}$ and the admittance $\underline{Y}$. For example, $\underline{Z}$ appears in Chapter 7 in several forms:

- $[\underline{Z}]$ complex impedance matrix
- $\underline{Z}_{34}$ complex impedance of element in 3rd row 4th column of $[\underline{Z}]$
- $[\underline{Z}']$ "referred" form of $[\underline{Z}]$
- $[\underline{Z}_r]$ "reduced" complex impedance matrix obtained from $[\underline{Z}']$
- $\underline{Z}_{r,23}$ complex impedance element of the matrix $[\underline{Z}_r]$. The element is a linear combination of short-circuit impedances involving windings 3 and 4.
- $\underline{Z}_{(34)}$ complex short-circuit impedance between windings 3 and 4
- $\underline{z}_{34}$ complex impedance element in a circuit. This symbol is not actually found in the report, but its inverse, the complex admittance element $\underline{y}_{34}$, does appear.

The table of symbols is alphabetized as follows. The relative order of two symbols is determined by the first pair of non-matching characters in the two symbols being compared. The order of the symbols is the same as the order of the two characters in an outline with the following hierarchy of headings:

1. **Alphabet:** Arabic, Greek, numerals, other characters
2. **Case:** upper, lower
3. **Style:** bold, italic, special, Roman
4. **Letter:** No next character, meaning the end of a symbol, comes before additional characters.

To form the outline, the four items in the third level "**Style:**" appear as subheadings for each of the items in the next higher level "**Case:**", and so on. According to this outline, the italicized upper-case W comes before the upper-case special character (subscript) $_W$, which comes before the lower-case w. Greek letters follow all Arabic letters.

If a particular symbol is not found in the table, its root and subscript are probably listed separately. The page numbers refer to Part I of this report. If "Part II" is given in the page-number column, the symbol first appears in Part II of the report, and a page reference is listed instead in the glossary near the front of Part II. SI units are used throughout.

Glossary of Symbols

Symbol	*Meaning*	*Page*
A	cross-sectional area	19
AWG	American Wire Gauge	156
$\hat{\mathbf{a}}_x$, $\hat{\mathbf{a}}_y$, $\hat{\mathbf{a}}_z$	unit vectors in the reference directions x, y, and z	9
$\mathbf{B}$	magnetic flux density, a vector	A-1
$_{BASE}$	(subscript) basis value for normalizing a variable	9
b	breadth	36
b_{cu}	breadth of each conductor in a winding layer	15
b_{max}	maximum breadth available in which to place a winding	15
b_w	breadth of a winding layer	15
b_{win}	breadth of the core window; $b_{win} \geq b_{max} \geq b_w$	15
$_{bob}$	(subscript) "bobbin"	156
$_C$	(subscript) "cross-section"	31
$_c$	(subscript) "critical"	89
c.m.	units of circular mils; 1 c.m. $= 5.067 \times 10^{-10}$ m^2	156
$_{cu}$	(subscript) copper, or more generally, the conductor	15
$\mathbf{D}$	electric flux density, a vector	A-1
$_d$	(subscript) "dissipated"	56
d_{cu}	diameter of the conductor alone in a round wire	16
d_o	outside diameter of a wire, including insulation	16
$\underline{\mathbf{E}}$	electric field intensity, a vector phasor	58
$_E$	(subscript) "eddy-current"	45
	(subscript) "excited-winding"	137
e	constant, 2.71828	8
F_1, F_2	dimensionless functions of Δ, where $\Delta = h_{cu}/\delta$	118
F_3, F_4	dimensionless functions of Δ, where $\Delta = h_{cu}/\delta$	123
f	frequency	72
$\underline{\mathcal{F}}$	magnetomotive force, a vector phasor	136
g_a	"additional" interlayer gap, a length used to correct the calculations	159
g_{inters}	gap between surfaces of conducting layers of adjacent winding	159
g_{intras}	gap between surfaces of conducting layers within a winding	159
g_n	gap height between winding layers n and $n+1$	147

(continued)

Symbol	*Meaning*	*Page*
g_n	(subscript) "in interlayer gap number n"	136
$\underline{\mathbf{H}}$	magnetic field intensity, a vector phasor	53
$\mathcal{H}_{jk}$	gain of the voltage source in secondary j that is controlled by the current in secondary k	226
$H_{(jk)}$	magnetic field intensity in the z-direction with winding j excited and winding k short-circuited	133
$H_{(jk)(lm)}$	product of $H_{(jk)}$ and $H_{(lm)}$	232
HF	"high-frequency"	179
h_{cu}	height of copper in a layer of foil, strip, or equivalent rectangular conductors	15
h_t	height of insulating tape	156
I	a constant value of current, rms unless indicated otherwise by a subscript	8
$\underline{I}$	complex current phasor	8
[I]	identity matrix	216
I_j	integral expression j	G-2
$\underline{I}_m$	magnetizing current phasor	131
Im	"imaginary" operator to signify "imaginary part of ..."	67
i	instantaneous current	8
$\underline{\mathbf{J}}$	current density, a vector phasor	60
j	$\sqrt{-1}$	8
	winding number	129
	row index of a matrix	191
(jk)	(subscript) refers to a short-circuit test where winding j is excited and winding k is short-circuited	129
K	total number of windings in a transformer	190
K_T	temperature coefficient of resistivity; $K_T = 3.93 \times 10^{-11}$ Ω-m/°C for annealed copper wire [22, p. E-88]	156
k	winding number	129
	column index of a matrix	191
$\underline{k}$	complex wave number	58
L	inductance	130
LF	"low-frequency"	179

(continued)

Glossary of Symbols (continued)

Symbol	*Meaning*	*Page*
$L_{(jk)}$	short-circuit inductance at winding j with winding k short-circuited	149
$L_{\ell n}$	leakage inductance associated with winding n	130
L_m	magnetizing inductance	130
ℓ	length	19
l	loop	34
ℓ_{gn}	"length of turn" for the interlayer gap number n	147
ℓ_m	magnetic path length	Part II
ℓ_T	length of turn in a winding layer	16
ℓ	(subscript) "layer"	16
	(subscript) "leakage"	130
M	mutual inductance	191
N_c	number of current-carrying conductors in a winding layer; $N_c = n_s N_\ell$	16
N_j	number of turns in winding j	26
N_ℓ	number of turns in one winding layer	16
$_N$	(subscript) "normalized"	9
n	number of turns per meter across the breadth of a winding	37
	layer or interlayer-gap number, counted from the innermost outward	112
n_s	number of electrically-paralleled conductors with the same height coordinate	16
$_n$	(subscript) layer number	112
$_{OC}$	(subscript) "open-circuit"	130
P	power	139
$< P_D >$	average power dissipated in all the windings of a transformer	139
$P_{R(jk)}$	power dissipated in a resistance $R_{(jk)}$	139
P_n	total power dissipated in winding layer n	112
$\mathcal{P}$	permeance	Part II
p_d	power dissipated per unit volume (power density)	56
$< Q_H >$	average magnetic energy storage per square meter in the y-z plane	123

(continued)

Glossary of Symbols (continued)

Symbol	*Meaning*	*Page*
$< Q_J >$	average power dissipated per square meter of current sheet in the y-z plane	119
$< Q'_H >$	normalized average magnetic energy storage in a layer, a dimensionless function of α, β, and Δ	123
$< Q'_J >$	normalized average power dissipation in a layer, a dimensionless function of α, β, and Δ	119
R	resistance	19
	radius	31
R_c	core loss resistance	130
$R_{(jk)}$	short-circuit resistance at winding j with winding k short-circuited	149
R_{wn}	resistance of winding n	130
$_R$	(subscript) "ring"	31
$\mathcal{R}$	reluctance	24
Re	"real" operator to signify "real part of ..."	8
r	"radius" direction in a cylindrical coordinate system where a point is specified as (r, ϕ, z); distance in the radius direction	34
$_r$	(subscript) "reduced"	200
S	surface	34
S_ℓ	center-to-center distance between two adjacent layers of the same winding section	18
$S_{\ell s}$	center-to-center distance between two adjacent layers of different winding sections	18
S_s	center-to-center distance between two adjacent sections of the same winding	18
$_S$	(subscript) "secondary"	226
$_{SC}$	(subscript) "short-circuit"	8
$_{S,j}$	(subscript) "secondary j"	226
T	period of a waveform	113
	temperature	Part II
T_S	switching period	Part II
TEM	"transverse electromagnetic"	105
$_T$	(subscript) "total"	144

(continued)

Glossary of Symbols (continued)

Symbol	*Meaning*	*Page*
^{T}	(superscript) transpose of a matrix or vector	200
t	time	7
$_(t)$	"time" as an independent variable; indicates that the preceding quantity is instantaneous or time-varying	7
$[\underline{V}_{d4}]$	vector of differential voltages $\underline{V}_{j4}$, all referenced to terminal 4	200
$\underline{V}$	complex voltage phasor	8
$\underline{V}_{jk}$	differential-voltage phasor between terminals j and k	199
V_n	volume of winding layer n	113
v	instantaneous voltage	177
	distance from $\chi = h_{cu}$, in the negative χ direction, in units of skin depth; $v = (h_{cu} - \chi)/\delta$; $v = w - \Delta$	E-3
W	energy	112
w	distance measured along the χ-axis in units of skin depth δ; $w = \chi/\delta$	117
$< W_g >$	time-average magnetic energy stored in all the interlayer gaps of a transformer	144
$W_{L(jk)}$	magnetic energy stored in an inductance $L_{(jk)}$	144
$< W_\ell >$	time-average magnetic energy stored in all the winding layers of a transformer	144
W_n	magnetic energy stored in winding layer n	112
$< W_T >$	total time-average magnetic energy stored in a transformer	144
w_m	magnetic energy stored per unit volume (energy density)	56
X_{bob}	height of the center leg of the bobbin	156
x, y, z	the three axes in a right-handed Cartesian coordinate system which correspond to the dimensions of *height*, *depth*, and *breadth* respectively; distance in the corresponding reference direction; as subscripts, a quantity in the designated direction	55
χ	(actually the Greek letter chi) variable denoting a position across the finite dimension of an infinite current sheet	66
$\underline{Y}$	admittance	190
Y_{bob}	depth of the center leg of the bobbin	156
$\underline{Y}_{jk}$	admittance element between terminals j and k of the admittance-link equivalent circuit	205

(continued)

Glossary of Symbols (continued)

Symbol	*Meaning*	*Page*
Y_o	distance across the windings in the y direction	158
y_j	expression j	F-1
$\underline{y}_{jk}$	admittance of branches or "links" in equivalent circuit	205
$\underline{Z}$	impedance	8
$\underline{Z}_{(jk)}$	short-circuit impedance with winding j excited and winding k short-circuit	149
$[\underline{Z}_S]$	coupled-secondaries equivalent-circuit impedance matrix	228
z_n	(subscript) component in z-direction in layer n	136
α	real part of the boundary-condition ratio $\underline{\Gamma}$	67
β	imaginary part of the boundary-condition ratio $\underline{\Gamma}$	67
$\underline{\Gamma}$	boundary-condition ratio; $\underline{\Gamma} = \alpha + j\beta$	67
Δ	height of a winding layer in skin depths; $\Delta = h_{cu}/\delta$	117
δ	skin depth; $\delta = \sqrt{2/\omega\mu\sigma}$	59
ε	variable which is either 1 or 0 depending upon the magnetic-field-intensity boundary conditions	68
ϵ	permittivity	58
ϵ_r	relative permittivity; $\epsilon_r = \epsilon/\epsilon_0$	A-2
ϵ_0	permittivity of free space, 8.854×10^{-12} [F/m]	58
η	layer porosity; $\eta = N_c b_{cu}/b_{win}$	22
θ	phase angle	8
Λ	flux linkage	Part II
λ	wavelength	D-8
μ	permeability	23
μ_r	relative permeability; $\mu_r = \mu/\mu_0$	A-2
μ_0	permeability of free space, $4\pi \times 10^{-7}$ [H/m]	23
ν	volume; $d\nu$ is a differential volume element	112
π	constant, 3.14159	72
ρ	resistivity in general, which could be the actual resistivity of a material or an "effective" resistivity; $\rho = 1/\sigma$	
	charge density	A-1

(continued)

Glossary of Symbols (continued)

Symbol	*Meaning*	*Page*
ρ_{cu}	resistivity of copper; for annealed copper wire: 1.7241×10^{-8} Ω-m at 20°C with temperature coefficient 3.93×10^{-11} Ω-m/°C [22, p. E-88]; $\rho_{cu} = 1.8813 \times 10^{-8}$Ω-m at 60°C	164
σ	conductivity in general, which could be the actual conductivity of a material or an "effective" conductivity	19
σ_{cu}	conductivity of copper; $\sigma_{cu} = 1/\rho_{cu} = 5.315 \times 10^{-7}$ S/m at 60°C	164
σ_{eff}	effective conductivity; replaces the σ in the equations of Part I when calculating for equivalent-foil windings; $\sigma_{eff} = \eta\sigma_{cu}$	126
$\underline{\Phi}$	flux phasor	Part II
ϕ	instantaneous magnetic flux	24
	the angle dimension in a cylindrical coordinate system where a point is specified as (r, ϕ, z)	53
χ	variable denoting a position across the finite dimension of an infinite current sheet	66
ω	angular frequency of a periodic waveform	8
$'$	prime, the identifier for a circuit-element value which has been multiplied by a transformer turns ratio to reflect it from its original-winding location to a location in another winding circuit	195
*	(superscript) "star," meaning the complex conjugate of the preceding quantity	116
$< _ >$	angle brackets, denoting the time average of the enclosed quantity	8
$\tilde{}$	block-partitioned matrix	216
	complex quantity	D-3

This page has been left blank intentionally.

Acknowledgments

The authors would like to acknowledge and thank several members and former members of the Center for Solid-State Power Conditioning and Control for their contributions to the research and documentation represented by this report.

First, we wish to acknowledge those former members of the research group who contributed to the writing of this report: Glenn Skutt[1] and Charles Hawkes.[2] Part I of this report, *Modeling Multiwinding Transformers for High-Frequency Applications: Analysis*, incorporates many ideas and figures plus some text originally presented in the Master's Thesis, *Modeling Multiwinding Transformers for High-Frequency Applications*, by Glenn Skutt. Glenn's work laid the cornerstone for much of the research presented in this report. As part of his master's degree work, Charles Hawkes wrote Sections 4.3 and 4.4, Appendix D, and the computer program which generated the phasor distribution plots of Chapter 4. In addition, he oversaw revisions to Sections 4.1 and 4.2 and Appendices A, B, and C of Part I, and coauthored a paper for the 1989 Power Electronics Specialists Conference which is included as Appendix K of Part I.

Second, we wish to acknowledge those persons whose contributions have been primarily toward the research presented in this report and to the mechanics of producing this document: Yain-Nan Chang[3], Dr. Harry A. Owen, Jr., and Margrid Krueger. The acquisition of most of the laboratory data presented in this report was carried out by Yain-Nan (Steve) Chang. Steve wrote the computer program to generate the calculated short-circuit impedance data presented in Chapter 6, and spent numerous hours in the Macintosh cluster drawing and revising figures. A special thanks goes to Dr. Owen whose advice on the laboratory measurements and on the interpretation of the resultant data were invaluable. Lastly, we wish to thank our administrative assistant, Margrid Krueger, for her LaTeX advice and expertise and for her time spent generating the various versions of this report.

Additionally, we would like to thank Dr. Anil K. Ohri and Dr. Joseph V. Thottuvelil of Digital Equipment Corporation for their guidance and direction in the conduct of this research, and to Mr. P. S. Venkatraman for consultation on many of the fine points of magnetics and for providing numerous sample transformers for testing and evaluation.

---

[1]Now with Digital Equipment Corporation, Northboro, MA.

[2]Now with Harris Corporation, Melbourne, FL.

[3]Now with Deltron, Inc., North Wales, PA.

This page has been left blank intentionally.

Chapter 1

Introduction

There are many advantages to using high excitation frequencies in power conditioning circuits. One of the most important of these advantages is the reduction in transformer size that can be achieved as the frequency increases. Other benefits which are not related to the transformer magnetic structure include a decrease in the size of output filter inductors and capacitors, faster output response to changes in input voltage, and easier filtering of radiated switching noise.

High-frequency excitation clearly has advantages in power conditioning circuits, but as with all things there must also be associated drawbacks. In this case, the drawbacks arise due to the so-called skin and proximity effects which cause the currents in the transformer windings to distribute unevenly over the cross-sectional areas of these windings. The results of these redistributions of current are an increase in the copper losses in the windings of the transformer and a reduction in the magnetic energy stored in the window of the transformer core.

The increase in the copper losses in the transformer windings appears in a circuit as an increase in the resistance of each of the transformer windings. This increase in the apparent winding resistance is often referred to as *ac winding resistance* and is a deleterious effect that results in more power dissipation in a winding that carries a given current. The increased power dissipation translates into an increase in the heat generated in the winding space. This increased thermal stress can affect the performance of the transformer enough to outweigh other advantages of high-frequency operation; in fact, the thermal problems related to high-frequency winding losses can place an upper limit on the frequency that can be used in a given device. Since transformer performance is so heavily influenced by dissipative loss, the quantification of ac winding resistance effects has been the major focus of most of the recent work that has appeared concerning the high-frequency operation of transformers.

The reduction of the amount of magnetic energy in the transformer window area that results from high-frequency excitation can be related to a corresponding decrease in the inductance of the various windings of the transformer. This winding inductance is often referred to as transformer *ac leakage inductance*. We must be clear however that the

concept of leakage inductance or more specifically leakage flux is defined only as leakage *between two windings*. There is no way to designate what the leakage inductance of a winding is in and of itself, but rather this must always be defined in reference to some other winding. In this report we refer to the inductances associated with the leakage flux between any two windings as the reactive component of the leakage *impedance* between the two windings.

The reduction of magnetic energy in the transformer window area is a more benign and generally a more beneficial phenomenon than the corresponding increase in apparent winding resistance. It has not, therefore, received a great deal of attention in the literature. However, this inductance of transformer windings warrants closer examination. At sufficiently high frequencies the winding inductance may interact with other stray elements in the circuit and significantly affect the circuit operation. In certain types of circuits such as quasi-resonant switching converters, this is a desirable and important interaction.

In other applications, however, the inductances in the windings cause undesirable effects. Such a situation exists in the multioutput voltage regulator where the inductances in the secondary windings of a multisecondary transformer create cross-regulation problems that impact the steady-state output voltages that appear on unregulated outputs. The analysis presented in this report is aimed more toward quantifying these cross-regulation effects than toward describing the interaction between transformer winding inductances and other parasitic circuit parameters. The focus of this analysis influences many of the assumptions used in deriving a suitable model for multiwinding transformers with high-frequency current excitations.

1.1 OVERVIEW OF THE REPORT

This report is divided into two separate parts: *Part I: Analysis*, and *Part II: Literature Review*. The document you are reading currently is *Part I: Analysis*. Throughout the rest of this report *Part I: Analysis* is called "Part I" or "Part I of this report" and *Part II: Literature Review* is called "Part II" or "Part II of this report." Part I of this report deals primarily with deriving the field solution to determine the redistribution of currents in high-frequency transformer windings and how this redistribution affects the power dissipation and energy storage of the transformer windings. It is designed to aid the reader's understanding of high-frequency effects in transformer windings and to provide the reader with simple equivalent circuits for the transformer which account for these effects. Part II of this report is an in-depth review of several important articles pertaining to high-frequency transformer windings and describes the strengths, weaknesses and significant contributions of each article. It is designed to aid the reader's comprehension of the reviewed articles.

1.1.1 Overview of Part I of the Report

Part I of this report provides a means by which the impedances which characterize a multiwinding transformer can be calculated for high-frequency sinusoidal excitations. The general aim of this analysis is to replace laboratory measurements of transformer characteristics with calculated values that are based on the geometry of the transformer and the excitation conditions in the transformer windings. The results of such an analysis hopefully will provide the foundation for determining via computer simulation the interactions between the various windings of a multiwinding transformer. The ability to simulate the behavior of a given transformer design without actually building the device should prove useful in the design of multiwinding transformer circuits for use in high-frequency applications.

Another and perhaps equally significant purpose of Part I of this report is to review critical concepts of high-frequency transformer analysis and to familiarize the reader with the set of assumptions that are used in such an analysis. This should provide the reader with the tools necessary to understand similar derivations presented in recently published articles such as [19]. In deriving the full solution for the field distribution in an infinite current sheet used to model a transformer winding layer, Part I of this report fills in many of the details that are often left out of shorter journal articles. The mathematical detail presented herein should allow the reader to follow the trail of analysis without having to derive the intermediate steps and should aid the reader's understanding of the journal articles discussed in Part II. Also, the sections on modeling an actual transformer winding structure should provide a guideline for applying these results to specific transformers. At the outset of the solution for the fields associated with the transformer winding space, certain assumptions are made and the winding layers of the physical transformer are replaced by infinite current sheets to make the solution tractable. At the conclusion of the field solution, two equivalent circuits are proposed to model the transformer's behavior in an electrical system.

1.1.2 Goals and Assumptions of Part I

Generally it is very difficult if not impossible to calculate the leakage impedance values between transformer windings, so the measurement of these parameters in the laboratory is usually the only reasonable alternative. This is rather inconvenient to the design engineer who would like to predict the performance of a certain transformer design without first building the device. In addition, the dependency of the leakage impedances of a transformer on the excitation conditions that exist in the windings means that it is usually not sufficient to measure the transformer characteristics only once; rather, the measurements must be performed over the expected range of harmonics for the excitation waveform.

The goal of Part I of this report, therefore, is to develop appropriate methods for calculating the values of the various winding impedances of a multiwinding transformer based on the geometry of the winding structure and the winding excitation conditions.

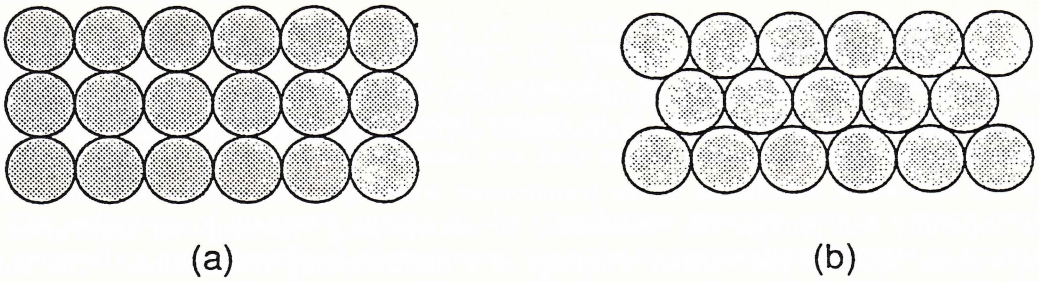


Figure 1.1: Definition of winding arrangements (a) square and (b) hexagonal [17, page 338].

To accomplish this goal, we must make several simplifying assumptions about the transformer that allow us to analyze the magnetic field distribution in and around the windings of the transformer in a single dimension. The main assumption that we use to perform such a one-dimensional analysis—indeed it is with the purpose of allowing this one assumption that other approximations are made—is that throughout the winding space of a pot- or EE-core transformer, the magnetic leakage flux is parallel to the surfaces of the various layers of conductors that comprise the transformer windings. We specify our assumptions and define the geometry of the winding structures in detail later in this report. We make no attempt in this report to address the variations of the magnetic fields in the windings in more than one dimension.

In this report, we are interested only in the high-frequency behavior of the transformer windings. No attempt is made to model core loss, nor analyze the frequency dependence of core loss. Rather, it is assumed that the magnetizing current of the transformer core is negligible and that the core appears to be ideal, i.e., it is lossless and stores no energy. Also, the analysis presented herein predicts only the apparent winding resistances and leakage inductances of the transformer windings. Throughout this analysis, capacitive effects caused by voltage gradients between adjacent conductors are ignored. For the frequencies of interest, this does not seriously affect the agreement between the measured transformer impedances and the predicted values as is shown in Chapter 6. At higher frequencies though, capacitance in the transformer windings will cause the measured and predicted values to diverge.

For the analysis presented in Part I of this report, certain assumptions are made about the configuration of the windings in the transformer window. It is assumed that winding layers are arranged in a "square" configuration as in Fig. 1.1(a) rather than a "hexagonal" arrangement as in Fig. 1.1(b). Hence, turns from one layer are not permitted to sink into the spaces between the turns of an adjacent layer. Likewise, it is assumed that transformer winding layers contain only conductors of one transformer winding. Bifilar windings, where wires from two separate windings are wound simultaneously,

are not considered. However, no restriction is placed on the relationship between the conductors in adjacent layers, and conductors of the same winding may be paralleled and wound simultaneously.

The analysis presented in this report is based solely on sinusoidal-current-excitation conditions in the windings of a transformer. Nonsinusoidal-current excitations can be accommodated by applying Fourier analysis to the nonsinusoidal waveforms. Such Fourier analysis is discussed in [2,19,20],[1] but we do not examine it any further in Part I. From the purely sinusoidal analysis, we derive expressions for the resistance and inductance values between two windings and then use these results in two different equivalent-circuit models of a multiwinding transformer. These circuit models are intended to be used in a circuit simulation tool such as SPICE for predicting the behavior of a multiwinding transformer under load. We have not performed such simulations and we can make no claim about the adequacy of the equivalent-circuit models discussed in this report.

The assumptions used in the analytical development limit the applicability of the results. Although measurement verification for different transformers operated under various excitation conditions is not complete, the analysis should apply to transformers wound on pot- or EE-core structures. Of particular interest are multiwinding transformers for use in multioutput dc-to-dc converters with PWM control. It should be stressed that the fundamentals of the analysis techniques employed here can be found in many early references on transformer analysis; however, the particulars of the analysis are adapted toward predicting and modeling the effects of high-frequency current excitations on the leakage impedances of multiple-winding transformers.

We should remember that the analysis of transformers and the calculation of transformer device characteristics is one of the oldest and most thoroughly investigated topics in electrical engineering. The reader should recognize that many of the ideas and solutions that are addressed in Part I were investigated in much earlier work. The primary advantage that the present analysis enjoys that earlier works could not incorporate is computer calculation of complex magnetic field equations. In essence, the major contribution of the following analysis is our ability to calculate and display the distributions of magnetic energy and current density inside a transformer winding space, thus increasing the reader's understanding of high-frequency effects in transformer windings.

1.2 OUTLINE OF ANALYTICAL STEPS PRESENTED IN PART I

In Chapter 2, we show how an actual transformer winding structure can be converted into the geometrical model of a transformer that we use in the analysis of Chapter 4. This chapter concentrates on the definition of certain winding parameters and provides detailed explanations for terms encountered in the rest of this report and in recently

[1] We list all references in Part I of this report alphabetically. See the bibliography for the specific reference.

published articles. In addition, Chapter 2 addresses the term *leakage flux* and what is meant by this term throughout this report.

Chapter 3 sets up the problem we address in the analytical development of later chapters. In this chapter, we initially assume that we can model the transformer as a multilayer, infinitely long solenoid. We then describe the magnetic-field-intensity distribution that exists in a two-layer infinite solenoid when the currents in the windings are constant or varying at low-frequencies. Following the development of the low-frequency field distribution in the solenoid, we discuss the effect that time-varying magnetic fields have on conductors in general. This discussion provides detailed qualitative explanations of both the skin and proximity effects that occur in the conductors of the transformer windings. Following this general discussion of the eddy-current effects in conductors, we introduce the infinite current sheet as an approximate representation of the infinitely long cylindrical conducting layers of the infinite solenoid. We conclude Chapter 3 by setting up the geometry of the current sheet which we proceed to analyze in Chapter 4.

Chapter 4 presents the bulk of the mathematical work in this report. In this chapter, we begin with Maxwell's field equations and apply them to the infinite current sheet under sinusoidal field variations. From these equations, we derive one-dimensional differential equations for the magnetic field intensity and current density inside a current sheet. We then solve these differential field equations to determine expressions for the distribution of magnetic field intensity and current density as functions of excitation frequency and the values of the magnetic field intensity on the boundaries of the sheet. An extensive number of plots are presented in this chapter to illustrate the impact of the skin and proximity effects on the distribution of the magnetic field intensity and current density in the conducting layers. The remainder of Chapter 4 shows how these two field distributions are used to calculate the power dissipated and energy stored in any winding layer.

Chapter 5 takes the general expressions for the power dissipated and energy stored in any winding layer, developed in Chapter 4, and applies them to the calculation of the apparent resistance and inductance for transformer windings under specific hypothetical short-circuit tests. The low-frequency field-intensity diagrams developed in Chapter 3 are used to determine the boundary conditions of field intensity for each layer in the winding space. The boundary conditions are used with the layer-based expressions of Chapter 4 to determine the total dissipated power and energy stored in the winding space. Finally, the total power loss and energy stored are represented in an equivalent circuit by a resistor and an inductor, respectively.

An example calculation of the short-circuit resistance and inductance for an actual transformer at a specific frequency is presented in Chapter 6. This chapter takes the reader through the steps necessary to determine these values given the geometry of the transformer winding and the specific short-circuit excitation. Many of the more important concepts of the previous chapters are recapitulated in Chapter 6 and clarified by use. Calculated short-circuit resistance and inductance data are plotted versus frequency and compared with measured data to demonstrate the validity of the analytic results.

Two equivalent circuits which fully characterize a four-winding transformer for sinusoidal excitation at a specific frequency are the subjects of Chapters 7 and 8. The elements of these equivalent circuits are determined using the short-circuit impedances calculated using the expressions derived in Chapter 5. Chapter 7 focuses on the admittance-link model which is also discussed in [1,13,18]. At the beginning of Chapter 7, we review the general K-port-network description of a transformer with K windings and express the winding voltages and currents using port voltages and currents of the K-port network. This K-port network description is used to derive expressions for the admittance-link-circuit elements in terms of the transformer short-circuit impedances. Chapter 7 concludes with a sample calculation of the admittance links for the example transformer used in Chapter 6. Chapter 8 focuses on a coupled-secondaries equivalent circuit which is an extension of a model proposed by Rosa in [15]. The relationship between the admittance-link model and the coupled-secondaries model and the relative merits of each are also discussed in Chapter 8.

Finally, Chapter 9 reviews some of the major assumptions made in this analysis, and provides some general guidelines for reducing the leakage impedances of multiwinding transformers. In this chapter we also comment on the future prospects for the application of the type of analysis presented here.

The analysis methods presented in this report have been summarized in two papers which are to be presented at the 1989 Power Electronics Specialists Conference. Preprints of these papers are included in this report as Appendices J and K.

1.3 NOTATIONAL CONVENTIONS USED IN THE REPORT

While writing Parts I and II of this report, a consistent set of symbols and nomenclature was adopted by the authors. A summary of these symbols and their definitions appears in the Glossary of Symbols which is located immediately after the Table of Contents. Throughout this report, all quantities are presented in SI units. The adopted nomenclature is defined throughout the text of Part I but primarily in Chapter 2. To cue the reader on the specific usage of the adopted symbols, certain notational conventions are used throughout Parts I and II of this report.

Variables that represent time-varying density functions are given lower case symbols, as shown below. The corresponding total time-varying variables resulting from integrating these density functions over space are given upper case symbols. For these variables, the case of the subscript follows no convention and is defined upon the first use of the variable. The time-varying nature of these functions is emphasized by the presence of (t) in the variable. Examples are:

- $p_d(t)$: instantaneous power dissipated per unit volume (power density)
- $w_m(t)$: instantaneous magnetic energy stored per unit volume (energy density)
- $P_n(t)$: total instantaneous power in the n^{th} layer of a transformer

- $W_g(t)$: total time-varying energy stored in the interlayer gaps

The time average value of any of these variables is represented by enclosing the symbol in angle brackets $\langle\ \rangle$. An example of this is $\langle p_d \rangle$, the time-average power density at a point.

With the above density functions as an exception, a time-varying quantity is generally designated as a lower-case variable with an upper-case subscript, and the corresponding time-average variable is given in angle brackets. For example, i_{SC} or $i_{SC}(t)$ might represent the instantaneous current under short-circuit (SC) conditions, and $\langle i_{SC} \rangle$ represent the time-average short-circuit current. Variables that refer to rms values of currents or voltages are written in upper case with an upper-case subscript. For example, an rms current in a short-circuited transformer winding is designated I_{SC}.

In the special case of sinusoidally varying waveforms, time-varying quantities may alternatively be written using phasor notation. Phasor notation is a shorthand notation used to represent the magnitude and phase information of a sinusoidally varying quantity. A phasor is a complex number with a magnitude equal to either the peak value or the rms value of a sinusoidal waveform and a phase angle that corresponds to the difference in phase between the particular time-varying quantity and some chosen sinusoidal reference. *In this text, we choose the magnitude of a phasor quantity to be equal to the rms value of the sinusoidally varying quantity that it represents.* We designate phasor quantities as upper-case letters with an underline. For example, the symbol $\underline{I}_{SC}$ denotes the phasor for the sinusoidally varying short-circuit current $i_{SC}(t)$. A phasor can be written as a complex number in terms of its real and imaginary components, or in terms of its magnitude and phase angle. In the latter case, called the polar form, two conventions are commonly encountered—either $\underline{I}_{SC} = I_{SC}\angle\theta$ or $\underline{I}_{SC} = I_{SC}\, e^{j\theta}$—where the magnitude of the phasor, which in this report is equal to the rms value I_{SC} of the sinusoid, is followed either by the angle symbol $\angle$ and the phase angle θ or by the expression $e^{j\theta}$. Phasor quantities are converted from polar to rectangular form using the Euler identity

$$e^{j\theta} = \cos\theta + j\sin\theta \tag{1.1}$$

Phasor quantities are transformed into their corresponding time functions by multiplying the phasor by the time function $e^{j\omega t}$, then taking the real part (for the case of a cosinusoidal reference function) and multiplying the result by $\sqrt{2}$. That is,

$$\begin{aligned} i_{SC}(t) &= \sqrt{2}\,\mathrm{Re}(\underline{I}_{SC}\, e^{j\omega t}) \\ &= \sqrt{2}\,\mathrm{Re}(I_{SC}\, e^{j\theta}\, e^{j\omega t}) \\ &= \sqrt{2}\, I_{SC}\cos(\omega t + \theta) \end{aligned} \tag{1.2}$$

In addition to being used in the symbols for phasor quantities, underlines are used to denote all complex variables. This includes any complex numbers that are the ratio of phasor quantities which are written as upper case letters with an underline. An example of this is an impedance that is determined from the ratio of a phasor voltage $\underline{V}$ and a phasor current $\underline{I}$. For this case, we write $\underline{Z} = \underline{V}/\underline{I}$.

Another notational convention in this report is the use of boldface characters to designate vector quantities. An example of this is $\mathbf{E}(x, y, z, t)$ which is the three-dimensional time-varying vector electric field. If this electric field is varying sinusoidally in time, then we can combine the phasor and vector notations and write

$$\mathbf{E}(x, y, z, t) = \sqrt{2}\,\mathrm{Re}(\underline{\mathbf{E}}(x, y, z)e^{j\omega t}) \tag{1.3}$$

where $\underline{\mathbf{E}}(x, y, z)$ is a vector phasor quantity. This vector phasor can be written in terms of its phasor components as

$$\underline{\mathbf{E}}(x, y, z) = \underline{E}_x\hat{\mathbf{a}}_\mathbf{x} + \underline{E}_y\hat{\mathbf{a}}_\mathbf{y} + \underline{E}_z\hat{\mathbf{a}}_\mathbf{z} \tag{1.4}$$

where $\underline{E}_x$ can be expressed as $E_x\angle\theta_x$ or $E_x e^{j\theta_x}$ and can be a function of x, y and z. In the text of this report, the explicit argument dependence of a vector quantity is sometimes dropped if the vector nature of the quantity is clear. For example, in writing Maxwell's equations, we may write $\nabla \times \mathbf{E} = -\partial\mathbf{B}/\partial t$ where the spatial and time dependencies of $\mathbf{E}$ and $\mathbf{B}$ are understood.

Finally, an expression that represents a normalized value is written with an additional N subscript appended, if necessary, by a hyphen to any preexisting subscript. For example, the magnetic field intensity in the n^{th} layer $\underline{H}_{z_n}(x)$ can be normalized to some base value $\underline{H}_{BASE}$, to yield the normalized field intensity for the layer $\underline{H}_{z_n\text{-}N}(x) = \underline{H}_{z_n}(x)/\underline{H}_{BASE}$.

This page has been left blank intentionally.

Chapter 2

Deriving a Model Transformer Structure From An Actual Transformer Winding Arrangement

Any analysis of high-frequency effects in transformer windings must, of course, begin with a determination of the fields in and around the windings which is based upon Maxwell's equations. Before this can be done though, certain assumptions must be made so that the transformer windings can be modeled and the field solution made tractable. Also, a set of terminology must be adopted to facilitate discussion of the transformer windings and any resultant model. In this chapter, we demonstrate the techniques and terminology used to transform an actual winding structure that consists of round wire, rectangular conductors, or foil windings into a model structure which we use in subsequent chapters that contains only equivalent foil conductors which extend across the full breadth of the core window. We also examine two aspects of leakage flux and clarify what is meant by this term in subsequent chapters.

2.1 EXAMPLE WINDING STRUCTURES

The key to the transformer analysis presented in this report lies in the geometry and layout of the transformer winding structure. Therefore, it is important to state clearly what types of devices are addressed here and to define clearly a set of variables that can be used in the analytical expressions. Much of the published work that addresses the issue of ac winding impedances uses somewhat conflicting terminology when referring to both transformer geometry and winding parameters. In the following discussion, we choose a single set of definitions and conventions to refer to the magnetic structures. Some terms are taken directly from the literature where a relatively clear consensus

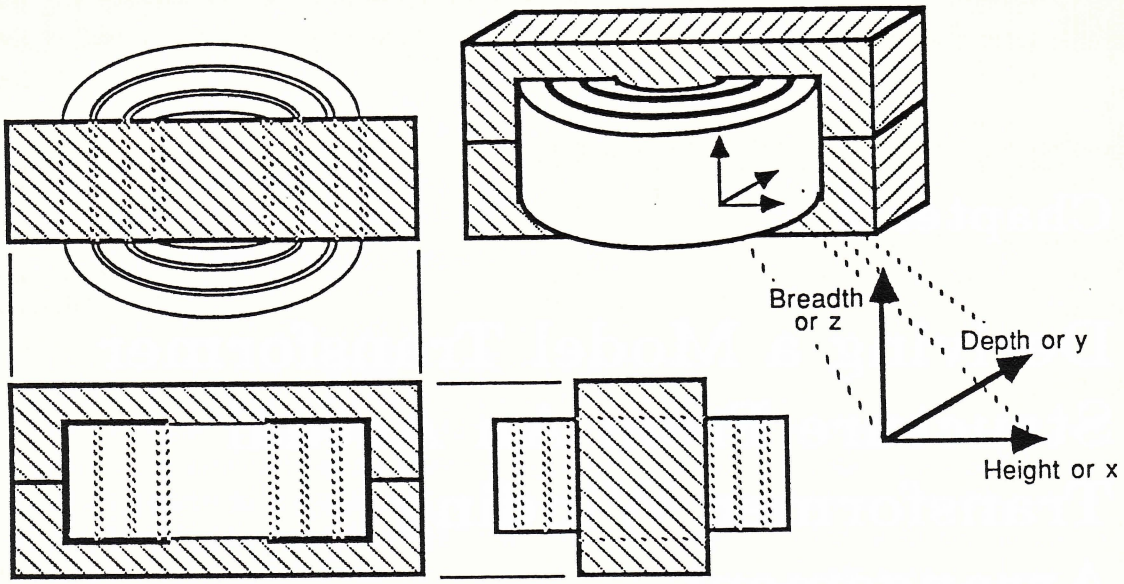


Figure 2.1: Wound EE-core transformer with shell windings.

exists among several authors. Where no such clear agreement exists, we pick a suitable symbol and use this symbol throughout our discussion. Not all of the symbols that we define in this chapter are necessarily used in any calculations given in this report. The justification for providing the specific and detailed definitions for all geometrical quantities is that such definitions should prove useful in the future for such pursuits as developing any type of computer program for the analysis of devices such as those examined in this report. For ease of reference, the symbols defined within this chapter and in later parts of this report have been collected in the Glossary of Symbols which follows the Table of Contents.

2.1.1 Transformer Configuration of Interest

The focus of our analysis is transformers with windings that are wound on pot cores although it is our opinion that the analysis is equally valid for EE cores such as those shown in Fig. 2.1. A transformer of the type shown in Fig. 2.1 has windings which form concentric cylindrical "shells" with the outer layers of wire completely surrounding the inner winding layers. Such a structure is referred to as a shell transformer in [13], and we shall use that designation in the discussion which follows. In a shell winding arrangement, the flux in the window of the transformer is assumed to be parallel to the axis of the winding. This leakage flux pattern is shown for an example transformer in Fig. 2.2.

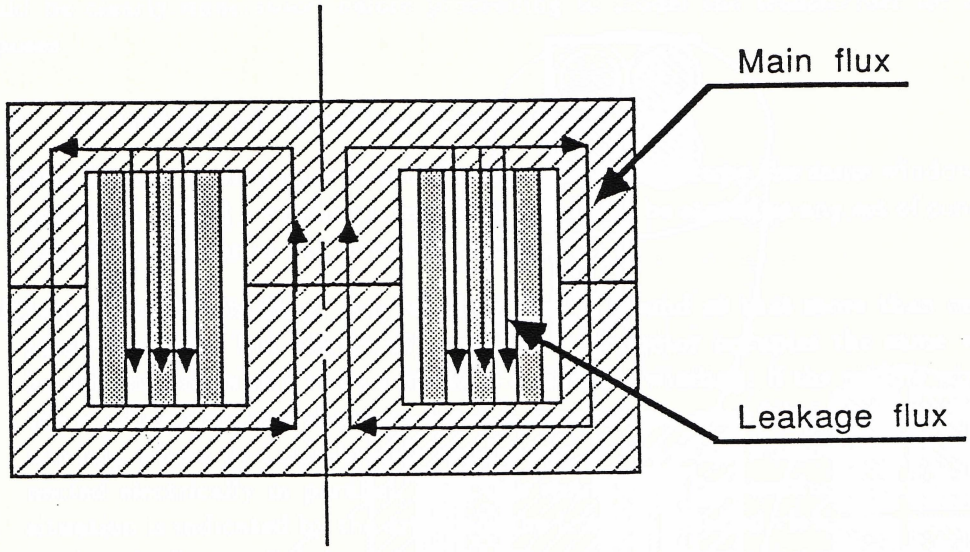


Figure 2.2: Window flux pattern in a shell winding structure.

2.1.2 Dimension Directions

The coil dimensions shown for the winding structure of Fig. 2.1 employ the following conventions:

- The **breadth** direction is in the same direction as the flux in the transformer window. For a shell winding structure, this direction is parallel to the axis of the center leg of the core. This is later referred to as the z-axis direction. This convention is indicated in Fig. 2.1.

- The **height** direction is normal to the direction of the flux in the window of the transformer and in the direction of the buildup of the windings. For the shell windings in Fig. 2.1, the height direction is normal to the core center leg. The height direction is later referred to as the x-axis direction. Figure 2.1 shows the height direction definition for the structure.

- The **depth** direction is always normal to the plane of the core window and is later referred to as the y-axis direction.

Figure 2.3 shows the cross section of the core and windings of a shell winding structure in greater detail. In this figure, there are three different types of windings illustrated. The innermost winding is made up of insulated round wire as shown in the upper detailed view of the winding. The center winding consists of insulated rectangular wire or insulated "strip conductor" as shown in the left-side detailed view; and the outermost winding is made of foil. The following definitions and features of this figure are of importance and

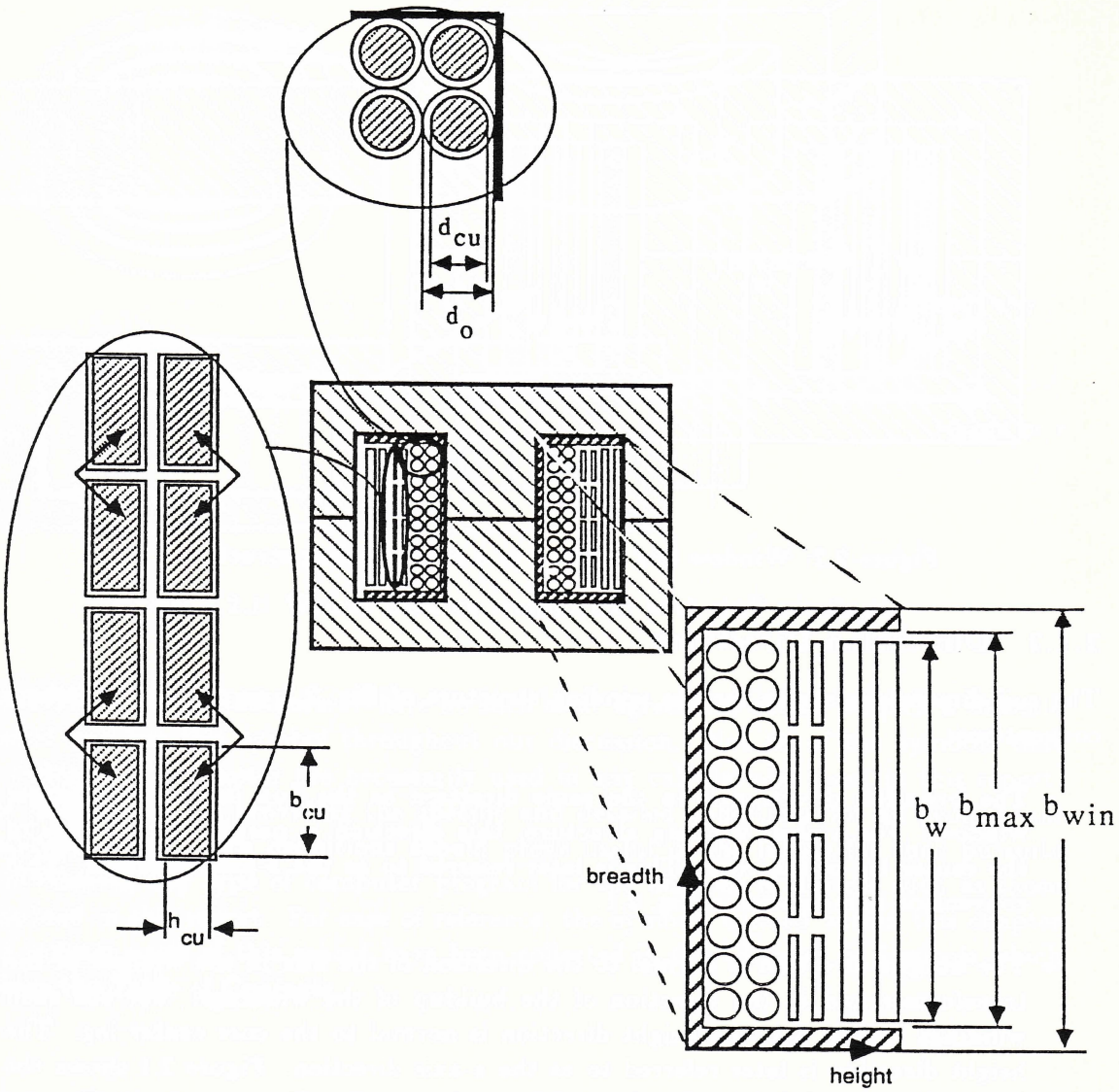


Figure 2.3: Detailed view of the cross-section of an EE-core transformer with shell windings. The innermost winding is made up of insulated round wire as shown in the upper detailed view of the winding. The center winding consists of insulated rectangular wire as shown in the left-side detailed view; and the outermost winding is made of foil.

should be clearly understood before proceeding to model the transformer for analysis purposes.

2.1.3 Definition of Winding Geometry Terms

Winding layer: A conductor or set of conductors that occupy the same window-height position is called a winding layer. This could also be stated as any set of conductors that are collinear in the direction of breadth.

Multi-conductor winding: Any winding that is wound so that more than one separately insulated but electrically paralleled conductor occupies the same window-height position is said to be a multiple-conductor winding. If the middle winding of the winding structure shown in Fig. 2.3, for example, were fabricated as a four-turn winding where two side-by-side conductors at the same window height were connected electrically in parallel, then this would be a two-conductor winding. This situation is indicated by the arrows in the left-side detailed view. The arrows point to electrically paralleled conductors. The term multi-conductor winding does not refer to Litz wire windings or to twisted-strand windings which are not considered in Part I of this report; these types of windings are discussed briefly in [2,11,12,20].

The following symbols are defined with respect to the drawing of Fig. 2.3:

b_{win} = the breadth of the core window itself.

b_{max} = the maximum breadth available in which to place a winding. This dimension is limited by a bobbin or a winding former or by the core itself. In the latter case, $b_{max} = b_{win}$.

b_w = the breadth of a winding layer. This is the actual physical extent of a winding layer including the insulation on the conductors. It cannot exceed the maximum available winding breadth b_{max} as shown in Fig. 2.3.

b_{cu} = the breadth of each of the copper conductors in a winding layer. For a foil conductor such as used in the outermost winding in Fig. 2.3 or a rectangular conductor such as used in the center winding, b_{cu} is simply the breadth of the conductive material in the foil or the rectangular wire. This does not include any insulation on the conductor. For round conductors, b_{cu} is computed by considering each round wire in the winding layer to be equivalent to a square conductor of equal cross-sectional area as discussed in detail later in connection with Fig. 2.5.

h_{cu} = The height of copper in a winding layer. For a foil conductor such as used in the outermost winding in Fig. 2.3 or a rectangular conductor such as used in the center winding, h_{cu} is the height of the conductive material in the foil or the rectangular wire. This does not include any insulation on the conductor. For round conductors, h_{cu} is computed by considering each round wire in the winding layer

to be equivalent to a square conductor of equal cross-sectional area as discussed in detail later in connection with Fig. 2.5.

d_o = the outside diameter of a round wire. This includes wire insulation.

d_{cu} = the diameter of the copper alone in a round wire.

ℓ_T = the length-of-turn of the layer. Often called the mean length-of-turn because it is calculated using the center of the layer in the x-direction, this value depends upon the actual shape of the windings of any particular transformer. Also, it is often assumed that the length-of-turn for each layer can be approximated by the length-of-turn for an entire winding or for an entire winding structure.

N_ℓ = the number of turns of winding wire in a winding layer. For a foil conductor winding, $N_\ell = 1$. For other winding types, N_ℓ is always the number of *turns* of the winding that have the same height coordinate.

N_c = the number of current-carrying conductors in a winding layer. The number of conductors in a layer may be the same as, or an integer multiple of the number of turns in a layer N_ℓ.

n_s = the number of electrically paralleled conductors in a multi-conductor winding.[1] In the cross-section shown in Fig. 2.3, the rectangular-conductor winding has two conductors per turn (i.e., $n_s = 2$). This is indicated by the connected arrows that point to the electrically paralleled conductors in the detailed view of the winding at the left of the figure. In terms of the above definitions, we can write $N_c = n_s N_\ell$. We assume throughout Part I of this report that the n_s electrically paralleled conductors each carry the same amount of current, i.e., they share the winding current equally.

There are other features of the windings yet to be defined, but for this we need another figure. Figure 2.4 shows a shell winding transformer with three windings. One winding is of foil conductors and consists of the inner three layers plus the sixth layer. A second winding consists of two layers of round wires, layers number four and five; and a third winding consists of the outermost layer of round wire. From Fig. 2.4, we can define the concepts of winding section, build, layer spacing, and section spacing.

Winding section: A winding section is any set of layers of a particular winding that are located next to each other with no layers of other windings separating them. If all the layers of a winding are physically next to each other then there is only one winding section for that winding. In Fig. 2.4 we see that the winding composed of foil layers has two winding sections, whereas each of the round-wire windings has only one section. The maximum number of winding sections a winding can have is equal to the number of layers in the winding.

[1] Multi-conductor windings are defined on page 15.

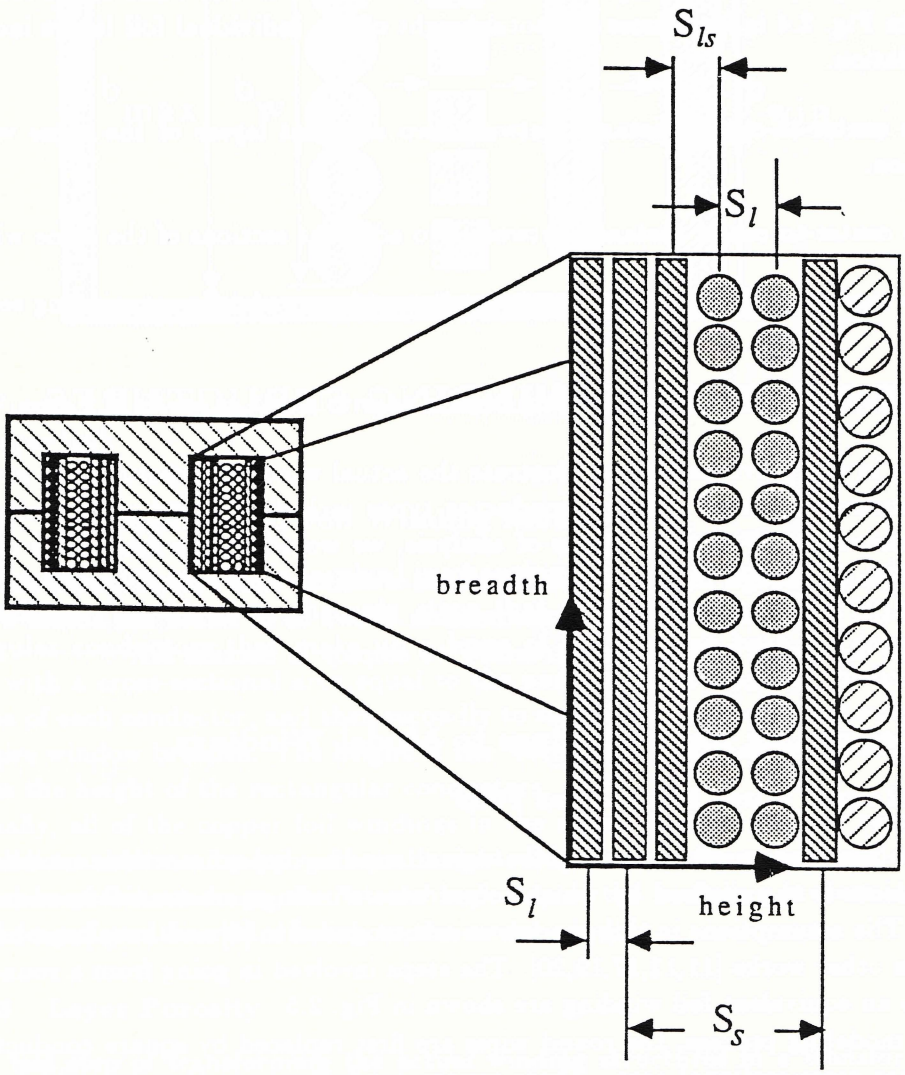


Figure 2.4: Detailed view of section and layer spacing in a three winding EE-core transformer with shell windings. One winding is of foil conductors and consists of the innermost three layers plus the sixth layer. A second winding consists of the fourth and fifth layers of round wire; a third winding consists of the outermost layer of round wire.

Build: The build of a winding is simply the total height—wire height plus wire insulation height—of all the layers of the winding. The sum of the builds of the different windings is limited by the core window height minus any allowance for a bobbin, insulating tape between layers or windings, shields, etc. The build of the foil winding in Fig. 2.4 is four times the total height of the individual foil layers including insulation.

S_ℓ = the center-to-center distance between two adjacent layers of the same winding section.

S_s = the center-to-center distance between two adjacent sections of the same winding.

$S_{\ell s}$ = the center-to-center spacing between adjacent layers of different winding sections.

2.2 GEOMETRICAL WINDING STRUCTURES

The figures in the previous section illustrate the actual winding structures for a variety of shell windings made of differing conductor types including round wire, rectangular and foil conductors. For the purpose of analysis, we would like to treat each of these winding types as though they are made up of foil windings that extend across the entire breadth of the core window. *This approximation allows us to relate the actual winding structure to the model transformer structure we employ in Section 3.1.*

2.2.1 Converting Real Windings to Model Windings

2.2.1.1 Round Wires Modeled as Foils

One key to the process of converting the actual winding types into their model winding equivalents is the method by which round wire windings are transformed into foil windings. The assumptions in this process were introduced in [6] and have been used extensively in other works [11,12,17,19,20]. The steps involved in going from a round-wire winding to an equivalent foil winding are shown in Fig. 2.5.

In the modeling process, the round wires are first replaced by square conductors of equal copper cross-sectional area. These square conductors are then brought together to form an equivalent foil winding with a height[2] equal to that of the square-wire height and a breadth equal to the number of conductors in the layer times the breadth of the equivalent square conductors. This foil winding, which does not extend the entire breadth of the core window, is then in effect "stretched" in the breadth direction and is replaced by a foil of equal height that does extend across the entire window breadth. This stretching increases the total area of the foil layer which must be compensated for in some fashion in the analysis process. This is discussed further below.

[2]Remember that winding *height* is defined in the direction of winding buildup.

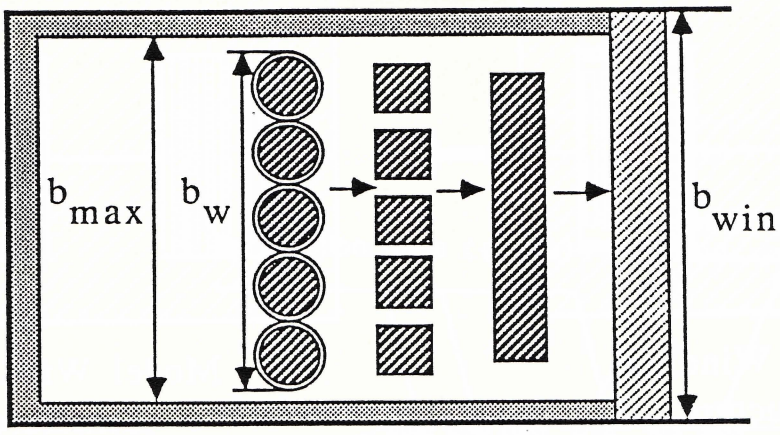


Figure 2.5: Steps in transforming a layer of a round-wire winding into a foil layer [19].

2.2.1.2 Rectangular and Foil Winding Models

A similar modeling process is involved in changing rectangular-conductor windings into foil windings. In this case, the only steps that are required are first to replace the rectangular conductors that make up a layer of the winding by a foil layer of equal height with a cross-sectional area equal to the number of rectangular conductors times the area of each conductor, and then secondly to stretch this foil so that it extends across the entire window breadth. The height of the "stretched" foil of copper conductor is the same as the height of the rectangular conductors.

Finally, all of the copper foil windings in the actual transformer are represented in the model transformer by foils of equal height which extend the entire window breadth. In the case of foil windings, the "stretching" step of the modeling process is all that is needed to go from the real winding to the model winding.

2.2.1.3 Layer Porosity

In the last step of transforming the actual winding structures in a transformer to foil windings (that is, when we "stretch" the equivalent foil winding so that it crosses the *entire window breadth*), we are in effect increasing the cross-sectional area of each of the layers in the winding. In order for this transformation to be valid, there must be some compensating factor introduced which will insure that the dc resistance of the model winding is the same as the dc resistance of the original winding that it replaces.

Since, for any conductor with a given conductivity σ, copper cross-sectional area A_{cu} and length ℓ the resistance R is given as

$$R = \frac{\ell}{\sigma A_{cu}} \tag{2.1}$$

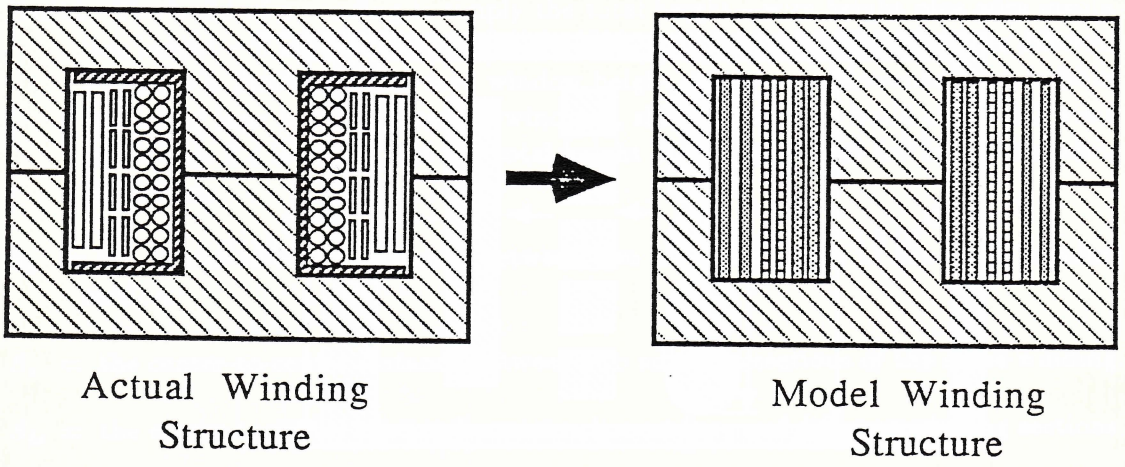


Figure 2.6: Modeling a real winding structure as a set of stretched foil windings that extend across the entire core-window breadth.

we can compensate for the increase in cross-sectional area by dividing this relationship by a factor which will offset the increase. That is, since resistance is inversely proportional to both conductivity and cross-sectional area, we can offset an increase in area by decreasing the conductivity by a corresponding amount. This multiplicative factor is called the *layer porosity* η. The layer porosity is simply the percentage of the total core-window breadth b_{win} that is occupied by conductive material in any winding layer. The value of η is always positive and less than unity. Using this compensating factor we can rewrite (2.1) as

$$R = \frac{\ell}{\eta \sigma A} \tag{2.2}$$

where A is the effective cross sectional area of the stretched foil. A general value of conductivity σ is used in the fields analysis of Chapter 4, but the significant resultant equations are recast in terms of the effective conductivity $\sigma_{eff} = \eta\sigma$ in Section 4.6.

The transformers shown in Fig. 2.6 illustrate how a practical winding structure that contains different kinds of windings is modeled by a transformer with porous-foil windings stretched across the full breadth of the core window. Figure 2.7 shows this type of geometric model in greater detail for a three-winding seven-layer transformer. The parameters shown in the geometric model of the transformer in Fig. 2.7 are defined as follows:

h_{cu} = height of a winding layer modeled as a foil winding. For rectangular and foil windings this is exactly the same as the height of the conductive material in the conductor. In round-wire windings, this is the height of the equal-area square conductors. For a round conductor with a diameter of copper d_{cu} this height is

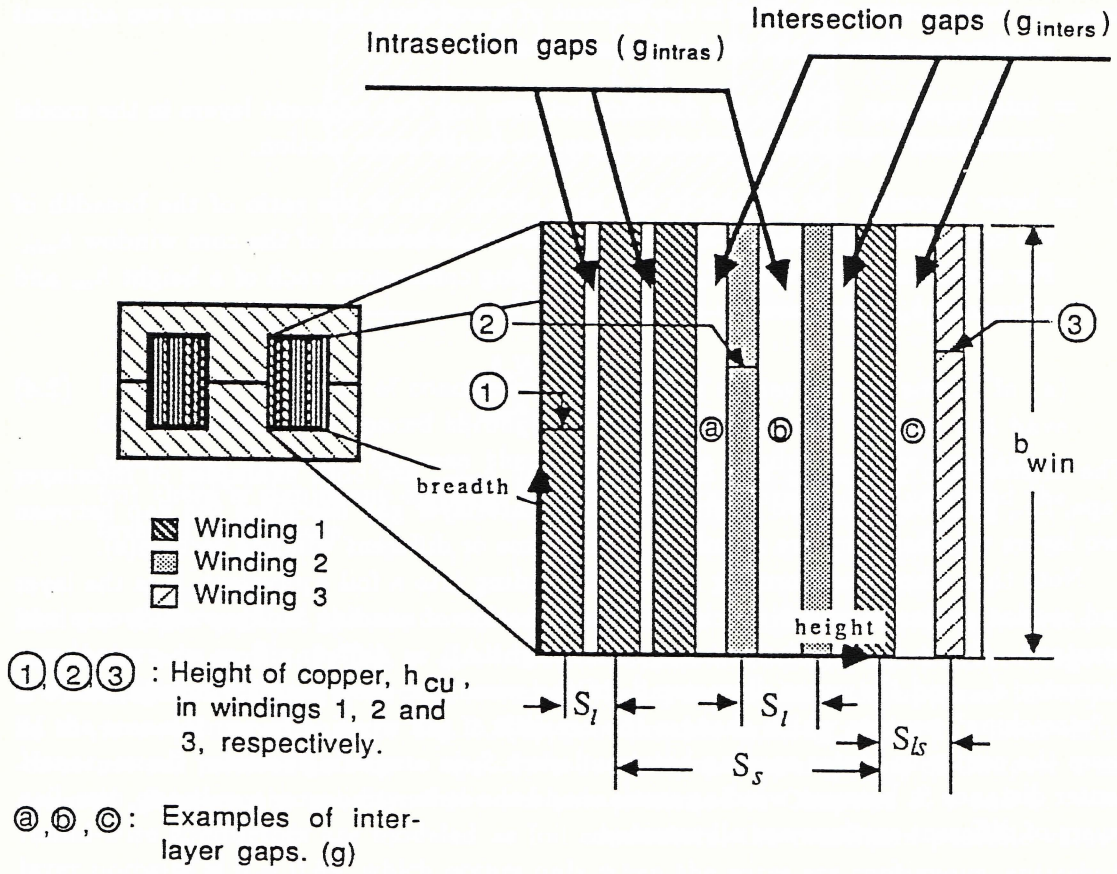


Figure 2.7: Detailed view of the structure of a transformer modeled as a set of foil windings that extend across the entire core-window breadth.

given by

$$h_{cu} = \sqrt{\frac{\pi}{4}}\, d_{cu} \tag{2.3}$$

g_{intras} = intrasection layer gap. This is the distance between adjacent layers of a winding section after the transformer has been modeled as a set of foil windings.

g_{inters} = intersection gap. This is the amount of space there is between any two adjacent winding sections in the model transformer.

g = interlayer gap. This is the distance between any two adjacent layers in the model transformer regardless of whether they are in the same section.

η = layer porosity. As defined in the text above, this is the ratio of the breadth of the conductive material in a winding layer to the breadth of the core window b_{win}. For a winding layer with N_c current-carrying conductors each of a height h_{cu} and a breadth b_{cu}, the porosity η is given by

$$\eta = \frac{N_c b_{cu}}{b_{win}} \tag{2.4}$$

The intersection gap g_{inters} and intrasection gap g_{intras} are both examples of interlayer gaps, i.e., gaps between two layers. The term interlayer gap describes the gap between two layers whether they are members of the same or different winding section(s).

Note that when transforming an actual winding into a foil equivalent, it is the layer and section center-to-center spacings in the direction of winding buildup which are held constant. For a round-wire winding, the height h_{cu} is different from the conductor diameter d_{cu} and the outer diameter d_o of the wire. For all types of windings, there is a "stretching" process which changes the breadth of the winding layer. However, in all cases the center-to-center spacing between layers S_ℓ in a winding section, the center-to-center distance S_s between winding sections and the center-to-center spacing $S_{\ell s}$ between layers of different sections are all retained.

2.2.2 Admonitions Concerning the Use of Layer Porosity η

Although the concept of layer porosity[3] is generally accepted in the reviewed literature [6,11,12,20], the reader should be warned that the indiscriminate use of layer porosity can lead to erroneous results. The analyses performed here and in [6] are "reliable" only for values of η which are not "too small" [17, pages 322,323]. A cornerstone of the analysis presented in Chapters 3, 4 and 5 is that the flux in the core window is parallel to the winding layers across the entire breadth of the core window as shown in Fig. 2.2. When discrete conductors constitute the winding layers, the validity of the assumption of parallel flux depends largely on the value of η. When conductors in a layer

[3]Layer porosity is also referred to as layer space factor and horizontal porosity in the literature reviewed in Part II.

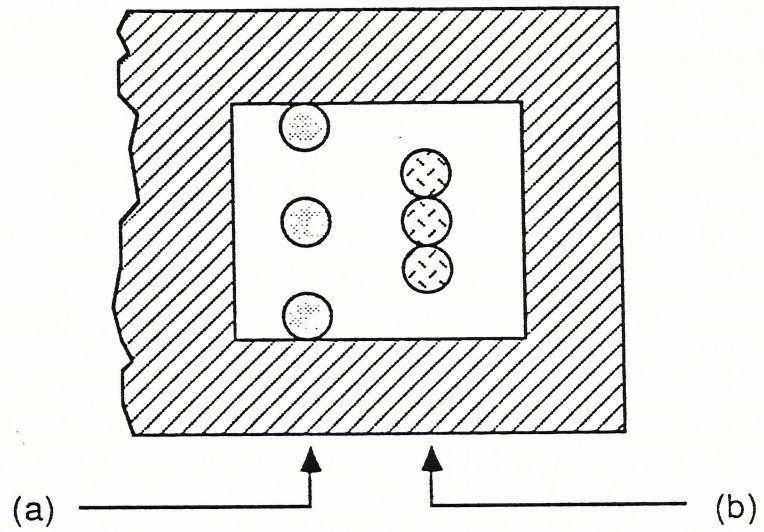


Figure 2.8: Example of conductor layers where η may be too small. In (a) the conductors are spaced throughout the breadth of the window but have significant distances between them. In (b) the conductors are contiguous but there is significant distance between the transformer-core yolk and the layer of conductors.

are spread throughout the window breadth and have significant distances between the conductors, as in Fig. 2.8(a), or if all the conductors in the layer are bunched together with significant distance between the ends of the layer and either the upper or lower yoke of the transformer core, as in Fig. 2.8(b), considerable bending of the flux lines occurs. Hence, small values of η negate one of the fundamental assumptions of Chapter 3 and call into question the validity of the analysis presented in Chapters 3, 4 and 5. When round-wire conductors are modeled as foil conductors, the maximum possible value of layer porosity is $\eta = 0.89$, which occurs only when the wires are contiguous, entirely fill the core-window breadth b_{win} and have negligible insulation.

2.3 DIFFERENT COMPONENTS OF LEAKAGE FLUX

Throughout Parts I and II of this report, we discuss the effects of leakage flux on transformer windings and how to predict these effects. The use of the term *leakage flux* may lead to some confusion since leakage flux in transformers can be considered to be made up of two components, only one of which is covered in this report and in the literature reviewed in Part II. In a transformer, leakage flux arises because of the following:

1. The effective permeability of the transformer core is low, i.e., not much greater than that of free space ($\mu \not\gg \mu_0$). This occurs when a core has substantial intentional or

unintentional air gaps, or when the core material has a low intrinsic permeability as do some ferrites.

2. The winding height h_{cu} of the transformer windings and the heights of the interlayer gaps between windings and within each winding are of nonzero value.

Since core materials with infinite permeability and winding layers of zero height do not exist in nature, both of these components of leakage flux occur, to some degree, in any physical transformer; however, often one or the other component can be considered negligible depending upon the transformer design and application.

Figure 2.9(a) shows the right half of a transformer where the permeability μ of the core is low and the winding and interlayer-gap heights are nonzero, so both components of leakage flux are present in the winding space. To examine the two separate causes of leakage flux, we modify Fig. 2.9(a) appropriately to produce Fig. 2.9(b) and (d). In Fig. 2.9(b), we examine the condition in item 1 and retain the same permeability for the core material as in (a), but shrink the winding heights so that $h_{cu} = 0$ for both primary and secondary. In Fig. 2.9(d), we examine the condition in item 2 and retain the same winding heights as in (a) but assume an ideal core material with $\mu = \infty$ and zero coercive force.

If we examine Fig. 2.9(b) more carefully, we note the points A and E located in the top and bottom core yolks, respectively, points B and D located in the inner and outer legs of the core, respectively, and point C in the center of the interlayer gap. Magnetic flux ϕ which flows through the center leg of the transformer—path (EBA)—can flow both through path (ADE) in the outer leg of the core and through path (ACE), the air in the transformer window. The amount of flux which flows in each path is dependent upon the relative reluctance values of paths (ADE) and (ACE).

Viewing the transformer as a lumped magnetic circuit as is shown in Fig. 2.9(c), we note that the reluctance $\mathcal{R}$ of a magnetic flux path is

$$\mathcal{R} = \frac{\ell}{\mu A} \tag{2.5}$$

where ℓ is the magnetic path length and A is the cross-sectional area of the magnetic path. In addition, we can describe the magnetic circuit in terms of its magnetomotive force $\mathcal{F}$, the flux in the center leg of the core $\phi_{(EBA)}$, and $\mathcal{R}_{(EBA)}$, $\mathcal{R}_{(ACE)}$ and $\mathcal{R}_{(ADE)}$ the reluctances of the various flux paths marked in Fig. 2.9(b). Viewing flux as the analog of current, mmf as the analog of voltage, reluctance as the analog of resistance and assuming that the inner winding is excited and the outer winding is open-circuited, the flux $\phi_{(EBA)}$ encounters the reluctance $\mathcal{R}_{(EBA)}$ in series with the parallel paths $\mathcal{R}_{(ACE)}$ and $\mathcal{R}_{(ADE)}$. Thus, we can write the magnetic analog of Ohm's law for the transformer.

$$\mathcal{F} = N_1 i_1 = \phi_{(EBA)} \left(\mathcal{R}_{(EBA)} + \frac{\mathcal{R}_{(ACE)} \mathcal{R}_{(ADE)}}{\mathcal{R}_{(ACE)} + \mathcal{R}_{(ADE)}} \right) \tag{2.6}$$

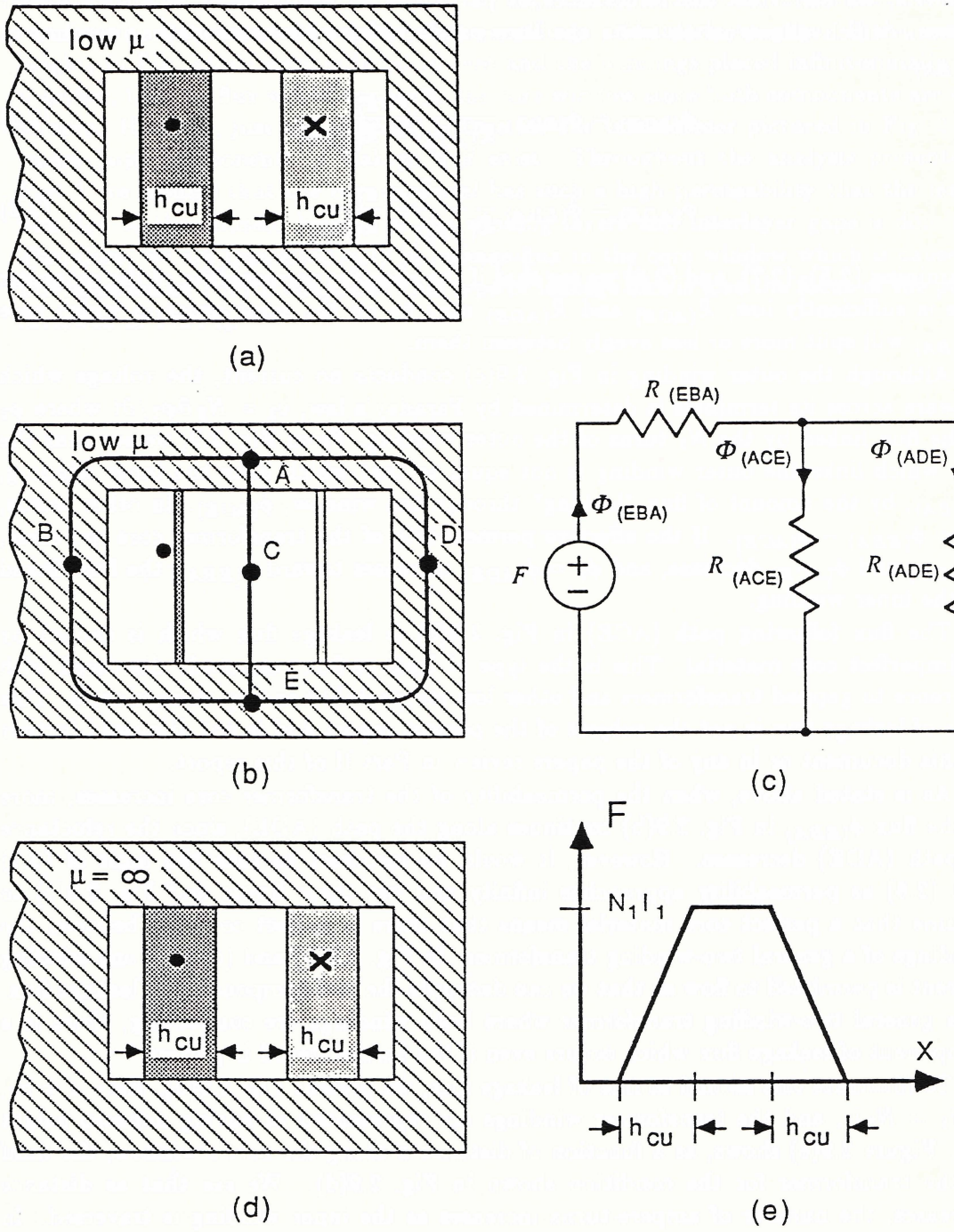


Figure 2.9: Leakage flux in a transformer is due to $\mu \neq \infty$ *and* $h_{cu} \neq 0$. Part (a) shows such a transformer. In (b), $h_{cu} = 0$ but $\mu \not\gg \mu_0$ and the reluctance of flux path (ACE) is on the same order of magnitude as that of path (ADE). (c) shows the magnetic equivalent circuit for the core of (b) when the inner winding is excited. In (d), $h_{cu} \neq 0$ and $\mu = \infty$; leakage flux is due to the variation of mmf shown in (e).

Likewise, we can view the reluctances of paths (ACE) and (ADE) as a flux-divider network which allows us to write the fluxes associated with those paths in terms of $\phi_{(EBA)}$

$$\phi_{(ACE)} = \phi_{(EBA)} \frac{\mathcal{R}_{(ADE)}}{\mathcal{R}_{(ACE)} + \mathcal{R}_{(ADE)}} \tag{2.7}$$

$$\phi_{(ADE)} = \phi_{(EBA)} \frac{\mathcal{R}_{(ACE)}}{\mathcal{R}_{(ACE)} + \mathcal{R}_{(ADE)}} \tag{2.8}$$

Examining (2.5), (2.7), and (2.8) we see that if the effective permeability of the magnetic core is sufficiently low, $\mathcal{R}_{(ACE)}$ and $\mathcal{R}_{(ADE)}$ may be on the same order in which case $\phi_{(EBA)}$ will split more or less evenly between them.

Although the outer winding in Fig. 2.9(c) conducts no current, the voltage which appears across its terminals is determined by Faraday's law, $v_2 = N_2 \partial\phi_2/\partial t$ where ϕ_2 is the flux linked by the N_2 turns of the outer winding. From Fig. 2.9, we see that the flux which links the outer winding is not equal to that which links the inner winding, $\phi_{(EBA)}$, by the amount of flux "leaking" through the window, $\phi_{(ACE)}$. In other words, $\phi_2 = \phi_{(EBA)} - \phi_{(ACE)}$. If the effective permeability of the transformer core increases, $\mathcal{R}_{(ADE)}$ and $\phi_{(ACE)}$ decrease, and $\phi_2 = \phi_{(ADE)}$ increases toward $\phi_{(EBA)}$, the flux linked by the inner winding.

The flux following path (ACE) in Fig. 2.9(b) is leakage flux which is caused by an imperfect core material. This is the type of leakage flux commonly discussed with reference to gapped transformers and other low-permeability energy-storage cores. This type of leakage flux is *not* the subject of the present report and is not discussed further in this document or in any of the papers review in Part II of this report.

As is stated above, when the permeability of the transformer core increases, more of the flux $\phi_{(EBA)}$ in Fig. 2.9(b) continues along the path (ADE), since the reluctance of path (ADE) decreases. However, it would be incorrect to take the limit of (2.7) and (2.8) as permeability approaches infinity and use these limits and Fig. 2.9(c) to assume that a perfect core material means that there is perfect coupling between the windings of a general two-winding transformer. In Fig. 2.9(b) and (c) only one winding current is permitted to flow so that we can decouple the two components of leakage flux. In a general two-winding transformer where both windings are conducting, there is a component of leakage flux which occurs even if the core material is perfect.

To illustrate this second source of leakage flux, we present Fig. 2.9(d). Here $\mu = \infty$, $N_1 I_1 = N_2 I_2$, and the transformer windings are represented as having nonzero height h_{cu}. Figure 2.9(e) shows, as a function of distance x along the core's window, the mmf of the transformer for the condition shown in Fig. 2.9(d). We see that as distance increases, the number of ampere-turns increases as the inner winding is traversed. In the interlayer gap, the magnetomotive force $\mathcal{F}$ remains constant and then decreases as the outer winding is traversed. Field-intensity or mmf diagrams such as that shown in Fig. 2.9(e) are discussed in detail in Section 3.1.2, but for now it is sufficient to note that since flux is proportional to mmf, the leakage flux in the winding space varies with

distance in the same fashion as does $\mathcal{F}$ in Fig. 2.9(e), and is due to the current in the windings and the nonzero heights of the windings and interlayer gaps. If the winding heights in Fig. 2.9(d) were reduced to zero and the windings placed infinitesimally close together, then no flux would appear in the core window since both components are equal to zero. However, just the opposite is true for the transformer pictured in Fig. 2.9(a), where both components of leakage flux exist. Throughout the analysis presented in Part I we assume that the core material has such a high permeability that the leakage flux due to the nonzero heights of the winding layers and interlayer gaps is dominant. Therefore, we are interested only in leakage flux in the core window which is caused by the variation of $\mathcal{F}$ with distance. This type of leakage flux is also the focus of the papers reviewed in Part II.

This page has been left blank intentionally.

Chapter 3

Magnetic-Field Distribution in the Winding Space of a Transformer

The leakage impedance between each pair of windings is important information for modeling high-frequency effects in a transformer. The resistive part of the leakage impedance arises from the resistivity of the conducting material and the uneven distribution of current in the conductors at high frequency. The inductive part exists because part of the magnetic flux generated by a current in any one winding fails to link with all the turns of both windings. In the following discussion, the infinite-solenoid model is introduced as a way of representing the essential structure of a multiwinding transformer. Because the magnetic-field distribution in such a solenoid is similar to that in a shell-winding transformer wound on a relatively high-permeability core, an understanding of the leakage-flux pattern in an actual transformer may be gained by examining the leakage flux in a multilayer infinite solenoid.

It is shown in Chapter 5 how the two components of leakage impedance, ac winding resistance and leakage inductance, are calculated from the power dissipated and the magnetic energy stored in the windings of a transformer. In Section 4.5, equations are derived by which values for power dissipation and energy storage can be calculated from the spatial distribution of magnetic field intensity in the volume occupied by the transformer windings. That magnetic-field-intensity distribution is derived for the air-and-insulation spaces between winding layers in this chapter, and for the interior of each winding layer in Chapter 4. Also in this chapter, the basic principles that govern the behavior of the magnetic field in the transformer winding space are explained.

In Section 3.1 below, it is shown how a hypothetical infinite solenoid carrying dc current is used to predict the frequency-*independent* magnetic-field distribution between the winding layers of a real transformer. That distribution depends only on the net current flowing in each winding, not how the current is distributed within each winding layer. Section 3.2 contains a qualitative discussion of eddy-current effects, which cause a

frequency-*dependent* redistribution of magnetic field intensity and current density inside each winding layer. Finally, Section 3.3 shows how an infinite current sheet is used to model each winding layer to solve for the magnetic-field-intensity distribution inside each layer as a function of frequency. The magnetic-field-intensity distribution and the associated current-density distribution in an infinite current sheet are derived in the next chapter. Here and throughout Part I of the report, all time-varying currents and fields are assumed to be sinusoidal.

3.1 INFINITE-SOLENOID MODEL OF A TRANSFORMER

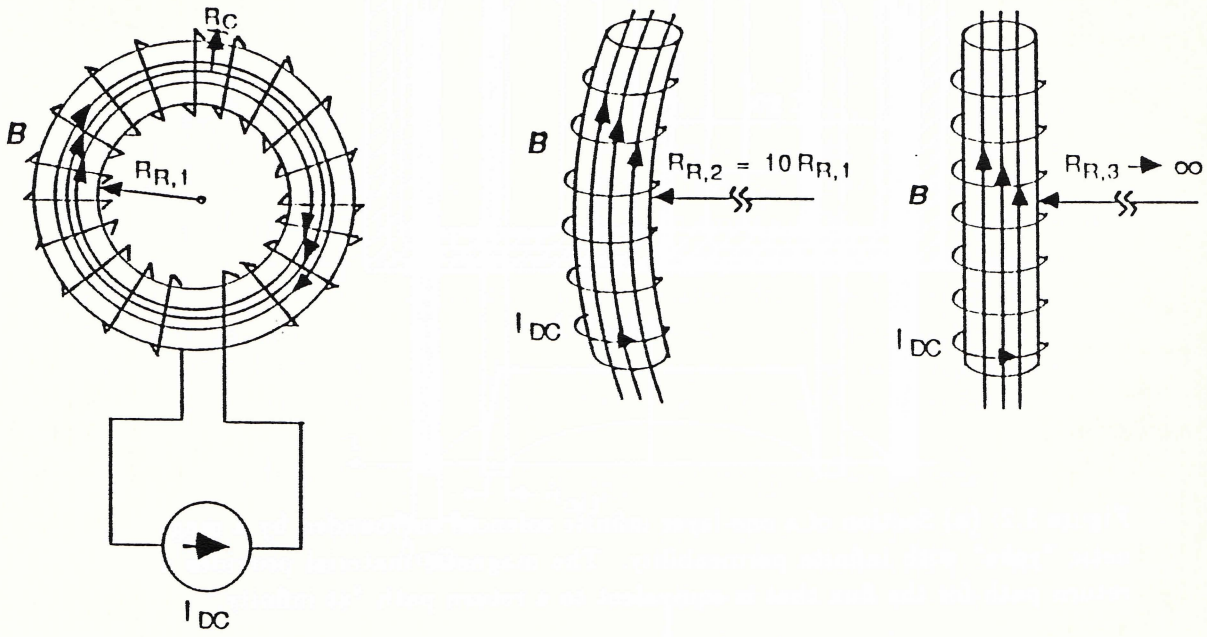
To simplify the problem of calculating the fields present in the winding space of a real transformer, it is shown in Section 2.2.1 how actual winding layers are modeled as foil layers that extend the entire breadth of the core window. Here, it is asserted that the leakage-flux pattern in and between those model winding layers, *when surrounded by a pot core of infinite permeability*, is exactly the same as the flux pattern present in a slice of a hypothetical infinite solenoid. An *infinite solenoid* is defined as a *tightly* wound torus with a finite circular cross section and a ring radius that approaches infinity, illustrated in Fig. 3.1. A *loosely* wound torus is shown instead in the figure to avoid obscuring the flux lines, which never leave the inside of the torus.

The magnetic flux in the infinitely long solenoid of Fig. 3.1(c) is said to follow a return path "at infinity." If a finite section of such a single-layer infinite solenoid is enclosed in infinitely permeable magnetic material as shown in Fig. 3.2, the leakage flux in the winding space is unchanged. The reason is that the axially directed flux of the infinite solenoid already satisfies the boundary condition required by Maxwell's equations, that is, the flux must be perpendicular to the surface of the ideal magnetic material where it enters the material. Essentially, the ideal magnetic material provides a return path for the flux that is equivalent to the path "at infinity" in Fig. 3.1(c).

With a magnetic yoke of less than infinite permeability, the leakage-flux pattern is close to that in an infinite solenoid as long as the component of the primary current that excites the core is small with respect to the component that supplies the loads. This condition is used as the definition of "high" permeability.

The structure of the model pot-core transformer in Fig. 3.3(b) is basically the same as that of Fig. 3.2. The only differences are multiple conducting layers, addressed in Section 3.1.2.2 below, and a center leg of the core. Although adding the center leg substantially increases the permeance of the core by eliminating a large air gap, it does not affect the distribution of the leakage flux in the winding space outside of the center leg.[1] If the transformer being modeled has an EE core of high permeability instead of a pot core, the infinite-solenoid model is less accurate, but it is shown in Chapter 6 that

[1]This leakage flux is due to the second cause discussed in Section 2.3, namely, layer current distributed over the finite height of the conductor.



(a) (b) (c)

Figure 3.1: Steps of the limiting process which defines the term *infinite solenoid*. (a) A toroidal solenoid of ring radius $R_{R,1}$, which may or may not have a core present. A current I_{DC} flowing in the solenoid produces a magnetic field intensity B inside the torus. (b) If the ring radius is increased by a factor of ten, but the current in the winding and the number of turns per meter along the solenoid remain constant, the same magnetic field intensity B is produced inside the solenoid. (c) As the ring radius approaches infinity, the device approaches an infinite solenoid.

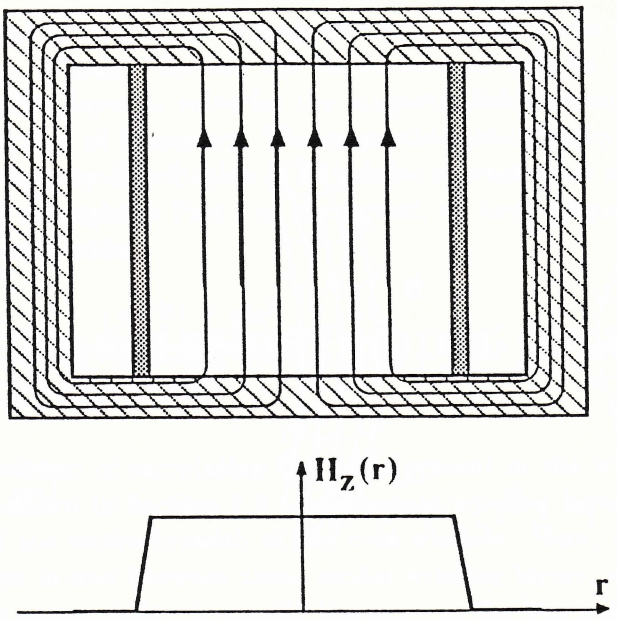


Figure 3.2: (a) Section of a one-layer infinite solenoid surrounded by a magnetic "yoke" with infinite permeability. The magnetic material provides a return path for the flux that is equivalent to a return path "at infinity."

the model still gives good results.

As seen in this discussion, the multilayer infinite solenoid in Fig. 3.3(a) may be analyzed to determine the magnetic-field distribution in the winding space of the transformer model in Fig. 3.3(b), which has equivalent-foil windings surrounded by a high-permeability magnetic core. The value of the magnetic field outside an infinite solenoid, the starting point of any analysis, is established in Section 3.1.1. Then dc field distributions are analyzed in Section 3.1.2, followed by a brief discussion of ac field distributions in Section 3.1.3.

3.1.1 The Magnetic Field Outside an Infinite Solenoid

In the infinite solenoid of Fig. 3.1(c), all of the magnetic flux generated by current flowing in the solenoid remains inside the torus, which implies that the magnetic field is zero everywhere outside the infinite solenoid regardless of the current flowing. For this statement to be true, is must be assumed that no externally generated magnetic fields are present. Another necessary assumption is that the component of the current along the axis of the solenoid is negligible, which requires that the solenoid be tightly wound. Both of these assumptions are made throughout this report.

The fact that the magnetic field is zero everywhere outside an infinite solenoid can also be proven rigorously from the Biot-Savart law, which gives the magnetic field produced at any point in space by a differential current element at another point in space. By

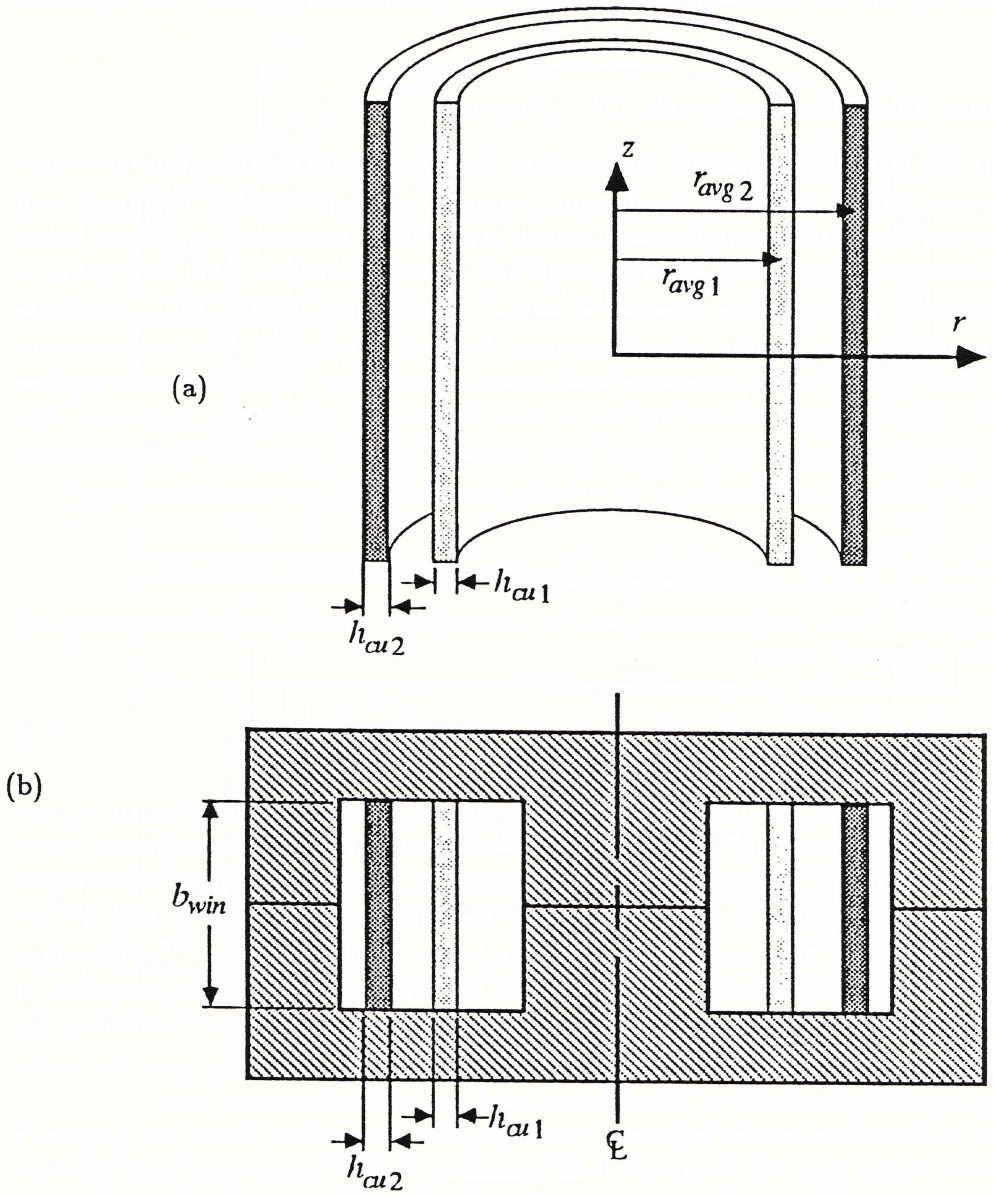


Figure 3.3: (a) Section of a two-layer infinite solenoid. (b) Pot-core transformer model containing the infinite-solenoid section in Part (a). The transformer model has winding layers of height h_{cu1} and h_{cu2} and breadth b_{win} as indicated.

integrating over a finite-length cylinder of current, and letting the length of the cylinder approach infinity, the net magnetic field at any point outside the cylinder can be shown to be zero.

3.1.2 Field Distribution with DC Current

It is stated in the introduction of this chapter that the magnetic field intensity everywhere in a transformer, except inside the conducting material, is independent of frequency and depends only on the net current flowing in each layer. This statement is proven below using Ampere's law. This fact, together with the earlier deduction that the fields in an infinite solenoid approximate those in an actual transformer, implies that an infinite solenoid with *dc* currents flowing in its layers may be used to calculate the instantaneous *ac* magnetic field present in the interlayer spaces of a transformer. Such a dc analysis does not, however, give accurate results for the ac field inside the conducting material. The analysis is carried out below for a single-layer air-core infinite solenoid, then extended to a two-layer solenoid, and finally to an infinite solenoid that has a magnetic core.

3.1.2.1 Ampere's Law Applied to a Single-Layer Infinite Solenoid

Having established that the magnetic field is always zero outside an infinite solenoid, Ampere's law for static fields

$$\oint_{l(S)} \mathbf{H} \bullet \mathbf{dl} = \iint_{S(l)} \mathbf{J} \bullet \mathbf{dS} \tag{3.1}$$

may be used to calculate the magnetic field distribution inside an infinite solenoid carrying dc current as shown in Fig. 3.4. The integration path $l(S)$ is the closed curve or loop l which bounds a surface S, while the surface of integration $S(l)$ is a surface S bounded by the closed curve l. The directions of the differential vectors **dl** and **dS** are chosen to be consistent with each other according to the right-hand rule. The direction of the differential-length element **dl** is chosen to be "clockwise," and the direction of the differential-surface-element vector **dS** is chosen to be "into the paper" as shown for loop l_1. The dots and the crosses in the current-conducting foil indicate that current is flowing into the right-hand side of the solenoid and out of the left-hand side.

By using the pictured series of closed curves as the integration paths for Ampere's law, it is shown below that the magnetic field is uniform inside the solenoid and directed vertically in what is defined as the positive z-direction. In addition, it is shown that the field changes linearly with the radius r across the height of the conducting layer.

First the following conditions are established to simplify the problem:

1. Only dc current flows in the solenoid, for which the current density in the conducting layer is uniform. Uniform current density is also a very good approximation whenever the excitation current is varying slowly.

2. There are no externally generated magnetic fields present.

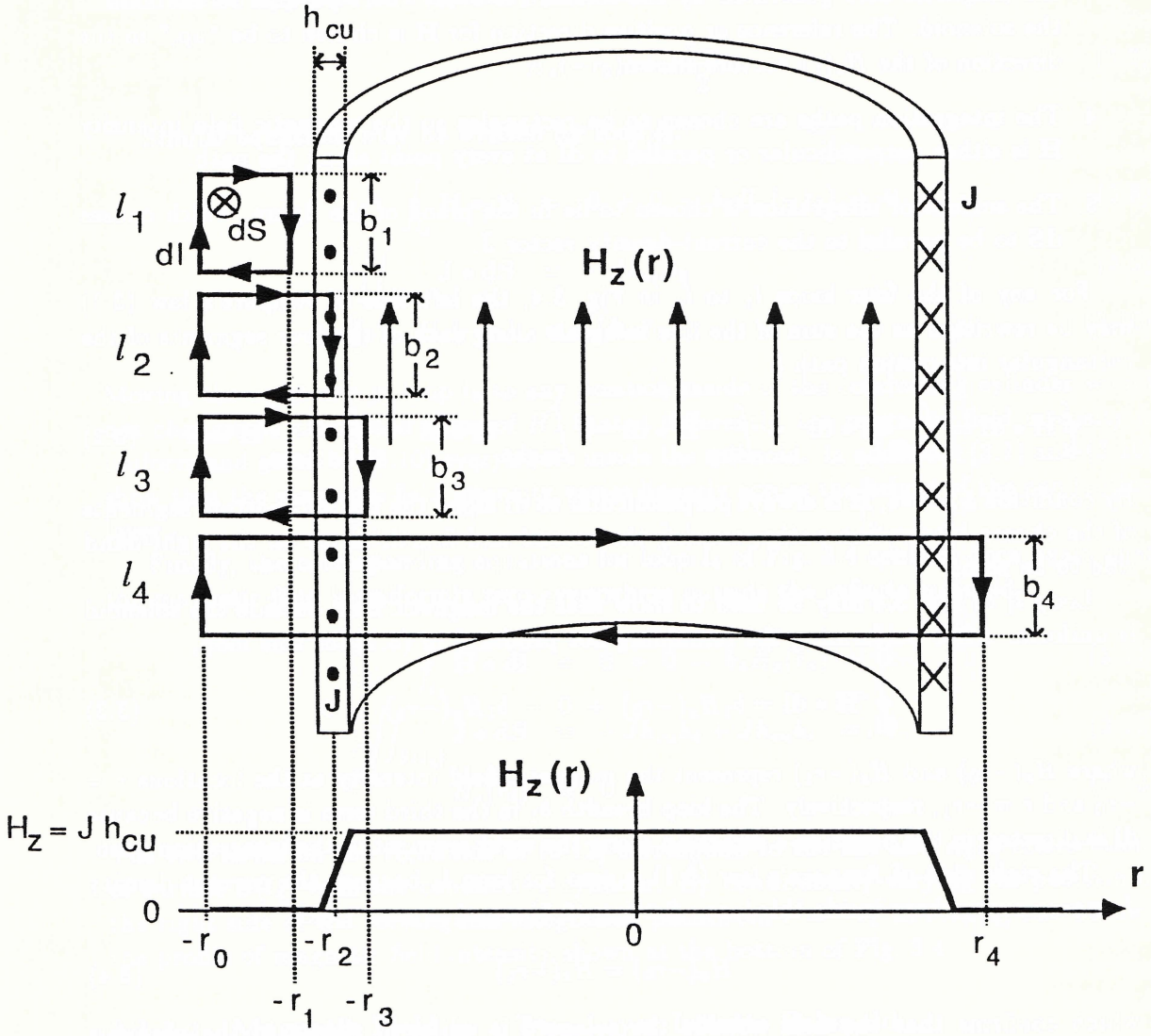


Figure 3.4: Integration paths used with Ampere's law to calculate the magnetic field intensity $H_z(r)$ in an infinitely long solenoid conducting at a uniform current density J.

3. The infinite length of the solenoid and its uniformity in the z-direction dictate that the magnetic field generated by the solenoid is everywhere parallel to the axis of the solenoid. The reference or positive direction for $\mathbf{H}$ is chosen to be "up," in the direction of the $H_z(r)$ vectors shown.

4. The integration paths are chosen to be rectangles so the magnetic field intensity $\mathbf{H}$ is either perpendicular or parallel to $\mathbf{dl}$ at every point along the path.

5. The surface of integration is chosen to lie in the plane of the figure, which causes $\mathbf{dS}$ to be parallel to the current-density vector $\mathbf{J}$.

For any of the four loops l_1 to l_4 in Fig. 3.4, the left side of Ampere's law (3.1) may be rewritten as the sum of the line integrals along each of the four segments of the rectangular integration path l.

$$\oint_l \mathbf{H} \bullet \mathbf{dl} = \int_{\text{left}} \mathbf{H} \bullet \mathbf{dl} + \int_{\text{top}} \mathbf{H} \bullet \mathbf{dl} + \int_{\text{right}} \mathbf{H} \bullet \mathbf{dl} + \int_{\text{bottom}} \mathbf{H} \bullet \mathbf{dl} \qquad (3.2)$$

By condition 3 above, $\mathbf{H}$ is always perpendicular to $\mathbf{dl}$ along the top and bottom segments of the chosen integration paths, causing the second and fourth terms on the right-hand side to be zero.

Loop l_1 of Fig. 3.4 may be used to show that the magnetic field outside the solenoid is uniform. After performing the remaining dot products in (3.2) for this loop,

$$\oint_{l_1} \mathbf{H} \bullet \mathbf{dl} = b_1 H_z(-r_0) + 0 - b_1 H_z(-r_1) + 0 \qquad (3.3)$$

where $H_z(-r_0)$ and $H_z(-r_1)$ represent the magnetic field intensity at the locations $r = -r_0$ and $r = -r_1$, respectively. The loop breadth b_1 in the third term is negative because $\mathbf{dl}$ is directed in the negative-z direction along the right segment of the integration path.

The right side of Ampere's law (3.1) is zero for loop l_1 because the current density J is zero everywhere inside this loop. Setting (3.3) equal to zero yields

$$H_z(-r_0) = H_z(-r_1) \qquad (3.4)$$

which confirms that the field outside the solenoid is uniform, shown in the previous section to be zero.

For loop l_2 in Fig. 3.4, where $r = r_2$ is the midpoint of the conducting layer of height h_{cu}, the left side of Ampere's law may be written from (3.2) as

$$\oint_{l_2} \mathbf{H} \bullet \mathbf{dl} = 0 + 0 - b_2 H_z(-r_2) + 0 \qquad (3.5)$$

which makes use of the fact that $H_z(-r_0) = 0$. With r_2 exactly at the center of the conducting layer, the corresponding right side of Ampere's law (3.1) is

$$\iint_{S(l_2)} \mathbf{J} \bullet \mathbf{dS} = -J \frac{h_{cu}}{2} b_2 \qquad (3.6)$$

where J is the dc value of the current-density vector $\mathbf{J}$. The negative sign occurs because $\mathbf{J}$ is directed opposite $\mathbf{dS}$. Equating (3.5) and (3.6)

$$H_z(-r_2) = J\frac{h_{cu}}{2} \tag{3.7}$$

Similar equations may be written for loop l_3.

$$\oint_{l_3} \mathbf{H} \bullet \mathbf{dl} = 0 + 0 - b_3 H_z(-r_3) + 0 \tag{3.8}$$

$$\iint_{S(l_3)} \mathbf{J} \bullet \mathbf{dS} = -J h_{cu} b_3 \tag{3.9}$$

$$H_z(-r_3) = J h_{cu} \tag{3.10}$$

Moving the right side of loop l_3 to any position inside of the conducting cylinder would not change the calculated value of H. Stated differently, the magnetic field intensity is uniform and given by (3.10) everywhere inside the solenoid. In addition, (3.7) and (3.10) show that the magnetic field intensity varies linearly across the height of the conducting layer.

Finally, the corresponding equations for loop l_4 of Fig. 3.4 confirm once again that the magnetic field is uniformly zero everywhere outside the infinite solenoid.

$$\oint_{l_4} \mathbf{H} \bullet \mathbf{dl} = 0 + 0 - b_4 H_z(r_4) + 0 \tag{3.11}$$

$$\iint_{S(l_4)} \mathbf{J} \bullet \mathbf{dS} = -J h_{cu} b_4 + J h_{cu} b_4 = 0 \tag{3.12}$$

$$H_z(r_4) = 0 \tag{3.13}$$

The two terms on the right side of (3.12) correspond to the left and right intersections of surface $S(l_4)$ with the conducting cylinder. By continuously varying the position of the right side of the rectangular integration path from $r = -r_1$ to $r = r_4$, one obtains the profile of magnetic field intensity shown at the bottom of Fig. 3.4.

3.1.2.2 Magnetic Field in a Two-Layer Infinite Solenoid

Figure 3.5 shows a solenoid which has two concentric and infinitely long layers with layer heights h_{cu1} and h_{cu2} and average radii r_{avg_1} and r_{avg_2} respectively. These radii are different from the "ring" radii in Fig. 3.1, which approach infinity for any infinite solenoid. The inner layer of the solenoid in Fig. 3.5 is called layer 1 and is wound with n_1 turns of rectangular conductor per meter of the solenoid in the z-direction. The outer layer is wound with n_2 turns of square conductor per meter of the solenoid in the z-direction. For convenience of discussion for the remainder of this illustration, n_2 is chosen to be twice n_1. The layers are shaded differently to emphasize that they are not necessarily two layers of a single winding. Rather, each layer is considered to be a separate element that can carry current in either direction independent of the current in

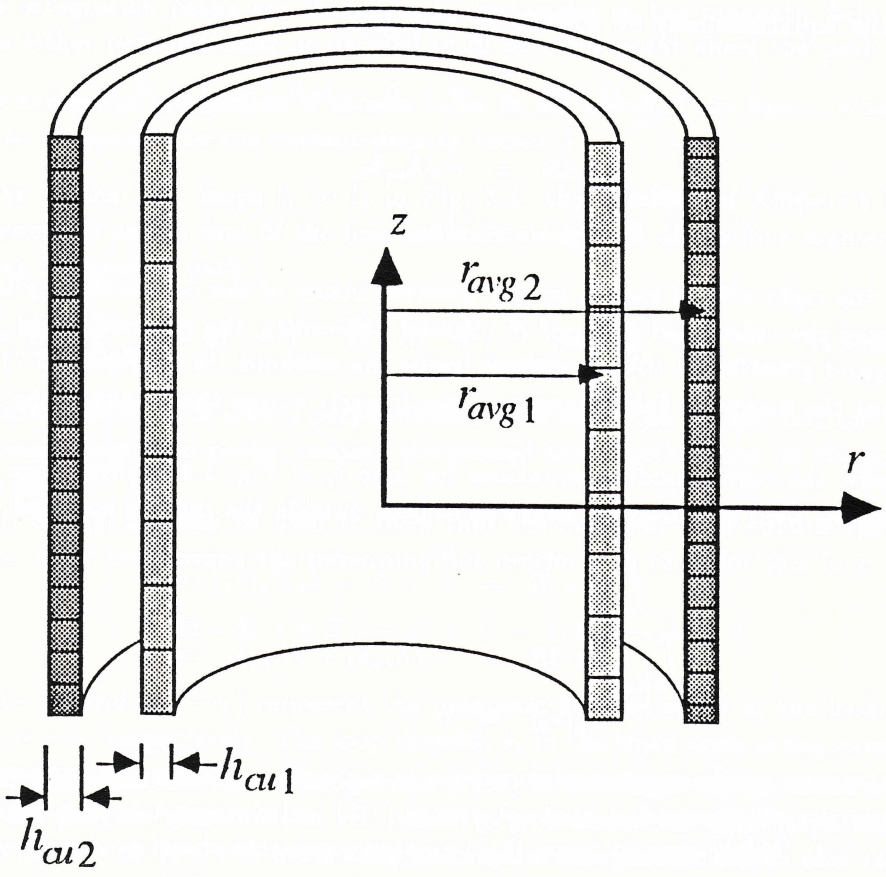


Figure 3.5: Infinitely long solenoid with two layers. The inner layer has n_1 turns per meter, average radius r_{avg_1}, and height h_{cu1}. The outer layer has n_2 turns per meter, average radius r_{avg_2}, and height h_{cu2}.

the other layer of the solenoid. The layers could carry the same current, but this is not required.

Assuming no external magnetic field is present, Fig. 3.6(a) shows the field distribution that exists around the solenoid when the outer winding layer is carrying a current $I_{2,DC}$ and the inner layer is carrying no current. Because the relative permeability of copper is close to one, and because there are no time-varying fields which would induce eddy currents in the inner conducting layer, the magnetic field distribution is exactly the same as in Fig. 3.4 where no inner layer is present. From (3.10), the magnetic field intensity everywhere inside the inner surface of layer 2 is given by

$$H_z = Jh_{cu} = \left(\frac{n_2 I_{2,DC}}{h_{cu2}}\right) h_{cu2} = n_2 I_{2,DC} \tag{3.14}$$

where n_2 has units of turns per meter.

Instead, if the inner layer is excited with a current $I_{1,DC}$ and the outer layer is left open-circuited, the plot of magnetic-field-intensity distribution appears as in Fig. 3.6(b). As in the case above for current flowing only in the outer layer, there is no z-directed magnetic field created outside an infinitely long cylindrical layer *by a current flowing in that layer*. The magnetic field in the region surrounded by layer 1 is $n_1 I_{1,DC}$, produced by the current in layer 1. In this illustration, the magnetic field intensity $n_1 I_{1,DC}$ is shown as half the value $n_2 I_{2,DC}$ in Part (a). Thus for this example, since $n_1 = n_2/2$,the magnitudes of the two currents $I_{1,DC}$ and $I_{2,DC}$ are equal.

The individual magnetic fields described above can be superposed to give the net magnetic field that exists in a solenoid of two layers. The currents $I_{1,DC}$ and $I_{2,DC}$ need not be equal and their directions need not be the same. In fact, there are no restrictions placed on these currents at all.

However, if $I_{1,DC} = I_{2,DC}$, which implies that the currents are equal and flow in the same direction, the magnetic field contributions of the two layers in the solenoid add, producing the field distribution shown in Fig. 3.6(c). The field strength between the two layers is the same as when only the outer layer carries current, but the field inside the inner layer is the sum of the fields produced by the individual layer currents. If the direction of the current in layer 1 is reversed, the net magnetic field distribution in the solenoid is the difference between the two contributions. This is illustrated in Fig. 3.6(d). Again, the field intensity between the two layers is that due to current in the outer layer only, while the field intensity inside the inner layer is the result of superposing the fields generated by the currents in both layers. These same plots of magnetic field intensity versus radius may be obtained by applying Ampere's law to a series of rectangular integration paths similar to those in Fig. 3.4.

The magnetic field intensity H that exists in the space surrounded by any winding layer establishes lines of magnetic flux ϕ which link the turns of that infinitely long layer *by closing on themselves via a flux path at infinity* [19, p. 356]. That flux path lies inside the torus of infinite ring radius shown in Fig. 3.1(c). Any flux in the innermost region of the solenoid links all the layers of the solenoid, but the flux in the conducting layers themselves and in the spaces between the conducting layers links only the layers further

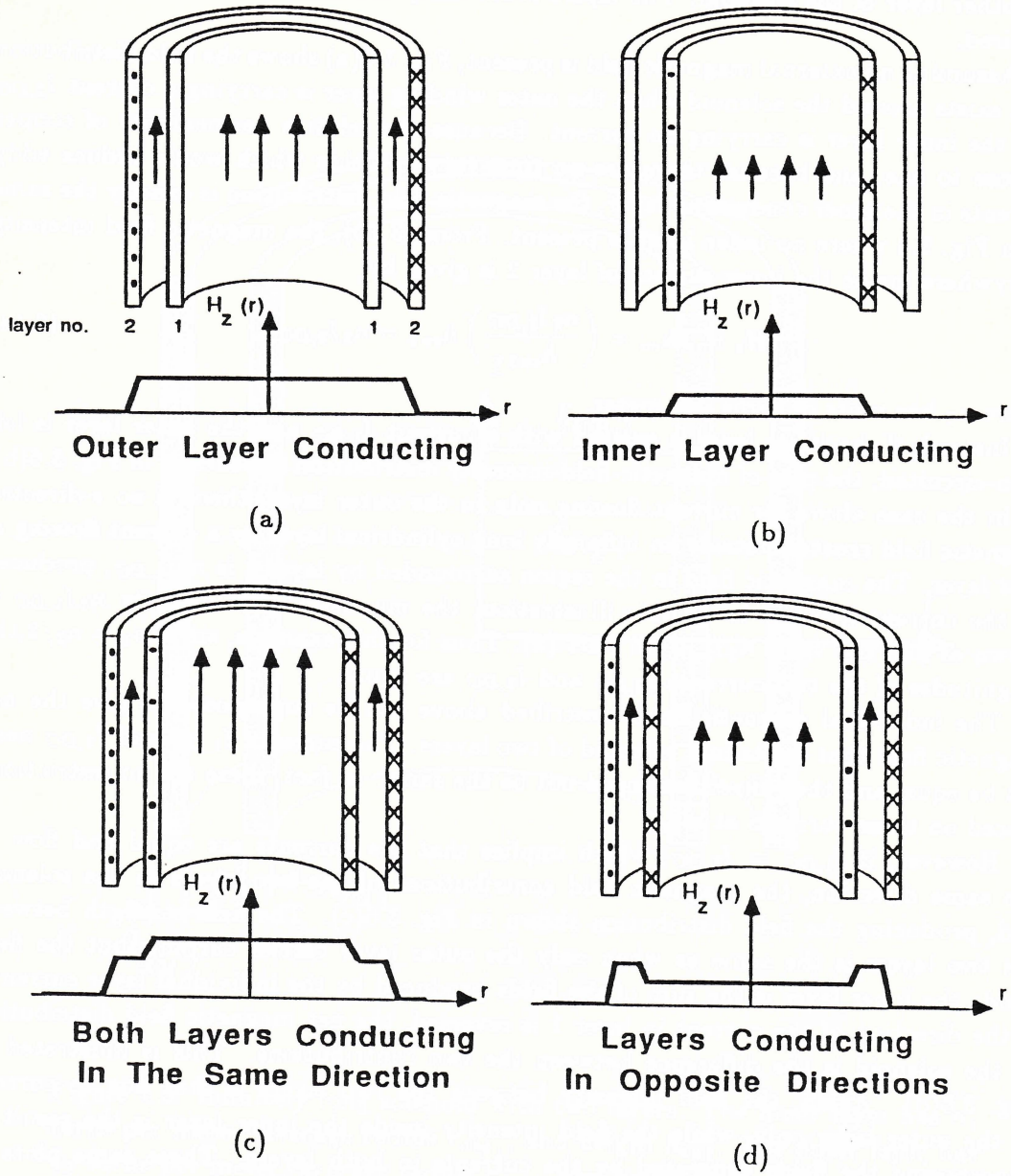


Figure 3.6: Field distribution inside an infinitely long two-layer solenoid with (a) only the outer layer conducting, (b) only the inner layer conducting but at half the current density, (c) both layers conducting the stated currents in the same direction, and (d) both layers conducting the stated currents but in opposite directions. The lengths of the arrows are proportional to the strength of the magnetic field in the different regions.

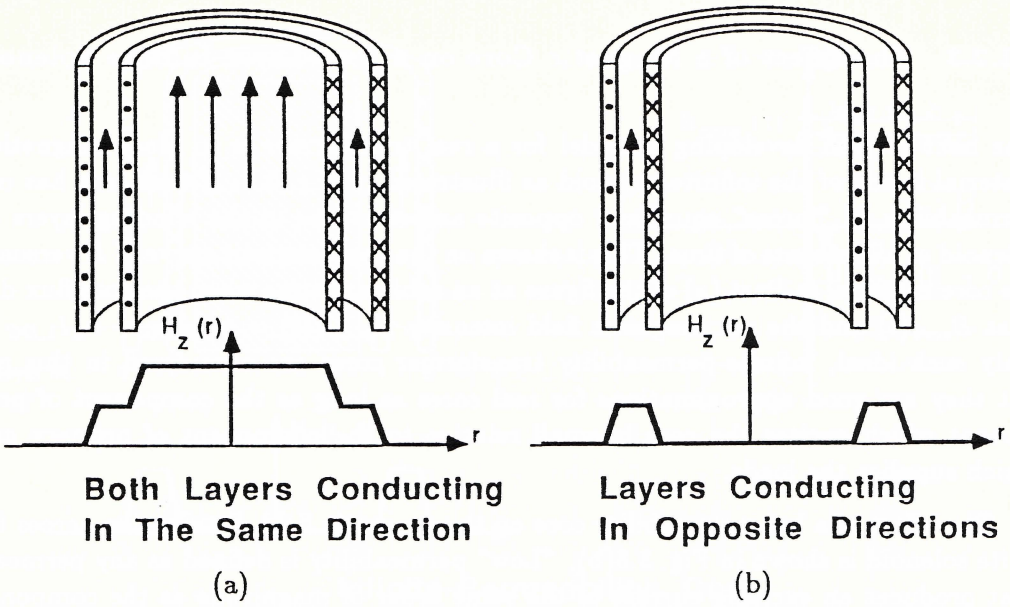


Figure 3.7: Field distribution inside an infinitely long two-layer solenoid with (a) the same current density in both layers, and (b) current densities of equal magnitude but opposite direction in the two layers. The lengths of the arrows are proportional to the strength of the magnetic field in the different regions.

from the center axis. Thus the winding space of the infinite solenoid, which includes the layers of conducting material and the spaces between them, contains the flux which is of particular interest to us because it is directly analogous to the leakage flux in a transformer.

To apply the infinite-solenoid model to the transformers that are of interest here, particular relationships are assumed between the magnetic fields generated by each of the two layers of the infinite solenoid. If $n_1 = n_2$ and $I_{1,DC} = I_{2,DC}$, then the two layers can be viewed as simply two series-connected layers of a single winding. This is the type of problem, namely one of single-winding multilayer series-connected solenoids, that M. P. Perry examines in [14]. In this instance, the equal magnetic-field contributions of the two layers $n_1 I_{1,DC}$ and $n_2 I_{2,DC}$ add, resulting in the field distribution shown in Fig. 3.7(a). If, however, the direction of the current in the inner layer is reversed such that $n_1 I_{1,DC} = -n_2 I_{2,DC}$, the magnetic field contributions of the two layers oppose each other, producing the net magnetic field distribution shown in Fig. 3.7(b). This case is similar to the condition of instantaneously equal and opposite ampere-turns in the windings of a transformer, where it is significant to note that the magnetic field inside the inner layer is completely canceled to give zero magnetic field intensity.

3.1.2.3 The Effect of a Magnetic Core on a Two-Layer Infinite Solenoid

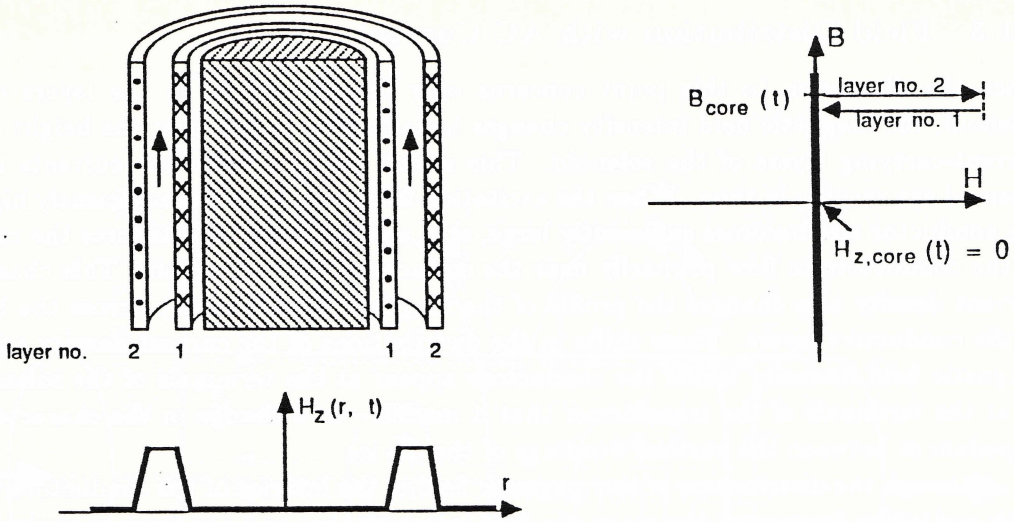
The next step in developing a model for a real transformer is to place magnetic core material inside of the infinite solenoid as illustrated in Fig. 3.8. If that core has infinite permeability, it "forces" equal and opposite ampere-turns in the winding layers of the solenoid at all instants of time. This is shown on the characteristic curve of B versus H for the core material in Part (a) of the figure at an arbitrary time when the core flux density is at $B_{core}(t)$ and the net magnetic field intensity $H_{z,core}(t) = n_2 I_{2,DC} - n_1 I_{1,DC} = 0$.[2] Only such ideal, infinite-permeability transformer cores are considered in this report, but they are good approximations for real cores as long as the component of primary current which excites the core is small relative to the component of primary current which supplies the loads.

The effect of a low-permeability core on the magnetic field distribution across the infinite solenoid is shown in Fig. 3.8(b). "Low" permeability is defined as any permeabiltiy that produces an exciting current of the same order of magnitude as the component of primary current that supplies the loads. With a low-permeability core, the net field in the center of the solenoid is not zero. In fact, it is a function of the flux density B in the core, which depends upon the history of the voltage applied to the core. At the particular instant t_1 shown in the figure, the core flux density is at $B_{core}(t_1)$, and the B versus H characteristic of the core material requires that the net magnetic field intensity be $H_{z,core}(t_1)$. With the current directions shown, this net magnetic field intensity can only be achieved by having the field produced by the outer winding layer greater than that produced by the inner winding layer by just this amount, that is, $H_{z,core}(t_1) = |n_2 I_{2,DC}(t_1)| - |n_1 I_{1,DC}(t_1)|$. This situation is shown in the associated plot of $H_z(r, t_1)$ versus r, where the magnetic field intensity inside the inner winding is not zero but varies in direct proportion to the flux density in the core. For the outer winding to contribute a larger component of field intensity inside the core than the inner winding, as shown in the figure, the outer winding must be connected to a source while the inner winding may be connected to a load. The case of a low-permeability core is not considered further in this report.

In summary, for an infinite solenoid having any number of concentric layers, no magnetic field is produced outside the solenoid for any combination of currents flowing in the layers. In contrast, the magnetic field in the space enclosed by the innermost layer depends on the currents flowing in all the layers, and it is zero only if the net field intensity—or mmf—produced by all the currents is zero. Because the material characteristics of a high-permeability magnetic core require a transformer to operate with essentially zero net mmf, the requirement of zero net mmf is imposed on a multilayer infinite solenoid when modeling such a transformer.

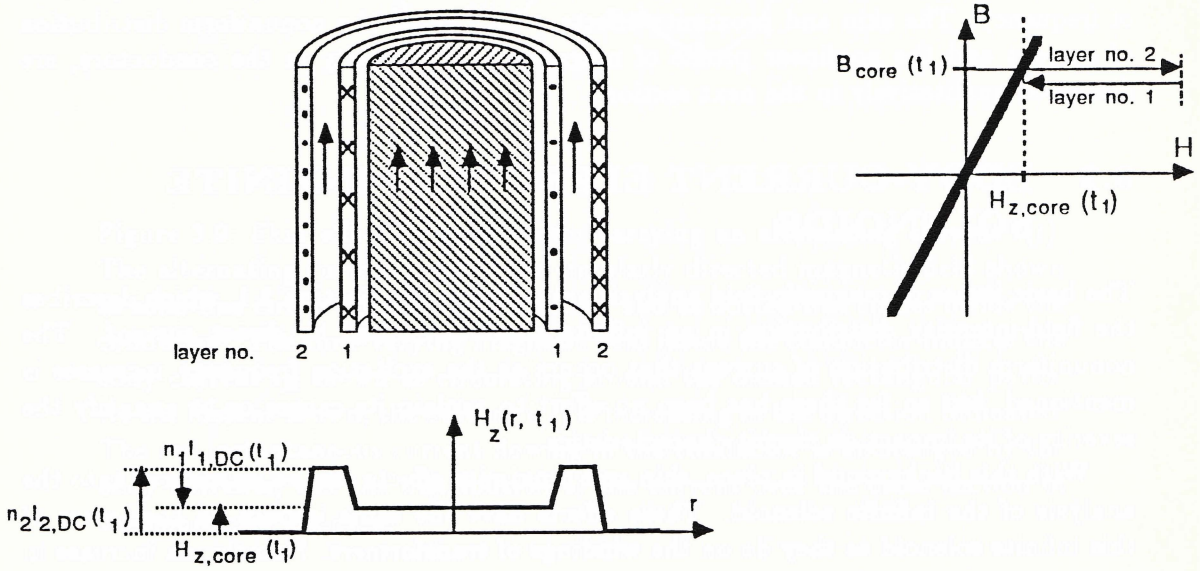
---

[2] The magnetic path length is implicit in n_1 and n_2, which have units of turns per meter.



Infinite-Permeability Core

(a)



Finite-Permeability Core

(b)

Figure 3.8: For an infinitely long two-layer solenoid containing a magnetic core, the field distribution in the winding space and the B versus H characteristic for (a) infinite-permeability core material and (b) finite-permeability core material. The horizontal vectors associated with the B versus H curves represent the magnetic field intensity in the center of the solenoid produced by each of the two winding layers. The difference between the horizontal vectors gives the magnetic field intensity inside the inner winding layer.

3.1.3 Field Distribution with AC Current

Since the discussion to this point concerns only direct currents in the layers of the solenoid, the magnetic field intensity changes linearly with radius over the height of the current-carrying layers of the solenoid. This is not the case when the currents in the solenoid are varying in time. When the excitation frequency becomes sufficiently high, or the conductor size becomes sufficiently large, skin and proximity effects force the current in the conductors to flow primarily near the surfaces of the conductors. This change in current density also changes the profile of the magnetic field intensity across the height of the conductive layers. These shifts in the distributions of the current density and the magnetic field intensity inside the conductors appear at the terminals of the solenoid—or at the terminals of the transformer that it models—as a change in the characteristic impedances between the various windings of the device.

Although the distribution of the magnetic field in the interior of the conductors varies with excitation frequency, the magnetic field intensity that any one layer contributes to the net magnetic field in the space between winding layers is independent of frequency. The field between layers is a function only of the *net* current in each of the surrounding layers. As long as the net current in each layer of conductors remains constant for changes in excitation frequency, the magnetic field in the spaces between the layers is independent of frequency. The skin and proximity effects, which cause the nonuniform distribution of current and the nonlinear profile of magnetic field intensity in the conductors, are discussed qualitatively in the next section.

3.2 EDDY-CURRENT EFFECTS IN INFINITE SOLENOIDS

The basic issues of magnetic-field analysis are addressed in Section 3.1, which describes the field-intensity distribution in an infinite solenoid excited by direct current. The nonuniform distribution of current that occurs as the excitation frequency increases is mentioned, but so far there has been no effort to explain its causes or to quantify the severity of its impact on circuit characteristics.

With this background in place, skin and proximity effects can be introduced into the analysis of the infinite solenoid. These effects have the same impact on the layers of this infinite solenoid as they do on the windings of transformers. Namely, an increase in excitation frequency causes an increase in the loss in the winding layers and a reduction in the total amount of energy stored in the magnetic field that exists in the winding layers.

3.2.1 Skin Effect

An isolated conductor carrying alternating current $i(t)$ generates a time-varying circular magnetic field $H(t)$ which exists both inside and outside the conductor. Such a conductor and its associated field are shown in Fig. 3.9.

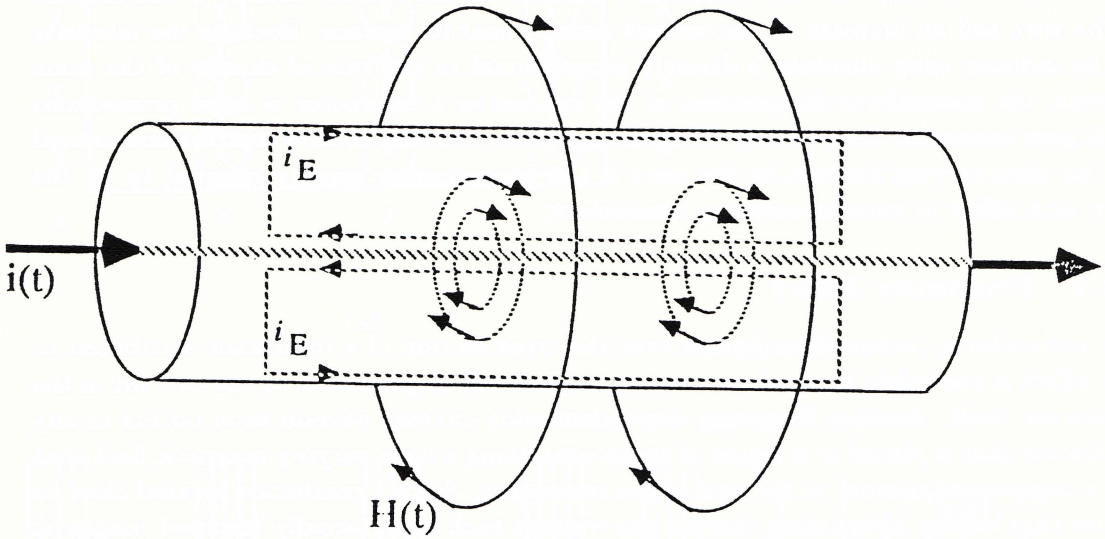


Figure 3.9: Skin effect in a conductor carrying an alternating current $i(t)$. The alternating current creates the circularly directed magnetic field shown as solid-line circles outside the conductor and as dotted-line circles inside the conductor. The time-varying magnetic field inside the conductor induces the eddy current i_E shown as circulating around the dashed rectangular paths. At the instant shown, the current $i(t)$ is increasing in the direction indicated. The net instantaneous current flowing in the conductor is unchanged by the eddy currents, but the distribution of the current over the cross section of the conductor changes.

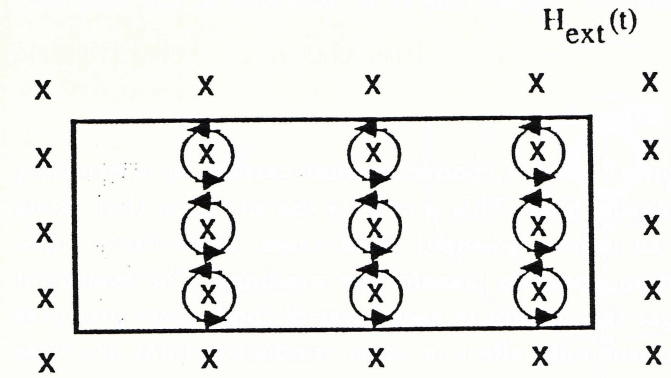
The circular alternating field inside the conductor induces eddy currents i_E in the conductor which are directed to produce a field that partially cancels the "main" alternating field produced by the time-varying current. These induced eddy currents are directed such that they add to the main current on the surface of the conductor and subtract from it in the interior region. The superposition of the main alternating current and the induced eddy currents results in a decrease in the current density in the interior of the wire and an increase in the current density near its surface. Because the intensity of the induced eddy currents is directly proportional to the rate of change of the main current, the nonuniform distribution of the current in a conductor is more pronounced for higher excitation frequencies. This change in the current-density distribution caused by the time-varying current in the wire is the phenomenon usually referred to by the term *skin effect* in current-carrying conductors.

3.2.2 Proximity Effect

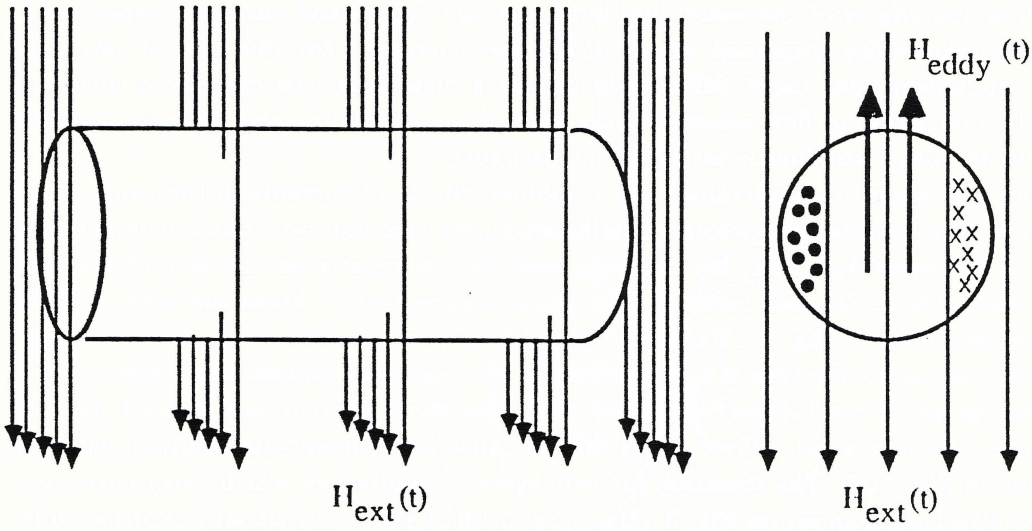
The nonuniform current distribution over the cross section of a conductor attributed to skin effect is due solely to the time-varying magnetic field generated by the current in the conductor itself. Another frequency-dependent eddy-current phenomenon occurs in any conductor that is placed in a region of space containing a time-varying magnetic field that has a component normal to the axis of the conductor. Since a conductor located close to a wire that carries alternating current experiences such an externally imposed magnetic field, this eddy-current phenomenon is often called the *proximity effect*. It would be more accurate perhaps to call this the *external-field effect* since it is actually the presence of the time-varying magnetic fields generated by nearby windings that causes the so-called proximity effect. In this document, however, the common term *proximity effect* is used.

Whenever a conductor is located in a region of space that contains an alternating magnetic field which is directed normal to the axis of the conductor, there are eddy currents induced in the conductor which act to oppose the penetration of this external field. Fig. 3.10 shows such a situation for a conductor with a circular cross section in a uniform time-varying magnetic field that is normal to the axis of the conductor. The conductor is isolated in space and carries no net current. The uniform external field H_{ext} in Fig. 3.10 is assumed to be increasing in magnitude in the indicated direction. The time-varying field lines which pass through the conductor induce eddy currents in the conductor, and these eddy currents are directed to oppose the increasing magnetic field. In Fig. 3.10(a), the eddy currents are shown as circular currents which surround each of the crosses that represent the downward directed external field H_{ext}.

The cross-sectional view of the conductor in Fig. 3.10(c) shows that the net effect of the induced eddy currents is the generation of a circulating current that flows into the right side of the cross section and out of the left side. The upwardly directed arrows in this cross-sectional view show the opposing magnetic field generated by the eddy currents. The superposition of this reaction field and the external field that induces it results in a reduction in the net amount of magnetic flux that penetrates the conductor. Since the energy stored in the magnetic field in any region of space is directly related



(a)



(b) (c)

Figure 3.10: Proximity effect for a cylindrical conductor in a uniform time-varying magnetic field. (a) Top view, showing an eddy current induced around each field line that passes through the conductor (b) Side view. (c) Cross-sectional view, showing the net opposing field H_{eddy} generated by the eddy currents.

to the magnetic field intensity there as explained in Section 3.3.2, a reduction in the magnetic flux that penetrates a conductor corresponds to a reduction in the magnetic energy stored in the conductor.

3.2.3 Combined Frequency Effects

Skin and proximity effects are combined when a conductor that carries an alternating current is placed in an external alternating field. This is exactly the situation that exists for the conductors in the layers of an infinite solenoid when these layers carry time-varying currents, and the same situation exists for transformer windings. The essence of the combination of these effects is that the current in each layer of conductors produces a skin effect in itself and produces a proximity effect in other conductors that are close to it.

While the infinite solenoid is the object of this analysis, a structure which has an infinite number of conductors in each layer, all carrying the same current, skin and proximity effects are just as evident in two side-by-side conductors. Figure 3.11 illustrates the combination of these effects for two round conductors located next to each other when the conductors carry currents in opposite directions. Parts (a) and (b) of the figure show the effects of the individual left-hand and right-hand currents respectively; Fig. 3.11(c) shows the combined effects of the two currents. For this case of two side-by-side conductors that carry currents in opposite directions, the current in either of the conductors tends to flow mostly on the skin of the conductor and more on the side nearest to the other conductor as shown in the figure.

Figure 3.12 shows the individual and combined effects of currents in the same direction in two side-by-side conductors. This figure shows that for two conductors carrying current in the same direction, the currents tend to flow mostly on the skin of the conductors and more on the side furthest from the other conductor. From the density of the magnetic field lines in Fig. 3.11(c) and Fig. 3.12(c), it can be seen that, in both cases, the current in the conductors is concentrated in the region of highest flux density.

When layers of conductors which all carry the same current are located next to each other, the combined eddy-current effects cause the current-distribution patterns illustrated in Fig. 3.13. The situation for two layers of conductors which carry current in the same direction is shown in Fig. 3.13(a); Fig. 3.13(b) shows the situation for two side-by-side layers which carry oppositely directed currents. As with the single conductors in Figs. 3.11 and 3.12, the currents in the layers of Fig. 3.13 concentrate in the region of highest magnetic flux density. This fact is important to remember when considering the current distribution in the winding layers of an infinite solenoid or a transformer.

This entire discussion of eddy currents concerns alternating magnetic fields. An alternating magnetic field induces the eddy currents that cause the nonuniform distribution of the current over the cross section of the conductors. For direct current flowing in the conductors, the magnetic field patterns in Figs. 3.11 to 3.13 would be similar to those shown, but there would be no crowding of current in the conductors in the regions of highest field strength. Instead, the current density would be uniform across all the

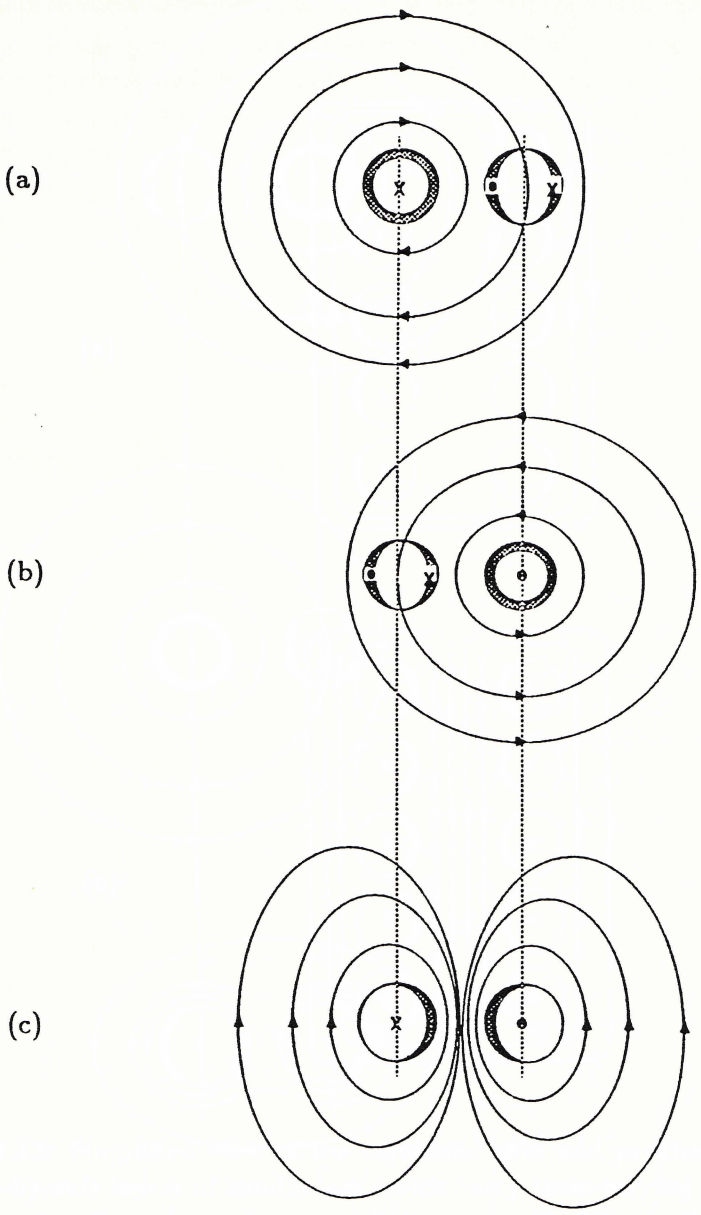


Figure 3.11: Combined skin and proximity effects in two side-by-side round conductors that carry time-varying currents in opposite directions. Dark regions show areas of high current density. (a) The effect of a current in the left-hand conductor. (b) The effect of an oppositely directed current in the right-hand conductor. (c) The combined effects of the two currents.

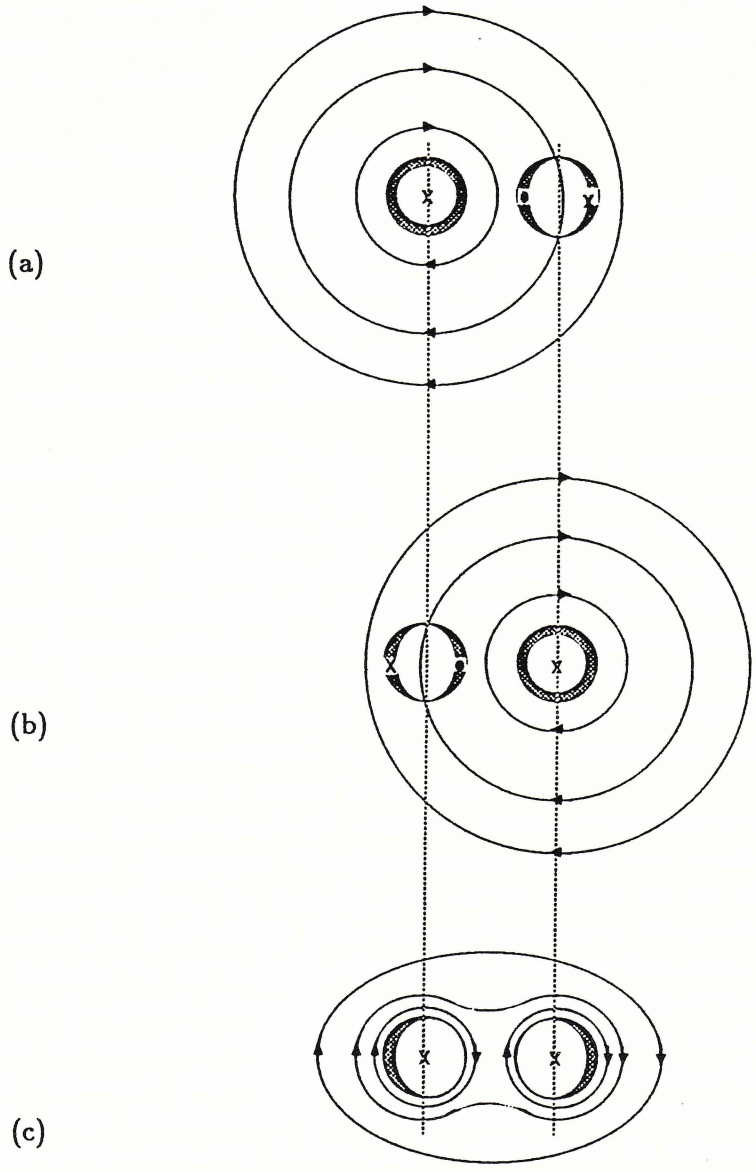


Figure 3.12: Combined skin and proximity effects in two side-by-side round conductors that carry time-varying currents in the same direction. Dark regions show areas of high current density. (a) The effect of a current in the left-hand conductor. (b) The effect of an equal current in the right-hand conductor. (c) The combined effects of the two currents.

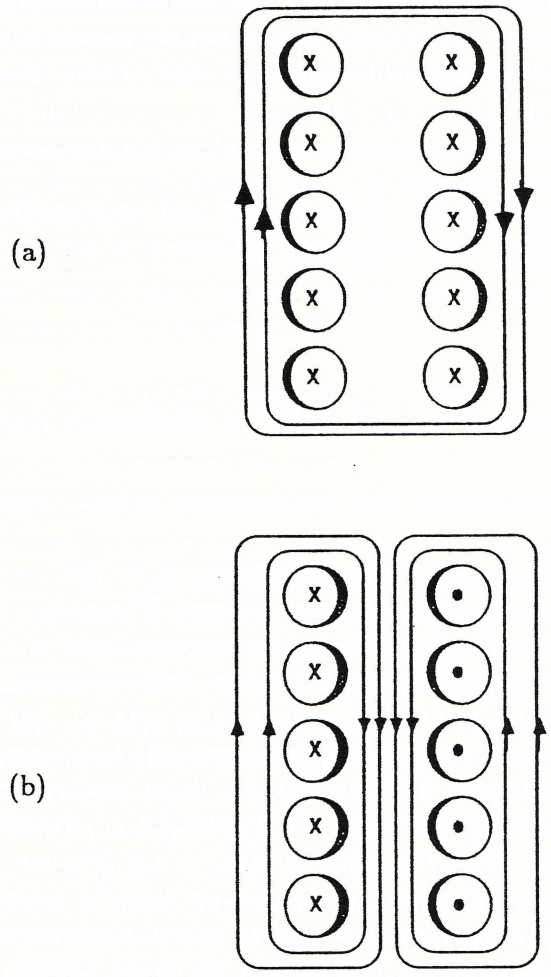


Figure 3.13: Simplified view of the combined skin and proximity effects in two side-by-side layers of conductors which carry time-varying currents. (a) Approximate effect of equal currents in the same direction in the two layers. In reality, the field lines are not straight and they do not entirely cancel in the region between layers. (b) The approximate effect of equal but oppositely directed currents in the two layers.

conductors.

It is also important to realize that the net magnetic field between the layers of conductors is assumed to be tangential to the layers. This is usually true near the "middle" of a winding layer with respect to the z-direction in Fig. 3.5, but it is less likely to be true at the ends of the layer. As stated in Section 1.1.2, this *parallel-field* assumption is critical to the analysis developed in Part I of the present document.

3.2.4 The Effect of the Field Distribution on Impedance Values

The crowding of current due to the effects of time-varying magnetic fields increases the effective resistance of a wire. The resistance R of any wire is given by

$$R = \frac{l}{\sigma A} \tag{3.15}$$

where l is the length of the wire, σ is the conductivity of the material, and A is the effective cross-sectional area of the conductor. Since current tends to flow only near the surface of the conductor as the frequency of the sinusoidal magnetic fields increases, the effective cross-sectional area of the wire decreases, which causes an increase in the resistance of the wire.

The relationship between the current distribution in the conductors and leakage inductance can be explained qualitatively as follows. The eddy currents induced near the surfaces of the conductors contribute to the magnetic field in a direction that tends to oppose the penetration of the external flux into the conductors. As a consequence, the magnetic field intensity inside the conductors is reduced. A lower magnetic field intensity produces less energy storage, which corresponds to a lower leakage inductance.

The distribution of magnetic field intensity for dc or low-frequency excitation in an infinite solenoid is developed in Section 3.1.2. Figure 3.4 in that section shows that the current distributes evenly across the solenoid layer at low frequencies and the magnetic field intensity for such a low-frequency case changes linearly across the height of each winding layer. When the frequency of the layer currents increases, however, skin and proximity effects combine to cause the current to crowd toward the surfaces of the conductors in the regions of highest flux density. This redistribution of current in the conductors of a winding layer acts to shield the interior of the layer from the time-varying magnetic fields, which means that at high frequencies, the total amount of energy stored in the magnetic field that exists in any winding layer is lower than it is with low-frequency excitation.

The decrease in the average magnetic energy stored in and around the layers of any two windings under short-circuit conditions correlates to a decrease in the leakage inductance between those two windings. One of the main objectives of the analysis in the next chapter is to develop analytical expressions for the variation of the magnetic field and the current density in a layer of conductors as a function of the excitation frequency. Such results are then used to formulate expressions for the frequency-variation of the characteristic impedance between each pair of windings in a multiwinding transformer.

3.3 CURRENT-SHEET APPROXIMATION OF A WINDING LAYER

The analysis described so far establishes the groundwork needed to solve for the spatial distribution of the magnetic field intensity and current density in the winding layers of an infinite solenoid, and for the magnetic field intensity between the winding layers, under conditions of high-frequency sinusoidal excitation. In Section 3.3.1 below, the problem of calculating these distributions is set up to be solved in the next chapter. There, it is seen that the current-density and field-intensity distributions are determined solely by the phasor values of the magnetic field intensity that exist at the surfaces of the winding layers. Section 3.3.2 then tells how the solutions for the magnetic-field-intensity and current-density distributions can be used to find the power dissipation and magnetic-energy storage in the layers.

3.3.1 Modeling an Infinite Cylindrical Layer as an Infinite Current Sheet

In an infinitely long cylindrical winding layer, the magnetic field intensity depends only on the distance r from the center axis and is directed purely in the z-direction. The general expression in cylindrical coordinates for a three-dimensional time-varying magnetic field intensity function $\mathbf{H}(r, \phi, z, t)$ can be written as simply $\mathbf{H}_z(r, t)$. When the excitation currents are sinusoidal, the magnetic field intensity can be written as a vector phasor field, representing a vector field in which all magnitudes vary sinusoidally with time. In symbols, $\underline{\mathbf{H}}(r) = \underline{H}_z(r)\hat{\mathbf{a}}_\mathbf{z}$ where $\underline{H}_z(r)$ is a scalar complex phasor which is a function of the radius coordinate r, and $\hat{\mathbf{a}}_\mathbf{z}$ is the unit vector in the z-direction.[3]

The above assumptions permit us to solve for the current distribution in the winding layers using Maxwell's equations written in their one dimensional form for cylindrical coordinates. M. P. Perry presents such an analysis in [14] where he shows that for the cylindrical current sheet problem, the current density in a winding layer can be written in terms of Bessel functions. Perry also argues, however, that it is often possible to neglect the curvature in the cylindrical winding layers and simply treat the layers as current sheets that extend infinitely in the direction of depth. He asserts that the curvature of the winding layers can be neglected if "the conductor thickness (designated here the layer *height* h_{cu}) is small compared to the total coil diameter [14, p. 118]." Figure 3.14 shows a cylindrical current sheet which is modeled by an infinite rectangular current sheet. Looking down at the top of any particular part of the cylindrical sheet as shown in Fig. 3.14(b), it seems reasonable that as long as the curvature of the surface of the cylinder is relatively small, each local section of the cylindrical conductor can be approximated by a flat surface without introducing substantial error. If such an approximation is valid, the winding layers can be analyzed as current sheets in rectangular coordinates, which is substantially easier than the analysis in cylindrical coordinates. It is seen later

[3]See Section 1.3 for a discussion of the use of phasor notation.

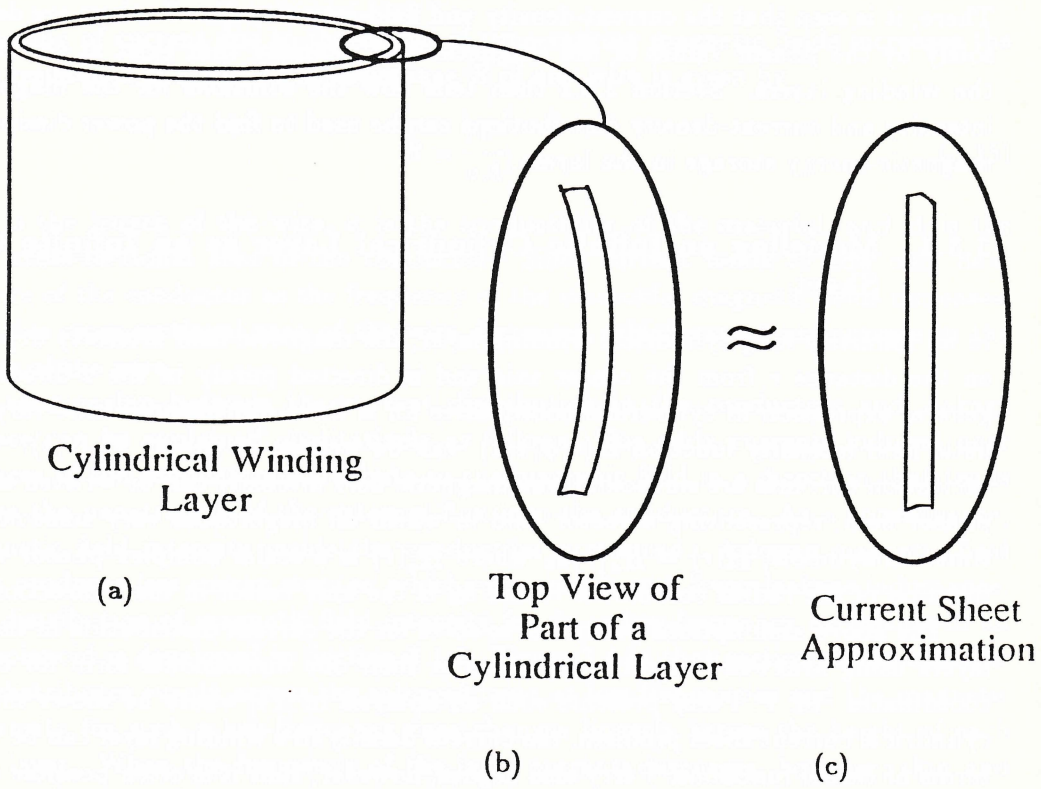


Figure 3.14: (a) Cylindrical layer of an infinite solenoid. (b) Detailed top view of the cylinder. (c) Infinite current sheet used to approximate the layer if the radius of the cylinder is large relative to the height of the layer.

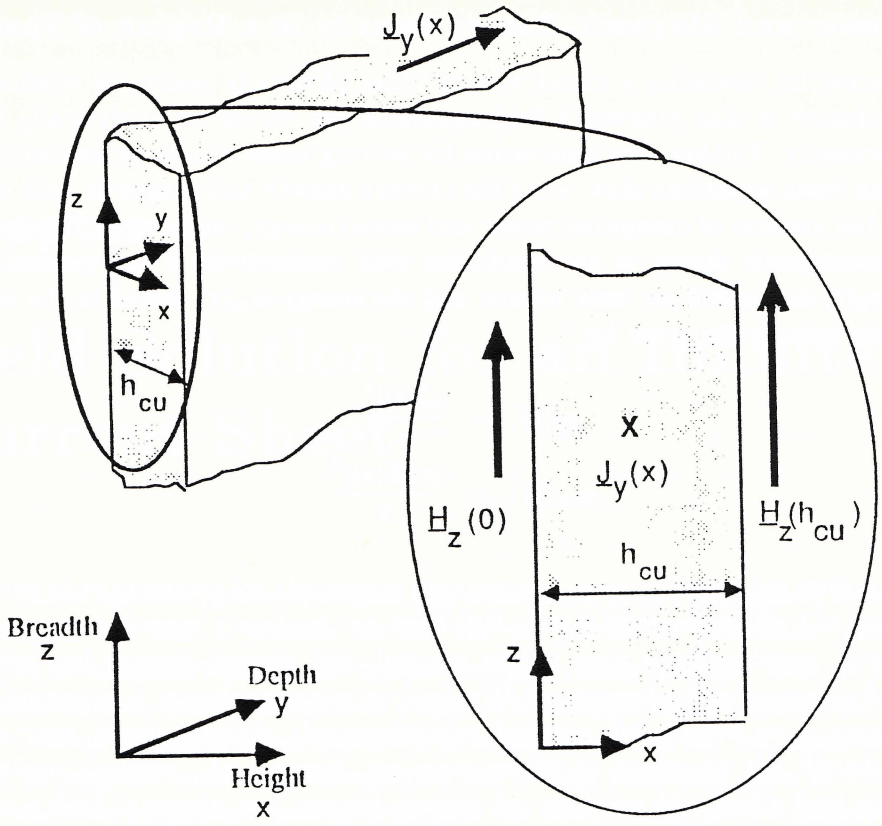


Figure 3.15: Model of an infinite current sheet. The sheet extends to infinity in the y (*depth*) and z (*breadth*) directions. The *height* of the sheet is shown as h_{cu} in the x-direction.

in this report that the results of a rectangular-coordinate analysis can be written in terms of hyperbolic sines and cosines instead of Bessel functions. In this document, it is always assumed that the radius of curvature of any winding is much larger than the height of the conductors; therefore, only rectangular coordinates are used.

For the current-sheet approximation, a general three-dimensional time-varying magnetic field intensity function is written as $\mathbf{H}(x, y, z, t)$ where the x, y, z directions are as defined as the height, depth, and breadth, respectively, as shown in Fig. 3.15.

For sinusoidal excitation, phasor notation is used to represent the time-varying magnetic field intensity $\mathbf{H}(x, y, z, t)$. The result is the vector phasor function $\underline{\mathbf{H}}(x, y, z)$ of the x, y and z coordinates. As the magnetic field intensity in an infinitely long conducting cylinder is a function of the radius r only, in the infinite current sheet it is a function of the x-direction only as defined in Fig. 3.15. Therefore, in the one-dimensional case, $\underline{\mathbf{H}}(x, y, z)$ is written as simply $\underline{H}_z(x)\hat{\mathbf{a}}_\mathbf{z}$.

3.3.2 Power and Magnetic-Energy Density in a Region of Space

The motivation for modeling a round-wire or other physically realizable winding as an infinite conductor is that Maxwell's field equations can be solved analytically for such a simple geometry. Further, the motivation for solving these equations explicitly lies in the following basic equations that relate the current density and magnetic field intensity in space to the amount of dissipated power and stored energy, respectively, in that space. From electromagnetic theory, in any conductor with conductivity σ and permeability μ, the power $p_d(t)$ dissipated per unit volume and the energy $w_m(t)$ stored in the magnetic field per unit volume are given by

$$p_d(t) = \frac{|\mathbf{J}(t)|^2}{\sigma} \tag{3.16}$$

$$w_m(t) = \frac{\mu\,|\mathbf{H}(t)|^2}{2} \tag{3.17}$$

The task of finding the power dissipation and magnetic-energy storage in any winding space reduces, therefore, to solving for the current density $\mathbf{J}$ and the magnetic-field intensity $\mathbf{H}$ in that winding space, and evaluating the volume integrals of (3.16) and (3.17) over the space. In this chapter, it is shown how the frequency-independent values of $\mathbf{H}$ are calculated for the interlayer spaces of a transformer winding structure. Because $\mathbf{H}$ is uniform in each interlayer space, the corresponding volume integral of (3.17) is trivial. Of course, no current flows in the interlayer spaces, making p_d zero there.

Inside the conductors, the current density and magnetic field intensity are complicated functions of frequency. By modeling each cylindrical winding layer as an infinite current sheet, it is possible to derive expressions which give the field distribution in each layer of conductors based solely on the thickness of the layer and the magnetic field intensity $\mathbf{H}$ at the two surfaces of the layer, determined by the methods of this chapter. The derivation for the magnetic field intensity $\mathbf{H}$ and the current density $\mathbf{J}$ in an infinite current sheet is carried out in the next chapter. Afterwards, the volume integrals of (3.16) and (3.17) can be calculated for the winding layers as well as the interwinding spaces, and the total power dissipation and energy storage are thus obtained. Then the goal of this analysis can be addressed: deriving expressions for the high-frequency impedances between the windings of actual transformers.

Chapter 4

Field Solution for an Infinite Current Sheet

To arrive at expressions for the energy storage and power dissipation within the winding space of a transformer structure, we must first obtain expressions for the magnetic-field-intensity and current-density distributions within each winding layer. However, when the windings of a transformer are excited with ac currents, the magnetic field intensity and current density within the conductors become distributed in a complicated and nonuniform fashion. As a result, we must resort to analyzing the distribution of the magnetic field intensity and current density by applying Maxwell's field equations. As argued in Chapter 3, we can model a given layer of a transformer winding structure as an infinite current sheet. Therefore, in this chapter we apply Maxwell's equations to an infinite current sheet and arrive at analytical expressions that approximately describe the magnetic-field-intensity and current-density distributions within transformer windings. We then make a detailed investigation into the peculiar nature of these distributions through an extensive array of examples and graphical illustrations. Finally, using the expressions for the magnetic-field-intensity and current-density distributions, we derive expressions for the average power dissipation and average energy storage per square meter for an infinite current sheet.

4.1 APPLICATION OF MAXWELL'S EQUATIONS TO THE INFINITE CURRENT SHEET

4.1.1 Description of Problem

Figure 3.15 shows the infinite current sheet we use to model the cylindrical winding layer. In this figure, a set of axes designates the coordinate system that applies to the following analysis. The origin of the system is located at the left-hand side of the current sheet. The x-coordinate axis is in the direction of layer height; the y-direction is normal to the indicated cross section of the current sheet and lies along the direction of depth; and the

z-axis is in the direction of breadth. The infinite sheet has a height designated as h_{cu}. To analyze the fields in such a current sheet, we need only the following assumptions:

- The current density and the magnetic field intensity vary sinusoidally with time.
- The media are linear.
- The magnetic field at the surfaces of the sheet are directed purely in the breadth or z-direction. That is, $\underline{\mathbf{H}}(x,y,z) = \underline{H}_z(x)\hat{\mathbf{a}}_\mathbf{z}$ where $\hat{\mathbf{a}}_\mathbf{z}$ is the unit vector in the z-direction. The boundary values of this field are given as $\underline{H}_z(0)$ and $\underline{H}_z(h_{cu})$.
- The current sheet is long enough in the breadth and depth directions that the spatial variation of the magnetic field depends only on changes in the x-direction, which is to say that the magnetic field is determined by the height, or x-coordinate, and does not vary with changes in depth or breadth. This is an alternate statement of the infinite-current-sheet assumption.
- The current sheet is stationary with respect to the observer.

What we seek in this analysis is a method for describing the fields inside the conductive sheet of a material with conductivity σ and permeability μ that is based only on the values of the sinusoidally varying magnetic fields on the surfaces of the sheet. This type of boundary-value problem where the spatial magnetic field intensity decreases as the field penetrates the material is the same mathematically as the problem of the diffusion of heat or gases into a medium where the surface temperature or gas concentration is made to vary sinusoidally with time. The mathematical statement of the differential equation that defines this problem is sometimes referred to as *the diffusion equation*, and we shall use this term in the analysis which follows.

4.1.2 Derivation of the Diffusion Equations

The diffusion equation for the case of sinusoidal steady-state variations of the electric field $\mathbf{E}$ is derived in Appendix A in terms of the the complex wave number $\underline{k}$ and the complex vector phasor $\underline{\mathbf{E}}$ as

$$\nabla^2\underline{\mathbf{E}} = \underline{k}^2\underline{\mathbf{E}} \tag{4.1}$$

where the complex wave number is a material characteristic given by

$$\underline{k} = \sqrt{j\omega\mu\sigma - \omega^2\mu\epsilon}. \tag{4.2}$$

In the *good conductor* case—which is the only case of importance here—the permittivity ϵ and the permeability μ are given by their free-space values $\epsilon_o = 8.854 \times 10^{-12}$ F/m and $\mu_o = 4\pi \times 10^{-7}$ H/m , respectively. Since the conductivity σ is far greater than the product of the permittivity of free space ϵ_o and the angular frequency ω, we can assume,

for any frequency of interest in our analysis[1], that $\omega\mu_o\sigma \gg \omega^2\mu_o\epsilon_o$. Therefore, for a good conductor, we can write the complex wave number as

$$\boxed{\underline{k} \approx \sqrt{j\omega\mu_o\sigma}} \tag{4.3}$$

Using the relation for the square root of j

$$\begin{aligned}\sqrt{j} &= (e^{j\frac{\pi}{2}})^{\frac{1}{2}} \\ &= e^{j\frac{\pi}{4}} \\ &= \cos\frac{\pi}{4} + j\sin\frac{\pi}{4} \\ &= \frac{1}{\sqrt{2}} + j\frac{1}{\sqrt{2}} = \frac{1}{\sqrt{2}}(1+j)\end{aligned} \tag{4.4}$$

we can write (4.3) as

$$\underline{k} = \sqrt{\frac{\omega\mu_o\sigma}{2}}(1+j) \tag{4.5}$$

$$\boxed{\underline{k} = \tfrac{1}{\delta}(1+j)} \tag{4.6}$$

where

$$\boxed{\delta = \sqrt{\frac{2}{\omega\mu_o\sigma}}} \tag{4.7}$$

The expression for δ above is referred to as the *skin depth* for the conductive material at the excitation frequency ω. For any general conducting sheet with a sinusoidally varying electric field at the surface of the conductor, the magnitude of the field strength at a distance equal to one skin depth into the material is equal to e^{-1} times the value of the field at the material surface. That is, at one skin depth, the strength of the electric field is 36.8% of its value at the conductor surface; and at a depth of 3δ, the electric field strength is reduced to 5.0% of the value at the surface. The solution to (4.1) is a phasor from which the instantaneous spatial distribution of the electric field can be determined. The solution is general and applicable for any good conductor under sinusoidal steady-state field conditions.

The diffusion equation given above in (4.1) is written in terms of the electric field; an analogous relationship can be written in terms of current density $\mathbf{J}$ by using the constitutive relationship $\mathbf{J} = \sigma\mathbf{E}$. Also, Maxwell's equations can be manipulated to

[1]For copper with $\sigma = 5.315 \times 10^7$ S/m at 60°C, this assumption is good for frequencies below approximately 1×10^{12} hertz. Above this frequency, the conductivity of copper becomes frequency dependent and the simple classical analysis of this report is not valid [7].

yield a diffusion equation in terms of the magnetic field $\mathbf{H}$; this derivation is detailed in Appendix B. The three diffusion equations are collected below.

$$\nabla^2 \underline{\mathbf{E}} = \underline{k}^2 \underline{\mathbf{E}} \tag{4.8}$$

$$\nabla^2 \underline{\mathbf{H}} = \underline{k}^2 \underline{\mathbf{H}} \tag{4.9}$$

$$\nabla^2 \underline{\mathbf{J}} = \underline{k}^2 \underline{\mathbf{J}} \tag{4.10}$$

What is important to see in the above equations is that, when there are no free charges in the conducting material, i.e., the volume charge density ρ in the material is zero, the diffusion equation is of exactly the same form for all three field quantities $\underline{\mathbf{E}}$, $\underline{\mathbf{H}}$ and $\underline{\mathbf{J}}$. This does not, however, mean that the solutions are the same because different boundary conditions apply.

For the infinite-current-sheet problem we are considering, we can make several simplifying assumptions. First, the spatial magnetic-field phasor $\underline{\mathbf{H}}(x, y, z)$ is assumed to be a function of x only and to be directed in the z-direction. Likewise, the spatial current-density phasor $\underline{\mathbf{J}}(x, y, z)$ is assumed to be a function of x only and to be directed in the y-direction. We can write these mathematically as

$$\underline{\mathbf{H}}(x, y, z) = \underline{H}_z(x)\hat{\mathbf{a}}_\mathbf{z} \tag{4.11}$$

$$\underline{\mathbf{J}}(x, y, z) = \underline{J}_y(x)\hat{\mathbf{a}}_\mathbf{y} \tag{4.12}$$

where $\hat{\mathbf{a}}_\mathbf{y}$ and $\hat{\mathbf{a}}_\mathbf{z}$ are the unit vectors in the y and z directions respectively. Then the three dimensional diffusion equations given in (4.9), and (4.10) above become the one-dimensional partial differential equations,

$$\boxed{\frac{\partial^2 \underline{H}_z(x)}{\partial x^2} = \underline{k}^2 \underline{H}_z(x)} \tag{4.13}$$

$$\boxed{\frac{\partial^2 \underline{J}_y(x)}{\partial x^2} = \underline{k}^2 \underline{J}_y(x)} \tag{4.14}$$

These are the equations that we now undertake to solve.

4.1.3 Form of Solution of the Boundary Value Problem

Before we continue with the mathematical development, it is useful to pause for a moment and consider the type of solution we expect to find in the analysis that follows. Figure 4.1(a) shows as a vertically shaded plot a hypothetical distribution over the layer height of the phasor magnitude(rms value) of the magnetic field intensity in a current sheet similar to that in Fig. 3.15 that is subject to an arbitrary pair of cosinusoidal magnetic-field-intensity boundary conditions. What we seek to find in our analysis is an analytical expression for the distribution of the magnetic field—and for the related

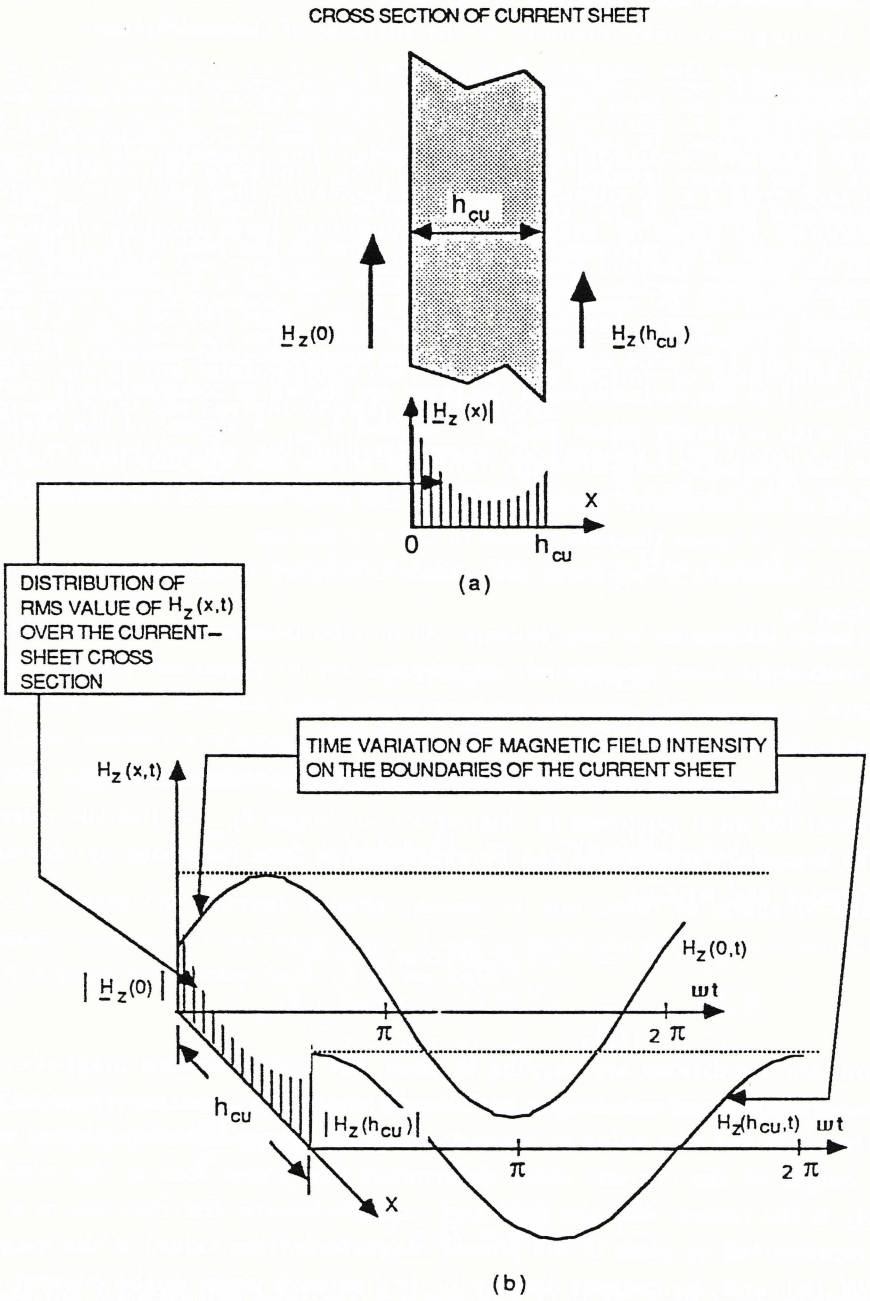


Figure 4.1: (a) Hypothetical distribution of the magnitude of the magnetic-field-intensity phasor $\underline{H}_z(x)$ across a layer of height h_{cu}. (b) The boundary conditions of the cosinusoidal waveforms $H_z(0,t) = \sqrt{2}\,|\underline{H}_z(0)|\cos(\omega t + \theta_0)$ and $H_z(h_{cu},t) = \sqrt{2}\,|\underline{H}_z(h_{cu})|\cos(\omega t + \theta_{h_{cu}})$ are shown.

current-density distribution—in a winding layer based on the excitation frequency and on the values of the magnetic field intensity at the surfaces of the conductor.

The boundary values of the magnetic field intensity play an important part in the derivations that follow, and we need to be somewhat explicit about the notation we use in describing these quantities. In part (a) of Fig. 4.1, we see a cross-sectional view of the current sheet. The arrows labeled $\underline{H}_z(0)$ and $\underline{H}_z(h_{cu})$ indicate the location of the magnetic-field-intensity phasor $\underline{H}_z(x)$ at the boundaries $x = 0$ and $x = h_{cu}$ on the two sides of the current sheet. The succession of vertical lines in the plot of $|\underline{H}_z(x)|$ versus x below the conductor cross section show how the rms value of a hypothetical phasor magnetic field might vary across the height of the layer. Part (b) of Fig. 4.1 shows in a perspective drawing two time axes on which the magnetic-field-intensity functions $H_z(0,t)$ and $H_z(h_{cu},t)$ at the boundaries of the layer are shown as cosinusoidally varying functions of time with arbitrary phase angles of θ_0 and $\theta_{h_{cu}}$. A repeat of the sketch of the rms value of the magnetic-field-intensity function across the winding-layer height is shown at the origin of the waveform plots. Note that the peak values of the cosinusoidally varying time wave is $\sqrt{2}$ times the rms values of the waveforms.

As explained in Section 1.2, we write the phasor boundary conditions in magnitude and phase notation as

$$\underline{H}_z(0) = H_z(0)\angle\theta_0 \tag{4.15}$$

$$\underline{H}_z(h_{cu}) = H_z(h_{cu})\angle\theta_{h_{cu}} \tag{4.16}$$

The angles θ_0 and $\theta_{h_{cu}}$ must be expressed in relation to some reference angle. We find that it is convenient for most purposes in this report to choose $\theta_{h_{cu}} = 0$ as the reference phase angle. The boundary conditions can be expressed as time functions by choosing a cosinusoidal reference and writing,

$$H_z(0,t) = \sqrt{2}\,H_z(0)\cos(\omega t + \theta_0) \tag{4.17}$$

$$H_z(h_{cu},t) = \sqrt{2}\,H_z(h_{cu})\cos(\omega t + \theta_{h_{cu}}) \tag{4.18}$$

Since these boundary conditions are varying in time, the instantaneous magnetic-field-intensity profile across the current sheet is continually changing. It is important to point out, however, that it is the rms value or magnitude of the current-density phasor whose effect over the height of the current sheet determines the power loss in the windings. This presumably is the reason why the field and current-density distributions in a layer are commonly represented by plots of the phasor *magnitude* (rms value) of the magnetic field intensity $|\underline{H}_z(x)|$ and the current density $|\underline{J}_z(x)|$ at each point in the current sheet [10]. In one reference [10], the magnitude plots are accompanied by plots of the real and imaginary parts as well.

4.1.4 Differential Relationships between $\underline{H}_z(x)$ and $\underline{J}_y(x)$ in the Current Sheet

With the above conceptual picture of the magnetic-field distribution across a winding layer in mind, we return our attention to deriving an analytical expression for the magnetic-field-intensity and current-density distributions. We start this development by writing two of the field equations given in Appendix A in a form that is appropriate for the infinite-current-sheet problem considered here. In doing so, we obtain two equations that interrelate the magnetic field intensity and current density so that we can easily determine the expression for one given an expression for the other. In the next section, we first calculate an expression for the magnetic-field-intensity distribution, and then apply one of the relationships derived in this section to determine the corresponding expression for the current-density distribution.

If we write the Maxwell field expression for Faraday's law from (A.1) as $\nabla \times \mathbf{E} = -\frac{\partial \mathbf{B}}{\partial t}$ in terms of $\mathbf{J}$ and $\mathbf{H}$ by using the relations $\mathbf{B} = \mu_o \mathbf{H}$ and $\mathbf{J} = \sigma \mathbf{E}$, we get

$$\nabla \times \mathbf{J}(x,y,z,t) = -\mu_o \sigma \frac{\partial}{\partial t} \mathbf{H}(x,y,z,t) \tag{4.19}$$

Since we are interested only in the special case of sinusoidal steady-state excitation at an angular frequency ω, we can remove the explicit time dependence from (4.19) by replacing $\mathbf{J}$ and $\mathbf{H}$ with their corresponding phasors. As shown in Appendix A, taking the time derivative of a real quantity is equivalent to multiplying its corresponding phasor by $j\omega$. Therefore, we can rewrite (4.19) in phasor form as

$$\nabla \times \underline{\mathbf{J}}(x,y,z) = -j\omega \mu_o \sigma \underline{\mathbf{H}}(x,y,z) \tag{4.20}$$

which relates the current-density phasor at any point in space to the magnetic-field-intensity phasor at that same point. Finally, using the definition of complex wave number $\underline{k}$ for a good conductor from (4.3) we have

$$\nabla \times \underline{\mathbf{J}}(x,y,z) = -\underline{k}^2 \underline{\mathbf{H}}(x,y,z) \tag{4.21}$$

Similarly, we can write the Maxwell-field expression for Ampere's law given by (A.2) as $\nabla \times \mathbf{H} = \mathbf{J} + \frac{\partial \mathbf{D}}{\partial t}$ in the form

$$\nabla \times \mathbf{H} = \sigma \mathbf{E} + \epsilon_o \frac{\partial \mathbf{E}}{\partial t} \tag{4.22}$$

where the constitutive relations $\mathbf{J} = \sigma \mathbf{E}$ and $\mathbf{D} = \epsilon \mathbf{E}$ have been used. In the sinusoidal steady-state case, we have

$$\nabla \times \underline{\mathbf{H}}(x,y,z) = \sigma \underline{\mathbf{E}}(x,y,z) + j\omega \epsilon_o \underline{\mathbf{E}}(x,y,z) \tag{4.23}$$

Now, if

$$\omega \mu_o \sigma \gg \omega^2 \mu_o \epsilon_o \tag{4.24}$$

as is assumed in deriving the complex wave number $\underline{k}$ for the good conductor in (4.3), then

$$\sigma \gg \omega\epsilon_o \tag{4.25}$$

and we can approximate (4.23) by

$$\begin{aligned} \nabla \times \underline{\mathbf{H}}(x,y,z) &\approx \sigma \underline{\mathbf{E}}(x,y,z) \\ &\approx \underline{\mathbf{J}}(x,y,z) \end{aligned} \tag{4.26}$$

We show in Appendix C that for the one dimensional sinusoidal analysis where the spatial components of $\underline{\mathbf{J}}$ and $\underline{\mathbf{H}}$ are functions only of x, (4.21) and (4.26) reduce to the one-dimensional equations,

$$\frac{\partial \underline{J}_y(x)}{\partial x}\hat{\mathbf{a}}_\mathbf{z} = -\underline{k}^2 \underline{H}_z(x)\hat{\mathbf{a}}_\mathbf{z} \tag{4.27}$$

$$\frac{\partial \underline{H}_z(x)}{\partial x}\hat{\mathbf{a}}_\mathbf{y} = -\underline{J}_y(x)\hat{\mathbf{a}}_\mathbf{y} \tag{4.28}$$

These two results are the one-dimensional field relations that we find useful in solving the diffusion-equation boundary-value problem for the infinite current sheet. Also, (4.27) and (4.28) point out that the current density and the magnetic field intensity are directly related and that we can always express one function in terms of the other. We make use of this fact in the following section where, after solving equation (4.13) for $\underline{H}_z(x)$, we obtain the equation for $\underline{J}_y(x)$ directly by applying the differential relationship (4.28).

4.2 SOLUTION TO FIELD EQUATIONS FOR $\underline{H}_z(x)$ AND $\underline{J}_y(x)$ FOR AN INFINITE CURRENT SHEET

Equation (4.13) is the one-dimensional diffusion equation written in terms of magnetic field intensity. The general solution of an equation of this form is

$$\underline{H}_z(x) = \underline{H}_1 e^{\underline{k}x} + \underline{H}_2 e^{-\underline{k}x} \tag{4.29}$$

where $\underline{H}_1$ and $\underline{H}_2$ are arbitrary quantities yet to be determined; $\underline{H}_1$ and $\underline{H}_2$ are written as underlined symbols to indicate that these quantities are in fact complex numbers representing phasor quantities. We use the boundary values of the magnetic field intensity, $\underline{H}_z(0)$ and $\underline{H}_z(h_{cu})$, to solve this differential equation as follows:

1. Use the boundary values to write two independent expressions involving $\underline{H}_1$ and $\underline{H}_2$. Evaluating (4.29) at $x = 0$ gives

$$\underline{H}_z(0) = \underline{H}_1 + \underline{H}_2 \tag{4.30}$$

and at $x = h_{cu}$ gives

$$\underline{H}_z(h_{cu}) = \underline{H}_1 e^{\underline{k}h_{cu}} + \underline{H}_2 e^{-\underline{k}h_{cu}} \tag{4.31}$$

2. Solve simultaneously for $\underline{H}_1$ and $\underline{H}_2$. Using (4.30) to substitute for $\underline{H}_2$ in (4.31) gives

$$\underline{H}_z(h_{cu}) = \underline{H}_1 e^{\underline{k}h_{cu}} + \left[\underline{H}_z(0) - \underline{H}_1\right] e^{-\underline{k}h_{cu}}$$

or,

$$\underline{H}_1 = \frac{\underline{H}_z(h_{cu}) - \underline{H}_z(0)e^{-\underline{k}h_{cu}}}{e^{\underline{k}h_{cu}} - e^{-\underline{k}h_{cu}}} \tag{4.32}$$

and a second use of (4.30) gives

$$\underline{H}_2 = \frac{\underline{H}_z(0)e^{\underline{k}h_{cu}} - \underline{H}_z(h_{cu})}{e^{\underline{k}h_{cu}} - e^{-\underline{k}h_{cu}}} \tag{4.33}$$

3. Substitute (4.32) and (4.33) back into the general solution (4.29) to give

$$\begin{aligned}\underline{H}_z(x) &= \frac{1}{e^{\underline{k}h_{cu}} - e^{-\underline{k}h_{cu}}}\Big[\underline{H}_z(h_{cu})e^{\underline{k}x} - \underline{H}_z(0)e^{\underline{k}(x-h_{cu})} \\ &\qquad + \underline{H}_z(0)e^{-\underline{k}(x-h_{cu})} - \underline{H}_z(h_{cu})e^{-\underline{k}x}\Big] \\ &= \frac{1}{e^{\underline{k}h_{cu}} - e^{-\underline{k}h_{cu}}}\Big[\underline{H}_z(h_{cu})\left(e^{\underline{k}x} - e^{-\underline{k}x}\right) \\ &\qquad - \underline{H}_z(0)\left(e^{\underline{k}(x-h_{cu})} - e^{-\underline{k}(x-h_{cu})}\right)\Big]\end{aligned} \tag{4.34}$$

4. Use the identity

$$\sinh\theta = \frac{e^{\theta} - e^{-\theta}}{2} \tag{4.35}$$

to rewrite equation (4.34) as

$$\boxed{\underline{H}_z(x) = \frac{1}{\sinh \underline{k}h_{cu}}\left[\underline{H}_z(h_{cu})\sinh \underline{k}x + \underline{H}_z(0)\sinh \underline{k}(h_{cu} - x)\right]} \tag{4.36}$$

5. Calculate $\underline{J}_y(x)$ by applying the differential relationship (4.28) to our solution for $\underline{H}_z(x)$ in (4.36). We can rewrite equation(4.28) as

$$\underline{J}_y(x) = -\frac{\partial \underline{H}_z(x)}{\partial x} \tag{4.37}$$

and then apply this result by differentiating (4.36) with respect to x to yield

$$\frac{\partial \underline{H}_z(x)}{\partial x} = \frac{\underline{k}}{\sinh \underline{k}h_{cu}}\left[\underline{H}_z(h_{cu})\cosh \underline{k}x - \underline{H}_z(0)\cosh \underline{k}(h_{cu} - x)\right] \tag{4.38}$$

so that

$$\boxed{\underline{J}_y(x) = \frac{-\underline{k}}{\sinh \underline{k}h_{cu}}\left[\underline{H}_z(h_{cu})\cosh \underline{k}x - \underline{H}_z(0)\cosh \underline{k}(h_{cu}-x)\right]} \tag{4.39}$$

The above equation (4.39) for current density $\underline{J}_y(x)$ and equation (4.36) for magnetic field intensity $\underline{H}_z(x)$ are the solutions we are seeking. Based only on the values of $\underline{H}_z(0)$ and $\underline{H}_z(h_{cu})$, the thickness of the winding layer h_{cu}, and the angular frequency ω of the sinusoidal excitation, we can now calculate the value of the current density and the magnetic field intensity at any point within a winding layer. In addition, equations (4.36) and (4.39) highlight the fact that the distributions of the magnetic field intensity and the current density across the current sheet actually result from the superposition of two independent effects. That is, the two boundary magnetic fields $\underline{H}_z(0)$ and $\underline{H}_z(h_{cu})$ have mathematically equivalent effects on the distributions of $\underline{H}_z(x)$ and $\underline{J}_y(x)$, except, of course, that the magnetic field $\underline{H}_z(0)$ dominates the total magnetic field in the region near the surface at $x = 0$ while the magnetic field $\underline{H}_z(h_{cu})$ dominates the total magnetic field in the region near the surface at $x = h_{cu}$. This characteristic of the solutions is discussed in greater detail in Section 4.3.2 as we explore more thoroughly the meaning of equations (4.36) and (4.39).

Before beginning such a detailed investigation, however, we first introduce some new notation that proves useful later in our analysis of energy storage and power loss. For convenience, we define a new variable χ such that

$$\chi = \begin{cases} x & \text{if } |\underline{H}_z(x=h_{cu})| \geq |\underline{H}_z(x=0)| \\ h_{cu}-x & \text{if } |\underline{H}_z(x=h_{cu})| < |\underline{H}_z(x=0)| \end{cases} \tag{4.40}$$

which means that we always have $\chi = h_{cu}$ at the surface which has the *larger* of the two boundary magnetic fields, and $\chi = 0$ at the surface which has the *smaller* of the two boundary magnetic fields. In other words, regardless of the relative magnitudes of the boundary magnetic fields, we have now defined χ such that

$$|\underline{H}_z(\chi=h_{cu})| \geq |\underline{H}_z(\chi=0)| \tag{4.41}$$

If we rewrite our solution for magnetic field intensity (4.36) in terms of χ, we obtain

$$\underline{H}_z(\chi) = \frac{1}{\sinh \underline{k}h_{cu}}\left[\underline{H}_z(\chi=h_{cu})\sinh \underline{k}\chi + \underline{H}_z(\chi=0)\sinh \underline{k}(h_{cu}-\chi)\right] \tag{4.42}$$

and factoring out the term $\underline{H}_z(\chi=h_{cu})$ gives

$$\underline{H}_z(\chi) = \frac{\underline{H}_z(\chi=h_{cu})}{\sinh \underline{k}h_{cu}}\left[\sinh \underline{k}\chi + \frac{\underline{H}_z(\chi=0)}{\underline{H}_z(\chi=h_{cu})}\sinh \underline{k}(h_{cu}-\chi)\right] \tag{4.43}$$

The form of equation (4.43) can be simplified somewhat by introducing the boundary-condition ratio $\underline{\Gamma} = \alpha + j\beta$ as

$$\underline{\Gamma} = \frac{\underline{H}_z(\chi = 0)}{\underline{H}_z(\chi = h_{cu})} \tag{4.44}$$

where

$$\alpha = \mathrm{Re}(\underline{\Gamma}) \tag{4.45}$$

$$\beta = \mathrm{Im}(\underline{\Gamma}) \tag{4.46}$$

and because of the way in which we define χ, we know that

$$0 \leq |\underline{\Gamma}| \leq 1 \tag{4.47}$$

for all possible choices of boundary magnetic fields, except of course for the trivial case where $|\underline{H}_z(0)|$ and $|\underline{H}_z(h_{cu})|$ are both equal to zero. In Section 4.1.3 above, we write $\underline{H}_z(0)$ and $\underline{H}_z(h_{cu})$ in magnitude and phase notation. We can use these expressions here to write

$$\begin{aligned}
\alpha &= \mathrm{Re}(\underline{\Gamma}) = \mathrm{Re}\left[\frac{\underline{H}_z(\chi = 0)}{\underline{H}_z(\chi = h_{cu})}\right] \\
&= \mathrm{Re}\left[\frac{H_z(\chi = 0)\angle\theta_{\chi=0}}{H_z(\chi = h_{cu})\angle\theta_{\chi=h_{cu}}}\right] \\
&= \frac{H_z(\chi = 0)}{H_z(\chi = h_{cu})}\cos(\theta_{\chi=0} - \theta_{\chi=h_{cu}})
\end{aligned} \tag{4.48}$$

$$\begin{aligned}
\beta &= \mathrm{Im}(\underline{\Gamma}) = \mathrm{Im}\left[\frac{\underline{H}_z(\chi = 0)}{\underline{H}_z(\chi = h_{cu})}\right] \\
&= \mathrm{Im}\left[\frac{H_z(\chi = 0)\angle\theta_{\chi=0}}{H_z(\chi = h_{cu})\angle\theta_{\chi=h_{cu}}}\right] \\
&= \frac{H_z(\chi = 0)}{H_z(\chi = h_{cu})}\sin(\theta_{\chi=0} - \theta_{\chi=h_{cu}})
\end{aligned} \tag{4.49}$$

where $\theta_{\chi=0}$ and $\theta_{\chi=h_{cu}}$ are understood to be the arguments of the magnetic field intensity phasor at $\chi = 0$ and $\chi = h_{cu}$, respectively. Finally, we may rewrite (4.43) to obtain an expression for the magnetic field intensity phasor in terms of the real component α and the imaginary component β of $\underline{\Gamma}$.

$$\boxed{\underline{H}_z(\chi) = \frac{\underline{H}_z(\chi = h_{cu})}{\sinh \underline{k}h_{cu}}\left[\sinh \underline{k}\chi + (\alpha + j\beta)\sinh \underline{k}(h_{cu} - \chi)\right]} \tag{4.50}$$

The corresponding equation for current density is

$$\underline{J}_y(X) = \frac{(-1)^{\varepsilon}\, \underline{k}\, \underline{H}_z(X = h_{cu})}{\sinh \underline{k} h_{cu}} \Big[\cosh \underline{k} X - (\alpha + j\beta) \cosh \underline{k}(h_{cu} - X)\Big] \tag{4.51}$$

where

$$\varepsilon = \begin{cases} 1 & \text{if } |\underline{H}_z(x = h_{cu})| \geq |\underline{H}_z(x = 0)| \\ 0 & \text{if } |\underline{H}_z(x = h_{cu})| < |\underline{H}_z(x = 0)| \end{cases} \tag{4.52}$$

so that the sign of equation (4.51) changes depending upon which case in equation (4.52) applies.

Equation (4.51) is the phasor expression for the current density function in the infinite current sheet subject to the given boundary conditions, and is equivalent to the result given by Perry [13] in his equation (8b). In Chapter 7, Part II of this report, the equivalence of these two equations is shown. Furthermore, except for minor differences in symbols, equation (4.51) is identical to equation (A-15) in the appendix of the paper by Vandelac and Ziogas [19].

Equations (4.50) and (4.51) are key equations. They are important in their own right because they give the phasor expressions for the sinusoidal steady-state magnetic field intensity and the current-density distributions at an arbitrary height X in a current sheet of height h_{cu} when a sinusoidal magnetic field of $\underline{H}_z(X = 0)$ is present on one side and a field of $\underline{H}_z(X = h_{cu})$ is on the other. They are also important because they lead, as shown in Section 4.5, to the calculation of energy storage and power loss within the winding structure of multi-winding transformers, which in turn can lead to the determination of the parameter values for an equivalent circuit, which is our ultimate goal.

4.3 GRAPHICAL ILLUSTRATIONS OF $\underline{H}_z(x)$ AND $\underline{J}_y(x)$ IN AN INFINITE CURRENT SHEET

Before continuing with the application of equations (4.50) and (4.51) to the winding space of a transformer, we first explore more thoroughly the meaning of the solutions for $\underline{H}_z(x)$ and $\underline{J}_y(x)$ through an extensive array of illustrations. In this section, we define specific numerical examples involving both single-layer and four-layer structures and, using the equations developed in the above sections, we provide a large number of plots and data tables that illuminate many of the important aspects of the magnetic-field-intensity and current-density distributions. Although the forms of equations (4.50) and (4.51) are well-defined and appropriate for their application in Section 4.5, we find that equations (4.36) and (4.39) are, in their simplicity, better-suited for the purposes of this Section. As shown in the development of Section 4.2, equations (4.50) and (4.51) really contain the same information as (4.36) and (4.39), although (4.50) and (4.51) have a slightly more generalized form.

4.3.1 Plots of Phasor Magnitudes for a Single-Layer Example

Plots of the magnitudes of the phasors of equations (4.36) and (4.39) reveal the impact that excitation frequency has on the current-density and magnetic-field-intensity distributions in a current sheet. Figure 4.2 shows the dramatic changes in magnitude of the phasor magnetic-field-intensity distribution over the height of a winding layer that take place as the excitation frequency increases. This plot represents the distribution of the magnitude $|\underline{H}_z(x)|$ of the magnetic-field-intensity phasor across a single layer given a particular set of boundary conditions. Figure 4.3 shows the corresponding variation of the magnitude of the current-density phasor in the same layer.

For this example, the magnetic-field-intensity boundary conditions are chosen as $\underline{H}_z(0) = 1\angle 0°$ and $\underline{H}_z(h_{cu}) = 2\angle 0°$. The plots in Figs. 4.2 and 4.3 represent the variation of $|\underline{H}_z(x)|$ and $|\underline{J}_y(x)|$ in an arbitrarily chosen winding layer of height $h_{cu} = 7.0 \times 10^{-4}$ meters over a frequency range of one kilohertz to one megahertz. At 1 kHz, the magnitude of the magnetic field intensity varies approximately linearly from one layer surface to the other, and the magnitude of the current density is approximately constant at a value of 1.43 kA/m^2 over the 0.7 mm height of the winding. At higher frequencies, the magnitude of the magnetic field intensity decreases substantially away from the layer boundaries, but remains constant over frequency at the two surfaces of the layer—as it must since the boundary conditions of the problem are the same for all these four frequencies. Also, the magnitude of the current density increases near the surfaces of the winding layer and drops to approximately zero in the interior regions. At 1 MHz, the magnitude of the current density at the surface where the magnetic-field-intensity magnitude is 1 A-t/m rises to 20.5 kA/m^2, and it reaches 41.0 kA/m^2 at the surface where the magnetic-field-intensity is 2 A-t/m in magnitude.

4.3.2 Plots of Phasors for a Single-Layer Example

In Section 4.3.1, we show the result of an example involving a single layer for which we plot the magnitudes of the magnetic-field-intensity and current-density phasors found in equations (4.36) and (4.39). These plots are shown in Figs. 4.2 and 4.3 for a range of excitation frequencies. In interpreting these two figures, however, we must be careful to remember that they are only *magnitude* plots, and therefore do not contain any information on the phase angles that are associated with $\underline{H}_z(x)$ and $\underline{J}_y(x)$. One way to incorporate this information is to accompany each of the magnitude plots with a corresponding phase plot, or similarly, with plots of the corresponding real and imaginary parts of the phasors. Magnitude plots such as those in Figs. 4.2 and 4.3, together with plots of the corresponding real and imaginary parts of the phasors are found in [9]. Although this approach does illustrate all of the information contained in the phasors of equations (4.36) and (4.39), it is generally quite difficult to gain physical insight into these solutions when the magnitude and phase information appears in two or more separate plots. To remedy this, we might wish to show the phasors of equations (4.36) and (4.39) at equally spaced intervals across the layer. Such a representation, however,

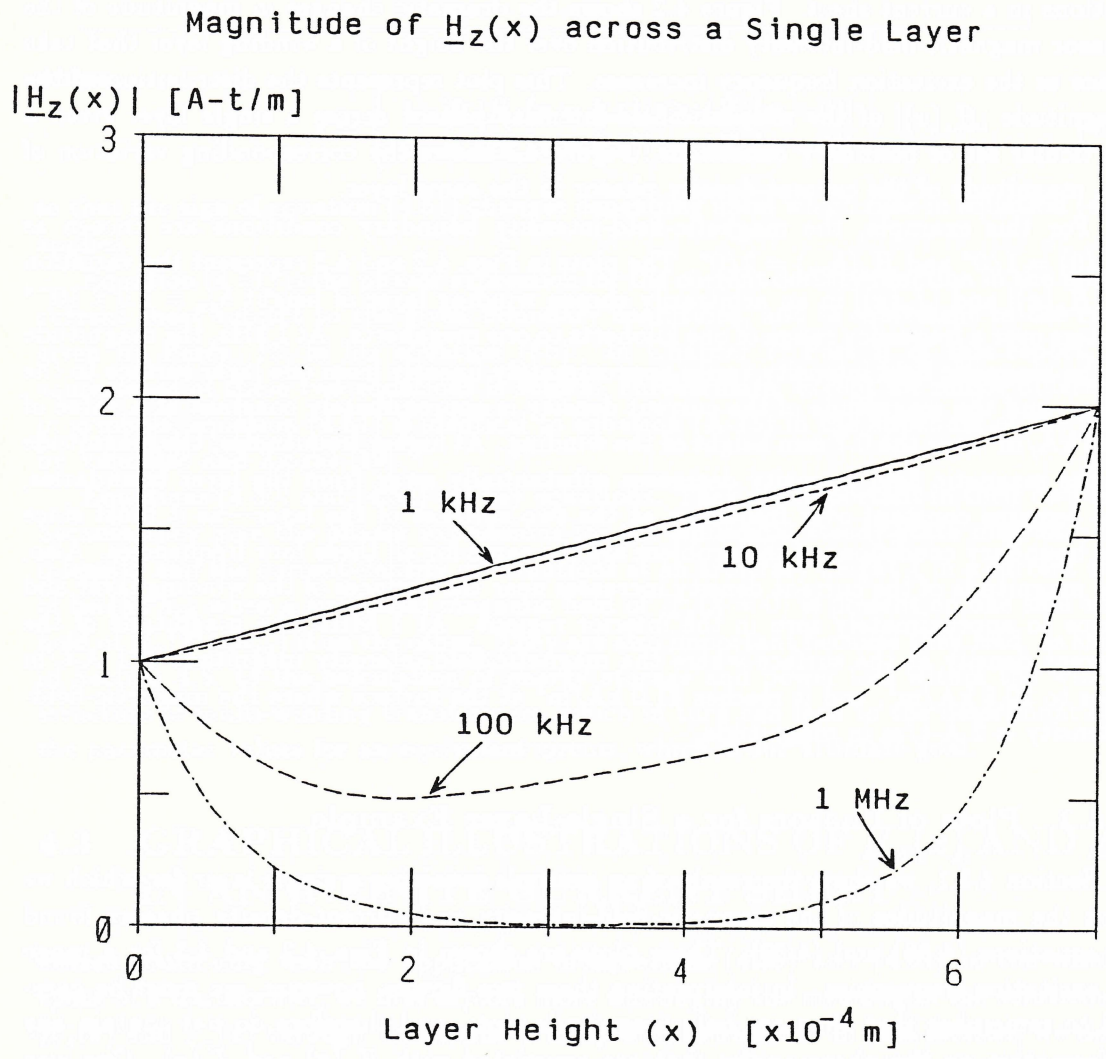


Figure 4.2: Plot of the magnitude of the magnetic-field-intensity phasor $\underline{H}_z(x)$ in an infinite current sheet at 1 kHz, 10 kHz, 100 kHz, and 1 MHz.

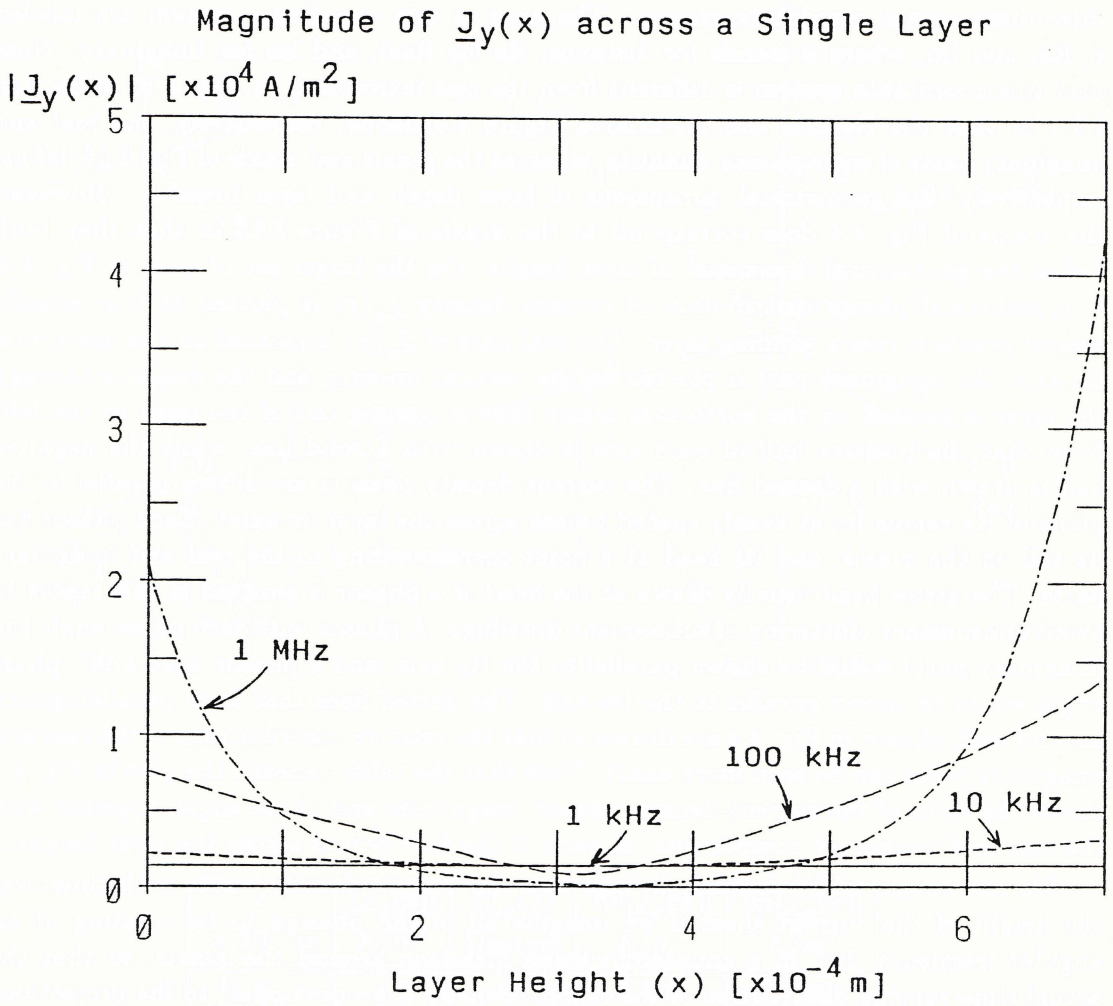


Figure 4.3: Plot of the magnitude of the current-density phasor $\underline{J}_y(x)$ in an infinite current sheet at excitation frequencies of 1 kHz, 10 kHz, 100 kHz, and 1 MHz.

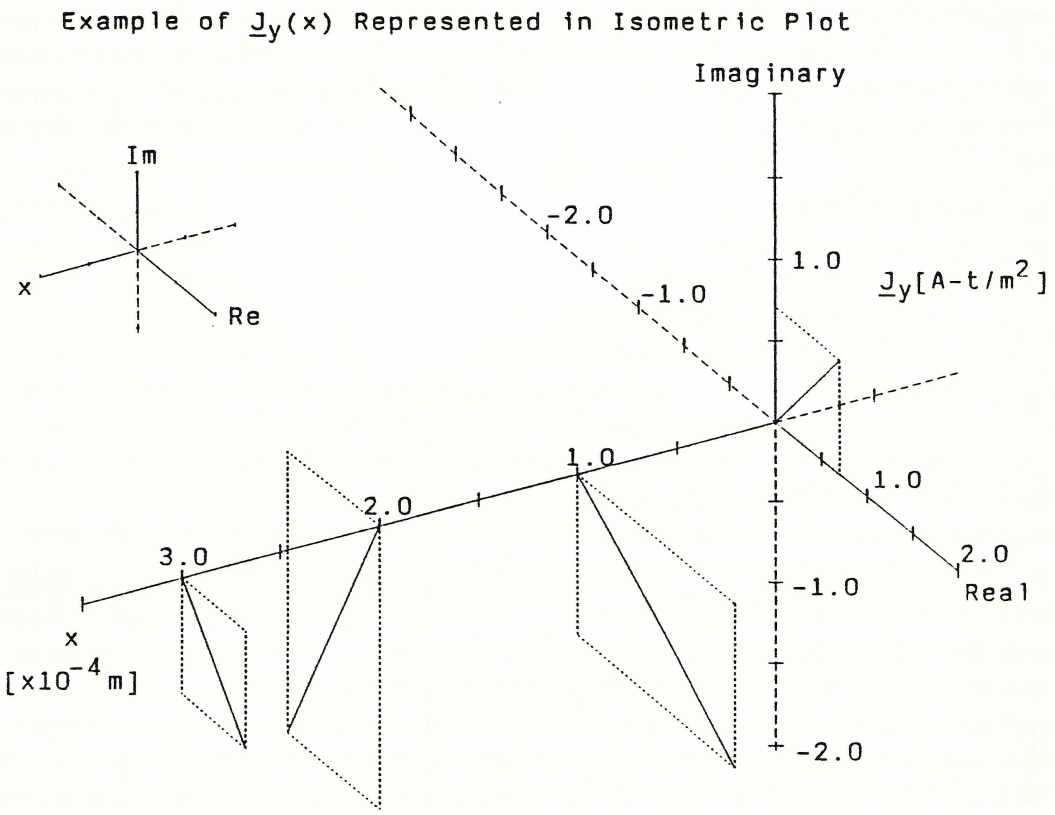
needs to be three-dimensional, since each phasor has two components (real and imaginary) and the location of each phasor across the layer height requires a third dimension. Although a geometrical model is the most appropriate solution, we can also represent this information in an isometric plot.

As an introduction to the concept of plotting phasors in three dimensions, we first look at a simple example. The upper left corner of Fig. 4.4 shows for reference a right-hand three-dimensional coordinate system. The axes of this coordinate system are labeled x, Re, and Im, where x stands for distance, Re for Real, and Im for Imaginary. Note that this coordinate system is different from the one introduced in Fig. 3.15 of Section 3.3.1 in that the Re-axis and Im-axis of Figure 4.4 define, respectively, the real and imaginary parts of some phasor quantity, whereas the y-axis and z-axis of Fig. 3.15 define, respectively, the geometrical dimensions of layer depth and layer breadth. However, the x-axis of Fig. 4.4 *does* correspond to the x-axis of Figure 3.15 in that they both define the geometrical dimension of layer height. On the larger set of axes in Fig. 4.4, a hypothetical phasor distribution of current density $\underline{J}_y(x)$ is plotted at four equally spaced points across a winding layer. The real part of $\underline{J}_y(x)$ is plotted on the horizontal Re-axis, the imaginary part is plotted on the vertical Im-axis, and the distance through the layer is plotted on the horizontal x-axis that is coming out of the page to the left. Note that the positive half of each axis is drawn with a solid line, while the negative half is drawn with a dashed line. The current density phasors are drawn parallel to the plane of Re versus Im at evenly spaced points across the layer (x-axis). Each phasor has its tail on the x-axis, and its head at a point corresponding to the real and imaginary parts. The arrow head usually drawn at the head of a phasor is omitted in this report to avoid unnecessary cluttering of subsequent drawings. A phasor with zero phase angle (no imaginary part) would be shown parallel to the Re-axis, and a phasor with a 90° phase angle would be shown parallel to the Im-axis. The dotted lines that form parallelograms around each phasor in Fig. 4.4 are drawn so that the relative contributions of the real and imaginary parts can be seen more easily. Note that the table beneath the plot in Fig. 4.4 shows the value of the current-density phasor, magnitude and phase angle, together with the real and imaginary components, at each of the four points across the layer height.

We can obtain additional insight into how the current density varies with time over the height of the current sheet if we imagine all of the phasors to be rotating at an angular frequency $2\pi f$ in a counterclockwise direction around the x-axis, so that the actual time-varying distribution of the current density is proportional[2] to the projections of the phasors onto the plane of x versus Re. Illustrations of the results of such a process are shown later in this section.

In Section 4.3.1 we plot the magnitudes of the phasors $\underline{H}_z(x)$ and $\underline{J}_y(x)$ for a particular numerical example in Figs 4.2 and 4.3. We now return to this same numerical example, but instead of plotting the magnitudes of the phasors, we now plot the phasors

[2]We have defined the magnitude of the phasor as the rms value of the actual sinusoid. Therefore, the actual sinusoidal waveform can be recovered from the rotating phasor by multiplying the real projection of the phasor by $\sqrt{2}$.



x $\times 10^{-4}$m	$\lvert\underline{J}_y(x)\rvert$ A/m^2	$/\underline{J}_y(x)$ Degrees	Re$[\underline{J}_y(x)]$ A/m^2	Im$[\underline{J}_y(x)]$ A/m^2
0	1.0	45°	0.707	0.707
1	2.0	−30°	1.732	−1.000
2	2.0	−120°	−1.000	−1.732
3	1.0	−45°	0.707	−0.707

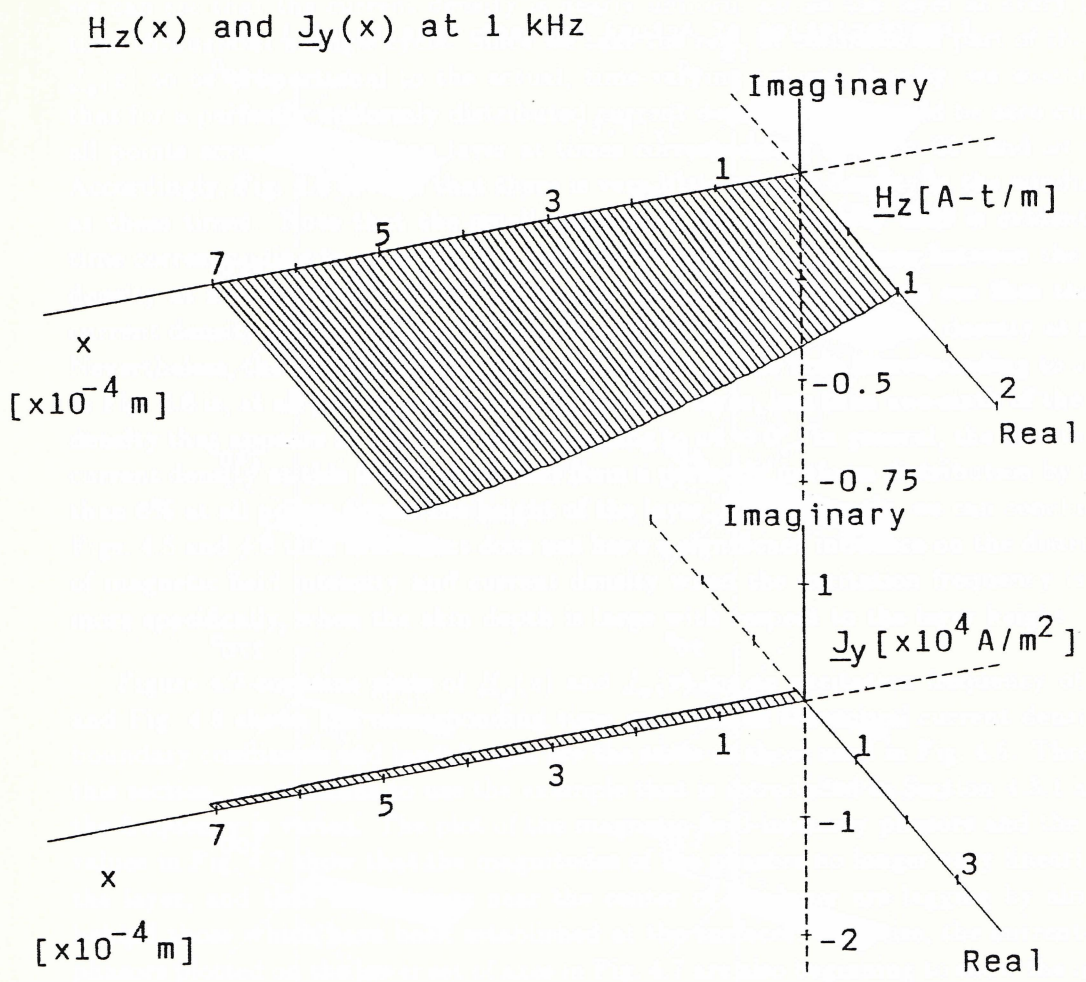
Figure 4.4: Plot of hypothetical current-density phasor $\underline{J}_y(x)$ at four points across the winding layer.

themselves. Figure 4.5 consists of plots of these $\underline{H}_z(x)$ and $\underline{J}_y(x)$ phasors as a function of layer height x at 1 kHz. The magnetic-field-intensity phasors at the boundaries are again given as $\underline{H}_z(0) = 1\angle 0°$ and $\underline{H}_z(h_{cu}) = 2\angle 0°$, and the height of the copper current sheet is given as $h_{cu} = 7.0 \times 10^{-4}$ m. Our arbitrary choice of zero phase angle for the phasors $\underline{H}_z(0)$ and of $\underline{H}_z(h_{cu})$ simply means that the magnetic field at $x = 0$ is oscillating in phase with the field at $x = h_{cu}$. In addition to the plots of the magnetic-field-intensity and current-density phasors, Fig. 4.5 also contains a data table that provides the values for the $\underline{H}_z(x)$ and $\underline{J}_y(x)$ phasors at eight equally spaced points across the layer height.

The upper set of three-dimensional axes in Fig. 4.5 shows the variation of the magnetic-field-intensity phasors across the height of the layer calculated using equation (4.36). Note that the heads of the phasors are all connected with a single, solid line to enhance the appearance of a surface. The plot and associated tabular values of $\underline{H}_z(x)$ in Fig. 4.5 reveals that the magnitude of the magnetic field at 1 kHz varies linearly within two significant figures across the layer. Also, since none of the phasors differ by more than 2° from being parallel to the real axis, we know that the magnetic field at every point across the layer must be oscillating very nearly in phase with the magnetic field at the surfaces. This simple linear distribution of magnetic field intensity is similar to the result obtained in Section 3.1.2.1 for the case of a uniform dc current except, of course, that the distribution obtained from the phasors in Fig. 4.5 is varying sinusoidally with time.

The current-density phasors associated with these magnetic-field-intensity phasors have been calculated using equation (4.39) and the results are plotted on the lower set of axes in Fig. 4.5. Note that on this plot the scaling on the real and imaginary axes has been changed from the upper plot to accommodate the current-density phasors, while the scaling on the x-axis is the same as that on the upper set of axes. The plot of the current-density phasors and the table of values in Fig. 4.5 reveal that the magnitude of $\underline{J}_y(x)$ remains essentially constant across the layer while the phase angle varies by less than $\pm 10°$. Therefore, we conclude that the actual current density is almost uniform across the layer and varies sinusoidally with time. Once again, this result agrees rather closely with the dc field calculation of Section 3.1.2.1 which shows that a uniform current is associated with a linearly distributed magnetic field intensity.

We mention above that the actual distributions of the magnetic field intensity and current density are proportional to the real projections of the phasor distributions in Fig. 4.5. We can, therefore, see how these distributions vary with time by imagining that all of the phasors are rotating in a counterclockwise direction about the x-axis with an angular frequency ω. This principle can be illustrated by looking at a time sequence of such real projections. Figure 4.6, which is a companion piece to Fig. 4.5, shows the actual distribution of current density across the winding layer for an excitation frequency of 1 kHz at various points in time throughout one cycle. Each small plot is labeled with an angle measure, corresponding to the angular measure of time ωt. The plots divide a single period of oscillation into twelve equal intervals, and they are ordered in time from top to bottom down the left column, and then down the right. From Figure 4.6,



x $\times 10^{-4}$m	$\underline{H}_z(x)$ A-t/m	$\underline{J}_y(x)$ $\times 10^4$A/m^2	x $\times 10^{-4}$m	$\underline{H}_z(x)$ A-t/m	$\underline{J}_y(x)$ $\times 10^4$A/m^2
0	$1.00\angle 0.00°$	$0.144\angle 172.18°$	4	$1.57\angle -1.40°$	$0.143\angle 180.80°$
1	$1.14\angle -0.87°$	$0.143\angle 173.96°$	5	$1.71\angle -1.10°$	$0.143\angle 183.55°$
2	$1.29\angle -1.34°$	$0.143\angle 175.99°$	6	$1.86\angle -0.63°$	$0.144\angle 186.53°$
3	$1.43\angle -1.49°$	$0.143\angle 178.28°$	7	$2.00\angle 0.00°$	$0.145\angle 189.70°$

Figure 4.5: Plots of the magnetic-field-intensity phasor $\underline{H}_z(x)$ and the current-density phasor $\underline{J}_y(x)$ at an excitation frequency of 1 kHz.

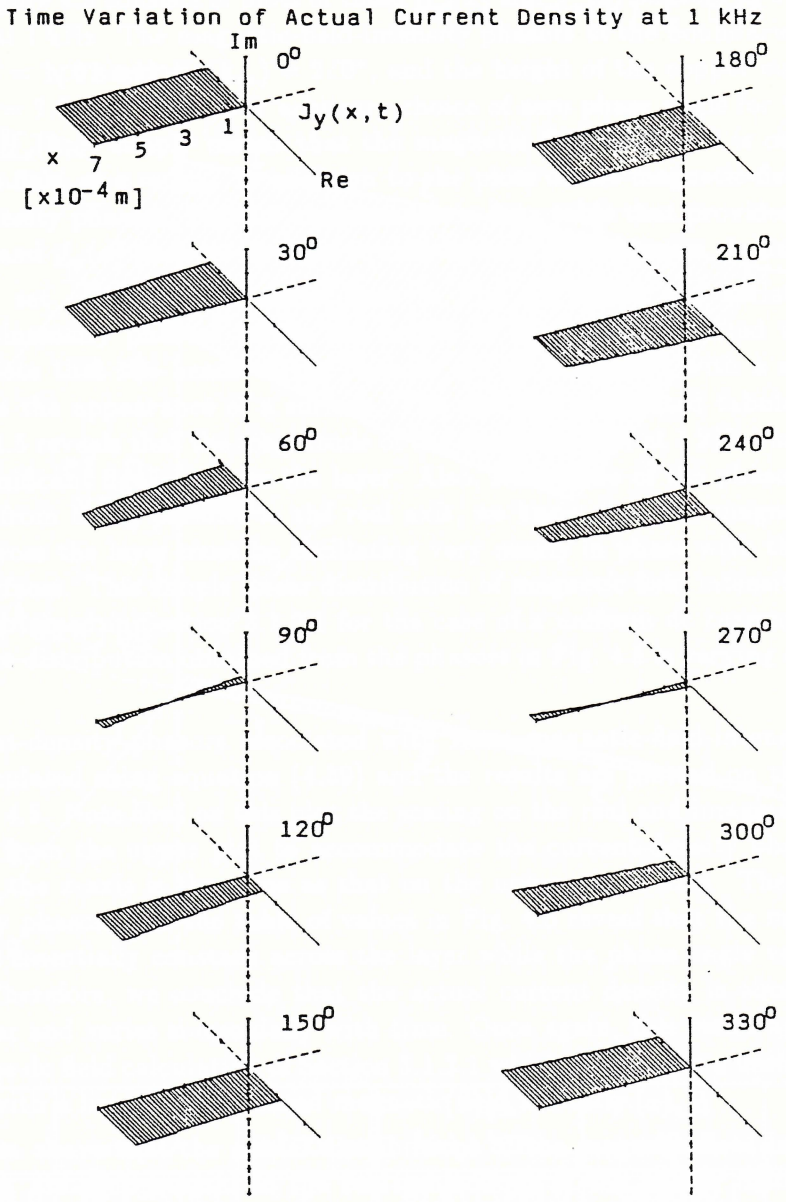
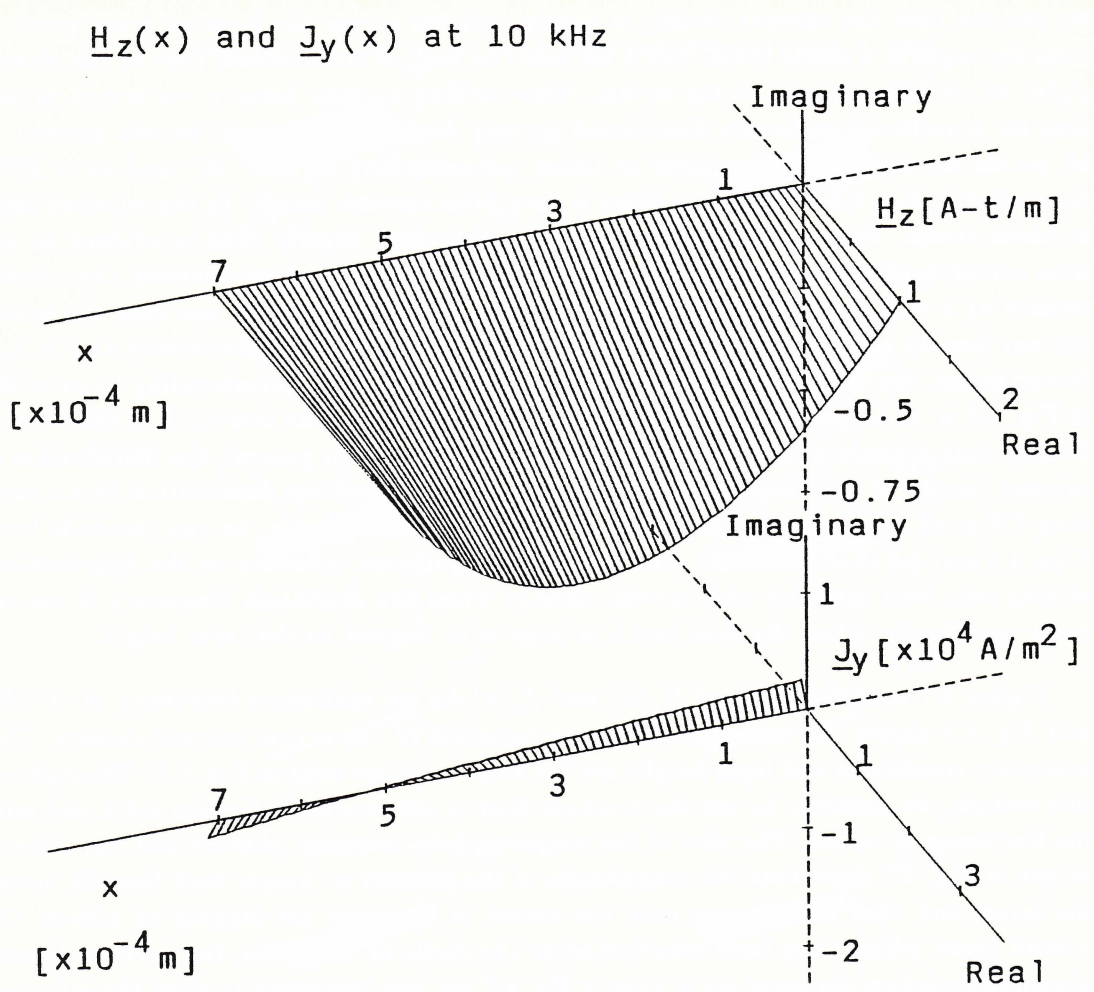


Figure 4.6: Plots of the actual current-density distribution at twelve different instants of ωt spaced evenly throughout a single cycle of oscillation at 1 kHz. The progression advances from top to bottom down the left column and then down the right.

we can see that the current density is nearly uniform across the layer at every point in time throughout a single cycle. Since we take the real, or cosinusoidal part of the phasor $\underline{J}_y(x)$ to be proportional to the actual, time-varying current density, we would expect that for a perfectly uniformly distributed current density there would be zero current at all points across the winding layer at times corresponding to $\omega t = 90°$ and $\omega t = 270°$. Accordingly, Fig. 4.6 reveals that there is very little current density in the winding layer at these times. Note that the small amount of current density that is evident at the time corresponding to $\omega t = 90°$ is a result of the difference in phase between the current density at $x = 0$ and at $x = h_{cu}$. From the table of Fig. 4.5, we can see that the actual current density at $x = 0$ is lagging in phase 17.52° behind the current density at $x = h_{cu}$. Nevertheless, the current density that does appear at the time corresponding to $\omega t = 90°$ in Fig. 4.6 is, at all points across the height of the layer, less than one-sixth of the current density that appears at the time corresponding to $\omega t = 0°$. In general, the distribution of current density at this frequency differs from a perfectly uniform distribution by no more than 6% at all points across the height of the layer. Consequently, we can conclude from Figs. 4.5 and 4.6 that skin effect does not have a significant influence on the distributions of magnetic field intensity and current density when the excitation frequency is low or, more specifically, when the skin depth is large with respect to the layer height.

Figure 4.7 contains plots of $\underline{H}_z(x)$ and $\underline{J}_y(x)$ for an excitation frequency of 10 kHz and Fig. 4.8 shows the corresponding time variation of the actual current density. The boundary conditions and layer height are the same as those used in Fig. 4.5. Throughout this section, we continue to use the example that is introduced in Section 4.3.1 and only the frequency is varied. The plot of the magnetic-field-intensity phasors and the table of values in Fig. 4.7 show that the magnitudes of the phasors no longer vary linearly across the layer, and that the phasors near the center of the layer are lagging by almost 15° behind those which have been established at the surfaces. Likewise, the current-density phasors plotted on the lower set of axes in Fig. 4.7 are also beginning to show the influence of skin effect. There is now a noticeable increase in the magnitude of the current-density phasors near the surfaces of the layer, by about 50% over that at 1 kHz at $x = 0$ and by about 100% at $x = h_{cu}$, while the magnitude near the center has decreased slightly below that at 1 kHz. More importantly, this plot reveals that there is now a substantial phase difference of 113° between the current-density phasors at $x = 0$ and at $x = h_{cu}$. It appears as though the small ribbon of current density that is seen in the lower set of axes in Fig. 4.5 has been twisted and widened at the ends to give us the distribution of Fig. 4.7. As a result of this phase difference, there is now an appreciable portion of a cycle during which the actual current flows in an opposite direction on one side of the current sheet than it does on the other. This can be seen more clearly in Fig. 4.8, which shows the actual current-density distribution at twelve instants of time during a single cycle of oscillation, at an excitation frequency of 10 kHz. This figure reveals, for example, that during the interval $60° \leq \omega t \leq 150°$ the current near the surface at $x = 0$ is flowing in the $-y$-direction, while the current near the surface at $x = h_{cu}$ is flowing in the $+y$-direction.



x $\times 10^{-4}$m	$\underline{H}_z(x)$ A-t/m	$\underline{J}_y(x)$ $\times 10^4$A/m^2	x $\times 10^{-4}$m	$\underline{H}_z(x)$ A-t/m	$\underline{J}_y(x)$ $\times 10^4$A/m^2
0	$1.00\angle 0.00°$	$0.217\angle 119.70°$	4	$1.54\angle -13.82°$	$0.151\angle 186.99°$
1	$1.12\angle -8.55°$	$0.182\angle 127.62°$	5	$1.68\angle -10.86°$	$0.185\angle 207.14°$
2	$1.26\angle -13.19°$	$0.154\angle 141.74°$	6	$1.83\angle -6.16°$	$0.236\angle 221.84°$
3	$1.40\angle -14.74°$	$0.141\angle 162.94°$	7	$2.00\angle 0.00°$	$0.298\angle 232.84°$

Figure 4.7: Plots of the magnetic-field-intensity phasor $\underline{H}_z(x)$ and the current-density phasor $\underline{J}_y(x)$ at an excitation frequency of 10 kHz.

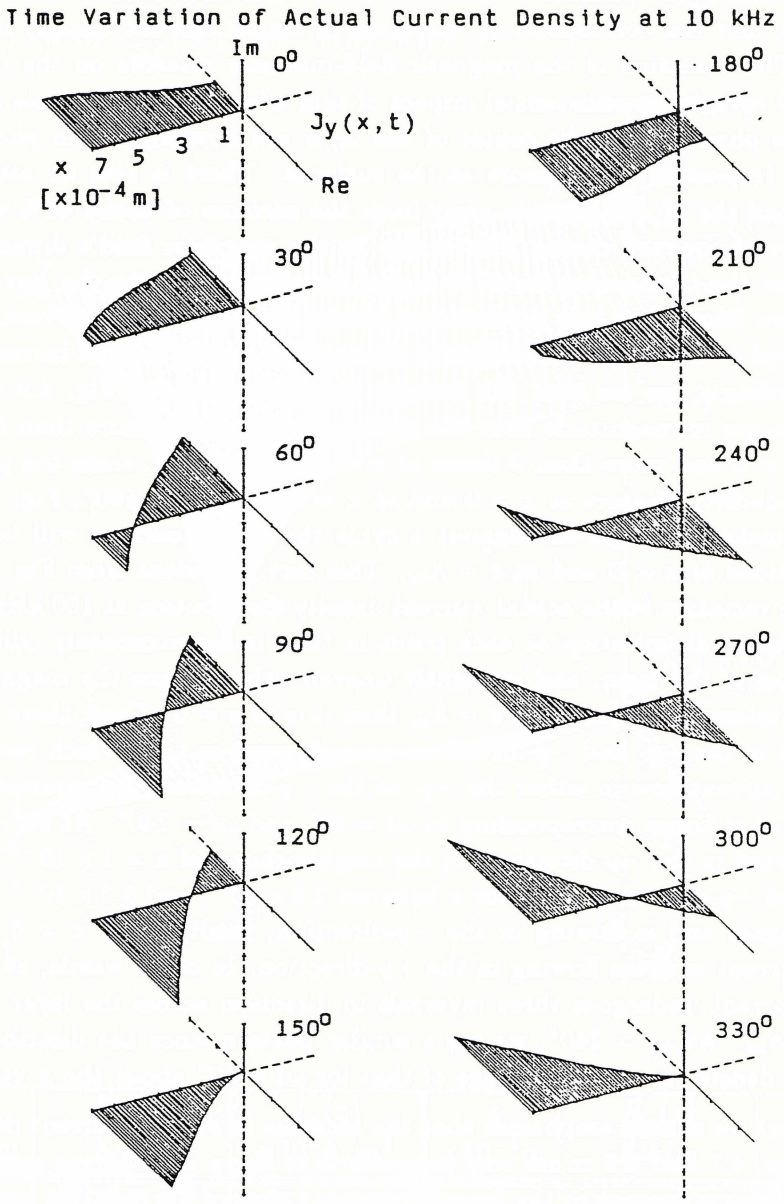
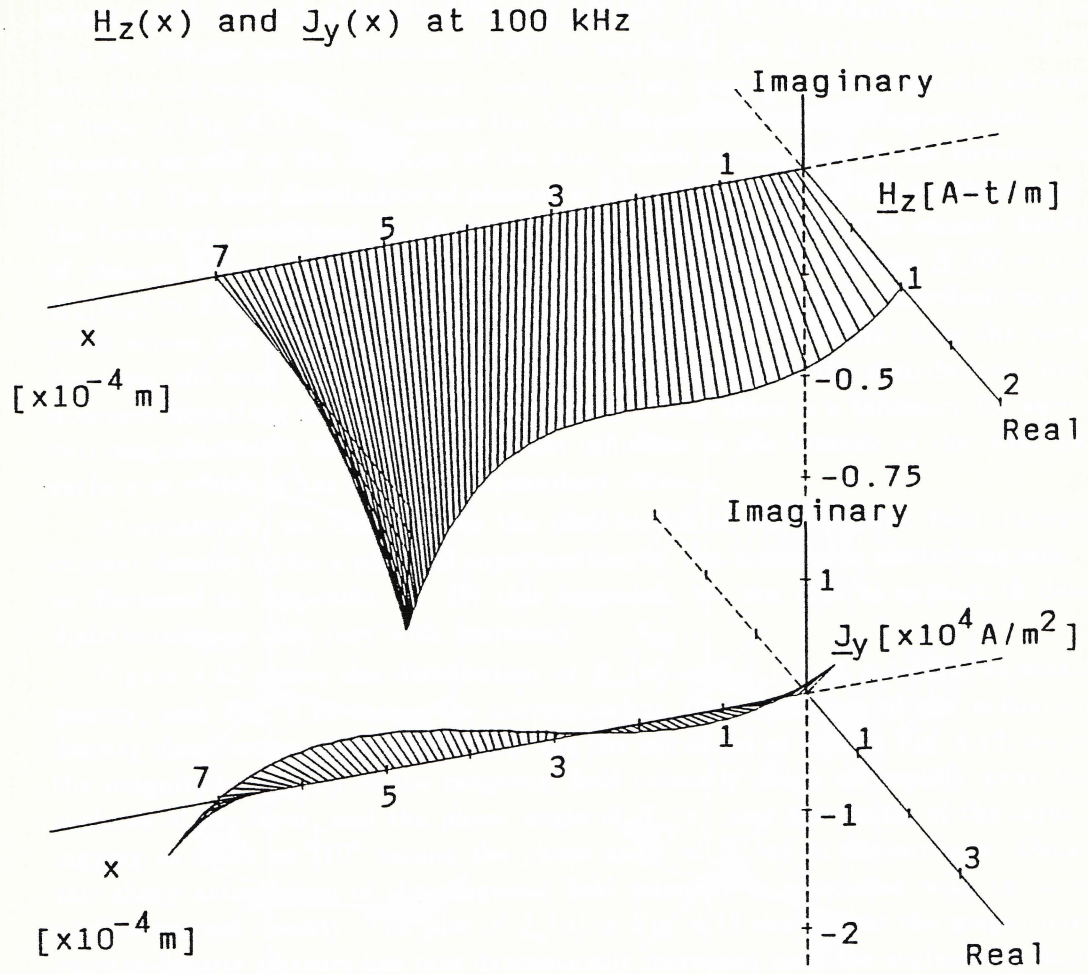


Figure 4.8: Plots of the actual current-density distribution at twelve different instants of ωt spaced evenly throughout a single cycle of oscillation at 10 kHz. The progression advances from top to bottom down the left column and then down the right.

The $\underline{H}_z(x)$ and $\underline{J}_y(x)$ phasors for the case of 100-kHz excitation frequency are plotted in Fig. 4.9, and the corresponding variation of actual current density is plotted in Figure 4.10. The variation of the magnetic-field-intensity phasors on the upper set of axes in Fig. 4.9 reveals the substantial impact of skin effect on this example layer at this frequency. The phasors near the center of the layer are now lagging in phase by more than 90^o with respect to the phasors at the surfaces. There is also an attenuation in the magnitude of the $\underline{H}_z(x)$ phasors away from the surfaces of about 40% with respect to the two lower frequency cases. This is due to the magnetic field's diminishing ability to penetrate the conducting layer at higher frequencies. From the development of Appendix D, we know that this attenuation in the magnetic field is a result of energy being transferred (via the electric field) into the medium in the form of increased current density. Accordingly, we see that the current density phasors of Fig. 4.9 are, in fact, substantially larger in magnitude near the surfaces of the layer, more than 5 times that for 1 kHz at $x = 0$ and more than 9 times at $x = h_{cu}$. Moreover, since the phase angles of the current-density phasors at $x = 0$ and at $x = h_{cu}$ differ by 180°, Fig. 4.9 suggests that at every instant of time throughout a cycle the actual current will be flowing in opposite directions at $x = 0$ and at $x = h_{cu}$. This fact is evident from Fig. 4.10, which shows the time variation of the actual current density distribution at 100 kHz. Note that the current-density distribution at each point in time is approximately odd-symmetric about the center of the layer, and is slightly uneven only because the magnitude of the magnetic field intensity is greater at $x = h_{cu}$ than it is at $x = 0$. Thus, there is an imbalance of current in the $+y$- and $-y$-directions at each point in time which results in a net instantaneous current flow in either the $+y$- or the $-y$-direction. An interesting effect is seen in Fig. 4.10 at times corresponding to $\omega t = 60°$ and $\omega t = 240°$. At 60°, the current at $x = 0$ is flowing in the $-y$-direction; in the neighborhood of $x = 1 \times 10^{-4}$, the current is flowing in the $+y$-direction; then, for x between 2.6×10^{-4} and 6.3×10^{-4}, the current has reversed again and is flowing in the $-y$-direction; finally, from $x = 6.4 \times 10^{-4}$ to $x = h_{cu}$ the current is again flowing in the $+y$-direction. In other words, at this instant in time, the current undergoes three reversals in direction across the layer height from $x = 0$ to $x = h_{cu}$. At $\omega t = 240°$, we see a similar pattern since the distribution of the actual current density is a mirror image of that for $\omega t = 60°$ about the x vs Im-plane.

At this point we should emphasize that the increase in surface current densities that appears in Figs. 4.7 and 4.9 in no way suggests that there is a "larger current" in the winding layer than is present in the lowest frequency case of Fig 4.5. We can see this by taking the actual current density at any instant of time in either Fig. 4.8 or Fig. 4.10 and spatially averaging it across the winding layer to obtain the *net*, instantaneous current density. In each case, the net or average current density that we obtain is exactly the same as the almost uniform current density of Fig. 4.6 for the same instant in time. This is expected since we force the same net sinusoidal current into the layer at all of these four frequencies.

In Section 4.2, immediately following the derivation of equations (4.36) and (4.39), we make the claim that the distribution of the magnetic field intensity and current



x $\times 10^{-4}$m	$\underline{H}_z(x)$ A-t/m	$\underline{J}_y(x)$ $\times 10^4$A/m^2	x $\times 10^{-4}$m	$\underline{H}_z(x)$ A-t/m	$\underline{J}_y(x)$ $\times 10^4$A/m^2
0	$1.00\angle 0.00°$	$0.755\angle 44.46°$	4	$0.68\angle -85.37°$	$0.240\angle 158.21°$
1	$0.61\angle -35.90°$	$0.503\angle 25.76°$	5	$0.85\angle -59.89°$	$0.521\angle 180.11°$
2	$0.52\angle -75.93°$	$0.286\angle 19.57°$	6	$1.25\angle -28.72°$	$0.868\angle 200.89°$
3	$0.59\angle -93.22°$	$0.094\angle 63.88°$	7	$2.00\angle 0.00°$	$1.352\angle 224.83°$

Figure 4.9: Plots of the magnetic-field-intensity phasor $\underline{H}_z(x)$ and the current-density phasor $\underline{J}_y(x)$ at an excitation frequency of 100 kHz.

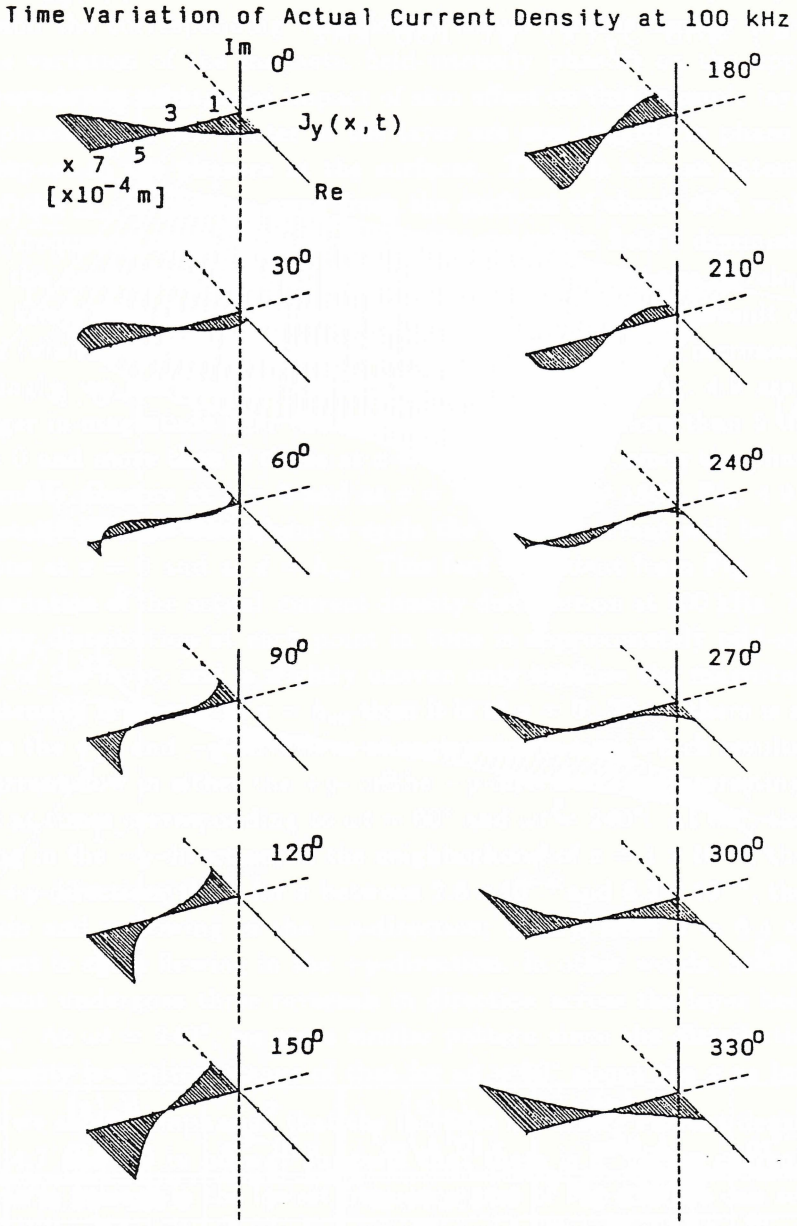


Figure 4.10: Plots of the actual current-density distribution at twelve different instants of ωt spaced evenly throughout a single cycle of oscillation at 100 kHz. The progression advances from top to bottom down the left column and then down the right.

density can be thought of as resulting from the superposition of the two independently established boundary magnetic fields—$\underline{H}_z(0)$ and $\underline{H}_z(h_{cu})$. We can graphically illustrate this fact for the case of equation (4.36) by replotting the $\underline{H}_z(x)$ distribution of Fig. 4.9 with the individual contributions of each boundary magnetic field explicitly shown. This is done in Fig. 4.11, which shows the two independent sets of magnetic-field-intensity phasors, as well as the envelope of the sum, which corresponds to the envelope seen in Fig. 4.9. The first distribution of phasors is marked by a dashed-line envelope, and it has the boundary conditions $\underline{H}_z(0) = 1\angle 0°$ and $\underline{H}_z(h_{cu}) = 0\angle 0°$. The second distribution of phasors has a solid line envelope and has the boundary conditions $\underline{H}_z(0) = 0\angle 0°$ and $\underline{H}_z(h_{cu}) = 2\angle 0°$. The envelope of the sum of these two phasor distributions at every point across the layer is represented by the dotted line. Note that near the surfaces of the layer the sum of the distributions more closely follows the distribution that has a non-zero boundary condition at that surface. Thus, there is a tendency for each of the two magnetic fields to exert a dominant influence in the interior of the layer near the surface at which it has a non-zero boundary value.

Alternatively, we can consider the distribution of the magnetic field intensity and current density to be a physical superposition of two transverse electromagnetic waves, as discussed in Appendix D. By this approach, we are able to explain in detail the distributions as they vary with frequency.

Figure 4.12 shows the distribution of $\underline{H}_z(x)$ and $\underline{J}_y(x)$ at a 1-MHz excitation frequency, and Fig. 4.13 shows the corresponding time variation of the actual current-density distribution at this frequency. On the upper set of axes in Fig. 4.12, we see that the magnitude $|\underline{H}_z(x)|$ of the magnetic field intensity drops off rapidly away from the surfaces of the layer, and the phase angle of $\underline{H}_z(x)$ near the center of the layer is now lagging as much as 270° behind the phase angle of $\underline{H}_z(x)$ at the surfaces. Once again, this sharp attenuation of the magnetic field intensity is associated with an increase in surface current density. The plot of $\underline{J}_y(x)$ in Fig. 4.12 shows that the magnitude of the current-density phasors has now dramatically increased near the surfaces by more than 14 times the 1 kHz value at $x = 0$ and more than 28 times at $x = h_{cu}$. Near the center of the layer, the magnitude of the current-density phasors has attenuated substantially to only 20% of the 1 kHz value. Note that the current-density phasors between $x = 0$ and $x \approx 2 \times 10^{-4}$ are all leading their corresponding magnetic-field-intensity phasors over this same region by a phase angle of approximately 45°. Likewise, the current-density phasors between $x \approx 5 \times 10^{-4}$ and $x = h_{cu}$ are leading their corresponding magnetic-field-intensity phasors by approximately 225°. Also, the phase angle of $\underline{H}_z(x)$ over these same regions exhibits even symmetry about the center of the layer, so that for $0 \leq x \leq 2 \times 10^{-4}$ we have

$$\angle \underline{H}_z(x) \approx \angle \underline{H}_z(h_{cu} - x) \tag{4.53}$$

where $\angle \underline{H}_z(x)$ denotes the phase angle of the phasor quantity $\underline{H}_z(x)$. As a result of this symmetry and the phase relationship between $\underline{J}_y(x)$ and $\underline{H}_z(x)$, the current density

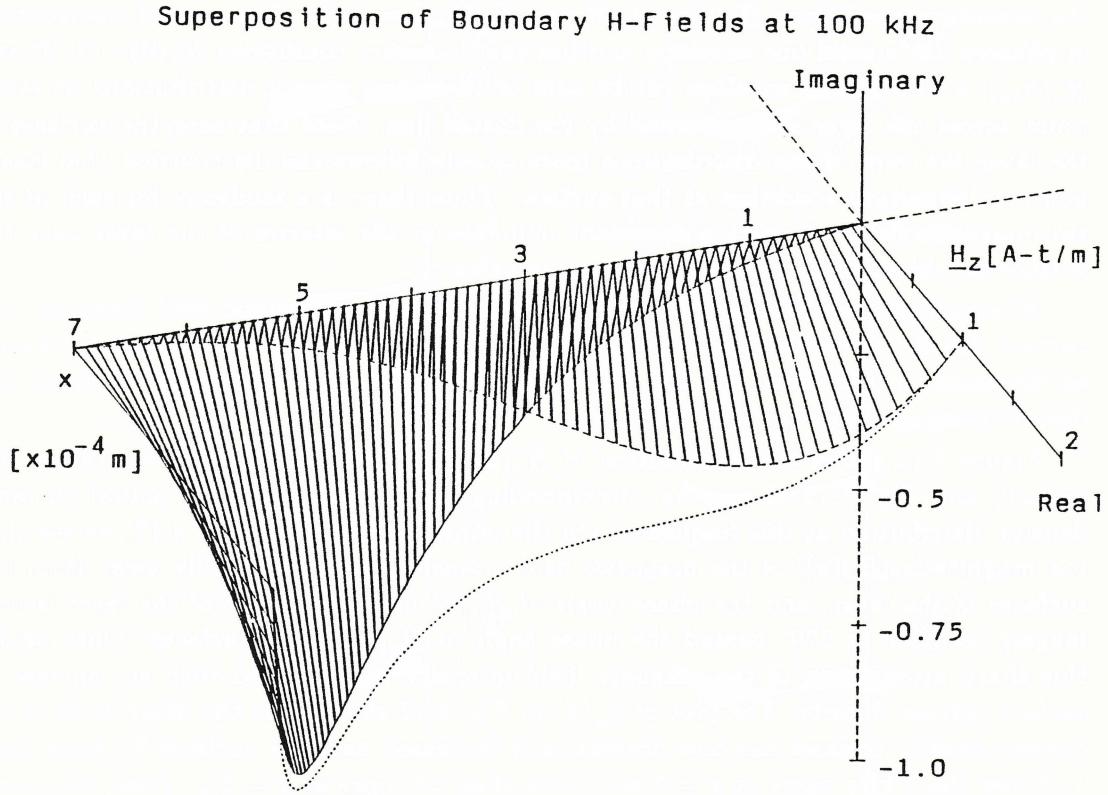


Figure 4.11: Superposition of two magnetic-field-intensity phasor distributions at 100 kHz showing the individual contributions from the magnetic fields established at each of the surfaces.

$\underline{J}_y(x)$ for $0 \leq x \leq 2 \times 10^{-4}$ must also obey

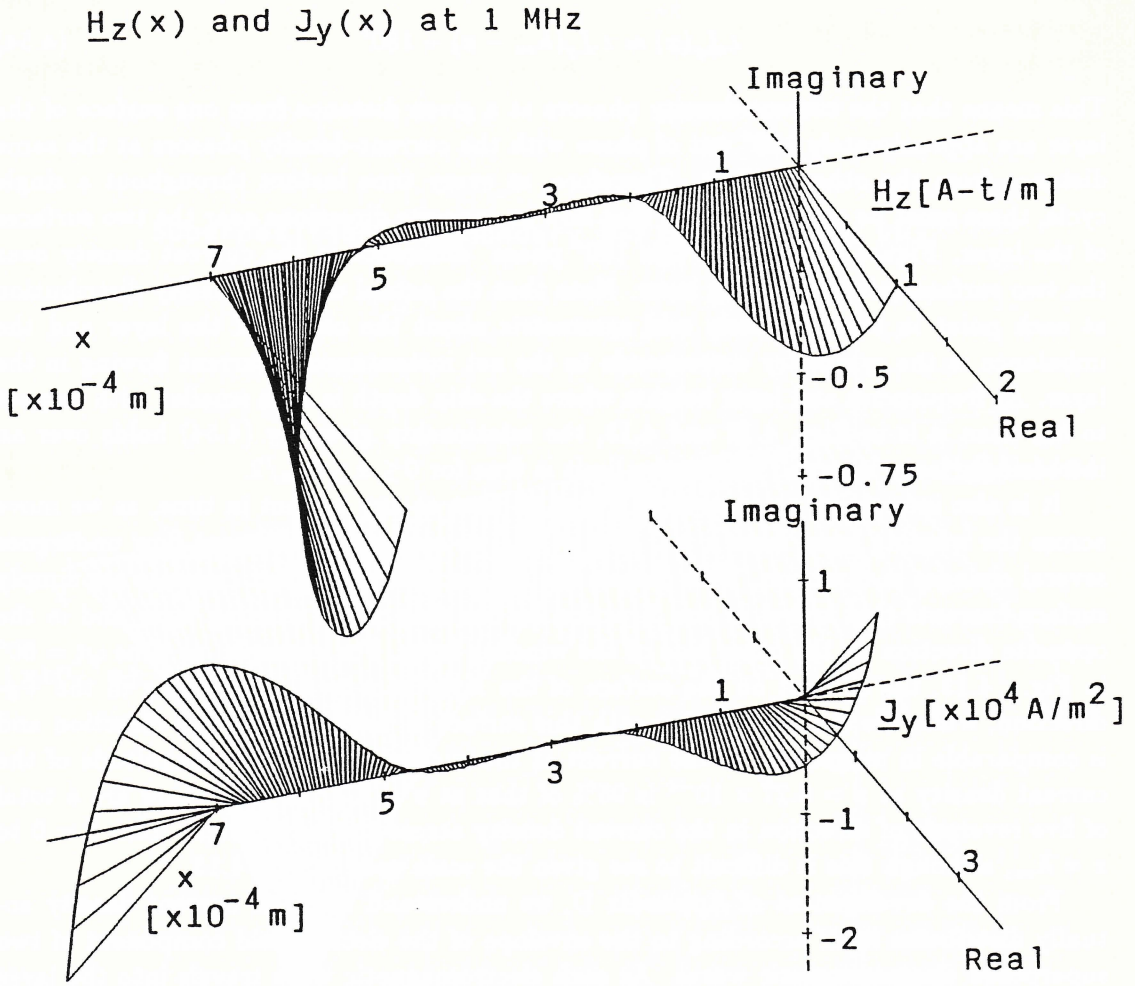
$$\angle \underline{J}_y(x) \approx \angle \underline{J}_y(h_{cu} - x) - 180^\circ \tag{4.54}$$

This means that the current-density phasors at a given distance from one surface of the layer are approximately 180° out of phase with the current-density phasors at the same distance from the other surface. Therefore, at every time instant throughout a single cycle, there must be actual currents that flow in opposite directions near the two surfaces of the layer. Figure 4.13 reveals this 180° phase difference in the current density near the two surfaces of the winding layer. Note that the actual current-density distribution at each point in time is nearly odd symmetric about the center of the layer and the imbalance in the symmetry corresponds to the net instantaneous current flowing in the layer. At frequencies and layer heights where the skin depth is even smaller with respect to h_{cu} than it is in Figs. 4.12 and 4.13, the relationship given by (4.54) holds over an increasingly large interval, and in the limit is true for $0 \leq x \leq h_{cu}/2$.

It is also interesting to observe in Fig. 4.13 that at any instant in time, as we move across the winding layer from $x = 0$ to $x = h_{cu}$, we see that the current flow undergoes several changes in direction. This dispels the notion that skin-effect currents are simply surface currents that travel in one direction on one side of the winding layer and in the opposite direction on the other side of the winding layer. For example, at time $\omega t = 60^\circ$ in Fig. 4.13, the current on the surface of the layer at $x = h_{cu}$ is flowing in the $+y$-direction, while the current just beneath this surface is flowing in the $-y$-direction and is comparable in magnitude to the current at the surface, so that the magnitude of the current density at $x = 6.27 \times 10^{-4}$ is 95% of that at $x = h_{cu}$. In fact, there are a total of five reversals of direction in the current density across the layer height from $x = 0$ to $x = h_{cu}$, although this is difficult to see given the scale used in Fig. 4.13.

From the development of Appendix D, we understand that the current density actually distributes itself according to the envelope of the electric-field component of two superposed electromagnetic waves. As each electromagnetic wave travels into the layer from one of the two surfaces, its electric field oscillates as a damped sinusoid, generating a current at each point that is proportional to the electric field at that same point. When the skin depth is small with respect to layer height ($\delta \approx 0.1 h_{cu}$ in Fig. 4.13), then there is very little interference between the two waves as they travel towards the center from opposite sides, and so the sinusoidal nature of the electric fields becomes apparent in the behavior of the current-density distribution. Therefore, it is this wavelike behavior which is responsible for the large number of direction changes in the actual current density at any instant in time.

Throughout this document, we have emphasized the fact that the importance of skin effect is in no way restricted to high-frequency applications. Indeed, skin effect can have a significant impact on the power-loss and energy-storage characteristics at what might be considered relatively low frequencies. Figure 4.14 dramatizes this fact. The example illustrated in this figure is in every way the same as the 1-kHz example of Figure 4.5 except one—that the copper height is now increased to $h_{cu} = 10 \times 10^{-3}$ m, or by a factor



x $\times 10^{-4}$m	$\underline{H}_z(x)$ A-t/m	$\underline{J}_y(x)$ $\times 10^4$A/m^2	x $\times 10^{-4}$m	$\underline{H}_z(x)$ A-t/m	$\underline{J}_y(x)$ $\times 10^4$A/m^2
0	$1.00\angle 0.00°$	$2.049\angle 44.99°$	4	$0.03\angle -255.54°$	$0.053\angle -17.24°$
1	$0.24\angle -83.07°$	$0.481\angle -37.93°$	5	$0.11\angle -165.64°$	$0.227\angle 58.66°$
2	$0.05\angle -164.59°$	$0.114\angle -122.37°$	6	$0.47\angle -83.01°$	$0.962\angle 142.02°$
3	$0.01\angle -272.79°$	$0.028\angle -177.67°$	7	$2.00\angle 0.00°$	$4.097\angle 225.00°$

Figure 4.12: Plots of the magnetic field intensity phasor $\underline{H}_z(x)$ and the current density phasor $\underline{J}_y(x)$ at an excitation frequency of 1 MHz.

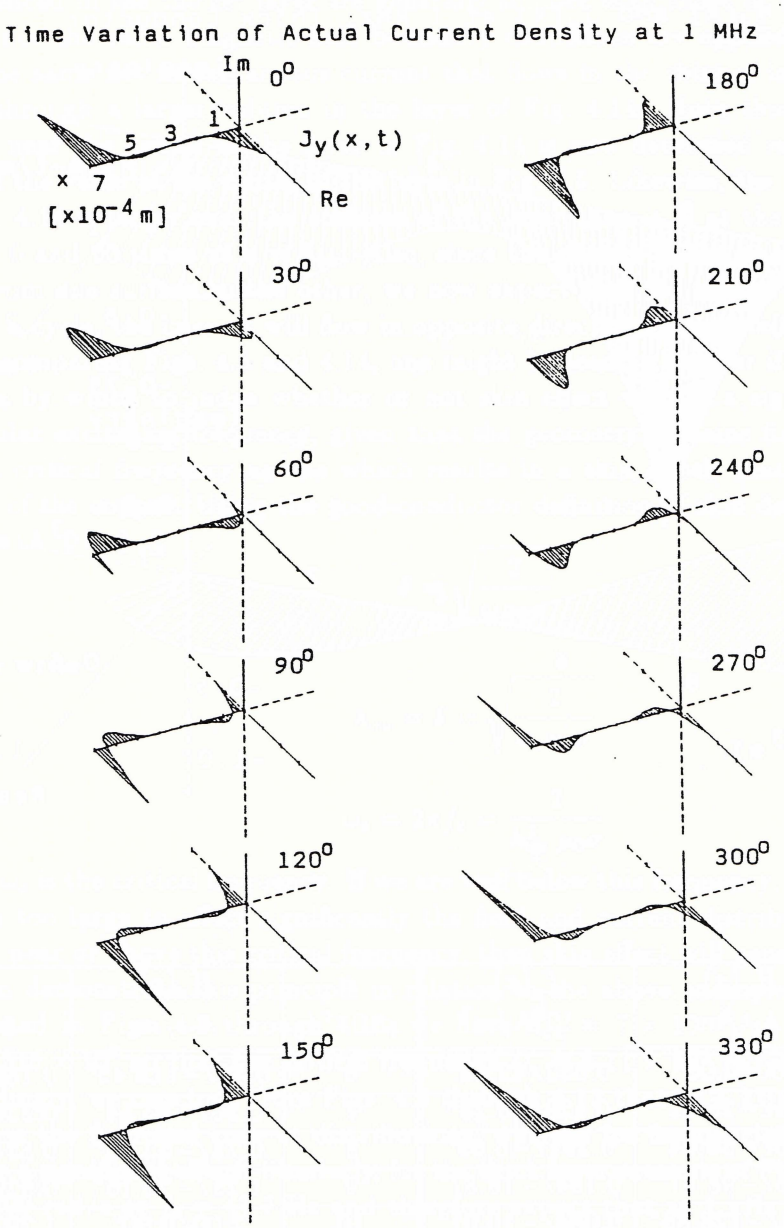
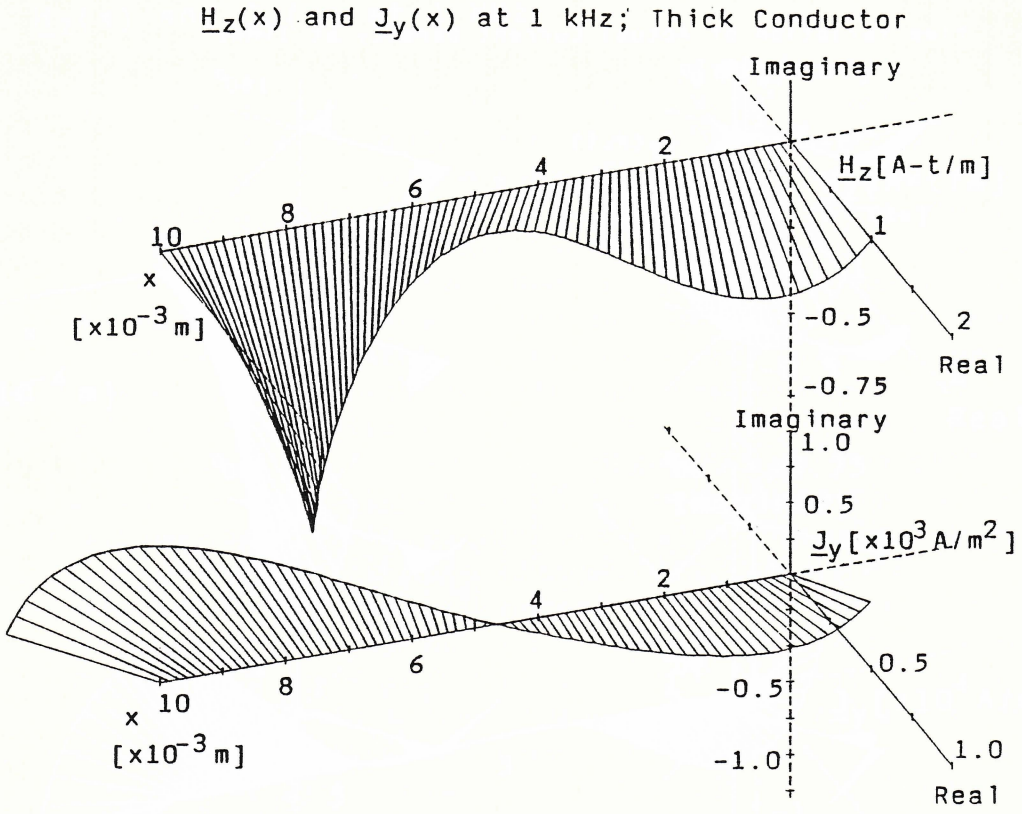


Figure 4.13: Plots of the actual current-density distribution at twelve different times (ωt) spaced evenly throughout a single cycle of oscillation at 1 MHz. The progression advances from top to bottom and then from left to right.



x $\times 10^{-4}$m	$\underline{H}_z(x)$ A-t/m	$\underline{J}_y(x)$ $\times 10^3$A/m^2	x $\times 10^{-4}$m	$\underline{H}_z(x)$ A-t/m	$\underline{J}_y(x)$ $\times 10^3$A/m^2
0	$1.00\angle 0.00°$	$0.652\angle 42.68°$	6	$0.36\angle -113.45°$	$0.186\angle 130.08°$
1	$0.61\angle -25.92°$	$0.429\angle 16.23°$	7	$0.50\angle -83.54°$	$0.336\angle 150.29°$
2	$0.35\angle -56.94°$	$0.291\angle -6.05°$	8	$0.78\angle -53.48°$	$0.534\angle 172.88°$
3	$0.25\angle -98.47°$	$0.184\angle -18.87°$	9	$1.25\angle -26.16°$	$0.829\angle 198.09°$
4	$0.26\angle -128.85°$	$0.084\angle -10.01°$	10	$2.00\angle 0.00°$	$1.297\angle 224.42°$
5	$0.30\angle -131.81°$	$0.065\angle 94.35°$			

Figure 4.14: Plots of the magnetic field intensity phasor $\underline{H}_z(x)$ and the current density phasor $\underline{J}_y(x)$ at an excitation frequency of 1 kHz where the thickness of the copper layer is increased to $h_{cu} = 10 \times 10^{-3}$ m.

of about 14. The scale on the plot of $\underline{J}_y(x)$ in Fig. 4.14 indicates that the current densities experienced in the thicker layer are generally smaller than those of Fig. 4.5. This is the case since the same magnetic-field boundary conditions are applied to both layers, so that the same net instantaneous current that flows in the thinner layer of Fig. 4.5 now flows through a larger volume in the layer of Fig. 4.14. Note that the magnitude of $\underline{H}_z(x)$ near the center of the layer in Fig. 4.14 is now decreased substantially to only 20% of the value at the center of the layer in Fig. 4.5. Likewise, the magnitude of $\underline{J}_y(x)$ in Fig. 4.14 is larger near the surfaces of the layer than it is at the center by 10 times at $x = 0$ and 20 times at $x = h_{cu}$. Also, since the change in the phase angle of $\underline{J}_y(x)$ is 182° from one surface to the other, we now expect that for almost all instants of time within a cycle, the current will flow in opposite directions near $x = 0$ and $x = h_{cu}$.

In comparing Figs. 4.5 and 4.14, one might be lead to wonder if there is some solid criteria by which to judge whether or not skin effect will be a significant factor at a particular excitation frequency, given that the geometry remains fixed. We can define such a *critical frequency* as one which results in a skin depth that exactly equals the height of the copper. Using the good-conductor definition of skin depth from (4.7)

$$\delta = \sqrt{\frac{2}{\omega \mu_0 \sigma}} \tag{4.55}$$

we can write

$$h_{cu} = \delta = \sqrt{\frac{2}{\omega_c \mu_0 \sigma}} \tag{4.56}$$

or

$$\omega_c = 2\pi f_c = \frac{2}{h_{cu}^2 \, \mu_0 \sigma} \tag{4.57}$$

where ω_c is the critical frequency. If we are well below this frequency, then the skin depth will be too large to affect significantly the field and current distributions. However, if we are near or above this critical frequency, then skin effect will generally be important. We can demonstrate this principle in relation to the above examples. For the example illustrated in Figs. 4.5 through 4.13, we have $h_{cu} = 7 \times 10^{-4}$, $\mu_0 = 4\pi \times 10^{-7}$, and $\sigma = 5.315 \times 10^7$ so that the critical frequency $\omega_c = 6.11 \times 10^4$ rad/s, or $f_c = 9.73$ kHz. Accordingly, we conclude from Figs. 4.5 through 4.13 that at 1 kHz there is very little effect on the field and current distributions, whereas for frequencies well above 10 kHz there is a significant effect. Similarly, for the thick layer example of Fig. 4.14, we find that $\omega_c = 299$ rad/s or $f_c = 47.7$ Hz and therefore expect that at 1 kHz there would indeed be a substantial impact of skin effect on the magnetic-field-intensity and current-density distributions.

We can further utilize the concept of critical frequency to examine the behavior of equations (4.36) and (4.39) in the limit of low frequency, where the excitation frequency is very much less than the critical frequency, or

$$\omega \ll \omega_c = \frac{2}{h_{cu}^2 \, \mu_0 \sigma} \tag{4.58}$$

Since (4.36) and (4.39) are in terms of complex wave number $\underline{k}$ instead of the frequency ω, we first rewrite the inequality of (4.58) in terms of the complex wave number. From (4.5) of Section 4.1.2 we can write

$$|\underline{k}| = \sqrt{\omega\mu_0\sigma} \tag{4.59}$$

and replacing the ω under the radical in (4.59) with the right-hand side of (4.58) we obtain

$$|\underline{k}| \ll \frac{\sqrt{2}}{h_{cu}} \tag{4.60}$$

$$|\underline{k}|h_{cu} \ll \sqrt{2} \tag{4.61}$$

or, approximately

$$|\underline{k}|h_{cu} \ll 1 \tag{4.62}$$

Furthermore, since $0 \leq (h_{cu} - x) \leq h_{cu}$ and $0 \leq x \leq h_{cu}$, we also know that

$$|\underline{k}|(h_{cu} - x) \ll 1 \tag{4.63}$$

and

$$|\underline{k}|x \ll 1 \tag{4.64}$$

so that the inequalities of (4.62), (4.63) and (4.64) are all implied by (4.58). Expanding now the sinh terms in (4.36) yields

$$\begin{aligned} \underline{H}_z(x) = \frac{1}{e^{\underline{k}h_{cu}} - e^{-\underline{k}h_{cu}}} \Big\{ & \underline{H}_z(h_{cu}) \left[e^{\underline{k}x} - e^{-\underline{k}x} \right] \\ & + \underline{H}_z(0) \left[e^{\underline{k}(h_{cu} - x)} - e^{-\underline{k}(h_{cu} - x)} \right] \Big\} \end{aligned} \tag{4.65}$$

The Taylor series approximation for $e^{\underline{u}}$ is given by

$$e^{\underline{u}} \approx 1 + \underline{u} \qquad \text{for } |\underline{u}| \ll 1 \tag{4.66}$$

where $\underline{u}$ is any complex number. Using (4.62), (4.63) and (4.64) together with the approximation of (4.66), we can replace each of the exponentials in (4.65) with its corresponding linear term

$$\begin{aligned} \underline{H}_z(x) &= \frac{1}{1 + \underline{k}h_{cu} - 1 + \underline{k}h_{cu}} \Big\{ \underline{H}_z(h_{cu}) \left[1 + \underline{k}x - 1 + \underline{k}x \right] \\ &\qquad + \underline{H}_z(0) \left[1 + \underline{k}h_{cu} - \underline{k}x - 1 + \underline{k}h_{cu} - \underline{k}x \right] \Big\} \\ &= \frac{1}{2\underline{k}h_{cu}} \Big\{ \underline{H}_z(h_{cu}) \left[2\underline{k}x \right] + \underline{H}_z(0) \left[2\underline{k}h_{cu} - 2\underline{k}x \right] \Big\} \end{aligned}$$

After making cancellations and factoring, we obtain

$$\underline{H}_z(x) = \left[\frac{\underline{H}_z(h_{cu}) - \underline{H}_z(0)}{h_{cu}}\right] x + \underline{H}_z(0) \tag{4.67}$$

In a similar manner, we can apply the Taylor series approximation to the expression for the current-density phasor $\underline{J}_y(x)$ (4.39) and obtain

$$\underline{J}_y(x) = \underline{J}_y = \frac{\underline{H}_z(0) - \underline{H}_z(h_{cu})}{h_{cu}} \tag{4.68}$$

Equations (4.67) and (4.68) are the low-frequency forms for the magnetic-field-intensity and current-density distributions across the height of a layer. Naturally, the results obtained in (4.67) and (4.68) could have been obtained equally well by a direct application of Ampere's law assuming dc-excitation current. Note that the low-frequency form (4.67) of $\underline{H}_z(x)$ is the equation of a straight line corresponding to the linear distribution of $\underline{H}_z(x)$, while the low-frequency form (4.68) of $\underline{J}_y(x)$ is independent of x. This corresponds to the result obtained for the dc-case of Section 3.1.2 as well as the low-frequency-case of Fig. 4.5. Equation (4.68) is also useful in that it provides a value for the average current-density phasor $\underline{J}_y$ across the height of a layer, given the magnetic-field boundary conditions for that layer.

4.4 GRAPHICAL ILLUSTRATIONS OF $\underline{H}_z(x)$ AND $\underline{J}_y(x)$ IN AN IDEALIZED TRANSFORMER

4.4.1 Plots of Phasor Magnitudes Across Four Layers

The reader will recall that in Section 3.1.2 we introduce the concept of dc straight-line magnetic-field-intensity diagrams that are used to determine the values of magnetic field that exist at the boundaries of each winding layer in a two-layer infinite solenoid. In Section 4.1, we demonstrate that these boundary values are sufficient information to solve for both the current density and the magnetic-field intensity in the interior of an infinite current sheet. We now take the results of our infinite-current-sheet analysis and apply them to a four-layer infinite solenoid similar to the two-layer one developed in Section 3.1.2.

Figure 4.15 shows a four-layer solenoid in which the inner three layers are part of one winding and the outermost layer is a different winding. Each winding layer in the structure has a height h_{cu} of 7.0×10^{-4} m, the same as that of the single layer of Figs. 4.2 and 4.3. Each layer is separated by an air gap of 2×10^{-4} m, and the magnetic field boundary conditions for the four layers are given by $\underline{H}_z(0) = 0\angle 0°$, $\underline{H}_z(7 \times 10^{-4}) = \underline{H}_z(9 \times 10^{-4}) = 1\angle 0°$, $\underline{H}_z(16 \times 10^{-4}) = \underline{H}_z(18 \times 10^{-4}) = 2\angle 0°$, $\underline{H}_z(25 \times 10^{-4}) = \underline{H}_z(27 \times 10^{-4}) = 3\angle 0°$, and $\underline{H}_z(34 \times 10^{-4}) = 0\angle 0°$. Following the pattern used in Figs. 4.2 and 4.3, Figs. 4.16 and 4.17 show plots of the magnitude of

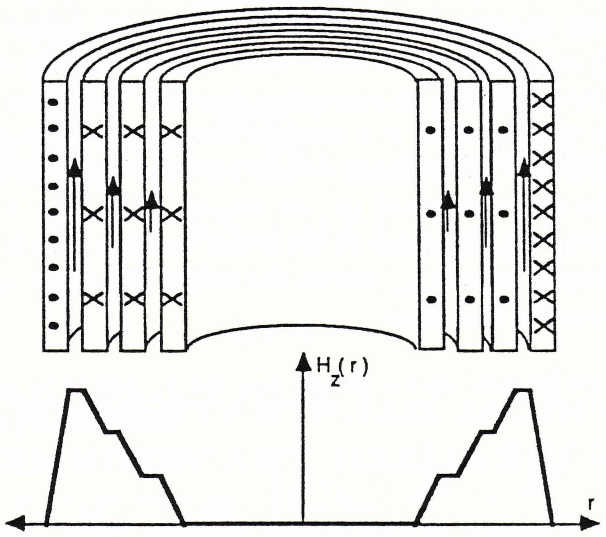


Figure 4.15: Structure of a four-layer solenoid. The three inner layers are all of one winding and the outer layer is of a different winding. The outer winding carries a current equal to the sum of the currents in the other layers.

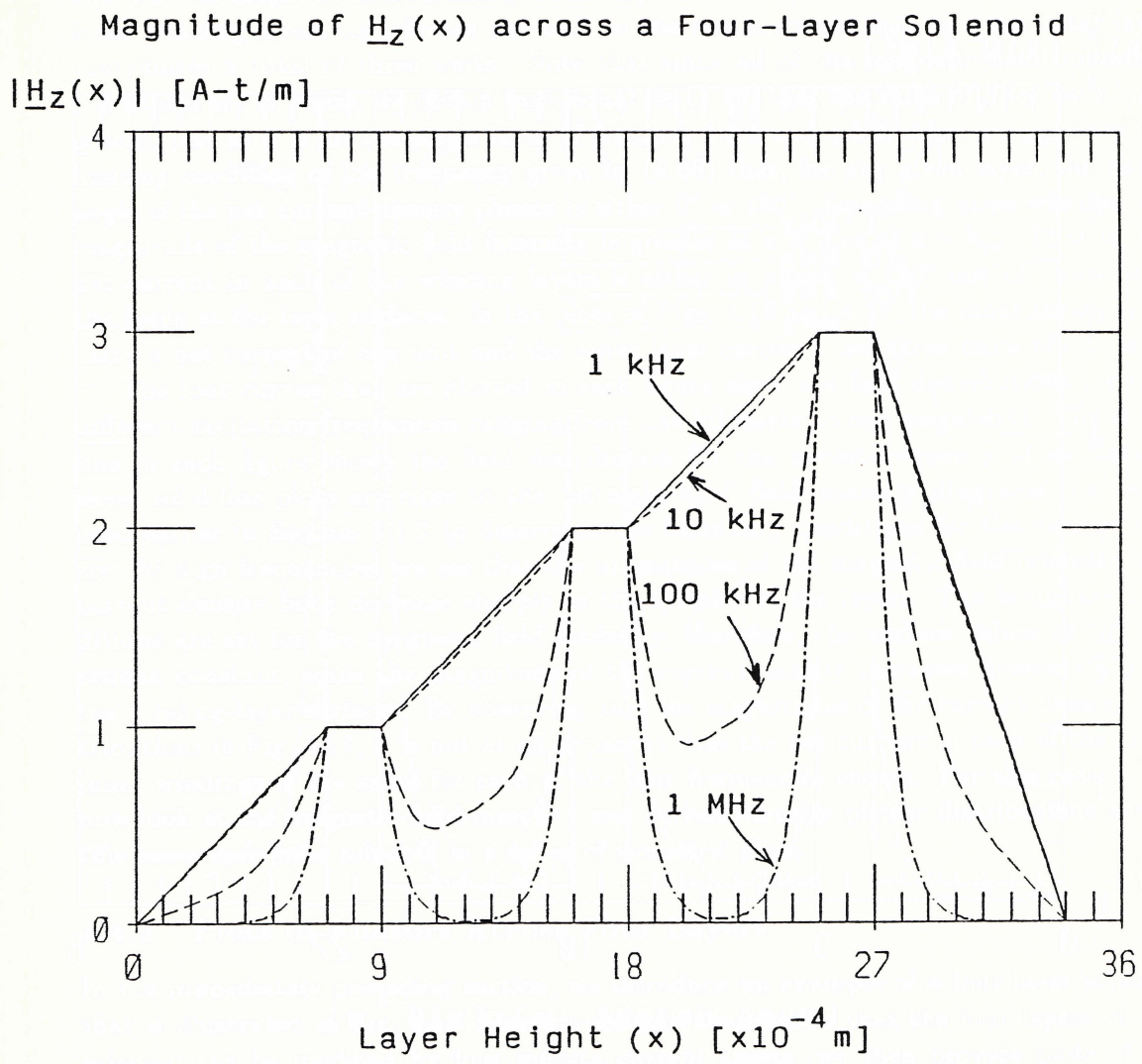


Figure 4.16: The magnitude of the magnetic-field-intensity phasor distribution for the solenoid shown in Fig. 4.15.

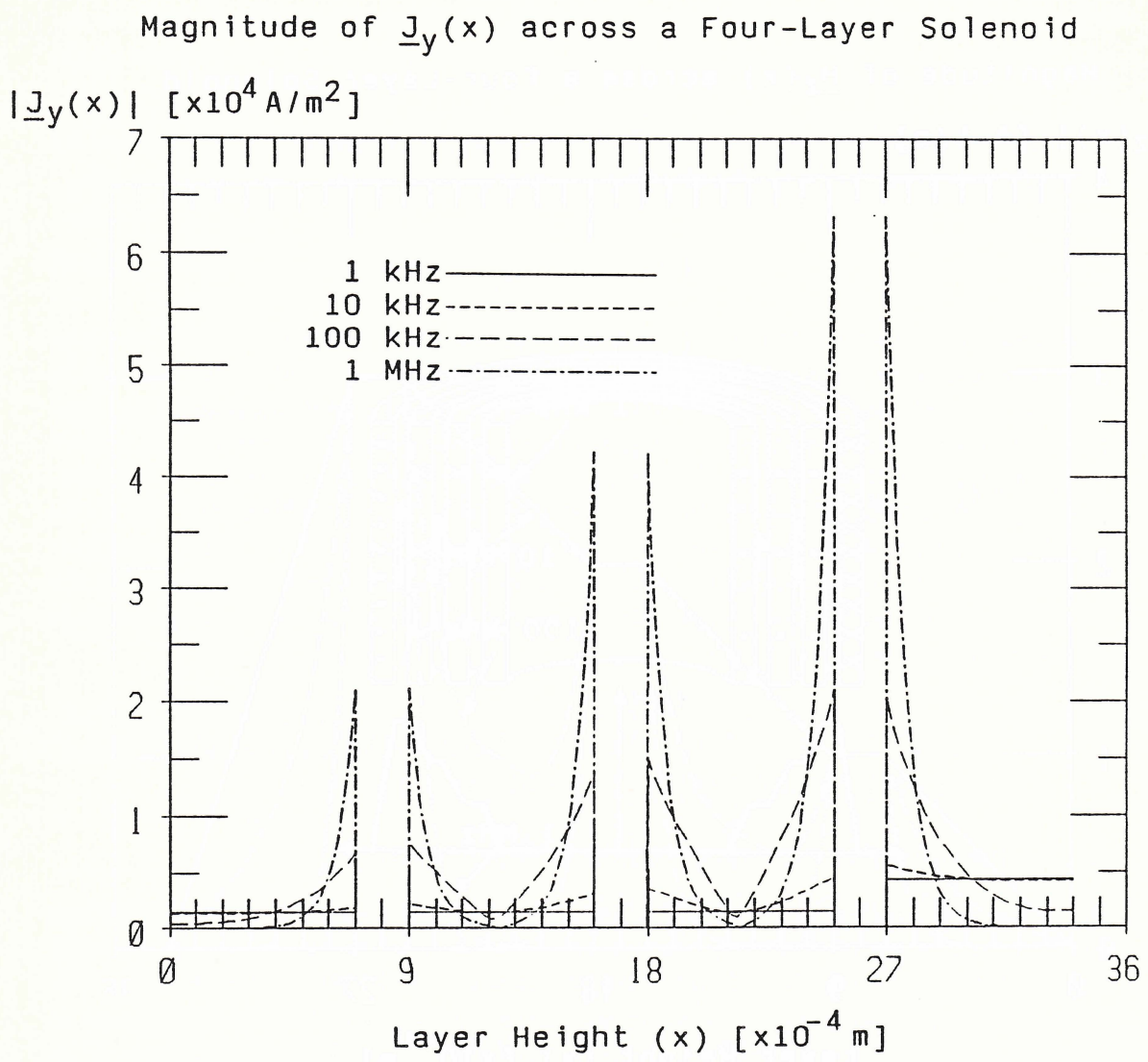


Figure 4.17: The magnitude of the current-density phasor distribution for the solenoid shown in Fig. 4.15.

the magnetic-field-intensity and current-density distributions, respectively, for the different layers of this four-layer solenoid. These plots are similar to those of Figs. 4.2 and 4.3; the magnetic-field-intensity boundary conditions are chosen so that each of the inner winding layers contributes one unit to the net magnetic field and the outer layer contributes a total of three units. Note that since all of the magnetic-field boundary conditions are in phase, we obtain from equation (4.49) that the value of β for each layer is zero, just as it is for the single layer of Sections 4.3.1 and 4.3.2. Also, we see from the limiting condition of low frequency given by (4.68) that, for any given layer, the phase angle of the net current-density phasor is either 0° or 180°, depending upon whether the magnitude of the magnetic field intensity is greater at $x = 0$ or at $x = h_{cu}$. That is, the *net* current in each of the winding layers is either in phase or 180° out of phase with the fields at the layer surfaces. In the plots of Figs. 4.16 and 4.17, the inner three layers carry a net current of one unit and the outer layer carries a net three units of current.

The four curves that are plotted in each figure show the field distributions for four different excitation frequencies ranging from one kilohertz to one megahertz. The solid-line in each figure shows the field distribution for the lowest-frequency of excitation; these solid-line plots are close to the "straight-line" field-intensity diagrams that were used earlier in Section 3.1.2 to determine the boundary conditions for the various layers. At high frequencies, we see that the magnitudes of the magnetic field intensity and current density both decrease sharply in the interior of the layers. The boundary conditions are set for the magnetic field intensity; therefore, the surface values of $|\underline{H}_z(x)|$ remain constant, while the magnitude of the current density increases dramatically on the winding-layer surfaces. By observing only the magnitudes of the current-density distributions in Fig. 4.17, it is not at all apparent that the net current in each of the three inner windings is the same for each of the four frequencies shown. For this reason, we now look at the magnetic-field-intensity and current-density phasor distributions across this same four-layer solenoid in a series of isometric plots.

4.4.2 Plots of Phasors Across Four Layers

In the immediately preceding section, we introduce an example of a four-layer solenoid that is illustrated in Fig. 4.15. Based upon the assumption that the four layers of this solenoid can be modeled by four infinite current sheets, we then provide plots of the magnitude of $\underline{H}_z(x)$ and $\underline{J}_y(x)$ in Figs. 4.16 and 4.17. It is important to realize that the four-layer infinite solenoid of Fig. 4.15 is not a transformer *per se*, since there is no magnetic core. In other words, there is nothing inherent in this structure that places any constraints whatever on the magnetic fields in any of the three inter-layer gaps, or in the center of the solenoid. Therefore, we *intentionally* choose values for these magnetic fields so that our example four-layer solenoid has the appearance of a transformer with a core material of infinite permeability. That is, we choose the values of the magnetic fields in the air spaces so that the total number of ampere-turns across the four layers is zero. In Section 4.3.2, we use isometric plots to illustrate the complete $\underline{H}_z(x)$ and $\underline{J}_y(x)$ phasors for the single-layer example originally introduced in Section 4.3.1. In the same way, we

now wish to show the complete phasors across all four layers for the infinite solenoid example that is introduced in Section 4.4.1. Figures 4.18 through 4.21 contain plots of the magnetic-field-intensity and current-density phasors for this four-layer example at the same four frequencies that are used in Figs. 4.16 and 4.17 where only the magnitudes of the phasors are plotted.

Figure 4.18 shows the variation of the $\underline{H}_z(x)$ and the $\underline{J}_y(x)$ phasors across four layers at an excitation frequency of 1 kHz, and Table 4.1 contains an illustrative set of data points corresponding to the two plots in Fig. 4.18. The magnetic-field-intensity phasor distribution is plotted on the upper set of axes in Figure 4.18, while the current-density phasor distribution is plotted on the lower set of axes. The upper set of axes in Fig. 4.18 and Table 4.1 reveal that, although there is some small variation in the phase of $\underline{H}_z(x)$ (less than 2°), the magnitude of $\underline{H}_z(x)$ varies essentially linearly across each of the four layers. Note that to avoid unnecessary cluttering of the drawings, there are no magnetic-field-intensity phasors plotted in the three interlayer gaps; the solid line that would be connecting their tips is shown, however. This is because we have assumed that the magnetic field intensity in each interlayer gap is a sinusoid of constant magnitude and phase, regardless of the excitation frequency. Therefore, the magnetic-field-intensity phasor $\underline{H}_z(x)$ remains constant in the interlayer gaps and need not be plotted. Also note that the layer between $x = 9 \times 10^{-4}$ m and $x = 16 \times 10^{-4}$ m has *exactly* the same boundary conditions as the single layer that is illustrated in Section 4.3.2. Therefore, at each frequency, the layer between $x = 9 \times 10^{-4}$ m and $x = 16 \times 10^{-4}$ m exhibits the exact same $\underline{H}_z(x)$ and $\underline{J}_y(x)$ distributions as is seen for the single-layer example of Section 4.3.2.

The plot of the current-density phasors on the lower set of axes in Fig. 4.18 and the values in Table 4.1 suggest that at 1 kHz the currents in each of the four layers is almost uniformly distributed, since the magnitude and phase of $\underline{J}_y(x)$ across each layer is approximately constant. The magnitude of $\underline{J}_y(x)$ across any of the four layers varies by no more than 5%, while the phase varies by no more than 29°. Also, we see from Fig. 4.18 that the current density in the outer layer is three times greater in magnitude, and 180° out of phase with respect to the current density in each of the three inner layers. Therefore, if we consider each of our layers to consist of a single turn of conductor, then the instantaneous sum of the ampere-turns across the four layers is in fact zero.

Figures 4.19 through 4.21 show the progression of the magnetic-field-intensity and current-density phasor distributions for excitation frequencies of 10 kHz, 100 kHz and 1 MHz, and Tables 4.2 through 4.4 contain corresponding data points. The changes in the phasor distributions of a single layer as the frequency increases have already been discussed above in Section 4.3.2, and the same arguments apply to each of the four layers in this section. In general, we see that as the frequency increases, the magnitude of both $\underline{H}_z(x)$ and $\underline{J}_y(x)$ becomes attenuated near the center of each layer, while the magnitude of $\underline{J}_y(x)$ becomes much greater near the surfaces of each layer. In other words, the alternating magnetic field's diminishing ability to penetrate deep into each winding layer causes the current to be concentrated in regions near the surfaces of each

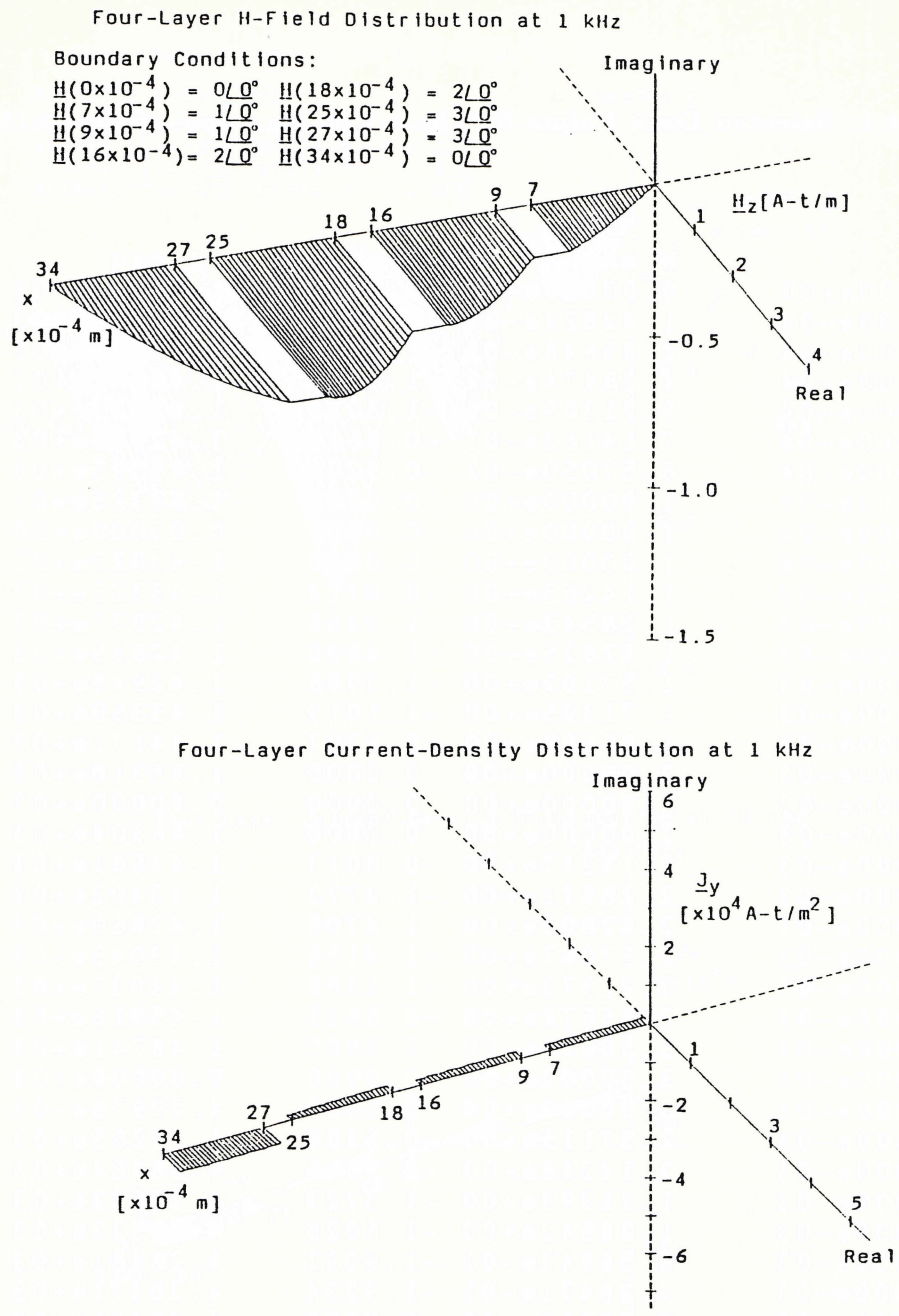


Figure 4.18: The magnetic-field-intensity and current-density phasor distributions across the four-layer solenoid of Fig. 4.15 at an excitation frequency of 1 kHz.

Table 4.1: Selected Data Points for the 1 kHz Example of Fig. 4.18

1 kHz

X	H_mag	H_phase	J_mag	J_phase
0.00000e+00	0.00000e+00	0.0000	1.42824e+03	178.0365
1.00000e-04	1.42824e-01	-1.9234	1.42824e+03	178.1568
2.00000e-04	2.85648e-01	-1.8032	1.42827e+03	178.5174
3.00000e-04	4.28474e-01	-1.6028	1.42841e+03	179.1185
4.00000e-04	5.71309e-01	-1.3223	1.42877e+03	179.9597
5.00000e-04	7.14162e-01	-0.9616	1.42955e+03	181.0406
6.00000e-04	8.57050e-01	-0.5209	1.43095e+03	182.3602
7.00000e-04	1.00000e+00	0.0000	1.43326e+03	183.9164
8.00000e-04	1.00000e+00	0.0000	0.00000e+00	0.000000
9.00000e-04	1.00000e+00	0.0000	1.43827e+03	172.1772
1.00000e-03	1.14263e+00	-0.8714	1.43322e+03	173.9600
1.10000e-03	1.28542e+00	-1.3356	1.42977e+03	175.9946
1.20000e-03	1.42825e+00	-1.4906	1.42835e+03	178.2770
1.30000e-03	1.57109e+00	-1.3988	1.42945e+03	180.8003
1.40000e-03	1.71395e+00	-1.1019	1.43359e+03	183.5545
1.50000e-03	1.85688e+00	-0.6287	1.44131e+03	186.5254
1.60000e-03	2.00000e+00	0.0000	1.45318e+03	189.6950
1.70000e-03	2.00000e+00	0.0000	0.00000e+03	0.000000
1.80000e-03	2.00000e+00	0.0000	1.46304e+03	166.4577
1.90000e-03	2.14247e+00	-0.8013	1.44581e+03	169.8144
2.00000e-03	2.28521e+00	-1.2772	1.43402e+03	173.4819
2.10000e-03	2.42803e+00	-1.4708	1.42860e+03	177.4356
2.20000e-03	2.57087e+00	-1.4158	1.43043e+03	181.6400
2.30000e-03	2.71373e+00	-1.1388	1.44037e+03	186.0494
2.40000e-03	2.85672e+00	-0.6611	1.45916e+03	190.6099
2.50000e-03	3.00000e+00	0.0000	1.48741e+03	195.2626
2.60000e-03	3.00000e+00	0.0000	0.00000e+03	0.000000
2.70000e-03	3.00000e+00	0.0000	4.29978e+03	3.9164
2.80000e-03	2.57115e+00	-0.5209	4.29285e+03	2.3602
2.90000e-03	2.14248e+00	-0.9616	4.28864e+03	1.0406
3.00000e-03	1.71393e+00	-1.3223	4.28632e+03	-0.0403
3.10000e-03	1.28542e+00	-1.6028	4.28522e+03	-0.8815
3.20000e-03	8.56943e-01	-1.8032	4.28481e+03	-1.4826
3.30000e-03	4.28471e-01	-1.9234	4.28471e+03	-1.8432
3.40000e-03	0.00000e+00	0.0000	4.28471e+03	-1.9635

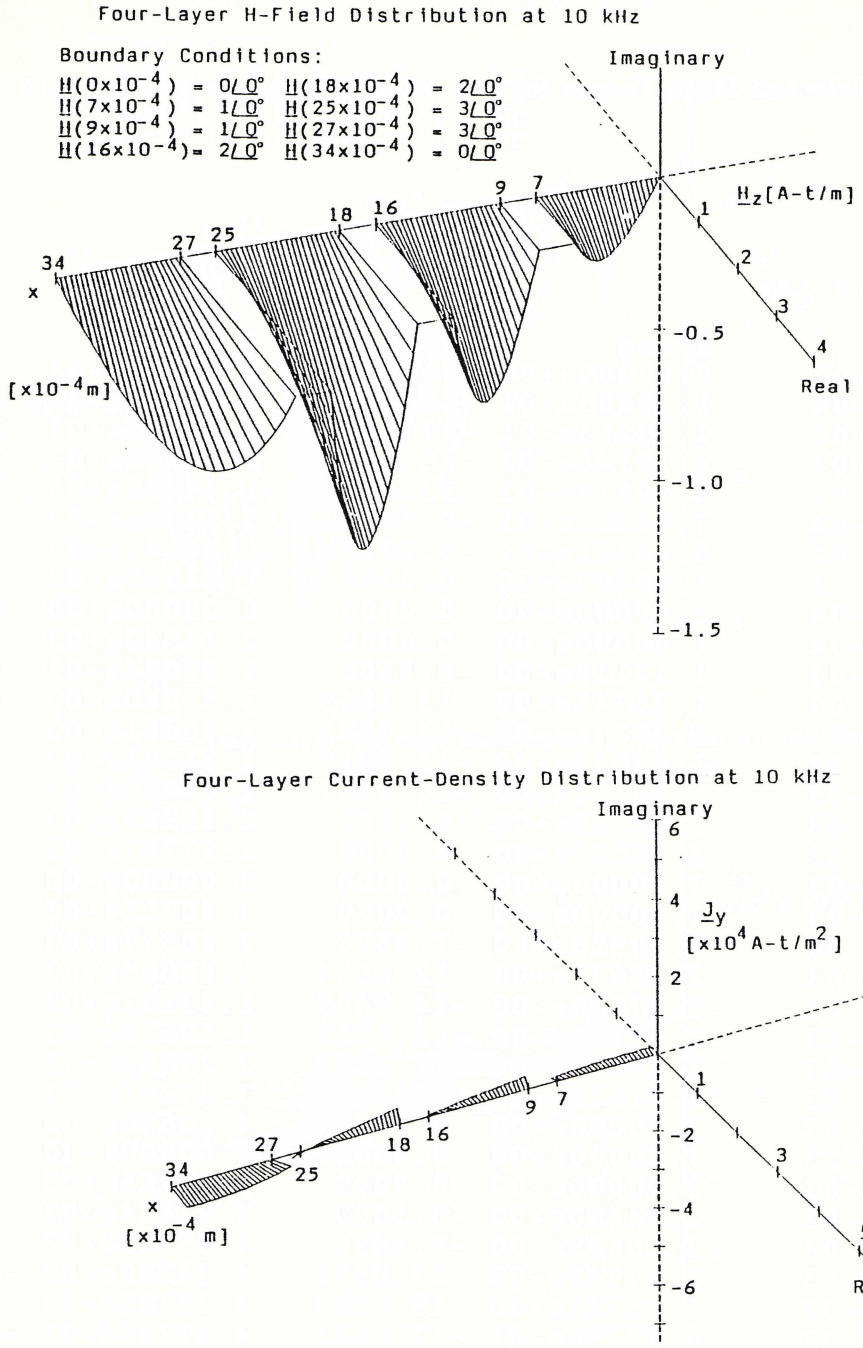


Figure 4.19: The magnetic-field-intensity and current-density phasor distributions across the four-layer solenoid of Fig. 4.15 at an excitation frequency of 10 kHz.

Table 4.2: Selected Data Points for the 10 kHz Example of Fig. 4.19

10 kHz

X	H_mag	H_phase	J_mag	J_phase
0.00000e+00	0.00000e+00	0.0000	1.39605e+03	160.5350
1.00000e-04	1.39606e-01	-19.0642	1.39625e+03	161.7372
2.00000e-04	2.79253e-01	-17.8621	1.39932e+03	165.3379
3.00000e-04	4.19145e-01	-15.8594	1.41255e+03	171.2874
4.00000e-04	5.59816e-01	-13.0592	1.44760e+03	179.4014
5.00000e-04	7.02282e-01	-9.4696	1.51902e+03	189.2615
6.00000e-04	8.48201e-01	-5.1070	1.64145e+03	200.2059
7.00000e-04	1.00000e+00	0.0000	1.82655e+03	211.4858
8.00000e-04	1.00000e+00	0.0000	0.00000e+00	0.000000
9.00000e-04	1.00000e+00	0.0000	2.16940e+03	119.7010
1.00000e-03	1.12119e+00	-8.5506	1.82064e+03	127.6220
1.10000e-03	1.25745e+00	-13.1865	1.53880e+03	141.7406
1.20000e-03	1.39771e+00	-14.7382	1.40691e+03	162.9370
1.30000e-03	1.53841e+00	-13.8219	1.51001e+03	186.9886
1.40000e-03	1.68132e+00	-10.8587	1.84820e+03	207.1418
1.50000e-03	1.83220e+00	-6.1601	2.35569e+03	221.8426
1.60000e-03	2.00000e+00	0.0000	2.97797e+03	232.8359
1.70000e-03	2.00000e+00	0.0000	0.00000e+00	0.000000
1.80000e-03	2.00000e+00	0.0000	3.40711e+03	104.1605
1.90000e-03	2.10528e+00	-7.8573	2.60577e+03	110.1328
2.00000e-03	2.23670e+00	-12.6034	1.88065e+03	124.4120
2.10000e-03	2.37636e+00	-14.5405	1.43102e+03	154.6951
2.20000e-03	2.51707e+00	-13.9915	1.59658e+03	193.8641
2.30000e-03	2.66062e+00	-11.2253	2.29856e+03	218.8485
2.40000e-03	2.81638e+00	-6.4772	3.24257e+03	232.6002
2.50000e-03	3.00000e+00	0.0000	4.30640e+03	241.7189
2.60000e-03	3.00000e+00	0.0000	0.00000e+00	0.000000
2.70000e-03	3.00000e+00	0.0000	5.47965e+03	31.4858
2.80000e-03	2.54460e+00	-5.1070	4.92434e+03	20.2059
2.90000e-03	2.10685e+00	-9.4696	4.55705e+03	9.2615
3.00000e-03	1.67945e+00	-13.0592	4.34280e+03	-0.5986
3.10000e-03	1.25744e+00	-15.8594	4.23765e+03	-8.7126
3.20000e-03	8.37758e-01	-17.8621	4.19796e+03	-14.6621
3.30000e-03	4.18818e-01	-19.0642	4.18875e+03	-18.2628
3.40000e-03	0.00000e+00	0.0000	4.18814e+03	-19.4650

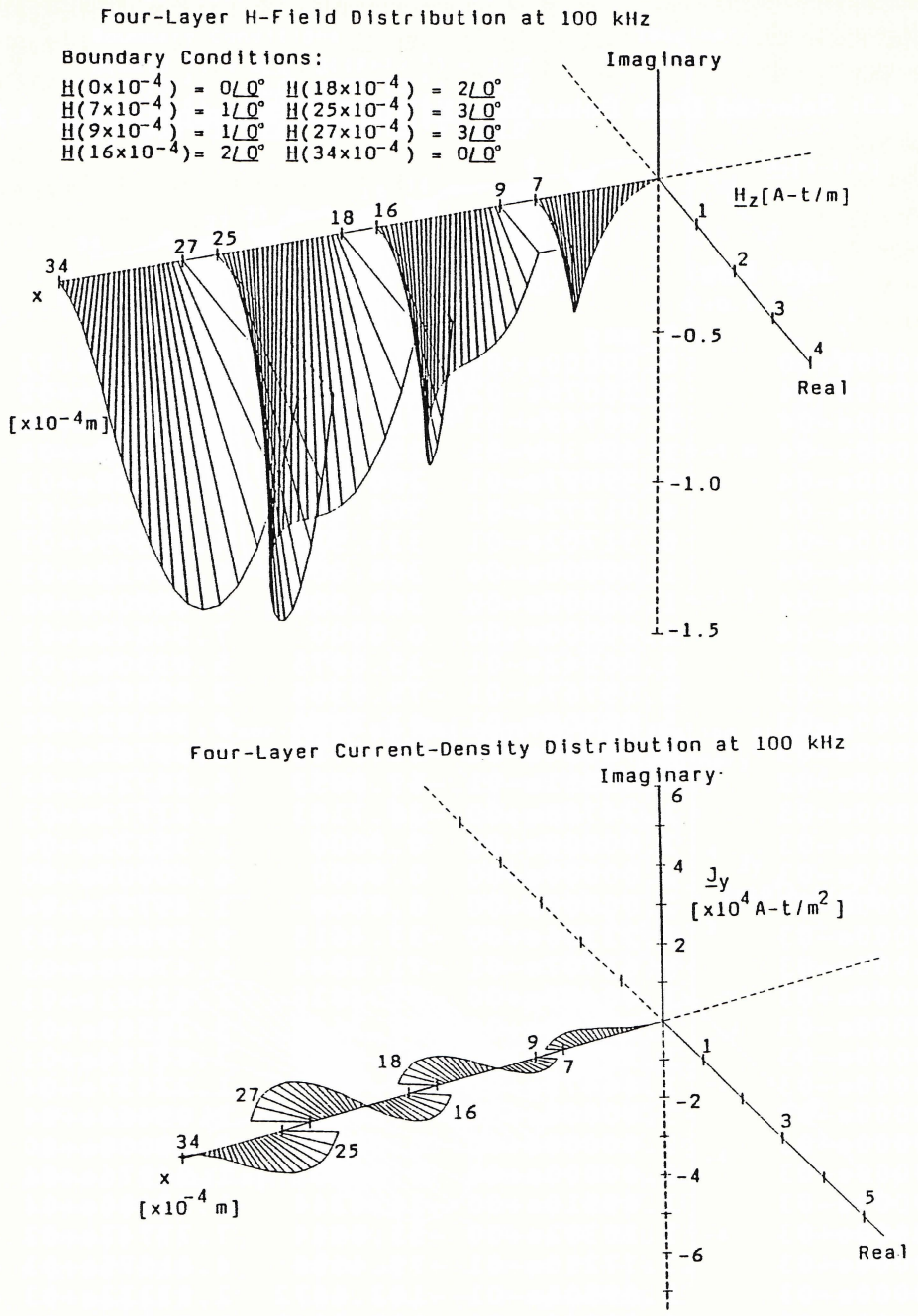


Figure 4.20: The magnetic-field-intensity and current-density phasor distributions across the four-layer solenoid of Fig. 4.15 at an excitation frequency of 100 kHz.

Table 4.3: Selected Data Points for the 100 kHz Example of Fig. 4.20

100 kHz

X	H_mag	H_phase	J_mag	J_phase
0.00000e+00	0.00000e+00	0.0000	5.25562e+02	41.2696
1.00000e-04	5.26076e-02	225.2756	5.33222e+02	53.1994
2.00000e-04	1.06749e-01	237.2053	6.37812e+02	84.5987
3.00000e-04	1.69836e-01	256.3328	9.77408e+02	118.5125
4.00000e-04	2.59097e-01	280.5344	1.60558e+03	147.0011
5.00000e-04	4.01272e-01	306.9156	2.59249e+03	173.0797
6.00000e-04	6.31702e-01	333.5756	4.11599e+03	198.9081
7.00000e-04	1.00000e+00	360.0000	6.49919e+03	224.9757
8.00000e-04	1.00000e+00	360.0000	0.00000e+00	0.000000
9.00000e-04	1.00000e+00	0.0000	7.54842e+03	44.4600
1.00000e-03	6.06942e-01	-35.8975	5.03306e+03	25.7643
1.10000e-03	5.15767e-01	-75.9305	2.85883e+03	19.5702
1.20000e-03	5.85708e-01	-93.2190	9.39182e+02	63.8825
1.30000e-03	6.76694e-01	-85.3711	2.39787e+03	158.2123
1.40000e-03	8.45511e-01	-59.8853	5.20725e+03	180.1128
1.50000e-03	1.24788e+00	-28.7183	8.67772e+03	200.8921
1.60000e-03	2.00000e+00	0.0000	1.35229e+04	224.8317
1.70000e-03	2.00000e+00	0.0000	0.00000e+00	0.000000
1.80000e-03	2.00000e+00	0.0000	1.45721e+04	44.5750
1.90000e-03	1.22306e+00	-33.4615	9.59601e+03	24.2973
2.00000e-03	9.61707e-01	-71.2844	5.47898e+03	13.5126
2.10000e-03	1.00487e+00	-91.4626	1.53561e+03	32.6161
2.20000e-03	1.09599e+00	-86.7649	3.23589e+03	163.7482
2.30000e-03	1.29345e+00	-61.9907	7.84794e+03	182.4309
2.40000e-03	1.86475e+00	-29.4952	1.32427e+04	201.5086
2.50000e-03	3.00000e+00	0.0000	2.05466e+04	224.7862
2.60000e-03	3.00000e+00	0.0000	0.00000e+00	0.000000
2.70000e-03	3.00000e+00	0.0000	1.94976e+04	44.9757
2.80000e-03	1.89510e+00	-26.4244	1.23480e+04	18.9081
2.90000e-03	1.20382e+00	-53.0844	7.77747e+03	-6.9203
3.00000e-03	7.77290e-01	-79.4656	4.81675e+03	-32.9989
3.10000e-03	5.09508e-01	-103.6672	2.93222e+03	-61.4875
3.20000e-03	3.20246e-01	-122.7947	1.91344e+03	-95.4013
3.30000e-03	1.57823e-01	-134.7244	1.59967e+03	-126.8006
3.40000e-03	0.00000e+00	0.0000	1.57668e+03	-138.7304

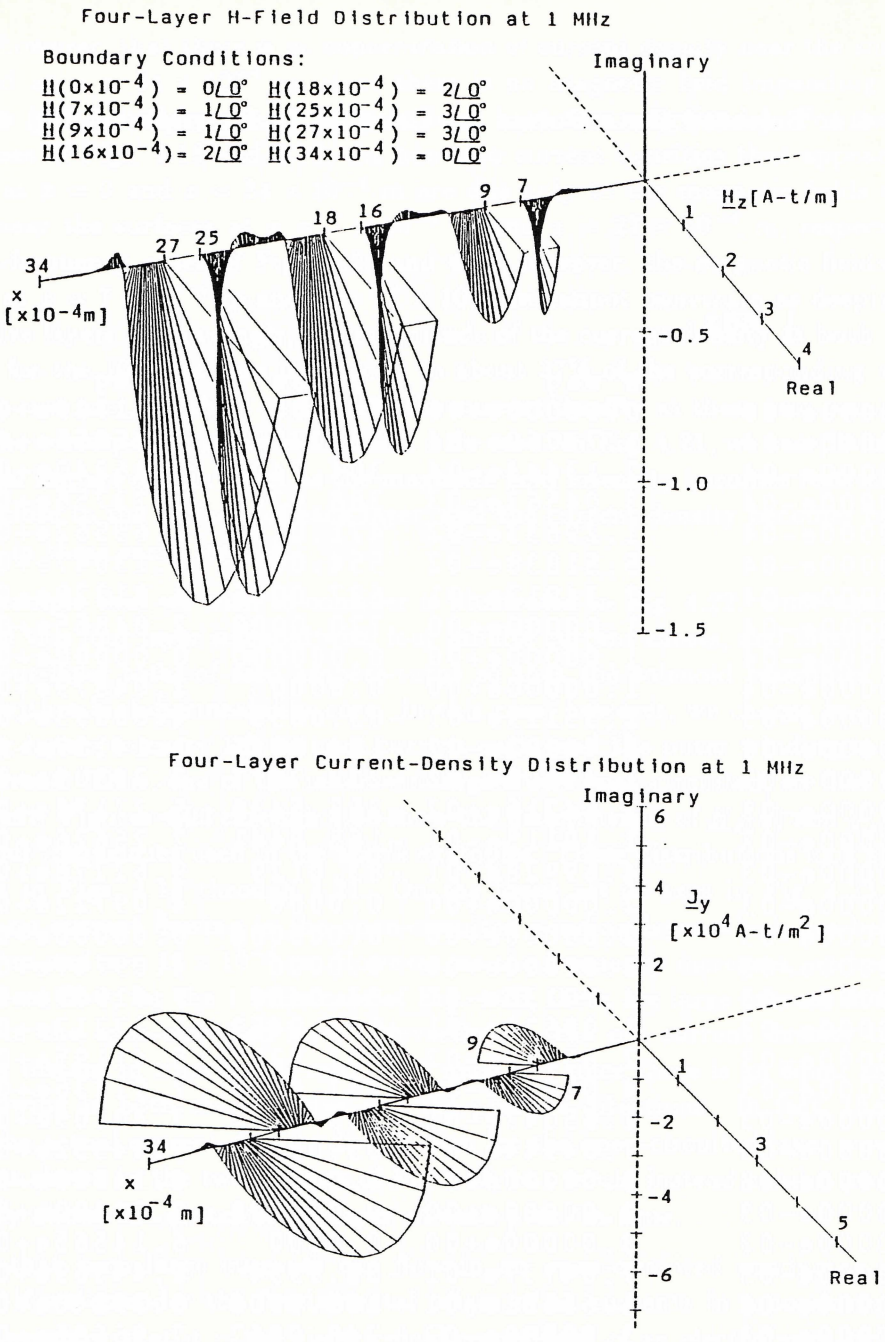


Figure 4.21: The magnetic-field-intensity and current-density phasor distributions across the four-layer solenoid of Fig. 4.15 at an excitation frequency of 1 MHz.

Table 4.4: Selected Data Points for the 1 MHz Example of Fig. 4.21

1 MHz

X	H_mag	H_phase	J_mag	J_phase
0.00000e+00	0.00000e+00	0.0000	1.61739e+00	4.0321
1.00000e-04	1.77060e-04	222.7539	3.25855e+00	86.2188
2.00000e-04	7.13443e-04	304.9407	1.46940e+01	170.1046
3.00000e-04	3.04563e-03	388.0248	6.23756e+01	253.0119
4.00000e-04	1.29633e-02	471.0133	2.65562e+02	336.0142
5.00000e-04	5.51838e-02	554.0092	1.13047e+03	419.0091
6.00000e-04	2.34912e-01	637.0046	4.81229e+03	502.0046
7.00000e-04	1.00000e+00	720.0000	2.04855e+04	585.0000
8.00000e-04	1.00000e+00	0.000000	0.00000e+00	0.00000
9.00000e-04	1.00000e+00	0.0000	2.04879e+04	44.9941
1.00000e-03	2.35119e-01	-83.0655	4.80863e+03	-37.9312
1.10000e-03	5.46902e-02	-164.5945	1.14137e+03	-122.3674
1.20000e-03	1.49809e-02	-272.7877	2.79309e+02	-177.6703
1.30000e-03	2.64715e-02	-255.5438	5.27172e+02	-17.2415
1.40000e-03	1.10115e-01	-165.6441	2.26626e+03	58.6625
1.50000e-03	4.69928e-01	-83.0129	9.62276e+03	142.0206
1.60000e-03	2.00000e+00	0.0000	4.09722e+04	224.9985
1.70000e-03	2.00000e+00	0.000000	0.00000e+00	0.00000
1.80000e-03	2.00000e+00	0.0000	4.09747e+04	44.9956
1.90000e-03	4.70135e-01	-83.0480	9.61909e+03	-37.9473
2.00000e-03	1.09621e-01	-164.9459	2.27717e+03	-122.0257
2.10000e-03	2.85219e-02	-267.5257	5.41195e+02	-183.9144
2.20000e-03	4.00918e-02	-257.6598	7.91236e+02	-14.9825
2.30000e-03	1.65047e-01	-165.5282	3.40209e+03	58.5474
2.40000e-03	7.04944e-01	-83.0188	1.44332e+04	142.0260
2.50000e-03	3.00000e+00	-0.0000	6.14589e+04	224.9980
2.60000e-03	3.00000e+00	0.000000	0.00000e+00	0.00000
2.70000e-03	3.00000e+00	-0.0000	6.14565e+04	45.0000
2.80000e-03	7.04737e-01	-82.9954	1.44369e+04	-37.9954
2.90000e-03	1.65551e-01	-165.9908	3.39140e+03	-120.9909
3.00000e-03	3.88898e-02	-248.9867	7.96685e+02	-203.9858
3.10000e-03	9.13688e-03	-331.9752	1.87127e+02	-286.9881
3.20000e-03	2.14033e-03	-415.0593	4.40821e+01	-369.8954
3.30000e-03	5.31180e-04	-497.2461	9.77566e+00	-453.7812
3.40000e-03	0.00000e+00	0.0000	4.85218e+00	-535.9679

layer. Note, however, that there is no concentration of current density near the surfaces at $x = 0$ and at $x = 34 \times 10^{-4}$ m, since there is no magnetic field impending upon these surfaces (the boundary-value magnetic fields have zero magnitude). For the low-frequency cases of Figs. 4.18 and 4.19, the non-zero current densities that appear near the surfaces at $x = 0$ and $x = 34 \times 10^{-4}$ m are due only to the magnetic fields which are present near the surfaces at $x = 7 \times 10^{-4}$ m and $x = 27 \times 10^{-4}$ m, respectively. For the high-frequency cases of Figs. 4.20 and 4.21, however, the magnetic fields near the surfaces at $x = 7 \times 10^{-4}$ m and $x = 27 \times 10^{-4}$ m cannot penetrate as deeply into their respective layers. Accordingly, the magnitude of the current density at both $x = 0$ and $x = h_{cu}$ for the 100 kHz-case is reduced to about 37% of the corresponding values for the 1 kHz-case and, for the 1 MHz-case, the current density at these two points less than 1% of the corresponding values for the 1 kHz case. In Fig. 4.21, we can plainly see the substantial impact of skin effect as the magnetic field intensity becomes restricted to regions very close to the surfaces of each layer, and the current density becomes heavily concentrated in these same regions.

A final example that we wish to consider is illustrated in Fig. 4.22. Once again, we wish to model this four layer solenoid with four infinite current sheets, and intentionally establish a four-layer total of zero ampere-turns so that the solenoid resembles a real transformer with a high-permeability core. In this case, however, we choose two of the inner winding layers to carry 1.5 units of current each, and the outer winding to carry 3 units of current. Thus, one of the inner windings is left open-circuited, so that it has zero net current. Figures 4.23 through 4.26 show the distributions of $\underline{H}_z(x)$ and $\underline{J}_y(x)$ at each of the four frequencies used in the above examples. These distributions look similar to those seen in Figs. 4.18 through 4.21. On the lower set of axes in Fig. 4.23, note that there is no current flowing in the open-circuited winding layer which lies between $x = 9 \times 10^{-4}$ m and $x = 16 \times 10^{-4}$ m. However, as the frequency increases, we begin to see some current flow; for the 1 MHz case of Fig. 4.26, there are large current densities that appear in the open-circuited layer. Nevertheless, the net current density in this layer at every instant in time is still zero (as it must be) since there is an equal amount of current flowing in both the negative and the positive directions. In fact, the time variation of the actual current-density distribution for the open-circuited layer would be similar to that shown in the twelve plots of Fig 4.13, but would instead exhibit *precisely* odd symmetry about the center of the layer at each point in time.

The fact that such large currents can flow in an open-circuited conductor is not so surprising if we consider the fundamental origin of ac currents in a conductor. In Appendix D we show that it is the electric-field component of an electromagnetic wave that causes the sinusoidal currents to flow in a winding layer. If we focus on the open-circuited layer of Fig. 4.26, then we can say that the resulting distribution of magnetic field intensity and current density across this layer actually consists of a superposition of two transverse electromagnetic (TEM) waves. One wave originates at $x = 9 \times 10^{-4}$ m and travels to the left, while the other wave originates at $x = 16 \times 10^{-4}$ m and travels to the right. We know that the projection of the current-density phasors in the open-circuited

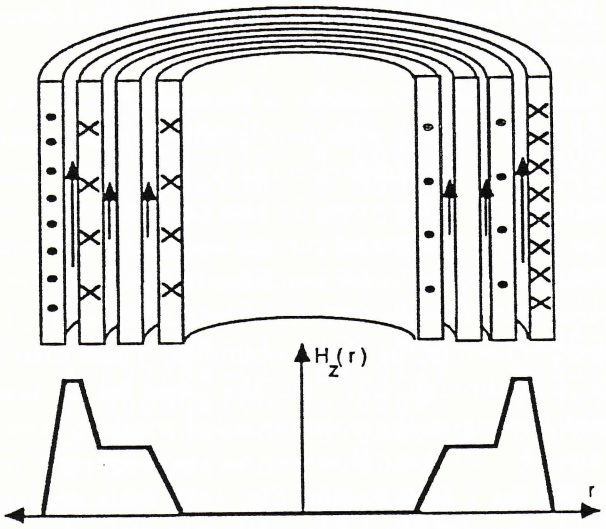
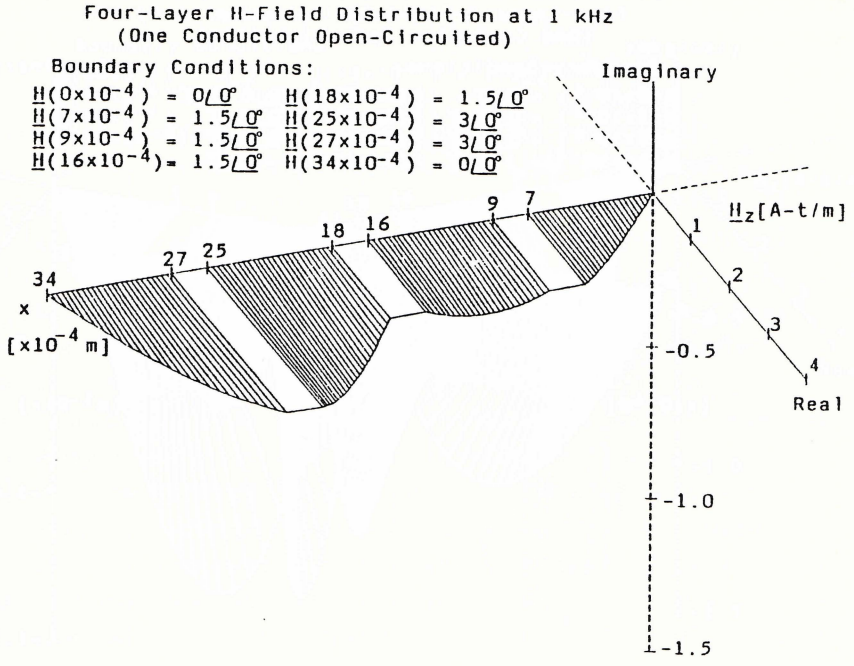


Figure 4.22: Structure of a four-layer solenoid. Two of the three inner layers are of the same winding while the other inner layer is left open circuited. The outer layer carries a current equal to the sum of the currents in the two current-carrying inner layers.



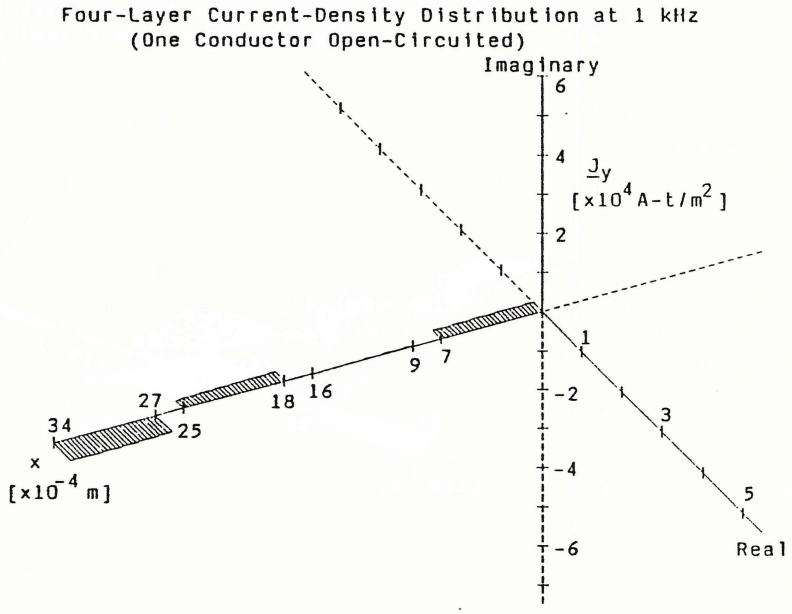


Figure 4.23: The magnetic-field-intensity and current-density phasor distributions across the four-layer solenoid of Fig. 4.22 at an excitation frequency of 1 kHz.

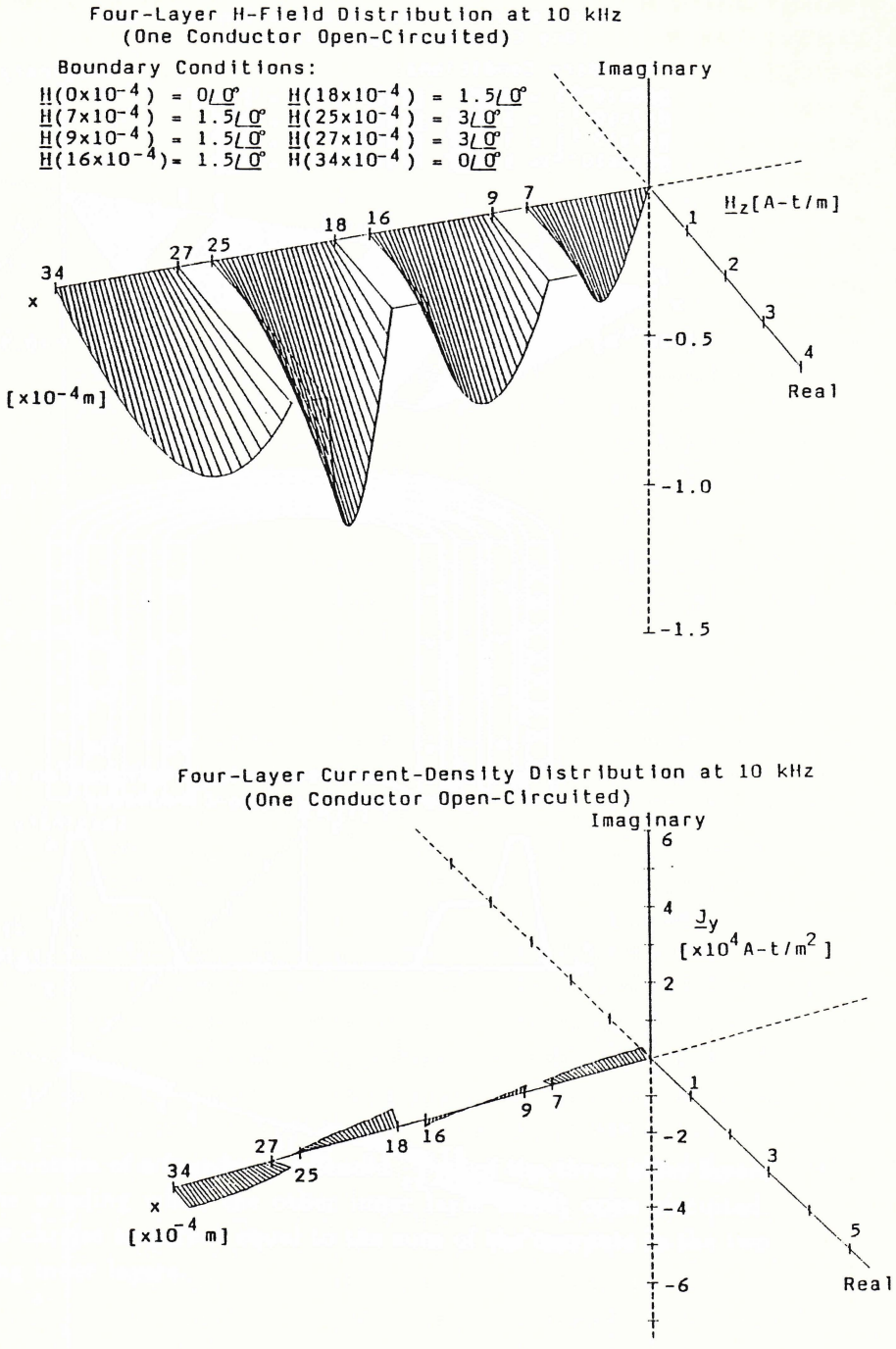
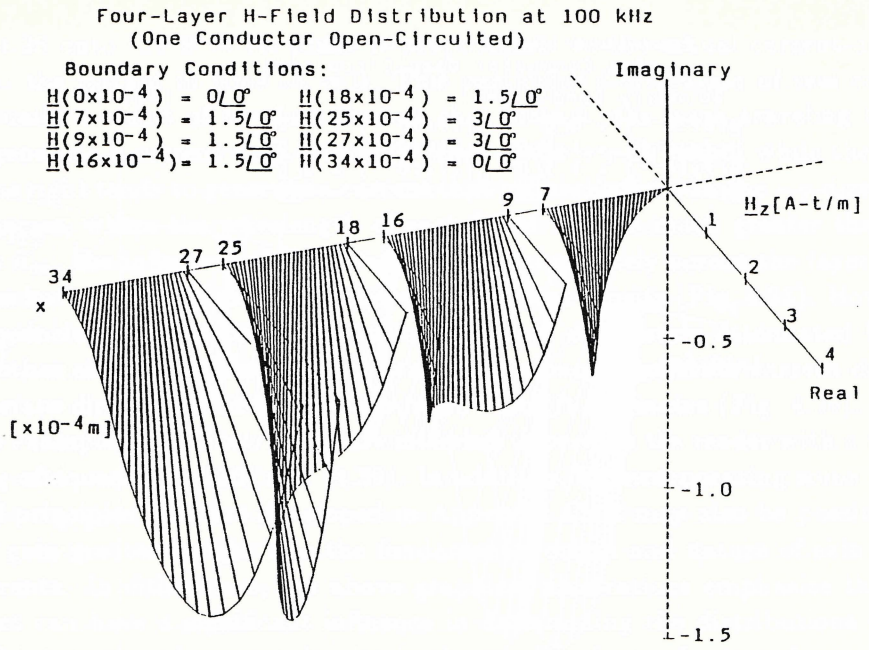


Figure 4.24: The magnetic-field-intensity and current-density phasor distributions across the four-layer solenoid of Fig. 4.22 at an excitation frequency of 10 kHz.



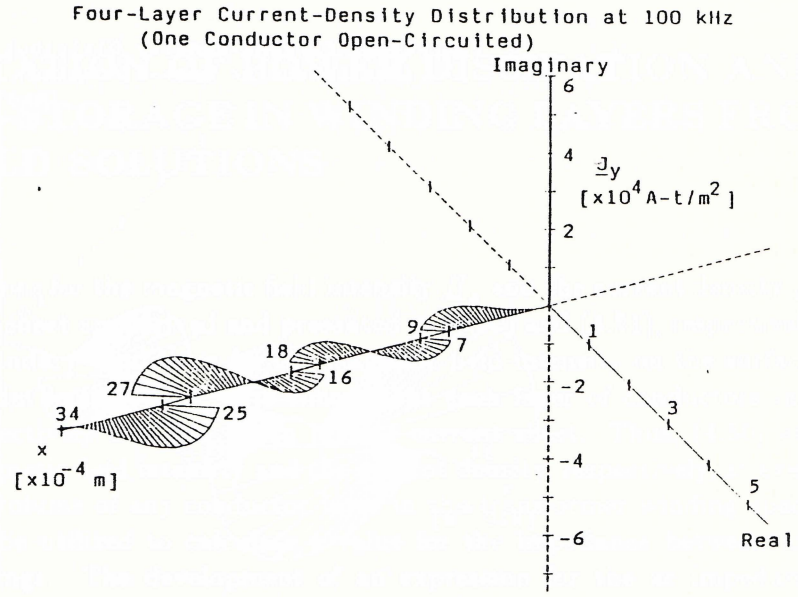
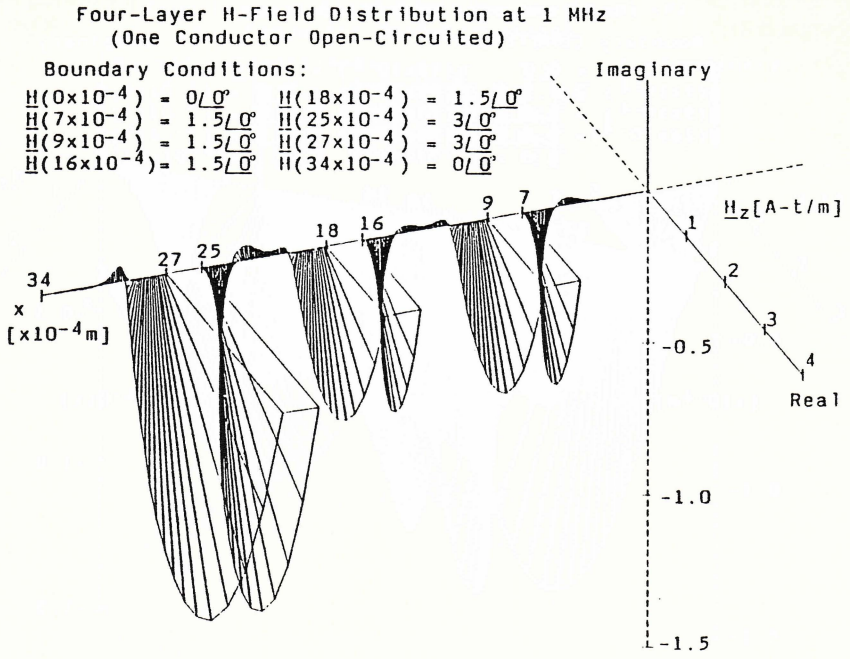


Figure 4.25: The magnetic-field-intensity and current-density phasor distributions across the four-layer solenoid of Fig. 4.22 at an excitation frequency of 100 kHz.



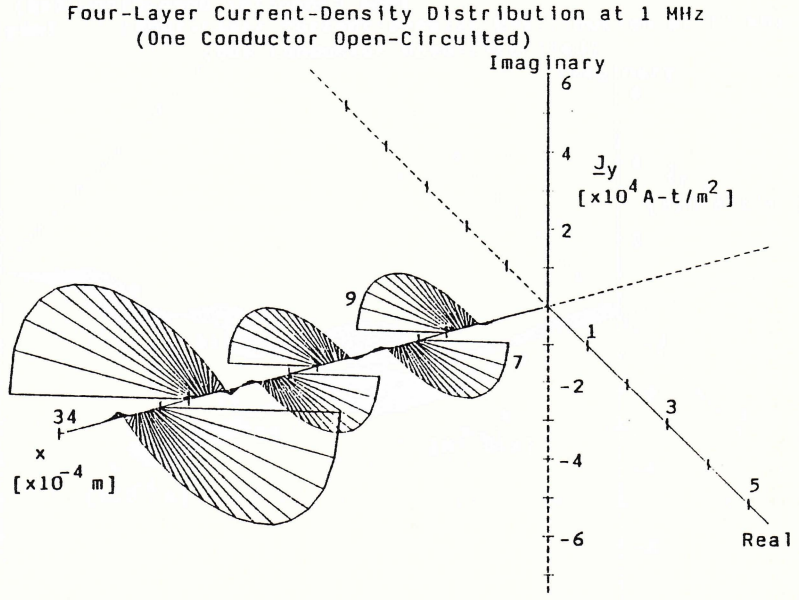


Figure 4.26: The magnetic-field-intensity and current-density phasor distributions across the four-layer solenoid of Fig. 4.22 at an excitation frequency of 1 MHz.

layer of Fig. 4.26 onto the x vs Re plane is proportional to the actual current-density distribution at the instant in time $\omega t = 0$. This particular distribution of real current density is actually a result of the fact that at that instant, the wave traveling to the left tends to generate a current that primarily flows in the $+y$-direction, while the wave traveling to the right tends to generate a current that primarily flows in the $-y$-direction. At low frequencies, where the wavelength of each TEM wave is much greater than the copper height h_{cu}, the influence of each wave extends completely across the layer, and, since the waves have opposing influences, there is no current density (Fig. 4.23). However, at higher frequencies, each of the TEM waves is almost completely attenuated before reaching the other side, and therefore each wave acts alone to generate current density in the appropriate direction near the surface from which it originates (Fig. 4.26).

The above examples and illustrations are intended to provide the reader with a better understanding of equations (4.36) and (4.39). In addition, by incorporating some of the basic physical principles that are developed in Appendix D, it may also be possible for the reader to gain greater insight into the fundamental origin and nature of skin effect and eddy currents. In either case, the above graphical illustrations emphasize the fact that skin effect can have a significant influence in determining the distributions of the magnetic field intensity and current density in the winding layer of a transformer. Our next logical step is to determine the effect of these distributions on the energy-storage and power-loss characteristics of a winding layer.

4.5 COMPUTATION OF POWER DISSIPATION AND ENERGY-STORAGE IN WINDING LAYERS FROM THE FIELD SOLUTIONS

4.5.1 Overview

In Section 4.2, expressions for the magnetic field intensity $\underline{H}_z$ and the current density $\underline{J}_y$ for any infinite current sheet are derived and presented in (4.50) and (4.51), respectively, as functions of the boundary conditions for the magnetic field intensity on the surfaces of the current sheet. In Section 3.1.2, it is shown that each layer of conductors in a transformer can be effectively modeled by an infinite current sheet. Thus, (4.50) and (4.51) describe the magnetic field intensity and the current density, respectively, at every point throughout the volume of any conductor layer in the transformer winding space. Such expressions can be utilized to calculate a value for the impedance between any two transformer windings. The development of an expression for the ac impedance requires the calculation of the ac winding resistance and the ac leakage inductance of the transformer under the appropriate winding-excitation conditions. Several additional new ideas apply to these calculations in general and are worth being emphasized at this point.

Providing the magnetizing inductance is relatively large, reflection indicates that the only reasonable use of the term *leakage inductance* is with reference to the total inductance that exists between *two windings taken as a pair.* For a simple two-winding transformer, there is only one such leakage inductance; in more complicated devices, however, there is a leakage inductance between each pair of windings. Therefore, in calculating formulae for leakage inductance in transformers, we want to keep in mind that the formulae are written for situations where only two windings of the device carry a net current. This is the same situation that exists when measuring the short-circuit impedance of a transformer in the laboratory. In such a test, one winding is short-circuited and one winding is excited from a source; if the device has any other windings, they are left open-circuited. The expressions that we derive for the impedance between two windings in the following discussion are based on such a *short-circuit test* condition.

The calculation of impedance can be divided into a calculation of the real and imaginary parts of the impedance. We derive separate expressions for both the resistive and the inductive components of the impedance between any two windings.

After the field solution has been obtained for the magnetic field intensity and the current density, the next step is to apply the field solution to model a transformer. Depending on the model assumed for the transformer—two models are proposed in Chapters 7 and 8—the various parameters associated with the equivalent model can be estimated either through laboratory measurements or through calculation based on the solutions to the magnetic field intensity and the current density derived in this chapter. It is shown in Chapter 5 that the estimation of the model parameters centers on the computation of the power losses and on the energy stored in the magnetic field in the space occupied by the winding layers. Hence, the calculation of the power losses and the energy stored in the winding layers is a crucial step in obtaining parameters for such models.

In general, the instantaneous power loss per unit volume $p_d(t)$ at a point is given by (3.16) and the instantaneous energy stored in the magnetic field per unit volume $w_m(t)$ at a point is given by (3.17). They are repeated here for convenience.

$$p_d(t) = \frac{|\mathbf{J}(t)|^2}{\sigma} \tag{4.69}$$

$$w_m(t) = \frac{\mu_0 |\mathbf{H}(t)|^2}{2} \tag{4.70}$$

The total instantaneous conduction loss $P_n(t)$ and the total instantaneous energy $W_n(t)$ stored in the magnetic field in the n^{th} conducting layer are then equal, respectively, to the volume integrals of $p_d(t)$ and $w_m(t)$ over the volume occupied by the n^{th} layer.

$$P_n(t) = \iiint_{V_n} p_d(t)\, d\nu = \iiint_{V_n} \frac{|\mathbf{J}(t)|^2}{\sigma}\, d\nu \tag{4.71}$$

$$W_n(t) = \iiint_{V_n} w_m(t)\, d\nu = \iiint_{V_n} \frac{\mu_0 |\mathbf{H}(t)|^2}{2}\, d\nu \tag{4.72}$$

where the subscript V_n in the integration symbol is used to remind us that this volume integral is carried out over the winding space occupied by the n^{th} layer. Since the current density in the air space between winding layers is equal to zero, the resistive portion of the leakage impedance can be computed entirely from the power loss P_n in the winding layers. On the other hand, the magnetic field intensity is not equal to zero in the air space between winding layers. Therefore, the estimation of the reactive portion of the leakage impedance requires not only the computation of W_n, the energy stored in the magnetic field in the winding layers, but also the computation of the energy stored in the magnetic field in the air space between winding layers. The computation of the energy stored in the air space will be discussed in more detail in Section 5.2.5.2.

As will be shown later in Sections 4.5.2 and 4.5.3, it is easier in the case of sinusoidal excitation to work with the average power loss and average energy storage over one period T of the sinusoid. Taking the average of the instantaneous conducting loss $P_n(t)$ and the instantaneous energy storage $W_n(t)$ defined in (4.71) and (4.72) then gives

$$\langle P_n \rangle = \frac{1}{T} \int_T \iiint_{V_n} \frac{|\mathbf{J}(t)|^2}{\sigma} \, d\nu \, dt \tag{4.73}$$

$$\langle W_n \rangle = \frac{1}{T} \int_T \iiint_{V_n} \frac{\mu_0 \, |\mathbf{H}(t)|^2}{2} \, d\nu \, dt \tag{4.74}$$

where the symbols $\langle P_n \rangle$ and $\langle W_n \rangle$ are used to represent the power loss and the energy storage in the space of the n^{th} winding layer, respectively, averaged over one period of excitation. The integration with respect to volume and the integration with respect to time can be interchanged:

$$\langle P_n \rangle = \iiint_{V_n} \left(\frac{1}{T} \int_T \frac{|\mathbf{J}(t)|^2}{\sigma} \, dt \right) d\nu \tag{4.75}$$

$$\langle W_n \rangle = \iiint_{V_n} \left(\frac{1}{T} \int_T \frac{\mu_0 \, |\mathbf{H}(t)|^2}{2} \, dt \right) d\nu \tag{4.76}$$

By defining the results of the integration with respect to time as

$$\langle p_d \rangle = \frac{1}{T} \int_T \frac{|\mathbf{J}(t)|^2}{\sigma} \, dt \tag{4.77}$$

$$\langle w_m \rangle = \frac{1}{T} \int_T \frac{\mu_0 \, |\mathbf{H}(t)|^2}{2} \, dt \tag{4.78}$$

where $\langle p_d \rangle$ and $\langle w_m \rangle$ are the average power loss per unit volume and the average energy storage per unit volume, respectively, the average power dissipated and the average energy storage in the volume of the n^{th} layer can be rewritten as:

$$\langle P_n \rangle = \iiint_{V_n} \langle p_d \rangle \, d\nu \tag{4.79}$$

$$\langle W_n \rangle = \iiint_{V_n} \langle w_m \rangle \, d\nu \tag{4.80}$$

For the n^{th} winding layer, the height x varies from zero to h_{cu}, the depth y varies from zero to the mean length of turn for the n^{th} layer ℓ_{T_n}, and the breadth z varies from zero to b_{win}. The terms *height*, *breadth*, and *depth* are defined in Section 2.1. The integrations in (4.79) and (4.80) become

$$\langle P_n \rangle = \int_0^{b_{win}} \int_0^{\ell_{T_n}} \int_0^{h_{cu}} \langle p_d \rangle \, dx \, dy \, dz \tag{4.81}$$

$$\langle W_n \rangle = \int_0^{b_{win}} \int_0^{\ell_{T_n}} \int_0^{h_{cu}} \langle w_m \rangle \, dx \, dy \, dz \tag{4.82}$$

The expressions derived for the phasors of the magnetic field intensity and for the current density, (4.50) and (4.51), indicate that the magnetic field intensity and the current density are dependent on the height x but not on the depth y nor the breadth z. This implies that the average loss density $\langle p_d \rangle$ and the average energy storage density $\langle w_m \rangle$ are dependent on x but not on y nor z. As a result, it is advantageous to evaluate the volume integrals in (4.81) and (4.82) in two steps; the first step is a single integration in the x-direction, and the second step is a double integration involving the y- and z-directions. Let us define the results of the integrations with respect to x as:

$$\langle Q_J \rangle = \int_0^{h_{cu}} \langle p_d \rangle \, dx \tag{4.83}$$

$$\langle Q_H \rangle = \int_0^{h_{cu}} \langle w_m \rangle \, dx \tag{4.84}$$

Then the double integration with respect to y and z becomes trivial multiplication processes as the integrands $\langle Q_J \rangle$ and $\langle Q_H \rangle$ are independent of y and z, giving

$$\begin{aligned} \langle P_n \rangle &= \int_0^{b_{win}} \int_0^{\ell_{T_n}} \langle Q_J \rangle \, dy \, dz \\ &= b_{win} \, \ell_{T_n} \langle Q_J \rangle \end{aligned} \tag{4.85}$$

$$\begin{aligned} \langle W_n \rangle &= \int_0^{b_{win}} \int_0^{\ell_{T_n}} \langle Q_H \rangle \, dy \, dz \\ &= b_{win} \, \ell_{T_n} \langle Q_H \rangle \end{aligned} \tag{4.86}$$

The benefit of evaluating the integral over the x coordinate first is that the resulting formulae yield the average power dissipation $\langle Q_J \rangle$ and the average energy storage $\langle Q_H \rangle$

per square meter of conductor in the y-z plane. These expressions are written in terms of the boundary conditions so that the results are general for any winding layer. Once the integrations have been evaluated over the height (x-coordinate) of a current sheet, the results can be multiplied by the depth and breadth of the winding layer to get the complete volume integrals. The derivation of $\langle Q_J \rangle$ and $\langle Q_H \rangle$ are presented in details in the next two sections.

J.P. Vandelac and P. Ziogas follow a procedure such as this to calculate the total power dissipation in a winding layer [19]; M.P. Perry in [13] evaluates the integration only over the layer height to derive expressions for power dissipation *per square meter of conductor in the breadth-depth plane.* These two analyses are both dependent on the actual currents in the transformer windings under load, and neither of them address the inductance of the windings at all. Their techniques are general and form the basis for the discussion here, but we do not follow the application of their results directly since we are interested in determining the load-independent circuit impedances. The type of analysis that both of these authors pursue is aimed more at a quantification of total winding *losses* than toward the development of a *circuit model* which can be used to predict the transformer terminal voltage characteristics. In the next sections, we present the main points of the solution for both average power loss $\langle Q_J \rangle$ and average energy storage $\langle Q_H \rangle$ per square meter in the y-z plane in a winding layer. The results of this solution for a single layer are then used to calculate the characteristic impedances of a multiwinding transformer.

4.5.2 Average Power Dissipation Per Square Meter of an Infinite Current Sheet

Equation (4.77) defines, for the case of periodic excitation, the average power dissipated per unit volume as

$$\langle p_d \rangle = \frac{1}{T} \int_T \frac{|\mathbf{J}(t)|^2}{\sigma} \, dt \tag{4.87}$$

where $\mathbf{J}(t)$ is the instantaneous current density at any point in an infinite current sheet. Since the current density in our model transformer has a nonzero component only in the y-direction, (4.87) can be further simplified to

$$\langle p_d \rangle = \frac{1}{T} \int_T \frac{|J_y(t)|^2}{\sigma} \, dt \tag{4.88}$$

The solutions for the current density and the magnetic field intensity derived in the previous sections, however, are in the form of phasor variables. Although the equivalent time-domain functions can always be computed from the phasor variables, one can take advantage of the complex arithmetic and work directly with the phasor variables. First, consider that the excitation is at an angular frequency ω where $\omega = 2\pi/T$. Since the

excitation is sinusoidal, the current density $J_y(t)$ and its corresponding phasor representation $\underline{J}_y$ can be assumed to take the forms of

$$J_y(t) = \sqrt{2}\,|\underline{J}_y|\,\cos(\omega t + \theta_J) \tag{4.89}$$

$$\underline{J}_y = |\underline{J}_y|\,e^{j\,\theta_J} \tag{4.90}$$

where $|\underline{J}_y|$, the magnitude of $\underline{J}_y$, is also the rms value of the current density. It is understood that the current density is also a function of the height x and its dependence on x is not explicitly shown here. Substituting (4.89) into (4.88) and carrying out the integration with respect to time yields

$$\begin{aligned}\langle p_d \rangle &= \frac{1}{T}\int_T \frac{2\,|\underline{J}_y|^2\cos^2(\omega t + \theta_J)}{\sigma}\,dt \\ &= \frac{|\underline{J}_y|^2}{\sigma}\end{aligned} \tag{4.91}$$

By definition, the product of the phasor $\underline{J}_y$ and its complex conjugate $\underline{J}_y^*$ gives the square of the magnitude of the phasor

$$\underline{J}_y\underline{J}_y^* = |\underline{J}_y|^2 \tag{4.92}$$

Hence, it is possible to express the average loss density $\langle p_d \rangle$ at a point in terms of the phasor of $J_y(t)$ as

$$\langle p_d \rangle = \frac{\underline{J}_y\,\underline{J}_y^*}{\sigma} \tag{4.93}$$

It is shown in the analysis of the infinite current sheet that the current density **J** has a nonzero component $\underline{J}_y$ in the y-direction which varies with respect to the height x. Reinserting the dependence of $\underline{J}_y$ on the height x gives

$$\langle p_d \rangle = \frac{\underline{J}_y(x)\,\underline{J}_y^*(x)}{\sigma} \tag{4.94}$$

As indicated earlier in (4.83), the integration of $\langle p_d \rangle$ from $x = 0$ to $x = h_{cu}$ yields the average power dissipated per square meter of current sheet in the y-z plane, designated as $\langle Q_J \rangle$, to match the symbol used in [13,19]. For ease of expressing the solution for the current density and the magnetic field intensity, we have introduced a variable χ earlier in (4.40). Depending on the magnitude of the magnetic field intensity on the boundaries of the conductor, χ is defined either as $\chi = x$ or $\chi = h_{cu} - x$. Instead of integrating (4.94) with respect to x, the average power dissipated in watts per square meter $\langle Q_J \rangle$ can also be obtained by integrating

$$\langle p_d \rangle = \frac{\underline{J}_y(\chi)\,\underline{J}_y^*(\chi)}{\sigma} \tag{4.95}$$

from $X = 0$ to $X = h_{cu}$. That is,

$$\begin{aligned} \langle Q_J \rangle &= \int_0^{h_{cu}} \frac{\underline{J}_y(X)\,\underline{J}_y^*(X)}{\sigma}\,dX \\ &= \frac{1}{\sigma}\int_0^{h_{cu}} \underline{J}_y(X)\,\underline{J}_y^*(X)\,dX \end{aligned} \tag{4.96}$$

To evaluate this integral, we must expand the product of the complex conjugates inside the integrand. This is done in detail in Appendix E; the results of this expansion are restated here. In order to simplify the form of the following expressions, we introduce the relationships

$$\Delta = \frac{h_{cu}}{\delta} \tag{4.97}$$

$$w = \frac{X}{\delta} \tag{4.98}$$

$$\begin{aligned} v &= \frac{h_{cu} - X}{\delta} \\ &= \Delta - w \end{aligned} \tag{4.99}$$

The variables w and v above are used simply to make the derivation given in Appendix E easier to read. The variable Δ also serves to simplify the derivation, but it has a physical interpretation that is important to understand.

Equation (4.97) above states that Δ *is the height of a winding layer in units of skin depth.* Bear in mind that the skin depth of a conducting layer depends upon the frequency of the transformer excitation. We show in the expressions below that the power dissipated and energy stored in any winding layer of a transformer is a function of the boundary values of the magnetic field intensity $\underline{H}_z(X = 0)$ and $\underline{H}_z(X = h_{cu})$, the skin depth δ of the conducting material at the excitation frequency, and Δ, the height of the layer normalized to the skin depth of the material.

This fact is important because it reminds us that it is not simply the frequency of the current in a transformer that causes the ac resistance and ac inductance effects in the device. Rather, it is the size of the conductors of the windings *relative to the skin depth of the conductive material for the particular frequency of excitation.* In other words, the so-called high-frequency effects that we are addressing in this document can occur at any excitation frequency provided the conductor size is large enough. Let us examine the case of 60-Hz power transmission lines. At 60°C, for example, the conductivity of annealed copper wire is $\sigma = 5.315 \times 10^7$ S/m. Together with $\omega = 120\pi$ and $\mu_0 = 4\pi \times 10^{-7}$ H/m, this gives a skin depth δ of 8.9 mm according to (4.7). Hence, there is a practical limit on the effectiveness of the size of conductors used in 60-Hz power transmission lines and power bus bars [21, p.201].

Returning to the integration of the average power-density function expressed by (4.96), the equation for the current density (4.51) is used in Appendix E to derive

$$\underline{J}_y(\chi)\underline{J}_y^*(\chi) = \frac{|\underline{k}|^2\,|\underline{H}_z(\chi = h_{cu})|^2}{(\cosh 2\Delta - \cos 2\Delta)} \times \Big\{ (\cosh 2w + \cos 2w) + (\alpha^2+\beta^2)(\cosh 2v + \cos 2v) - 2\alpha\big(\cosh\Delta\cos(\Delta-2w) + \cosh(\Delta-2w)\cos\Delta\big) + 2\beta\big(\sinh\Delta\sin(\Delta-2w) + \sinh(\Delta-2w)\sin\Delta\big) \Big\} \tag{4.100}$$

To see how the product $\underline{J}_y(\chi)\underline{J}_y^*(\chi)$ varies as a function of χ, v and w need to be eliminated from the above equation. From (4.98), we have $w = \chi/\delta$. From (4.99) we have $v = \Delta - w = \Delta - (\chi/\delta)$. So this product of $\underline{J}_y(\chi)\underline{J}_y^*(\chi)$ can be rewritten as:

$$\underline{J}_y(\chi)\underline{J}_y^*(\chi) = \frac{|\underline{k}|^2\,|\underline{H}_z(\chi = h_{cu})|^2}{(\cosh 2\Delta - \cos 2\Delta)} \times \Big\{ \Big[\cosh\Big(\frac{2\chi}{\delta}\Big) + \cos\Big(\frac{2\chi}{\delta}\Big)\Big] + \Big(\alpha^2+\beta^2\Big)\Big[\cosh\Big(2\Delta - \frac{2\chi}{\delta}\Big) + \cos\Big(2\Delta - \frac{2\chi}{\delta}\Big)\Big] - 2\alpha\Big[\cosh\Delta\cos\Big(\Delta - \frac{2\chi}{\delta}\Big) + \cosh\Big(\Delta - \frac{2\chi}{\delta}\Big)\cos\Delta\Big] + 2\beta\Big[\sinh\Delta\sin\Big(\Delta - \frac{2\chi}{\delta}\Big) + \sinh\Big(\Delta - \frac{2\chi}{\delta}\Big)\sin\Delta\Big] \Big\} \tag{4.101}$$

The details in the integration of (4.101) from $\chi = 0$ to $\chi = h_{cu}$ are shown in Appendix G, and the results are restated here:

$$\int_0^{h_{cu}} \underline{J}_y(\chi)\underline{J}_y^*(\chi)\,d\chi = \frac{|\underline{k}|^2\,|\underline{H}_z(\chi = h_{cu})|^2\,\delta}{2\,(\cosh 2\Delta - \cos 2\Delta)} \times \Big\{ (1+\alpha^2+\beta^2)(\sinh 2\Delta + \sin 2\Delta) - 4\alpha(\sinh\Delta\cos\Delta + \cosh\Delta\sin\Delta) \Big\} \tag{4.102}$$

Defining F_1 and F_2 as

$$F_1(\Delta) = \frac{\sinh 2\Delta + \sin 2\Delta}{\cosh 2\Delta - \cos 2\Delta} \tag{4.103}$$

$$F_2(\Delta) = \frac{\sinh\Delta\cos\Delta + \cosh\Delta\sin\Delta}{\cosh 2\Delta - \cos 2\Delta} \tag{4.104}$$

and recalling from (4.6) that $\underline{k} = (1+j)/\delta$, or $|\underline{k}|^2 = 2/\delta^2$, we can write the final result from (4.96) for the average power dissipation per square meter $\langle Q_J \rangle$ in the y-z plane as

$$\boxed{\begin{aligned}\langle Q_J \rangle &= \frac{|\underline{H}_z(X = h_{cu})|^2}{\sigma\delta}\left[(1+\alpha^2+\beta^2)F_1(\Delta) - 4\alpha F_2(\Delta)\right] \\ &= \frac{|\underline{H}_z(X = h_{cu})|^2}{\sigma\delta}\langle Q'_J(\alpha,\beta,\Delta)\rangle\end{aligned}} \tag{4.105}$$

where

$$\boxed{\langle Q'_J(\alpha,\beta,\Delta)\rangle = (1+\alpha^2+\beta^2)F_1(\Delta) - 4\alpha F_2(\Delta)} \tag{4.106}$$

These two equations essentially state the same result given by Vandelac and Ziogas in equation (A-17) of [19].

Since the functions $F_1(\Delta)$ and $F_2(\Delta)$ depend only on the parameter Δ, they are generally applicable to a winding layer of arbitrary height h_{cu} driven at an arbitrary excitation frequency ω. The plots of $F_1(\Delta)$ and $F_2(\Delta)$ are provided in Fig. 4.27. Once the conductivity σ and the frequency of excitation ω are known, the skin depth δ can be computed from (4.7). Then Δ, the height of a winding layer in units of skin depth, can be computed from h_{cu} and δ from (4.97). The functional values of F_1 and F_2 can be read directly from Fig. 4.27. Given the boundary conditions on the magnetic field intensity phasors $\underline{H}_z(X = 0)$ and $\underline{H}_z(X = h_{cu})$, the parameters α and β can be computed according to (4.48) and (4.49). With the knowledge of the parameters α and β, and the values of F_1 and F_2, $\langle Q'_J \rangle$ can be computed from (4.106). Finally, the average power dissipation per square meter $\langle Q_J \rangle$ in the y-z plane is computed according to (4.105). When Δ is large, the functions F_1 and F_2 approach to their respective limits:

$$\lim_{\Delta\to\infty} F_1(\Delta) = 1 \tag{4.107}$$

$$\lim_{\Delta\to\infty} F_2(\Delta) = 0 \tag{4.108}$$

To obtain a quick estimation of $\langle Q'_J \rangle$ in such a situation, F_1 and F_2 can be approximated by one and zero, respectively. The error introduced to $\langle Q'_J \rangle$ through such approximations is less than 10% for $\Delta \geq 2.2$ and less than 5% for $\Delta \geq 4.1$ for all values of α and β.

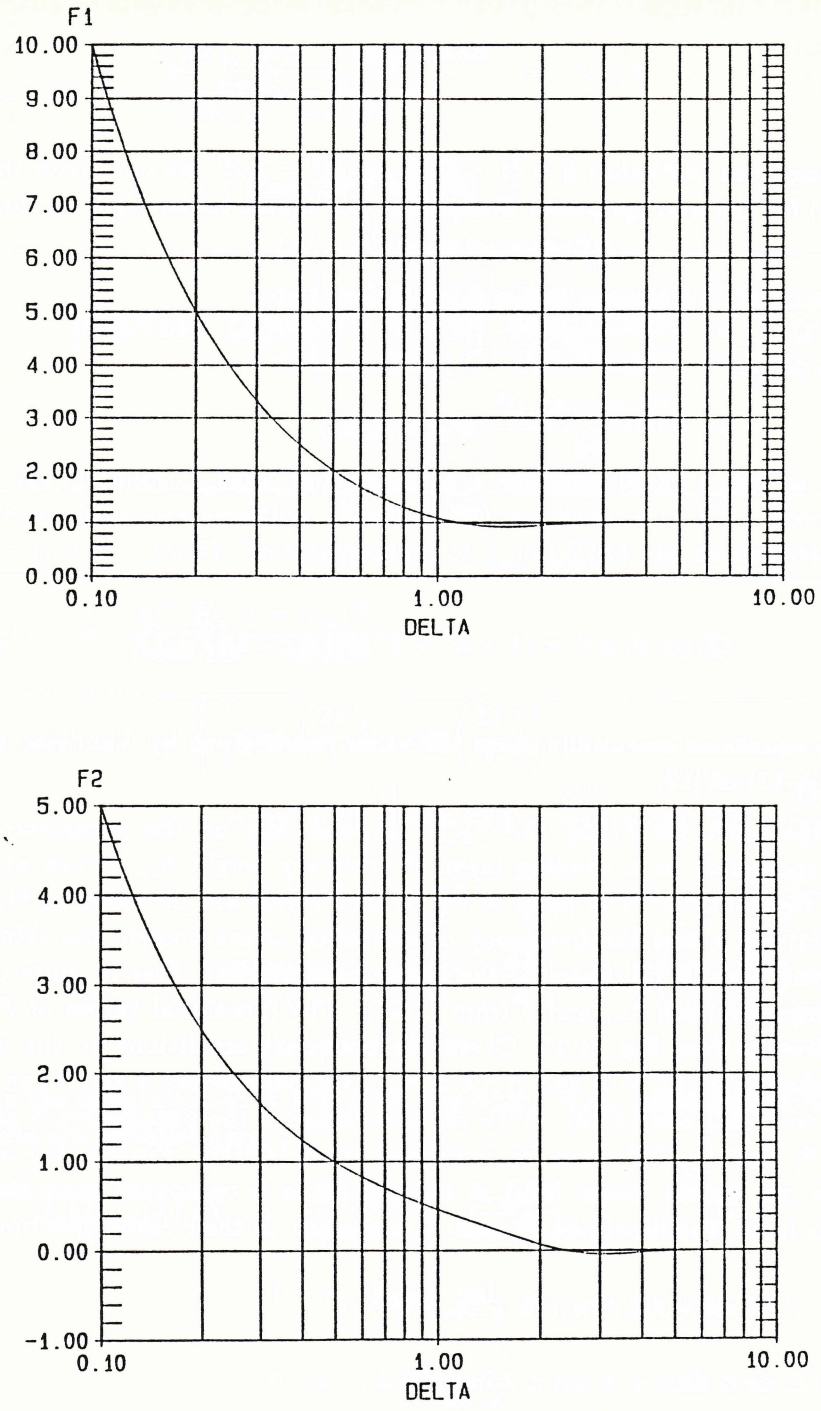


Figure 4.27: The variation of (a) F_1 and (b) F_2 with respect to Δ.

4.5.3 Average Energy Storage Per Square Meter of an Infinite Current Sheet

We can carry out a completely parallel derivation for $\langle Q_H \rangle$, the average energy stored in the magnetic field per square meter in the y-z plane. The starting point of this derivation is (4.78), which is restated here:

$$\langle w_m \rangle = \frac{1}{T} \int_T \frac{\mu_0 \, |\mathbf{H}(t)|^2}{2} \, dt \tag{4.109}$$

Since the magnetic field intensity in our model transformer has a nonzero component only in the z-direction, the above equation can be further simplified to

$$\langle w_m \rangle = \frac{1}{T} \int_T \frac{\mu_0 \, |H_z(t)|^2}{2} \, dt \tag{4.110}$$

With the excitation being sinusoidal, the magnetic field intensity $H_z(t)$ and its corresponding phasor representation $\underline{H}_z$ can be assumed to take the forms of

$$H_z(t) = \sqrt{2} \, |\underline{H}_z| \, \cos(\omega t + \theta_H) \tag{4.111}$$

$$\underline{H}_z = |\underline{H}_z| \, e^{j \, \theta_H} \tag{4.112}$$

where $|\underline{H}_z|$, the magnitude of $\underline{H}_z$, is also the rms value of the magnetic field intensity. It is understood that the magnetic field intensity is also a function of the height x and its dependence on x is not explicitly shown here. Substituting (4.111) into (4.110) and carrying out the integration with respect to time yields

$$\begin{aligned} \langle w_m \rangle &= \frac{1}{T} \int_T \mu_0 \, |\underline{H}_z|^2 \cos^2(\omega t + \theta_H) \, dt \\ &= \frac{\mu_0 \, |\underline{H}_z|^2}{2} \end{aligned} \tag{4.113}$$

By definition, the product of the phasor $\underline{H}_z$ and its complex conjugate $\underline{H}_z^*$ gives the square of the magnitude of the phasor $|\underline{H}_z|^2$. Hence, the average energy storage density $\langle w_m \rangle$ can be written as

$$\langle w_m \rangle = \frac{\mu_0 \, \underline{H}_z \underline{H}_z^*}{2} \tag{4.114}$$

Reinserting the dependence of $\underline{H}_z$ on the height x gives

$$\langle w_m \rangle = \frac{\mu_0 \, \underline{H}_z(x) \underline{H}_z^*(x)}{2} \tag{4.115}$$

The per cycle average of the energy stored in the magnetic field in joules per square meter of winding layer $\langle Q_H \rangle$ in the y-z plane can then be obtained by integrating $\langle w_m \rangle$ from $x = 0$ to $x = h_{cu}$

$$\begin{aligned} \langle Q_H \rangle &= \int_0^{h_{cu}} \frac{\mu_0 \underline{H}_z(x)\underline{H}_z^*(x)}{2}\, dx \\ &= \frac{\mu_0}{2}\int_0^{h_{cu}} \underline{H}_z(x)\underline{H}_z^*(x)\, dx \end{aligned} \tag{4.116}$$

Since the solution for $\underline{H}_z$ is derived earlier in terms of the variable χ, the above integration can also be carried out with respect to the variable χ for $\chi = 0$ and $\chi = h_{cu}$

$$\langle Q_H \rangle = \frac{\mu_0}{2}\int_0^{h_{cu}} \underline{H}_z(\chi)\underline{H}_z^*(\chi)\, d\chi \tag{4.117}$$

Using the same simplifying definitions for Δ, w, and v given in (4.97), (4.98), and (4.99), we show in Appendix F that the product $\underline{H}_z(\chi)\underline{H}_z^*(\chi)$ is equal to

$$\begin{aligned} \underline{H}_z(\chi)\underline{H}_z^*(\chi) &= \frac{|\underline{H}_z(\chi = h_{cu})|^2}{\cosh 2\Delta - \cos 2\Delta} \\ &\quad \times \Big\{ (\cosh 2w - \cos 2w) \\ &\quad + (\alpha^2 + \beta^2)(\cosh 2v - \cos 2v) \\ &\quad + 2\alpha\Big[\cosh\Delta\cos(\Delta - 2w) - \cosh(\Delta - 2w)\cos\Delta\Big] \\ &\quad - 2\beta\Big[\sinh\Delta\sin(\Delta - 2w) - \sinh(\Delta - 2w)\sin\Delta\Big] \Big\} \end{aligned} \tag{4.118}$$

From (4.98), we have $w = \chi/\delta$. From (4.99) we have $v = \Delta - w = \Delta - (\chi/\delta)$. So this product of $\underline{H}_z(\chi)\underline{H}_z^*(\chi)$ can be rewritten as:

$$\begin{aligned} \underline{H}_z(\chi)\underline{H}_z^*(\chi) &= \frac{|\underline{H}_z(\chi = h_{cu})|^2}{(\cosh 2\Delta - \cos 2\Delta)} \\ &\quad \times \Bigg\{ \left[\cosh\left(\frac{2\chi}{\delta}\right) - \cos\left(\frac{2\chi}{\delta}\right)\right] \\ &\quad + \left(\alpha^2 + \beta^2\right)\left[\cosh\left(2\Delta - \frac{2\chi}{\delta}\right) - \cos\left(2\Delta - \frac{2\chi}{\delta}\right)\right] \\ &\quad + 2\alpha\left[\cosh\Delta\cos\left(\Delta - \frac{2\chi}{\delta}\right) - \cosh\left(\Delta - \frac{2\chi}{\delta}\right)\cos\Delta\right] \\ &\quad - 2\beta\left[\sinh\Delta\sin\left(\Delta - \frac{2\chi}{\delta}\right) - \sinh\left(\Delta - \frac{2\chi}{\delta}\right)\sin\Delta\right] \Bigg\} \end{aligned} \tag{4.119}$$

The details in the integration of the above equation from $X = 0$ to $X = h_{cu}$ are shown in Appendix H, and the results are repeated here for convenience:

$$\int_0^{h_{cu}} \underline{H}_z(X)\underline{H}_z^*(X)\, dX = \frac{|\underline{H}_z(X = h_{cu})|^2\, \delta}{2\,(\cosh 2\Delta - \cos 2\Delta)} \times \Big\{ (1 + \alpha^2 + \beta^2)(\sinh 2\Delta - \sin 2\Delta) - 4\alpha(\sinh\Delta\cos\Delta - \cosh\Delta\sin\Delta) \Big\} \quad (4.120)$$

To help visualizing the dependence of $\langle Q_H \rangle$, the per cycle average of the energy storage per square meter in the y-z plane, on the variable Δ, we define F_3 and F_4 as

$$F_3(\Delta) = \frac{\sinh 2\Delta - \sin 2\Delta}{\cosh 2\Delta - \cos 2\Delta} \quad (4.121)$$

$$F_4(\Delta) = \frac{\sinh\Delta\cos\Delta - \cosh\Delta\sin\Delta}{\cosh 2\Delta - \cos 2\Delta} \quad (4.122)$$

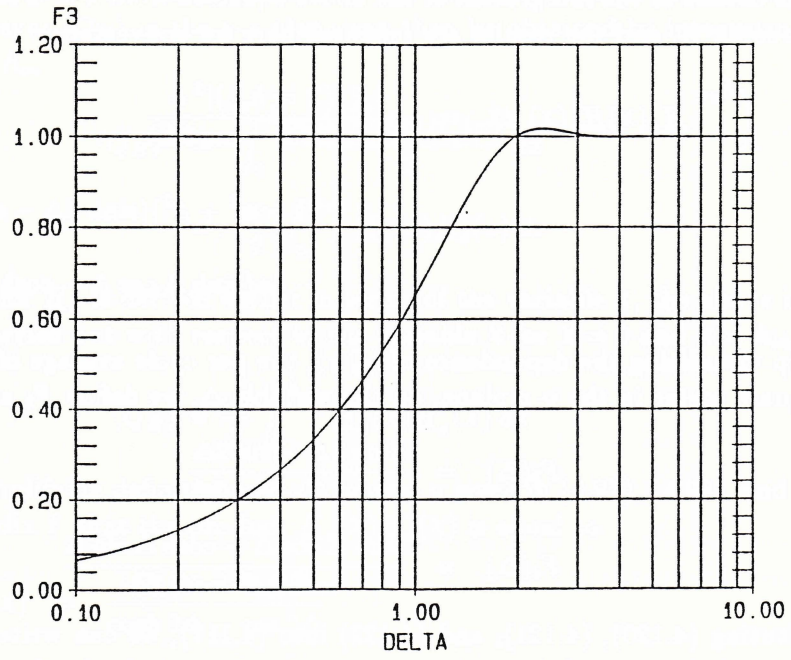
Substituting (4.120), (4.121), and (4.122) into (4.117), we can write the final result for the per cycle average of the energy storage per square meter in the y-z plane $\langle Q_H \rangle$ as,

$$\boxed{\begin{aligned} \langle Q_H \rangle &= \frac{\mu_0 \delta |\underline{H}_z(X = h_{cu})|^2}{4} \Big[(1 + \alpha^2 + \beta^2)F_3(\Delta) - 4\alpha F_4(\Delta)\Big] \\ &= \frac{\mu_0 \delta |\underline{H}_z(X = h_{cu})|^2}{4} \langle Q'_H(\alpha, \beta, \Delta) \rangle \end{aligned}} \quad (4.123)$$

where

$$\boxed{\langle Q'_H(\alpha, \beta, \Delta) \rangle = (1 + \alpha^2 + \beta^2)F_3(\Delta) - 4\alpha F_4(\Delta)} \quad (4.124)$$

The plots of the two functions $F_3(\Delta)$ and $F_4(\Delta)$ are provided in Fig. 4.28. Once the conductivity σ and the frequency of excitation ω are known, the skin depth δ can be computed from (4.7). Then Δ, the height of a winding layer in units of skin depth, can be computed from h_{cu} and δ from (4.97). The functional values of F_3 and F_4 can be read directly from Fig. 4.28. Given the boundary conditions on the magnetic field intensity phasors $\underline{H}_z(X = 0)$ and $\underline{H}_z(X = h_{cu})$, the parameters α and β can be computed according to (4.48) and (4.49). With the knowledge of the parameters α and β, and the values of F_3 and F_4, $\langle Q'_H \rangle$ can be computed from (4.124). Finally, the average energy



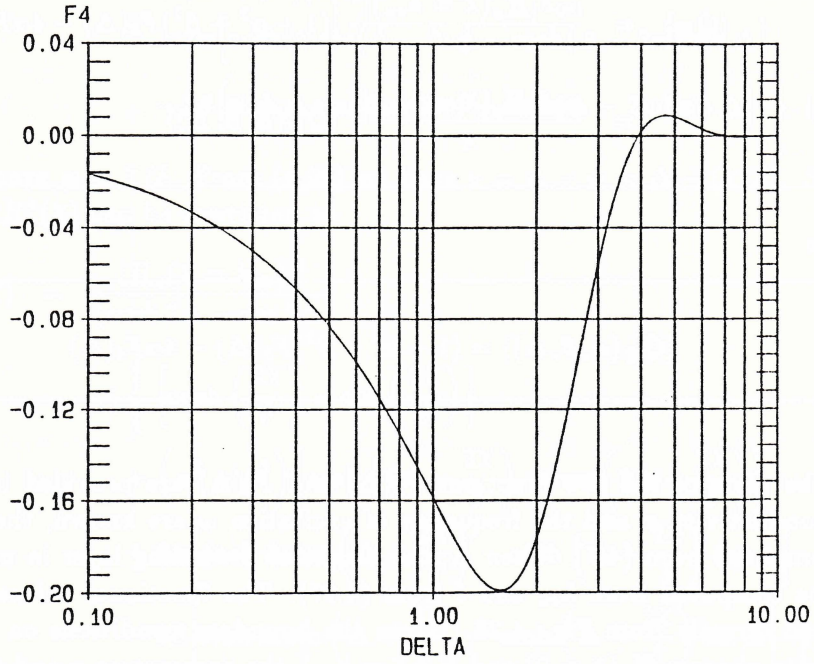


Figure 4.28: The variation of (a) F_3 and (b) F_4 with respect to Δ.

storage per square meter $\langle Q_H \rangle$ in the y-z plane is computed according to (4.123). Similar to F_1 and F_2, the functions F_3 and F_4 approach to the limiting values of

$$\lim_{\Delta \to \infty} F_3(\Delta) = 1 \tag{4.125}$$

$$\lim_{\Delta \to \infty} F_4(\Delta) = 0 \tag{4.126}$$

To obtain a quick estimation of $\langle Q'_H \rangle$ in such a situation, F_3 and F_4 can be approximated by one and zero, respectively. The error introduced to $\langle Q'_H \rangle$ through such approximations is less than 10% for $\Delta \geq 3.1$ and less than 5% for $\Delta \geq 3.4$ for all values of α and β.

4.6 SUMMARY OF THE FIELD SOLUTION FOR AN INFINITE CURRENT SHEET

4.6.1 Introduction of Layer Porosity η Into the Equations

Before making further use of the equations derived in this chapter, we should pause to restate some of the underlying assumptions that limit their domain of application. In Chapters 1 through 3, we make a series of simplifying assumptions concerning the structure of a transformer that eventually lead us to the infinite current sheet model of this chapter. These assumptions and their resulting implications may be summarized as follows :

1. Assume that the discrete conductors that make up the transformer windings may be modeled by an equivalent foil that entirely fills the window breadth.
   Implications: Layer porosity must be introduced, and each layer may now be treated as a one-turn solenoid.
2. Assume that the transformer has a pot core of infinite magnetic permeability.
   Implications: Only the leakage flux due to finite conductor thickness and finite interlayer gaps appears in the model, and we may now treat the solenoid that models a winding layer as an infinite solenoid.
3. Assume for the purpose of field solution that a small portion of the surface of an infinite solenoid may be modeled by a flat sheet of conductor that extends infinitely in both the breadth and the depth directions.
   Implications: The calculation of the fields is greatly simplified, but the validity of the resulting equations is limited by the curvature in the windings of the transformer to be modeled.

It is important to note that the infinite current sheet model that is obtained from assumption 3 above is for the purpose of obtaining the field solution *only*, and the equations that result from this model are to be used in conjunction with the model of assumption 2. However, before applying the equations of this chapter to a physical

transformer, we must incorporate the concept of layer porosity. In Section 2.2.1.3, we argue that the introduction of layer porosity as a multiplicative factor insures that the dc resistance of the model winding is the same as that of the original winding that it replaces. This multiplicative factor appears as an effective decrease in conductivity. Based upon equation (2.2), we can define an effective conductivity σ_{eff} as

$$\sigma_{eff} = \eta\sigma \tag{4.127}$$

Thus, we can incorporate the layer porosity into the equations of this chapter simply by using the numerical value of σ_{eff} as determined by (4.127) instead of the intrinsic conductivity of the conductors. In the next section, we restate all of the significant equations of this chapter, and incorporate the use of σ_{eff} wherever appropriate.

4.6.2 Restatement of Significant Equations

Using the definition of effective conductivity σ_{eff} given in (4.127), we can restate the significant equations derived in this chapter as follows:

The complex wave number $\underline{k}$ is given by

$$\boxed{\underline{k} \approx \sqrt{j\omega\mu_o\sigma_{eff}}} \tag{4.128}$$

The skin depth δ is given by

$$\boxed{\delta = \sqrt{\frac{2}{\omega\mu_o\sigma_{eff}}}} \tag{4.129}$$

The magnetic-field-intensity and current-density phasor distributions across the height of a layer are given by

$$\boxed{\underline{H}_z(x) = \frac{1}{\sinh \underline{k}h_{cu}}\left[\underline{H}_z(h_{cu})\sinh \underline{k}x + \underline{H}_z(0)\sinh \underline{k}(h_{cu}-x)\right]} \tag{4.130}$$

$$\boxed{\underline{J}_y(x) = \frac{-\underline{k}}{\sinh \underline{k}h_{cu}}\left[\underline{H}_z(h_{cu})\cosh \underline{k}x - \underline{H}_z(0)\cosh \underline{k}(h_{cu}-x)\right]} \tag{4.131}$$

or, if we define χ as

$$\chi = \begin{cases} x & \text{if } |\underline{H}_z(x=h_{cu})| \geq |\underline{H}_z(x=0)| \\ h_{cu}-x & \text{if } |\underline{H}_z(x=h_{cu})| < |\underline{H}_z(x=0)| \end{cases} \tag{4.132}$$

and $\underline{\Gamma}$ as

$$\underline{\Gamma} = \alpha + j\beta = \frac{\underline{H}_z(\chi = 0)}{\underline{H}_z(\chi = h_{cu})} \tag{4.133}$$

then we can rewrite the distributions of (4.130) and (4.131) as

$$\boxed{\underline{H}_z(\chi) = \frac{\underline{H}_z(\chi = h_{cu})}{\sinh \underline{k} h_{cu}} \Big[\sinh \underline{k}\chi + (\alpha + j\beta) \sinh \underline{k}(h_{cu} - \chi)\Big]} \tag{4.134}$$

$$\boxed{\underline{J}_y(\chi) = \frac{(-1)^{\varepsilon}\, \underline{k}\, \underline{H}_z(\chi = h_{cu})}{\sinh \underline{k} h_{cu}} \Big[\cosh \underline{k}\chi - (\alpha + j\beta) \cosh \underline{k}(h_{cu} - \chi)\Big]} \tag{4.135}$$

where

$$\varepsilon = \begin{cases} 1 & \text{if } |\underline{H}_z(x = h_{cu})| \geq |\underline{H}_z(x = 0)| \\ 0 & \text{if } |\underline{H}_z(x = h_{cu})| < |\underline{H}_z(x = 0)| \end{cases} \tag{4.136}$$

If we define Δ as

$$\Delta = \frac{h_{cu}}{\delta} \tag{4.137}$$

and F_1,F_2,F_3 and F_4 as

$$F_1(\Delta) = \frac{\sinh 2\Delta + \sin 2\Delta}{\cosh 2\Delta - \cos 2\Delta} \tag{4.138}$$

$$F_2(\Delta) = \frac{\sinh \Delta \cos \Delta + \cosh \Delta \sin \Delta}{\cosh 2\Delta - \cos 2\Delta} \tag{4.139}$$

$$F_3(\Delta) = \frac{\sinh 2\Delta - \sin 2\Delta}{\cosh 2\Delta - \cos 2\Delta} \tag{4.140}$$

$$F_4(\Delta) = \frac{\sinh \Delta \cos \Delta - \cosh \Delta \sin \Delta}{\cosh 2\Delta - \cos 2\Delta} \tag{4.141}$$

then we can use (4.134) and (4.135) above to write the average power dissipation per square meter in the y-z plane as

$$\boxed{\begin{aligned} \langle Q_J \rangle &= \frac{|\underline{H}_z(\chi = h_{cu})|^2}{\sigma_{eff}\, \delta} \Big[(1 + \alpha^2 + \beta^2) F_1(\Delta) - 4\alpha F_2(\Delta)\Big] \\ &= \frac{|\underline{H}_z(\chi = h_{cu})|^2}{\sigma_{eff}\, \delta} \langle Q'_J(\alpha, \beta, \Delta) \rangle \end{aligned}} \tag{4.142}$$

where

$$\langle Q'_J(\alpha,\beta,\Delta)\rangle = (1+\alpha^2+\beta^2)F_1(\Delta) - 4\alpha F_2(\Delta) \tag{4.143}$$

Likewise, the average energy storage per square meter in the y-z plane is given by

$$\begin{aligned}\langle Q_H\rangle &= \frac{\mu_0\delta|\underline{H}_z(\chi=h_{cu})|^2}{4}\left[(1+\alpha^2+\beta^2)F_3(\Delta) - 4\alpha F_4(\Delta)\right] \\ &= \frac{\mu_0\delta|\underline{H}_z(\chi=h_{cu})|^2}{4}\langle Q'_H(\alpha,\beta,\Delta)\rangle\end{aligned} \tag{4.144}$$

where

$$\langle Q'_H(\alpha,\beta,\Delta)\rangle = (1+\alpha^2+\beta^2)F_3(\Delta) - 4\alpha F_4(\Delta) \tag{4.145}$$

The above equations, together with the assumptions and the derivations that have produced them, form the mathematical framework for the modeling of a multiwinding transformer for high-frequency applications. Using these equations, we are now in a position to obtain expressions for the short-circuit impedances that exist between two windings of a multiwinding transformer.

Chapter 5

Derivation of Short-Circuit Impedances from Field Solutions

In Chapter 4 we present equations (4.105) and (4.123) to determine, respectively, the average energy dissipated per square meter $\langle Q_J \rangle$ and the average energy stored per square meter $\langle Q_H \rangle$ for an infinite current sheet. In Section 4.6, these equations are applied to transformer winding layers where they are rewritten as (4.142) and (4.144), respectively. The discussion in Chapter 4 is very general and (4.142) and (4.144) do not depend upon the specific excitation of the transformer winding; however, most of the terms in (4.142) and (4.144) do depend upon the layer porosity of the winding layer, although this dependence is not always explicit. We now wish to determine the values of the impedances associated with specific hypothetical short-circuit tests between two windings of a multiwinding transformer. We adopt the nomenclature throughout this chapter and the rest of this report that $Z_{(jk)}$ is the impedance seen at the terminals of winding j when winding j is excited and winding k is shorted and all other windings are left open. First, we discuss the basic impedance measurements frequently performed on two-winding transformers and the extension of these tests to multiple-windings transformers. Then, we use equations (4.142) and (4.144) to derive equations for the short-circuit resistance $R_{(jk)}$ and the short-circuit inductance $L_{(jk)}$.

5.1 IMPEDANCE MEASUREMENTS OF TRANSFORMER WINDINGS

Before calculating transformer winding short-circuit impedances, we must first look at what measurements are commonly performed on transformers and what parameters can be determined by these tests. Although the emphasis in this report is on multiwinding transformers, it is instructive to understand how the results of open-circuit and short-circuit tests are used to determine the values of the circuit components for a two-winding transformer equivalent circuit.

5.1.1 Two-Winding Transformer Measurements

Figure 5.1(a) shows what is often referred to as the T-equivalent circuit of a two-winding transformer. The two-winding T-equivalent circuit consists of an ideal transformer, a magnetizing impedance on the primary side of the ideal transformer, and primary and secondary leakage impedances. In this figure, the ideal transformer is denoted by the two coils with two parallel dashed lines between them. The magnetizing impedance is made up of the magnetizing inductance L_m in parallel with the core-loss equivalent resistance R_c. The primary leakage impedance is made up of a series combination of a winding resistance R_{w1} and a primary leakage inductance $L_{\ell 1}$; the secondary leakage impedance has similar elements R_{w2} and $L_{\ell 2}$. Although widely used, the T-equivalent circuit cannot be extended to a transformer with four windings which is the model being sought in this report. Transformer open-circuit and short-circuit tests to determine the values of the circuit elements in Fig. 5.1 are commonly performed as follows:

1. Figure 5.1(b) shows the primary winding excited with rated voltage—designated $\underline{V}_{OC}$—and the secondary winding left open-circuited. In the case of a transformer with magnetic core material of high effective permeability, the leakage impedance presented by R_{w1} in series with $L_{\ell 1}$ usually can be assumed to be much smaller than the magnetizing impedance represented by R_c in parallel with L_m. In this case, the impedance seen by the source under open-circuit conditions is approximately equal to the magnetizing impedance of R_c in parallel with L_m.

2. Figure 5.1(c) shows the primary winding excited with rated current—designated $\underline{I}_{SC}$—with the secondary winding short-circuited. Since the leakage impedance of the secondary winding referred to the primary winding is assumed to be much smaller than the magnetizing impedance, the impedance seen by the source is approximately equal to the sum of the primary and secondary leakage impedances referred to the primary winding, and the effect of R_c and L_m can be neglected in this test.

3. The assumption is often made that the primary and secondary leakage impedances are approximately the same value *when referred to the same winding*. Therefore, we can split the impedance measured under short-circuit test into two equal impedances, one half represented by R_{w1} and $L_{\ell 1}$ and the other half represented by R'_{w2} and $L'_{\ell 2}$, the latter when reflected by the turns ratio squared into the secondary gives us values for R_{w2} and $L_{\ell 2}$.

The above discussion of the short-circuit and open-circuit tests of a two-winding transformer as usually encountered is useful to us here because it demonstrates three very important points about transformer measurements. First, when considering a transformer with rated winding current applied under short-circuit conditions, whether it is a two-winding transformer or a multiwinding transformer, it is often *acceptable to assume that the magnetizing impedance* of the transformer is so large that its effect *can*

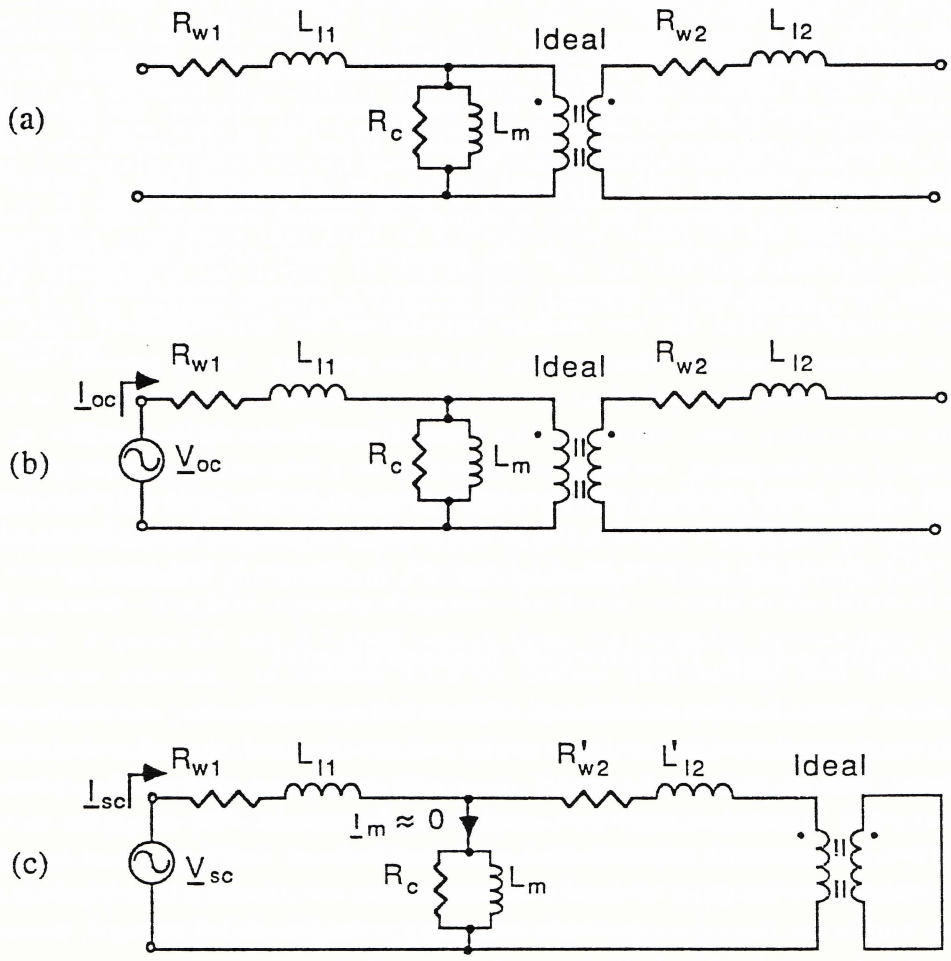


Figure 5.1: (a) The T-equivalent circuit of a two-winding transformer. (b) The T-equivalent circuit under open-circuit test conditions. (c) The T-equivalent circuit under short-circuit conditions where R'_{w2} and $L'_{\ell 2}$ represent the values of R_{w2} and $L_{\ell 2}$, respectively, when reflected through the ideal transformer to the primary winding.

be neglected in comparison to the leakage impedance effects. We use this assumption throughout our discussion of multiwinding transformers, particularly in Chapters 7 and 8 where two equivalent circuits for four-winding transformers are proposed. Second, the magnetizing or excitation impedance of a transformer appears in the equivalent-circuit model effectively as a shunt element. In Chapter 7, we use this fact in modeling a multiwinding transformer using a circuit model that neglects all such shunt elements. Finally, the short-circuit test shows that in a measurement situation, the primary and secondary leakage impedances cannot be separated. When we short-circuit one winding and excite another winding with a current source, the impedance that is measured is the leakage impedance *between the two windings*; we cannot measure only one leakage parameter at a time. In order to divide the measured short-circuit impedance for the two-winding case above into a primary and secondary leakage impedance, we had to make the assumption that the two leakage impedances are approximately equal when referred to the same winding, which in Fig. 5.1 is the primary. In the general case of an n-winding transformer, the equivalent circuit that represents the device is not as simple as for the two-winding case, therefore, this type of impedance division is not so easy. For the rest of our discussion, we focus our attention on a four-winding transformer, and we present methods for calculating analytically the short-circuit impedance between any two windings. In Chapters 7 and 8, we then relate these impedance values to component values in two equivalent-circuit representations of a multiwinding transformer.

5.1.2 Multiwinding Transformer Measurements

When a short-circuit test is performed on a four-winding transformer, one winding is excited with rated current while another winding is short-circuited; the other two windings are left open. Here we do not refer to any one winding as the primary winding but rather consider the four windings simply as a single, coupled circuit. We adopt the notation used in [13] and denote the short-circuit impedance between windings j and k as $\underline{Z}_{(jk)}$. More specifically, we use $\underline{Z}_{(jk)}$ to denote the impedance seen looking into winding j, the first index number in the subscript, when winding j is excited and winding k, the second subscripted index number, is shorted.

Now, by taking two windings at a time, we can specify twelve different short-circuit tests for the four-winding transformer. In other words, if we number the windings 1 through 4 and take any two windings at a time, we can measure the short-circuit impedances $\underline{Z}_{(12)}$, $\underline{Z}_{(13)}$, $\underline{Z}_{(14)}$, $\underline{Z}_{(21)}$, $\underline{Z}_{(23)}$, $\underline{Z}_{(24)}$, $\underline{Z}_{(31)}$, $\underline{Z}_{(32)}$, $\underline{Z}_{(34)}$, $\underline{Z}_{(41)}$, $\underline{Z}_{(42)}$, and $\underline{Z}_{(43)}$. Except for the turns ratio, the impedance between a pair of windings is independent of which winding is excited and which is shorted, so $\underline{Z}_{(jk)} = (N_j/N_k)^2 \underline{Z}_{(kj)}$, which reduces the number of short-circuit tests to six. Thus, for the four-winding transformer under consideration it is sufficient to measure impedances $\underline{Z}_{(12)}$, $\underline{Z}_{(13)}$, $\underline{Z}_{(14)}$, $\underline{Z}_{(23)}$, $\underline{Z}_{(24)}$, $\underline{Z}_{(34)}$. In general, there are $n(n-1)/2$ different short-circuit tests that can be performed on a multiwinding transformer [1,13,18] which yield the same number of leakage impedances among the n windings. Therefore, for a four-winding transformer, there are $(4 \times 3)/2 = 6$ different short-circuit tests, yielding six leakage impedances.

5.2 DETERMINATION OF THE SHORT-CIRCUIT IMPEDANCE FORMULAE

In Section 5.1.2 we describe the symbol $\underline{Z}_{(jk)}$ used to denote the short-circuit impedance between windings j and k of a multiwinding transformer, and we state that there are a total of six different short-circuit impedances which characterize a four-winding transformer. We now wish to derive equations to calculate these short-circuit impedances by using *hypothetical* short-circuit tests. The mathematical development of the field solution in an infinite current sheet gives a quantitative description of the high-frequency leakage-flux conditions that exist in a transformer based on the excitation conditions in the windings of the device. In this section, we use this field description to calculate values for the leakage impedance between any possible pair of windings in a four-winding transformer.

5.2.1 Short-Circuit Conditions

To calculate the short-circuit impedance between two windings based on the leakage flux in the transformer, we must first describe the flux pattern that exists in the windings for the short-circuit test of interest. In Section 3.1.2, we generate the profile of the magnetic field intensity—the field-intensity diagram—for direct currents in the layers of an infinite solenoid. Figures 3.6 and 3.7 show sets of these diagrams for various layer currents in a two-layer solenoid. In Section 3.1.3 we discuss qualitatively, and in Section 4.3.1 we demonstrate pictorially that the straight-line field-intensity diagram applies only at relatively low frequencies, but that the values of $\underline{H}_z$ in the gaps between winding layers are independent of the excitation frequency. Since the solutions for the current-density and the magnetic-field-intensity distributions are written in terms of these values of $\underline{H}_z$ in the gaps, we find that the low-frequency field-intensity diagrams are useful tools for visualizing the flux pattern in a transformer and for determining the boundary conditions necessary to solve for the high-frequency distributions.

Figure 5.2 shows a four-winding transformer under various short-circuit test conditions. Part (a) of the figure shows the right-hand side of a cross-sectional view of the transformer. The four windings of the device each contain two adjacent layers of conductors which gives a total of eight winding layers in the transformer. Figure 5.2(b) shows the low-frequency field-intensity distributions for each of the six different short-circuit tests mentioned in Section 5.1.2. These plots of $H_z(x,t)$ at an arbitrary time instant t are labeled $H_{(jk)}$ in keeping with the use of $\underline{Z}_{(jk)}$ to designate the short-circuit impedance between windings j and k.

Figure 5.2(c) shows a schematic representation of the terminal connections for each of the six short-circuit tests. In this figure, each layer of conductors is shown by a separate coil symbol; the internal connections between the layers, for example between layers 1 and 2, 3 and 4, etc., are indicated by the lines connecting the various coils. The external connections between the excitation source and the transformer as well as the various

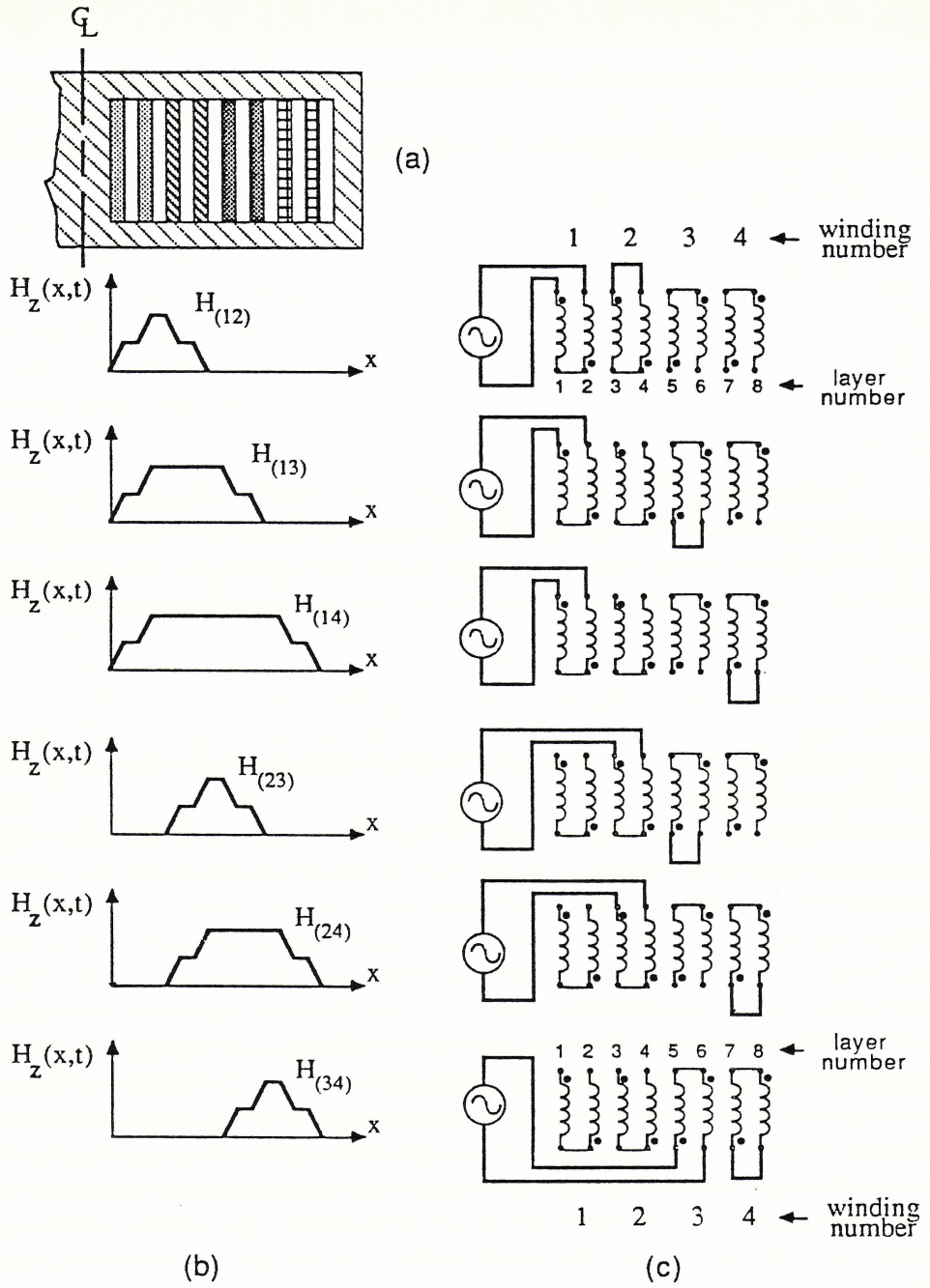


Figure 5.2: A four-winding transformer under various short-circuit conditions. In the winding cross-section of (a), the instantaneous current is assumed in each case to be flowing into the paper in the outer conducting winding and flowing out of the paper in the inner windings. Also shown are (b) the $H_z(x,t)$ profiles at an arbitrary time instant t and (c) the schematic representations for the six different short-circuit tests including relative positions of external leads from the windings and internal shorts between the layers.

short-circuit connections are also shown.

Magnetic-field-intensity profiles such as those of Fig. 5.2(b) typically are shown with a field intensity of zero at the center leg of the transformer core which is justified as follows. In the discussion of a two-layered infinite solenoid in Section 3.1.2, it is pointed out that with no external fields present, the magnetic field intensity is always zero outside the solenoid, but inside the inner layer of the solenoid the field is zero only if the sum of the currents in all of the layers is zero. This condition is equivalent to having zero net ampere-turns in the windings of a transformer.

The assumption of zero net ampere-turns is made throughout this report. In other words, the exciting current of the transformer core is assumed to be negligible relative to the load currents, which is the case for a core of very high permeability. Thus, the magnetic field intensity in the center leg of the core is assumed to be zero.

5.2.2 Deriving the Magnetic-Field-Intensity Boundary Conditions for a Winding Layer

The field-intensity diagrams $H_z(x,t)$ given in Fig. 5.2(b) appear without labels defining the actual values of field intensity at any point in the window. This is done to emphasize the generality of these diagrams. Before calculating values of resistance and inductance for a transformer under a particular short-circuit test, we need to determine the boundary conditions of $\underline{H}_z(x)$ for each layer of the transformer winding using parameters which describe the physical layout and the excitation of the layer. In this section, we derive such a formula which expresses the difference between the boundary conditions as a function of the number of turns in the layer N_ℓ and the current being conducted by the layer $\underline{I}_\ell$.

Equation (4.68) in Section 4.3.2,

$$\frac{\underline{H}_z(0) - \underline{H}_z(h_{cu})}{h_{cu}} = \underline{J}_y \tag{5.1}$$

states that at low frequencies, the difference in the boundary conditions of the field intensity for any layer is proportional to the current density $\underline{J}_y$ of that layer which is independent of x. This equation is consistent with Ampere's law and results from a Taylor series approximation of (4.39) for frequencies significantly below the critical frequency.

For an actual transformer winding layer consisting of N_ℓ turns conducting a slowly-varying current of $i_\ell(t)$, the instantaneous, uniform current density $J_y(t)$ is

$$J_y(t) = \frac{N_\ell\, i_\ell(t)}{b_{win} h_{cu}} \tag{5.2}$$

If the current and current density are expressed as phasors, this becomes

$$\underline{J}_y = \frac{N_\ell \underline{I}_\ell}{b_{win} h_{cu}} \tag{5.3}$$

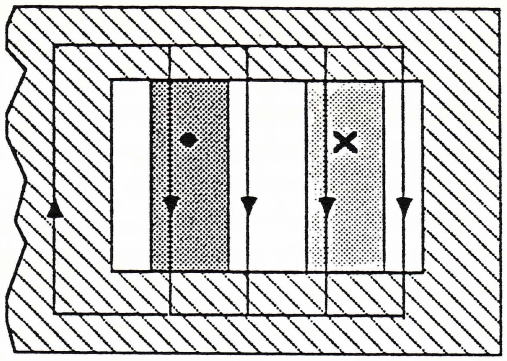


Figure 5.3: Closed paths chosen to determine $\underline{\mathcal{F}}(x) = \oint \underline{H}_z(x) \bullet \mathbf{dl} = \underline{H}_z(x) b_{win}$. The field intensity in the center leg of the core is assumed to be zero.

Substituting this into (5.1) gives

$$\underline{H}_z(0) - \underline{H}_z(h_{cu}) = \frac{N_\ell \underline{I}_\ell}{b_{win}} \tag{5.4}$$

$\underline{I}_\ell$ is the net layer current seen at the terminals of the layer and is not affected by the distribution of $\underline{J}_y(x)$; therefore, (5.4) is true at all frequencies.

5.2.3 Normalized Values of Field Intensity and MMF

Before beginning the derivation of the short-circuit impedances, two ideas need to be stressed. First, the magnetic field intensity $\underline{H}_z(x)$ in the winding space is proportional to the magnetomotive force or mmf $\underline{\mathcal{F}}(x)$ of the winding space, since the integral of $\underline{H}_z(x) \bullet \mathbf{dl}$ around any of the closed paths in Fig. 5.3 yields $\underline{\mathcal{F}}(x) = \underline{H}_z(x) b_{win}$. Second, the values of $\underline{H}_z(x)$ or $\underline{\mathcal{F}}(x)$ can be normalized to any useful reference value. Therefore, the values of $\underline{H}_z(x)$ in the layers and in the gaps between layers can be normalized to any convenient value of magnetic field intensity. Using the subscript appendage "-N" to indicate a normalized value, we can write the normalized value of $\underline{H}_z(x)$ in layer n as

$$\underline{H}_{z_n\text{-}N}(x) = \frac{\underline{H}_{z_n}(x)}{\underline{H}_{BASE}} \tag{5.5}$$

and in gap n as

$$\underline{H}_{g_n\text{-}N} = \frac{\underline{H}_{g_n}}{\underline{H}_{BASE}} \tag{5.6}$$

where $\underline{H}_{BASE}$ is the base unit of magnetic field intensity and $\underline{H}_{g_n}$ is the actual value of the magnetic field intensity in the n^{th} gap of the winding structure. A completely similar expression for the normalized value of mmf in a gap is

$$\underline{\mathcal{F}}_{g_n\text{-}N} = \frac{\underline{\mathcal{F}}_{g_n}}{\underline{\mathcal{F}}_{BASE}} \tag{5.7}$$

where $\underline{\mathcal{F}}_{BASE}$ is a convenient base unit of mmf and $\underline{\mathcal{F}}_{g_n}$ is the value of the magnetomotive force in the gap.

The base value of mmf can be expressed as

$$\underline{\mathcal{F}}_{BASE} = N_{BASE}\underline{I}_{BASE} \tag{5.8}$$

A convenient value for N_{BASE} is the number of turns of the excited winding N_E, since the calculated short-circuit impedances are reflected into the excited winding. At first glance, it appears that a convenient value for I_{BASE} would be $\underline{I}_{SC}$, the short-circuit current in the excited winding. This is not the case, however, as explained below.

In Section 3.1.2 we adopted the convention that current "into the paper" on the right side of a solenoid produces magnetic field intensity in the positive z-direction inside the solenoid. Likewise, current "out of the paper" on the right side of the solenoid produces a negatively directed field intensity inside the solenoid. Using this convention, the transformer layer currents shown in Fig. 5.4(a) are associated with the low-frequency field-intensity plots of Fig. 5.4(b), regardless of which layer is excited and which is shorted.

It is important that $\underline{I}_{BASE}$ be consistent with this convention so that the diagrams of $\underline{H}_{z\text{-}N}(x)$ have the same polarity as those of $H_z(x)$. To accomplish this, $\underline{I}_{BASE}$ cannot be set universally to $\underline{I}_{SC}$, the short-circuit current in the excited winding. Rather, $\underline{I}_{BASE}$ can be set equal to $\underline{I}_{SC}$ only when $\underline{I}_{SC}$ flows "into the paper" on the right half of the transformer cross section. If the current in the excited winding flows "out of the paper" on the right half of the transformer, then $\underline{I}_{BASE}$ should be set equal to $-\underline{I}_{SC}$. For example, $\underline{I}_{BASE} = -\underline{I}_{SC}$ for each of the short-circuit tests represented in Fig. 5.2, since in each case, the current in the excited winding flows "out of the paper." Adopting this definition for $\underline{I}_{BASE}$ means that $\underline{I}_{BASE}$ flows in the "positive" direction ("into the paper" on the right side of the transformer) whether $\underline{I}_{SC}$ flows in the positive or negative ("out of the paper") direction.

Returning to the discussion of normalization, we can chose a value for $\underline{\mathcal{F}}_{BASE}$ which is both convenient and consistent with the convention shown in Fig. 5.4:

$$\underline{\mathcal{F}}_{BASE} = N_E\underline{I}_{BASE} \tag{5.9}$$

where

$$\underline{I}_{BASE} = \begin{cases} \underline{I}_{SC} & \text{if } \underline{I}_{SC} \text{ flows in "positive" direction} \\ -\underline{I}_{SC} & \text{if } \underline{I}_{SC} \text{ flows in "negative" direction} \end{cases} \tag{5.10}$$

The related base for normalizing the field intensity is

$$\underline{H}_{BASE} = N_E\underline{I}_{BASE}/b_{win} \tag{5.11}$$

The usefulness of normalizing the field intensity becomes clear if we substitute (5.5) and (5.11) into (5.4)

$$[\underline{H}_{z\text{-}N}(0) - \underline{H}_{z\text{-}N}(h_{cu})]\frac{N_E\underline{I}_{BASE}}{b_{win}} = \frac{N_\ell\underline{I}_\ell}{b_{win}}$$

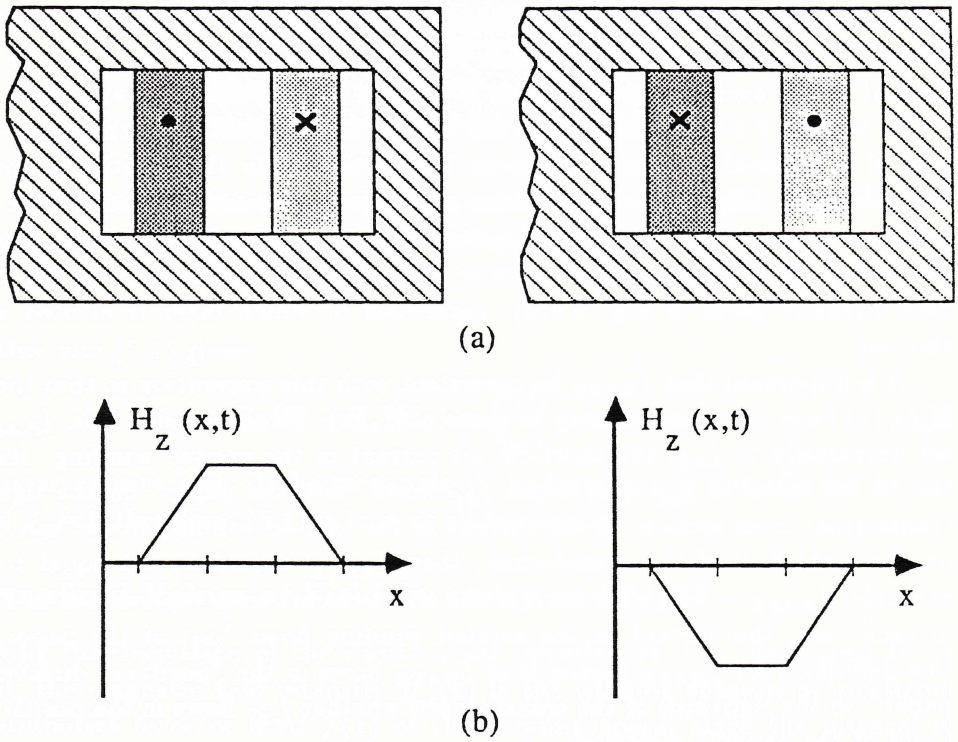


Figure 5.4: Convention adopted for drawing field-intensity diagrams from layer currents. (a) Right-hand sides of two transformer cross sections showing directions of layer currents. (b) Field-intensity diagrams associated with transformer cross sections of (a).

$$\underline{H}_{z\text{-}N}(0) - \underline{H}_{z\text{-}N}(h_{cu}) = \frac{N_\ell \underline{I}_\ell}{N_E \underline{I}_{BASE}} \tag{5.12}$$

Equation (5.12) allows us to determine the difference between the normalized boundary conditions for a layer provided we know the ampere-turns of that layer relative to the ampere-turns of the excited winding.

5.2.4 Calculation of Resistance Values

Under a short-circuit test, a driving source (usually a sinusoidal voltage source in series with a source impedance to limit the current) is applied to a certain j^{th} winding while a certain k^{th} winding is shorted. Depending on the layout of the transformer, the j^{th} and the k^{th} windings may be made up of one or more winding layers. Naturally, the current density in the winding layers associated with these two windings is non-zero and net current flows through them. If the excitation frequency is high enough, any winding layer which is "sandwiched" between the winding layers of the j^{th} and k^{th} windings can develop non-zero current-density distribution due to the eddy currents induced from the high rate of change of magnetic flux, even though the net current flowing through such a winding layer is always equal to zero. An example of a layer with zero net current but non-zero current distribution is shown in Fig. 4.25 of Section 4.4.2. Due to the finite conductivity of the winding layers, a non-zero current-density distribution implies energy dissipated as heat.

Since measurements of terminal voltages and currents do not reveal the actual current-density distribution, the excitation source applied to the j^{th} winding can only see an aggregate lumped-circuit effect of all of the dissipative loss. As a result, the leakage impedance between windings j and k, referred to winding j, is modeled as a resistance $R_{(jk)}$ in series with an inductance $L_{(jk)}$. The resistance $R_{(jk)}$ is used to account for the total loss dissipated in the transformer windings while the inductance $L_{(jk)}$ is used to account for the total energy stored in the magnetic field in the whole winding structure including both the winding layers and the interlayer air gaps. The value of $R_{(jk)}$ is defined so that the average loss over one cycle $\langle P_{R(jk)} \rangle$ developed in this model resistor is equal to the total average loss over one cycle $\langle P_D \rangle$ in all winding layers in the transformer under the particular test conditions.

$$\langle P_{R(jk)} \rangle = \langle P_D \rangle \tag{5.13}$$

where the average powers $\langle P_{R(jk)} \rangle$ and $\langle P_D \rangle$ are calculated from the instantaneous power loss $P_{R(jk)}(t)$ in the model resistor, and the instantaneous power loss $P_D(t)$ in the transformer windings, respectively.

$$\langle P_{R(jk)} \rangle = \frac{1}{T} \int_T P_{R(jk)}(t)\, dt \tag{5.14}$$

$$\langle P_D \rangle = \frac{1}{T} \int_T P_D(t)\, dt \tag{5.15}$$

The symbol $P_D(t)$ is the total loss in all winding layers of a transformer and should not be confused with the symbol $p_d(t)$, which stands for the power density at a point.

Since the resistor $R_{(jk)}$ is referred to the excited winding, the instantaneous current flowing through such a model resistor is equal to the current $i_{SC}(t)$, the short-circuit excitation current. Therefore,

$$P_{R(jk)}(t) = i_{SC}^2(t)\, R_{(jk)} \tag{5.16}$$

It can be further assumed that in the case of sinusoidal excitation,

$$i_{SC}(t) = \sqrt{2} I_{SC} \cos(\omega t + \theta) \tag{5.17}$$

or for a phasor current,

$$\underline{I}_{SC} = I_{SC}\, e^{j\theta} \tag{5.18}$$

Pursuing the usual procedure to compute the average loss in a resistor under sinusoidal excitation, the integration in (5.14) is carried out after substituting (5.16) and (5.17), yielding

$$\langle P_{R(jk)} \rangle = I_{SC}^2\, R_{(jk)} \tag{5.19}$$

From (5.18), $|\underline{I}_{SC}|^2 = \underline{I}_{SC}\, \underline{I}_{SC}^* = I_{SC}^2$, thus

$$\langle P_{R(jk)} \rangle = |\underline{I}_{SC}|^2\, R_{(jk)} \tag{5.20}$$

After finding the average loss $\langle P_{R(jk)} \rangle$ in the model resistor, we can now focus our attention on the computation of $\langle P_D \rangle$, the total loss in the transformer averaged over one cycle. Since the current density in an interlayer air gap is equal to zero, there is no power loss in any of these air gaps. In a transformer that is made up of N layers, the total instantaneous loss $P_D(t)$ in the whole transformer can be expressed as

$$P_D(t) = \sum_{n=1}^{N} P_n(t) \tag{5.21}$$

where $P_n(t)$ is the instantaneous power loss in the n^{th} winding layer. Substituting (5.21) into the right hand side of (5.15), and interchanging the averaging process with the summation process, we have

$$\langle P_D \rangle = \sum_{n=1}^{N} \left(\frac{1}{T} \int_T P_n(t)\, dt \right) \tag{5.22}$$

The symbol $\langle P_n \rangle$ is introduced in Section 4.5.1[1] to represent the loss in the n^{th} winding averaged over one period T of excitation

$$\langle P_n \rangle = \frac{1}{T} \int_T P_n(t)\, dt \tag{5.23}$$

[1]Some of this discussion is presented in Sections 4.5.1, and 4.5.2, but is repeated here for convenience and clarity.

Then (5.22) can be rewritten as

$$\langle P_D \rangle = \sum_{n=1}^{N} \langle P_n \rangle \tag{5.24}$$

Hence, the task of computing $\langle P_D \rangle$, the total loss in the transformer averaged over one cycle, can be broken down into the computation of the loss in each individual layer averaged over one cycle.

To find $\langle P_n \rangle$, the average loss in the n^{th} layer, we need to compute first the instantaneous loss $P_n(t)$ in this layer. The instantaneous loss in the specified volume is equal to

$$P_n(t) = \iiint_{V_n} p_d(t)\, d\nu \tag{5.25}$$

where the symbol V_n associated with the integral signs is used to signify that the triple integration is carried out over the volume V_n of the n^{th} layer and $p_d(t)$ is the instantaneous loss density at an arbitrary point in the specified volume.

Combining (5.23) and (5.25) yields

$$\langle P_n \rangle = \frac{1}{T} \int_T \iiint_{V_n} p_d(t)\, d\nu\, dt \tag{5.26}$$

The integration with respect to time and the integration with respect to volume can be interchanged to give

$$\langle P_n \rangle = \iiint_{V_n} \left(\frac{1}{T} \int_T p_d(t)\, dt \right) d\nu \tag{5.27}$$

In Section 4.5.2, the power density averaged over one cycle, i.e.,

$$\langle p_d \rangle = \frac{1}{T} \int_T p_d(t)\, dt \tag{5.28}$$

is shown to be related to the phasor of the current density $\underline{J}_y$. Rewriting (4.95) to be consistent with the notation discussed in Section 4.6 gives

$$\langle p_d \rangle = \frac{\underline{J}_y(\chi)\, \underline{J}_y^*(\chi)}{\sigma_{eff}} \tag{5.29}$$

Substituting (5.28) and (5.29) into (5.27) yields

$$\langle P_n \rangle = \iiint_{V_n} \frac{\underline{J}_y(\chi)\, \underline{J}_y^*(\chi)}{\sigma_{eff}}\, d\nu \tag{5.30}$$

For the n^{th} layer of the transformer-winding arrangement, the height χ varies from zero to h_{cu}, the depth y varies from zero to the length of turn for the n^{th} layer ℓ_{Tn}, and the breadth z varies from zero to b_{win}. Thus, (5.30) can be expanded into

$$\langle P_n \rangle = \int_0^{b_{win}} \int_0^{\ell_{Tn}} \int_0^{h_{cu}} \frac{\underline{J}_y(\chi)\, \underline{J}_y^*(\chi)}{\sigma_{eff}}\, d\chi\, dy\, dz \tag{5.31}$$

In Section 4.5.2, the symbol $\langle Q_J \rangle$ is defined as the average power dissipated per square meter in the y-z plane. To be consistent with Section 4.6, (4.96) can be rewritten as

$$\langle Q_J \rangle = \frac{1}{\sigma_{eff}} \int_0^{h_{cu}} \underline{J}_y(X)\, \underline{J}_y^*(X)\, dX \tag{5.32}$$

Substituting (5.32) into (5.31), we have

$$\langle P_n \rangle = \int_0^{b_{win}} \int_0^{\ell_{Tn}} \langle Q_J \rangle \, dy \, dz \tag{5.33}$$

Since $\langle Q_J \rangle$ is not a function of the depth y nor the breadth z, the above double integration amounts to a trivial multiplication. The net result is

$$\langle P_n \rangle = \langle Q_J \rangle \, b_{win} \, \ell_{Tn} \tag{5.34}$$

After determining the average loss $\langle P_n \rangle$ over the n^{th} layer of the transformer winding arrangement, we can now return to find the average total loss $\langle P_D \rangle$ of the transformer. Combining (5.24) and (5.34) and using the results in (4.142) for $\langle Q_J \rangle$, the following derivation is obtained.

$$\begin{aligned}
\langle P_D \rangle &= \sum_{n=1}^{N} \langle P_n \rangle \\
&= \sum_{n=1}^{N} \langle Q_J \rangle \, b_{win} \, \ell_{Tn} \\
&= \sum_{n=1}^{N} b_{win} \ell_{Tn} \left[\frac{|\underline{H}_z(X = h_{cu})|^2}{\sigma_{eff}\, \delta} \left\{ (1 + \alpha^2 + \beta^2) F_1(\Delta) - 4\alpha F_2(\Delta) \right\} \right]_n \\
&= b_{win} \sum_{n=1}^{N} \left[\frac{\ell_T}{\sigma_{eff}\, \delta} \, |\underline{H}_z(X = h_{cu})|^2 \, \langle Q'_J(\alpha, \beta, \Delta) \rangle \right]_n
\end{aligned} \tag{5.35}$$

where all of the terms inside the summation depend upon which layer is being considered. The skin depth δ is retained inside the summation because its value depends upon the value of the effective conductivity for the layer as shown in (4.129).

It is worth noting here that the β term in the expression for $\langle Q'_J \rangle$ is zero for all of the short-circuit tests we are considering in this chapter. If we assume that the ampere-turns of the two current-carrying windings sum to zero, $N_j \underline{I}_j = N_k \underline{I}_k$, then in each short-circuit test, the currents in the winding layers are either in phase with one another or 180° out of phase with one another. This causes the z-directed magnetic-field-intensity phasors at the boundaries of each winding layer to be in phase or 180° out of phase with each other. When this is the case, Equation (4.49) for β evaluates to zero since $\sin(\theta_{X=0} - \theta_{X=h_{cu}})$. We continue to write $\langle Q'_J \rangle$ as a function of all three variables α, β and Δ in order to keep the resulting equations as general as possible, but we do not need to consider β in the present discussion.

We can use the normalization procedures discussed in Section 5.2.3 to relate the values of $\underline{H}_z(\chi = h_{cu})$ in the above expression for $\langle P_D \rangle$ to the short-circuit current in the excited winding, $\underline{I}_{SC}$. Recalling (5.11), $\underline{H}_{BASE} = N_E \underline{I}_{BASE}/b_{win}$, we have

$$\underline{H}_{z\text{-}N}(\chi = h_{cu}) = \frac{\underline{H}_z(\chi = h_{cu})}{\underline{H}_{BASE}} = \frac{b_{win}\,\underline{H}_z(\chi = h_{cu})}{N_E \underline{I}_{BASE}} \tag{5.36}$$

We can solve this expression for $\underline{H}_z(\chi = h_{cu})$ as

$$\underline{H}_z(\chi = h_{cu}) = \frac{N_E \underline{I}_{BASE} \underline{H}_{z\text{-}N}(\chi = h_{cu})}{b_{win}} \tag{5.37}$$

Using this expression in (5.35) and noting that

$$|\underline{I}_{BASE}|^2 = |\underline{I}_{SC}|^2 \tag{5.38}$$

we get the final expression for the total time-averaged power dissipated in the transformer for any short-circuit test condition.

$$\boxed{\langle P_D \rangle = \frac{N_E^2 |\underline{I}_{SC}|^2}{b_{win}} \sum_{n=1}^{N} \left[\frac{\ell_T}{\sigma_{eff}\,\delta} |\underline{H}_{z\text{-}N}(\chi = h_{cu})|^2 \langle Q'_J(\alpha, \beta, \Delta) \rangle \right]_n} \tag{5.39}$$

Recalling equations (5.13) and (5.20), we can use (5.39) to write $R_{(jk)}$, the apparent short-circuit resistance that represents the losses in the windings of a transformer for any short-circuit test, as

$$R_{(jk)} = \frac{\langle P_D \rangle}{|\underline{I}_{SC}|^2}$$

$$\boxed{R_{(jk)} = \frac{N_E^2}{b_{win}} \sum_{n=1}^{N} \left[\frac{\ell_T}{\sigma_{eff}\,\delta} |\underline{H}_{z\text{-}N}(\chi = h_{cu})|^2 \langle Q'_J(\alpha, \beta, \Delta) \rangle \right]_n} \tag{5.40}$$

In the above equations, ℓ_T, σ_{eff}, δ, $|\underline{H}_{z\text{-}N}(\chi = h_{cu})|$ and $\langle Q'_J \rangle$ must be determined for each individual layer.

5.2.5 Winding-Inductance Calculations

The calculation of energy stored in the magnetic field in a winding layer from the solution for energy stored per square meter $\langle Q_H \rangle$ of the layer given in (4.144) follows a very similar path to that used in the calculation of power dissipation from $\langle Q_J \rangle$. However, in the energy storage case, we must account not only for the energy in the winding layers

themselves, but also for the energy in the interlayer gap regions. This poses no real problem since the phasors of the magnetic field in these gap regions are independent of frequency. In this section, we demonstrate a method for calculating the amount of stored energy in a winding structure by first calculating the energy stored in the winding layers then calculating the energy stored in the gaps. The total energy stored in the entire winding structure is then used to determine the apparent inductance $L_{(jk)}$ as seen by winding j for the (jk) short-circuit test.

For an inductance $L_{(jk)}$ to model the energy-storage behavior of the transformer for a given short-circuit test, the average energy stored $\langle W_{L(jk)} \rangle$ by $L_{(jk)}$ must be equal to the total average energy stored by the winding structure $\langle W_T \rangle$.

$$\langle W_{L(jk)} \rangle = \langle W_T \rangle \tag{5.41}$$

The total average energy stored by the transformer winding structure $\langle W_T \rangle$ is composed of two parts: the average energy stored in the layers of the windings $\langle W_\ell \rangle$, and the average energy stored in the interlayer gaps $\langle W_g \rangle$.

$$\langle W_T \rangle = \langle W_\ell \rangle + \langle W_g \rangle \tag{5.42}$$

The energies $\langle W_{L(jk)} \rangle$, $\langle W_\ell \rangle$, and $\langle W_g \rangle$ are determined by averaging over one cycle their respective instantaneous quantities $W_{L(jk)}(t)$, $W_\ell(t)$, and $W_g(t)$.

$$\langle W_{L(jk)} \rangle = \frac{1}{T} \int_T W_{L(jk)}(t)\, dt \tag{5.43}$$

$$\langle W_\ell \rangle = \frac{1}{T} \int_T W_\ell(t)\, dt \tag{5.44}$$

$$\langle W_g \rangle = \frac{1}{T} \int_T W_g(t)\, dt \tag{5.45}$$

5.2.5.1 Energy Stored in the Winding Layers

In this subsection, we derive the equations necessary to determine $\langle W_\ell \rangle$, the average energy stored in the layers of the transformer windings. The determination of $\langle W_g \rangle$, the average energy stored in the interlayer gaps, is deferred until Section 5.2.4.2. Using the symbol $W_n(t)$ to represent the instantaneous energy stored in the n^{th} layer of an N-layer winding structure, we can state that the instantaneous energy $W_\ell(t)$ stored in all the layers is equal to the sum of the energy stored $W_n(t)$ in each layer.

$$W_\ell(t) = \sum_{n=1}^{N} W_n(t) \tag{5.46}$$

Taking the time average of each side of (5.46), replacing the left-hand side with (5.44) and interchanging the integration and summation in the right-hand side gives

$$\langle W_\ell \rangle = \sum_{n=1}^{N} \frac{1}{T} \int_T W_n(t)\, dt$$

$$= \sum_{n=1}^{N} \langle W_n \rangle \tag{5.47}$$

where $\langle W_n \rangle$ is the average energy storage in the n^{th} layer.

Recalling from Section 4.5.3[2] that $\langle w_m \rangle$ represents the average over one period of excitation of the energy density at a point, we can calculate $\langle W_n \rangle$ by taking the integral of $\langle w_m \rangle$ over the volume of the specified n^{th} layer

$$\langle W_n \rangle = \iiint_{V_n} \langle w_m \rangle \, d\nu \tag{5.48}$$

Adopting the bounds of integration used in Section 5.2.4, this can be rewritten

$$\langle W_n \rangle = \int_0^{b_{win}} \int_0^{\ell_{Tn}} \int_0^{h_{cu}} \langle w_m \rangle \, dX \, dy \, dz \tag{5.49}$$

The innermost integral in (5.49) is calculated in Section 4.5.3 and is equal to $\langle Q_H \rangle$, the average energy storage per square meter in the y-z plane. Since $\langle Q_H \rangle$ is invariant with y and z, the integrations with respect to y and z in (5.49) are trivial and

$$\langle W_n \rangle = \langle Q_H \rangle \, b_{win} \, \ell_{Tn} \tag{5.50}$$

Substituting this into (5.47) and using the expression for $\langle Q_H \rangle$ given in (4.144) results in the total stored energy averaged over one cycle in the N layers of the winding structure.

$$\begin{aligned}
\langle W_\ell \rangle &= \sum_{n=1}^{N} \langle W_n \rangle \\
&= \sum_{n=1}^{N} \langle Q_H \rangle b_{win} \ell_{Tn} \\
&= \sum_{n=1}^{N} b_{win} \ell_{Tn} \left[\frac{\mu_0 \delta |\underline{H}_z(X = h_{cu})|^2}{4} \left\{ (1 + \alpha^2 + \beta^2) F_3(\Delta) - 4\alpha F_4(\Delta) \right\} \right]_n \\
&= \frac{b_{win} \mu_0}{4} \sum_{n=1}^{N} \left[\ell_T \delta |\underline{H}_z(X = h_{cu})|^2 \langle Q'_H(\alpha, \beta, \Delta) \rangle \right]_n
\end{aligned} \tag{5.51}$$

where all of the terms inside the final summation depend on which layer is being considered. As is the case for the expression for $\langle Q'_J \rangle$, the value of β in the expression for $\langle Q'_H \rangle$ above is equal to zero for all of the short-circuit tests considered here.

Again as in (5.36) and (5.37), we write $\underline{H}_z(X = h_{cu}) = \underline{H}_{z\text{-}N}(X = h_{cu}) \underline{H}_{BASE}$ with $\underline{H}_{BASE} = N_E \underline{I}_{BASE} / b_{win}$ and $|\underline{I}_{BASE}|^2 = |\underline{I}_{SC}|^2$ to yield

$$\langle W_\ell \rangle = \frac{b_{win} \mu_0}{4} \frac{N_E^2 |\underline{I}_{SC}|^2}{b_{win}^2} \sum_{n=1}^{N} \left[\ell_T \delta |\underline{H}_{z\text{-}N}(X = h_{cu})|^2 \langle Q'_H(\alpha, \beta, \Delta) \rangle \right]_n$$

[2]Some of this discussion is also presented in Sections 4.5.1, and 4.5.3, but is repeated here for convenience and clarity.

$$\langle W_\ell \rangle = \frac{\mu_0}{2} \left\{ \frac{N_E^2 |\underline{I}_{SC}|^2}{2 b_{win}} \sum_{n=1}^{N} \left[\ell_T \delta |\underline{H}_{z\text{-}N}(\chi = h_{cu})|^2 \langle Q'_H(\alpha, \beta, \Delta) \rangle \right]_n \right\} \tag{5.52}$$

5.2.5.2 Energy Stored in the Gaps Between the Winding Layers

The determination of the energy stored in the interlayer gaps of a transformer winding follows much the same trail as is presented in Section 5.2.5.1 for the layer energy. The total instantaneous energy stored in all the gaps $W_g(t)$ is composed of the energies $W_{g_n}(t)$ stored in each of the $(N-1)$ interlayer gaps of the N-layer winding. Likewise, the total gap energy averaged over one cycle $\langle W_g \rangle$ is composed of the individual, averaged, gap energies $\langle W_{g_n} \rangle$. Algebraically this can be expressed as

$$W_g(t) = \sum_{n=1}^{N-1} W_{g_n}(t) \tag{5.53}$$

$$\langle W_g \rangle = \sum_{n=1}^{N-1} \langle W_{g_n} \rangle \tag{5.54}$$

The summations in (5.53) and (5.54) include only the $(N-1)$ gaps between any two adjacent layers of the winding structure. Thus, gap one is located between layers one and two, and gap $(N–1)$ is located between layers $(N–1)$ and N. Neither the gap between the the innermost layer and the core (the "0^{th}" gap), nor the gap between the outermost layer and the core (the N^{th} gap) is of interest when determining energy storage, since the magnetic field intensity in these two gaps is assumed to be zero at all times.[3]

We continue by expressing the total instantaneous energy $W_{g_n}(t)$ in gap n in terms of the instantaneous magnetic energy density $w_m(t)$ in the gap.

$$W_{g_n}(t) = \iiint_{V_n} w_m(t)\, d\nu \tag{5.55}$$

Taking the time average of both sides of (5.55) and reversing the order of integration gives

$$\begin{aligned} \langle W_{g_n} \rangle &= \frac{1}{T} \int_T \iiint_{V_n} w_m(t)\, d\nu\, dt \\ &= \iiint_{V_n} \frac{1}{T} \int_T w_m(t)\, dt\, d\nu \\ &= \iiint_{V_n} \langle w_m \rangle\, d\nu \end{aligned} \tag{5.56}$$

[3] See Section 5.2.1.

Each gap extends from zero to the height of the gap g_n in the x-direction, from zero to the "length-of-turn" for the gap ℓ_{gn} in the y-direction, and from zero to b_{win} in the z-direction. Inserting these limits of integration in (5.56) gives

$$\langle W_{g_n} \rangle = \int_0^{b_{win}} \int_0^{\ell_{gn}} \int_0^{g_n} \langle w_m \rangle \, dx \, dy \, dz \tag{5.57}$$

From (4.115), the averaged energy-storage density $\langle w_m \rangle$ at any point x where the magnetic-field-intensity phasor is equal to $\underline{H}_z(x)$ is given by

$$\langle w_m \rangle = \frac{\mu_0 \underline{H}_z(x) \underline{H}_z^*(x)}{2} \tag{5.58}$$

Examining the magnetic-field-intensity diagrams of Fig. 5.2 we see that, for any excitation of the winding structure, the magnetic field intensity in any gap is invariant in the x-dimension and that the value of the field-intensity phasor $\underline{H}_g$ in the n^{th} gap is equal to $\underline{H}_z(x = h_{cu})$ of the n^{th} layer and to $\underline{H}_z(x = 0)$ of the $(n+1)^{th}$ layer. As is discussed in Section 3.1.3, $\underline{H}_{g_n}$ depends only on the net ampere-turns of the conducting layers and is independent of frequency. Substituting $\underline{H}_{g_n}$ into (5.58), we can express the average energy density in the gap as

$$\langle w_m \rangle = \frac{\mu_0 \underline{H}_{g_n} \underline{H}_{g_n}^*}{2} = \frac{\mu_0 |\underline{H}_{g_n}|^2}{2} \tag{5.59}$$

Since this expression for $\langle w_m \rangle$ is invariant in all three directions, the integrations in (5.57) are trivial.

$$\begin{aligned} \langle W_{g_n} \rangle &= \iiint_{V_n} \langle w_m \rangle \, d\nu = \int_0^{b_{win}} \int_0^{\ell_{gn}} \int_0^{g_n} \frac{\mu_0 |\underline{H}_{g_n}|^2}{2} \, dx \, dy \, dz \\ &= \frac{\mu_0 |\underline{H}_{g_n}|^2}{2} \times \text{Volume} \\ &= \frac{\mu_0 |\underline{H}_{g_n}|^2 b_{win} \ell_{gn} g_n}{2} \end{aligned} \tag{5.60}$$

From (5.54), we know that the total amount of gap energy is the sum of the individual gap energies, so, for a winding structure with N layers and $(N-1)$ interlayer gaps, the total gap energy averaged over one cycle is

$$\begin{aligned} \langle W_g \rangle &= \sum_{n=1}^{N-1} \langle W_{g_n} \rangle \\ &= \frac{\mu_0 b_{win}}{2} \sum_{n=1}^{N-1} |\underline{H}_{g_n}|^2 \ell_{gn} g_n \\ &= \frac{\mu_0 b_{win}}{2} \frac{N_E^2 |\underline{I}_{SC}|^2}{b_{win}^2} \sum_{n=1}^{N-1} |\underline{H}_{g_n - N}|^2 \ell_{gn} g_n \end{aligned}$$

$$\langle W_g \rangle = \frac{\mu_0}{2} \left\{ \frac{N_E^2 |\underline{I}_{SC}|^2}{b_{win}} \sum_{n=1}^{N-1} \left[|\underline{H}_{g\text{-}N}|^2 \ell_g \, g \right]_n \right\} \tag{5.61}$$

where the magnetic field intensity has been normalized to the value of $\underline{H}_{BASE}$ used earlier.

5.2.5.3 Total Stored Energy in a Transformer

As discussed in the introductory text in Section 5.2.5.1, the total energy stored, averaged over one cycle, in the transformer winding for any short-circuit test is designated $\langle W_T \rangle$, and is given by the sum of the average energy $\langle W_\ell \rangle$ in the layers and the average energy $\langle W_g \rangle$ in the gaps between the layers. Combining equations (5.52) and (5.61)

$$\langle W_T \rangle = \langle W_\ell \rangle + \langle W_g \rangle$$

$$\langle W_T \rangle = \frac{\mu_0}{2} \frac{N_E^2 |\underline{I}_{SC}|^2}{b_{win}} \left\{ \frac{1}{2} \sum_{n=1}^{N} \left[\ell_T \delta |\underline{H}_{z\text{-}N}(\chi = h_{cu})|^2 \langle Q'_H(\alpha, \beta, \Delta) \rangle \right]_n + \sum_{n=1}^{N-1} \left[\ell_g \, g |\underline{H}_{g\text{-}N}|^2 \right]_n \right\} \tag{5.62}$$

5.2.5.4 The Short-Circuit Inductance

Now that an expression for $\langle W_T \rangle$ exists, we need to determine an expression for $\langle W_{L(jk)} \rangle$ on the left-hand side of equation (5.41) which is the average energy stored in the apparent short-circuit inductance.

We know that $w(t) = (1/2) L i^2(t)$ is the instantaneous energy stored in any inductor L. Assuming that the inductor $L_{(jk)}$ models the energy stored in the transformer windings for short-circuit test (jk), the instantaneous current flowing through the model inductor is equal to the short-circuit current $i_{SC}(t)$ in the excited winding since $L_{(jk)}$ is referred to winding j.

$$W_{L(jk)}(t) = \frac{1}{2} L_{(jk)} \, i_{SC}^2(t) \tag{5.63}$$

As is given in equations (5.17) and (5.18), for the case of sinusoidal excitation the instantaneous exciting current can be expressed as

$$i_{SC}(t) = \sqrt{2} I_{SC} \cos(\omega t + \theta) \tag{5.64}$$

$$\underline{I}_{SC} = I_{SC} \, e^{j\theta} \tag{5.65}$$

Taking the average over one cycle of $W_{L(jk)}(t)$ using equation (5.43) after substituting (5.63) in for $W_{L(jk)}(t)$ and (5.64) in for $i_{SC}(t)$, yields

$$\langle W_{L(jk)} \rangle = \frac{1}{2} {I_{SC}}^2 \, L_{(jk)} \tag{5.66}$$

From (5.65), $|\underline{I}_{SC}|^2 = {I_{SC}}^2$, thus

$$\langle W_{L(jk)} \rangle = \frac{1}{2} |\underline{I}_{SC}|^2 \, L_{(jk)} \tag{5.67}$$

Substituting this expression into the left-hand side of (5.41) and rearranging lets us relate the average energy stored in the transformer winding structure to the short-circuit leakage inductance $L_{(jk)}$ between the excited and shorted windings

$$L_{(jk)} = \frac{2 \langle W_T \rangle}{|\underline{I}_{SC}|^2}$$

$$\boxed{L_{(jk)} = \frac{\mu_0 N_E^2}{b_{win}} \left\{ \frac{1}{2} \sum_{n=1}^{N} \left[\ell_T \delta |\underline{H}_{z\text{-}N}(\chi = h_{cu})|^2 \langle Q'_H(\alpha, \beta, \Delta) \rangle \right]_n + \sum_{n=1}^{N-1} \left[\ell_g g |\underline{H}_{g\text{-}N}|^2 \right]_n \right\}} \tag{5.68}$$

where $\langle W_T \rangle$ is defined by (5.62).

5.2.6 Short-Circuit Impedance Formula

We can combine the results for the resistance and inductance calculations above to write an expression for the impedance between any two windings of a transformer. The short-circuit impedance $\underline{Z}_{(jk)}$ between windings j and k referred to winding j is in general,

$$\underline{Z}_{(jk)} = R_{(jk)} + j\omega L_{(jk)} \tag{5.69}$$

where $R_{(jk)}$ is the short-circuit resistance given in (5.40) that corresponds to the power dissipation in the conductors and $L_{(jk)}$ is the short-circuit leakage inductance related to the energy stored in the transformer winding space as given above in (5.68). For a four-winding transformer there are six different short-circuit impedances to calculate. The results of these calculations can be used in place of measured short-circuit impedances to determine values for the six admittance links of the circuit shown in Fig. 7.9. The details of such a development are presented in Chapter 7 and are built upon the work in [1,13,18]. The six calculated short-circuit impedances can also be used to determine the six impedances used in the coupled-secondaries equivalent circuit discussed in Chapter 8.

5.2.7 Relating Field Solutions to Winding Layout

In order to compute an actual numerical value for the leakage impedance between any two windings, we must know the specific layout of the winding layers. The expressions developed above depend only on the boundary conditions of the magnetic field intensity that exist for each winding layer and not on how those conditions arise. In order to use these expressions, however, we must in fact determine values for the various boundary conditions.

A simple algorithm for calculating the power dissipation and energy storage of a winding for sinusoidal excitation which includes the determination of the various boundary conditions is as follows:

1. Describe in detail the geometry of the transformer and its windings including important mechanical parameters such as core-window breadth. Decide upon operating points such as excitation frequency and winding-temperature rise. Calculate necessary parameters such as skin depth and layer porosity.[4]

2. Given the positions of the layers of the respective windings of the transformer and the excitation conditions in these layers—short-circuit current in this case—construct the low-frequency field-intensity diagram for the transformer as detailed in Section 3.1.2.

3. From this diagram and (5.12), determine the normalized values of the magnetic field intensity at all interlayer-gap positions.

4. If desired, determine the losses in the transformer windings using the boundary conditions determined above and equation (5.39).

5. If desired, determine the energy stored in the winding structure from the above determined boundary conditions and (5.62).

6. Use the boundary conditions determined above to compute the apparent short-circuit resistance and the apparent short-circuit inductance using (5.40) and (5.68) respectively.

7. Use (5.69) to determine the leakage impedance between the windings of interest.

The algorithm given above is straightforward enough to be easily implemented with a computer for any winding structure. In order to expand and clarify the procedure for determining $R_{(jk)}$ and $L_{(jk)}$, we present in the next chapter a detailed example calculation of these quantities and sample plots of how they vary with frequency for a sample winding structure.

The present chapter is based upon short-circuit tests in which current flows in only two windings of the transformer, and those currents are of equal but opposite ampere-turns. Under these conditions, $\beta = 0$ always, since the phase difference of the magnetic

[4] A more complete description of this step is given in Sections 6.1.1, 6.1.2, and 6.1.3.

field across a layer is always 0° or 180°. This excitation condition gives us the short-circuit impedances which are used to determine the components of the admittance-link circuit of Chapter 7 and the coupled-secondaries circuit of Chapter 8. Yet, the equations developed above for the short-circuit impedances require only that the specific layout of the windings and the boundary conditions of the field intensity for each layer be known. Because of this, equations (5.39) and (5.62) for $\langle P_D \rangle$ and $\langle W_T \rangle$, respectively, are given as general functions of α, β and Δ. Therefore, equations (5.40) and (5.68) are applicable to any winding excitation, not just the short-circuit conditions assumed in this chapter, and represent the resistance and inductance seen at winding j due to the field distribution in the transformer windings when current flows in winding j.

This page has been left blank intentionally.

Chapter 6

Calculation and Verification of Short-Circuit Impedances

In this chapter, we present both calculated and measured data for $R_{(jk)}$ and $L_{(jk)}$ for an example EE-core transformer and an example pot-core transformer. The winding structure for both transformers under analysis corresponds to that in Fig. 5.2(a). Section 6.1 contains a detailed example wherein the values of $R_{(13)}$ and $L_{(13)}$ at 100 kHz are calculated in a step-by-step fashion for the EE-core transformer. Section 6.2 contains computer-generated plots of $R_{(jk)}$ and $L_{(jk)}$ versus frequency for the EE-core transformer under the six short-circuit tests of Fig. 5.2(c). In Section 6.3 we discuss how short-circuit tests were performed on the actual transformers, and compare the measured data for the EE-core transformer with the results of the calculations in Section 6.2. Also in Section 6.3, we compare measured and calculated values of short-circuit impedances for the pot-core transformer, and we discuss the validity of the predicted impedance values.

6.1 STEP-BY-STEP NUMERICAL EXAMPLE OF DETERMINING $R_{(jk)}$ AND $L_{(jk)}$

In this section, the reader is guided through a complete numerical determination of the short-circuit resistance $R_{(jk)}$ and inductance $L_{(jk)}$ for an example EE-core transformer at a specified frequency for a given dc field-intensity diagram. Through this example, we tie together the various issues presented throughout this report: modeling a layer of conducting wires as a foil conductor as presented in Section 2.2; determining the average normalized power dissipation in a layer $\langle Q'_J \rangle$ and the average normalized energy stored in a layer $\langle Q'_H \rangle$ as discussed in Sections 4.5.2 and 4.5.3, respectively; and determining the short-circuit resistance $R_{(jk)}$ and inductance $L_{(jk)}$ from $\langle Q'_J \rangle$ and $\langle Q'_H \rangle$, discussed in Sections 5.2.4 and 5.2.5. This numerical example should help explain the process of calculating the short-circuit impedances so that the reader may do similar hand calculations or automate the calculation procedure by programming a computer with the

pertinent equations.

As with any calculations, the precision of the results presented below depends upon the precision of the input data and the calculation technique. Data culled from manufacturer's data books are only as accurate and precise as the manufacturer's specifications. For the most part, calculation results presented in this numerical example are rounded to reflect the number of accurate digits. When the calculations presented below were performed, however, intermediate results were stored in calculator memory for use in subsequent calculations. Therefore, data actually used for these calculations was of higher resolution than that of the presented intermediate results. If the reader chooses to replicate these calculations using the provided data, some variation in the last digit of the results may be seen. This should not effect the final calculation of the short-circuit resistance and inductance since they have been rounded to only two significant digits.

6.1.1 Step 1—Collect Known Quantities

To begin the analysis, we must first collect the needed mechanical and electrical parameters which are known from the transformer design. It is assumed that the transformer has already been wound, or that the transformer design is detailed enough to provide all the necessary information. The parameters of initial interest are:

- General layout of transformer including number of layers, and the relative positions and interconnections of the layers
- Size, type and number of conductors in each layer, and the total number of turns in the excited winding
- Frequency of interest
- Mechanical dimensions of the core and bobbin
- Resistivity and its thermal coefficient for the wires, and the temperature of the windings
- Low-frequency magnetic-field-intensity diagram for the chosen short-circuit test, if known
- Thickness of interlayer insulation or shields

In this example, we use an eight-layer four-winding transformer[1] with a cross-section similar to that shown in Fig. 6.1. Each layer is composed of $N_\ell = 13$ turns of $n_s = 2$ paralleled twenty-gauge wires, amounting to $N_c = 26$ insulated wires per layer. Each winding has twenty-six turns and is composed of two layers of thirteen turns each. The six possible short-circuit low-frequency magnetic-field-intensity diagrams for this winding arrangement are shown in Fig. 5.2(b). For this numerical example, we develop in detail only the (13) case—winding one excited and winding three shorted—as is shown in Fig. 6.2. Derivation of low-frequency field-intensity diagrams for short-circuit tests

[1]Vekatraman's transformer number W835-2, alias Duke's number ec03b03.

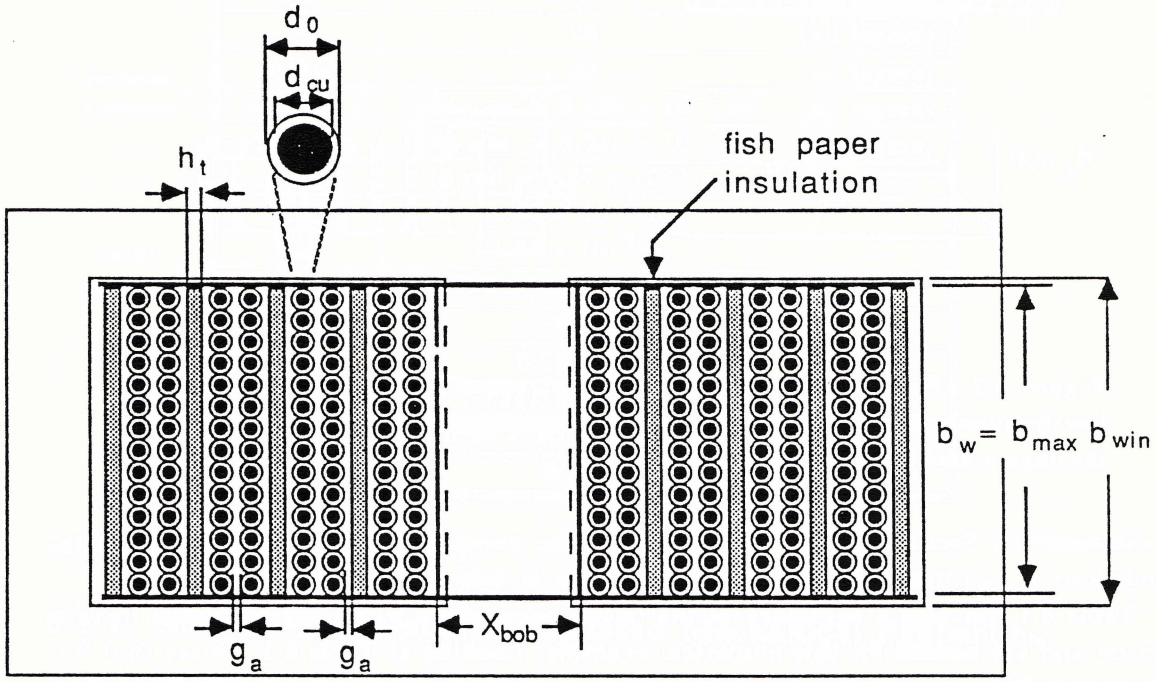


Figure 6.1: Cross-section of an eight-layer four-winding EE-core transformer showing its relevant dimensions. Displayed layers are composed of seven turns of two paralleled wires for a total of 14 conductors per layer. In the actual transformer under analysis, there are 13 turns of two paralleled wires for a total of 26 conductors per layer.

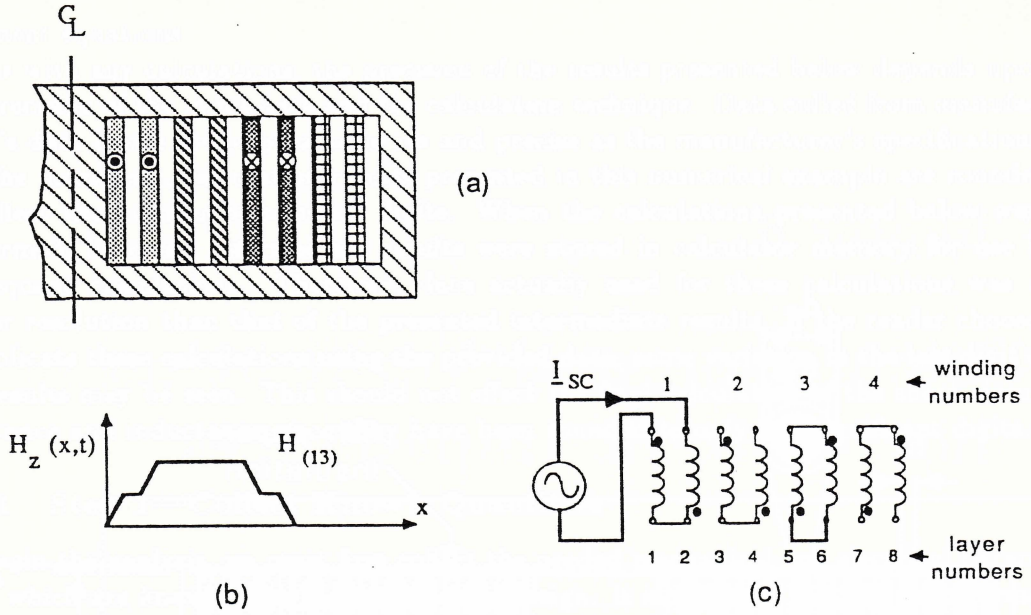


Figure 6.2: For short-circuit test (13), (a) transformer cross section, (b) low-frequency field-intensity diagram, (c) interconnections among the winding layers and the excitation source.

is discussed in Section 5.2.2. Calculation of the normalized field-intensity boundary conditions $\underline{H}_{z\text{-}N}(0)$ and $\underline{H}_{z\text{-}N}(h_{cu})$ for each layer is deferred until Section 6.1.3.

Table 6.1 contains a summary of the initial parameters which are discussed in this section and are needed for this numerical example. Looking at Table 6.1, we see that for the sample EE-core transformer, the thickness h_t of the fish paper insulation separating the windings is 5 mil or 1.27×10^{-4} m. An "additional gap" g_a is introduced later to account for overlap of the fish-paper insulation, tape and unevenness of the windings. A frequency f of 100 kHz is used for this example. The chosen wire size, 20 AWG, has a copper area[2] of 1024 circular mils (c.m.) and an area[3] with heavy insulation of 1246 c.m. Using the conversion factor 1 c.m. $= 5.067 \times 10^{-10}$ m^2, these areas can be rewritten in SI units as shown in Table 6.1. If different layers employ different wire sizes, then the areas of each wire size should be noted. The center-leg dimensions of the chosen bobbin were measured from other bobbins of the same type and found to be $X_{bob} = 1.45 \times 10^{-2}$ m and $Y_{bob} = 1.83 \times 10^{-2}$ m; X_{bob} and Y_{bob} are defined in Fig. 6.4. The chosen EE core has a window breadth[4] b_{win} of 3.02×10^{-2} m. For completeness, the resistivity $\rho_{cu,20°C}$ of annealed copper wire at 20 °C and its temperature coefficient of resistivity K_T, which are given in the Glossary of Symbols, are included in Table 6.1 along with the chosen

[2]Magnetics, Inc., *Design Manual featuring Tape Wound Cores*, Publication TWC-300R, pp. 64.
[3]Ibid.
[4]Stackpole Corp. *Stackpole Cermag Products*, Bulletin 59-107, pp. 17. **Core Material**: 24B. **Core Number**: 50-0348.

Table 6.1: Initial Collection of Mechanical and Electrical Parameters

Parameter	*Value*	
N_ℓ	13	(all layers)
n_s	2	(all layers)
N_c	26	(all layers)
AWG	20	(all layers)
$A_{cu,20\text{AWG}}$	1024 c.m. $= 5.189 \times 10^{-7}$ m^2	(all layers)
$A_{o,20\text{AWG}}$	1246 c.m. $= 6.313 \times 10^{-7}$ m^2	(all layers)
h_t	5 mil $= 1.27 \times 10^{-4}$ m	
X_{bob}	1.45×10^{-2} m	
Y_{bob}	1.83×10^{-2} m	
b_{win}	$2(0.595 \text{ in}) = 3.02 \times 10^{-2}$ m	
f	100 kHz	
ω	6.28×10^5	
$\rho_{cu,20°\text{C}}$	1.7241×10^{-8} Ω-m	
K_T	3.93×10^{-11} Ω-m/C°	
T	60 °C	

winding operating temperature T.

6.1.2 Step 2—Determine the Related Mechanical Properties

After collecting the initial list of electrical and mechanical parameters associated with the transformer under analysis, certain other parameters must be determined. In this section, we discuss the mechanical parameters to be determined. These are:

- The diameters of the wires with and without insulation
- The height h_{cu} of each of the foil layers used to model the layers of wire conductors
- The layer porosity for each layer
- The heights of the gaps between the layers
- The mean length of each layer and each interlayer gap

The diameter d_{cu} of the copper in each conductor and the diameter d_o of the wire with insulation can be determined from their associated areas by the formula $d = \sqrt{4\,A/\pi}$.

$$d_{cu} = \sqrt{\frac{4\,A_{cu}}{\pi}} = \sqrt{\frac{4(5.189 \times 10^{-7})}{\pi}} = 8.128 \times 10^{-4} \text{ m}$$

$$d_o = \sqrt{\frac{4\,A_o}{\pi}} = \sqrt{\frac{4(6.313 \times 10^{-7})}{\pi}} = 8.966 \times 10^{-4}\,\text{m}$$

Since in Section 2.2 the round wire conductors are initially modeled as square conductors of equal cross-sectional area, we can determine both the height h_{cu} and the breadth b_{cu} of the equivalent square conductors using (2.3)

$$h_{cu} = b_{cu} = \sqrt{\frac{\pi}{4}}\,d_{cu} = \sqrt{\frac{\pi}{4}}\,(8.128 \times 10^{-4}) = 7.203 \times 10^{-4}\,\text{m}$$

Note that h_{cu} is also the height of the "stretched" foil conductor finally used to model a layer of round-wire conductors. As discussed in Sections 2.2.1, the foil conductors have an associated layer porosity which results from the "stretching" process. The value of layer porosity for each layer can be determined using (2.4) and the above calculated value of b_{cu},

$$\eta = \frac{N_c b_{cu}}{b_{win}} = \frac{26(7.203 \times 10^{-4})}{3.02 \times 10^{-2}} = 0.620$$

If wire size or conductor type differ among the winding layers, values of d_{cu}, d_o, b_{cu}, h_{cu} and η must be determined for each layer. If the number of turns per layer differs, η must be determined for each layer.

If round-wire windings are wound as tightly as possible without permitting wires in layer $(n+1)$ to slip into the notches between the wires in layer n, in other words, if the winding is "square" as represented in Fig. 1.1(a), then the minimum center-to-center distance between adjacent layers n and $(n+1)$ is equal to the sum of the radii of the two layers. For layers in a square winding which are separated by a layer of fish paper insulation, the minimum center-to-center separation between the layers is equal to the sum of the radii of the two layers and the thickness of the fish paper. For our particular transformer, it is assumed that the windings are "square," so the minimum possible center-to-center distance between adjacent layers, such as between layers one and two, is equal to d_o, since all the wires have the same radii. The minimum possible center-to-center distance between layers separated by fish paper, such as between layers two and three, is $(d_o + h_t)$.

In an actual transformer, it is unlikely that the separation between the winding layers will be equal to the minimum possible. Whether it is due to the overlapping of the ends of the fish paper insulation, or to loosely wound layers, some additional gap between the layers is generally present. For a transformer which is still being designed, an estimation must be made of the amount of this additional gap. For a transformer which is being wound with this analysis in mind, exact measurements can be made of the buildup after each layer of wires or fish paper is wound. To analyze an already existent transformer winding, the additional interlayer gaps can be approximated by comparing the actual buildup of the winding to the minimum possible value. For our particular winding, the minimum possible outside measurement $Y_{o,min}$ is equal to the number of winding layers multiplied by d_o the outer diameter of the round wire used in each layer, plus the number

of layers of fish paper insulation used multiplied by h_t the thickness of the insulation, plus Y_{bob} the y-direction dimension of the bobbin, or algebraically,

$$\begin{aligned} Y_{o,min} &= 16d_o + 8h_t + Y_{bob} \\ &= 16(8.966 \times 10^{-4}) + 8(1.27 \times 10^{-4}) + 1.83 \times 10^{-2} \\ &= 3.366 \times 10^{-2} \text{ m} \end{aligned}$$

It is recognized that a result with four-digit precision cannot be obtained in this calculation because of the imprecision of h_t and Y_{bob}, but the result is treated as exact for convenience in subsequent calculations.

When the actual buildup of the windings in the y-direction was measured, however, a value of $Y_{o,meas} = 3.423 \times 10^{-2}$ m was obtained. Clearly some additional gaps must exist between the layers. For the transformer being analyzed, we assume that the difference between $Y_{o,meas}$ and $Y_{o,min}$ is a distributed gap appearing in equal portions in all 24 possible locations, i.e., in the eight spaces between two winding layers, the 14 spaces between a winding layer and a layer of insulation, and the two spaces between a winding layer and the bobbin. The value of the approximate additional gap g_a appearing in each of these locations is

$$g_a = \frac{3.423 \times 10^{-2} - 3.366 \times 10^{-2}}{24} = 2.4 \times 10^{-5} \text{ m}$$

Using this value of g_a and referring to Fig. 6.3, the values of the intrasection gaps g_{intras} and the intersection gaps g_{inters}, defined in Section 2.2.1, are

$$\begin{aligned} g_{intras} &= d_o - h_{cu} + g_a \\ &= 8.966 \times 10^{-4} - 7.203 \times 10^{-4} + 2.4 \times 10^{-5} \\ &= 2.0 \times 10^{-4} \text{ m} \end{aligned}$$

$$\begin{aligned} g_{inters} &= d_o - h_{cu} + h_t + 2g_a \\ &= 8.966 \times 10^{-4} - 7.203 \times 10^{-4} + 1.27 \times 10^{-4} + 2(2.4 \times 10^{-5}) \\ &= 3.5 \times 10^{-4} \text{ m} \end{aligned}$$

The last mechanical parameters that we must determine are the length-of-turn ℓ_{Tn} for each layer of the winding, and the length ℓ_{gn} of each interlayer gap. Although it is common to use one average turn length for the entire winding, in this example, we calculate individual lengths for each layer and each interlayer gap.

The model which is adopted to determine the length of an individual layer wound on a rectangular bobbin is shown in Fig. 6.4. We assume that each corner forms a quarter-circle and that the radii r_n are the distances from the corner of the bobbin to the centers of the n layers. For the first layer,

$$r_1 = g_a + \frac{d_o}{2} = 2.4 \times 10^{-5} + \frac{1}{2}(8.966 \times 10^{-4})$$

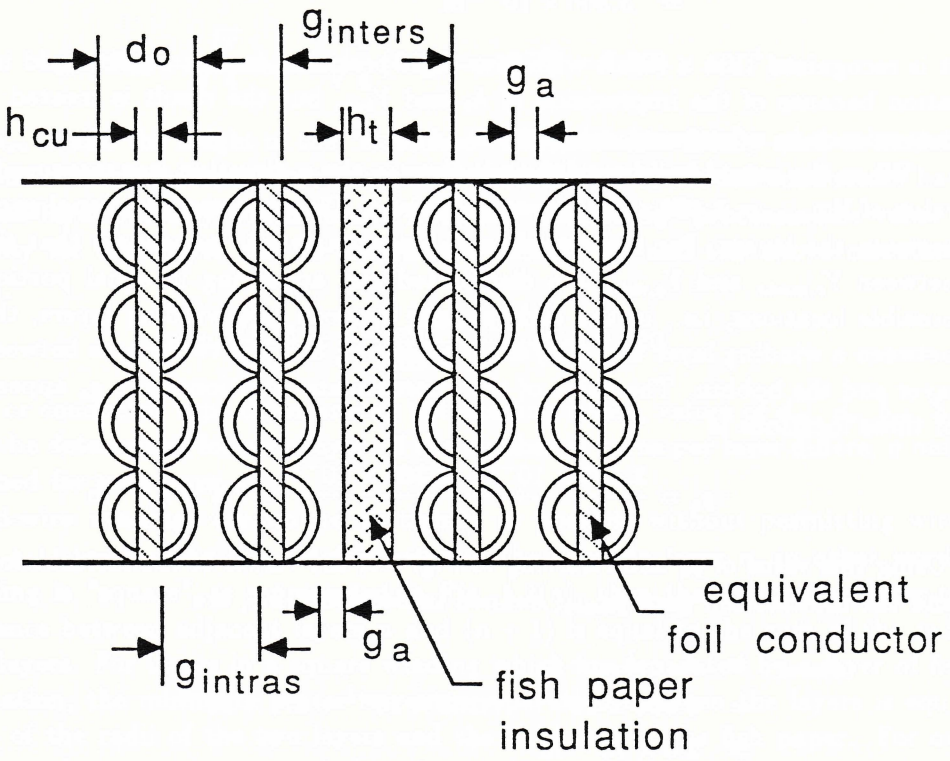


Figure 6.3: Detailed drawing of modeled layers showing the intrasection gaps g_{intras} and the intersection gaps g_{inters}.

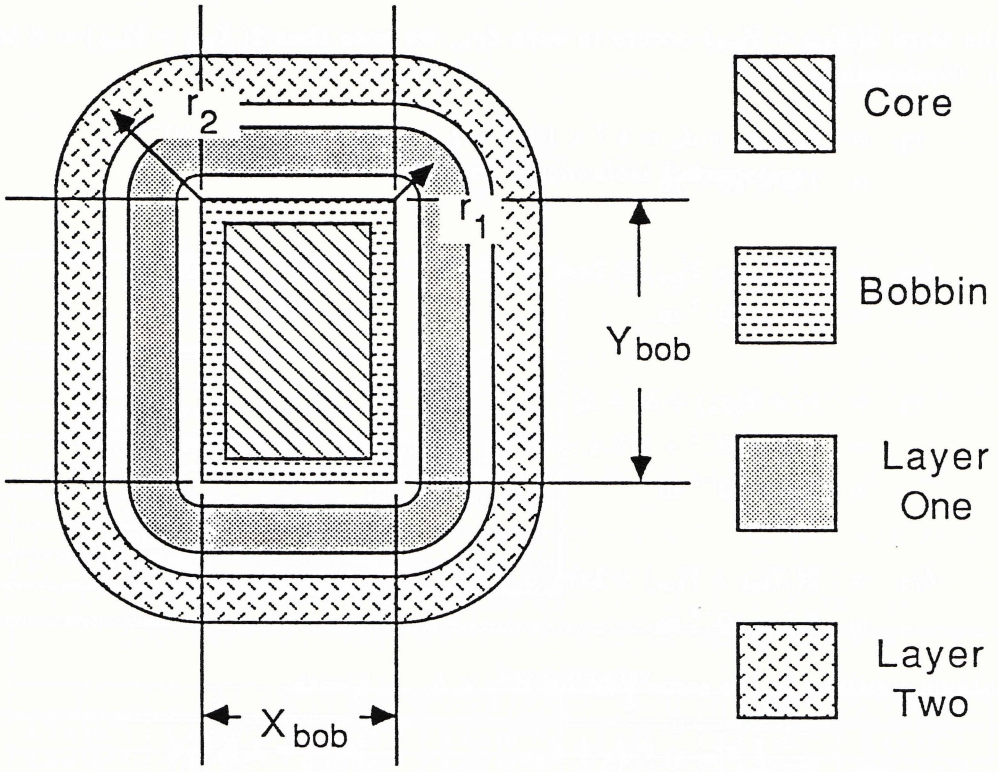


Figure 6.4: Top view of layers one and two of the transformer under analysis showing corner radii r_1 and r_2. Length of turn for a layer is calculated at the center of the layer.

$$= 4.7 \times 10^{-4}\ \text{m}$$

$$\begin{aligned} \ell_{T1} &= 2(X_{bob} + Y_{bob}) + 2\pi r_1 \\ &= 2\left(1.45 \times 10^{-2} + 1.83 \times 10^{-2}\right) + 2\pi\left(4.7 \times 10^{-4}\right) \\ &= 6.9 \times 10^{-2}\ \text{m} \end{aligned}$$

Since the term $2(X_{bob} + Y_{bob})$ occurs in each ℓ_{Tn}, we note that $2(X_{bob} + Y_{bob}) = 6.56 \times 10^{-2}$ m. Continuing,

$$\begin{aligned} r_2 &= r_1 + g_a + d_o = 4.7 \times 10^{-4} + 2.4 \times 10^{-5} + 8.966 \times 10^{-4} \\ &= 1.4 \times 10^{-3}\ \text{m} \end{aligned}$$

$$\begin{aligned} \ell_{T2} &= 2(X_{bob} + Y_{bob}) + 2\pi r_2 = 6.56 \times 10^{-2} + 2\pi(1.4 \times 10^{-3}) \\ &= 7.4 \times 10^{-2}\ \text{m} \end{aligned}$$

$$\begin{aligned} r_3 &= r_2 + 2(g_a) + h_t + d_o \\ &= 1.4 \times 10^{-3} + 2(2.4 \times 10^{-5}) + 1.27 \times 10^{-4} + 8.966 \times 10^{-4} \\ &= 2.5 \times 10^{-3}\ \text{m} \end{aligned}$$

$$\begin{aligned} \ell_{T3} &= 2(X_{bob} + Y_{bob}) + 2\pi r_3 = 6.56 \times 10^{-2} + 2\pi(2.5 \times 10^{-3}) \\ &= 8.1 \times 10^{-2}\ \text{m} \end{aligned}$$

Calculations continue in the same vein for $n = 4, 5, \ldots, 8$ with

$$r_n = \begin{cases} r_{(n-1)} + g_a + d_{o,n} & \text{for } n = 2, 4, 6, 8 \\ r_{(n-1)} + 2g_a + h_t + d_{o,n} & \text{for } n = 3, 5, 7 \end{cases}$$

$$\ell_{Tn} = 2(X_{bob} + Y_{bob}) + 2\pi r_n \qquad \text{for all } n$$

The complete results of these calculation for the sample transformer are presented in Table 6.2.

The lengths of the interlayer gaps are calculated using the formulae

$$r_{gn} = \frac{1}{2}\left[\left(r_n + \frac{d_{o,n}}{2}\right) + \left(r_{(n+1)} - \frac{d_{o,(n+1)}}{2}\right)\right] \tag{6.1}$$

$$\ell_{gn} = 2(X_{bob} + Y_{bob}) + 2\pi r_{gn} \tag{6.2}$$

For the case of $d_{o,n} = d_{o,(n+1)}$ for all n, (6.2) degenerates to

$$\ell_{gn} = \frac{1}{2}\left[\ell_{Tn} + \ell_{T(n+1)}\right]$$

Table 6.2: Calculated Mechanical Parameters

Symbol	*Value*	
d_{cu}	8.128×10^{-4} m	(all layers)
d_o	8.966×10^{-4} m	(all layers)
h_{cu}	7.203×10^{-4} m	(all layers)
b_{cu}	7.203×10^{-4} m	(all conductors)
η	0.620	(all layers)
g_a	2.4×10^{-5} m	
g_{intra}	2.0×10^{-4} m	
g_{inter}	3.5×10^{-4} m	

Symbol	*Layer Number*							
	1	2	3	4	5	6	7	8
r	4.7×10^{-4}	1.4×10^{-3}	2.5×10^{-3}	3.4×10^{-3}	4.5×10^{-3}	5.4×10^{-3}	6.4×10^{-3}	7.4×10^{-3}
ℓ_T	6.9×10^{-2}	7.4×10^{-2}	8.1×10^{-2}	8.7×10^{-2}	9.4×10^{-2}	9.9×10^{-2}	1.06×10^{-1}	1.12×10^{-1}

Symbol	*Gap Number*						
	1	2	3	4	5	6	7
g	2.0×10^{-4}	3.5×10^{-4}	2.0×10^{-4}	3.5×10^{-4}	2.0×10^{-4}	3.5×10^{-4}	2.0×10^{-4}
ℓ_g	7.1×10^{-2}	7.8×10^{-2}	8.4×10^{-2}	9.0×10^{-2}	9.6×10^{-2}	1.0×10^{-1}	1.1×10^{-1}

The first interlayer gap of interest is g_1 the gap in between layers ℓ_1 and ℓ_2. Gaps which appear outside the winding area are not of interest, so for an eight-layer transformer only seven interlayer gaps are analyzed. The calculation results for the various values of ℓ_{gn} appear in Table 6.2.

Often it is assumed that one average turn length can be used for the entire winding. For the example transformer, this assumption yields a value of $\ell_{Tn} = \ell_{gn} = \ell_{T,avg} = 9.0 \times 10^{-2}$ m. This value is determined by computing the average of the lengths-of-turn for the eight layers or the seven interlayer gaps given in Table 6.2.

$$\left(\frac{1}{8}\right)\sum_{n=1}^{8}\ell_{Tn} = \left(\frac{1}{7}\right)\sum_{n=1}^{7}\ell_{gn} = \ell_{T,avg}$$

This value can also be calculated by averaging the radii r_n of Table 6.2 and using the averaged radius in (6.2). Although easier to use, we expect that use of this average length will cause error in calculating $R_{(13)}$ and $L_{(13)}$ since the (13) short-circuit test involves only the inner six layers and not the entire winding space. More is said about this and other possible contributors of calculation error in Section 6.3.3.

6.1.3 Step 3—Determine the Electrical and Magnetic Properties

Now that we have determined all the necessary mechanical specifications for the transformer under analysis, we must determine several electrical and magnetic properties before finally solving the fields problem and determining the short-circuit resistance and inductance. The electrical and magnetic parameters which need to be determined are:

- Conductivity of the wire at the expected operating temperature
- Effective conductivity of the "stretched" foil conductors
- Skin depth and the height of the equivalent foil conductors in skin depths
- Normalized magnetic-field-intensity boundary conditions
- The phasor boundary-condition ratio $\underline{\Gamma} = \alpha + j\beta$

To calculate the conductivity of an annealed copper wire at the expected temperature of 60 °C we use the equation and constants from [22, page E-88].

$$\begin{aligned}
\rho_{cu,T} &= \rho_{cu,20°C} + K_T(T - 20\ °C) \\
\rho_{cu,60°C} &= 1.7241 \times 10^{-8} + 3.93 \times 10^{-11}(60 - 20) \\
&= 1.88 \times 10^{-8}\ \Omega\text{-m}
\end{aligned}$$

$$\sigma_{cu,60°C} = \frac{1}{\rho_{cu,60°C}} = 5.32 \times 10^{7}\ \text{S/m}$$

Table 6.3: Calculated Electrical and Magnetic Properties

Symbol	*Value*	
$\sigma_{cu,60°C}$	5.32×10^7 S/m	(all layers)
σ_{eff}	3.29×10^7 S/m	(all layers)
δ	2.77×10^{-4} m	(all layers)
Δ	2.60	(all layers)

Symbol	*Layer*							
	1	2	3	4	5	6	7	8
$\underline{I_\ell}/\underline{I_{BASE}}$	−1	−1	0	0	1	1	0	0
$\underline{H}_{z\text{-}N}(0)$	0	0.5	1	1	1	0.5	0	0
$\underline{H}_{z\text{-}N}(h_{cu})$	0.5	1	1	1	0.5	0	0	0
$\underline{H}_{z\text{-}N}(X = 0)$	0	0.5	1	1	0.5	0	0	0
$\underline{H}_{z\text{-}N}(X = h_{cu})$	0.5	1	1	1	1	0.5	0	0
α	0	0.5	1	1	0.5	0	—	—

Symbol	*Gap*						
	1	2	3	4	5	6	7
$\underline{H}_{g\text{-}N}$	0.5	1	1	1	0.5	0	0

The effective conductivity σ_{eff} of the foil conductors which model the layers of conducting wire is determined using the equation $\sigma_{eff} = \eta\sigma_{cu}$. For the example transformer, the layer porosity η is the same for all eight layers so each layer has the same effective conductivity

$$\sigma_{eff} = 0.620\left(5.32 \times 10^7\right) = 3.29 \times 10^7 \text{ S/m}$$

Table 6.3 contains a recapitulation of the calculated results presented in this section. Once we have the effective conductivity, we can calculate the skin depth for the foil conductors using equation (4.129).

$$\begin{aligned} \delta &= \sqrt{\frac{2}{\omega\mu_0\sigma_{eff}}} = \sqrt{\frac{2}{(6.28 \times 10^5)(4\pi \times 10^{-7})(3.29 \times 10^7)}} \\ &= 2.77 \times 10^{-4} \text{ m} \end{aligned}$$

Using the definition given in (4.137) and the information already at hand, we can calculate the height of each foil conductor in skin depths.

$$\Delta = \frac{h_{cu}}{\delta} = \frac{7.203 \times 10^{-4}}{2.77 \times 10^{-4}} = 2.60$$

Note that if the different layers of the transformer were composed of different wire types or sizes, or had different numbers of turns, then values of σ_{eff}, δ and Δ would have to be determined for each layer.

Figure 6.2, (5.10), and (5.12) are used to determine the normalized field-intensity boundary conditions, $\underline{H}_{z_n\text{-}N}(0)$ and $\underline{H}_{z_n\text{-}N}(h_{cu})$, for each of the eight layers, and the normalized field intensity, $\underline{H}_{g_n\text{-}N}$, for each of the seven interlayer gaps. Examining Fig. 6.2, we see that layers one and two constitute the excited winding and layers five and six constitute the shorted winding. Thus,

$$\begin{array}{rcl} \underline{I}_{\ell 1} = \underline{I}_{\ell 2} & = & \underline{I}_{SC} \\ \underline{I}_{\ell 3} = \underline{I}_{\ell 4} & = & 0 \\ \underline{I}_{\ell 5} = \underline{I}_{\ell 6} & = & -\underline{I}_{SC} \\ \underline{I}_{\ell 8} = \underline{I}_{\ell 9} & = & 0 \end{array}$$

From Fig. 6.2(a), it is clear that $\underline{I}_{\ell 1} = \underline{I}_{SC}$ flows in the negative direction ("out of the paper"), so for this short-circuit test

$$\underline{I}_{BASE} = -\underline{I}_{SC}$$

per the definition in (5.10). For layer one, $N_{\ell 1} = 13$ while $N_E = 26$, so (5.12) becomes

$$\underline{H}_{z_1\text{-}N}(0) - \underline{H}_{z_1\text{-}N}(h_{cu}) = \frac{13\,(\underline{I}_{SC})}{26\,(-\underline{I}_{SC})} = -0.5$$

As discussed in Section 5.2.1, $\underline{H}_{z_1\text{-}N}(0) = 0$ for layer one, so $\underline{H}_{z_1\text{-}N}(h_{cu}) = 0.5$. Since the field intensity remains constant in the interlayer gaps,

$$\underline{H}_{z_2\text{-}N}(0) = \underline{H}_{g_1\text{-}N} = \underline{H}_{z_1\text{-}N}(h_{cu}) = 0.5$$

Applying (5.12) to layer two, which also belongs to the excited winding, gives

$$\begin{aligned} \underline{H}_{z_2\text{-}N}(h_{cu}) &= \underline{H}_{z_1\text{-}N}(0) - \frac{N_{\ell 2}\underline{I}_{\ell 2}}{N_E \underline{I}_{BASE}} \\ &= 0.5 - \frac{13\,(\underline{I}_{SC})}{26\,(-\underline{I}_{SC})} \\ &= 1.0 \end{aligned}$$

The ratio $\underline{I}_\ell / \underline{I}_{BASE}$ and the boundary conditions for all eight layers plus the normalized field-intensity values for the seven interlayer gaps are presented in Table 6.3. Because

the layer currents are either in phase or 180° out of phase with $\underline{I}_{BASE}$, the values in Table 6.3 are presented as signed real numbers, rather than as complex numbers.

In Table 6.3, $\underline{H}_{z\text{-}N}(0)$ represents the inner boundary of each winding layer and $\underline{H}_{z\text{-}N}(h_{cu})$ represents the outer boundary as the winding space is traversed radially. Adopting the change of reference from x to X proposed in equation (4.132), we can also write the boundary values $\underline{H}_{z\text{-}N}(X = 0)$ and $\underline{H}_{z\text{-}N}(X = h_{cu})$ for the winding layers. These, too, are given in Table 6.3.

Having collected the boundary conditions $\underline{H}_{z\text{-}N}(X = 0)$ and $\underline{H}_{z\text{-}N}(X = h_{cu})$, we can now determine the phasor boundary condition ratio $\underline{\Gamma}$ for the foil-conductor layers. From (4.133), the definition of this ratio is

$$\begin{aligned} \underline{\Gamma} &= \frac{\underline{H}_z(X = 0)}{\underline{H}_z(X = h_{cu})} = \frac{\underline{H}_{z\text{-}N}(X = 0)}{\underline{H}_{z\text{-}N}(X = h_{cu})} \\ &= \alpha + j\beta \end{aligned}$$

As is discussed on page 142, $\beta = 0$ for short-circuit tests such as the (13) test being analyzed. Using this we can determine α for the same short-circuit tests.

$$\alpha = \frac{\underline{H}_z(X = 0)}{\underline{H}_z(X = h_{cu})} = \frac{\underline{H}_{z\text{-}N}(X = 0)}{\underline{H}_{z\text{-}N}(X = h_{cu})} \tag{6.3}$$

When a layer has both boundary conditions equal to zero, then, $\underline{H}_z(x)$ is zero throughout the layer as (4.130) shows. Such a layer is inactive and stores no energy. Likewise, when both boundary conditions are zero, $\underline{J}_y(x)$ is zero throughout the layer as (4.131) shows, and the layer dissipates no power. Equations (4.134) and (4.135), which give $\underline{H}_z(X)$ and $\underline{J}_y(X)$ in terms of α and β, *do not apply* when $\underline{H}_{z\text{-}N}(X = 0) = \underline{H}_{z\text{-}N}(X = h_{cu}) = 0$. *No attempt should be made* to determine the energy storage or power dissipation in such layers using the methods presented in this and subsequent sections of this example.

Since layers seven and eight have zero boundary conditions on both sides, the value of α is undefined for these layers and a dash is entered in the table. Continuing on with the boundary conditions given in Table 6.3 for layers one through six, (6.3) yields values of α for these layers as

$$\begin{aligned} \alpha_1 &= \alpha_6 = 0/(0.5) = 0 \\ \alpha_2 &= \alpha_5 = (0.5)/1 = 0.5 \\ \alpha_3 &= \alpha_4 = 1/1 = 1 \end{aligned}$$

6.1.4 Step 4—Determine Short-Circuit Resistance and Inductance

The calculation of $R_{(jk)}$ and $L_{(jk)}$ now follows these steps:

- For each layer having at least one nonzero boundary condition, determine $F_1(\Delta)$, $F_2(\Delta)$, $F_3(\Delta)$ and $F_4(\Delta)$.
- For the same layers, calculate $\langle Q'_J \rangle$ and $\langle Q'_H \rangle$.

- Evaluate the terms inside the summations of the formulae for $R_{(jk)}$ and $L_{(jk)}$, (5.40) and (5.68), respectively.
- Using (5.40) and (5.68), carry out the summations and complete the calculations for $R_{(jk)}$ and $L_{(jk)}$.

Using the value of Δ given in Table 6.3 for all the excited layers at 100 kHz, values of $F_1(\Delta)$, $F_2(\Delta)$, $F_3(\Delta)$ and $F_4(\Delta)$ can be determined using equations (4.138), (4.139), (4.140) and (4.141), respectively. Substituting $\Delta = 2.60$ into (4.138) gives

$$F_1(\Delta) = \frac{\sinh 2\Delta + \sin 2\Delta}{\cosh 2\Delta - \cos 2\Delta} = \frac{\sinh 2(2.60) + \sin 2(2.60)}{\cosh 2(2.60) - \cos 2(2.60)} = 0.995$$

and into (4.139) gives

$$\begin{aligned} F_2(\Delta) &= \frac{\sinh \Delta \cos \Delta + \cosh \Delta \sin \Delta}{\cosh 2\Delta - \cos 2\Delta} \\ &= \frac{\sinh(2.60)\cos(2.60) + \cosh(2.60)\sin(2.60)}{\cosh 2(2.60) - \cos 2(2.60)} = -2.49 \times 10^{-2} \end{aligned}$$

From (4.140) we get

$$F_3(\Delta) = \frac{\sinh 2(2.60) - \sin 2(2.60)}{\cosh 2(2.60) - \cos 2(2.60)} = 1.01$$

and from (4.141)

$$F_4(\Delta) = \frac{\sinh(2.60)\cos(2.60) - \cosh(2.60)\sin(2.60)}{\cosh 2(2.60) - \cos 2(2.60)} = -0.103$$

Since the layers are composed of identical numbers of turns and wire size, these four functions have the same values for all six layers. If the composition of the layers differs, individual values of $F_1(\Delta)$, $F_2(\Delta)$, $F_3(\Delta)$ and $F_4(\Delta)$ must be calculated for each layer.

$F_1(\Delta)$, $F_2(\Delta)$ and the values of α calculated in Section 6.1.3 are substituted into (4.143) to determine $\langle Q'_J \rangle$, the normalized power dissipation for each layer. For layer one with $\beta = 0$, (4.143) yields

$$\begin{aligned} \langle Q'_J \rangle &= (1 + \alpha^2 + \beta^2)F_1(\Delta) - 4\alpha F_2(\Delta) \\ &= (1 + 0^2 + 0^2)(0.995) - 4(0)(-2.49 \times 10^{-2}) \\ &= 0.995 \end{aligned}$$

and for layer two

$$\begin{aligned} \langle Q'_J \rangle &= (1 + 0.5^2 + 0^2)(0.995) - 4(0.5)(-2.49 \times 10^{-2}) \\ &= 1.29 \end{aligned}$$

Table 6.4: Intermediate Results in the Numerical Example

Quantity	*Layer*					
	1	2	3	4	5	6
$F_1(\Delta)$	0.995		(same for all layers)			
$F_2(\Delta)$	-2.49×10^{-2}		(same for all layers)			
$F_3(\Delta)$	1.01		(same for all layers)			
$F_4(\Delta)$	-0.103		(same for all layers)			
$\langle Q'_J \rangle$	0.995	1.29	2.09	2.09	1.29	0.995
$\langle Q'_H \rangle$	1.01	1.47	2.44	2.44	1.47	1.01
$\frac{\ell_T \lvert \underline{H}_{z\text{-}N} \rvert^2 \langle Q'_J \rangle}{\sigma_{eff}\delta}$	1.87×10^{-6}	1.05×10^{-5}	1.85×10^{-5}	1.99×10^{-5}	1.33×10^{-5}	2.71×10^{-6}
$\ell_T\delta \lvert \underline{H}_{z\text{-}N} \rvert^2 \langle Q'_H \rangle$	4.82×10^{-6}	3.01×10^{-5}	5.47×10^{-5}	5.88×10^{-5}	3.83×10^{-5}	6.92×10^{-6}

Quantity	*gap*				
	1	2	3	4	5
$g\ell_g \lvert \underline{H}_{g\text{-}N} \rvert^2$	3.57×10^{-6}	2.73×10^{-5}	1.68×10^{-5}	3.16×10^{-5}	4.82×10^{-6}

The values of $\langle Q'_J \rangle$ for all six layers are given in Table 6.4.

$F_3(\Delta)$, $F_4(\Delta)$ and the values of α calculated in Section 6.1.3 are substituted into (4.145) to determine $\langle Q'_H \rangle$, the normalized energy storage of each layer. For layer one, (4.145) becomes

$$\begin{aligned} \langle Q'_H \rangle &= (1+\alpha^2+\beta^2)F_3(\Delta) - 4\alpha F_4(\Delta) \\ &= (1+0^2+0^2)(1.01) - 4(0)(-0.103) \\ &= 1.01 \end{aligned}$$

and for layer two,

$$\begin{aligned} \langle Q'_H \rangle &= (1+0.5^2+0^2)(1.01) - 4(0.5)(-0.103) \\ &= 1.47 \end{aligned}$$

Using the lengths-of-turn for the equivalent foil conductors presented in Table 6.2, the values of σ_{eff}, δ and $\underline{H}_{z\text{-}N}(\chi = h_{cu})$ presented in Table 6.3, and the values of $\langle Q'_J \rangle$ and $\langle Q'_H \rangle$ calculated above, the following terms can be calculated. For layer one,

$$\begin{aligned} \frac{\ell_T \lvert \underline{H}_{z\text{-}N}(\chi = h_{cu}) \rvert^2 \langle Q'_J \rangle}{\sigma_{eff}\delta} &= \frac{(6.9\times10^{-2})(0.5)^2(0.995)}{(3.29\times10^{7})(2.77\times10^{-4})} \\ &= 1.87\times10^{-6}\ \Omega\text{-m} \end{aligned}$$

$$\begin{aligned} \ell_T\delta \lvert \underline{H}_{z\text{-}N}(\chi = h_{cu}) \rvert^2 \langle Q'_H \rangle &= (6.9\times10^{-2})(2.77\times10^{-4})(0.5)^2(1.01) \\ &= 4.82\times10^{-6}\ \text{m}^2 \end{aligned}$$

The results of these calculations for all excited layers are given in Table 6.4.

Using the values for the lengths of the gaps ℓ_g between the layers listed in Table 6.2, the values of gap heights g given in Table 6.2, and the values of $\underline{H}_{g\text{-}N}$ given in Table 6.3, we can determine the value of the following quantity associated with each interlayer gap within the excited layers. For gap one,

$$g\ell_g|\underline{H}_{g\text{-}N}|^2 = (2.0\times10^{-4})(7.1\times10^{-2})(0.5)^2 = 3.6\times10^{-6}\ \mathrm{m}^2$$

The results of these calculations for the five gaps between excited layers are given in Table 6.4.

The last step in this rather lengthy procedure is the actual calculation of $R_{(jk)}$ and $L_{(jk)}$. To calculate $R_{(13)}$, (5.40) is used where $N_E = 26$, $N = 6$, b_{win} is found Table 6.1, and the values of the terms in the summation appear in Table 6.4.

$$\begin{aligned} R_{(13)} &= \frac{N_E^2}{b_{win}}\sum_{n=1}^{N}\left[\frac{\ell_T}{\sigma_{eff}\delta}|\underline{H}_{z\text{-}N}(\chi=h_{cu})|^2\langle Q'_J(\alpha,\beta,\Delta)\rangle\right]_n \\ &= \frac{26^2}{3.02\times10^{-2}}\left[6.68\times10^{-5}\right] \\ &= 1.5\ \Omega \end{aligned}$$

To calculate $L_{(13)}$, recall equation (5.68):

$$\begin{aligned} L_{(jk)} &= \frac{\mu_0 N_E^2}{b_{win}}\left\{\frac{1}{2}\sum_{n=1}^{N}\left[\ell_T\delta|\underline{H}_{z\text{-}N}(\chi=h_{cu})|^2\,\langle Q'_H(\alpha,\beta,\Delta)\rangle\right]_n \right. \\ &\qquad \left. +\sum_{n=1}^{N-1}\left[\ell_g g|\underline{H}_{g\text{-}N}|^2\right]_n\right\} \\ &= \frac{(4\pi\times10^{-7})\,(26^2)}{3.02\times10^{-2}}\left\{\frac{1}{2}\,(1.94\times10^{-4})+8.41\times10^{-5}\right\} \\ &= 5.1\ \mu\mathrm{H} \end{aligned}$$

In Section 6.1.2, we mention that it is possible to use one average turn length for the entire winding rather than calculate individual lengths for each winding layer, and we mention that this practice can be expected to produce some error in the calculation of $R_{(jk)}$ and $L_{(jk)}$. The average of the eight turn lengths presented in Table 6.2 is 9.0×10^{-2}, and the values of the calculated short-circuit data using this average length-of-turn are

$$R_{(13)} = 1.6\ \Omega \qquad L_{(13)} = 5.5\ \mu\mathrm{H}$$

which are 7% and 8% higher than those calculated using the individual lengths-of-turn. For the other short-circuit tests given in Fig. 5.2, the error produced by using the average length-of-turn depended upon the test. For the (12) test, both the resistance and

inductance calculated at 100 kHz using the average length-of-turn were 16% over those calculated using the individual turn lengths. At the other extreme, the resistance and inductance values using the average length of turn was 12% under for the (34) test. For the (14) and (23) tests, the difference between the data calculated by the two methods was insignificant.

6.2 PLOTS OF SHORT-CIRCUIT RESISTANCES AND INDUCTANCES VERSUS FREQUENCY

In the previous section, we present a detailed step-by-step calculation of $R_{(13)}$ and $L_{(13)}$ at a single frequency of 100 kHz. In this section, the results of calculating values of $R_{(jk)}$ and $L_{(jk)}$ for the six short-circuit tests of Fig. 5.2(c) over a five-decade range of frequencies, from 100 Hz to 10 MHz, are presented for the same transformer used in Section 6.1. For all of the short-circuit tests, the inner conducting winding is excited and the outer conducting winding is shorted. Current is assumed to flow out of the paper in the inner conducting winding and into the paper in the outer winding. The specific length-of-turn given in Table 6.2 for each layer was used to calculate the data presented in Sections 6.2 and 6.3.

Table 6.5 shows the different normalized boundary conditions of magnetic field intensity for each of the eight winding layers and each of the six short-circuit tests shown in Fig. 5.2(c). We recall that in the expressions for the short-circuit resistance and inductance between two windings given in (5.40) and (5.68), respectively, we write the boundary conditions of the magnetic field intensity in terms of a normalized value $\underline{H}_{z\text{-}N}(\chi = h_{cu})$. The normalizing base value ($\underline{H}_{BASE} = N_E \underline{I}_{BASE}/b_{win}$) is described in Section 5.2.3. Table 6.5 also shows the value of the ratio of the field boundary values α that applies to each of the layers which were calculated using (6.3). With the information in Tables 6.1, 6.2, and 6.5, we can now compute the values of each of the six short-circuit resistances $R_{(jk)}$ and inductances $L_{(jk)}$ as given by (5.40) and (5.68), respectively. In Table 6.5, entries for α are not given when both $\underline{H}_z(\chi = 0)$ and $\underline{H}_z(\chi = h_{cu})$ are equal to zero and $\alpha = 0/0$. This situation arises for a winding layer that lies in a region of zero magnetic field intensity; such a layer neither stores energy nor dissipates power, so this undetermined value of α is of no concern.

Figure 6.5 shows computer-generated plots of the six short-circuit resistances versus excitation frequency; Figure 6.6 shows similar plots for the short-circuit inductances of the example transformer. These plots show the dramatic changes in the leakage impedances of a transformer predicted by the field solution that is developed in this report. For example, the short-circuit resistance $R_{(14)}$ at 1 MHz is approximately 100 times its dc value.

For a simple winding layout such as that of the transformer under consideration, it is possible to predict the top-to-bottom ordering of the curves of $R_{(jk)}$ and $L_{(jk)}$ before performing any calculations. In general, the greater the number of open-circuit layers which exist between the excited winding and the shorted winding, i.e., layers which exist

Table 6.5: Values of $\underline{H}_{z\text{-}N}$ and α for the Layers of the Example Transformer Under Six Different Short-Circuit Conditions.

Short-Circuit Test (12)								
Symbol	*Layer*							
	1	2	3	4	5	6	7	8
$\underline{I}_\ell/\underline{I}_{BASE}$	−1	−1	1	1	0	0	0	0
$\underline{H}_{z\text{-}N}(0)$	0	0.5	1	0.5	0	0	0	0
$\underline{H}_{z\text{-}N}(h_{cu})$	0.5	1	0.5	0	0	0	0	0
$\underline{H}_{z\text{-}N}(\chi = 0)$	0	0.5	0.5	0	0	0	0	0
$\underline{H}_{z\text{-}N}(\chi = h_{cu})$	0.5	1	1	0.5	0	0	0	0
α	0	0.5	0.5	0	—	—	—	—

Short-Circuit Test (13)								
Symbol	*Layer*							
	1	2	3	4	5	6	7	8
$\underline{I}_\ell/\underline{I}_{BASE}$	−1	−1	0	0	1	1	0	0
$\underline{H}_{z\text{-}N}(0)$	0	0.5	1	1	1	0.5	0	0
$\underline{H}_{z\text{-}N}(h_{cu})$	0.5	1	1	1	0.5	0	0	0
$\underline{H}_{z\text{-}N}(\chi = 0)$	0	0.5	1	1	0.5	0	0	0
$\underline{H}_{z\text{-}N}(\chi = h_{cu})$	0.5	1	1	1	1	0.5	0	0
α	0	0.5	1	1	0.5	0	—	—

Short-Circuit Test (14)								
Symbol	*Layer*							
	1	2	3	4	5	6	7	8
$\underline{I}_\ell/\underline{I}_{BASE}$	−1	−1	0	0	0	0	1	1
$\underline{H}_{z\text{-}N}(0)$	0	0.5	1	1	1	1	1	0.5
$\underline{H}_{z\text{-}N}(h_{cu})$	0.5	1	1	1	1	1	0.5	0
$\underline{H}_{z\text{-}N}(\chi = 0)$	0	0.5	1	1	1	1	0.5	0
$\underline{H}_{z\text{-}N}(\chi = h_{cu})$	0.5	1	1	1	1	1	1	0.5
α	0	0.5	1	1	1	1	0.5	0

Continued on Next Page

Table 6.5: (cont.) Values of $\underline{H}_{z\text{-}N}$ and α for the Layers of an Example Transformer under Six Different Short-Circuit Conditions. For all six tests: $\underline{I}_{BASE} = -\underline{I}_{SC}$.

Short-Circuit Test (23)								
Symbol	*Layer*							
	1	2	3	4	5	6	7	8
$\underline{I}_\ell / \underline{I}_{BASE}$	0	0	−1	−1	1	1	0	0
$\underline{H}_{z\text{-}N}(0)$	0	0	0	0.5	1	0.5	0	0
$\underline{H}_{z\text{-}N}(h_{cu})$	0	0	0.5	1	0.5	0	0	0
$\underline{H}_{z\text{-}N}(X = 0)$	0	0	0	0.5	0.5	0	0	0
$\underline{H}_{z\text{-}N}(X = h_{cu})$	0	0	0.5	1	1	0.5	0	0
α	—	—	0	0.5	0.5	0	—	—

Short-Circuit Test (24)								
Symbol	*Layer*							
	1	2	3	4	5	6	7	8
$\underline{I}_\ell / \underline{I}_{BASE}$	0	0	−1	−1	0	0	1	1
$\underline{H}_{z\text{-}N}(0)$	0	0	0	0.5	1	1	1	0.5
$\underline{H}_{z\text{-}N}(h_{cu})$	0	0	0.5	1	1	1	0.5	0
$\underline{H}_{z\text{-}N}(X = 0)$	0	0	0	0.5	1	1	0.5	0
$\underline{H}_{z\text{-}N}(X = h_{cu})$	0	0	0.5	1	1	1	1	0.5
α	—	—	0	0.5	1	1	0.5	0

Short-Circuit Test (34)								
Symbol	*Layer*							
	1	2	3	4	5	6	7	8
$\underline{I}_\ell / \underline{I}_{BASE}$	0	0	0	0	−1	−1	1	1
$\underline{H}_{z\text{-}N}(0)$	0	0	0	0	0	0.5	1	0.5
$\underline{H}_{z\text{-}N}(h_{cu})$	0	0	0	0	0.5	1	0.5	0
$\underline{H}_{z\text{-}N}(X = 0)$	0	0	0	0	0	0.5	0.5	0
$\underline{H}_{z\text{-}N}(X = h_{cu})$	0	0	0	0	0.5	1	1	0.5
α	—	—	—	—	0	0.5	0.5	0

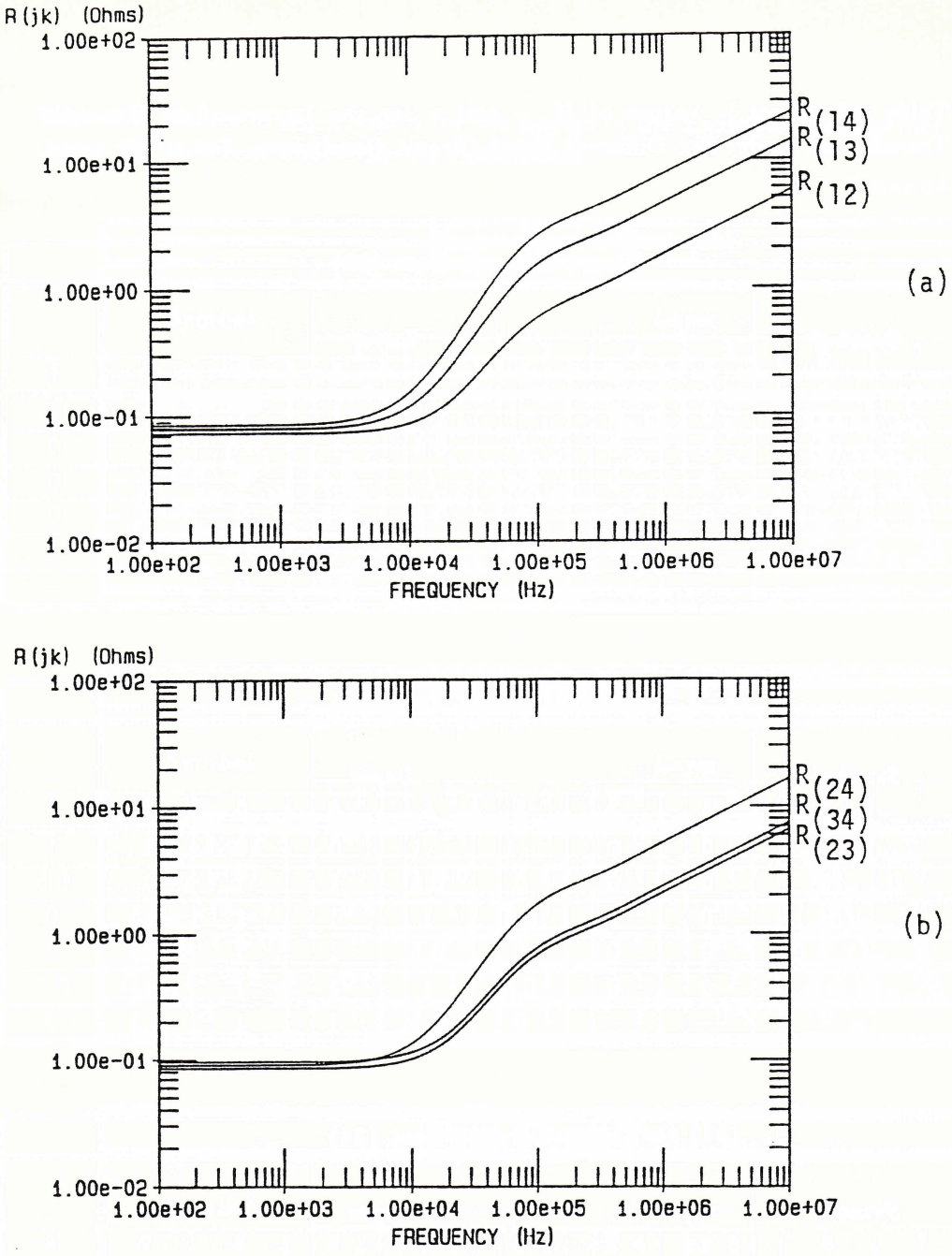


Figure 6.5: Plots of calculated values for $R_{(jk)}$ versus frequency for the short-circuit tests of Fig. 5.2(c). (a) shows $R_{(12)}$, $R_{(13)}$ and $R_{(14)}$. (b) shows $R_{(23)}$, $R_{(24)}$ and $R_{(34)}$.

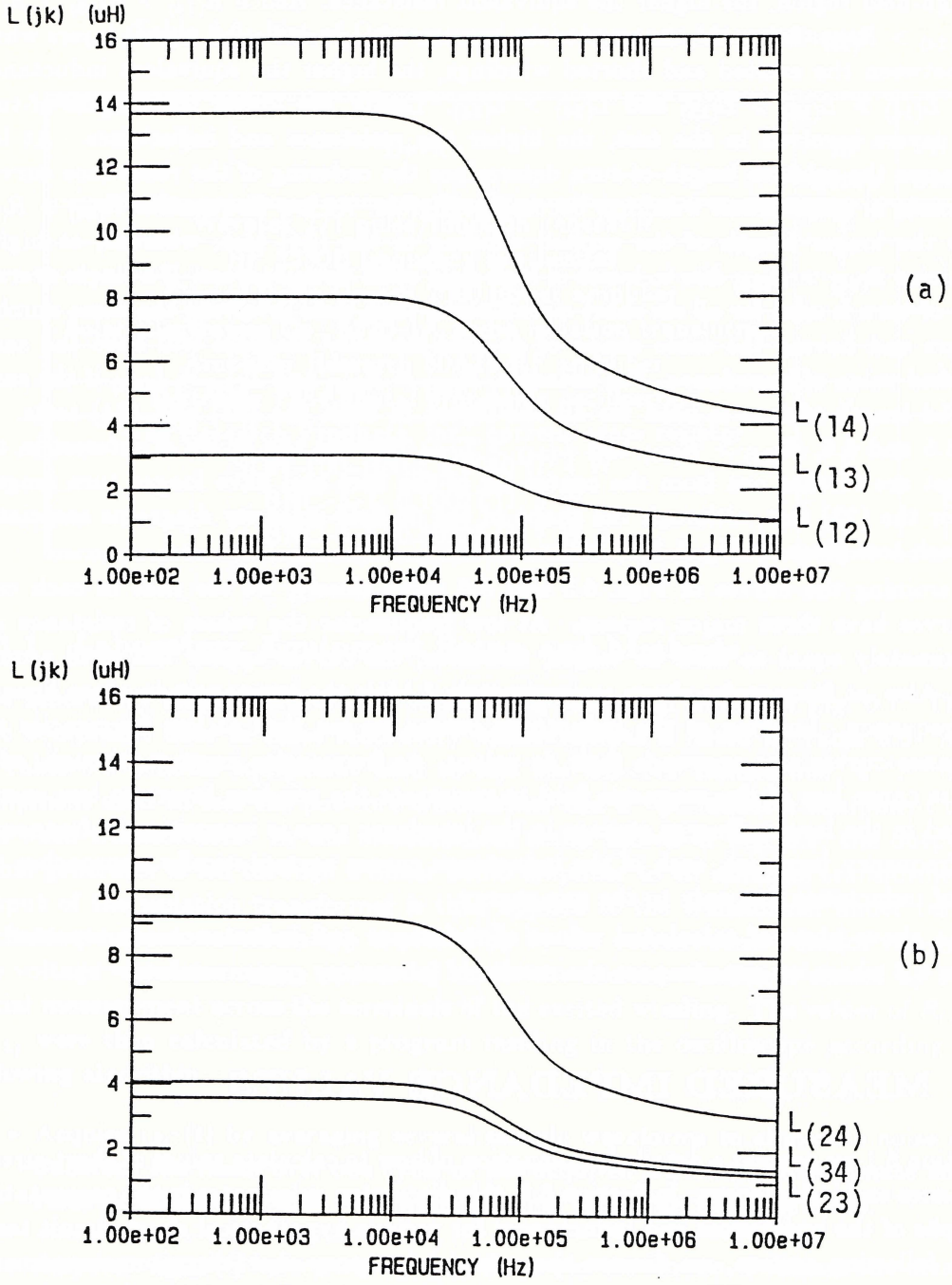


Figure 6.6: Plots of calculated values for $L_{(jk)}$ versus frequency for the short-circuit tests of Fig. 5.2(c). (a) shows $L_{(12)}$, $L_{(13)}$ and $L_{(14)}$. (b) shows $L_{(23)}$, $L_{(24)}$ and $L_{(34)}$.

in a high-field region, the higher the equivalent resistance. Hence $R_{(14)} > R_{(13)} > R_{(12)}$ and $R_{(24)} > R_{(23)}$. Likewise, the greater the number of gaps and open-circuit layers which exist between the excited and shorted windings, the higher the equivalent inductance, hence, $L_{(14)} > L_{(13)} > L_{(12)}$ and $L_{(24)} > L_{(34)}$. Lastly, the longer the lengths-of-turn of the layers involved in the test, the higher the resistance and inductance. At low frequencies the relative length-of-turn determines the ordering of the resistance curves, since losses in open-circuit windings become negligible. At low frequencies $R_{(34)} > R_{(24)}$ due to the longer length of the excited winding in the (34) test, whereas, at higher frequencies $R_{(24)} > R_{(34)}$ due to losses in high-field open-circuit layers. If a single average length-of-turn is used for all six short circuit tests, then tests involving the same number of layers and having the same shape of dc field-intensity diagram will have the same calculated value of impedance. For example, $R_{(23)} = R_{(34)}$ and $L_{(23)} = L_{(34)}$ if the same averaged length-of-turn is used for all the layers in both the (23) and (34) tests. In Figs. 6.5 and 6.6, $R_{(34)} > R_{(23)}$ and $L_{(34)} > L_{(23)}$ because the layers of interest in the (34) test are further out from the center leg of the core and have longer turn lengths than for the (23) test, although the shape of the dc field-intensity diagrams associated with each test given in Fig. 5.2(b) is the same.

Examining the curves of Figs. 6.5 and 6.6 more closely, we see that in each case the curves have three major regions. At low frequencies the values of resistance are approximately equal to their dc values, therefore, the curves appear flat until around 4 kHz. Also, at frequencies above approximately 1 MHz the resistances increase linearly with frequency. Looking at the inductance curves we see that at low frequencies the inductance curves also approach their dc values. As frequencies increase, though, eddy currents cause less of the magnetic field to penetrate the winding layers so less energy is stored in the layers. Energy storage in the interlayer gaps is insensitive to frequency, so as frequency increases, each of the inductance curves asymptotically approaches the value of inductance due only to the gap energy.

The above plots of calculated values of resistance and inductance are repeated in Section 6.3 where we superimpose the results of laboratory measurements.

6.3 MEASURED IMPEDANCE VALUES

In Section 6.1 we present a detailed explanation of how to calculate values of short-circuit resistances and inductances. In Section 6.2, this discussion culminates in the presentation of graphs of the resistances and inductances for various hypothetical short-circuit tests. In the following section, we discuss the actual laboratory short-circuit measurements performed on the same EE-core transformer used in Sections 6.1 and 6.2, and performed on a sample pot-core transformer described in Appendix I. We present the measured short-circuit resistances and inductances for both the EE-core and pot-core transformers superimposed on computer-generated plots of calculated data and discuss the agreement between the measured and calculated data.

Table 6.6: List of Devices used in Laboratory Measurements

Device	*LF Setup*	*HF Setup*
Wavetek 271 pulse/function generator	E	
HP 3330B frequency synthesizer	P	√
Crown Delta Omega 2000 power amplifier	√	
Solar Electronics Co., 6220–1A audio isolation transformer	√	
Amplifier Research 50A15 RF amplifier		√
Tektronix 7854 digital processing oscilloscope	√	√
T+M Research Products, Inc., current-sense resistor		
SDN–100–BNC, 1.0080 Ω, 4 W	E	
BNC–5–1, 0.10027 Ω, 5 W		E
BNC–5–5, 0.50235 Ω, 7 W	P	P

6.3.1 Laboratory Equipment Setup and Methods

The laboratory measurements were made using the setup shown in Fig. 6.7. The specific equipment used in these laboratory measurements is listed in Table 6.6. An "E" in Table 6.6 denotes equipment used to test the EE-core transformer, a "P" denotes equipment used to test the pot-core transformer and a "√" denotes equipment used to test both transformers. In the measurement setup shown in Fig. 6.7, the output of a signal generator is fed through a linear audio amplifier to an isolation transformer. The output of the isolation transformer is then applied to the transformer under test. The excitation current waveform i_{SC} is picked up by the current-sense resistor R_{SENSE}, and the voltage waveform v_{MEAS} appearing across the excited winding is sensed by a differential measurement across the terminals of the excited winding. The values of $R_{(jk)}$ and $L_{(jk)}$ were then calculated by a program residing in the oscilloscope according to the following algorithm:

- Acquire $i_{SC}(t)$ by averaging several sample waveforms to eliminate noise effects. Subtract the mean over one cycle of the acquired waveform to eliminate any spurious dc offset, and then determine the rms value I_{SC} over one cycle.

- Acquire $v_{MEAS}(t)$ by averaging several sample waveforms. Subtract the mean over one cycle of the acquired waveform, and then determine the rms value V_{MEAS} over one cycle.

- Multiply $i_{SC}(t)$ and $v_{MEAS}(t)$ to obtain $P_D(t)$, then determine the average power over one cycle $\langle P_D \rangle$.

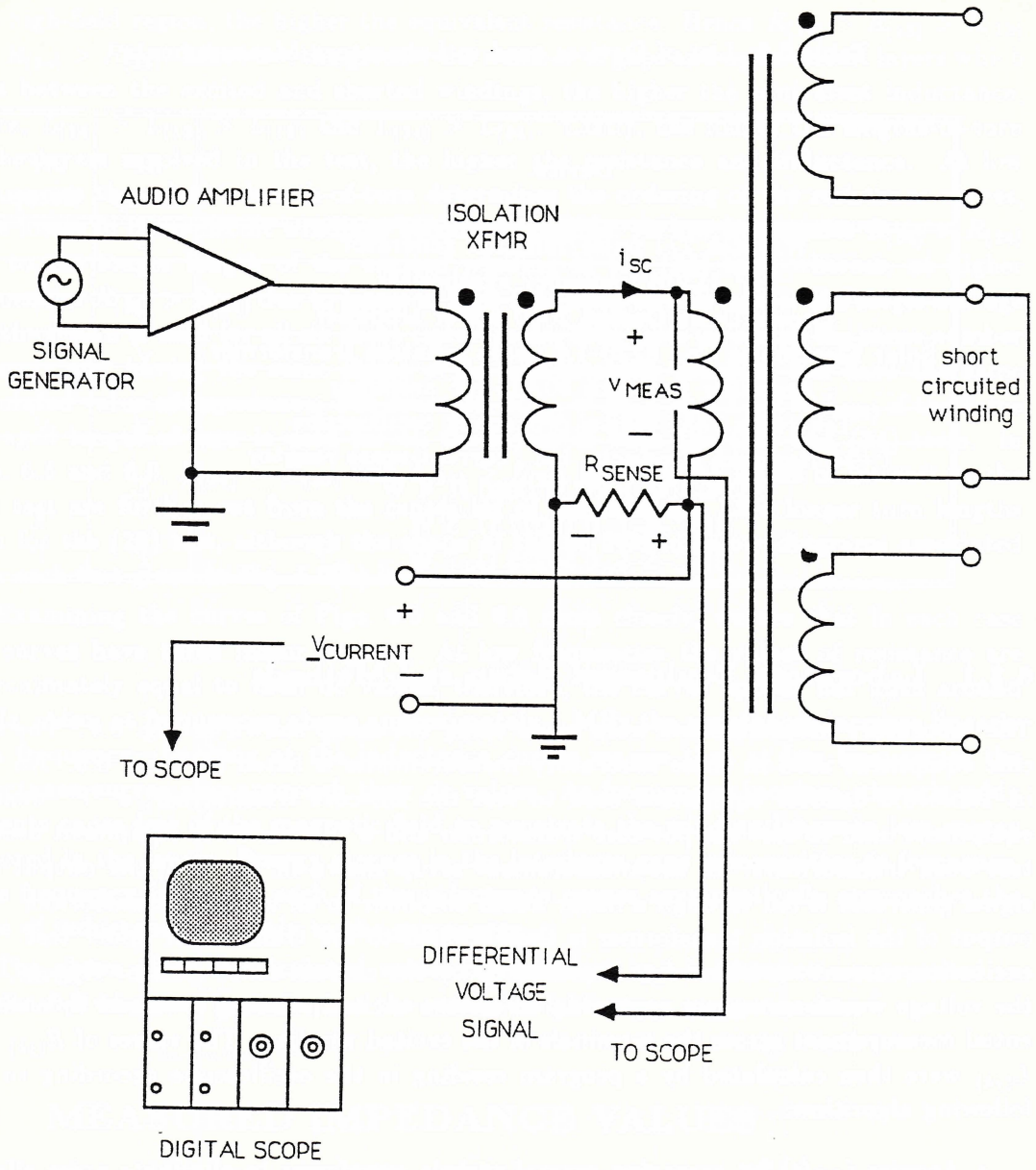


Figure 6.7: Laboratory equipment setup used for low-frequency short-circuit testing of transformers.

- Determine the magnitude of the impedance from the rms values of excitation current and measured voltage using $|\underline{Z}| = V_{MEAS}/I_{SC}$.
- Determine the short-circuit resistance by dividing the time average power by the square of the rms excitation current, $R_{(jk)} = \langle P_D \rangle / I_{SC}^2$.
- Determine the short-circuit inductance by the formula

$$L_{(jk)} = \left(\frac{T}{2\pi}\right)\sqrt{|\underline{Z}|^2 - R_{(jk)}^2)}$$

  where T is the period of $v_{MEAS}(t)$.

This algorithm assumes that the measured waveforms i_{SC} and v_{MEAS} are sinusoidal.

To acquire data over the full range of desired frequencies, two different setups were required. These are referred to as the LF or low-frequency setup and the HF or high-frequency setup in Table 6.6 and in the subsequent text. Data acquired with the low-frequency setup are represented by diamonds in Figs. 6.8, 6.9, 6.11 and 6.12. Triangles in these figures denote data acquired with the high-frequency setup. For measurements performed on the EE-core transformer, the low-frequency setup was used from 500 Hz to 200 kHz and consisted of the equipment listed in Table 6.6 marked with an E or a $\surd$ in the column "LF Setup". At frequencies ranging from 18 kHz to 5.6 MHz, the EE-core transformer was tested using the equipment in Table 6.6 denoted by an E or a $\surd$ under "HF Setup." For the pot-core transformer, the low-frequency setup was used from 320 Hz to 100 kHz and the high-frequency setup from 18 kHz to 10 MHz. The overlap of frequency ranges for the two setups mutually confirms the data acquired by both setups. For the high-frequency setup, the combination of the audio amplifier and the isolation transformer shown in Fig. 6.7 was replaced by the RF amplifier. The RF amplifier has internal isolation making the external transformer unnecessary. For the low-frequency testing of the EE-core transformer, a Wavetek 271 pulse/function generator was used as the voltage source. For all the other tests, an HP 3330B frequency synthesizer was used because it produced a superior sinusoidal voltage waveform at the higher frequencies.

In general, no effort was made in these short-circuit tests to maintain either a constant excitation current or excitation voltage between measurement frequencies.[5] Rather, the amplifier gain was adjusted to maintain measured waveforms which were apparently clean sinusoids. When too much gain was used, then the waveforms tended to distort; when too little gain was used, then the measured voltages became corrupted by noise and were too small to digitize without error. Only for the low-frequency measurement of the EE-core transformer was an effort made to maintain a constant input current. For the low-frequency tests on the EE-core transformer, the excitation current was maintained at approximately one ampere rms, or the largest rms value possible when the amplifier was

[5]Only normalized values of $\underline{H}_{x-N}$ are used to calculate $R_{(jk)}$ and $L_{(jk)}$, and the transformer is assumed to have negligible magnetizing current. Therefore, the actual magnitude of the current should not effect either the calculated or measured values for a square-loop core. Initial measurements have shown this hypothesis to be true.

unable to deliver a current of one ampere. Maintaining this level of excitation current lead to some distortion of the measured waveforms at low frequencies. For the other tests, the excitation currents ranged from 0.1 to 0.7 amperes rms.

As is stated above, the algorithm used to acquire measured values of $R_{(jk)}$ and $L_{(jk)}$ is accurate only when v_{MEAS} and i_{SC} are sinusoidal. No attempt was made to determine quantitatively how close the acquired waveforms were to perfect sinusoids.

6.3.2 Laboratory Results

Using the above described laboratory equipment, the six short-circuit tests of Fig. 5.2(c) were performed on the EE-core transformer. The results of these tests are given in Figs. 6.8 and 6.9, superimposed on the computer-generated data discussed in Section 6.2. The pot-core transformer was similarly tested using the equipment described above. The six short-circuit tests of Fig. 6.10(c) yielded the data presented in Figs. 6.11 and 6.12 along with the data calculated for the pot-core transformer. Observing the curves for the two transformers, we see that in one case, i.e., the pot-core transformer, the agreement between the measured data and the calculated data appears to be quite good over a frequency range of 320 Hz to 560 kHz. For frequencies above 560 kHz, the capacitance of the windings can no longer be considered negligible as evidenced by the dramatic nonlinear increase in the measured resistance. Although for the EE-core transformer the analytical results predict the relative magnitudes and the variation in parameter values fairly well, there appears to be significant disagreement between the actual measured and calculated data. To get idea on how close the measured and calculated data actually are, let us now look at the values at two specific frequencies for both transformers and determine the actual percentage differences involved.

For the EE-core transformer at 100 kHz, values of

$$R_{(13),calc} = 1.5\,\Omega \quad \text{and} \quad L_{(13),calc} = 5.1\,\mu\text{H}$$

are calculated in Section 6.1.4. In the laboratory, the following values of $R_{(jk)}$ and $L_{(jk)}$ for the EE-core transformer were measured at 100 kHz for the (13) short-circuit test.

$$R_{(13),meas} = 1.65\,\Omega \qquad L_{(13),meas} = 6.24\,\mu\text{H}$$

Using the formula

$$\frac{X_{(jk),calc} - X_{(jk),meas}}{X_{(jk),meas}} \times 100\% = \%\,\text{difference} \tag{6.4}$$

where X stands for R or L, we get percentage differences of -9% and -18% for the $R_{(13)}$ and $L_{(13)}$ cases, respectively. At a frequency of 1 kHz, the calculated and measured data for the EE-core transformer are

$$\begin{aligned} R_{(13),calc} &= 79.5\,\text{m}\Omega & L_{(13),calc} &= 8.03\,\mu\text{H} \\ R_{(13),meas} &= 112.\,\text{m}\Omega & L_{(13),meas} &= 9.63\,\mu\text{H} \end{aligned}$$

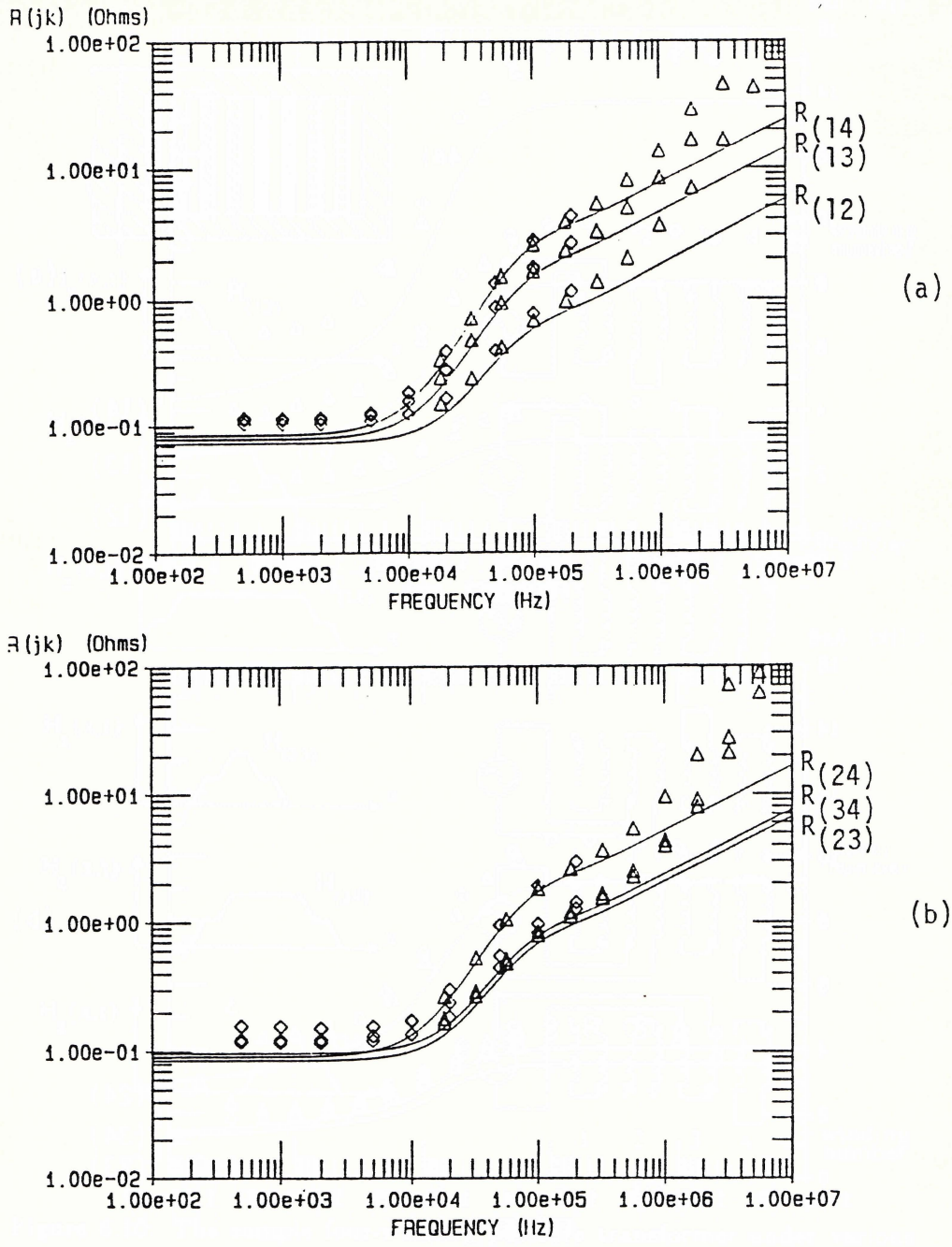


Figure 6.8: Comparison of measured and calculated values of $R_{(jk)}$ versus frequency for the short-circuit tests of Fig. 5.2(c) using EE-core transformer. Lines = calculation data; Diamonds = data measured using LF setup; Triangles = data measured using HF setup. (a) shows $R_{(12)}$, $R_{(13)}$ and $R_{(14)}$. (b) shows $R_{(23)}$, $R_{(24)}$ and $R_{(34)}$.

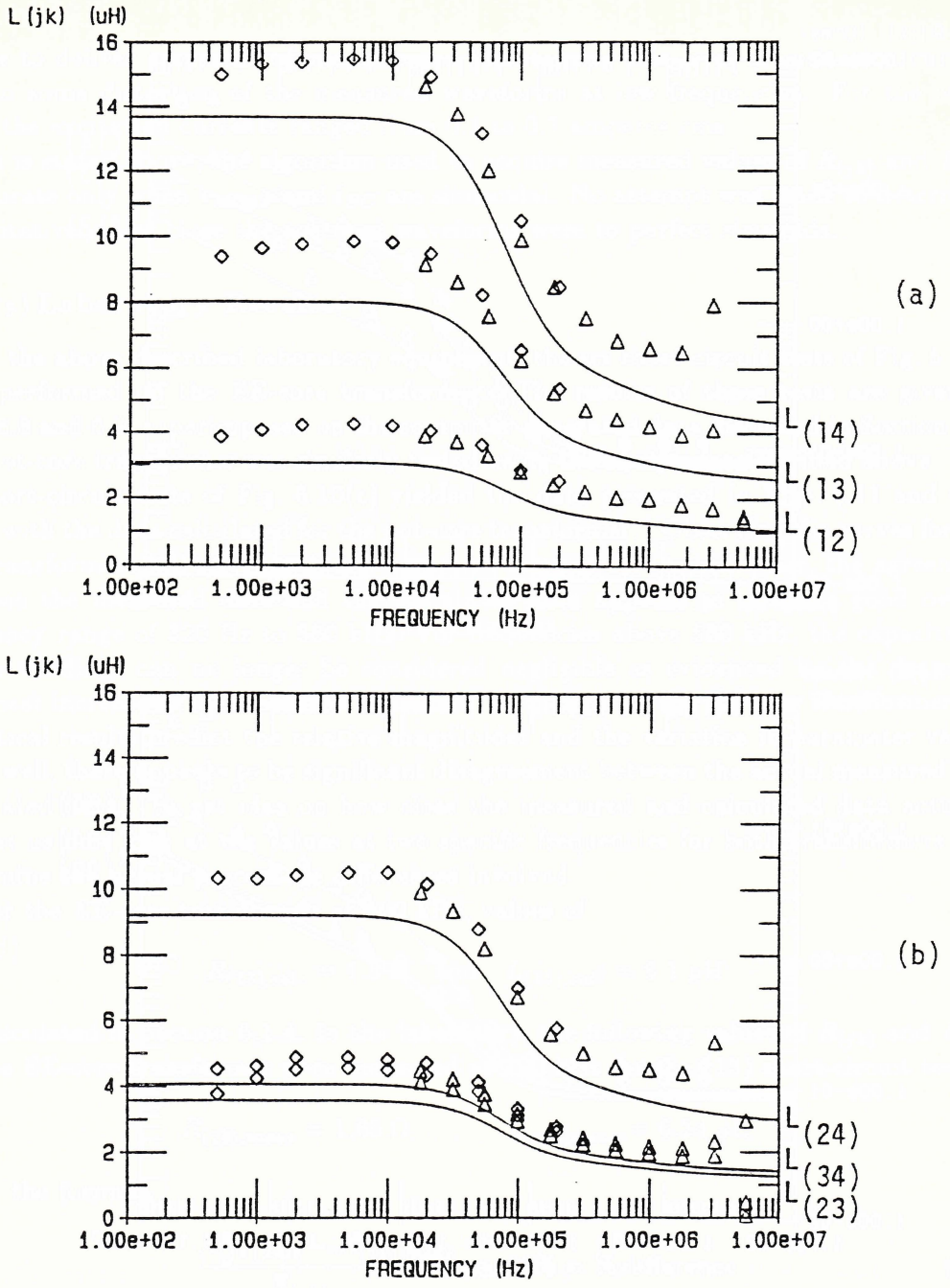


Figure 6.9: Comparison of measured and calculated values of $L_{(jk)}$ versus frequency for the short-circuit tests of Fig. 5.2(c) using EE-core transformer. Lines = calculation data; Diamonds = data measured with LF setup; Triangles = data measured using HF setup. (a) shows $L_{(12)}$, $L_{(13)}$ and $L_{(14)}$. (b) shows $L_{(23)}$, $L_{(24)}$ and $L_{(34)}$.

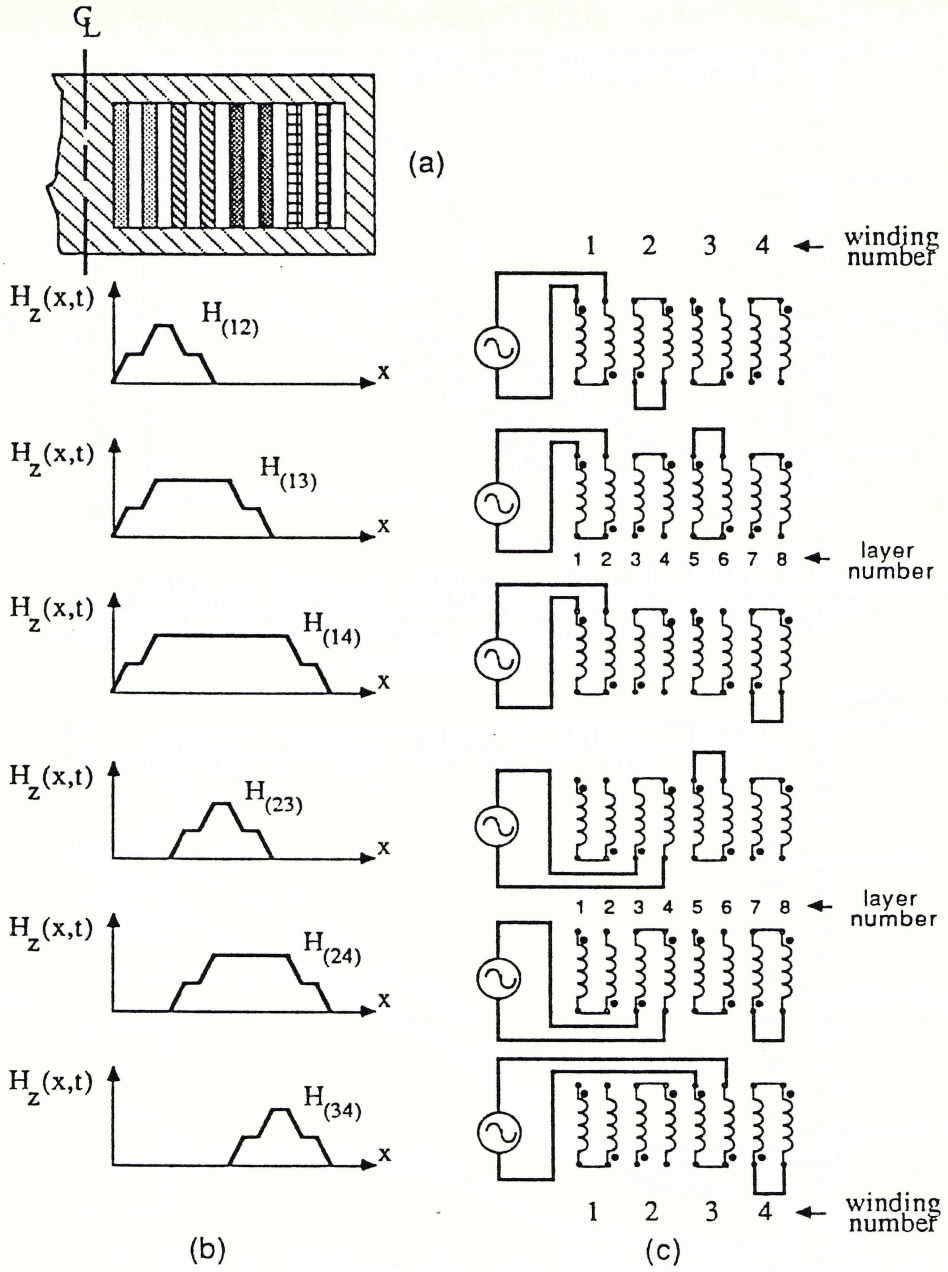


Figure 6.10: The sample four-winding pot-core transformer under various short-circuit conditions. In the winding cross-section of (a), the instantaneous current is assumed in each case to be flowing into the paper in the outer conducting winding and flowing out of the paper in the inner windings. Also shown are (b) the $H_z(x,t)$ profiles at an arbitrary time instant t and (c) the schematic representations for the six different short-circuit tests including relative positions of external leads from the windings and internal shorts between the layers.

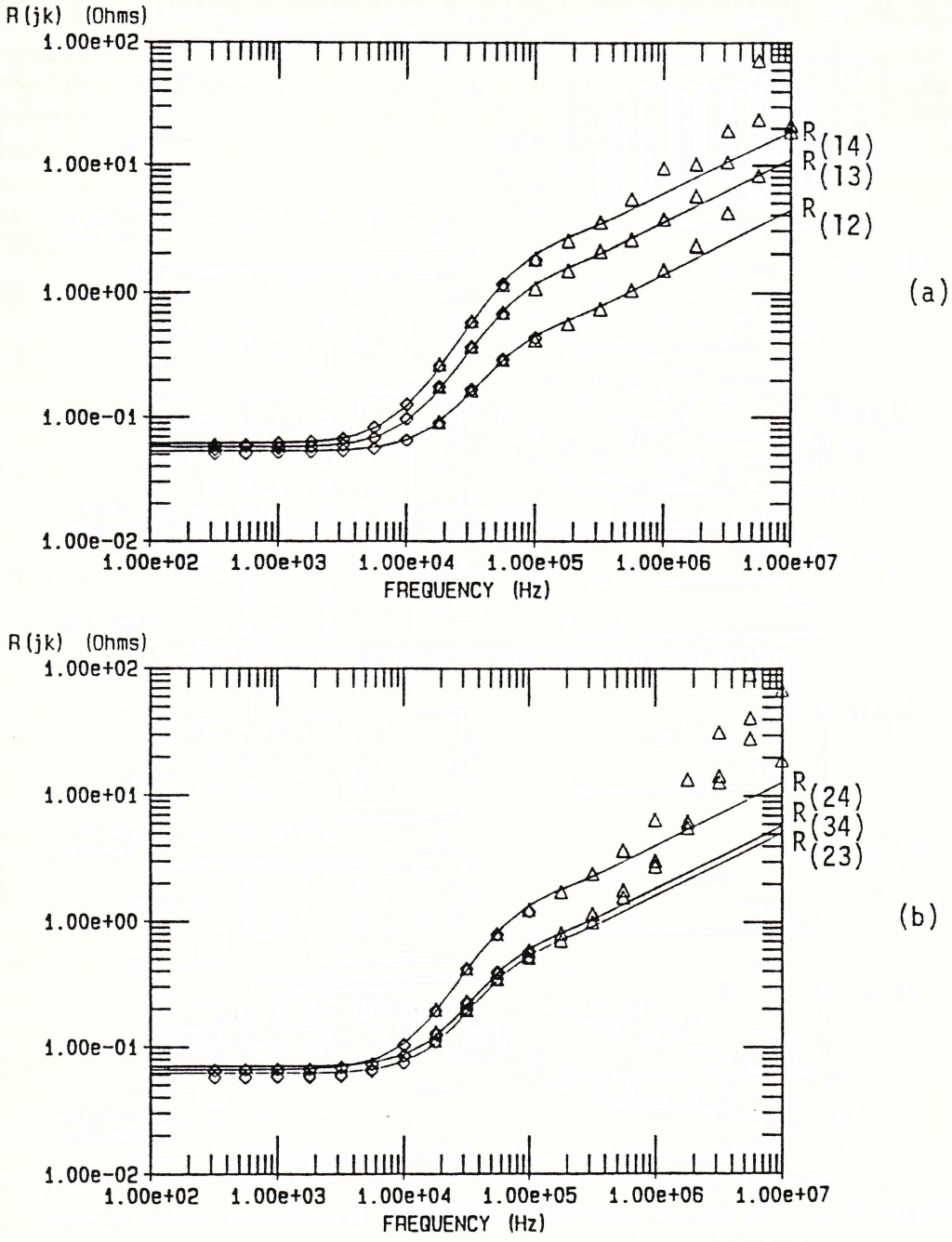


Figure 6.11: Comparison of measured and calculated values of $R_{(jk)}$ versus frequency for the short-circuit tests of Fig. 6.10(c) using pot core. Lines = calculation data; Diamonds = data measured with LF setup; Triangles = data measured with HF setup. (a) shows $R_{(12)}$, $R_{(13)}$ and $R_{(14)}$. (b) shows $R_{(23)}$, $R_{(24)}$ and $R_{(34)}$.

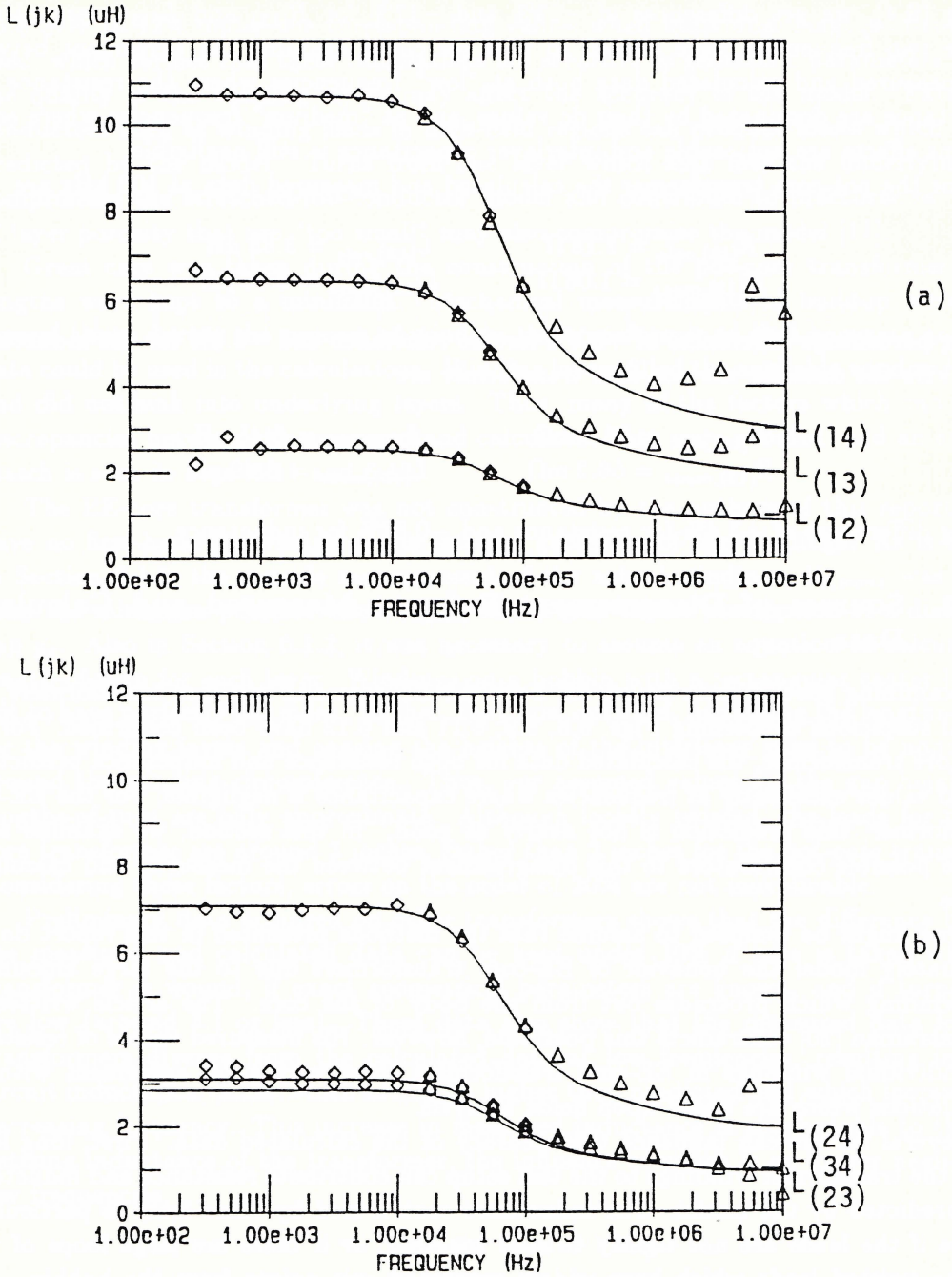


Figure 6.12: Comparison of measured and calculated values of $L_{(jk)}$ versus frequency for the short-circuit tests of Fig. 6.10(c) using pot core. Lines = calculation data; Diamonds = data measured with LF setup; Triangles = data measured with HF setup. (a) shows $L_{(12)}$, $L_{(13)}$ and $L_{(14)}$. (b) shows $L_{(23)}$, $L_{(24)}$ and $L_{(34)}$.

Using (6.4), we get differences of -29% and -17% for $R_{(13)}$ and $L_{(13)}$, respectively. These two frequencies were chosen so that we could examine the agreement between the measured and calculated data both at "low" frequencies where the resistance and inductance are dominated by their dc values, and at "medium" frequencies where eddy-current effects are noticeable and interlayer capacitance is still negligible.

For the pot-core transformer the calculated and measured data at 100 kHz are

$$R_{(13),calc} = 1.18\,\Omega \qquad L_{(13),calc} = 3.85\,\mu\text{H}$$
$$R_{(13),meas} = 1.08\,\Omega \qquad L_{(13),meas} = 3.98\,\mu\text{H}$$

giving percentage differences of $+9.3\%$ for the resistance and -3.3% for the inductance. At 1 kHz the data for the pot-core transformer are

$$R_{(13),calc} = 58.1\,\text{m}\Omega \qquad L_{(13),calc} = 6.45\,\mu\text{H}$$
$$R_{(13),meas} = 56.2\,\text{m}\Omega \qquad L_{(13),meas} = 6.49\,\mu\text{H}$$

giving differences of $+3.4\%$ for resistance and -0.62% for inductance.

6.3.3 Sources of Disagreement Between Measured and Calculated Data

By examining specific data points for both the EE-core and pot-core transformers, our initial suspicions concerning Figs. 6.8, 6.9, 6.11 and 6.12 have been confirmed. For the pot-core transformer, the calculated data for both resistance and inductance predict the actual values excellently at frequencies where capacitance is negligible. For the EE-core transformer, this prediction is not nearly as good. In this section, we examine some of the possible contributors to this disagreement between the measured and calculated values.

One might be tempted to assume that the methods presented in this report do not adequately model the behavior of EE-core transformers due to the large amount of the winding which protrudes out from the body of the core. The article written by Venkatraman [20] contradicts this postulate, however. His measured values of resistance for individual windings in EE-core transformers show very good agreement with his calculations which are based upon fields analysis.

Several factors can influence the accuracy of the calculated data. First, long leads from the transformer windings to the test setup can contribute resistance and inductance not predicted by the model. The inductance contributed by these leads is particularly severe if the leads are not tightly twisted together, or if there are large loops of wire due to twisted leads which have widely separated exit points from the bobbin. The effect of these lead inductances is exacerbated by turn ratios which are much greater or smaller than one. Second, for the model to adequately predict the behavior of the transformer, accurate information about the geometry of the transformer is needed. As shown in Section 6.1.4, the assumption of a single average length-of-turn for the EE-core transformer lead to calculated resistance and inductance values that ranged from

16% over to 12% under the corresponding values when individual lengths-of-turn were used, which verifies that these calculations are sensitive to geometric parameters. Third, the quality of the winding layers may affect the accuracy of the model. Extraneous conductors such as winding leads in high-field regions can produce losses which are not predicted by the model. Turns from one layer which sink into the underlying layer compromise the stretched-foil-conductor model and contribute to inaccuracies. Values of layer porosity that are "too small" may also compromise the model [17].

Great care was taken during the construction of the pot-core transformer. Lead lengths were kept to a minimum. Mechanical measurements of buildup were taken several times during the process of winding the transformer so that accurate geometric data could be used in the calculations. Winding layers filled the available window breadth and did not sink into underlying layers. Thus, many of the factors which can lead to discrepancies between the measured and calculated data were avoided, and an excellent match is seen in Figs. 6.11 and 6.12.

The EE-core transformer was not constructed by the authors of this report, so we have no first-hand knowledge of the internal geometry of the windings. As is detailed in Section 6.1.2, the outside measurement of the actual windings, $Y_{o,meas}$ was greater than the minimum possible value $Y_{o,min}$ which lead to the assumption of a distributed gap g_a. Also in Section 6.1.2, it was necessary to assume an equation to calculate the length-of-turn for each layer. Windings on a bobbin with a rectangular center leg tend not to have perfectly flat sides. Rather, they bow outward, increasing the lengths-of-turn for the winding layers and causing the heights of the interlayer gaps to be nonuniform around the winding circumference. Thus, our assumed values for the gap heights and lengths-of-turn are only approximate. Although loosely twisted, the leads for the EE-core transformer are around 3 inches, rather than 2 inches for the pot-core transformer. Considering these factors, errors on the order of 20% are not inexplicable.

Preliminary data acquired on other transformers shows that the difference between the measured and calculated data can be kept under 10% if care is taken while the transformer is wound, if exact geometrical parameters are known, and if turns ratios are low (around 3:1 or less). These data also show that the measured data for some transformers diverge from the calculated data at low frequencies, resulting in short-circuit inductance values which are much higher than predicted and which increase with decreasing frequency. This increase in measured inductance is attributable to the magnetizing inductance of the transformer, the influence of which is no longer negligible at low frequencies.

This page has been left blank intentionally.

Chapter 7

Admittance-Link Equivalent Circuit

Chapter 6 illustrates how the short-circuit resistances and inductances of a multiwinding transformer can be calculated from its geometry. The next step in predicting the high-frequency behavior of such a transformer is to use these short-circuit resistances and inductances to obtain the parameters associated with some circuit model of the transformer. Two such equivalent-circuit models are presented; the admittance-link model is developed in this chapter and the coupled-secondaries model in the next chapter. It is shown in Section 8.3 that these two models are essentially equivalent, but one or the other might be preferable depending on the circumstances of its application.

The first circuit model that we examine is the linear network of admittance links given in Fig. 7.9. This circuit dates to the early part of this century and is well documented in the literature [1,13,18], but with the passage of time, these references have become less readily accessible and less widely known. Yet, with the assistance of computers to carry out the often lengthy calculations, the admittance-link transformer model might become a valuable tool for the power-electronics designer faced with the task of predicting cross-regulation effects in power supplies with multiple, isolated outputs. For these reasons, we go into some depth to show the basis of this circuit model and develop expressions for the values of the admittance links in terms of the short-circuit impedances of the transformer. The model is general for a transformer with any number of windings, but once again we use a 4-winding transformer as an example.

Section 7.1 shows that for sinusoidal excitation, the familiar coupled-coils model of a linear K-winding transformer can be represented by a general K-port network with its associated phasor equations in either impedance or admittance form. From this K-port network, the admittance-link equivalent circuit is derived in Section 7.2 through a series of circuit transformations made possible by applying some simplifying assumptions. In Section 7.3, equations are derived by which the values of the elements in the admittance-link model can be calculated from the short-circuit impedances of the transformer, and an example calculation is shown. Finally, Section 7.4 contains general comments about

the applicability of the admittance-link model.

7.1 GENERAL TRANSFORMER EQUIVALENT CIRCUITS

A multicircuit transformer is a device in which the voltage across the terminals of each of a set of windings depends on the current in that winding and on the current in each of the other windings. The coupled-coils model pictured in Fig. 7.1 is a familiar description of the linear inductive interactions between the different windings of a transformer. In each of the equations for winding voltage, the coefficient that multiplies the time derivative of current in the same winding is called the *self*-inductance, and each of the coefficients that multiplies the time derivative of current in a different winding is called a *mutual* inductance.

Noticing that each of the mutual-inductance coefficients appears twice in the equations of Fig. 7.1, there are seem to be ten different coefficients that characterize a 4-winding transformer. After the series of circuit transformations in Section 7.2, it is found that only six coefficients are actually needed to characterize the leakage-impedance effects in a 4-winding transformer. After reducing the number of coefficients from ten to six, however, the turn ratios of the transformer must also be known in order to use the resulting circuit model.

More generally, a linear K -winding transformer can be represented by the "black box" K-port network shown in Fig. 7.2, with each port representing a different transformer winding. If such a general network is restricted to sinusoidal steady-state operation, we can specify the relationships between the various transformer windings by writing a set of phasor-current or phasor-voltage equations for the K windings as shown in the figure. In each of the equations for winding voltage, the coefficient that multiplies the current phasor of the same winding is called the *self-impedance* and each coefficient that multiplies the current phasor of a different winding is called a *mutual impedance.* When the set of K equations in Fig. 7.2(b) is expressed in vector form as

$$[\underline{V}] = [\underline{Z}][\underline{I}] \tag{7.1}$$

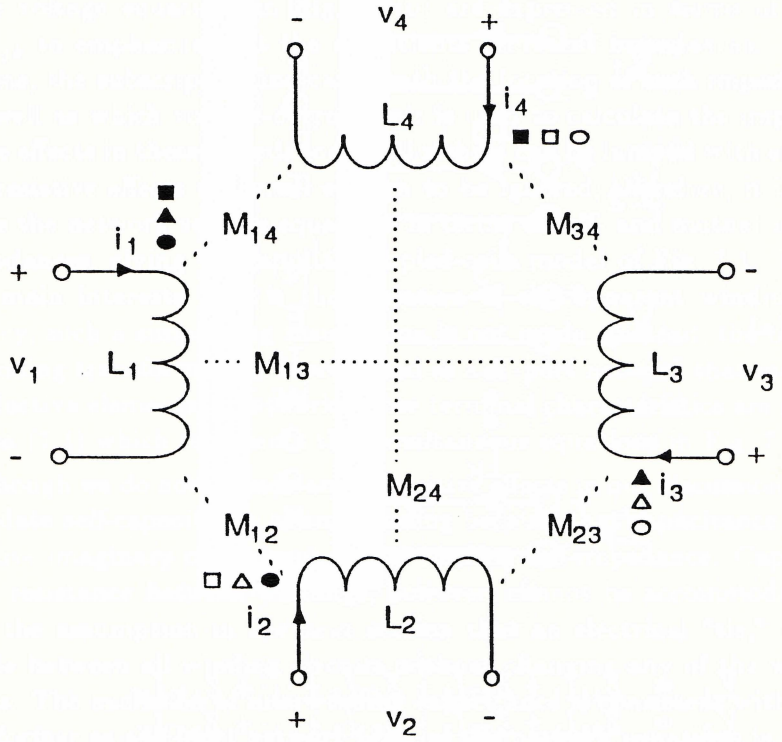
the matrix $[\underline{Z}]$ contains self-impedances along the diagonal and mutual impedances off the diagonal.

Alternatively, a vector equation for the current expressions in Fig. 7.2(c) can be written, where the coefficients that multiply the various winding voltages form the admittance matrix $[\underline{Y}]$.

$$[\underline{I}] = [\underline{Y}][\underline{V}] \tag{7.2}$$

For any realizable linear circuit, $[\underline{Z}]$ and $[\underline{Y}]$ are inverses of each other, that is,

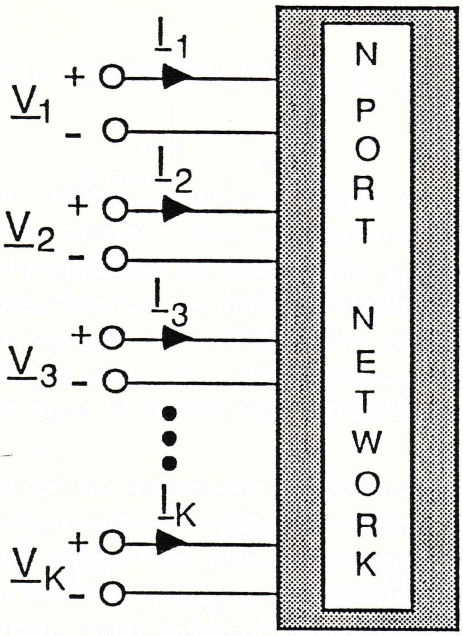
$$[\underline{Y}] = [\underline{Z}]^{-1} \tag{7.3}$$



$$
\begin{aligned}
v_1(t) &= L_1\frac{di_1}{dt} + M_{12}\frac{di_2}{dt} + M_{13}\frac{di_3}{dt} + M_{14}\frac{di_4}{dt} \\
v_2(t) &= M_{12}\frac{di_1}{dt} + L_2\frac{di_2}{dt} + M_{23}\frac{di_3}{dt} + M_{24}\frac{di_4}{dt} \\
v_3(t) &= M_{13}\frac{di_1}{dt} + M_{23}\frac{di_2}{dt} + L_3\frac{di_3}{dt} + M_{34}\frac{di_4}{dt} \\
v_4(t) &= M_{14}\frac{di_1}{dt} + M_{24}\frac{di_2}{dt} + M_{34}\frac{di_3}{dt} + L_4\frac{di_4}{dt}
\end{aligned}
$$

Figure 7.1: Coupled-coils model of a linear 4-winding transformer, with the self-inductance of winding j designated L_j and the mutual inductance between windings j and k designated M_{jk}.

(a)



(b)

$$\begin{aligned}
\underline{V}_1 &= \underline{Z}_{11}\underline{I}_1 + \underline{Z}_{12}\underline{I}_2 + \underline{Z}_{13}\underline{I}_3 + \cdots + \underline{Z}_{1K}\underline{I}_K \\
\underline{V}_2 &= \underline{Z}_{21}\underline{I}_1 + \underline{Z}_{22}\underline{I}_2 + \underline{Z}_{23}\underline{I}_3 + \cdots + \underline{Z}_{2K}\underline{I}_K \\
\underline{V}_3 &= \underline{Z}_{31}\underline{I}_1 + \underline{Z}_{32}\underline{I}_2 + \underline{Z}_{33}\underline{I}_3 + \cdots + \underline{Z}_{3K}\underline{I}_K \\
&\vdots \qquad\qquad\qquad\qquad\qquad\qquad \vdots \\
\underline{V}_K &= \underline{Z}_{K1}\underline{I}_1 + \underline{Z}_{K2}\underline{I}_2 + \underline{Z}_{K3}\underline{I}_3 + \cdots + \underline{Z}_{KK}\underline{I}_K
\end{aligned}$$

(c)

$$\begin{aligned}
\underline{I}_1 &= \underline{Y}_{11}\underline{V}_1 + \underline{Y}_{12}\underline{V}_2 + \underline{Y}_{13}\underline{V}_3 + \cdots + \underline{Y}_{1K}\underline{V}_K \\
\underline{I}_2 &= \underline{Y}_{21}\underline{V}_1 + \underline{Y}_{22}\underline{V}_2 + \underline{Y}_{23}\underline{V}_3 + \cdots + \underline{Y}_{2K}\underline{V}_K \\
\underline{I}_3 &= \underline{Y}_{31}\underline{V}_1 + \underline{Y}_{32}\underline{V}_2 + \underline{Y}_{33}\underline{V}_3 + \cdots + \underline{Y}_{3K}\underline{V}_K \\
&\vdots \qquad\qquad\qquad\qquad\qquad\qquad \vdots \\
\underline{I}_K &= \underline{Y}_{K1}\underline{V}_1 + \underline{Y}_{K2}\underline{V}_2 + \underline{Y}_{K3}\underline{V}_3 + \cdots + \underline{Y}_{KK}\underline{V}_K
\end{aligned}$$

Figure 7.2: (a) K-port phasor model of a linear, K-winding transformer. (b) A set of K equations that relates the K winding voltages to the K winding currents. (c) An equivalent set of equations that relates the K winding currents to the K winding voltages.

Since these two matrices are equivalent dual descriptions of the K-port network, we continue the discussion in terms of the impedance matrix $[\underline{Z}]$.

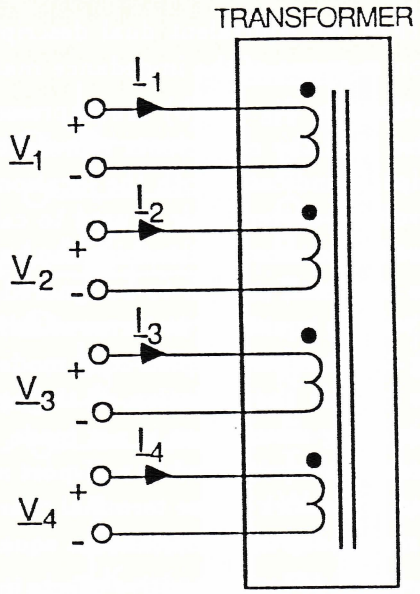
The voltage equations in Fig. 7.2(b) are expressed in terms of coefficients of the form $\underline{Z}_{jk}$ to emphasize that the coefficients represent impedances. Note that in these equations, the subscript jk indicates both the location of each impedance in the matrix $[\underline{Z}]$ as well as which voltage-current pair is used to calculate the impedance. Often the resistive effects in these impedance relationships can be lumped with external resistances, or the resistive effects are small enough to be ignored; therefore, it is common practice to write the network voltage equations in terms of self- and mutual *inductances* instead of *impedances*, giving the familiar coupled-coils model of Fig. 7.1. However, since one of the main interests here is the variation of the apparent winding resistances with frequency, such a simplifying assumption is not made. Instead, the coupled windings of a K-winding transformer are represented as a K-port network that may contain resistive and inductive elements, a network whose terminal characteristics are given by the vector equation (7.1) which represents the simultaneous equations in Fig. 7.2(b).

Although we do not include any capacitive effects in our discussion, the model can accommodate *self*-capacitance of any winding because that capacitance simply contributes a negative imaginary component to the winding self-impedance. Capacitive coupling or leakage resistance *between* windings, however, cannot be accommodated by this model due to the assumption in the next section that an electrical "tie," or connection, can be made between all winding circuits without changing any of the winding voltages or currents. The exclusion of interwinding capacitance is consistent with the description of a transformer as a K-port network because the network equations in Fig. 7.2(b) and (c) are incapable of describing the voltage across an interwinding capacitance, i.e., a voltage between two terminals of different ports. It is shown in the next section how some simplifying assumptions permit this K-port network to be replaced by the admittance-link equivalent circuit for modeling the transformer.

7.2 DERIVATION OF THE ADMITTANCE-LINK EQUIVALENT CIRCUIT

The admittance-link equivalent circuit for an example 4-winding transformer is derived below by a series of steps. In Section 7.2.1, equations are written for the 4-port network that represents the actual transformer, then equations are derived for all winding circuits referred to a common winding. Simplifying assumptions are applied which allow the "referred" transformer to be modeled by a 5-terminal circuit in Section 7.2.2, then by a 4-terminal circuit in Section 7.2.3. It is shown in Section 7.2.4 how this 4-terminal circuit may be viewed as a 3-port network, and finally, Section 7.2.5 explains how the 3-port network may be represented instead by a mesh of admittances, the admittance-link equivalent circuit.

(a)



(b)

$$
\begin{aligned}
\underline{V}_1 &= \underline{Z}_{11}\underline{I}_1 + \underline{Z}_{12}\underline{I}_2 + \underline{Z}_{13}\underline{I}_3 + \underline{Z}_{14}\underline{I}_4 \\
\underline{V}_2 &= \underline{Z}_{21}\underline{I}_1 + \underline{Z}_{22}\underline{I}_2 + \underline{Z}_{23}\underline{I}_3 + \underline{Z}_{24}\underline{I}_4 \\
\underline{V}_3 &= \underline{Z}_{31}\underline{I}_1 + \underline{Z}_{32}\underline{I}_2 + \underline{Z}_{33}\underline{I}_3 + \underline{Z}_{34}\underline{I}_4 \\
\underline{V}_4 &= \underline{Z}_{41}\underline{I}_1 + \underline{Z}_{42}\underline{I}_2 + \underline{Z}_{43}\underline{I}_3 + \underline{Z}_{44}\underline{I}_4
\end{aligned}
$$

Figure 7.3: (a) 4-winding transformer used as an example. (b) The corresponding network equations in impedance form.

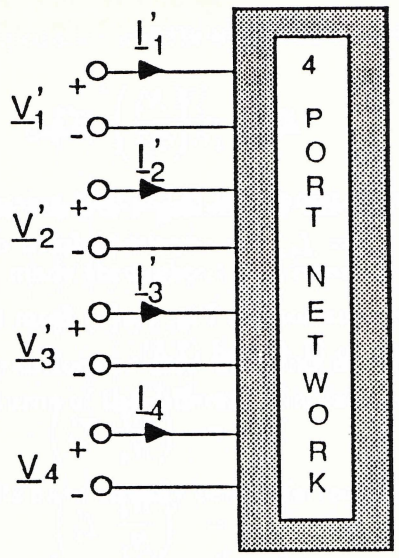
7.2.1 4-Port Network

A schematic diagram of the 4-winding transformer used as an example is shown in Fig. 7.3. The admittance-link model is derived without regard for which particular winding of the transformer is the primary winding.

If we assume that the only interactions between the different windings of the transformer are through mutual impedances; in particular, if we ignore any capacitive coupling between windings and assume that the load circuits are independent, we can deduce two important facts. First, the "mutual" nature of mutual impedances tells us that the impedance matrix $[\underline{Z}]$ in (7.1) is symmetric. It contains four self-impedances along the diagonal and six mutual impedances off the diagonal, a total of ten different elements. For a K-winding transformer, there are $K(K+1)/2$ different elements in the impedance matrix. The second fact deduced is that one side of each transformer winding can be connected to a common point without changing the operation of the circuit. This fact is used in Section 7.2.2.

An alternate form of the equivalent circuit in Fig. 7.3 that has no step-up or step-down of voltages due to ideal-transformer action can be drawn if all of the voltages,

(a)



(b)

$$
\begin{aligned}
\underline{V}'_1 &= \underline{Z}'_{11}\underline{I}'_1 + \underline{Z}'_{12}\underline{I}'_2 + \underline{Z}'_{13}\underline{I}'_3 + \underline{Z}'_{14}\underline{I}_4 \\
\underline{V}'_2 &= \underline{Z}'_{21}\underline{I}'_1 + \underline{Z}'_{22}\underline{I}'_2 + \underline{Z}'_{23}\underline{I}'_3 + \underline{Z}'_{24}\underline{I}_4 \\
\underline{V}'_3 &= \underline{Z}'_{31}\underline{I}'_1 + \underline{Z}'_{32}\underline{I}'_2 + \underline{Z}'_{33}\underline{I}'_3 + \underline{Z}'_{34}\underline{I}_4 \\
\underline{V}_4 &= \underline{Z}'_{41}\underline{I}'_1 + \underline{Z}'_{42}\underline{I}'_2 + \underline{Z}'_{43}\underline{I}'_3 + \underline{Z}'_{44}\underline{I}_4
\end{aligned}
$$

Figure 7.4: (a) 4-port-network equivalent circuit of the transformer which has all other winding circuits referred to winding number 4. (b) The corresponding network equations.

currents, and impedances associated with every winding of the transformer are referred to a single, preselected winding. Winding 4 is chosen here for convenience so later in this derivation, the impedance-matrix row and column numbers correspond to the winding numbers of the voltage and current used to calculate each impedance. With winding 4 designated as the winding to which all others are referred, the voltage and current transformation equations

$$\underline{V}'_j = \left(\frac{N_4}{N_j}\right)\underline{V}_j \tag{7.4}$$

$$\underline{I}'_j = \left(\frac{N_j}{N_4}\right)\underline{I}_j \tag{7.5}$$

may be applied to produce the equivalent circuit of Fig. 7.4. When modeling the transformer as part of a larger network, any external circuits connected to windings 1, 2, or 3 must also be referred to winding 4 using these equations. The effect is to refer the

impedance of each external circuit as follows.

$$\underline{Z}'_{ext,j} = \left(\frac{N_4}{N_j}\right)^2 \underline{Z}_{ext,j} \tag{7.6}$$

Because the voltage and current of winding 4 are not actually "referred" by (7.4) and (7.5), i.e., $\underline{V}'_4 = \underline{V}_4$ and $\underline{I}'_4 = \underline{I}_4$, the unprimed form of these symbols is used in the subsequent equations.

To obtain the network equations in Fig. 7.4(b) from those in Fig. 7.3(b), the inverse relationships corresponding to (7.4) and (7.5),

$$\underline{V}_j = \left(\frac{N_j}{N_4}\ \underline{V}'_j\right) \tag{7.7}$$

$$\underline{I}_j = \left(\frac{N_4}{N_j}\ \underline{I}'_j\right) \tag{7.8}$$

are substituted into the equations in Fig. 7.3(b) to give

$$\begin{aligned}
\left(\frac{N_1}{N_4}\ \underline{V}'_1\right) &= \underline{Z}_{11}\left(\frac{N_4}{N_1}\ \underline{I}'_1\right) + \underline{Z}_{12}\left(\frac{N_4}{N_2}\ \underline{I}'_2\right) + \underline{Z}_{13}\left(\frac{N_4}{N_3}\ \underline{I}'_3\right) + \underline{Z}_{14}\underline{I}_4 \\
\left(\frac{N_2}{N_4}\ \underline{V}'_2\right) &= \underline{Z}_{21}\left(\frac{N_4}{N_1}\ \underline{I}'_1\right) + \underline{Z}_{22}\left(\frac{N_4}{N_2}\ \underline{I}'_2\right) + \underline{Z}_{23}\left(\frac{N_4}{N_3}\ \underline{I}'_3\right) + \underline{Z}_{24}\underline{I}_4 \\
\left(\frac{N_3}{N_4}\ \underline{V}'_3\right) &= \underline{Z}_{31}\left(\frac{N_4}{N_1}\ \underline{I}'_1\right) + \underline{Z}_{32}\left(\frac{N_4}{N_2}\ \underline{I}'_2\right) + \underline{Z}_{33}\left(\frac{N_4}{N_3}\ \underline{I}'_3\right) + \underline{Z}_{34}\underline{I}_4 \\
\underline{V}_4 &= \underline{Z}_{41}\left(\frac{N_4}{N_1}\ \underline{I}'_1\right) + \underline{Z}_{42}\left(\frac{N_4}{N_2}\ \underline{I}'_2\right) + \underline{Z}_{43}\left(\frac{N_4}{N_3}\ \underline{I}'_3\right) + \underline{Z}_{44}\underline{I}_4
\end{aligned} \tag{7.9}$$

Rearranging,

$$\begin{aligned}
\underline{V}'_1 &= \left(\frac{N_4^2}{N_1^2}\ \underline{Z}_{11}\right)\underline{I}'_1 + \left(\frac{N_4^2}{N_1 N_2}\ \underline{Z}_{12}\right)\underline{I}'_2 + \left(\frac{N_4^2}{N_1 N_3}\ \underline{Z}_{13}\right)\underline{I}'_3 + \left(\frac{N_4}{N_1}\ \underline{Z}_{14}\right)\underline{I}_4 \\
\underline{V}'_2 &= \left(\frac{N_4^2}{N_2 N_1}\ \underline{Z}_{21}\right)\underline{I}'_1 + \left(\frac{N_4^2}{N_2^2}\ \underline{Z}_{22}\right)\underline{I}'_2 + \left(\frac{N_4^2}{N_2 N_3}\ \underline{Z}_{23}\right)\underline{I}'_3 + \left(\frac{N_4}{N_2}\ \underline{Z}_{24}\right)\underline{I}_4 \\
\underline{V}'_3 &= \left(\frac{N_4^2}{N_3 N_1}\ \underline{Z}_{31}\right)\underline{I}'_1 + \left(\frac{N_4^2}{N_3 N_2}\ \underline{Z}_{32}\right)\underline{I}'_2 + \left(\frac{N_4^2}{N_3^2}\ \underline{Z}_{33}\right)\underline{I}'_3 + \left(\frac{N_4}{N_3}\ \underline{Z}_{34}\right)\underline{I}_4 \\
\underline{V}_4 &= \left(\frac{N_4}{N_1}\ \underline{Z}_{41}\right)\underline{I}'_1 + \left(\frac{N_4}{N_2}\ \underline{Z}_{42}\right)\underline{I}'_2 + \left(\frac{N_4}{N_3}\ \underline{Z}_{43}\right)\underline{I}'_3 + \underline{Z}_{44}\underline{I}_4
\end{aligned} \tag{7.10}$$

These simultaneous equations are written in vector form as

$$[\underline{V}'] = [\underline{Z}'][\underline{I}'] \tag{7.11}$$

where $[\underline{Z}']$ is the "referred" impedance matrix obtained from the elements of $[\underline{Z}]$ by

$$\underline{Z}'_{jk} = \left(\frac{N_4^2}{N_j N_k}\right) \underline{Z}_{jk} \tag{7.12}$$

It can be seen from this expression that if $[\underline{Z}]$ is symmetric, as argued in Section 7.2.1, then $[\underline{Z}']$ is symmetric also.

The following assumption, made throughout this research report, is used to simplify the network equations above.

> **Assumption 1**: The transformer core material is of high enough permeability that the ampere-turns of the different windings sum to approximately zero.

Because the transformer circuits have already been referred to winding 4, this assumption implies

$$\underline{I}_4 = -(\underline{I}'_1 + \underline{I}'_2 + \underline{I}'_3) \tag{7.13}$$

Substituting (7.13) into the equations of Fig. 7.4(b) gives

$$\begin{aligned}
\underline{V}'_1 &= (\underline{Z}'_{11} - \underline{Z}'_{14})\underline{I}'_1 + (\underline{Z}'_{12} - \underline{Z}'_{14})\underline{I}'_2 + (\underline{Z}'_{13} - \underline{Z}'_{14})\underline{I}'_3 \\
\underline{V}'_2 &= (\underline{Z}'_{21} - \underline{Z}'_{24})\underline{I}'_1 + (\underline{Z}'_{22} - \underline{Z}'_{24})\underline{I}'_2 + (\underline{Z}'_{23} - \underline{Z}'_{24})\underline{I}'_3 \\
\underline{V}'_3 &= (\underline{Z}'_{31} - \underline{Z}'_{34})\underline{I}'_1 + (\underline{Z}'_{32} - \underline{Z}'_{34})\underline{I}'_2 + (\underline{Z}'_{33} - \underline{Z}'_{34})\underline{I}'_3 \\
\underline{V}_4 &= (\underline{Z}'_{41} - \underline{Z}'_{44})\underline{I}'_1 + (\underline{Z}'_{42} - \underline{Z}'_{44})\underline{I}'_2 + (\underline{Z}'_{43} - \underline{Z}'_{44})\underline{I}'_3
\end{aligned} \tag{7.14}$$

These equations are used in Section 7.2.2.

7.2.2 5-Terminal Circuit

In Section 7.2.1, it is argued that the absence of capacitive coupling between transformer windings makes the following assumption valid.

> **Assumption 2**: One side of each transformer winding may be connected to a common point without disturbing the operation of the circuit.

This assumption applies to the referred transformer equivalent circuit of Fig. 7.4 as well as to the actual transformer. If an electrical "tie" is added between all the terminals of one polarity, and the circuit is redrawn as shown in Fig. 7.5, the new equivalent circuit has only five terminals instead of eight. It is important to recognize that the circled terminal numbers in this figure, used throughout the rest of the chapter, do not correspond to the terminals of the actual transformer, but instead to the terminals of an equivalent circuit obtained by referring all the transformer winding circuits to a common winding. It is also helpful to note that in the diagrams of this chapter, multiport networks, which have terminals arranged in pairs, are typically drawn as solid boxes while other equivalent circuits of the transformer are drawn as dashed boxes.

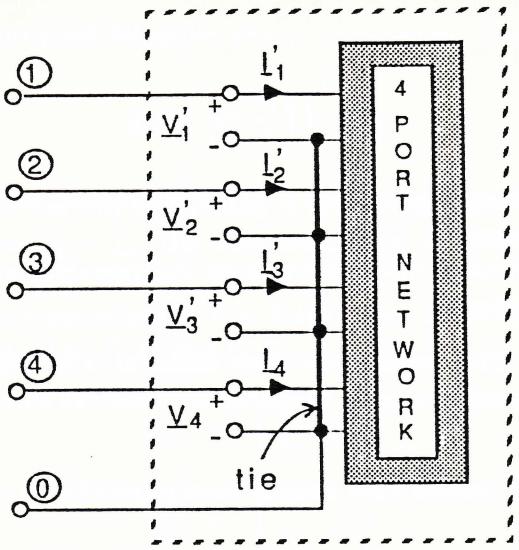


Figure 7.5: 4-port-network equivalent circuit of Fig. 7.4 with a "tie" connecting one side of each port to a common point. The resulting circuit has only the five nodes, labeled with circled numbers.

7.2.3 4-Terminal Circuit

Because equal and opposite currents must flow in the two leads of each port in the 4-port network of Fig. 7.5, the current flowing out of the circuit at terminal 0 is equal to the sum of the other four terminal currents. But (7.13) states that this sum is equal to zero, which means that for any configuration of sources and loads connected to the equivalent circuit, the connection between the tie and terminal 0 can always be broken as shown in Fig. 7.6 without affecting the operation of the circuit. A disconnected terminal 0 is shown as the "ground" node as a reminder that when using this equivalent circuit, one side of all sources and loads is connected to this node, which is external to the equivalent circuit.

The terminal voltages of the equivalent circuit in Fig. 7.6 can be described by selecting one terminal as the reference, and specifying all other voltages relative to this reference terminal. The choice of reference *terminal* is independent of the choice of reference *winding* outlined in Section 7.2.1. Again, for convenience in later subscript numbering, the number 4 is used here to designate the reference terminal as well. A new symbol of the form $\underline{V}_{j4}$ is chosen to stand for the differential-voltage phasor between terminal j and terminal 4. Note that the differential-voltage phasors defined here represent voltages in only those transformer equivalent circuits where all winding voltages, represented here by the four terminal voltages relative to ground, have already been referred to a chosen reference winding.

In general, a differential-voltage phasor may be specified between any two terminals of the equivalent circuit, regardless of which terminal is designated the reference. In

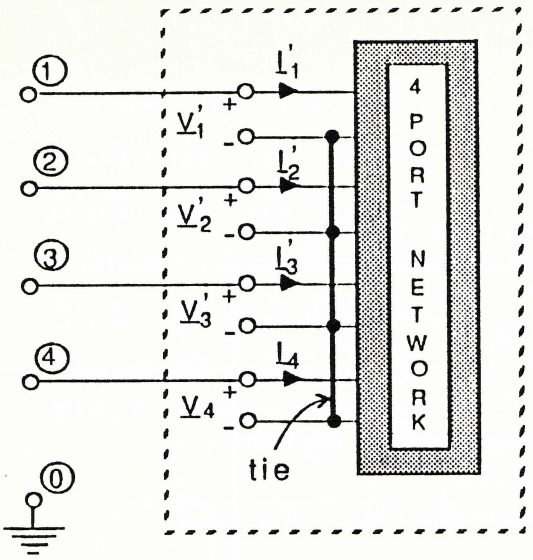


Figure 7.6: The 4-terminal equivalent circuit that results from breaking the connection between the tie and terminal 0.

terms of the actual winding voltages seen in Fig. 7.3, with winding 4 chosen as the reference winding for referral, differential voltages can be expressed as

$$\underline{V}_{jk} = \left(\frac{N_4}{N_j}\right)\underline{V}_j - \left(\frac{N_4}{N_k}\right)\underline{V}_k \tag{7.15}$$

For the choice of terminal 4 as the reference, this equation becomes

$$\underline{V}_{j4} = \left(\frac{N_4}{N_j}\right)\underline{V}_j - \underline{V}_4 = \underline{V}'_j - \underline{V}_4 \tag{7.16}$$

It is helpful in understanding differential-voltage phasors to recognize that if the stray effects in the transformer are neglected, all the transformer winding voltages referred to a common winding are equal, which implies that all the differential-voltage phasors given by (7.15) are equal to zero.

The set of equations in (7.14), which describe the 4-terminal equivalent circuit in Fig. 7.6, is transformed into the set of three expressions below for the differential-voltage phasors with respect to terminal 4. As indicated by (7.16), the difference is taken between each of the first three equations in (7.14) and the last one.

$$\begin{aligned}\underline{V}_{14} = \underline{V}'_1 - \underline{V}_4 = {} & (\underline{Z}'_{11} - \underline{Z}'_{14} - \underline{Z}'_{41} + \underline{Z}'_{44})\underline{I}'_1 \\ & + (\underline{Z}'_{12} - \underline{Z}'_{14} - \underline{Z}'_{42} + \underline{Z}'_{44})\underline{I}'_2 \\ & + (\underline{Z}'_{13} - \underline{Z}'_{14} - \underline{Z}'_{43} + \underline{Z}'_{44})\underline{I}'_3\end{aligned}$$

$$\begin{aligned}
\underline{V}_{24} = \underline{V}'_2 - \underline{V}_4 &= (\underline{Z}'_{21} - \underline{Z}'_{24} - \underline{Z}'_{41} + \underline{Z}'_{44})\underline{I}'_1 \\
&\quad + (\underline{Z}'_{22} - \underline{Z}'_{24} - \underline{Z}'_{42} + \underline{Z}'_{44})\underline{I}'_2 \\
&\quad + (\underline{Z}'_{23} - \underline{Z}'_{24} - \underline{Z}'_{43} + \underline{Z}'_{44})\underline{I}'_3 \\
\underline{V}_{34} = \underline{V}'_3 - \underline{V}_4 &= (\underline{Z}'_{31} - \underline{Z}'_{34} - \underline{Z}'_{41} + \underline{Z}'_{44})\underline{I}'_1 \\
&\quad + (\underline{Z}'_{32} - \underline{Z}'_{34} - \underline{Z}'_{42} + \underline{Z}'_{44})\underline{I}'_2 \\
&\quad + (\underline{Z}'_{33} - \underline{Z}'_{34} - \underline{Z}'_{43} + \underline{Z}'_{44})\underline{I}'_3
\end{aligned} \tag{7.17}$$

Each of the impedance coefficients above has the form

$$\underline{Z}_{r,jk} = \underline{Z}'_{jk} - \underline{Z}'_{j4} - \underline{Z}'_{4k} + \underline{Z}'_{44} \tag{7.18}$$

where the subscript r stands for *reduced*, which means that the array indices range from 1 to 3, one less than the number of windings in the transformer. Because $[\underline{Z}']$ is symmetric as pointed out below (7.12), the reduced impedance matrix $[\underline{Z}_r]$ is also symmetric:

$$\begin{aligned}
\underline{Z}_{r,kj} &= \underline{Z}'_{kj} - \underline{Z}'_{k4} - \underline{Z}'_{4j} + \underline{Z}'_{44} \\
&= \underline{Z}'_{jk} - \underline{Z}'_{4k} - \underline{Z}'_{j4} + \underline{Z}'_{44} \\
&= \underline{Z}_{r,jk}
\end{aligned} \tag{7.19}$$

Using the notation introduced in (7.18), (7.17) may be written in more compact form as

$$\begin{aligned}
\underline{V}_{14} &= \underline{Z}_{r,11}\underline{I}'_1 + \underline{Z}_{r,12}\underline{I}'_2 + \underline{Z}_{r,13}\underline{I}'_3 \\
\underline{V}_{24} &= \underline{Z}_{r,21}\underline{I}'_1 + \underline{Z}_{r,22}\underline{I}'_2 + \underline{Z}_{r,23}\underline{I}'_3 \\
\underline{V}_{34} &= \underline{Z}_{r,31}\underline{I}'_1 + \underline{Z}_{r,32}\underline{I}'_2 + \underline{Z}_{r,33}\underline{I}'_3
\end{aligned} \tag{7.20}$$

These equations are represented by the following vector equation.

$$[\underline{V}_{d4}] = [\underline{Z}_r][\underline{I}'_r] \tag{7.21}$$

The subscript $d4$ stands for *differential, referenced to terminal 4*, and as before, the subscript r stands for *reduced*. The r subscript is used to distinguish between the (3×3) *reduced* impedance matrix here and the (4×4) impedance matrix $[\underline{Z}]$ in (7.1), which represents a different set of quantities for the same transformer. The r is also used to distinguish $[\underline{I}'_r] = [\underline{I}'_1 \;\; \underline{I}'_2 \;\; \underline{I}'_3]^{\mathrm{T}}$ from $[\underline{I}'] = [\underline{I}'_1 \;\; \underline{I}'_2 \;\; \underline{I}'_3 \;\; \underline{I}_4]^{\mathrm{T}}$, although $[\underline{I}'_r]$ is contained in $[\underline{I}']$.

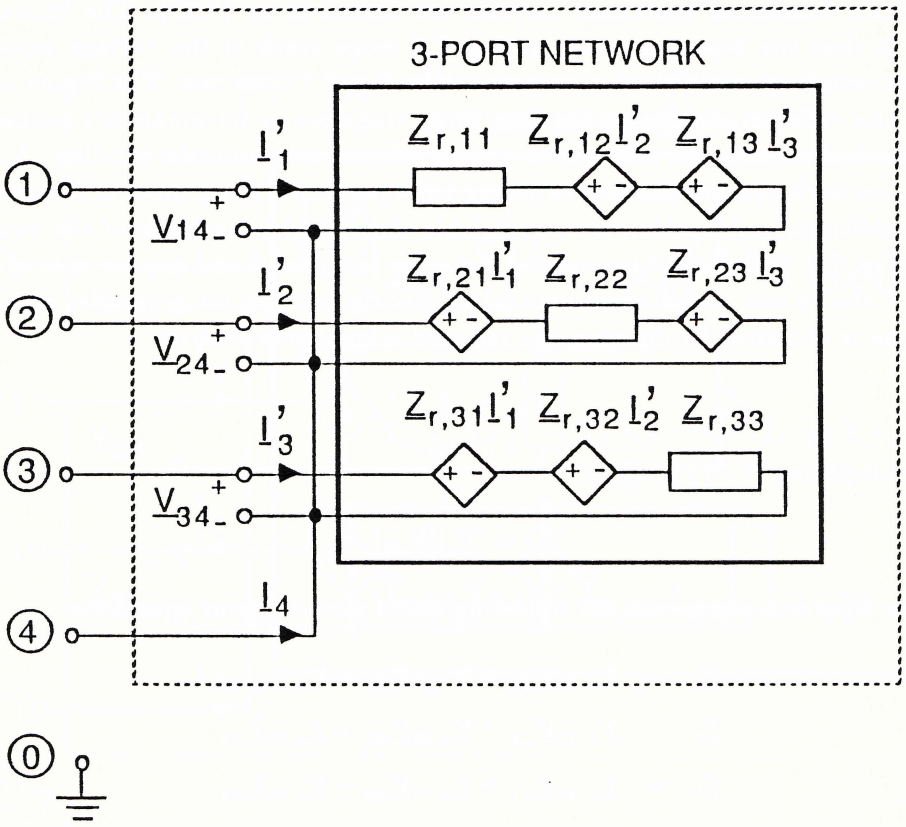


Figure 7.7: 3-port-network representation of the admittance-link equivalent circuit, showing the impedance form of the 3-port network.

7.2.4 3-Port Network

The form of (7.20) suggests that an equivalent representation of the 4-terminal equivalent circuit in Fig. 7.6 is the 3-port network shown in Fig. 7.7, synthesized from impedances and controlled-voltage sources. Although this network has one less port than the one in Fig. 7.6, both 4-terminal equivalent circuits are described by (7.20). The fundamental difference is that the 4-port network in Fig. 7.6 keeps track of the voltage across each transformer winding, while the 3-port network in Fig. 7.7 does not. The 3-port network gives only the *differential* voltages between those transformer terminals not connected to the hypothetical tie, after all voltages have been referred to a common winding. Although the 4-port network can provide four winding voltages rather than three differential voltages, the additional information is not available through the terminals of the equivalent circuit in Fig. 7.6 because the connection between terminal 0 and the tie is broken.

Fig. 7.7 shows one transformer equivalent circuit suitable for computer simulation. Another one is obtained by defining the *reduced admittance matrix*

$$[\underline{Y}_r] = [\underline{Z}_r]^{-1} \tag{7.22}$$

then premultiplying (7.21) by $[\underline{Y}_r]$.

$$[\underline{I}'_r] = [\underline{Y}_r][\underline{V}_{d4}] \tag{7.23}$$

This vector equation represents the following set of simultaneous equations.

$$\underline{I}'_1 = \underline{Y}_{r,11}\underline{V}_{14} + \underline{Y}_{r,12}\underline{V}_{24} + \underline{Y}_{r,13}\underline{V}_{34} \tag{7.24}$$

$$\underline{I}'_2 = \underline{Y}_{r,21}\underline{V}_{14} + \underline{Y}_{r,22}\underline{V}_{24} + \underline{Y}_{r,23}\underline{V}_{34} \tag{7.25}$$

$$\underline{I}'_3 = \underline{Y}_{r,31}\underline{V}_{14} + \underline{Y}_{r,32}\underline{V}_{24} + \underline{Y}_{r,33}\underline{V}_{34} \tag{7.26}$$

From this set of equations, the 3-port network can be represented using admittances and controlled-current sources as shown in Fig. 7.8. This new circuit, showing the admittance form of the 3-port network, is simply the dual of the impedance form of Fig. 7.7. Another, simpler transformer equivalent circuit is derived from the admittance form in Section 7.2.5.

7.2.5 Admittance-Link Equivalent Circuit

It is clear that (7.24) through (7.26) describe the terminal characteristics of the equivalent circuit in Fig. 7.8, which is redrawn in Fig. 7.9(a) without showing the internal elements of the 3-port network. Part (b) of Fig. 7.9 shows a general 4-terminal admittance-link equivalent circuit for the linear network of Fig. 7.9(a). For the correct choice of admittance values, the equivalent circuit can be made to have exactly the same terminal characteristics as the network in Fig. 7.9(a). The equivalence of the two circuits is proven in this section. The main advantage of the admittance-link equivalent circuit over the

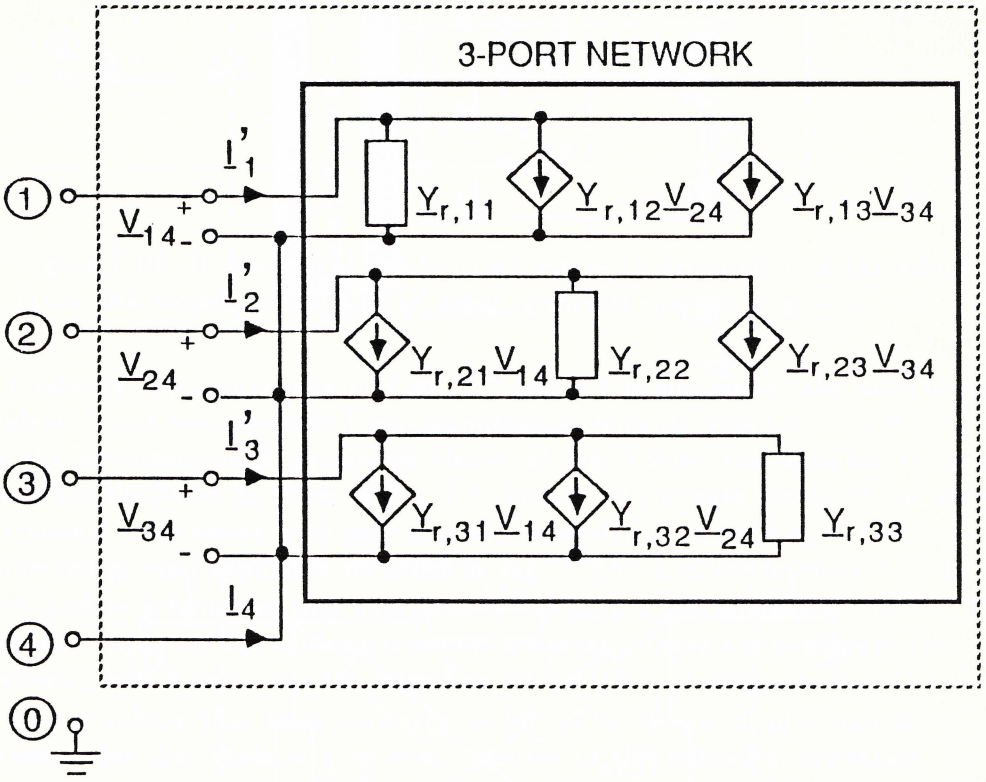
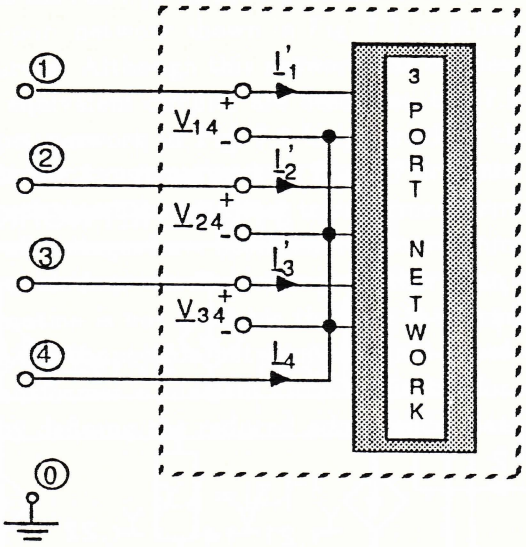


Figure 7.8: 3-port-network representation of the transformer equivalent circuit, showing the admittance form of the 3-port network.

(a)



(b)

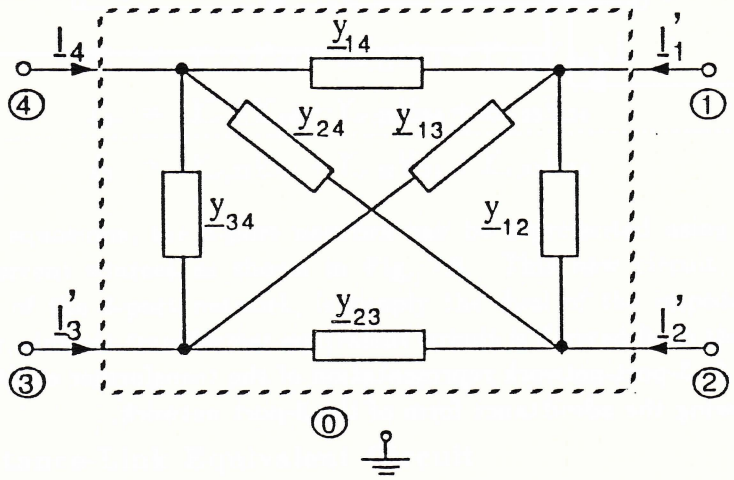


Figure 7.9: (a) 3-port-network equivalent circuit for a 4-winding transformer. (b) Corresponding 4-terminal admittance-link equivalent circuit.

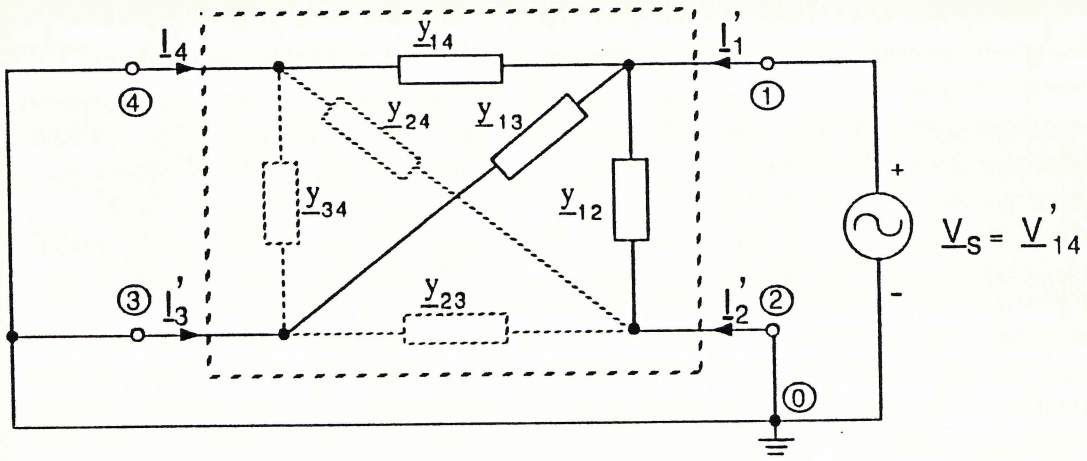


Figure 7.10: Hypothetical short-circuit test with terminal 1 of the admittance-link model excited and all other terminals shorted to ground.

3-port-network representations in Figs. 7.7 and 7.8 is simplicity; the admittance-link equivalent circuit contains only linear admittance elements with no controlled sources.

In the admittance-link equivalent circuit of Fig. 7.9(b), the terminal voltages and currents are the same as those in Fig. 7.5; hence, all currents except those associated with terminal 4 are shown with primes to indicate referral to winding 4. Once again, the unconnected ground symbol is included in Fig. 7.9(b) to allow terminal 0 to be called *ground*, and as a reminder that this node is not part of the equivalent circuit. The six branches or "links" of the equivalent circuit are labeled using the new lower-case symbol $\underline{y}_{jk}$, where j and k designate the adjoining terminals, to distinguish these admittances from all the others that have appeared so far. The choice of admittances instead of impedances for the labels is a natural outcome of the following derivation, but each admittance $\underline{y}_{jk}$ could be inverted to obtain the corresponding impedance of the link if that form is desired.

The simplest way to prove the equivalence of the two circuits in Fig. 7.9 is to derive the admittance values that cause the circuit in Part (b) to be described by the same equations as the circuit in Part (a), (7.24) through (7.26). This is done below by considering a series of hypothetical short-circuit-admittance tests in which one terminal of the equivalent circuit is excited relative to a common interconnection of the remaining three terminals as illustrated in Fig. 7.10. It is seen below how each of these tests causes several terms of network equations (7.24) through (7.26) to be zero, allowing superposition to be used in proving the equivalence of the two circuits.

These short-circuit-*admittance* tests are different from the short-circuit-*impedance* tests, usually called just *short-circuit tests*, which are the subject of Chapters 5 and 6. To represent a short-circuit-impedance test, one terminal of the admittance-link equivalent circuit would be excited relative to another, and the remaining terminals would be left unconnected or open-circuited.

To begin the derivation, the circuit in Fig. 7.10 has terminals 2, 3, and 4 shorted to ground, which sets voltages $\underline{V}_{24}$ and $\underline{V}_{34}$ to zero. This allows network equations (7.24) through (7.26) to be rewritten

$$\underline{I}'_1 = \underline{Y}_{r,11}\underline{V}_{14} \tag{7.27}$$

$$\underline{I}'_2 = \underline{Y}_{r,21}\underline{V}_{14} \tag{7.28}$$

$$\underline{I}'_3 = \underline{Y}_{r,31}\underline{V}_{14} \tag{7.29}$$

A new symbol, a double-subscripted current phasor of the form $\underline{I}_{jk}$, is now introduced to represent the current through each admittance link. For example, $\underline{I}_{12}$ represents the current flowing through admittance element $\underline{y}_{12}$ with a reference direction from terminal 1 to terminal 2.

Since no current flows through shorted admittance links, drawn with dashed lines in the figure, only the three admittance links connected to terminal 1 carry current in this short-circuit test, and

$$\underline{I}'_1 = \underline{I}_{12} + \underline{I}_{13} + \underline{I}_{14} \tag{7.30}$$

This also means, for example, that terminal current $\underline{I}'_2$ is equal to the admittance-link current $\underline{I}_{21}$, or $-\underline{I}_{12}$. It follows that

$$\underline{I}'_2 = -\underline{I}_{12} = -\underline{y}_{12}\underline{V}_{14} \tag{7.31}$$

$$\underline{I}'_3 = -\underline{I}_{13} = -\underline{y}_{13}\underline{V}_{14} \tag{7.32}$$

Equating the right-hand sides of (7.31) and (7.28), and doing the same for (7.32) and (7.29),

$$\underline{y}_{12} = -\underline{Y}_{r,21} = -\underline{Y}_{r,12} \tag{7.33}$$

$$\underline{y}_{13} = -\underline{Y}_{r,31} = -\underline{Y}_{r,13} \tag{7.34}$$

These are two of the admittance-link values in terms of elements in the reduced admittance matrix $[\underline{Y}_r]$. A third admittance-link value is obtained by combining (7.27) and (7.30).

$$\underline{Y}_{r,11} = \frac{\underline{I}'_1}{\underline{V}_{14}} = \frac{\underline{I}_{12} + \underline{I}_{13} + \underline{I}_{14}}{\underline{V}_{14}} = \underline{y}_{12} + \underline{y}_{13} + \underline{y}_{14} \tag{7.35}$$

Rearranging and substituting (7.33) and (7.34),

$$\underline{y}_{14} = \underline{Y}_{r,11} - \underline{y}_{12} - \underline{y}_{13} = \underline{Y}_{r,11} + \underline{Y}_{r,12} + \underline{Y}_{r,13} \tag{7.36}$$

Another short-circuit test is shown in Fig. 7.11, for which similar equations may be written as follows. Here, $\underline{V}_{14}$ and $\underline{V}_{34}$ are zero and the network equations (7.24) through (7.26) become

$$\underline{I}'_1 = \underline{Y}_{r,12}\underline{V}_{24} \tag{7.37}$$

$$\underline{I}'_2 = \underline{Y}_{r,22}\underline{V}_{24} \tag{7.38}$$

$$\underline{I}'_3 = \underline{Y}_{r,32}\underline{V}_{24} \tag{7.39}$$

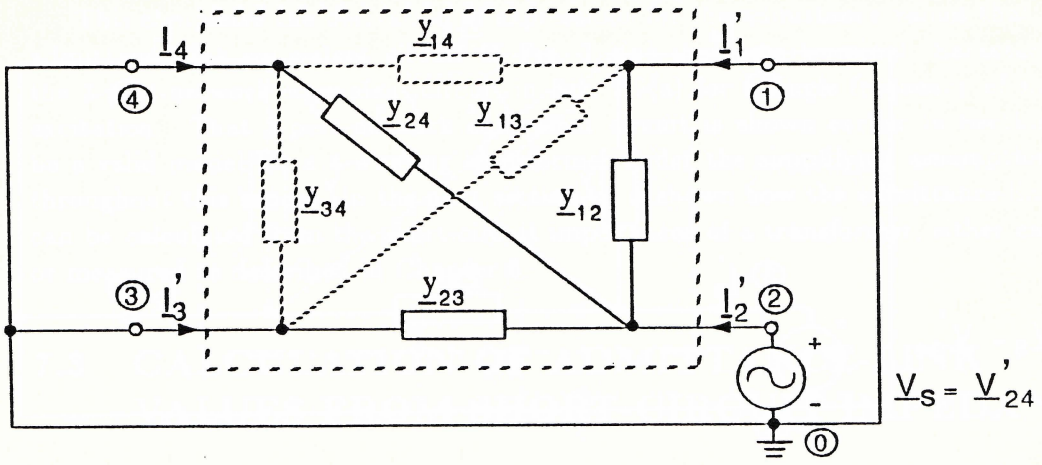


Figure 7.11: Hypothetical short-circuit test with terminal 2 of the admittance-link model excited and all other terminals shorted to ground.

In this case,

$$I'_2 = I_{21} + I_{23} + I_{24} \tag{7.40}$$

Each of the shorted-terminal currents flows through a single admittance link; for example,

$$I'_3 = I_{32} = y_{23}(-V_{24}) \tag{7.41}$$

Equating the right-hand sides of (7.39) and (7.41) gives

$$y_{23} = -Y_{r,32} = -Y_{r,23} \tag{7.42}$$

which is the fourth admittance-link value in terms of a reduced-admittance-matrix element. Another admittance-link value is obtained by combining (7.38) and (7.40).

$$Y_{r,22} = \frac{I'_2}{V_{24}} = \frac{I_{21} + I_{23} + I_{24}}{V_{24}} = y_{12} + y_{23} + y_{24} \tag{7.43}$$

Rearranging and substituting (7.33) and (7.42),

$$y_{24} = Y_{r,22} - y_{12} - y_{23} = Y_{r,22} + Y_{r,21} + Y_{r,23} \tag{7.44}$$

The sixth admittance-link value is calculated by considering the short-circuit test shown in Fig. 7.12. With V_{14} and V_{24} both zero, (7.26) may be written

$$Y_{r,33} = \frac{I'_3}{V_{34}} \tag{7.45}$$

Again, it is apparent from the circuit diagram that

$$I'_3 = I_{31} + I_{32} + I_{34} \tag{7.46}$$

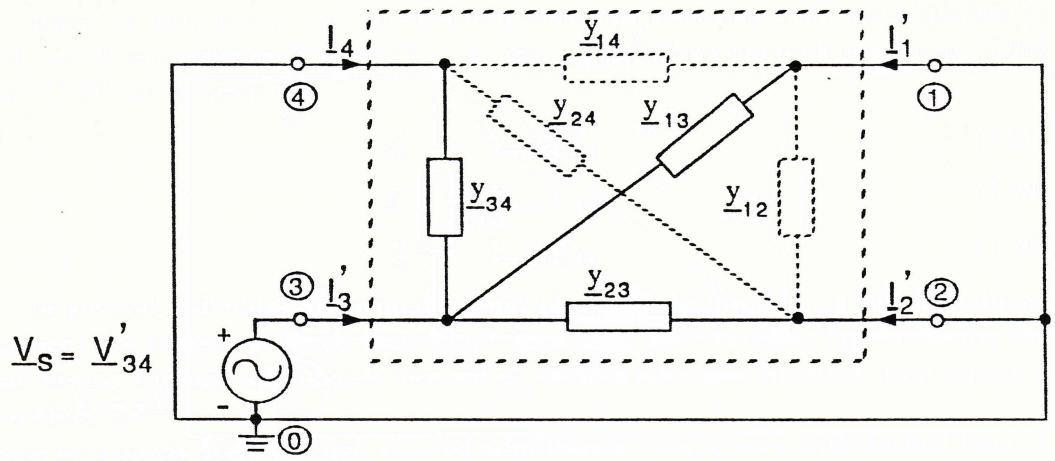


Figure 7.12: Hypothetical short-circuit test with terminal 3 of the admittance-link model excited and all other terminals shorted to ground.

which may be substituted into (7.45).

$$\underline{Y}_{r,33} = \frac{\underline{I}_{31} + \underline{I}_{32} + \underline{I}_{34}}{\underline{V}_{34}} = \underline{y}_{13} + \underline{y}_{23} + \underline{y}_{34} \tag{7.47}$$

Rearranging and substituting (7.34) and (7.42),

$$\underline{y}_{34} = \underline{Y}_{r,33} - \underline{y}_{13} - \underline{y}_{23} = \underline{Y}_{r,33} + \underline{Y}_{r,31} + \underline{Y}_{r,32} \tag{7.48}$$

The results of this derivation, which give the admittance-link values as functions of elements in the reduced admittance matrix $[\underline{Y}_r]$, may be expressed in just two equations with variable subscripts. The first encompasses (7.33), (7.34), and (7.42), and the second encompasses (7.36), (7.44), and (7.48).

$$\underline{y}_{jk} = -\underline{Y}_{r,jk} = -\underline{Y}_{r,kj} \qquad j < k;\ j,k = 1,2,3 \tag{7.49}$$

$$\underline{y}_{j4} = \sum_{k=1}^{3} \underline{Y}_{r,jk} \qquad j = 1,2,3 \tag{7.50}$$

The derivation here may be extended for a transformer with any number of windings K greater than or equal to two, with the following general results.

$$\underline{y}_{jk} = -\underline{Y}_{r,jk} = -\underline{Y}_{r,kj} \qquad j < k;\ j,k = 1,2,\ldots,(K-1) \tag{7.51}$$

$$\underline{y}_{jK} = \sum_{k=1}^{K-1} \underline{Y}_{r,jk} \qquad j = 1,2,\ldots,(K-1) \tag{7.52}$$

This completes the derivation of expressions for the admittance values that give the admittance-link equivalent circuit in Fig. 7.9(b) the same terminal characteristics as the 3-port-network equivalent circuit in Fig. 7.9(a) for a single frequency of sinusoidal excitation. That 3-port-network equivalent circuit is shown earlier in Section 7.2 to be a valid model for a 4-winding transformer under the simplifying assumptions made throughout this report. In the next section, it is shown how the admittance-link values can be calculated from the short-circuit impedances of a transformer, either calculated or measured as described in Chapter 6.

7.3 CALCULATION OF ADMITTANCE-LINK VALUES FROM SHORT-CIRCUIT IMPEDANCES

It is shown in Section 7.2 that, under the simplifying assumptions of negligible magnetizing current and no capacitive coupling between windings, the admittance-link model of Fig. 7.9(b) can completely characterize the ac behavior of a 4-winding transformer for any chosen frequency. In this section, equations are derived by which the necessary admittance-link values can be calculated from the short-circuit impedances of the transformer.

Although the values of the elements in the admittance-link model are frequency-dependent, they are independent of the particular combination of linear loads and sinusoidal excitation sources connected to the transformer. The principle of superposition allows transformer behavior to be predicted for an infinite number of source-load combinations from just a few pieces of information, namely, the short-circuit impedances of the transformer. Loads may be of any size, from as small as an open circuit to as large as a short circuit.

The following derivation is carried out for the example 4-winding transformer, then the results are generalized to a transformer with K windings. More specifically, equations are derived by which the values of six admittance links in circuit of Fig. 7.9(b) can be calculated from the six short-circuit impedances of the transformer. Although the derivation is somewhat involved, the resulting equations are quite simple and are summarized in Section 7.3.4. An example calculation of a set of admittance-link values is given in Section 7.3.5.

7.3.1 Obtaining the Reduced Impedance Martix from the Short-Circuit Impedances

Equations for the elements of the reduced impedance matrix $[\underline{Z}_r]$ are derived in this section by considering some hypothetical short-circuit-impedance tests performed on the admittance-link equivalent circuit of Fig. 7.9(b). After the entries of $[\underline{Z}_r]$ have been deduced, the reduced admittance matrix $[\underline{Y}_r]$ is obtained by inverting $[\underline{Z}_r]$ according to (7.22). The values of the individual admittance links are finally computed according to the generalized equations (7.51) and (7.52).

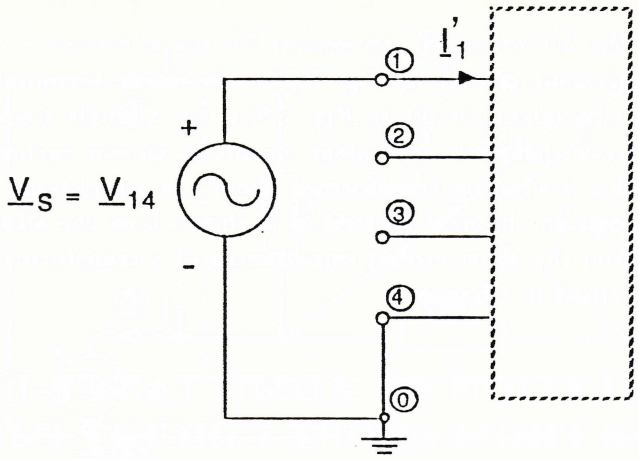


Figure 7.13: Short-circuit test (14) applied to the 4-terminal equivalent circuit to determine the impedance $\underline{Z}_{r,11}$.

The admittance-link equivalent circuit is represented here by the 4-terminal "black box" shown in Fig. 7.13, which corresponds to the dashed box in either part of Fig. 7.9. The network equations for the admittance-link equivalent circuit in terms of the elements of $[\underline{Z}_r]$ are repeated here from (7.20).

$$\underline{V}_{14} = \underline{Z}_{r,11}\underline{I}'_1 + \underline{Z}_{r,12}\underline{I}'_2 + \underline{Z}_{r,13}\underline{I}'_3 \tag{7.53}$$

$$\underline{V}_{24} = \underline{Z}_{r,21}\underline{I}'_1 + \underline{Z}_{r,22}\underline{I}'_2 + \underline{Z}_{r,23}\underline{I}'_3 \tag{7.54}$$

$$\underline{V}_{34} = \underline{Z}_{r,31}\underline{I}'_1 + \underline{Z}_{r,32}\underline{I}'_2 + \underline{Z}_{r,33}\underline{I}'_3 \tag{7.55}$$

To calculate the diagonal elements of $[\underline{Z}_r]$, terminal 4 of the equivalent circuit is connected to ground and each of the other terminals is excited in turn. This corresponds to short-circuiting winding 4 of the transformer and exciting each of the other windings, i.e., performing short-circuit tests (14), (24), and (34) in the notation introduced in Section 5.1.2.

For the first test, illustrated in Fig. 7.13, terminal 1 of the circuit is excited, terminal 4 is grounded, and the remaining terminals are left open-circuited. Since $\underline{I}'_2$ and $\underline{I}'_3$ are zero, (7.53) reduces to

$$\underline{Z}_{r,11} = \frac{\underline{V}_{14}}{\underline{I}'_1} \tag{7.56}$$

Substituting the expression for $\underline{V}_{14}$ from (7.16) and the value of $\underline{I}'_1$ from (7.5), and recognizing that $\underline{V}_4 = 0$ for this test, this equation can be written in terms of an actual, unprimed voltage and current as

$$\underline{Z}_{r,11} = \frac{\left(\frac{N_4}{N_1}\right)\underline{V}_1 - \underline{V}_4}{\left(\frac{N_1}{N_4}\right)\underline{I}_1} = \left(\frac{N_4}{N_1}\right)^2 \frac{\underline{V}_1}{\underline{I}_1} \tag{7.57}$$

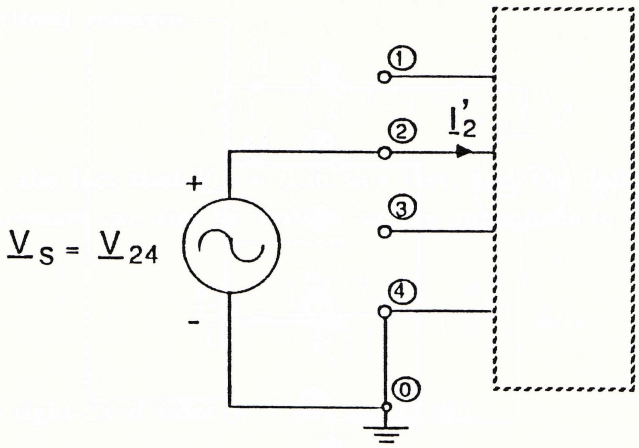


Figure 7.14: Short-circuit test (24) applied to the 4-terminal equivalent circuit to determine the impedance $\underline{Z}_{r,22}$.

Referring to Fig. 7.5, it can be seen that the external connections to the admittance-link equivalent circuit in Fig. 7.9 represent short-circuit-impedance test (14) on the actual transformer, in which winding 1 is excited, winding 4 is short-circuited, and the remaining windings are left open-circuited ($\underline{I}_2 = \underline{I}_3 = 0$). Under these circumstances, $\underline{V}_1/\underline{I}_1$ in (7.57) is simply short-circuit impedance $\underline{Z}_{(14)}$.

$$\underline{Z}_{r,11} = \left(\frac{N_4}{N_1}\right)^2 \underline{Z}_{(14)} \tag{7.58}$$

For the next hypothetical test, terminal 2 of the equivalent circuit is excited and terminal 4 is grounded as shown in Fig. 7.14. In the same manner as above,

$$\begin{aligned} \underline{Z}_{r,22} &= \frac{\underline{V}_{24}}{\underline{I}'_2} \\ &= \frac{\left(\frac{N_4}{N_2}\right)\underline{V}_2 - \underline{V}_4}{\left(\frac{N_2}{N_4}\right)\underline{I}_2} = \left(\frac{N_4}{N_2}\right)^2 \frac{\underline{V}_2}{\underline{I}_2} \end{aligned} \tag{7.59}$$

$$\underline{Z}_{r,22} = \left(\frac{N_4}{N_2}\right)^2 \underline{Z}_{(24)} \tag{7.60}$$

Similar equations could be written for the third test with terminal 3 excited and terminal 4 grounded, but the pattern is clear: From short-circuit tests with terminal 4 grounded, the diagonal elements of $[\underline{Z}_r]$ are obtained.

$$\underline{Z}_{r,jj} = \left(\frac{N_4}{N_j}\right)^2 \underline{Z}_{(j4)} \qquad j = 1,2,3 \tag{7.61}$$

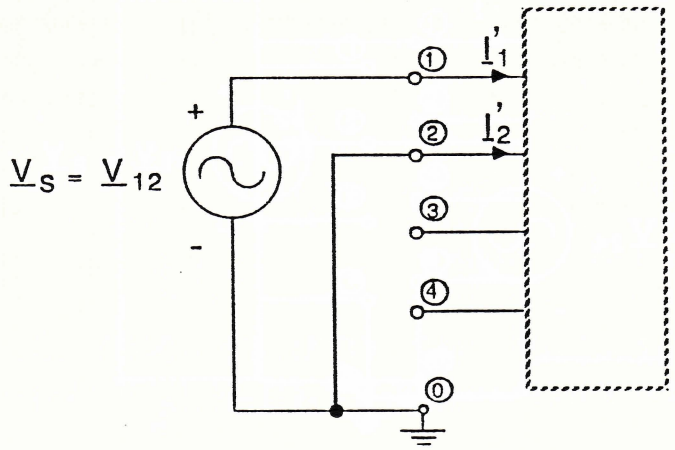


Figure 7.15: Short-circuit test (12) applied to the 4-terminal equivalent circuit to determine the impedance $\underline{Z}_{r,12}$.

Because only two windings are involved in each of these short-circuit tests, this result is easily extended to a transformer with K windings.

$$\underline{Z}_{r,jj} = \left(\frac{N_K}{N_j}\right)^2 \underline{Z}_{(jK)} \qquad j = 1, 2, \ldots, (K-1) \tag{7.62}$$

Expressions for the off-diagonal elements of the symmetric matrix $[\underline{Z}_r]$ are found by considering the remaining three hypothetical short-circuit tests, (12), (13), and (23). First, terminal 1 is excited and terminal 2 is grounded as shown in Fig. 7.15. With $\underline{I}'_3 = 0$, (7.53) and (7.54) may be written

$$\underline{V}_{14} = \underline{Z}_{r,11}\underline{I}'_1 + \underline{Z}_{r,12}\underline{I}'_2 \tag{7.63}$$

$$\underline{V}_{24} = \underline{Z}_{r,21}\underline{I}'_1 + \underline{Z}_{r,22}\underline{I}'_2 \tag{7.64}$$

Subtracting (7.64) from (7.63) and using $\underline{V}_{14} - \underline{V}_{24} = \underline{V}_{12}$ from (7.15), $\underline{Z}_{r,21} = \underline{Z}_{r,12}$ from (7.19), and $\underline{I}'_2 = -\underline{I}'_1$ from Fig. 7.15,

$$\begin{aligned} \underline{V}_{12} &= (\underline{Z}_{r,11} - \underline{Z}_{r,21})\underline{I}'_1 + (\underline{Z}_{r,12} - \underline{Z}_{r,22})\underline{I}'_2 \\ &= (\underline{Z}_{r,11} + \underline{Z}_{r,22} - 2\underline{Z}_{r,12})\underline{I}'_1 \end{aligned} \tag{7.65}$$

$$\frac{\underline{V}_{12}}{\underline{I}'_1} = \underline{Z}_{r,11} + \underline{Z}_{r,22} - 2\underline{Z}_{r,12} \tag{7.66}$$

By the definition of differential voltages in (7.15), the quantity $\underline{V}_{12}$ may be written in

terms of unprimed voltages.

$$\underline{V}_{12} = \left(\frac{N_4}{N_1}\right)\underline{V}_1 - \left(\frac{N_4}{N_2}\right)\underline{V}_2 \tag{7.67}$$

Using (7.67), the fact that $\underline{V}_2 = 0$ in this test, and the definition of $\underline{I}'_1$ in (7.5), the following expression can also be written for the impedance in (7.66).

$$\frac{\underline{V}_{12}}{\underline{I}'_1} = \frac{\left(\frac{N_4}{N_1}\right)\underline{V}_1}{\left(\frac{N_1}{N_4}\right)\underline{I}_1} = \left(\frac{N_4}{N_1}\right)^2 \underline{Z}_{(12)} \tag{7.68}$$

Equating the right-hand sides of (7.68) and (7.66),

$$\left(\frac{N_4}{N_1}\right)^2 \underline{Z}_{(12)} = \underline{Z}_{r,11} + \underline{Z}_{r,22} - 2\underline{Z}_{r,12} \tag{7.69}$$

Rearranging,

$$\underline{Z}_{r,12} = \frac{1}{2}\left[\underline{Z}_{r,11} + \underline{Z}_{r,22} - \left(\frac{N_4}{N_1}\right)^2 \underline{Z}_{(12)}\right] \tag{7.70}$$

Then substituting (7.58) and (7.60) gives

$$\begin{aligned} \underline{Z}_{r,12} = \underline{Z}_{r,21} &= \frac{1}{2}\left[\left(\frac{N_4}{N_1}\right)^2 \underline{Z}_{(14)} + \left(\frac{N_4}{N_2}\right)^2 \underline{Z}_{(24)} - \left(\frac{N_4}{N_1}\right)^2 \underline{Z}_{(12)}\right] \\ &= \frac{N_4^2}{2}\left(\frac{\underline{Z}_{(14)} - \underline{Z}_{(12)}}{N_1^2} + \frac{\underline{Z}_{(24)}}{N_2^2}\right) \end{aligned} \tag{7.71}$$

The next hypothetical short-circuit test has terminal 2 excited and terminal 3 grounded as shown in Fig. 7.16. The following equations which are analogous to (7.63) through (7.71) are obtained by a parallel argument.

With $\underline{I}'_1 = 0$, (7.54) and (7.55) may be written

$$\underline{V}_{24} = \underline{Z}_{r,22}\underline{I}'_2 + \underline{Z}_{r,23}\underline{I}'_3 \tag{7.72}$$

$$\underline{V}_{34} = \underline{Z}_{r,32}\underline{I}'_2 + \underline{Z}_{r,33}\underline{I}'_3 \tag{7.73}$$

Subtracting (7.73) from (7.72) and using $\underline{V}_{24} - \underline{V}_{34} = \underline{V}_{23}$, $\underline{Z}_{r,32} = \underline{Z}_{r,23}$, and for this test, $\underline{I}'_3 = -\underline{I}'_2$,

$$\begin{aligned} \underline{V}_{23} &= (\underline{Z}_{r,22} - \underline{Z}_{r,32})\underline{I}'_2 + (\underline{Z}_{r,23} - \underline{Z}_{r,33})\underline{I}'_3 \\ &= (\underline{Z}_{r,22} + \underline{Z}_{r,33} - 2\underline{Z}_{r,23})\underline{I}'_2 \end{aligned} \tag{7.74}$$

$$\frac{\underline{V}_{23}}{\underline{I}'_2} = \underline{Z}_{r,22} + \underline{Z}_{r,33} - 2\underline{Z}_{r,23} \tag{7.75}$$

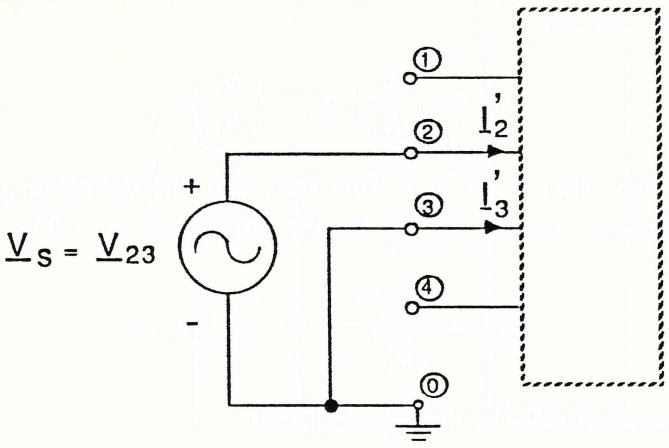


Figure 7.16: Short-circuit test (23) applied to the 4-terminal equivalent circuit to determine the impedance $\underline{Z}_{r,23}$.

By the definition of differential voltages (7.15), the quantity $\underline{V}_{23}$ may be written in terms of the voltages across the transformer windings in Fig. 7.3.

$$\underline{V}_{23} = \left(\frac{N_4}{N_2}\right)\underline{V}_2 - \left(\frac{N_4}{N_3}\right)\underline{V}_3 \tag{7.76}$$

Using (7.76), the fact that $\underline{V}_3 = 0$ in this test, and the definition of $\underline{I}'_2$ in (7.5), the following expression can also be written for the impedance in (7.75).

$$\frac{\underline{V}_{23}}{\underline{I}'_2} = \frac{\left(\frac{N_4}{N_2}\right)\underline{V}_2}{\left(\frac{N_2}{N_4}\right)\underline{I}_2} = \left(\frac{N_4}{N_2}\right)^2 \underline{Z}_{(23)} \tag{7.77}$$

Equating the right-hand sides of (7.77) and (7.75),

$$\left(\frac{N_4}{N_2}\right)^2 \underline{Z}_{(23)} = \underline{Z}_{r,22} + \underline{Z}_{r,33} - 2\underline{Z}_{r,23} \tag{7.78}$$

Rearranging,

$$\underline{Z}_{r,23} = \frac{1}{2}\left[\underline{Z}_{r,22} + \underline{Z}_{r,33} - \left(\frac{N_4}{N_2}\right)^2 \underline{Z}_{(23)}\right] \tag{7.79}$$

Then substituting (7.61) with $j = 2$ and $j = 3$,

$$\begin{aligned} \underline{Z}_{r,23} = \underline{Z}_{r,32} &= \frac{1}{2}\left[\left(\frac{N_4}{N_2}\right)^2 \underline{Z}_{(24)} + \left(\frac{N_4}{N_3}\right)^2 \underline{Z}_{(34)} - \left(\frac{N_4}{N_2}\right)^2 \underline{Z}_{(23)}\right] \\ &= \frac{N_4^2}{2}\left(\frac{\underline{Z}_{(24)} - \underline{Z}_{(23)}}{N_2^2} + \frac{\underline{Z}_{(34)}}{N_3^2}\right) \end{aligned} \tag{7.80}$$

Equations could be written for the last remaining short-circuit test with terminal 1 excited and terminal 3 grounded, but it is apparent from (7.71) and (7.80) that any off-diagonal element of $[\underline{Z}_r]$ may be calculated by

$$\underline{Z}_{r,jk} = \underline{Z}_{r,kj} = \frac{N_4^2}{2}\left(\frac{\underline{Z}_{(j4)} - \underline{Z}_{(jk)}}{N_j^2} + \frac{\underline{Z}_{(k4)}}{N_k^2}\right) \qquad j \neq k;\ \ j,k = 1,2,3 \tag{7.81}$$

Once again, this result may be generalized to a transformer with K windings.

$$\underline{Z}_{r,jk} = \underline{Z}_{r,kj} = \frac{N_K^2}{2}\left(\frac{\underline{Z}_{(jK)} - \underline{Z}_{(jk)}}{N_j^2} + \frac{\underline{Z}_{(kK)}}{N_k^2}\right) \qquad j \neq k;\ \ j,k = 1,2,\ldots,(K-1) \tag{7.82}$$

Using the boxed expressions (7.62) and (7.82), one may now calculate all the elements of the symmetric reduced impedance matrix $[\underline{Z}_r]$ defined in (7.21) from the short-circuit impedances of the transformer.

7.3.2 Inverting the Reduced Impedance Matrix

The symmetric reduced impedance matrix $[\underline{Z}_r]$ in (7.21) can be inverted to obtain the symmetric reduced admittance matrix, an equivalent description of the 3-port network in Fig. 7.9(a).

$$[\underline{Y}_r] = [\underline{Z}_r]^{-1} \tag{7.83}$$

The inverse of a complex matrix may be obtained by the same methods used for a real matrix, namely, by using cofactors or an LU decomposition, but complex arithmetic is avoided altogether in the following algorithm [10].

To invert an $(n \times n)$ complex matrix, let

$$[\underline{Z}] = [A] + j[B] \tag{7.84}$$

where $[A]$ and $[B]$ are real-valued. The following $(2n \times 2n)$ block-partitioned matrix is formed:

$$[\tilde{Z}] = \begin{bmatrix} [A] & -[B] \\ [B] & [A] \end{bmatrix} \tag{7.85}$$

The real-valued matrix $[\tilde{Z}]$ is inverted using any suitable method to obtain a result which may be partitioned as follows, giving two new $(n \times n)$ matrices $[C]$ and $[D]$.

$$[\tilde{Z}]^{-1} = \begin{bmatrix} [C] & -[D] \\ [D] & [C] \end{bmatrix} \tag{7.86}$$

By definition, the identity matrix results from multiplying a matrix by its inverse.

$$\begin{aligned}[I] &= [\tilde{Z}][\tilde{Z}]^{-1} \\ &= \begin{bmatrix} [A] & -[B] \\ [B] & [A] \end{bmatrix} \begin{bmatrix} [C] & -[D] \\ [D] & [C] \end{bmatrix} \\ &= \begin{bmatrix} \{[A][C]-[B][D]\} & \{-[A][D]-[B][C]\} \\ \{[B][C]+[A][D]\} & \{-[B][D]+[A][C]\} \end{bmatrix} \end{aligned} \tag{7.87}$$

Thus,

$$[A][C] - [B][D] = [I] \tag{7.88}$$

$$[A][D] + [B][C] = [0] \tag{7.89}$$

Now, let a new $(n \times n)$ complex matrix $[\underline{U}]$ be defined in terms of $[C]$ and $[D]$ from (7.86).

$$[\underline{U}] = [C] + j[D] \tag{7.90}$$

Multiplying (7.84) and (7.90),

$$\begin{aligned}[\underline{Z}][\underline{U}] &= \{[A] + j[B]\}\{[C] + j[D]\} \\ &= [A][C] - [B][D] + j\{[A][D] + [B][C]\} \end{aligned} \tag{7.91}$$

Substituting (7.88) and (7.89),

$$[\underline{Z}][\underline{U}] = [I] + j[0] = [I] \tag{7.92}$$

By the definition of the inverse of a matrix,

$$[\underline{Z}]^{-1} = [\underline{U}] = [C] + j[D] \tag{7.93}$$

Thus the inverse of an $(n \times n)$ complex matrix can be obtained by inverting a $(2n \times 2n)$ *real* matrix instead.

7.3.3 Obtaining the Admittance-Link Values from the Reduced Admittance Matrix

The values of the admittances in the admittance-link model for a K-winding transformer are calculated from the elements of its reduced admittance matrix $[\underline{Y}_r]$ using (7.51) and (7.52), derived in Section 7.2.5 and repeated in the following summary.

7.3.4 Summary of Equations

Using the equations derived in Sections 7.3.1 and 7.2.5, the values of the elements in the admittance-link equivalent circuit of Fig. 7.9(b) can be calculated from the short-circuit impedances of the transformer in three steps:

1. Calculate the reduced impedance matrix $[\underline{Z}_r]$ from the short-circuit impedances of the transformer using (7.62) and (7.82), repeated below. The short-circuit impedances are obtained either by calculation from the geometry of the winding layers as described in Section 6.1, or by measurement in the laboratory of the actual transformer as described in Section 6.3.

$$\underline{Z}_{r,jj} = \left(\frac{N_K}{N_j}\right)^2 \underline{Z}_{(jK)} \qquad j = 1,2,\ldots,(K-1) \tag{7.94}$$

$$\underline{Z}_{r,jk} = \underline{Z}_{r,kj} = \frac{N_K^2}{2}\left(\frac{\underline{Z}_{(jK)} - \underline{Z}_{(jk)}}{N_j^2} + \frac{\underline{Z}_{(kK)}}{N_k^2}\right) \qquad j \neq k;\ \ j,k = 1,2,\ldots,(K-1) \tag{7.95}$$

2. Invert the reduced impedance matrix $[\underline{Z}_r]$ by the algorithm in Section 7.3.2 or any suitable technique to obtain the reduced admittance matrix $[\underline{Y}_r]$.

3. Calculate the admittance-link values from the elements of the reduced admittance matrix $[\underline{Y}_r]$ using (7.51) and (7.52), repeated here.

$$\underline{y}_{jk} = -\underline{Y}_{r,jk} = -\underline{Y}_{r,kj} \qquad j < k;\ \ j,k = 1,2,\ldots,(K-1) \tag{7.96}$$

$$\underline{y}_{jK} = \sum_{k=1}^{K-1} \underline{Y}_{r,jk} \qquad j = 1,2,\ldots,(K-1) \tag{7.97}$$

After the admittance-link values are calculated by the three steps above, some simple checks can be performed to verify that the values are reasonable. First, the real and imaginary parts of each admittance-link value should have opposite signs [13, p. 638]. Second, for each complex sum

$$\underline{S}_j = \sum_{k<j} \underline{y}_{kj} + \sum_{k>j} \underline{y}_{jk} \qquad j,k = 1,2,\ldots,K \tag{7.98}$$

Table 7.1: Calculated Short-Circuit Impedances at 100 kHz

Test (jk)	*Resistance* $R_{(jk)}$ (ohms)	*Inductance* $L_{(jk)}$ (henrys)	*Impedance* $\underline{Z}_{(jk)}$ (ohms)
(12)	0.5869	2.031×10^{-6}	$(0.5869 + j1.276)$
(13)	1.493	5.091×10^{-6}	$(1.493 + j3.199)$
(14)	2.527	8.582×10^{-6}	$(2.527 + j5.392)$
(23)	0.6814	2.358×10^{-6}	$(0.6814 + j1.482)$
(24)	1.716	5.849×10^{-6}	$(1.716 + j3.675)$
(34)	0.7758	2.685×10^{-6}	$(0.7758 + j1.687)$

the real part should be positive, and for all but the highest frequencies where capacitive effects dominate, the imaginary part should be negative [13, p. 636]. And third, the first $(K-1)$ of these sums should be equal to the corresponding diagonal elements of $[\underline{Y}_r]$, an observation which follows directly from (7.35), (7.43), and (7.47).

$$\underline{S}_j = \underline{Y}_{r,jj} \qquad j = 1, 2, \ldots, (K-1) \tag{7.99}$$

7.3.5 Calculation Example

In this section, it is shown how the boxed equations in summary Section 7.3.4 are used to calculate the set of admittance-link values for an example transformer. The 4-winding EE-core transformer described in Section 6.1.1 and used for the numerical example there is used here as well.

Section 6.1 details the calculation of the short-circuit resistance $R_{(13)}$ and the short-circuit inductance $L_{(13)}$ of the transformer at 60°C and 100 kHz. Following that example, and using data from Tables 6.1, 6.2, 6.3, and 6.5, the remaining short-circuit resistances and inductances are calculated, with the results given in Table 7.1. These numbers are also contained in the plotted data of Figs. 6.5 and 6.6. The short-circuit impedances in the last column of Table 7.1 are calculated as

$$\underline{Z}_{(jk)} = R_{(jk)} + j\omega L_{(jk)} \tag{7.100}$$

where the angular frequency $\omega = 2\pi f$ for $f = 100$ kHz. These six impedances are all that is needed to calculate the parameters of the admittance-link model. However, *the resulting parameter values are valid only for a single frequency*; they must be recalculated for each frequency of interest.

Throughout this example, impedances and admittances are expressed in the rectangular form for complex numbers to facilitate their addition and subtraction. The data in this example are typically written with four significant figures to guard against rounding error in later calculations, although it is known that the actual precision of the data is

much less. The three subsections below correspond to the three steps for calculating the admittance-link values outlined in Section 7.3.4.

Step 1—Calculate the Reduced Impedance Matrix

From the six short-circuit impedances of the transformer listed in Table 7.1, and the fact that each of the four windings of the transformer has 26 turns, the elements of the reduced impedance matrix $[\underline{Z}_r]$ are calculated, thus defining the hypothetical 3-port network of Fig. 7.7. First, the self-impedances are obtained from (7.94), repeated here, with $K = 4$.

$$\underline{Z}_{r,jj} = \left(\frac{N_K}{N_j}\right)^2 \underline{Z}_{(jK)} \qquad j = 1, 2, \ldots, (K-1) \tag{7.101}$$

$$\begin{aligned} \underline{Z}_{r,11} &= \left(\frac{N_4}{N_1}\right)^2 \underline{Z}_{(14)} \\ &= \left(\frac{26}{26}\right)^2 (2.527 + j5.392) = (2.527 + j5.392)\ \Omega \end{aligned} \tag{7.102}$$

$$\underline{Z}_{r,22} = \left(\frac{N_4}{N_2}\right)^2 \underline{Z}_{(24)} = (1.716 + j3.675)\ \Omega \tag{7.103}$$

$$\underline{Z}_{r,33} = \left(\frac{N_4}{N_3}\right)^2 \underline{Z}_{(34)} = (0.7758 + j1.687)\ \Omega \tag{7.104}$$

The mutual impedances are obtained from (7.95), also repeated here.

$$\underline{Z}_{r,jk} = \underline{Z}_{r,kj} = \frac{N_K^2}{2}\left(\frac{\underline{Z}_{(jK)} - \underline{Z}_{(jk)}}{N_j^2} + \frac{\underline{Z}_{(kK)}}{N_k^2}\right) \tag{7.105}$$

$$j \neq k;\ \ j, k = 1, 2, \ldots, (K-1)$$

$$\begin{aligned} \underline{Z}_{r,12} &= \underline{Z}_{r,21} = \frac{N_4^2}{2}\left(\frac{\underline{Z}_{(14)} - \underline{Z}_{(12)}}{N_1^2} + \frac{\underline{Z}_{(24)}}{N_2^2}\right) \\ &= \frac{26^2}{2}\left(\frac{(2.527 + j5.392) - (0.5869 + j1.276)}{26^2} + \frac{(1.716 + j3.675)}{26^2}\right) \\ &= (1.828 + j3.896)\ \Omega \end{aligned} \tag{7.106}$$

$$\begin{aligned} \underline{Z}_{r,13} &= \underline{Z}_{r,31} = \frac{N_4^2}{2}\left(\frac{\underline{Z}_{(14)} - \underline{Z}_{(13)}}{N_1^2} + \frac{\underline{Z}_{(34)}}{N_3^2}\right) \\ &= \frac{26^2}{2}\left(\frac{(2.527 + j5.392) - (1.493 + j3.199)}{26^2} + \frac{(0.7758 + j1.687)}{26^2}\right) \\ &= (0.9049 + j1.940)\ \Omega \end{aligned} \tag{7.107}$$

$$\underline{Z}_{r,23} = \underline{Z}_{r,32} = \frac{N_4^2}{2}\left(\frac{\underline{Z}_{(24)} - \underline{Z}_{(23)}}{N_2^2} + \frac{\underline{Z}_{(34)}}{N_3^2}\right)$$

$$= \frac{26^2}{2}\left(\frac{(1.716 + j3.675) - (0.6814 + j1.482)}{26^2} + \frac{(0.7758 + j1.687)}{26^2}\right)$$

$$= (0.9052 + j1.940)\ \Omega \tag{7.108}$$

The reduced impedance matrix is thus

$$[\underline{Z}_r] = \begin{bmatrix} \underline{Z}_{r,11} & \underline{Z}_{r,12} & \underline{Z}_{r,13} \\ \underline{Z}_{r,21} & \underline{Z}_{r,22} & \underline{Z}_{r,23} \\ \underline{Z}_{r,31} & \underline{Z}_{r,32} & \underline{Z}_{r,33} \end{bmatrix}$$

$$= \begin{bmatrix} (2.527 + j5.392) & (1.828 + j3.896) & (0.9049 + j1.940) \\ (1.828 + j3.896) & (1.716 + j3.675) & (0.9052 + j1.940) \\ (0.9049 + j1.940) & (0.9052 + j1.940) & (0.7758 + j1.687) \end{bmatrix} \tag{7.109}$$

Step 2—Invert the Reduced Impedance Matrix

The reduced impedance matrix in (7.109) is inverted by the algorithm described in Section 7.3.2 to obtain the reduced admittance matrix.

$$[\underline{Y}_r] = [\underline{Z}_r]^{-1} = \begin{bmatrix} (0.3048 - j0.6661) & (-0.3481 + j0.7720) & (0.04908 - j0.1225) \\ (-0.3481 + j0.7720) & (0.6591 - j1.468) & (-0.3541 + j0.8040) \\ (0.04908 - j0.1225) & (-0.3541 + j0.8040) & (0.5723 - j1.277) \end{bmatrix}$$

$$= \begin{bmatrix} \underline{Y}_{r,11} & \underline{Y}_{r,12} & \underline{Y}_{r,13} \\ \underline{Y}_{r,21} & \underline{Y}_{r,22} & \underline{Y}_{r,23} \\ \underline{Y}_{r,31} & \underline{Y}_{r,32} & \underline{Y}_{r,33} \end{bmatrix} \tag{7.110}$$

Step 3—Calculate the Admittance-Link Values

The values of the elements in the admittance-link model of Fig. 7.9(b) are calculated from the elements of $[\underline{Y}_r]$ given in (7.110) as follows. Three of the values are obtained from (7.96), repeated here, with $K = 4$.

$$\underline{y}_{jk} = -\underline{Y}_{r,jk} \qquad j \neq k;\ j,k = 1,2,\ldots,(K-1) \tag{7.111}$$

$$\underline{y}_{12} = -\underline{Y}_{r,12} = (0.3481 - j0.7720)\ \text{S} \tag{7.112}$$

$$\underline{y}_{13} = -\underline{Y}_{r,13} = (-0.0491 + j0.1225)\ \text{S} \tag{7.113}$$

$$\underline{y}_{23} = -\underline{Y}_{r,23} = (0.3541 - j0.8040)\ \text{S} \tag{7.114}$$

The remaining three admittance-link values are obtained from (7.97), also repeated here.

$$\underline{y}_{jK} = \sum_{k=1}^{K-1} \underline{Y}_{r,jk} \qquad j = 1,2,\ldots,(K-1) \tag{7.115}$$

Table 7.2: Admittance-Link Values

Link jk	*Admittance* $\underline{y}_{jk}$ (siemens)
12	$(0.3481 - j0.7720)$
13	$(-0.0491 + j0.1225)$
14	$(0.0058 - j0.0166)$
23	$(0.3541 - j0.8040)$
24	$(-0.0431 + j0.1080)$
34	$(0.2673 - j0.5955)$

$$\begin{aligned}
\underline{y}_{14} &= \sum_{k=1}^{3} \underline{Y}_{r,1k} = \underline{Y}_{r,11} + \underline{Y}_{r,12} + \underline{Y}_{r,13} \\
&= (0.3048 - j0.6661) + (-0.3481 + j0.7720) + (0.04908 - j0.1225) \\
&= (0.0058 - j0.0166) \text{ S} \qquad (7.116)
\end{aligned}$$

$$\begin{aligned}
\underline{y}_{24} &= \sum_{k=1}^{3} \underline{Y}_{r,2k} = \underline{Y}_{r,21} + \underline{Y}_{r,22} + \underline{Y}_{r,23} \\
&= (-0.3481 + j0.7720) + (0.6591 - j1.468) + (-0.3541 + j0.8040) \\
&= (-0.0431 + j0.1080) \text{ S} \qquad (7.117)
\end{aligned}$$

$$\begin{aligned}
\underline{y}_{34} &= \sum_{k=1}^{3} \underline{Y}_{r,3k} = \underline{Y}_{r,31} + \underline{Y}_{r,32} + \underline{Y}_{r,33} \\
&= (0.04908 - j0.1225) + (-0.3541 + j0.8040) + (0.5723 - j1.277) \\
&= (0.2673 - j0.5955) \text{ S} \qquad (7.118)
\end{aligned}$$

These admittance-link values, repeated in Table 7.2, completely define the admittance-link model for the example transformer at 60°C and 100 kHz.

If desired, the checks for calculation errors described at the end of Section 7.3.4 may be carried out. First, the real and imaginary parts of each admittance-link value in Table 7.2 have opposite signs, as expected. Second, the following sums from (7.98) all have positive real parts and negative imaginary parts, as expected.

$$\begin{aligned}
S_1 &= \underline{y}_{12} + \underline{y}_{13} + \underline{y}_{14} \\
&= (0.3481 - j0.7720) + (-0.0491 + j0.1225) + (0.0058 - j0.0166) \\
&= (0.3048 - j0.6661) \text{ S} \qquad (7.119)
\end{aligned}$$

$$\begin{aligned} S_2 &= \underline{y}_{12} + \underline{y}_{23} + \underline{y}_{24} \\ &= (0.3481 - j0.7720) + (0.3541 - j0.8040) + (-0.0431 + j0.1080) \\ &= (0.6591 - j1.468) \text{ S} \end{aligned} \tag{7.120}$$

$$\begin{aligned} S_3 &= \underline{y}_{13} + \underline{y}_{23} + \underline{y}_{34} \\ &= (-0.0491 + j0.1225) + (0.3541 - j0.8040) + (0.2673 - j0.5955) \\ &= (0.5723 - j1.277) \text{ S} \end{aligned} \tag{7.121}$$

$$\begin{aligned} S_4 &= \underline{y}_{14} + \underline{y}_{24} + \underline{y}_{34} \\ &= (0.0058 - j0.0166) + (-0.0431 + j0.1080) + (0.2673 - j0.5955) \\ &= (0.2300 - j0.5041) \text{ S} \end{aligned} \tag{7.122}$$

And third, S_1, S_2, and S_3 above are equal to their respective diagonal elements in (7.110), as expected. No calculation errors are revealed by the three checks.

7.4 APPLICATION OF THE ADMITTANCE-LINK MODEL

Assumption 1 in Section 7.2.1, the assumption of high-permeability core material, is equivalent to saying that the core has negligible exciting current. For a real transformer, this is a reasonable assumption as long as the exciting current in the primary winding is small with respect to the primary current that drives the loads. It follows that the admittance-link equivalent-circuit model is unsuitable for transformers which are designed to store a large amount of energy. Also implied by this assumption is low core loss, often not the case for high-frequency operation. The inability of the admittance-link model to account for core loss is a recognized source of error, but no attempt has been made to quantify it.

It is shown in Section 8.3 that the admittance-link model and the coupled-secondaries model presented in the next chapter contain exactly the same information in different forms. This difference creates advantages and disadvantages of one model relative to the other which is discussed further in that section.

Another limitation of the admittance-link model, as well as the coupled-secondaries model, is that its parameter values vary with the frequency of sinusoidal excitation. In its basic form, the usefulness of this model for predicting transformer behavior under pulse-wave excitation is doubtful. However, the ease with which the admittance-link values can be calculated suggests that, using a computer, it might be practical to calculate the admittance-link values at the harmonics of the converter switching frequency, and in some manner apply those results to a Fourier decomposition of the excitation waveform. This possibility has not yet been investigated. Although the admittance-link model has not been thoroughly tested as part of the current research at Duke, its basis is sound

and it might be a useful tool for predicting stray effects in multiwinding transformers.

This page has been left blank intentionally.

Chapter 8

Coupled-Secondaries Equivalent Circuit

In Chapter 5, we detail how the field solutions of magnetic field intensity and current density in a transformer winding are applied to calculate the short-circuit impedances for the transformer. In Chapter 6 we present an example calculation of a short-circuit impedance at a specific frequency, and a comparison of measured and calculated short-circuit impedances over a range of frequencies. The goal in those two chapters is to replace laboratory measurement data with calculations based on field analysis in order to determine the component values for an equivalent circuit. One such equivalent circuit, the admittance-link model, is discussed in Chapter 7. A possible alternative to this admittance-link model for a multiwinding transformer is proposed by John Rosa in [15]. In the present chapter, we discuss the circuit proposed by Rosa and present two circuits which are modifications of Rosa's circuit. The second of these circuits, the *Coupled-Secondaries Equivalent Circuit*, is discussed in some detail and compared with the admittance-link model of Chapter 7.

8.1 CIRCUIT DESCRIPTIONS

Figure 8.1 shows a four-winding example of the circuit that Rosa proposes for modeling multiwinding transformers. Rosa considers only the inductive components of the transformer, and the calculations he presents for determining the values of inductance are limited to low-frequency excitations. Neglecting the resistances of the windings, the K coupled coils of the transformer circuit are represented by an ideal K-winding transformer and $(K-1)$ coupled secondaries. The mutual inductances between secondary windings are represented in Fig. 8.1 by the coupled inductors in each secondary winding; these are shown as linear inductors with dashed lines connecting related mutual components. Examining Rosa's model, we see that the terminal voltages in phasor form for

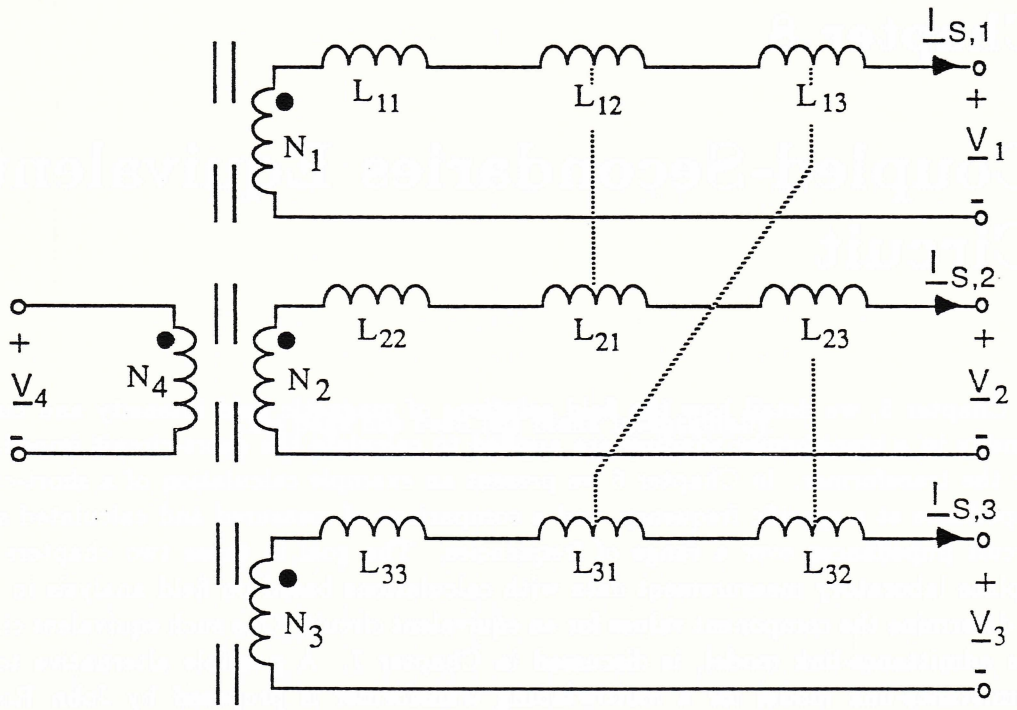


Figure 8.1: Equivalent circuit of a four-winding transformer as proposed by Rosa [15]. The transformer-leakage-inductance effects are modeled by the self- and mutual inductances.

this circuit are expressed as

$$\underline{V}_1 = \left(\frac{N_1}{N_4}\underline{V}_4\right) - j\omega L_{11}\underline{I}_{S,1} - j\omega L_{12}\underline{I}_{S,2} - j\omega L_{13}\underline{I}_{S,3} \tag{8.1}$$

$$\underline{V}_2 = \left(\frac{N_2}{N_4}\underline{V}_4\right) - j\omega L_{21}\underline{I}_{S,1} - j\omega L_{22}\underline{I}_{S,2} - j\omega L_{23}\underline{I}_{S,3} \tag{8.2}$$

$$\underline{V}_3 = \left(\frac{N_3}{N_4}\underline{V}_4\right) - j\omega L_{31}\underline{I}_{S,1} - j\omega L_{32}\underline{I}_{S,2} - j\omega L_{33}\underline{I}_{S,3} \tag{8.3}$$

$$\underline{V}_4 = \underline{V}_4 \tag{8.4}$$

where the L_{jj} terms are self-inductances and the L_{jk} terms are mutual inductances between the windings.

Rosa's circuit model as shown presents some conceptual difficulties because the mutual or coupled inductors in each secondary are not actual circuit elements that exist in series with the self-inductances of the secondary windings. The voltage drop in any particular secondary winding due to mutual coupling effects is produced not by current in the effected winding but rather by current flowing in some other secondary. Therefore it is confusing to draw these mutual terms as actual circuit elements as Rosa does in Fig. 8.1.

An alternate way to represent the coupling of the secondaries of a multiwinding transformer which avoids the use of such coupled inductors is shown in Fig. 8.2. In this figure, current-controlled voltage sources with gains $\underline{\mathcal{H}}_{jk}$

$$\underline{V}_{jk} = \underline{\mathcal{H}}_{jk}\underline{I}_{S,k} \tag{8.5}$$

are used to represent the coupling between the secondaries. The equations which describe this circuit are

$$\underline{V}_1 = \left(\frac{N_1}{N_4}\underline{V}_4\right) - \underline{\mathcal{H}}_{11}\underline{I}_{S,1} - \underline{\mathcal{H}}_{12}\underline{I}_{S,2} - \underline{\mathcal{H}}_{13}\underline{I}_{S,3} \tag{8.6}$$

$$\underline{V}_2 = \left(\frac{N_2}{N_4}\underline{V}_4\right) - \underline{\mathcal{H}}_{21}\underline{I}_{S,1} - \underline{\mathcal{H}}_{22}\underline{I}_{S,2} - \underline{\mathcal{H}}_{23}\underline{I}_{S,3} \tag{8.7}$$

$$\underline{V}_3 = \left(\frac{N_3}{N_4}\underline{V}_4\right) - \underline{\mathcal{H}}_{31}\underline{I}_{S,1} - \underline{\mathcal{H}}_{32}\underline{I}_{S,2} - \underline{\mathcal{H}}_{33}\underline{I}_{S,3} \tag{8.8}$$

$$\underline{V}_4 = \underline{V}_4 \tag{8.9}$$

As in (8.1) to (8.3), representing the circuit of Fig. 8.1, voltage drops in (8.6) to (8.8) are caused by each secondary's self-current and the currents in the other two secondary windings. Comparing the two circuit diagrams, we see that each of the self- and mutual inductances of Fig. 8.1 have been replaced in Fig. 8.2 by a current-controlled voltage source. For a direct equivalence to Fig. 8.1, the gains of the controlled sources should be written

$$\underline{\mathcal{H}}_{jj} = j\omega L_{jj} \quad \text{and} \quad \underline{\mathcal{H}}_{jk} = j\omega L_{jk} \tag{8.10}$$

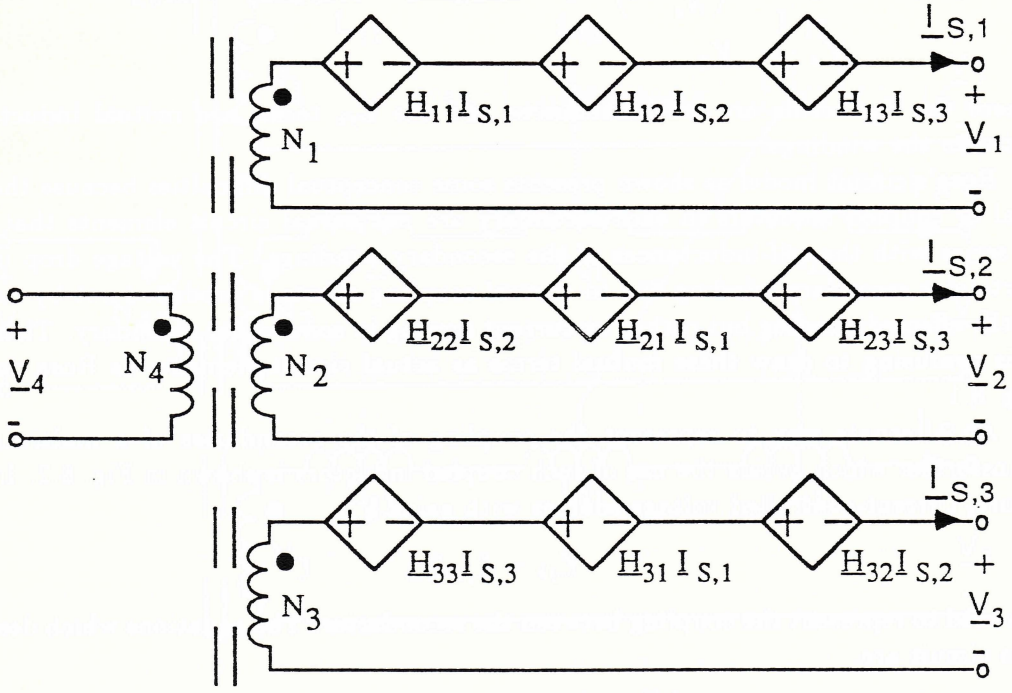


Figure 8.2: A modification of Rosa's circuit where the coupling between the secondaries is modeled using current-controlled voltage sources.

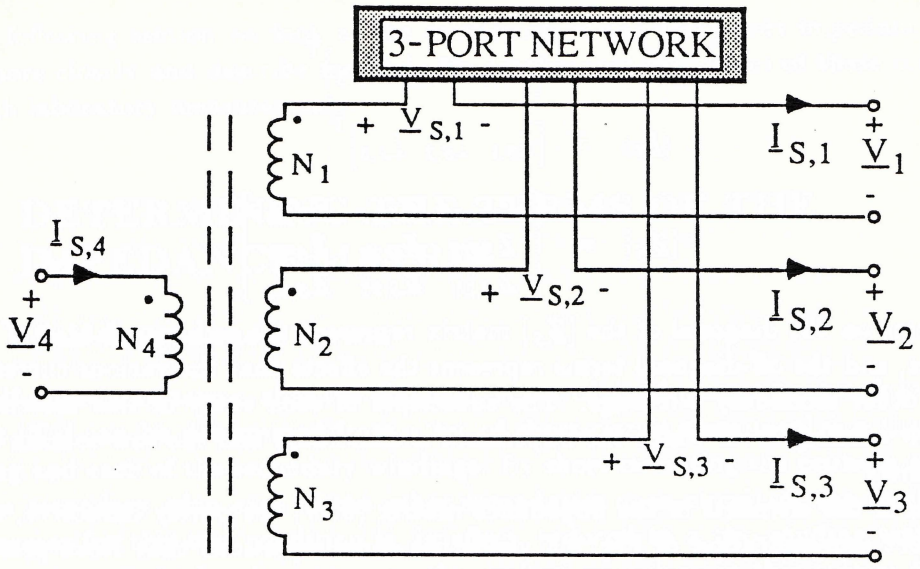


Figure 8.3: The 3-port coupled-secondaries model is a further modification of Rosa's circuit model that characterizes the coupled secondary windings of a four-winding transformer as a three-port network. For a K-winding transformer, a $(K-1)$-port network is used to model the $(K-1)$ coupled secondaries.

However, if the relationships between the currents and voltages are expressed in terms of gains, we no longer are limited to representing only the inductive effects in the multiwinding transformer, but can include more general impedance effects.

A third and potentially more useful way to represent the effects of leakage impedance is to treat the $(K-1)$ secondaries of the K-winding transformer as an $(K-1)$-port "black-box" network as shown in Fig. 8.3. This figure shows a three-port network in which each port models the voltage drop that appears in a particular secondary winding due to both the self- and mutual effects in the transformer secondary windings. As described in Section 7.1, these port voltages—labeled here as $\underline{V}_{S,1}$, $\underline{V}_{S,2}$, and $\underline{V}_{S,3}$—are written in general terms for a three-port network as

$$\underline{V}_{S,1} = \underline{Z}_{S,11}\underline{I}_{S,1} + \underline{Z}_{S,12}\underline{I}_{S,2} + \underline{Z}_{S,13}\underline{I}_{S,3} \tag{8.11}$$

$$\underline{V}_{S,2} = \underline{Z}_{S,21}\underline{I}_{S,1} + \underline{Z}_{S,22}\underline{I}_{S,2} + \underline{Z}_{S,23}\underline{I}_{S,3} \tag{8.12}$$

$$\underline{V}_{S,3} = \underline{Z}_{S,31}\underline{I}_{S,1} + \underline{Z}_{S,32}\underline{I}_{S,2} + \underline{Z}_{S,33}\underline{I}_{S,3} \tag{8.13}$$

This set of equations can be recast into matrix form as

$$[\underline{V}_S] = [\underline{Z}_S]\,[\underline{I}_S] \tag{8.14}$$

where

$$[\underline{V}_S] = \left[\underline{V}_{S,1}\ \underline{V}_{S,2}\ \underline{V}_{S,3}\right]^T \tag{8.15}$$

$$[\underline{I}_S] = \left[\underline{I}_{S,1}\ \underline{I}_{S,2}\ \underline{I}_{S,3}\right]^T \tag{8.16}$$

$$[\underline{Z}_S] = \begin{bmatrix} \underline{Z}_{S,11} & \underline{Z}_{S,12} & \underline{Z}_{S,13} \\ \underline{Z}_{S,21} & \underline{Z}_{S,22} & \underline{Z}_{S,23} \\ \underline{Z}_{S,31} & \underline{Z}_{S,32} & \underline{Z}_{S,33} \end{bmatrix} \tag{8.17}$$

The terms on the diagonal of the $[\underline{Z}_S]$ matrix represent the self-impedances of the secondaries, and the off-diagonal terms represent the effects that the various currents have on the other secondary windings. The subscripts of each entry in this matrix denote both the windings with which the impedance is associated and the row-column location of the entry.

If all of the elements in the impedance matrix (8.17) are purely inductive, then the three-port representation of Fig. 8.3 yields the same equations that Rosa presents for his purely inductive circuit model shown in Fig. 8.1. Since we are concerned here with both inductive and resistive effects in the transformer, we will maintain the generality of modeling the three-port network as a network that can contain both resistive and inductive components. We make the restriction that the network cannot contain any capacitive elements since this report does not address transformer winding capacitance.

From Fig. 8.3, we can write the terminal voltages in terms of the voltages of the ideal transformer and the port voltages of the 3-port network.

$$\underline{V}_1 = \left(\frac{N_1}{N_4}\underline{V}_4\right) - \underline{V}_{S,1} \tag{8.18}$$

$$\underline{V}_2 = \left(\frac{N_2}{N_4}\underline{V}_4\right) - \underline{V}_{S,2} \tag{8.19}$$

$$\underline{V}_3 = \left(\frac{N_3}{N_4}\underline{V}_4\right) - \underline{V}_{S,3} \tag{8.20}$$

$$\underline{V}_4 = \underline{V}_4 \tag{8.21}$$

Substituting (8.11) to (8.13) in for the port voltages $\underline{V}_{S,1}$, $\underline{V}_{S,2}$, and $\underline{V}_{S,3}$, we can express the transformer terminal voltages in terms of the currents and impedances associated with the coupled-secondaries (K–1)-port network

$$\underline{V}_1 = \left(\frac{N_1}{N_4}\underline{V}_4\right) - \underline{Z}_{S,11}\underline{I}_{S,1} - \underline{Z}_{S,12}\underline{I}_{S,2} - \underline{Z}_{S,13}\underline{I}_{S,3} \tag{8.22}$$

$$\underline{V}_2 = \left(\frac{N_2}{N_4}\underline{V}_4\right) - \underline{Z}_{S,21}\underline{I}_{S,1} - \underline{Z}_{S,22}\underline{I}_{S,2} - \underline{Z}_{S,23}\underline{I}_{S,3} \tag{8.23}$$

$$\underline{V}_3 = \left(\frac{N_3}{N_4}\underline{V}_4\right) - \underline{Z}_{S,31}\underline{I}_{S,1} - \underline{Z}_{S,32}\underline{I}_{S,2} - \underline{Z}_{S,33}\underline{I}_{S,3} \tag{8.24}$$

$$\underline{V}_4 = \underline{V}_4 \tag{8.25}$$

In the following section we look at the coefficients of the three-port impedance matrix $[\underline{Z}_S]$ more closely and describe methods for determining the values of these coefficients through laboratory measurements.

8.2 DETERMINING THE TERMS OF THE IMPEDANCE MATRIX

8.2.1 Self-Impedance Terms

The self-impedance terms, alias the diagonal terms, of the three-port-network impedance matrix $[\underline{Z}_S]$ can be determined from a set of short-circuit tests involving the primary winding and each of the secondary windings. By short-circuiting the primary and exciting one secondary with each of the other secondaries open-circuited, the multiwinding transformer for this test condition is, in effect, reduced to a two-winding transformer. The impedance seen by the source on the excited secondary in this case is the short-circuit impedance between the particular secondary and the primary winding. If the secondary winding labeled one in Fig. 8.3 is excited while the primary winding labeled four is short-circuited, the impedance that is measured is the short-circuit impedance between windings one and four reflected to winding one. Thus we see that the diagonal terms $\underline{Z}_{S,jj}$ of the impedance network are identical to the short-circuit impedances $\underline{Z}_{(j4)}$ discussed in Chapter 5.[1]

For the four-winding transformer of Fig. 8.3, we can perform three short-circuit tests in which the primary winding is shorted to determine the three diagonal elements of the coupled-secondaries 3-port-network matrix $[\underline{Z}_S]$. The recognition that each of these diagonal elements, or self-impedances, represents the same physical phenomenon that we earlier called the short-circuit impedance between two windings is critical to avoiding an erroneous assumption that one might make upon examining Figs. 8.1 and 8.3. In each of these diagrams, it initially appears that the presented model assumes perfect coupling between the primary winding and each secondary since there are no leakage elements in the primary circuit. This is not the case, however. Rather, the leakage impedance that exists between the primary and each of the secondaries is included as part of the three-port secondary network, therefore, no leakage-impedance elements exist in the primary winding.

Described above is the way in which the self-impedance for each of the secondaries can be measured in the laboratory. This is identical to the measurement of short-circuit impedance between each of the secondaries and the primary winding discussed in Section 6.3. Because of this relationship, the expressions derived in Section 5.2 for the short-circuit impedance between any two windings of a multiwinding transformer apply

[1]Since the primary is labeled winding four in the present chapter, the three short-circuit tests involving a shorted primary are $Z_{(14)}$, $Z_{(24)}$, and $Z_{(34)}$. In Chapters 5 and 6, the primary winding is labeled winding *one* so these three tests are called $Z_{(21)}$, $Z_{(31)}$, and $Z_{(41)}$, respectively, in these earlier chapters.

equally well for calculating the diagonal elements of the coupled-secondaries $(K-1)$-port-network impedance matrix $[\underline{Z}_S]$ where $\underline{Z}_{S,jj} = \underline{Z}_{(j4)}$ for $j = 1, 2, 3$.

8.2.2 Mutual Impedance Terms

In the previous section, the determination of the self-impedance or diagonal elements of the $[\underline{Z}_S]$ matrix for the three-port network in Fig. 8.3 is shown to be equivalent to the short-circuit impedance calculations derived earlier. The determination of the off-diagonal or mutual terms of the impedance matrix is also related to these short-circuit tests, but the application of the field solutions for calculating these off-diagonal $Z_{S,jk}$ terms is not so straightforward.

In the short-circuit tests of Chapter 6, we choose to excite one winding, short a second winding and then measure the current and voltage of the excited winding in order to determine the short-circuit impedance for each test. As is discussed above, if the primary winding is always shorted, then the $(K-1)$ possible short-circuit tests yield the self-impedances which constitute the diagonal of the impedance matrix given in (8.17). If the same tests are performed but, in addition, the voltages across the open-circuited windings are also measured, then the mutual impedances between the excited winding and the open-circuited windings can be determined. For example, if winding four of the transformer shown in Fig. 8.3 is shorted, windings two and three are left open, and winding one is excited by the voltage $\underline{V}_E$, then an excitation current of $\underline{I}_E$ flows into the positive terminal of winding one and

$$\underline{V}_1 = \underline{V}_E \tag{8.26}$$

$$\underline{I}_{S,1} = -\underline{I}_E \tag{8.27}$$

$$\underline{I}_{S,2} = \underline{I}_{S,3} = 0 \tag{8.28}$$

$$\underline{V}_4 = 0 \tag{8.29}$$

Under these conditions (8.22) to (8.24) become

$$\underline{V}_1 = \underline{Z}_{S,11}\underline{I}_E \tag{8.30}$$

$$\underline{V}_2 = \underline{Z}_{S,21}\underline{I}_E \tag{8.31}$$

$$\underline{V}_3 = \underline{Z}_{S,31}\underline{I}_E \tag{8.32}$$

Thus, the straightforward short-circuit tests described in Section 6.3 can be adapted to measure the mutual impedances between the secondaries of a multiwinding transformer. The (14) short-circuit test described here yields not only

$$\underline{Z}_{S,11} = \underline{Z}_{(14)} = \frac{\underline{V}_E}{\underline{I}_E} \tag{8.33}$$

but also

$$\underline{Z}_{S,21} = \frac{\underline{V}_2}{\underline{I}_E} \tag{8.34}$$

$$\underline{Z}_{S,31} = \frac{\underline{V}_3}{\underline{I}_E} \tag{8.35}$$

Additional short-circuit tests are needed to determine the other mutual impedances.

Thus far in this section, we have shown that the mutual-impedance values can be determined in the laboratory by measuring the voltage that appears at each of the open-circuited windings during a given short-circuit test. We have no difficulty, therefore, measuring the mutual impedance coefficients, but what we would like in addition is a way to calculate these terms based on the transformer analysis techniques introduced in earlier chapters of this report.

Figure 8.4(b) shows the low-frequency field-intensity diagrams labeled $H_{(14)}$, $H_{(24)}$, and $H_{(34)}$ for the three short-circuit tests involving a shorted primary for the transformer shown in Fig. 8.4(a). These field-intensity diagrams are equivalent to the top three field-intensity diagrams of Fig. 5.2(b) except that the primary winding, which is composed of the two innermost layers, is now numbered as winding four and the secondary windings are numbered from one to three. We know from our discussion of short-circuit impedances that the impedance between two windings is related to the field-intensity distribution in the transformer under short-circuit conditions. In particular, the leakage inductance is related to the volume integral of the $|\underline{H}_z(x)|^2$ function and the winding resistance is related to the volume integral of the square of the current-density function, $|\underline{J}_y(x)|^2$. The plots of $H_{(14)}$, $H_{(24)}$, and $H_{(34)}$ can be used to determine the layer boundary conditions of field intensity from which we can determine the self-impedance terms of $[\underline{Z}_S]$.

Figure 8.4(c) shows three low-frequency field-intensity diagrams that are unlike those we looked at earlier. These diagrams are labeled $H_{(14)(24)}$, $H_{(14)(34)}$, and $H_{(24)(34)}$. As these labels imply, these plots represent the products of each pair of low-frequency field-intensity diagrams for the various short-circuit tests. John Rosa, who discusses only low-frequency field effects, proposes in [15] that the inductive portion of the mutual impedance between any two secondary windings is related to the volume integral of the product of the individual short-circuit field distributions for the two secondary windings. It is not clear how this method for calculating the mutual inductances can be extended to high-frequency operation where the distributions of $\underline{H}_z(x)$ in the core window become highly nonlinear and fields must be described in terms of phasor notation. This is not a problem, however, because both the self- and mutual impedance terms for the matrix $[\underline{Z}_S]$ in (8.17) can be determined from the elements of the impedance matrix $[\underline{Z}_r]$ introduced in the derivation of the admittance-link model discussed in Chapter 7. How this computation is carried out is detailed in the next section.

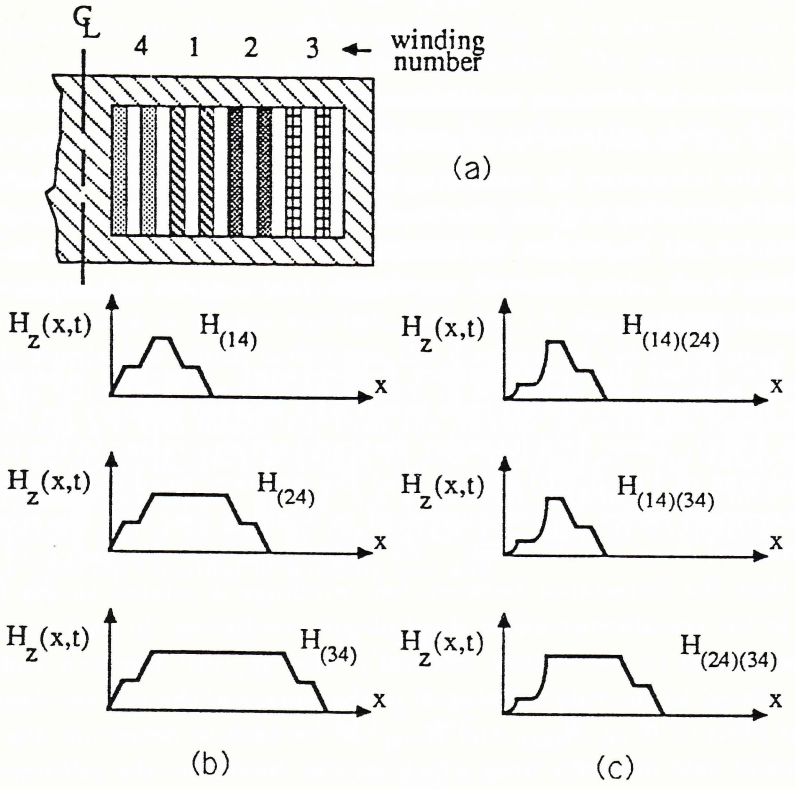


Figure 8.4: (a) Four-winding transformer cross section where the primary winding which comprises the two innermost layers has been numbered as the fourth winding to be consistent with Rosa. (b) Low-frequency short-circuit field-intensity diagrams for the three short-circuit tests which involve a shorted primary for the four-winding transformer. (c) Plots of the cross-products of each pair of short-circuit low-frequency field-intensity diagrams.

8.3 COMPARISON OF THE COUPLED-SECONDARIES AND ADMITTANCE-LINK MODELS

Using a four-winding transformer as an example, the admittance-link model is developed in Chapter 7 and the $(K-1)$-port coupled-secondaries model is presented in Section 8.1. Although the two models appear quite different, in fact, they contain exactly the same information. In Section 8.3.1, the equivalence of the two models is proven, again using a four-winding transformer as an example, and the relationship between the short-circuit impedances needed to determine the admittance-link-model parameters and the impedances of the coupled-secondaries model is derived. Since the frequency-dependent short-circuit impedances for a transformer can be calculated using the methods of Chapter 5, this relationship provides the information necessary to calculate the frequency-dependent elements of the coupled-secondaries-model impedance matrix $[\underline{Z}_S]$, which can not be done using the methods presented by Rosa in [15]. In Section 8.3.2, comments are made about some possible advantages of the admittance-link and coupled-secondaries models.

8.3.1 Relationship Between the Three-Port Networks

As an intermediate step in developing the admittance-link model, the three-port network of Fig. 7.9(a) is created. That network is characterized by the differential reduced impedance matrix $[\underline{Z}_r]$ of (7.21) which is repeated here.

$$[\underline{V}_{d4}] = [\underline{Z}_r][\underline{I}'_r] \tag{8.36}$$

Although the development of the admittance-link model is completed in Chapter 7 by inverting $[\underline{Z}_r]$ and considering more short-circuit tests, it is the matrix $[\underline{Z}_r]$ which is directly related to the matrix $[\underline{Z}_S]$ which defines the $(K-1)$-port coupled-secondaries model. The coupled-secondaries impedance matrix $[\underline{Z}_S]$ first appears in (8.14) which is repeated here for ease of reference.

$$[\underline{V}_S] = [\underline{Z}_S][\underline{I}_S] \tag{8.37}$$

The claim to be proven in this section is that the impedances in $[\underline{Z}_S]$ may be obtained from the impedances in $[\underline{Z}_r]$. This involves performing a simple referral of the impedances in $[\underline{Z}_S]$ to a common winding of the transformer, with a prime used in the conventional manner to indicate this referral.

The proof begins with the transformation of the coupled-secondaries equivalent circuit in Fig. 8.3. Its vector network equation (8.37) represents the following set of simultaneous equations originally presented in (8.11) to (8.13).

$$\underline{V}_{S,1} = \underline{Z}_{S,11}\underline{I}_{S,1} + \underline{Z}_{S,12}\underline{I}_{S,2} + \underline{Z}_{S,13}\underline{I}_{S,3} \tag{8.38}$$

$$\underline{V}_{S,2} = \underline{Z}_{S,21}\underline{I}_{S,1} + \underline{Z}_{S,22}\underline{I}_{S,2} + \underline{Z}_{S,23}\underline{I}_{S,3} \tag{8.39}$$

$$\underline{V}_{S,3} = \underline{Z}_{S,31}\underline{I}_{S,1} + \underline{Z}_{S,32}\underline{I}_{S,2} + \underline{Z}_{S,33}\underline{I}_{S,3} \tag{8.40}$$

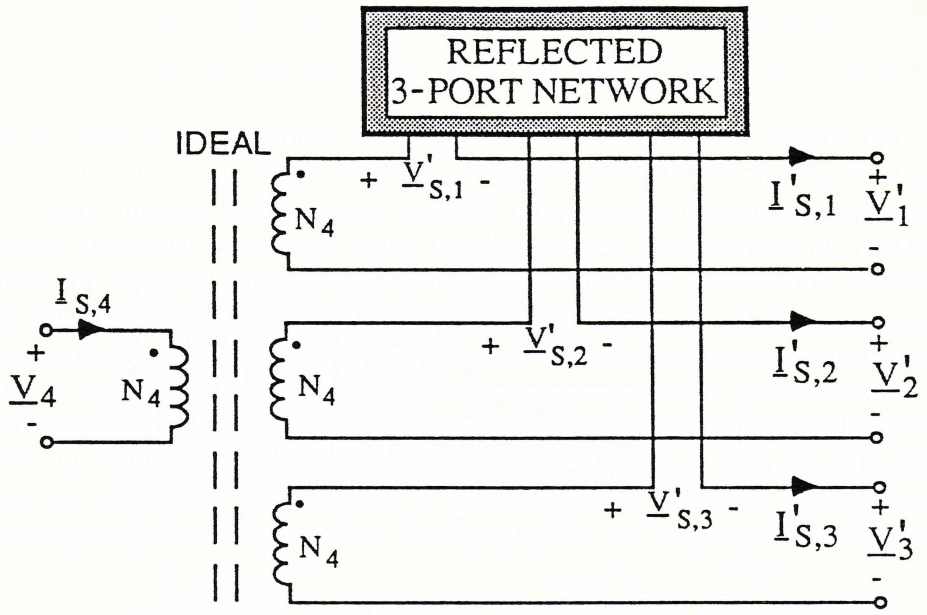


Figure 8.5: The coupled-secondaries equivalent circuit of Fig. 8.3 with all other winding circuits referred to winding number 4.

All voltages and currents in the circuit may be referred to winding number $K=4$ by the following equations, producing the circuit of Fig. 8.5. Equations (7.4) and (7.5)

$$\underline{V}'_j = \left(\frac{N_4}{N_j}\right)\underline{V}_j \tag{8.41}$$

$$\underline{I}'_j = \left(\frac{N_j}{N_4}\right)\underline{I}_j \tag{8.42}$$

can be written for our purposes as

$$\underline{V}'_{S,j} = \left(\frac{N_4}{N_j}\right)\underline{V}_{S,j} \tag{8.43}$$

$$\underline{I}'_{S,j} = \left(\frac{N_j}{N_4}\right)\underline{I}_{S,j} \tag{8.44}$$

To obtain the network equations associated with the new circuit, the inverses of relationships (8.43) and (8.44), given by

$$\underline{V}_{S,j} = \left(\frac{N_j}{N_4}\right)\underline{V}'_{S,j} \tag{8.45}$$

$$\underline{I}_{S,j} = \left(\frac{N_4}{N_j}\right)\underline{I}'_{S,j} \tag{8.46}$$

are substituted into (8.38) through (8.40) to give

$$\left(\frac{N_1}{N_4}\,\underline{V}'_{S,1}\right) = \underline{Z}_{S,11}\left(\frac{N_4}{N_1}\,\underline{I}'_{S,1}\right) + \underline{Z}_{S,12}\left(\frac{N_4}{N_2}\,\underline{I}'_{S,2}\right) + \underline{Z}_{S,13}\left(\frac{N_4}{N_3}\,\underline{I}'_{S,3}\right) \quad (8.47)$$

$$\left(\frac{N_2}{N_4}\,\underline{V}'_{S,2}\right) = \underline{Z}_{S,21}\left(\frac{N_4}{N_1}\,\underline{I}'_{S,1}\right) + \underline{Z}_{S,22}\left(\frac{N_4}{N_2}\,\underline{I}'_{S,2}\right) + \underline{Z}_{S,23}\left(\frac{N_4}{N_3}\,\underline{I}'_{S,3}\right) \quad (8.48)$$

$$\left(\frac{N_3}{N_4}\,\underline{V}'_{S,3}\right) = \underline{Z}_{S,31}\left(\frac{N_4}{N_1}\,\underline{I}'_{S,1}\right) + \underline{Z}_{S,32}\left(\frac{N_4}{N_2}\,\underline{I}'_{S,2}\right) + \underline{Z}_{S,33}\left(\frac{N_4}{N_3}\,\underline{I}'_{S,3}\right) \quad (8.49)$$

Rearranging,

$$\underline{V}'_{S,1} = \left(\frac{N_4^2}{N_1^2}\,\underline{Z}_{S,11}\right)\underline{I}'_{S,1} + \left(\frac{N_4^2}{N_1 N_2}\,\underline{Z}_{S,12}\right)\underline{I}'_{S,2} + \left(\frac{N_4^2}{N_1 N_3}\,\underline{Z}_{S,13}\right)\underline{I}'_{S,3} \quad (8.50)$$

$$\underline{V}'_{S,2} = \left(\frac{N_4^2}{N_2 N_1}\,\underline{Z}_{S,21}\right)\underline{I}'_{S,1} + \left(\frac{N_4^2}{N_2^2}\,\underline{Z}_{S,22}\right)\underline{I}'_{S,2} + \left(\frac{N_4^2}{N_2 N_3}\,\underline{Z}_{S,23}\right)\underline{I}'_{S,3} \quad (8.51)$$

$$\underline{V}'_{S,3} = \left(\frac{N_4^2}{N_3 N_1}\,\underline{Z}_{S,31}\right)\underline{I}'_{S,1} + \left(\frac{N_4^2}{N_3 N_2}\,\underline{Z}_{S,32}\right)\underline{I}'_{S,2} + \left(\frac{N_4^2}{N_3^2}\,\underline{Z}_{S,33}\right)\underline{I}'_{S,3} \quad (8.52)$$

These simultaneous equations are written in vector form as

$$[\underline{V}'_S] = [\underline{Z}'_S][\underline{I}'_S] \quad (8.53)$$

where $[\underline{Z}'_S]$ is the impedance matrix of the new three-port network in Fig. 8.5. It is apparent from (8.50) through (8.52) that the elements of $[\underline{Z}'_S]$ for a K-winding transformer may be obtained from the elements of the impedance matrix $[\underline{Z}_S]$ by

$$\underline{Z}'_{S,jk} = \left(\frac{N_K^2}{N_j N_k}\right)\underline{Z}_{S,jk} \quad (8.54)$$

The matrix $[\underline{Z}'_S]$ is proven below to be equal to $[\underline{Z}_r]$ of (8.36) by examining the equivalence of the voltage and current vectors in (8.36) and those in (8.53). To accomplish this, the relationship between the notation used in Chapters 7 and 8 to refer to the voltages and currents of the example four-winding transformer is first established. By comparing Figs. 7.3(a) and 8.3, it is clear that unprimed voltages of the form $\underline{V}_j$ are the same in both chapters. Also, the secondary currents $\underline{I}_j$ in Chapter 7 are equal but opposite to the currents $\underline{I}_{S,j}$ of Chapter 8 and the primary currents in both chapters are equal. For a general K-port network,

$$\underline{I}_{S,j} = \begin{cases} -\underline{I}_j & j = 1, 2, \ldots, (K-1) \\ \underline{I}_j & j = K \end{cases} \quad (8.55)$$

In Chapter 7, the transformation equation (8.42) is used to obtain the primed currents of the form $\underline{I}'_j$ from $\underline{I}_j$. Since this transformation equation is of exactly the same form

as (8.44) used to obtain $\underline{I}'_{S,j}$ from $\underline{I}_{S,j}$, (8.55) can be rewritten

$$\underline{I}'_{S,j} = \begin{cases} -\underline{I}'_j & j = 1,2,\ldots,(K-1) \\ \underline{I}'_j & j = K \end{cases} \tag{8.56}$$

For a four-winding transformer, $[\underline{I}'_S]$ in (8.53) contains three components:

$$[\underline{I}'_S] = [\underline{I}'_{S,1}\ \underline{I}'_{S,2}\ \underline{I}'_{S,3}]^{\mathrm{T}} \tag{8.57}$$

Similarly, the $[\underline{I}'_r]$ current vector in (8.36) contains three components:

$$[\underline{I}'_r] = [\underline{I}'_1\ \underline{I}'_2\ \underline{I}'_3]^{\mathrm{T}} \tag{8.58}$$

Comparing (8.56), (8.57), and (8.58), it can be concluded that

$$[\underline{I}'_S] = -[\underline{I}'_r] \tag{8.59}$$

To finish determining the relationship between $[\underline{Z}_r]$ of (8.36) and $[\underline{Z}'_S]$ of (8.53), we must look at the voltage vectors $[\underline{V}_{d4}]$ and $[\underline{V}'_s]$. To begin, the expressions for differential voltages (7.15) and (7.16) are repeated below.

$$\underline{V}_{jk} = \left(\frac{N_4}{N_j}\right)\underline{V}_j - \left(\frac{N_4}{N_k}\right)\underline{V}_k \tag{8.60}$$

$$\underline{V}_{j4} = \underline{V}'_j - \underline{V}_4 \tag{8.61}$$

Equation (8.61) reflects the choice of winding four as a reference by setting $k = 4$ in (8.60).

To compare the voltage vectors in (8.53) and (8.36), it is apparent from Fig. 8.5 and (8.61) that

$$\underline{V}'_{S,j} = \underline{V}_4 - \underline{V}'_j = -\underline{V}_{j4} \qquad j = 1,2,3 \tag{8.62}$$

Since $[\underline{V}_{d4}] = [\underline{V}_{14}\underline{V}_{24}\underline{V}_{34}]^{\mathrm{T}}$ and $[\underline{V}'_S] = [\underline{V}'_{S,1}\,\underline{V}'_{S,2}\,\underline{V}'_{S,3}]^{\mathrm{T}}$, we see from (8.61) and (8.62) that the two voltage vectors are equal but opposite.

$$[\underline{V}'_S] = -[\underline{V}_{d4}] \tag{8.63}$$

Since the current and voltage vectors in (8.53) are both the negative of those in (8.36), and since both equations describe the same transformer, the impedance matrices must be the same.

$$[\underline{Z}'_S] = [\underline{Z}_r] \tag{8.64}$$

Because of this equivalence, the elements of $[\underline{Z}_r]$ may be substituted into the left-hand side of (8.54) to give the relationship between corresponding elements in the $(K-1)$-port-network reduced impedance matrix $[\underline{Z}_r]$ for the admittance-link-model and the coupled-secondaries impedance matrix $[\underline{Z}_S]$.

$$\underline{Z}_{r,jk} = \left(\frac{N_K^2}{N_j N_k}\right)\underline{Z}_{S,jk} \tag{8.65}$$

Rearranging this gives us

$$\underline{Z}_{S,jk} = \left(\frac{N_j N_k}{N_K^2}\right) \underline{Z}_{r,jk} \tag{8.66}$$

Since the components of the impedance matrix $[\underline{Z}_S]$ of the coupled-secondaries model can be calculated from the components of the reduced matrix $[\underline{Z}_r]$, and the components of $[\underline{Z}_r]$ and be calculated from the short-circuit impedances for the transformer, we can substitute (7.94) and (7.95) into (8.66) to determine the elements of $[\underline{Z}_S]$ in terms of the short-circuit impedances $\underline{Z}_{(jK)}$, which is what we have been seeking.

$$\underline{Z}_{S,jj} = \underline{Z}_{(jK)} \qquad j = 1, 2, \ldots, (K-1) \tag{8.67}$$

$$\underline{Z}_{S,jk} = \underline{Z}_{S,kj} = \frac{N_j N_k}{2}\left(\frac{\underline{Z}_{(jK)} - \underline{Z}_{(jk)}}{N_j^2} + \frac{\underline{Z}_{(kK)}}{N_k^2}\right) \tag{8.68}$$

$$j \neq k; \quad j, k = 1, 2, \ldots, (K-1)$$

Equation (8.67) is consistent with our assertion in Section 8.2.1 that each diagonal term of the $(K-1)$-port coupled-secondaries impedance matrix $[\underline{Z}_S]$ is equal to the short-circuit impedance seen by the j^{th} secondary winding when the primary K^{th} winding is shorted. Equation (8.68) allows us to determine the off-diagonal terms of $[\underline{Z}_S]$ from the short-circuit impedances that can be obtained from laboratory measurements or calculated using the methods of Chapter 5, something we were unable to do in Section 8.2.2 by following Rosa's proposed procedure. Equations (8.67) and (8.68) together enable us to compute all parametric values in the coupled-secondaries model.

8.3.2 Merits of Each Model

As shown in the previous section, the admittance-link model and the coupled-secondaries model contain exactly the same information; therefore, the user may chose whichever model is best suited to a particular application. Neither the admittance-link model nor the coupled-secondaries model has yet been tested by the authors in computer-based circuit simulation; nevertheless, some general comments are included here about the expected advantages and disadvantages of each.

The admittance-link model pictured in Fig. 7.9(b) has simplicity as its primary advantage, with no transformers and no controlled voltage or current sources present. Each admittance link may be modeled as a resistor in combination with either an inductor or a capacitor, although the resistor may have a negative value. Negative resistances can be avoided by using the coupled-secondaries model instead. Disadvantages of

the admittance-link model are apparent from the advantages of the coupled-secondaries model described below.

A more realistic representation of the transformer can be had for the price of additional complexity with the coupled-secondaries model of Fig. 8.3. The actual voltages and currents of the transformer windings are present in this model, instead of those quantities referred to a common winding as in the admittance-link model. In addition, the winding circuits are all "floating" with respect to one another, instead of being tied together at either the dotted or the undotted terminals of the transformer. Although the three-port network of the coupled-secondaries model does "link" three of the winding circuits, it is evident in the controlled-source representations of that network in Fig. 8.2 that there is no direct connection there.

Because the coupled-secondaries model is more realistic, it is more versatile than the admittance-link model. The circuits associated with different windings may be tied together in ways other than what is internal to the admittance-link model. For instance, to model a power converter with output voltages of +12 Vdc and −12 Vdc, the dotted terminal of one winding of the transformer is typically connected to the undotted terminal of another. This configuration cannot be modeled directly with the admittance-link equivalent circuit; some form of external "isolation transformer" must be included in the model to reverse the polarity of one output. The coupled-secondaries model should be better suited for studying the effects of stray capacitances. Interwinding capacitances, calculated from the geometry of the transformer, can be inserted directly into the coupled-secondaries model as discrete elements which link one winding circuit to another. There, the capacitors experience the actual voltages expected to be present in the transformer, rather than some combination of referred voltages.

Although the coupled-secondaries model provides more versatility, its complexity is its main disadvantage. For a circuit-simulation program that does not accept the impedance or admittance matrix of a $(K-1)$-port network as input, the $(K-1)$-port network has to be modeled using current-controlled voltage sources as shown in Figs. 7.7 and 8.2, or voltage-controlled current sources as shown in Fig. 7.8. However, the real and imaginary parts of those controlled-source impedances and admittances must typically be modeled separately, producing a total of twelve controlled sources for a four-winding transformer. In spite of this large number of controlled sources, only three state variables are involved, usually chosen to be three of the winding currents. If a time-domain simulation were undertaken, this low number of state variables could be an advantage relative to the six state variables associated with the six admittance links of that model, albeit those six variables are not completely independent. Another potential problem with employing the admittance-link equivalent circuit in time-domain simulations stems from the possibility of developing cut-sets of inductive links for a multiple-output transformer experiencing switching load currents.

Based on these advantages and disadvantages, it is impossible to judge at this juncture which model is "better". Knowing the specific circumstances of the modeling to be performed can give some indication as described above, but, until some actual computer

simulations are run, it is difficult to predict which model will cause fewer computational difficulties.

This page has been left blank intentionally.

Chapter 9

CONCLUSIONS

In Part I of this report, a practical method is derived for calculating—prior to construction—the short-circuit impedances of a multiwinding transformer as a function of frequency. These short-circuit impedances completely describe the ac-winding-resistance and leakage-inductance properties of the transformer. Experimental data are provided to substantiate the derived results, and two transformer equivalent-circuit models are presented whose parameter values are obtained from these short-circuit impedances. The present chapter attempts to put the derived results in perspective relative to other work in the area of power-converter modeling. Section 9.1 describes how the present research is an extension of the existing literature, and Section 9.2 restates the assumptions underlying the derived results, explaining the limitations those assumptions impose on the application of the results. Finally, some ideas for future research are described in Section 9.3.

9.1 BACKGROUND AND REVIEW

The research embodied in this report was undertaken for the ultimate purpose of developing a better circuit model for the multiple-winding transformer, to be used for predicting cross-regulation in multiple-output dc-to-dc power converters. The research began with a comprehensive review of the existing literature, the subject of Part II of this report. The approach taken by each of several authors was evaluated and compared to the others, and through a combination of analysis and laboratory testing, one approach was selected as best meeting the needs of the research project. The approach adopted from the literature [7,14,19] uses the winding layer as the fundamental unit of analysis to successfully predict ac winding losses from the magnetic-field-intensity distribution in the winding space of a transformer. Extending that pattern, expressions are derived in this report by which the ac winding resistances and the leakage inductances of a transformer can be calculated from its dimensions and the layout of its windings. Such winding-resistance and leakage-inductance calculations are used to predict the short-circuit impedances which can be used to model a transformer.

Most of the related articles in the literature are devoted exclusively to calculating transformer losses for a given load condition [2,11,12,19,20]. The main issue addressed in these articles is the effect of winding layout and wire size on the total power dissipation in a given winding of a transformer. These articles do not apply the field solution to determine the terminal characteristics or equivalent-circuit parameters for a multiwinding transformer; instead, they are concerned with efficiency and the thermal limits of transformers operated at high frequencies. The reader is referred to the literature for more detail on such design considerations.

In this report, the actual winding layers of a transformer are approximated in Chapter 2 by equivalent-foil windings which span the entire breadth of the core window. Knowing only the arrangement of the windings and the currents flowing in them, Chapter 3 shows how a simplified low-frequency field analysis is applied to obtain the solution for the frequency-independent magnetic field intensity between winding layers. Each equivalent-foil layer is then modeled as a finite portion of an infinite current sheet, with the boundary conditions of magnetic field intensity at the surfaces of the sheet determined from the simplified field analysis. This approximation allows cumbersome Bessel functions to be avoided in deriving the results of Chapter 4.

The complete boundary-value solution for the frequency-dependent profile of magnetic field intensity inside a current sheet is derived from Maxwell's equations and illustrated graphically in Chapter 4. The corresponding solution for the profile of current density across the current sheet is also derived, giving the same result obtained by Vandelac and Ziogas by an alternate derivation [19]. From the profiles of magnetic field intensity and current density, expressions are then obtained for the profiles of power density and magnetic-energy density in a current sheet.

By applying the results of Chapter 4 to the set of short-circuit tests that can be performed on a multiwinding transformer, analytical expressions are derived in Chapter 5 for the leakage impedances between all pairs of transformer windings. These equations depend only on the winding geometry and the frequency of excitation. Laboratory experiments designed to confirm the analytical results are described in Chapter 6, and experimental data illustrate the accuracy and the limitations of both the ac-winding-resistance and the leakage-inductance calculations. A numerical example of these calculations is included. The experimental results have been further substantiated in other similar tests performed on several transformers not mentioned here.

Because the set of short-circuit impedances for a transformer completely characterizes its winding-loss and leakage-inductance characteristics at a particular frequency, the short-circuit impedances can be used to calculate the parameter values for some single-frequency circuit models of the transformer. Two different but closely related models are proposed, the admittance-link model of Chapter 7, and the coupled-secondaries model of Chapter 8, but neither has been tested yet in simulations. Although these single-frequency sinusoidal-excitation models are not directly usable in modeling the transformer in a power converter, it is believed that some derivatives of them may be.

Equations are now in hand for calculating the equivalent short-circuit resistances and

inductances for a trial transformer design. Because the calculations are lengthy and quite tedious, they are best done by computer. To be more useful, a computer program that calculates these results might also be written to calculate automatically the parameters associated with one of the proposed transformer models.

9.2 REVIEW OF THE ASSUMPTIONS

In deriving a simplified field solution for the magnetic-field and current-density distributions in the winding space of a transformer, some major assumptions or approximations are made. Because these assumptions may or may not be valid for a particular transformer, they impose certain limits on the applicability of the results reported in Part I. Therefore, it is worthwhile to review the assumptions and comment on their implications.

1. It is assumed throughout the field analysis that the currents in the transformer windings are purely sinusoidal. Because most power-electronics applications do not have sinusoidal excitation, the results given here cannot be applied directly to the analysis of transformers in such circuits. The method of analysis employed here can be expanded to include nonsinusoidal current excitations through Fourier-series decomposition of the nonsinusoidal waveforms. This technique is demonstrated in [2,19,20].

2. The magnetizing impedance of the transformer is always assumed to be so large that it is neglected in the analysis and modeling here. This is classically a safe assumption when considering transformers wound on high-permeability materials such as silicon-steel. However, the assumption that the magnetizing effects can be neglected may give erroneous results where the transformer is used for energy storage, as in a flyback converter. In general, if the component of primary current that excites the core is much smaller than the component of primary current that drives the loads, the assumption of infinite magnetizing impedance is reasonable.

3. All transformer winding layers are modeled as equivalent-foil layers that extend across the full breadth of the transformer core window. To match the dc resistance of the actual winding layer, the conductivity of the equivalent-foil layer is adjusted by the layer-porosity factor η. Windings of round, strip, and foil conductors arranged in concentric cylindrical layers can be analyzed, but bifilar windings and those of Litz wire or twisted-wire bundles cannot.

4. All magnetic flux in the transformer winding space is assumed to be parallel to the center leg of the core. This condition is brought about in the physical model of the transformer by assuming equivalent-foil windings and assuming that high-permeability magnetic material completely surrounds those windings. This parallel-flux assumption eliminates the difficult-to-compute "end effects," or curvature of the field lines, usually found near the ends of real layers. This approximation has produced generally good agreement between predicted and measured

short-circuit impedances for transformers having ungapped pot cores and EE cores of high-permeability material. Although the maximum number of turns that fit in the bobbin have been wound in all layers, η has been as low as 0.5. An alternative approach that does not ignore the end effects is presented in [1, p. 84].

5. All transformer winding layers are analyzed as infinite current sheets, neglecting the curvature of the layers. Perry states that the error is small as long as the thickness of the layer is small relative to its radius of curvature [14], but he does not give quantitative limits. Nevertheless, good agreement has generally been obtained between predicted and measured short-circuit impedances using the current-sheet approximation. If more accurate results are desired, Perry carries out the analysis in cylindrical coordinates [14], but the resulting expressions contain cumbersome Bessel functions. Goad, on the other hand, begins with the cylindrical-coordinate solution but uses approximations for the Bessel functions [7].

6. Winding capacitance is always neglected in the analysis and modeling reported here. Experiments have confirmed this to be a good assumption up to the frequency where the leakage inductance begins to resonate with the winding capacitance, the latter of which is not included in the present models. The importance of this shortcoming of the analysis has not been assessed.

These are the important assumptions and approximations upon which the field analysis of this report is based. It is important to keep them in mind when applying the results because circumstances can be imagined that would contradict each one of these assumptions to the extent that the analysis would be invalid.

9.3 FUTURE WORK

While the completed research offers improvements in the ability to predict the high-frequency behavior of multiwinding transformers, much work remains to be done before achieving the ultimate goal of predicting cross-regulation in multiple-output converters. Some areas in which research might be continued are described here.

The admittance-link and the coupled-secondaries equivalent circuits for a transformer have not yet been tested on a computer. Since they are mathematically equivalent, they should both give the same results when used with a circuit simulation program such as SPICE, but practical issues need to be addressed. For instance, how easy is it to calculate automatically the parameter values for each model from the short-circuit impedances of the transformer? Would the simulation program fail with one or the other of the models? Can results still be obtained if a magnetizing inductance, a resistor to account for core loss, lead inductances, and winding capacitances are added to the model? Under what conditions, if any, would significant numerical errors be generated in calculating the parameter values or performing the ac analysis? How easy would it be to extend each model to obtain a frequency-independent form that would be suitable

for simulating pulse-wave excitation as discussed below? To answer these questions, ac analyses could be performed with SPICE using model parameters calculated for actual test transformers.

Because the parameter values of the admittance-link and coupled-secondaries equivalent circuits are derived from short-circuit-test data, either model should predict the results of short-circuit tests with little error. Since the transformer models are linear at a given frequency, the proposed models should also predict transformer behavior for any linear-load condition, but this must be confirmed experimentally. The steady-state regulation predicted by computer simulation using one of the models could be compared to the regulation measured in laboratory tests. Such experiments should reveal at what frequencies and under what conditions is it necessary to incorporate into the model various effects that were previously neglected, namely, the magnetizing inductance, the core loss, lead inductances, and winding capacitances.

Once a solid understanding of transformer equivalent-circuit behavior is established for sinusoidal excitation, one can address the more challenging problem of nonsinusoidal excitation, specifically, the pulse-width-modulated current waveforms seen in dc-to-dc converters. Rather than a single frequency, many harmonics of the excitation frequency are present under conditions of pulse-wave excitation. To extend the single-frequency transformer model to predict transformer behavior with pulse-wave excitation, the following three alternatives are envisioned.

What seems to be the most promising approach is to devise a more complex circuit model whose elements are independent of frequency, yet whose equivalent impedances model the frequency dependance of ac winding resistance and leakage inductance. This might be done by replacing each frequency-dependent resistance and inductance in the single-frequency equivalent circuit with a small network of linear circuit elements that approximates the frequency dependence. A balance would have to be established between accurately approximating the frequency dependence and keeping the order of the resulting equivalent circuit manageable.

A second way of handling nonsinusoidal excitation is through Fourier analysis. For linear loads, the sinusoidal response for each harmonic component of the excitation waveform could be calculated, and the results could then be summed together to yield the equivalent time-domain response. For nonlinear loads, where diodes are present in the output circuits of the transformer, the "field harmonic analysis" proposed by Vandelac and Ziogas might prove useful [19]. There, the different waveforms of magnetic field intensity in the interlayer spaces of the transformer windings are examined, and the losses are calculated from Fourier decompositions of those waveforms, taking into account both magnitude and phase relationships.

The third possible way of analyzing nonsinusoidal excitation is to determine an "equivalent" sinusoidal frequency that could be used to predict essential features of the pulse-wave response. The equivalent frequency could be simply the fundamental frequency of the excitation, or it might be some other frequency that is derived from the shape of the excitation waveform. This approach appears less promising than the first

two, but due to its simplicity, it should not be discarded without further examination.

To model pulse-wave and high-frequency ac excitation, it is likely that winding capacitance will have to be included in the transformer model. The typical resonant peak observed in plots of measured short-circuit resistance and inductance causes a substantial deviation between measured and predicted values beginning only several harmonics higher than typical converter switching frequencies. By examining the energy stored in the electric fields inside the transformer winding space, a suitable method might be found for calculating the critical winding capacitances from the geometry of a trial transformer design.

Experience has shown that the most reliable way to advance the limits of knowledge is methodically, one step at a time. This research report represents a first step in developing techniques for predicting cross-regulation in multiple-output converters. It provides a complete derivation from Maxwell's equations of the important results, with all assumptions and approximations clearly identified. The purpose of such detail is to convince a reader of the integrity of the results, and to convey a fundamental understanding of their limitations. Having established this solid foundation of knowledge on the subject of high-frequency effects in transformers, and having obtained encouraging laboratory results to date, it is expected that further research in this direction will prove fruitful.

APPENDICES

This page has been left blank intentionally.

Appendix A

Derivation of Diffusion Equation (4.1) in Terms of E from Maxwell's Equations

For our purposes here, we choose to write Maxwell's field equations in their differential form as,

$$\nabla \times \mathbf{E} = -\frac{\partial \mathbf{B}}{\partial t} \tag{A.1}$$

$$\nabla \times \mathbf{H} = \mathbf{J} + \frac{\partial \mathbf{D}}{\partial t} \tag{A.2}$$

$$\nabla \bullet \mathbf{D} = \rho \tag{A.3}$$

$$\nabla \bullet \mathbf{B} = 0 \tag{A.4}$$

where

$$\begin{aligned} \mathbf{D} &= \text{electric flux density (in C/m}^2\text{)} \\ \mathbf{E} &= \text{electric field (in V/m)} \\ \mathbf{J} &= \text{current density (in A/m}^2\text{)} \\ \mathbf{B} &= \text{magnetic flux density (in T)} \\ \mathbf{H} &= \text{magnetic field intensity (in A-t/m)} \\ \rho &= \text{volume charge density (in C/m}^3\text{)} \end{aligned} \tag{A.5}$$

We also have the constitutive relations,

$$\mathbf{B} = \mu \mathbf{H} \tag{A.6}$$

$$\mathbf{J} = \sigma \mathbf{E} \tag{A.7}$$

$$\mathbf{D} = \epsilon \mathbf{E} \tag{A.8}$$

where

$$\mu = \text{permeability (in H/m)} = \mu_0\mu_r \tag{A.9}$$
$$\epsilon = \text{permittivity (in F/m)} = \epsilon_o\epsilon_r \tag{A.10}$$
$$\sigma = \text{conductivity (in S/m)}$$

with the permeability of free space $\mu_o = 4\pi \times 10^{-7}$ H/m and the permittivity of free space $\epsilon_o = 8.854 \times 10^{-12}$ F/m. For copper the relative permeability μ_r and the relative permittivity ϵ_r are both taken equal to one.

We can use these equations to derive the diffusion equation given in (4.1) as follows,

1. Take the curl of both sides of (A.1)

$$\nabla \times \nabla \times \mathbf{E} = \nabla \times (-\frac{\partial \mathbf{B}}{\partial t}) \tag{A.11}$$

2. Use (A.6) to replace $\mathbf{B}$ in (A.11) by $\mu\mathbf{H}$

$$\nabla \times \nabla \times \mathbf{E} = \nabla \times (-\mu\frac{\partial \mathbf{H}}{\partial t}) \tag{A.12}$$
$$= -\mu\frac{\partial}{\partial t}(\nabla \times \mathbf{H}) \tag{A.13}$$

3. Substitute (A.2) for $\nabla \times \mathbf{H}$

$$\nabla \times \nabla \times \mathbf{E} = -\mu\frac{\partial}{\partial t}(\mathbf{J} + \frac{\partial \mathbf{D}}{\partial t}) \tag{A.14}$$

4. Use (A.7) and (A.8), respectively, to write $\mathbf{J}$ and $\mathbf{D}$ in terms of $\mathbf{E}$ on the right side of (A.14)

$$\nabla \times \nabla \times \mathbf{E} = -\mu\frac{\partial}{\partial t}(\sigma\mathbf{E} + \epsilon\frac{\partial \mathbf{E}}{\partial t}) \tag{A.15}$$

5. Using the general vector identity for the curl of the curl of a vector

$$\nabla \times \nabla \times \mathbf{A} = \nabla(\nabla \bullet \mathbf{A}) - \nabla^2\mathbf{A} \tag{A.16}$$

we can write,

$$\nabla \times \nabla \times \mathbf{E} = \nabla(\nabla \bullet \mathbf{E}) - \nabla^2\mathbf{E}$$
$$= \nabla(\nabla \bullet \mathbf{D}/\epsilon) - \nabla^2\mathbf{E} \tag{A.17}$$

6. Now if we assume that there is no free charge density in the conductive material ($\rho = 0$), then $\nabla \bullet \mathbf{D} = 0$ according to (A.3), and we have

$$\nabla \times \nabla \times \mathbf{E} = -\nabla^2\mathbf{E} \tag{A.18}$$

7. Equations (A.15) and (A.18) combine to give,

$$\nabla^2\mathbf{E} = \mu\sigma\frac{\partial\mathbf{E}}{\partial t} + \mu\epsilon\frac{\partial^2\mathbf{E}}{\partial t^2} \tag{A.19}$$

8. If we now include in our derivation the assumption that the time-varying fields are sinusoidal, we can remove the explicit time dependence by rewriting equation (A.19) in phasor (complex variable) form. As is shown in equation (1.4) of Section 1.2 we can write the *vector phasor* for the electric field as

$$\underline{\mathbf{E}} = \underline{E}_x(x,y,z)\hat{\mathbf{a}}_\mathbf{x} + \underline{E}_y(x,y,z)\hat{\mathbf{a}}_\mathbf{y} + \underline{E}_z(x,y,z)\hat{\mathbf{a}}_\mathbf{z} \tag{A.20}$$

where the three phasor components $\underline{E}_x$, $\underline{E}_y$ and $\underline{E}_z$ are given by

$$\begin{aligned} \underline{E}_x(x,y,z) &= \underline{E}_x = E_x e^{j\theta_x} \\ \underline{E}_y(x,y,z) &= \underline{E}_y = E_y e^{j\theta_y} \\ \underline{E}_z(x,y,z) &= \underline{E}_z = E_z e^{j\theta_z} \end{aligned}$$

We can therefore write, for example, the *real*, time-varying x-component in terms of the associated *phasor* x-component as

$$E_x(x,y,z,t) = \sqrt{2}\,\mathrm{Re}\left(\underline{E}_x e^{j\omega t}\right) \tag{A.21}$$

$$= \sqrt{2}\,\mathrm{Re}\left(E_x e^{j(\omega t+\theta_x)}\right) \tag{A.22}$$

It is clear from the form of (A.22) that taking any spacial derivative of the real part $E_x(x,y,z,t)$ simply corresponds to taking the same derivative of the phasor component $\underline{E}_x(x,y,z)$. However, if we take a time derivative of the real part, we get

$$\frac{\partial}{\partial t}E_x(x,y,z,t) = \sqrt{2}\,\mathrm{Re}\left(j\omega E_x e^{j(\omega t+\theta_x)}\right) \tag{A.23}$$

which corresponds to the multiplication of the phasor component by $j\omega$. Each additional time derivative of the real part corresponds to an additional factor of $j\omega$ for the phasor component. We can therefore write three rules for transforming equation (A.19) into phasor form

$$\frac{\partial}{\partial i}E_x(x,y,z,t) \iff \frac{\partial}{\partial i}\underline{E}_x(x,y,z) \qquad \text{where } i = x, y \text{ or } z$$

$$\frac{\partial}{\partial t}E_x(x,y,z,t) \iff j\omega\underline{E}_x(x,y,z)$$

$$\frac{\partial^2}{\partial t^2}E_x(x,y,z,t) \iff -\omega^2\underline{E}_x(x,y,z)$$

Finally, using the above three rules, we can rewrite equation (A.19) as

$$\begin{aligned} \nabla^2\underline{\mathbf{E}} &= j\omega\mu\sigma\underline{\mathbf{E}} - \omega^2\mu\epsilon\underline{\mathbf{E}} \\ &= (j\omega\mu\sigma - \omega^2\mu\epsilon)\underline{\mathbf{E}} \end{aligned} \tag{A.24}$$

or, using $\underline{k} = \sqrt{j\omega\mu\sigma - \omega^2\mu\epsilon}$ we have

$$\boxed{\nabla^2\underline{\mathbf{E}} = \underline{k}^2\underline{\mathbf{E}}} \tag{A.25}$$

The above result is the diffusion equation that we seek. This equation states that the spacial distribution of a sinusoidally varying electric field in a medium is related through the complex coefficient $\underline{k}$ to the angular frequency ω of the field variation and to the characteristics of the transmitting media. In this expression the coefficient $\underline{k}$ is the complex wave number whose conjugate is designated as $\underline{k}^*$.

Appendix B

Derivation of Diffusion Equation (4.9) in Terms of H from Maxwell's Equations

We can follow a trail very similar to that used to derive the diffusion equation in terms of the electric field $\mathbf{E}$ to derive the the analogous diffusion equation given in (4.9) in terms of $\mathbf{H}$ as follows:

1. Take the curl of both sides of (A.2)

$$\nabla \times \nabla \times \mathbf{H} = \nabla \times (\mathbf{J} + \frac{\partial \mathbf{D}}{\partial t}) \tag{B.1}$$

2. Using the vector identity for the curl of the curl of a vector given in (A.16) and substituting $\mathbf{B}/\mu$ for $\mathbf{H}$ in the dot-product term we write,

$$\begin{aligned} \nabla \times \nabla \times \mathbf{H} &= \nabla(\nabla \bullet \mathbf{H}) - \nabla^2 \mathbf{H} \\ &= \nabla(\nabla \bullet \mathbf{B}/\mu) - \nabla^2 \mathbf{H} \\ &= -\nabla^2 \mathbf{H} \end{aligned} \tag{B.2}$$

   where (A.4) is used to eliminate the dot-product term.

3. Expanding the right side of (B.1) using the fact that the curl of the sum of two vectors is the sum of the curl of the vectors, we can combine (B.2) and (B.1)

$$\begin{aligned} -\nabla^2 \mathbf{H} &= (\nabla \times \mathbf{J}) + (\nabla \times \frac{\partial \mathbf{D}}{\partial t}) \\ &= (\nabla \times \sigma \mathbf{E}) + (\nabla \times \epsilon \frac{\partial \mathbf{E}}{\partial t}) \end{aligned} \tag{B.3}$$

4. Recalling (A.1) and (A.6) we can rewrite (B.3) as

$$\begin{aligned} -\nabla^2\underline{\mathbf{H}} &= -\sigma\frac{\partial\underline{\mathbf{B}}}{\partial t} - \epsilon\frac{\partial^2\underline{\mathbf{B}}}{\partial t^2} \\ \nabla^2\underline{\mathbf{H}} &= \mu\sigma\frac{\partial\mathbf{H}}{\partial t} + \mu\epsilon\frac{\partial^2\mathbf{H}}{\partial t^2} \end{aligned} \tag{B.4}$$

5. Assuming sinusoidal steady-state excitation, we can use the same approach as in Step 8 of Appendix A to write (B.4) in phasor notation

$$\nabla^2\underline{\mathbf{H}} = j\omega\mu\sigma\underline{\mathbf{H}} - \omega^2\mu\epsilon\underline{\mathbf{H}} \tag{B.5}$$

6. Finally, we can collect terms to yield

$$\begin{aligned} \nabla^2\underline{\mathbf{H}} &= (j\omega\mu\sigma - \omega^2\mu\epsilon)\underline{\mathbf{H}} \\ &= \underline{k}^2\underline{\mathbf{H}} \end{aligned} \tag{B.6}$$

where $\underline{k} = \sqrt{j\omega\mu\sigma - \omega^2\mu\epsilon}$ as before.

Equation (B.6) is the result we sought to prove. This diffusion relation is identical in form to the diffusion equation for the electric field given in (A.25). The magnetic field intensity and electric field at any point in the transmitting media are both related to the frequency of the field variation and the material characteristics of the media.

Appendix C

Derivation of Equation (4.27) from (4.21) and of Equation (4.28) from (4.26)

We are given in Equation (4.21),

$$\nabla \times \underline{\mathbf{J}}(x,y,z) = -\underline{k}^2 \underline{\mathbf{H}}(x,y,z) \tag{C.1}$$

In rectangular coordinates, we expand the curl on the left-hand side of the above equation as

$$\begin{aligned} \nabla \times \underline{\mathbf{J}} &= \begin{vmatrix} \hat{\mathbf{a}}_\mathbf{x} & \hat{\mathbf{a}}_\mathbf{y} & \hat{\mathbf{a}}_\mathbf{z} \\ \frac{\partial}{\partial x} & \frac{\partial}{\partial y} & \frac{\partial}{\partial z} \\ \underline{J}_x & \underline{J}_y & \underline{J}_z \end{vmatrix} \\ &= \hat{\mathbf{a}}_\mathbf{x}\left(\frac{\partial \underline{J}_z}{\partial y} - \frac{\partial \underline{J}_y}{\partial z}\right) + \hat{\mathbf{a}}_\mathbf{y}\left(\frac{\partial \underline{J}_x}{\partial z} - \frac{\partial \underline{J}_z}{\partial x}\right) + \hat{\mathbf{a}}_\mathbf{z}\left(\frac{\partial \underline{J}_y}{\partial x} - \frac{\partial \underline{J}_x}{\partial y}\right) \end{aligned} \tag{C.2}$$

In the case we are modeling, we assume there is current only in the y-direction and that this current varies only with x. Therefore we write

$$\underline{J}_x = \underline{J}_z = 0 \tag{C.3}$$

and,

$$\frac{\partial \underline{J}_y}{\partial z} = 0 \tag{C.4}$$

With these assumptions we can write the curl expansion above as

$$\nabla \times \underline{\mathbf{J}} = \frac{\partial \underline{J}_y(x)}{\partial x}\hat{\mathbf{a}}_\mathbf{z} \tag{C.5}$$

Our assumptions also state that the magnetic-field intensity function $\underline{\mathbf{H}}(x,y,z)$ is a function that varies only with x and is directed only in the z-direction. Therefore,

$$\underline{\mathbf{H}}(x,y,z) = \underline{H}_z(x)\hat{\mathbf{a}}_\mathbf{z} \tag{C.6}$$

If the result of (C.5) is used in the left side of (C.1) and the result of (C.6) is used in the right side of (C.1), we have as a result equation (4.27):

$$\boxed{\frac{\partial \underline{J}_y(x)}{\partial x}\hat{\mathbf{a}}_\mathbf{z} = -\underline{k}^2\underline{H}_z(x)\hat{\mathbf{a}}_\mathbf{z}} \tag{C.7}$$

A very similar derivation for Equation (4.28) follows from (4.26). Equation (4.26) is repeated here,

$$\nabla \times \underline{\mathbf{H}}(x,y,z) \approx \underline{\mathbf{J}}(x,y,z) \tag{C.8}$$

Then as in the above derivation, we expand the curl in rectangular coordinates as

$$\nabla \times \underline{\mathbf{H}} = \hat{\mathbf{a}}_\mathbf{x}\left(\frac{\partial \underline{H}_z}{\partial y} - \frac{\partial \underline{H}_y}{\partial z}\right) + \hat{\mathbf{a}}_\mathbf{y}\left(\frac{\partial \underline{H}_x}{\partial z} - \frac{\partial \underline{H}_z}{\partial x}\right) + \hat{\mathbf{a}}_\mathbf{z}\left(\frac{\partial \underline{H}_y}{\partial x} - \frac{\partial \underline{H}_x}{\partial y}\right) \tag{C.9}$$

In the case we are modeling, we assume the magnetic field is directed only in the z-direction and that this field varies only with x. Therefore we write,

$$\underline{H}_x = \underline{H}_y = 0 \tag{C.10}$$

and,

$$\frac{\partial \underline{H}_z}{\partial y} = 0 \tag{C.11}$$

With these assumptions, we can write the curl expansion above as,

$$\nabla \times \underline{\mathbf{H}} = -\frac{\partial \underline{H}_z(x)}{\partial x}\hat{\mathbf{a}}_\mathbf{y} \tag{C.12}$$

Since the current density is a function of x and is directed only in the y-direction, we have

$$\underline{\mathbf{J}}(x,y,z) = \underline{J}_y(x)\hat{\mathbf{a}}_\mathbf{y} \tag{C.13}$$

Equating the right hand sides of (C.12) and (C.13) gives (4.28) directly

$$\boxed{\frac{\partial \underline{H}_z(x)}{\partial x}\hat{\mathbf{a}}_\mathbf{y} = -\underline{J}_y(x)\hat{\mathbf{a}}_\mathbf{y}} \tag{C.14}$$

Appendix D

Physical Basis for the Distributions of $\underline{H}_z(x)$ and $\underline{J}_y(x)$

In Section 4.1.1, we describe the mathematical statement of the infinite-current-sheet field problem as the *diffusion equation*. Our mathematical analysis begins with Maxwell's equations and arrives at the diffusion equation as a result of making various simplifying assumptions. This concept of diffusion is useful here in obtaining a qualitative understanding of the field and current distributions across a layer. Indeed, if we examine Figs. 4.2 and 4.3 we can easily see what appears to be a diffusion-like attenuation away from the surfaces of the current sheet. We should point out, however, that the propagation of electromagnetic energy across a conducting layer is *physically distinct* from the thermodynamic process of diffusion, although in certain cases it is mathematically equivalent. For this reason, a more complete understanding of the distributions of $\underline{H}_z(x)$ and $\underline{J}_y(x)$ is best obtained by considering a more relevant physical model, namely, the traveling wave.

In Appendices A and B we derive the diffusion equation in terms of the electric field vector phasor $\underline{\mathbf{E}}$ and the magnetic field vector phasor $\underline{\mathbf{H}}$. In each case, before introducing phasor notation, we obtain as an intermediate result a single partial differential equation in terms of only one field quantity, either $\mathbf{E}$ or $\mathbf{H}$. These intermediate results appear as equations (A.19) and (B.4) in the Appendices, and are repeated here for clarity

$$\nabla^2\mathbf{E} = \mu\epsilon\frac{\partial^2\mathbf{E}}{\partial t^2} + \mu\sigma\frac{\partial\mathbf{E}}{\partial t} \tag{D.1}$$

$$\nabla^2\mathbf{H} = \mu\epsilon\frac{\partial^2\mathbf{H}}{\partial t^2} + \mu\sigma\frac{\partial\mathbf{H}}{\partial t} \tag{D.2}$$

Equations (D.1) and (D.2) are commonly known as the *telegraph equations* since they were originally derived to explain the propagation of electromagnetic pulses down telegraph lines. They are, however, a direct reformulation of Maxwell's equations and may consequently be applied to solve a variety of field problems, including that of an infinite current sheet. In our application of the telegraph equations to an infinite current

sheet, we arrive at the final field solutions in a series of steps that may be outlined as follows:

1. Assume that the fields are sinusoidal functions of time and introduce phasor notation to reduce the telegraph equations to the form of diffusion equations. (Appendices A and B)
2. Make the good conductor approximation that $\sigma \gg \omega\epsilon$ and use this to simplify the expression for the complex wave number $\underline{k}$. (Section 4.1.2)
3. Assume that the current density and the electric field are related through Ohm's law[1] by $\mathbf{J} = \sigma\mathbf{E}$, and use this to rewrite the equation for $\mathbf{E}$ in terms of $\mathbf{J}$. (Section 4.1.2)
4. Assume that both $\underline{\mathbf{J}}$ and $\underline{\mathbf{H}}$ are functions of x only. (Section 4.1.2)
5. Assume that $\underline{\mathbf{H}}$ is directed exclusively along z-axis while $\underline{\mathbf{J}}$ is directed exclusively along the y-axis. (Section 4.1.2)
6. Use Maxwell's equations to derive differential relationships between $\underline{H}_z(x)$ and $\underline{J}_y(x)$, so that one can easily be found from the other. (Section 4.1.4)
7. Assume that the solution to the diffusion equation for $\underline{H}_z(x)$ has the general form of
$$\underline{H}_z(x) = \underline{H}_1 e^{\underline{k}x} + \underline{H}_2 e^{-\underline{k}x} \tag{D.3}$$
and apply the boundary conditions at $x = 0$ and $x = h_{cu}$ to obtain the final solution for $\underline{H}_z(x)$. (Section 4.2)
8. Use the differential relationship found in Step 6 to directly calculate the solution for $\underline{J}_y(x)$. (Section 4.2)

A mathematically equivalent but physically more enlightening development might begin by directly solving the telegraph equations themselves, without using phasor notation to first remove the explicit time dependence and reduce them to the form of diffusion equations. As they are written above, equations (D.1) and (D.2) are in terms of the time-varying vector fields $\mathbf{E}(x, y, z, t)$ and $\mathbf{H}(x, y, z, t)$. However, the math involved in solving these equations directly is greatly simplified is we introduce complex-number notation. If we assume that $\mathbf{E}(x, y, z, t)$ and $\mathbf{H}(x, y, z, t)$ are varying sinusoidally in time, then we can make use of equations (A.20) and (A.22) to rewrite the vector $\mathbf{E}(x, y, z, t)$ in terms of its corresponding vector phasor $\underline{\mathbf{E}}$

$$\mathbf{E}(x, y, z, t) = \sqrt{2}\mathrm{Re}\left[\underline{\mathbf{E}}(x, y, z)e^{j\omega t}\right] \tag{D.4}$$

[1]The more familiar form of Ohm's law $V = IR$ is just a special case of $\mathbf{J} = \sigma\mathbf{E}$. We can see this by applying a voltage V across a round wire of cross-section A and length l, so that the electric field $E = \frac{J}{\sigma} = \frac{I}{\sigma A}$ is along the wire and given by $E = \frac{V}{l}$. Solving for V gives $V = \frac{l}{\sigma A} I = RI$, where $R = \frac{l}{\sigma A}$.

Now if we define a complex-valued function of time $\tilde{\mathbf{E}}(x,y,z,t)$ such that

$$\tilde{\mathbf{E}}(x,y,z,t) = \sqrt{2}\left[\underline{\mathbf{E}}(x,y,z)e^{j\omega t}\right] \tag{D.5}$$

where the tilde designates a complex quantity, then we can write the vector $\mathbf{E}(x,y,z,t)$ as

$$\mathbf{E}(x,y,z,t) = \text{Re}\left[\tilde{\mathbf{E}}(x,y,z,t)\right] \tag{D.6}$$

We henceforth refer to the quantity $\tilde{\mathbf{E}}(x,y,z,t)$ as the *complex electric field*, since its real part is precisely equal to the actual time-varying electric field. Note that the complex electric field may be obtained from the electric field phasor simply by multiplying the electric field phasor with $\sqrt{2}\,e^{j\omega t}$. Thus, we may visualize the complex electric field in the complex plane as being equivalent to a phasor, lengthened by a factor of $\sqrt{2}$, and rotating in a counterclockwise direction in the complex plane with an angular frequency ω. In a completely parallel fashion, we can also write the magnetic field vector $\mathbf{H}(x,y,z,t)$ in terms of its associated complex magnetic field[2] $\tilde{\mathbf{H}}(x,y,z,t)$ as

$$\mathbf{H}(x,y,z,t) = \text{Re}\left[\tilde{\mathbf{H}}(x,y,z,t)\right] \tag{D.7}$$

where $\tilde{\mathbf{H}}(x,y,z,t)$ is defined as

$$\tilde{\mathbf{H}}(x,y,z,t) = \sqrt{2}\left[\underline{\mathbf{H}}(x,y,z)e^{j\omega t}\right] \tag{D.8}$$

Given the above definitions for the complex electric field (D.5) and the complex magnetic field (D.8) we can now write the general solutions to the telegraph equations (D.1) and (D.2) in complex form as

$$\tilde{\mathbf{E}}(x,t) = \tilde{\mathbf{E}}_1 e^{(\underline{k}x+j\omega t)} + \tilde{\mathbf{E}}_2 e^{(-\underline{k}x+j\omega t)} \tag{D.9}$$

$$\tilde{\mathbf{H}}(x,t) = \tilde{\mathbf{H}}_1 e^{(\underline{k}x+j\omega t)} + \tilde{\mathbf{H}}_2 e^{(-\underline{k}x+j\omega t)} \tag{D.10}$$

where $\tilde{\mathbf{E}}_1$, $\tilde{\mathbf{E}}_2$, $\tilde{\mathbf{H}}_1$ and $\tilde{\mathbf{H}}_2$ are four arbitrary complex constants, and we have assumed that both the electric and magnetic fields are functions of x only. Thus, the *actual solutions* to equations (D.1) and (D.2) (which represent the physical fields) can be retrieved by taking the real part of (D.9) and (D.10), respectively. Note, however, that the complex form of the solutions as given in (D.9) and (D.10) satisfy the telegraph equations *themselves*, as can be verified easily by substituting (D.9) and (D.10) into the telegraph equations (D.1) and (D.2), replacing each real field quantity with its corresponding complex field quantity. Upon making such a substitution, we find that (D.9) and (D.10) are valid solutions to the telegraph equations provided that

$$\underline{k}^2 = j\omega\mu\sigma - \omega^2\mu\epsilon \tag{D.11}$$

[2]The complex electric and magnetic fields as we define them here have no real physical significance. We merely find them a convenient mathematical tool which, if properly used, provide all the desired information on the actual fields within an infinite current sheet.

which is the same result that we obtain in Appendix A. Indeed, at this point we *could* proceed by applying a series of steps similar to those outlined above to arrive at the same final solutions that are stated in Section 4.2. However, as they are now written, equations (D.9) and (D.10) are already very useful to us in that they describe a superposition of two electromagnetic waves. It is this physical model that we find fundamental to a thorough understanding skin effect.

Let us first consider equation (D.9) and explore some of its properties. Note that the first term on the right-hand side is a complex-number representation of a plane wave traveling in the $-x$-direction, and the second term on the right-hand side represents a plane wave traveling in the $+x$-direction. Equation (D.9), therefore, represents a superposition of two plane waves. These waves are called plane waves because they possess a surface of constant phase, or wavefront, that is planar. Another property of these two plane waves, although it is difficult to see from equation (D.9), is that they are sinusoidal in both time and space. We can more clearly see this sinusoidal behavior by focusing on the plane wave traveling in the $-x$-direction and extracting the real part, so as to obtain a mathematical description of the actual electric field plane wave. To do this, we first need to rewrite the complex wave number $\underline{k}$ as[3]

$$\underline{k} = k_1 + k_2 j \tag{D.12}$$

and the complex constant $\tilde{\mathbf{E}}_1$ as

$$\tilde{\mathbf{E}}_1 = |\tilde{\mathbf{E}}_1| e^{j\theta_{E1}} \tag{D.13}$$

The first term on the right-hand side of equation (D.9) can now be expanded as

$$\begin{aligned} \tilde{\mathbf{E}}_1 e^{(\underline{k}x + j\omega t)} &= |\tilde{\mathbf{E}}_1| e^{k_1 x} e^{j(k_2 x + \omega t + \theta_{E1})} \\ &= |\tilde{\mathbf{E}}_1| e^{k_1 x} [\cos(k_2 x + \omega t + \theta_{E1}) \\ &\quad + j \sin(k_2 x + \omega t + \theta_{E1})] \end{aligned} \tag{D.14}$$

and taking the real part gives

$$\text{Re}\left[\tilde{\mathbf{E}}_1 e^{\underline{k}x + j\omega t}\right] = |\tilde{\mathbf{E}}_1| e^{k_1 x} \cos(k_2 x + \omega t + \theta_{E1}) \tag{D.15}$$

From the form of equation (D.15) we can clearly see that, at every fixed point x in space, the electric field intensity varies sinusoidally in time with an angular frequency ω. Likewise, if we look at a snapshot of the electric field intensity at any instant of time t, we see that the electric field varies as a damped sinusoid in the $-x$-direction with an exponential envelope that decreases by $1/e$ in a distance of $1/k$, and shows a sinusoidal periodicity along the x-axis equal to $2\pi/k_2$. The amplitude of this wave, therefore, decreases as the wave "travels" in the $-x$-direction, and the amplitude of the

[3] Actually, there are two roots to equation (D.11), $\pm(k_1 + k_2 j)$. We choose the positive root, which gives positive values for k_1 and k_2. The negative root would give us a physically meaningless result.

electric field at $x = 0$ is given by $|\tilde{\mathbf{E}}_1|$. We can get a sense of traveling from equation (D.15) by considering the relative location of a single wave peak as time progresses. If the initial phase angle θ_{E1} is taken to be zero, then at time $t = 0$, there is a wave peak at $x = 0$; however, as time advances, the position along the x-axis at which the peak is located is $x = -\omega t/k_2$. In other words, the peak appears to move in the $-x$-direction and, since the envelope decreases in the $-x$-direction, the peak becomes attenuated as it moves.

In a similar manner, we can extract the real part of the wave traveling in the $+x$-direction (the second term on right-hand side of (D.9)). Again, we can write the complex constant $\tilde{\mathbf{E}}_2$ in polar form as

$$\tilde{\mathbf{E}}_2 = |\tilde{\mathbf{E}}_2| e^{j\theta_{E2}} \tag{D.16}$$

and use this together with (D.12) to expand the second term on right-hand side of (D.9) as

$$\begin{aligned} \tilde{\mathbf{E}}_2 e^{(-\underline{k}x + j\omega t)} &= |\tilde{\mathbf{E}}_2| e^{-k_1 x} e^{j(-k_2 x + \omega t + \theta_{E1})} \\ &= |\tilde{\mathbf{E}}_2| e^{-k_1 x} [\cos(-k_2 x + \omega t + \theta_{E1}) \\ &\quad + j \sin(-k_2 x + \omega t + \theta_{E1})] \end{aligned} \tag{D.17}$$

Using the identity $\cos(-x) = \cos(x)$ and taking the real part of (D.17) we obtain

$$\mathrm{Re}\left[\tilde{\mathbf{E}}_2 e^{-\underline{k}x + j\omega t}\right] = |\tilde{\mathbf{E}}_2| e^{-k_1 x} \cos(k_2 x - \omega t - \theta_{E2}) \tag{D.18}$$

which is also a sinusoidal plane wave. This wave, however, has its peaks driven in the $+x$-direction as time progresses. We can again demonstrate this by considering the relative location of a single wave peak as time progresses. Taking the initial phase angle θ_{E2} to be zero, we observe that at $t = 0$ there is a peak at $x = 0$, just as in the previous case. For time $t > 0$, however, the same wave peak occurs at $x = \omega t/k_2$; thus, the peak appears to move in the $+x$-direction. Nevertheless, since the exponential envelope of (D.18) decreases in the $+x$-direction, the wave peak is once again attenuated as it moves.

We measure the amount of attenuation that a wave experiences by the skin depth[4], which is defined as the distance that a wave must travel to be attenuated by a factor of e^{-1}. Note that this definition applies equally well to the wave traveling in the $+x$-direction as it does to the wave traveling in the $-x$-direction, and from equations (D.15) and (D.18) the skin depth is clearly given by

$$\delta = \frac{1}{k_1} \tag{D.19}$$

Likewise, at any instant in time, each wave has the same distance between adjacent peaks. This measure of spacial periodicity is called the wavelength λ, and for either

[4]Note that we have not, at this point, made the assumption that the conductor is a *good* one, i.e., that $\sigma \gg \omega\epsilon$.

wave it is given by

$$\lambda = \frac{2\pi}{k_2} \tag{D.20}$$

If we now examine the complex magnetic field solution (D.10) for $\tilde{\mathbf{H}}(x,t)$, we find it to be of the same form as the complex electric field solution (D.9) for $\tilde{\mathbf{E}}(x,t)$. Accordingly, we can also view equation (D.10) as a complex-number representation of a superposition of two plane waves: one traveling in the $-x$-direction and the other traveling in the $+x$-direction. Furthermore, the frequency, wavelength and skin depth associated with the two waves of equation (D.10) are all the same as those associated with (D.9). In fact, the only distinction whatever between the two solutions for the telegraph equations is that one describes the magnetic field and the other the electric field. Note that although the actual amplitudes of both the electric and magnetic waves are attenuated as the waves travel, we henceforth refer to the complex vectors $\tilde{\mathbf{E}}_1$ and $\tilde{\mathbf{E}}_2$ as the *complex amplitudes* of the electric fields, and $\tilde{\mathbf{H}}_1$ and $\tilde{\mathbf{H}}_2$ as the *complex amplitudes* of the magnetic fields.

Even though equations (D.1) and (D.2) are derived directly from Maxwell's equations (Appendices A and B), it is important to realize that, because they were arrived at by taking derivatives, they do not contain all of the information that Maxwell's equations contain. For this reason, we must now reconsider Maxwell's equations themselves in order to further explain the nature of our assumed traveling wave solutions (D.9) and (D.10). Let us first concentrate our attention on the electric and magnetic waves that are traveling in the $+x$-direction, and use Maxwell's equations to analyze each of these waves. Since there is no embedded free charge density inside an ideal conductor, we can use (A.8) to write Gauss's law (A.3) in complex form as

$$\nabla \bullet \tilde{\mathbf{E}} = 0 \tag{D.21}$$

If we expand the complex amplitude $\tilde{\mathbf{E}}_2$ in terms of its three spacial components as

$$\tilde{\mathbf{E}}_2 = (\tilde{E}_2)_x \hat{\mathbf{a}}_\mathbf{x} + (\tilde{E}_2)_y \hat{\mathbf{a}}_\mathbf{y} + (\tilde{E}_2)_z \hat{\mathbf{a}}_\mathbf{z} \tag{D.22}$$

where $(\tilde{E}_2)_i$ represents the $i^{\underline{\text{th}}}$ spacial component of the complex vector, then we can apply (D.21) to the second term on the right-hand side of equation (D.9) to yield

$$-\underline{k}(\tilde{E}_2)_x e^{-\underline{k}x+j\omega t} = 0 \tag{D.23}$$

or

$$(\tilde{E}_2)_x = 0 \tag{D.24}$$

Similarly, we can apply the relationship (A.6) to write (A.4) in complex form as

$$\nabla \bullet \tilde{\mathbf{H}} = 0 \tag{D.25}$$

and apply this to the second term on the right-hand side of equation (D.10) to yield

$$(\tilde{H}_2)_x = 0 \tag{D.26}$$

Equations (D.24) and (D.26) suggest that x-components of both the complex electric and the complex magnetic fields are zero. Since a complex quantity is zero only if both its real and its imaginary parts are zero, we can also conclude from (D.24) and (D.26) that the actual electric and magnetic fields have no component along the x-axis. Note that this is the axis along which both the electric and magnetic waves are traveling. Waves such as these, which exert influences or cause disturbances in directions perpendicular to their direction of travel, are called *transverse*.

Using Faraday's law (A.1), we can relate the complex electric and magnetic amplitudes of the waves traveling in the $+x$-direction by

$$\tilde{\mathbf{H}}_2 = \frac{k}{j\omega\mu}(\hat{\mathbf{a}}_\mathbf{x} \times \tilde{\mathbf{E}}_2) \tag{D.27}$$

Since the vector resulting from a cross-product is in a direction perpendicular to the plane containing the two crossed vectors, equation (D.27) implies that the complex magnetic field is perpendicular to the plane defined by the complex electric field and the x-axis (axis of travel). Consequently, it can be shown that the actual magnetic field must also be perpendicular to the plane containing the electric field and the x-axis, and because of equations (D.24) and (D.26) we know that the electric field, the magnetic field and the x-axis must all be mutually perpendicular. Therefore, since these magnetic and electric plane waves are so closely related, they are considered collectively to comprise a single transverse electromagnetic (TEM) wave, propagating (traveling) in the $+x$-direction.

In the same way, we can apply Maxwell's equations to the first term on the right-hand side of equation (D.9) and the corresponding term of equation(D.10) to yield the relations

$$(\tilde{E}_1)_x = (\tilde{H}_1)_x = 0 \tag{D.28}$$

and

$$\tilde{\mathbf{H}}_1 = \frac{k}{j\omega\mu}(-\hat{\mathbf{a}}_\mathbf{x} \times \tilde{\mathbf{E}}_1) \tag{D.29}$$

Once again, equations (D.28) and (D.29) imply that these electric and magnetic traveling waves comprise a single TEM wave, only now it is traveling in the $-x$-direction. We can therefore view our assumed solutions (D.9) and (D.10) to the telegraph equations as complex vector representation of the superposition of two TEM waves, one traveling in the $+x$- and the other in the $-x$-direction. In actuality, of course, it is the real parts of equations (D.9) and (D.10) that define these TEM waves.

It is important to note that, although we can conclude from (D.27) and (D.29) that the electric and magnetic fields within a TEM wave must both lie in the yz-plane and be mutually perpendicular, we still do not specifically know the direction of either field. This information concerning the orientation of the fields is called the *polarization* of the TEM wave, and it is, in general, determined by some additional physical constraint. In the case of an infinite solenoid, the polarization of the wave is determined solely by the orientation of the solenoid itself. This is the case because, as argued in Section 3.1.1, the magnetic field within an infinite solenoid is uniformly directed along its axis. If we

define our coordinate system as in Fig. 3.15, then we know that the magnetic field within an infinite solenoid is along the z-axis. Consequently, we can see from (D.27) that the electric field must be directed along the y-axis, and because of Ohm's law (A.7), the current density as well. Note that it is the TEM-wave property of mutual orthogonality of the electric field, magnetic field and direction of travel that forms a physical basis for the assumptions in Section 4.1.2 that the magnetic field is along the z-axis, the current density along the y-axis, and that both the magnetic field intensity and current density are functions of x only. We assume this same orientation or polarization of the TEM wave throughout the remainder of this appendix.

Before considering the behavior of the superposed TEM waves represented by (D.9) and (D.10), let us first concentrate on a single TEM wave traveling in the $+x$-direction with no obstructions. If the wave is traveling in free space, then $\sigma = 0$, and from equation (D.11) we see that

$$\underline{k} = j\omega\sqrt{\epsilon_0\mu_0} \tag{D.30}$$

and $\underline{k}$ is purely imaginary. Based upon equations (D.19) and (D.20), therefore, we expect that the wave will propagate unattenuated in the $+x$-direction with a wavelength given by

$$\lambda = \frac{2\pi}{\omega\sqrt{\epsilon_0\mu_0}} \tag{D.31}$$

In its upper left-hand corner, Fig. D.1 shows in an inset drawing the orientation of the x-, y- and z-axes. Note that the z-axis points upward on the page and lies in the plane of the page, while the x-axis comes out of the page to the left and the y-axis out of the page to the right. Figure D.1 also shows a representation of a 7.5 MHz TEM wave at a single instant in time, plotted in the same coordinate system as shown in the inset. The wave is traveling in free space in the $+x$-direction with a source of some kind at $x = 0$, which establishes a polarization of the TEM wave such that the magnetic field $\mathbf{H}(x)$ is directed along on the vertical (z) axis, and electric field $\mathbf{E}(x)$ is directed along the horizontal (y) axis. The source at the origin is maintaining a magnetic field that varies sinusoidally with an amplitude of 2 A-t/m, and the associated electric field satisfies equation (D.27). As time advances, the wave peaks shown move to the left on the page in the $+x$-direction, and new peaks periodically appear at $x = 0$. Each peak is traveling at the speed of light[5], since the wave is in free space where the magnetic permeability and the electric permittivity are equal to their free space values. Note that Fig. D.1 does not show the entire plane wave, but only the part that is traveling along our particular x-axis. In reality, the wave completely fills all space where $x \geq 0$, but regardless of which point we choose on the yz-plane as the origin of the x-axis, the variation of the fields along this axis will be identical to Fig. D.1.

Figure D.1 also reveals that the magnetic and electric fields are oscillating in phase. We can understand this by examining the phase relationship between the sinusoidally

[5]The speed of a wave is in general observed to be $v = f\lambda$. For an electromagnetic wave it is also given by $v = \frac{\omega}{\underline{k}}$, which, in free space, reduces to $v = \frac{1}{\sqrt{\mu_0\epsilon_0}} \approx 3.0 \times 10^8\ m/s$.

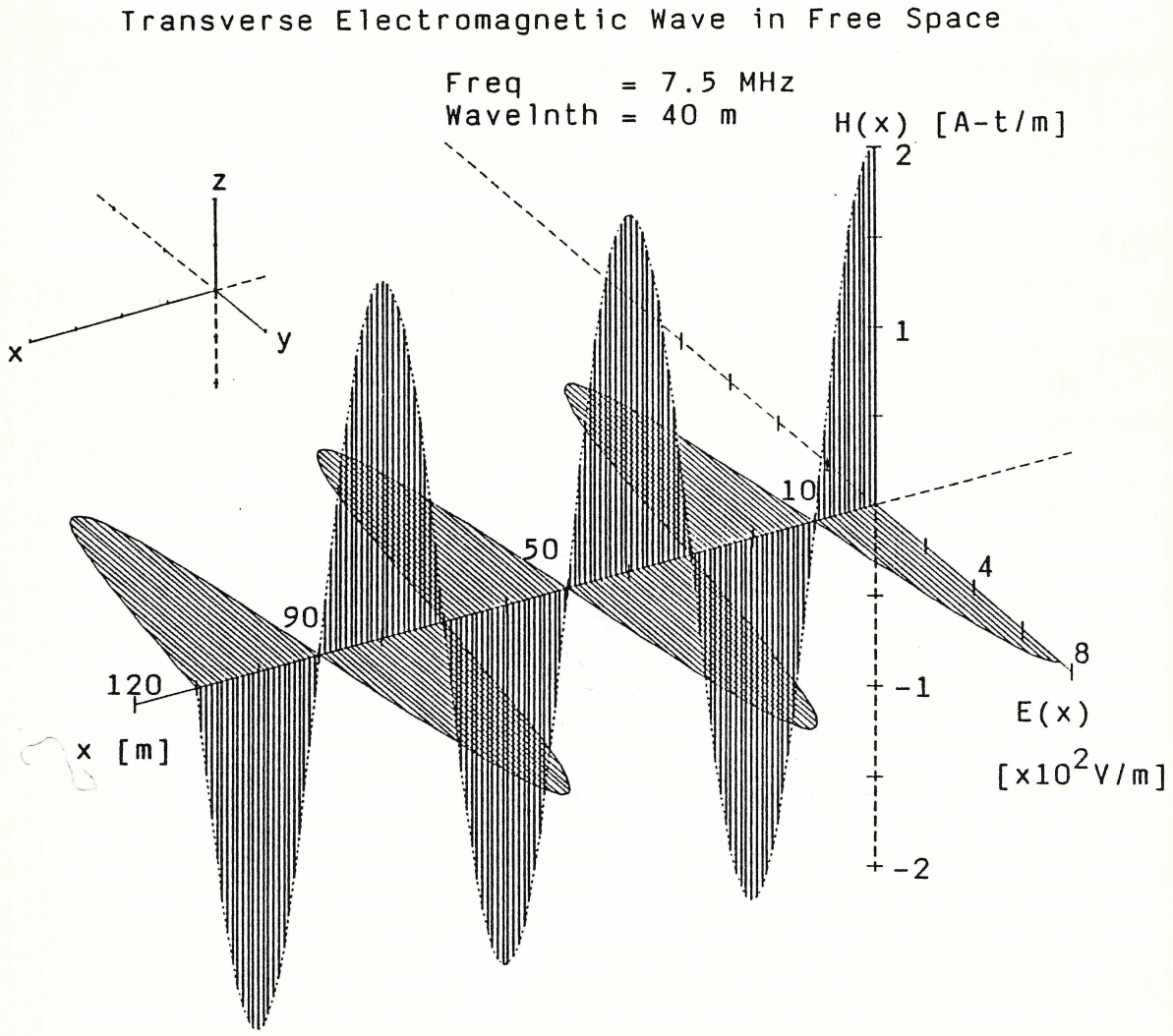


Figure D.1: Representation of a 7.5 MHz transverse electromagnetic wave traveling through free space in the $+x$-direction.

varying magnetic and electric fields suggested by (D.27). By comparing (D.13) and (D.15) we see that the phase angle associated with the polar form of the complex amplitude is also the initial phase angle of the actual, sinusoidal electric-field traveling wave. Thus, if we rewrite (D.27) in polar form as

$$|\tilde{\mathbf{H}}_2|e^{j\theta_{H2}} = \frac{|\underline{k}|e^{j\theta_k}}{e^{j(90°)}\omega\mu}(\hat{\mathbf{a}}_\mathbf{x} \times |\tilde{\mathbf{E}}_2|e^{j\theta_{E2}}) \tag{D.32}$$

we can equate the exponentials on the left-hand and right-hand sides to obtain

$$\theta_{H2} = \theta_k - 90° + \theta_{E2} \tag{D.33}$$

Since $\underline{k}$ is purely imaginary, its phase angle is also 90^o, and so

$$\theta_{H2} = \theta_{E2} \tag{D.34}$$

and the fields oscillate in phase.

If we now consider the TEM wave to be traveling in a slightly conductive medium ($\sigma > 0$), then the electric field will begin to interact with this medium to produce currents according to Ohm's law. This results in a transfer of energy from the fields to the medium, which is why the amplitudes of the fields attenuate as the wave travels. Figure D.2 shows a representation of a TEM wave traveling through a very weak conductor. The source at the origin is again establishing a magnetic field that varies sinusoidally with an amplitude of 2 A-t/m, and the magnetic permeability and electric permittivity are again taken to be their free space values. Note that both the electric and the magnetic fields are attenuated as the wave propagates, and the wavelength is slightly reduced from its free space value since the wave has been slowed down by its interaction with the medium. Note also that there is a slight phase difference between the magnetic and electric fields since the wave number $\underline{k}$ of equation (D.27) now has a non-zero real part. This can be seen more clearly in the expanded-view inset of Fig. D.2, which shows on a magnified scale the electric and magnetic fields in the vicinity of the zero-crossing near $x = 10$ m.

Figure D.3 shows a representation of a TEM wave propagating through a medium of five times greater conductivity than that of Fig. D.2. Now the wave is able to complete little more that a single cycle before being almost completely attenuated, the wavelength is greatly reduced, and the electric field is noticeably leading the magnetic field in phase. Finally, if we consider a medium of very high conductivity, we can make the assumption that $\sigma \gg \omega\epsilon$ in equation (D.11) and obtain (as in Section 4.1.2)

$$\underline{k} = \sqrt{\frac{2}{\omega\mu_0\sigma}}(1+j) \tag{D.35}$$

so that the skin depth δ is now given by

$$\delta = \sqrt{\frac{2}{\omega\mu_0\sigma}} \tag{D.36}$$

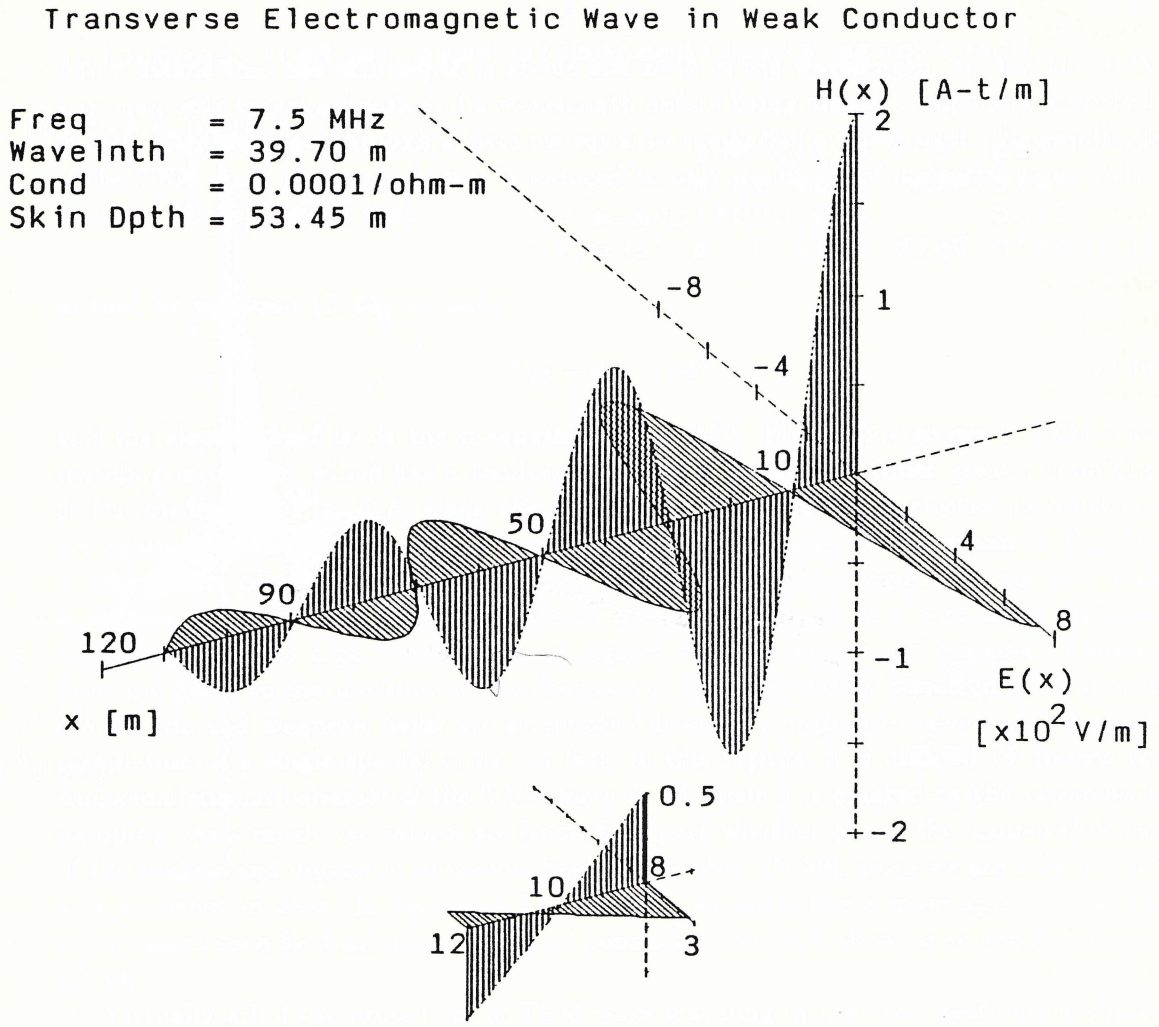


Figure D.2: Representation of a 7.5 MHz transverse electromagnetic wave traveling through a very weak conductor in the $+x$-direction.

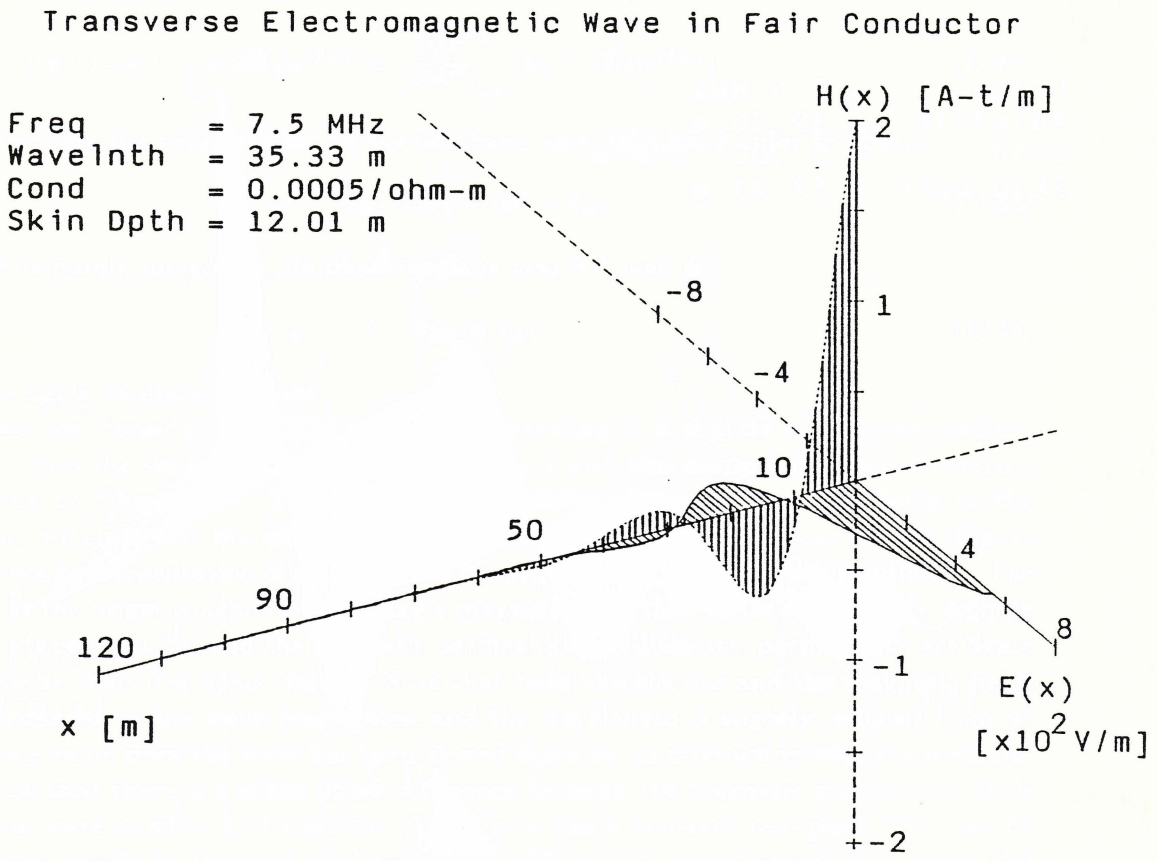


Figure D.3: Representation of a 7.5 MHz transverse electromagnetic wave traveling through a fair conductor in the $+x$-direction.

Since the real and imaginary parts of $\underline{k}$ are now equal, we can use equations (D.19) and (D.20) to write

$$\delta = \frac{\lambda}{2\pi} \tag{D.37}$$

which means that the skin depth is about one sixth of the wavelength, or that the TEM wave can only travel a fraction of a wavelength before being almost completely absorbed. In fact, after traveling through a distance equal to one half of a wavelength, the amplitude of the TEM wave in the conductor is reduced to only about 4% of its initial value. Also, equation (D.35) implies that

$$\theta_k = 45° \tag{D.38}$$

so that by equation (D.33) we have

$$\theta_{H2} = \theta_{E2} - 45° \tag{D.39}$$

and the electric field leads the magnetic field by 45^o. Figure D.4 shows a TEM wave traveling in copper, which has a conductivity that is about 10^{11} times greater than that of the medium of Fig. D.3, while the magnetic permeability and electric permittivity are again taken as their free space values. Note that the scale on the x-axis of Fig. D.4 is four orders of magnitude smaller than that of the previous figures. This new scale is necessary because the TEM wave is now attenuated heavily in a very short distance, indicating that the high conductivity of copper causes a very rapid transfer of energy from the fields to the medium at this frequency. As predicted by equation (D.37), both the electric and magnetic fields are attenuated down to a negligible value well before the completion of a single spacial cycle. In fact, in this regime, it is difficult to discern the sinusoidal spacial behavior of the TEM wave at all, since it is masked by the exponential damping. As a result, we cannot see from this figure whether or not the *temporal* phases of the electric and magnetic sinusoidal fields really obey (D.39), since we are only looking at a snapshot in time. In Section 4.3.2, however, we introduce a more appropriate way to represent such field solutions in a good conductor that will allow us to verify equation (D.39).

Virtually all of the properties of TEM wave traveling in the $+x$-direction are shared with a with a TEM wave traveling in the $-x$-direction. Regardless of the direction of propagation, a TEM wave responds in precisely the same manner to an increase in conductivity or frequency. In fact, the only distinguishing characteristic of a TEM wave traveling in the $-x$-direction is that the electric field oscillates 180° out of phase with respect to a wave traveling in the $+x$-direction, assuming that the magnetic fields are oscillating in phase. This is clear from equation (D.29), which suggests that

$$\theta_{H1} = \theta_k - 90° - 180° + \theta_E 1 \tag{D.40}$$

so that for a good conductor the phases of the magnetic and electric fields are related by

$$\theta_{H1} = 45° - 90° - 180° + \theta_{E1} \theta_{H1} = \theta_{E1} - 225° \tag{D.41}$$

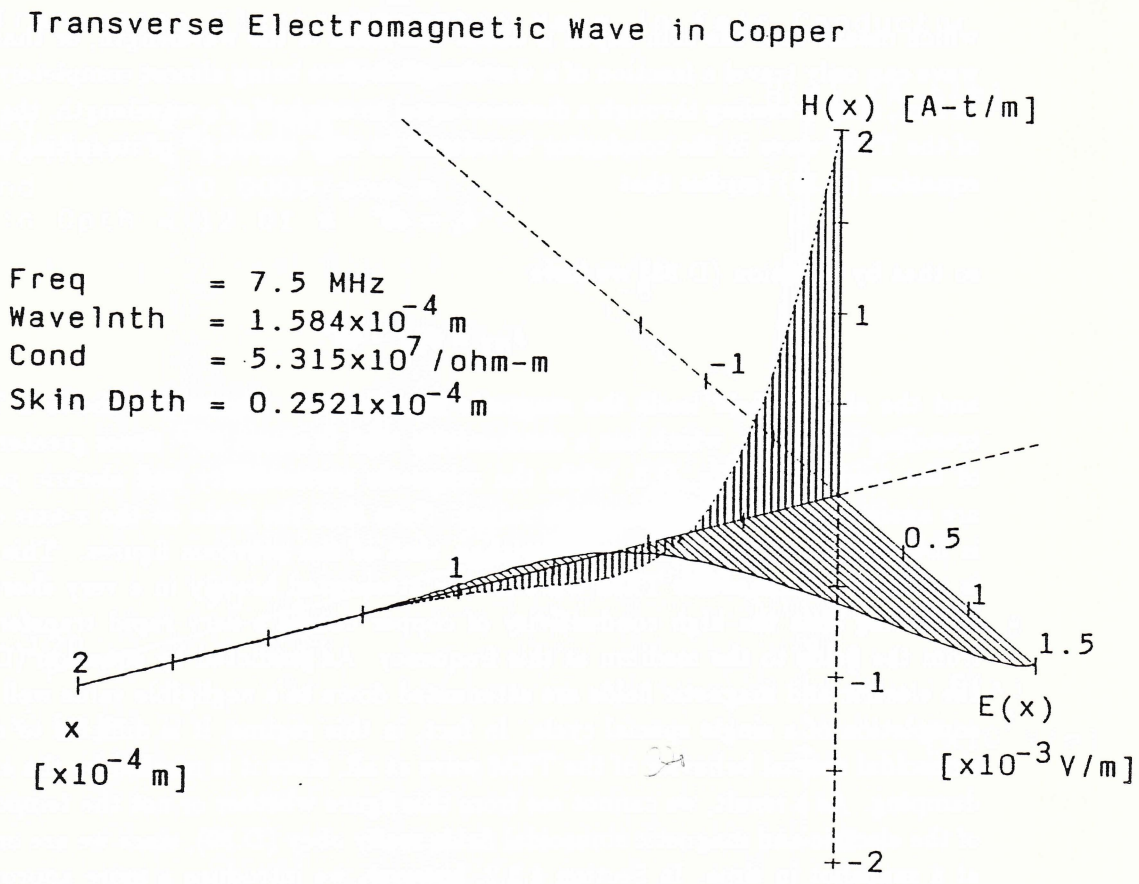


Figure D.4: Representation of a 7.5 MHz transverse electromagnetic wave traveling through copper in the $+x$-direction.

and the electric field leads the magnetic field in phase by 225°. This may seem to be a fairly insignificant result; however, as we shall see in Section 4.3.2, it is this property of TEM waves that is solely responsible for the circulating currents that are commonly known as eddy currents.

Having now investigated the behavior of a TEM wave traveling in both the $+x$- and the $-x$-directions, we are now in a position to analyze the field solutions in an infinite current sheet, which is, of course, our objective. According to the model introduced in Section 3.3.1, the values of the magnetic field at $x = 0$ and $x = h_{cu}$ can be arbitrarily specified and are assumed to be in sinusoidal steady state. It is evident from Figure D.4, however, that we cannot arbitrarily specify the magnetic field of a single TEM wave at two different points. Consider, for example, that in Fig. D.4 we choose $h_{cu} = 0.5 \times 10^{-4}$ m and we wish to arbitrarily specify the magnitude of magnetic field at this point to be zero. Clearly, we cannot, unless we also allow the magnetic field to change from its present value at every other point. Therefore, in order to be able to arbitrarily specify the magnetic field at two points on the interval between $x = 0$ and $x = h_{cu}$, it is necessary to introduce a second TEM wave, traveling in the opposite direction and originating at $x = h_{cu}$. Using a superposition of these two waves, it is now easy to adjust the initial value of each wave so as to satisfy any arbitrarily chosen boundary conditions at both $x = 0$ and $x = h_{cu}$. Note that if the height of the copper is much greater than the skin depth there is no significant interaction between the two waves. Figure D.5 shows such a situation where the magnetic field at $x = 0$ has been chosen to have an amplitude of 2 A-t/m with a phase angle of 0°, and the magnetic field at $x = h_{cu} = 3 \times 10^{-4}$ m has been chosen to have an amplitude of 2 A-t/m with a phase angle of 0°. In this case, since there is no interaction, these boundary values are also the initial values of the magnetic fields associated with the TEM waves traveling in the $+x$- and the $-x$-direction respectively. In Fig. D.6, however, there is significant interaction between the two TEM waves. In this example, we have chosen the same magnetic field boundary conditions as in Fig. D.5, but now we have decreased the copper height to $h_{cu} = 1 \times 10^{-4}$ m. As a result, each TEM wave does not die out completely before reaching the other side. Therefore, the initial value of each TEM wave constitutes only a portion of the total magnetic field boundary condition at $x = 0$ or $x = h_{cu}$. Moreover, in such cases where there is interaction between the two waves, the relative phase between the total electric field and the total magnetic field across the layer will not in general obey either of the relationships given for *single* TEM waves in equations (D.39) and (D.41). In fact, when the copper height is very small with respect to the wavelength, the two TEM waves combine in such a way that both the total electric and the total magnetic fields are constant across the height of the copper. Therefore, since the current density $\mathbf{J}$ is of the same form as the electric field at every point ($\mathbf{J} = \sigma\mathbf{E}$), this is why we do not see any circulating currents when the frequency is low with respect to the conductor height.

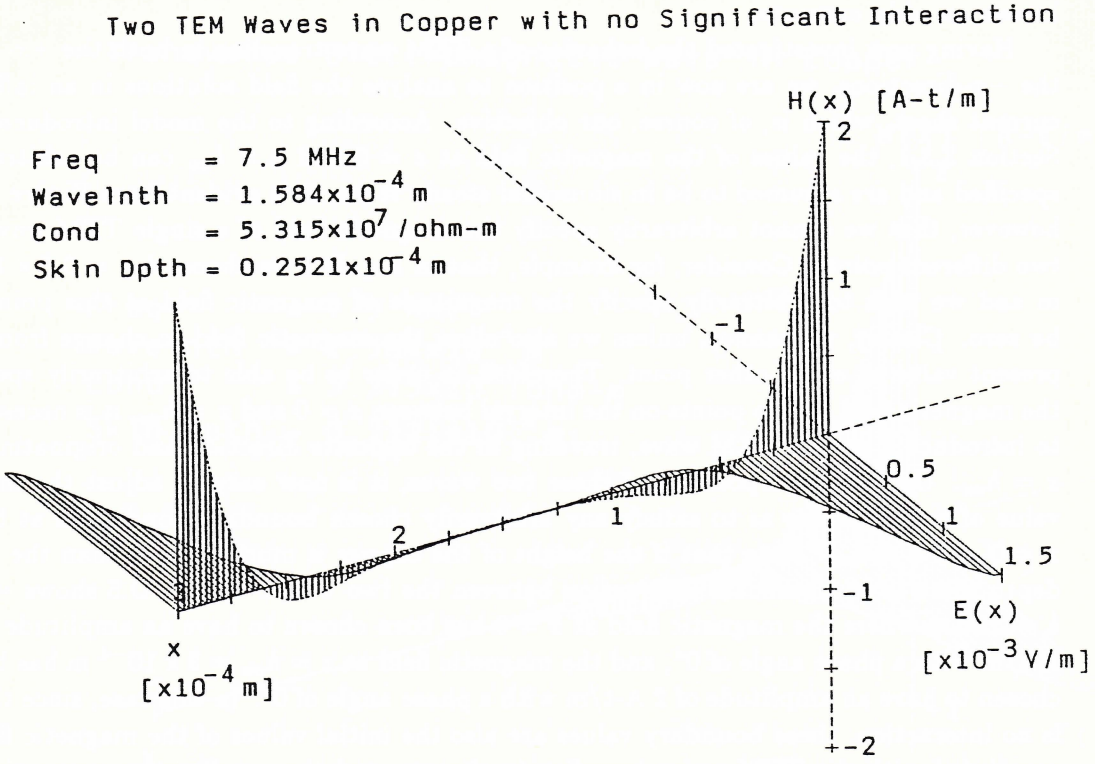


Figure D.5: Superposition of two 7.5 MHz transverse electromagnetic waves traveling in copper where there is no interaction. One wave has its source at $x = 0$ and travels in the $+x$-direction and the other wave has its source at $x = h_{cu}$ and travels in the $-x$-direction.

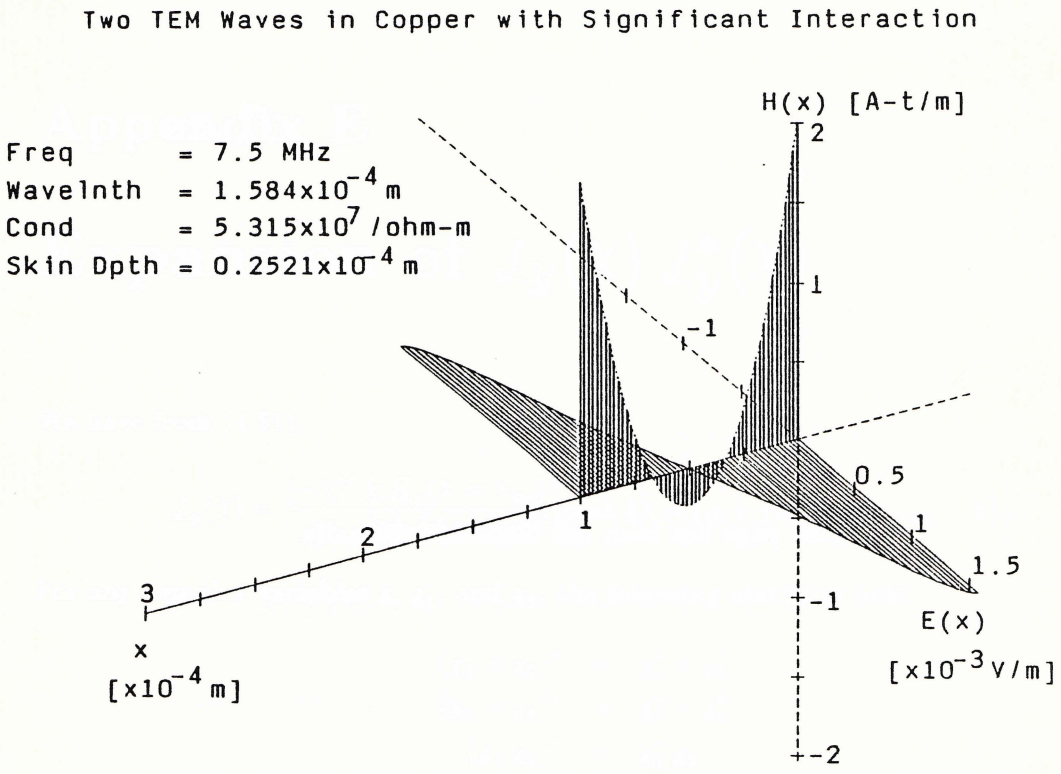


Figure D.6: Superposition of two 7.5 MHz transverse electromagnetic waves traveling through copper where there is significant interaction.

This page has been left blank intentionally.

Appendix E

Expansion of $\underline{J}_y(\chi)\,\underline{J}_y^*(\chi)$

We have from (4.51),

$$\underline{J}_y(\chi) = \frac{(-1)^{\varepsilon}\,\underline{k}\,\underline{H}_z(\chi = h_{cu})}{\sinh \underline{k} h_{cu}}\Big[\cosh \underline{k}\chi - (\alpha + j\beta)\cosh \underline{k}(h_{cu} - \chi)\Big] \qquad \text{(E.1)}$$

For any complex variables $\underline{z}$, $\underline{z}_1$, and $\underline{z}_2$, the following identities hold

$$\begin{aligned}
(\underline{z}_1 + \underline{z}_2)^* &= \underline{z}_1^* + \underline{z}_2^* \\
(\underline{z}_1 - \underline{z}_2)^* &= \underline{z}_1^* - \underline{z}_2^* \\
(\underline{z}_1\,\underline{z}_2)^* &= \underline{z}_1^*\,\underline{z}_2^* \\
\left(\frac{\underline{z}_1}{\underline{z}_2}\right)^* &= \frac{\underline{z}_1^*}{\underline{z}_2^*} \\
\underline{z} + \underline{z}^* &= 2\,\mathrm{Re}(\underline{z}) \\
\underline{z} - \underline{z}^* &= 2j\,\mathrm{Im}(\underline{z})
\end{aligned}$$

For the cosh and the sinh functions, we have

$$\begin{aligned}
(\cosh \underline{z})^* &= \cosh(\underline{z}^*) \\
(\sinh \underline{z})^* &= \sinh(\underline{z}^*)
\end{aligned}$$

Therefore, the complex conjugate of $\underline{J}_y(\chi)$ can be expressed as

$$\begin{aligned}
\underline{J}_y^*(\chi) &= \frac{(-1)^{\varepsilon}\,\underline{k}^*\,\underline{H}_z^*(\chi = h_{cu})}{(\sinh \underline{k} h_{cu})^*}\Big[\Big(\cosh \underline{k}\chi\Big)^* - (\alpha - j\beta)\Big(\cosh \underline{k}(h_{cu} - \chi)\Big)^*\Big] \\
&= \frac{(-1)^{\varepsilon}\,\underline{k}^*\,\underline{H}_z^*(\chi = h_{cu})}{\sinh \underline{k}^* h_{cu}}\Big[\cosh \underline{k}^*\chi - (\alpha - j\beta)\cosh \underline{k}^*(h_{cu} - \chi)\Big] \qquad \text{(E.2)}
\end{aligned}$$

as h_{cu} and χ are both real parameters.

Multiplying (E.1) and (E.2) gives the product $\underline{J}_y(\chi)\underline{J}_y^*(\chi)$:

$$\begin{aligned}\underline{J}_y(\chi)\underline{J}_y^*(\chi) &= \left(\frac{(-1)^e \underline{k}\underline{H}_z(\chi = h_{cu})}{\sinh \underline{k}h_{cu}}\right)\Big[\cosh \underline{k}\chi - (\alpha + j\beta)\cosh \underline{k}(h_{cu} - \chi)\Big] \\ &\quad \times \left(\frac{(-1)^e \underline{k}^* \underline{H}_z^*(\chi = h_{cu})}{\sinh \underline{k}^* h_{cu}}\right)\Big[\cosh \underline{k}^*\chi - (\alpha - j\beta)\cosh \underline{k}^*(h_{cu} - \chi)\Big] \\ &= \frac{|\underline{k}|^2\,|\underline{H}_z(\chi = h_{cu})|^2}{y_0}\Big\{\, y_1 + y_2 + y_3 + y_4 \,\Big\} \qquad \text{(E.3)}\end{aligned}$$

where

$$y_0 = \sinh \underline{k}h_{cu} \sinh \underline{k}^* h_{cu} \qquad \text{(E.4)}$$

$$y_1 = \cosh \underline{k}\chi \cosh \underline{k}^*\chi \qquad \text{(E.5)}$$

$$y_2 = (\alpha^2 + \beta^2)\cosh \underline{k}(h_{cu} - \chi) \cosh \underline{k}^*(h_{cu} - \chi) \qquad \text{(E.6)}$$

$$y_3 = -\alpha\Big[\cosh \underline{k}(h_{cu} - \chi) \cosh \underline{k}^*\chi + \cosh \underline{k}\chi \cosh \underline{k}^*(h_{cu} - \chi)\Big] \qquad \text{(E.7)}$$

$$y_4 = j\beta\Big[\cosh \underline{k}\chi \cosh \underline{k}^*(h_{cu} - \chi) - \cosh \underline{k}(h_{cu} - \chi) \cosh \underline{k}^*\chi\Big] \qquad \text{(E.8)}$$

At this point we introduce the following identities involving the trigonometric and hyperbolic functions:

$$\cosh \underline{z}_1 \cosh \underline{z}_2 = \frac{\cosh(\underline{z}_1 + \underline{z}_2) + \cosh(\underline{z}_1 - \underline{z}_2)}{2}$$

$$\sinh \underline{z}_1 \sinh \underline{z}_2 = \frac{\cosh(\underline{z}_1 + \underline{z}_2) - \cosh(\underline{z}_1 - \underline{z}_2)}{2}$$

$$\begin{aligned}\cosh(\underline{z}_1 + \underline{z}_2) &= \cosh \underline{z}_1 \cosh \underline{z}_2 + \sinh \underline{z}_1 \sinh \underline{z}_2 \\ \cosh(j\underline{z}) &= \cos(\underline{z}) \\ \sinh(j\underline{z}) &= j\sin(\underline{z}) \\ \cos(-\underline{z}) &= \cos(\underline{z}) \\ \sin(-\underline{z}) &= -\sin(\underline{z}) \\ \cosh(-\underline{z}) &= \cosh(\underline{z}) \\ \sinh(-\underline{z}) &= -\sinh(\underline{z})\end{aligned}$$

Using (4.6), we also write

$$\underline{k}h_{cu} = \left(\frac{1}{\delta} + j\frac{1}{\delta}\right) h_{cu} = \Delta + j\Delta \tag{E.9}$$

$$\underline{k}\chi = \left(\frac{1}{\delta} + j\frac{1}{\delta}\right) \chi = w + jw \tag{E.10}$$

$$\underline{k}(h_{cu} - \chi) = \left(\frac{1}{\delta} + j\frac{1}{\delta}\right) (h_{cu} - \chi) = v + jv \tag{E.11}$$

where $\Delta = h_{cu}/\delta$, $w = \chi/\delta$, and $v = (h_{cu} - \chi)/\delta$ are real numbers that have been introduced in Section 4.5.2. The variable Δ is defined as the ratio of the height of a layer to the skin depth; w and v are variables used here merely to simplify the writing of the expressions which follow. Using these definitions, we can start expanding the terms in (E.3) to (E.8). For example,

$$\begin{aligned} y_0 &= \sinh \underline{k}h_{cu} \sinh \underline{k}^* h_{cu} \\ &= \frac{\cosh[\Delta + j\Delta + (\Delta - j\Delta)] - \cosh[\Delta + j\Delta - (\Delta - j\Delta)]}{2} \\ &= \frac{\cosh(2\Delta) - \cosh(j2\Delta)}{2} \\ &= \frac{\cosh 2\Delta - \cos 2\Delta}{2} \end{aligned} \tag{E.12}$$

$$\begin{aligned} y_1 &= \cosh \underline{k}\chi \cosh \underline{k}^* \chi \\ &= \frac{\cosh 2w + \cos 2w}{2} \end{aligned} \tag{E.13}$$

$$\begin{aligned} y_2 &= (\alpha^2 + \beta^2)\left[\cosh \underline{k}(h_{cu} - \chi) \cosh \underline{k}^*(h_{cu} - \chi)\right] \\ &= (\alpha^2 + \beta^2)\left[\frac{\cosh 2v + \cos 2v}{2}\right] \end{aligned} \tag{E.14}$$

Using the identities of $\cosh(\underline{z}^*) = (\cosh \underline{z})^*$ and $\underline{z}_1 \, \underline{z}_2^* = (\underline{z}_1^* \, \underline{z}_2)^*$, the term y_3 can be regrouped step by step as follows:

$$\begin{aligned} y_3 &= -\alpha\left[\cosh \underline{k}(h_{cu} - \chi) \cosh \underline{k}^*\chi + \cosh \underline{k}\chi \cosh \underline{k}^*(h_{cu} - \chi)\right] \\ &= -\alpha\left[\cosh \underline{k}(h_{cu} - \chi) \cosh \underline{k}^*\chi + \cosh \underline{k}\chi \left(\cosh \underline{k}(h_{cu} - \chi)\right)^*\right] \\ &= -\alpha\left[\cosh \underline{k}(h_{cu} - \chi) \cosh \underline{k}^*\chi + \left((\cosh \underline{k}\chi)^* \cosh \underline{k}(h_{cu} - \chi)\right)^*\right] \\ &= -\alpha\left[\cosh \underline{k}(h_{cu} - \chi) \cosh \underline{k}^*\chi + \left(\cosh \underline{k}^*\chi \cosh \underline{k}(h_{cu} - \chi)\right)^*\right] \end{aligned} \tag{E.15}$$

Recognizing that $\left(\cosh \underline{k}^* \chi \ \cosh \underline{k}(h_{cu} - \chi)\right)^*$ is the complex conjugate of $\cosh \underline{k}(h_{cu} - \chi) \ \cosh \underline{k}^* \chi$, and applying the identity of $\underline{z} + \underline{z}^* = 2 \operatorname{Re}(\underline{z})$ to (E.15) gives

$$y_3 = -2\alpha \operatorname{Re}\left[\cosh \underline{k}(h_{cu} - \chi) \ \cosh \underline{k}^* \chi\right] \tag{E.16}$$

To find the product of $\cosh \underline{k}(h_{cu} - \chi) \cosh \underline{k}^* \chi$, we make use of the facts that $\underline{k}(h_{cu} - \chi) = v + jv = (\Delta - w) + j(\Delta - w)$ and $\underline{k}^* \chi = w - jw$ and the expansion formula for $\cosh \underline{z}_1 \cosh \underline{z}_2$ to write

$$\begin{aligned} & \cosh \underline{k}(h_{cu} - \chi) \ \cosh \underline{k}^* \chi \\ = \ & \frac{\cosh\Big([\Delta - w + j(\Delta - w)] + (w - jw)\Big)}{2} \\ & + \frac{\cosh\Big([\Delta - w + j(\Delta - w)] - (w - jw)\Big)}{2} \\ = \ & \frac{\cosh\Big(\Delta + j(\Delta - 2w)\Big)}{2} + \frac{\cosh\Big(\Delta - 2w + j\Delta\Big)}{2} \end{aligned} \tag{E.17}$$

Using the identities $\cosh(\underline{z}_1 + \underline{z}_2) = \cosh \underline{z}_1 \ \cosh \underline{z}_2 + \sinh \underline{z}_1 \ \sinh \underline{z}_2$, $\cosh(j\underline{z}) = \cos \underline{z}$, and $\sinh(j\underline{z}) = j \sin \underline{z}$, (E.17) can be regrouped as

$$\begin{aligned} & \cosh \underline{k}(h_{cu} - \chi) \cosh \underline{k}^* \chi \\ = \ & \frac{\cosh \Delta \ \cosh(j(\Delta - 2w)) + \sinh \Delta \ \sinh(j(\Delta - 2w))}{2} \\ & + \frac{\cosh(\Delta - 2w) \ \cosh(j\Delta)) + \sinh(\Delta - 2w) \ \sinh(j\Delta))}{2} \\ = \ & \frac{\cosh \Delta \ \cos(\Delta - 2w) + j \sinh \Delta \ \sin(\Delta - 2w)}{2} \\ & + \frac{\cosh(\Delta - 2w) \ \cos \Delta + j \sinh(\Delta - 2w) \ \sin \Delta}{2} \end{aligned} \tag{E.18}$$

Since Δ and w are real numbers, the functional values of the trigonometric and hyperbolic functions in (E.18), with Δ and $\Delta - 2w$ as arguments, are all real numbers. As a result, the real and imaginary parts of $\cosh \underline{k}(h_{cu} - \chi) \cosh \underline{k}^* \chi$ are easily identified as

$$\mathrm{Re}\Big[\cosh \underline{k}(h_{cu}-\chi)\cosh \underline{k}^{*}\chi\Big] = \frac{\cosh\Delta\,\cos(\Delta-2w)+\cosh(\Delta-2w)\,\cos\Delta}{2} \tag{E.19}$$

$$\mathrm{Im}\Big[\cosh \underline{k}(h_{cu}-\chi)\cosh \underline{k}^{*}\chi\Big] = \frac{\sinh\Delta\,\sin(\Delta-2w)+\sinh(\Delta-2w)\,\sin\Delta}{2} \tag{E.20}$$

Substituting (E.19) into (E.16) gives

$$y_3 = -\alpha\Big[\cosh\Delta\,\cos(\Delta-2w)+\cosh(\Delta-2w)\,\cos\Delta\Big] \tag{E.21}$$

A very similar derivation follows for the term y_4:

$$\begin{aligned} y_4 &= j\beta\Big[\cosh \underline{k}\chi\,\cosh \underline{k}^{*}(h_{cu}-\chi)-\cosh \underline{k}(h_{cu}-\chi)\,\cosh \underline{k}^{*}\chi\Big] \\ &= j\beta\Big[\cosh \underline{k}\chi\,\Big(\cosh \underline{k}(h_{cu}-\chi)\Big)^{*}-\cosh \underline{k}(h_{cu}-\chi)\,\cosh \underline{k}^{*}\chi\Big] \\ &= j\beta\Big[\Big((\cosh \underline{k}\chi)^{*}\,\cosh \underline{k}(h_{cu}-\chi)\Big)^{*}-\cosh \underline{k}(h_{cu}-\chi)\,\cosh \underline{k}^{*}\chi\Big] \\ &= j\beta\Big[\Big(\cosh \underline{k}^{*}\chi\,\cosh \underline{k}(h_{cu}-\chi)\Big)^{*}-\cosh \underline{k}(h_{cu}-\chi)\,\cosh \underline{k}^{*}\chi\Big] \end{aligned} \tag{E.22}$$

Recognizing that $\Big(\cosh \underline{k}^{*}\chi\,\cosh \underline{k}(h_{cu}-\chi)\Big)^{*}$ is the complex conjugate of $\cosh \underline{k}(h_{cu}-\chi)\,\cosh \underline{k}^{*}\chi$ and substituting the identity of $\underline{z}^{*}-\underline{z}=-2j\,\mathrm{Im}(\underline{z})$ into (E.22) gives

$$y_4 = 2\beta\,\mathrm{Im}\Big[\cosh \underline{k}(h_{cu}-\chi)\,\cosh \underline{k}^{*}\chi\Big] \tag{E.23}$$

Substituting (E.20) into (E.23) yields

$$y_4 = \beta\Big[\sinh\Delta\,\sin(\Delta-2w)+\sinh(\Delta-2w)\,\sin\Delta\Big] \tag{E.24}$$

Substituting (E.12), (E.13), (E.14), (E.21), and (E.24) into (E.3) gives

$$
\begin{aligned}
\underline{J}_y(X)\underline{J}_y^*(X) &= \frac{2\,|\underline{k}|^2\,|\underline{H}_z(X=h_{cu})|^2}{(\cosh 2\Delta-\cos 2\Delta)} \\
&\quad\times\Bigg\{\frac{(\cosh 2w+\cos 2w)}{2} \\
&\qquad+\frac{(\alpha^2+\beta^2)(\cosh 2v+\cos 2v)}{2} \\
&\qquad-\alpha\Big(\cosh\Delta\cos(\Delta-2w)+\cosh(\Delta-2w)\cos\Delta\Big) \\
&\qquad+\beta\Big(\sinh\Delta\sin(\Delta-2w)+\sinh(\Delta-2w)\sin\Delta\Big)\Bigg\} \\
&= \frac{|\underline{k}|^2\,|\underline{H}_z(X=h_{cu})|^2}{(\cosh 2\Delta-\cos 2\Delta)} \\
&\quad\times\Bigg\{(\cosh 2w+\cos 2w) \\
&\qquad+(\alpha^2+\beta^2)(\cosh 2v+\cos 2v) \\
&\qquad-2\alpha\Big(\cosh\Delta\cos(\Delta-2w)+\cosh(\Delta-2w)\cos\Delta\Big) \\
&\qquad+2\beta\Big(\sinh\Delta\sin(\Delta-2w)+\sinh(\Delta-2w)\sin\Delta\Big)\Bigg\}
\end{aligned}
\tag{E.25}
$$

which is the final result for the expansion of $\underline{J}_y(X)\underline{J}_y^*(X)$ as shown in (4.100).

Appendix F

Expansion of $\underline{H}_z(\chi)\,\underline{H}_z^*(\chi)$

We have from (4.50),

$$\underline{H}_z(\chi) = \frac{\underline{H}_z(\chi = h_{cu})}{\sinh \underline{k} h_{cu}} \Big[\sinh \underline{k}\chi + (\alpha + j\beta)\sinh \underline{k}(h_{cu} - \chi)\Big] \tag{F.1}$$

Applying the same arguments in deriving the expression for $\underline{J}_y^*(\chi)$ in (E.2), the complex conjugate of $\underline{H}_z(\chi)$ is derived and the result is presented here:

$$\underline{H}_z^*(\chi) = \frac{\underline{H}_z^*(\chi = h_{cu})}{\sinh \underline{k}^* h_{cu}} \Big[\sinh \underline{k}^*\chi + (\alpha - j\beta)\sinh \underline{k}^*(h_{cu} - \chi)\Big] \tag{F.2}$$

Multiplying (F.1) and (F.2) gives the product $\underline{H}_z(\chi)\underline{H}_z^*(\chi)$:

$$\begin{aligned}\underline{H}_z(\chi)\underline{H}_z^*(\chi) &= \left(\frac{\underline{H}_z(\chi = h_{cu})}{\sinh \underline{k} h_{cu}}\right)\Big[\sinh \underline{k}\chi + (\alpha + j\beta)\sinh \underline{k}(h_{cu} - \chi)\Big] \\ &\quad \times \left(\frac{\underline{H}_z^*(\chi = h_{cu})}{\sinh \underline{k}^* h_{cu}}\right)\Big[\sinh \underline{k}^*\chi + (\alpha - j\beta)\sinh \underline{k}^*(h_{cu} - \chi)\Big] \\ &= \frac{|\underline{H}_z(\chi = h_{cu})|^2}{y_0}\Big\{y_5 + y_6 + y_7 + y_8\Big\} \end{aligned} \tag{F.3}$$

where

$$y_0 = \sinh \underline{k} h_{cu}\ \sinh \underline{k}^* h_{cu} \tag{F.4}$$

$$y_5 = \sinh \underline{k}\chi\ \sinh \underline{k}^*\chi \tag{F.5}$$

$$y_6 = (\alpha^2 + \beta^2)\sinh \underline{k}(h_{cu} - \chi)\ \sinh \underline{k}^*(h_{cu} - \chi) \tag{F.6}$$

$$y_7 = \alpha\Big[\sinh \underline{k}(h_{cu} - \chi)\ \sinh \underline{k}^*\chi + \sinh \underline{k}\chi\ \sinh \underline{k}^*(h_{cu} - \chi)\Big] \tag{F.7}$$

$$y_8 = j\beta\left[\sinh \underline{k}(h_{cu} - \chi) \sinh \underline{k}^* \chi - \sinh \underline{k}\chi \sinh \underline{k}^*(h_{cu} - \chi)\right] \tag{F.8}$$

For convenience, we repeat here the trigonometric and hyperbolic identities introduced in Appendix E:

$$\cosh \underline{z}_1 \cosh \underline{z}_2 = \frac{\cosh(\underline{z}_1 + \underline{z}_2) + \cosh(\underline{z}_1 - \underline{z}_2)}{2}$$

$$\sinh \underline{z}_1 \sinh \underline{z}_2 = \frac{\cosh(\underline{z}_1 + \underline{z}_2) - \cosh(\underline{z}_1 - \underline{z}_2)}{2}$$

$$\begin{aligned}
\cosh(\underline{z}_1 + \underline{z}_2) &= \cosh \underline{z}_1 \cosh \underline{z}_2 + \sinh \underline{z}_1 \sinh \underline{z}_2 \\
\cosh(j\underline{z}) &= \cos(\underline{z}) \\
\sinh(j\underline{z}) &= j \sin(\underline{z}) \\
\cos(-\underline{z}) &= \cos(\underline{z}) \\
\sin(-\underline{z}) &= -\sin(\underline{z}) \\
\cosh(-\underline{z}) &= \cosh(\underline{z}) \\
\sinh(-\underline{z}) &= -\sinh(\underline{z})
\end{aligned}$$

We also write

$$\underline{k}h_{cu} = \left(\frac{1}{\delta} + j\frac{1}{\delta}\right) h_{cu} = \Delta + j\Delta \tag{F.9}$$

$$\underline{k}\chi = \left(\frac{1}{\delta} + j\frac{1}{\delta}\right) \chi = w + jw \tag{F.10}$$

$$\underline{k}(h_{cu} - \chi) = \left(\frac{1}{\delta} + j\frac{1}{\delta}\right) (h_{cu} - \chi) = v + jv \tag{F.11}$$

where $\Delta = h_{cu}/\delta$, $w = \chi/\delta$, and $v = (h_{cu} - \chi)/\delta$ are real numbers that have been introduced in Section 4.5.2. The variable Δ is defined as the ratio of the height of a layer to the skin depth; w and v are variables used here merely to simplify the writing of the expressions which follow. Using these definitions, we can start expanding the terms in (F.3) to (F.8).

$$\begin{aligned}
y_0 &= \sinh \underline{k}h_{cu} \sinh \underline{k}^* h_{cu} \\
&= \frac{\cosh[\Delta + j\Delta + (\Delta - j\Delta)] - \cosh[\Delta + j\Delta - (\Delta - j\Delta)]}{2} \\
&= \frac{\cosh(2\Delta) - \cosh(j2\Delta)}{2} \\
&= \frac{\cosh 2\Delta - \cos 2\Delta}{2}
\end{aligned} \tag{F.12}$$

$$\begin{aligned} y_5 &= \sinh \underline{k}\chi \sinh \underline{k}^*\chi \\ &= \frac{\cosh 2w - \cos 2w}{2} \end{aligned} \tag{F.13}$$

$$\begin{aligned} y_6 &= (\alpha^2+\beta^2)\Big[\sinh \underline{k}(h_{cu}-\chi) \sinh \underline{k}^*(h_{cu}-\chi)\Big] \\ &= (\alpha^2+\beta^2)\left[\frac{\cosh 2v - \cos 2v}{2}\right] \end{aligned} \tag{F.14}$$

In expanding the term y_7, we recognize that the product $\sinh \underline{k}\chi \sinh \underline{k}^*(h_{cu}-\chi)$ in (F.7) is the complex conjugate of the product $\sinh \underline{k}(h_{cu}-\chi) \sinh \underline{k}^*\chi$. A very similar argument is presented in Appendix E for the expansion of the term y_3. Therefore,

$$\begin{aligned} y_7 &= \alpha\Big[\sinh \underline{k}(h_{cu}-\chi) \sinh \underline{k}^*\chi + \sinh \underline{k}\chi \sinh \underline{k}^*(h_{cu}-\chi)\Big] \\ &= 2\alpha \operatorname{Re}\Big[\sinh \underline{k}(h_{cu}-\chi) \sinh \underline{k}^*\chi\Big] \end{aligned} \tag{F.15}$$

To find the product of $\sinh \underline{k}(h_{cu}-\chi) \sinh \underline{k}^*\chi$, we make use of the facts that $\underline{k}(h_{cu}-\chi) = v+jv = (\Delta-w)+j(\Delta-w)$ and $\underline{k}^*\chi = w-jw$ and the expansion formula for $\sinh \underline{z}_1 \sinh \underline{z}_2$ to write

$$\begin{aligned} &\sinh \underline{k}(h_{cu}-\chi) \sinh \underline{k}^*\chi \\ &= \frac{\cosh\Big([\Delta - w + j(\Delta-w)] + (w-jw)\Big)}{2} \\ &\quad - \frac{\cosh\Big([\Delta - w + j(\Delta-w)] - (w-jw)\Big)}{2} \\ &= \frac{\cosh\Big(\Delta + j(\Delta-2w)\Big)}{2} - \frac{\cosh\Big(\Delta - 2w + j\Delta\Big)}{2} \end{aligned} \tag{F.16}$$

Using the identities $\cosh(\underline{z}_1+\underline{z}_2) = \cosh \underline{z}_1 \cosh \underline{z}_2 + \sinh \underline{z}_1 \sinh \underline{z}_2$, $\cosh(j\underline{z}) = \cos \underline{z}$, and $\sinh(j\underline{z}) = j \sin \underline{z}$, (F.16) can be regrouped as

$$\begin{aligned}
&\sinh \underline{k}(h_{cu} - \chi) \sinh \underline{k}^* \chi \\
&= \frac{\cosh \Delta \cosh(j(\Delta - 2w)) + \sinh \Delta \sinh(j(\Delta - 2w))}{2} \\
&\quad - \frac{\cosh(\Delta - 2w) \cosh(j\Delta)) + \sinh(\Delta - 2w) \sinh(j\Delta))}{2} \\
&= \frac{\cosh \Delta \cos(\Delta - 2w) + j \sinh \Delta \sin(\Delta - 2w)}{2} \\
&\quad - \frac{\cosh(\Delta - 2w) \cos \Delta + j \sinh(\Delta - 2w) \sin \Delta}{2}
\end{aligned} \tag{F.17}$$

Since Δ and w are real numbers, the functional values of the trigonometric and hyperbolic functions in (F.17), with Δ and $\Delta - 2w$ as arguments, are all real numbers. Thus,

$$\mathrm{Re}\Big[\sinh \underline{k}(h_{cu} - \chi) \sinh \underline{k}^* \chi\Big] = \frac{\cosh \Delta \cos(\Delta - 2w) - \cosh(\Delta - 2w) \cos \Delta}{2} \tag{F.18}$$

$$\mathrm{Im}\Big[\sinh \underline{k}(h_{cu} - \chi) \sinh \underline{k}^* \chi\Big] = \frac{\sinh \Delta \sin(\Delta - 2w) - \sinh(\Delta - 2w) \sin \Delta}{2} \tag{F.19}$$

Substituting (F.18) into (F.15) gives

$$y_7 = \alpha\Big[\cosh \Delta \cos(\Delta - 2w) - \cosh(\Delta - 2w) \cos \Delta\Big] \tag{F.20}$$

Recognizing that the product $\sinh \underline{k}\chi \sinh \underline{k}^*(h_{cu} - \chi)$ in (F.8) is the complex conjugate of the product $\sinh \underline{k}(h_{cu} - \chi) \sinh \underline{k}^* \chi$, the term y_8 is expanded as

$$\begin{aligned}
y_8 &= j\beta\Big[\sinh \underline{k}(h_{cu} - \chi) \sinh \underline{k}^* \chi - \sinh \underline{k}\chi \sinh \underline{k}^*(h_{cu} - \chi)\Big] \\
&= -2\beta \,\mathrm{Im}\Big[\sinh \underline{k}(h_{cu} - \chi) \sinh \underline{k}^* \chi\Big]
\end{aligned} \tag{F.21}$$

Substituting (F.19) into (F.21) yields

$$y_8 = -\beta\Big[\sinh \Delta \sin(\Delta - 2w) - \sinh(\Delta - 2w) \sin \Delta\Big] \tag{F.22}$$

Substituting (F.12), (F.13), (F.14), (F.20), and (F.22) into (F.3) gives

$$\begin{aligned}
\underline{H}_z(\chi)\underline{H}_z^*(\chi) &= \frac{2\,|\underline{H}_z(\chi = h_{cu})|^2}{\cosh 2\Delta - \cos 2\Delta} \\
&\quad \times \Bigg\{ \frac{(\cosh 2w - \cos 2w)}{2} \\
&\qquad + \frac{(\alpha^2 + \beta^2)(\cosh 2v - \cos 2v)}{2} \\
&\qquad + \alpha\Big[\cosh\Delta\cos(\Delta - 2w) - \cosh(\Delta - 2w)\cos\Delta\Big] \\
&\qquad - \beta\Big[\sinh\Delta\sin(\Delta - 2w) - \sinh(\Delta - 2w)\sin\Delta\Big] \Bigg\}
\end{aligned}$$

$$\begin{aligned}
&= \frac{|\underline{H}_z(\chi = h_{cu})|^2}{\cosh 2\Delta - \cos 2\Delta} \\
&\quad \times \Bigg\{ (\cosh 2w - \cos 2w) \\
&\qquad + (\alpha^2 + \beta^2)(\cosh 2v - \cos 2v) \\
&\qquad + 2\alpha\Big[\cosh\Delta\cos(\Delta - 2w) - \cosh(\Delta - 2w)\cos\Delta\Big] \\
&\qquad - 2\beta\Big[\sinh\Delta\sin(\Delta - 2w) - \sinh(\Delta - 2w)\sin\Delta\Big] \Bigg\}
\end{aligned} \tag{F.23}$$

which is the final result for the expansion of $\underline{H}_z(\chi)\underline{H}_z^*(\chi)$ as shown in (4.118).

This page has been left blank intentionally.

Appendix G

Integration of $\underline{J}_y(\chi)\,\underline{J}_y^*(\chi)$ with respect to χ

Before the integration of $\underline{J}_y(\chi)\underline{J}_y{}^*(\chi)$ with respect to χ is shown, several mathematical formulae associated with hyperbolic functions are listed:

$$\begin{aligned}
\cosh(-\chi) &= \cosh(\chi) \\
\sinh(-\chi) &= -\sinh(\chi) \\
\int \cosh(a\chi)\,d\chi &= \frac{\sinh(a\chi)}{a} \\
\int \sinh(a\chi)\,d\chi &= \frac{\cosh(a\chi)}{a}
\end{aligned}$$

Equation (4.101), which defines the product of $\underline{J}_y(\chi)\underline{J}_y{}^*(\chi)$, is repeated here for convenience.

$$\begin{aligned}
\underline{J}_y(\chi)\underline{J}_y^*(\chi) &= \frac{|\underline{k}|^2\,|\underline{H}_z(\chi = h_{cu})|^2}{(\cosh 2\Delta - \cos 2\Delta)} \\
&\quad \times \left\{ \left[\cosh\left(\frac{2\chi}{\delta}\right) + \cos\left(\frac{2\chi}{\delta}\right)\right] \right. \\
&\quad + \left(\alpha^2 + \beta^2\right)\left[\cosh\left(2\Delta - \frac{2\chi}{\delta}\right) + \cos\left(2\Delta - \frac{2\chi}{\delta}\right)\right] \\
&\quad - 2\alpha\left[\cosh\Delta\cos\left(\Delta - \frac{2\chi}{\delta}\right) + \cosh\left(\Delta - \frac{2\chi}{\delta}\right)\cos\Delta\right] \\
&\quad \left. + 2\beta\left[\sinh\Delta\sin\left(\Delta - \frac{2\chi}{\delta}\right) + \sinh\left(\Delta - \frac{2\chi}{\delta}\right)\sin\Delta\right] \right\}
\end{aligned} \tag{G.1}$$

By factoring constants which do not vary with respect to X outside the integration operation, the integration can be split into four parts as:

$$\int_0^{h_{cu}} \underline{J}_y(X)\underline{J}_y^*(X)\,dX = \frac{|\underline{k}|^2\,|\underline{H}_z(X=h_{cu})|^2}{(\cosh 2\Delta - \cos 2\Delta)}\left\{I_1 + I_2 + I_3 + I_4\right\} \tag{G.2}$$

where

$$I_1 = \int_0^{h_{cu}} \left[\cosh\left(\frac{2X}{\delta}\right) + \cos\left(\frac{2X}{\delta}\right)\right] dX \tag{G.3}$$

$$I_2 = (\alpha^2+\beta^2)\int_0^{h_{cu}} \left[\cosh\left(2\Delta - \frac{2X}{\delta}\right) + \cos\left(2\Delta - \frac{2X}{\delta}\right)\right] dX \tag{G.4}$$

$$I_3 = -2\alpha\int_0^{h_{cu}} \left[\cosh\Delta\cos\left(\Delta - \frac{2X}{\delta}\right) + \cosh\left(\Delta - \frac{2X}{\delta}\right)\cos\Delta\right] dX \tag{G.5}$$

$$I_4 = 2\beta\int_0^{h_{cu}} \left[\sinh\Delta\sin\left(\Delta - \frac{2X}{\delta}\right) + \sinh\left(\Delta - \frac{2X}{\delta}\right)\sin\Delta\right] dX \tag{G.6}$$

The four integrals are now evaluated in sequence. First,

$$\begin{aligned} I_1 &= \int_0^{h_{cu}} \left[\cosh\left(\frac{2X}{\delta}\right) + \cos\left(\frac{2X}{\delta}\right)\right] dX \\ &= \frac{\delta}{2}\left[\sinh\left(\frac{2X}{\delta}\right) + \sin\left(\frac{2X}{\delta}\right)\right]_0^{h_{cu}} \\ &= \frac{\delta}{2}\left[\sinh\left(\frac{2h_{cu}}{\delta}\right) + \sin\left(\frac{2h_{cu}}{\delta}\right) - 0 - 0\right] \\ &= \frac{\delta}{2}\left[\sinh\left(\frac{2h_{cu}}{\delta}\right) + \sin\left(\frac{2h_{cu}}{\delta}\right)\right] \end{aligned} \tag{G.7}$$

Substituting the definition of $\Delta = h_{cu}/\delta$ into the above equation gives

$$I_1 = \frac{\delta}{2}\left[\sinh 2\Delta + \sin 2\Delta\right] \tag{G.8}$$

The integral I_2 is evaluated next. The reader is again reminded that Δ is defined as the ratio of h_{cu} to δ.

$$\begin{aligned}
I_2 &= (\alpha^2+\beta^2)\int_0^{h_{cu}} \left[\cosh\left(2\Delta-\frac{2\chi}{\delta}\right)+\cos\left(2\Delta-\frac{2\chi}{\delta}\right)\right] d\chi \\
&= \frac{-\delta(\alpha^2+\beta^2)}{2}\left[\sinh\left(2\Delta-\frac{2\chi}{\delta}\right)+\sin\left(2\Delta-\frac{2\chi}{\delta}\right)\right]_0^{h_{cu}} \\
&= \frac{-\delta(\alpha^2+\beta^2)}{2}\left[\sinh\left(2\Delta-\frac{2h_{cu}}{\delta}\right)+\sin\left(2\Delta-\frac{2h_{cu}}{\delta}\right)-\sinh(2\Delta)-\sin(2\Delta)\right] \\
&= \frac{-\delta(\alpha^2+\beta^2)}{2}\left[0+0-\sinh(2\Delta)-\sin(2\Delta)\right] \\
&= \frac{\delta(\alpha^2+\beta^2)}{2}\left(\sinh 2\Delta+\sin 2\Delta\right) \qquad \text{(G.9)}
\end{aligned}$$

The evaluation of I_3 proceeds in a similar manner:

$$\begin{aligned}
I_3 &= -2\alpha\int_0^{h_{cu}} \left[\cosh\Delta\cos\left(\Delta-\frac{2\chi}{\delta}\right)+\cosh\left(\Delta-\frac{2\chi}{\delta}\right)\cos\Delta\right] d\chi \\
&= \delta\alpha\left[\cosh\Delta\sin\left(\Delta-\frac{2\chi}{\delta}\right)+\sinh\left(\Delta-\frac{2\chi}{\delta}\right)\cos\Delta\right]_0^{h_{cu}} \\
&= \delta\alpha\left[\cosh\Delta\sin\left(\Delta-\frac{2h_{cu}}{\delta}\right)+\sinh\left(\Delta-\frac{2h_{cu}}{\delta}\right)\cos\Delta\right. \\
&\qquad \left.-\cosh\Delta\sin\Delta-\sinh\Delta\cos\Delta\right] \\
&= \delta\alpha\left[\cosh\Delta\sin(-\Delta)+\sinh(-\Delta)\cos\Delta-\cosh\Delta\sin\Delta-\sinh\Delta\cos\Delta\right] \\
&= -\delta\alpha\left[2\cosh\Delta\sin\Delta+2\sinh\Delta\cos\Delta\right] \\
&= -\left(\frac{\delta}{2}\right)4\alpha\left[\cosh\Delta\sin\Delta+\sinh\Delta\cos\Delta\right] \\
&= -\left(\frac{\delta}{2}\right)4\alpha\left[\sinh\Delta\cos\Delta+\cosh\Delta\sin\Delta\right] \qquad \text{(G.10)}
\end{aligned}$$

The evaluation of I_4 gives

$$\begin{aligned}
I_4 &= 2\beta \int_0^{h_{cu}} \left[\sinh\Delta \sin\left(\Delta - \frac{2\chi}{\delta}\right) + \sinh\left(\Delta - \frac{2\chi}{\delta}\right)\sin\Delta\right] d\chi \\
&= \delta\beta\left[\sinh\Delta\cos\left(\Delta - \frac{2\chi}{\delta}\right) - \cosh\left(\Delta - \frac{2\chi}{\delta}\right)\sin\Delta\right]_0^{h_{cu}} \\
&= \delta\beta\left[\sinh\Delta\cos\left(\Delta - \frac{2h_{cu}}{\delta}\right) - \cosh\left(\Delta - \frac{2h_{cu}}{\delta}\right)\sin\Delta\right. \\
&\qquad \left. - \sinh\Delta\cos\Delta + \cosh\Delta\sin\Delta\right] \\
&= \delta\beta\left[\sinh\Delta\cos(-\Delta) - \cosh(-\Delta)\sin\Delta - \sinh\Delta\cos\Delta + \cosh\Delta\sin\Delta\right] \\
&= \delta\beta\left[\sinh\Delta\cos\Delta - \cosh\Delta\sin\Delta - \sinh\Delta\cos\Delta + \cosh\Delta\sin\Delta\right] \\
&= 0 \qquad\qquad (G.11)
\end{aligned}$$

Substituting (G.8), (G.9), (G.10), and (G.11) into (G.2) yields the final result:

$$\begin{aligned}
\int_0^{h_{cu}} \underline{J}_y(\chi)\underline{J}_y^*(\chi)\, d\chi &= \frac{|\underline{k}|^2\,|\underline{H}_z(\chi = h_{cu})|^2\,\delta}{2\,(\cosh 2\Delta - \cos 2\Delta)} \\
&\quad \times \left\{ \left(1 + \alpha^2 + \beta^2\right)\left(\sinh 2\Delta + \sin 2\Delta\right)\right. \\
&\quad \left. - 4\alpha\left(\sinh\Delta\cos\Delta + \cosh\Delta\sin\Delta\right)\right\} \qquad (G.12)
\end{aligned}$$

Appendix H

Integration of $\underline{H}_z(\chi)\,\underline{H}_z^*(\chi)$ with respect to χ

Equation (4.119), which defines the product of $\underline{H}_x(\chi)\underline{H}_x{}^*(\chi)$, is repeated here for convenience.

$$\begin{aligned}\underline{H}_z(\chi)\underline{H}_z^*(\chi) &= \frac{|\underline{H}_z(\chi = h_{cu})|^2}{(\cosh 2\Delta - \cos 2\Delta)} \\ &\times \left\{ \left[\cosh\left(\frac{2\chi}{\delta}\right) - \cos\left(\frac{2\chi}{\delta}\right)\right] \right. \\ &+ \left(\alpha^2 + \beta^2\right)\left[\cosh\left(2\Delta - \frac{2\chi}{\delta}\right) - \cos\left(2\Delta - \frac{2\chi}{\delta}\right)\right] \\ &+ 2\alpha\left[\cosh\Delta\cos\left(\Delta - \frac{2\chi}{\delta}\right) - \cosh\left(\Delta - \frac{2\chi}{\delta}\right)\cos\Delta\right] \\ &\left. - 2\beta\left[\sinh\Delta\sin\left(\Delta - \frac{2\chi}{\delta}\right) - \sinh\left(\Delta - \frac{2\chi}{\delta}\right)\sin\Delta\right] \right\}\end{aligned} \tag{H.1}$$

Therefore,

$$\int_0^{h_{cu}} \underline{H}_z(\chi)\underline{H}_z^*(\chi)\,d\chi = \frac{|\underline{H}_z(\chi = h_{cu})|^2}{(\cosh 2\Delta - \cos 2\Delta)}\left\{I_5 + I_6 + I_7 + I_8\right\} \tag{H.2}$$

where

$$I_5 = \int_0^{h_{cu}} \left[\cosh\left(\frac{2\chi}{\delta}\right) - \cos\left(\frac{2\chi}{\delta}\right)\right] d\chi \tag{H.3}$$

$$I_6 = \left(\alpha^2 + \beta^2\right)\int_0^{h_{cu}} \left[\cosh\left(2\Delta - \frac{2\chi}{\delta}\right) - \cos\left(2\Delta - \frac{2\chi}{\delta}\right)\right] d\chi \tag{H.4}$$

$$I_7 = 2\alpha \int_0^{h_{cu}} \left[\cosh\Delta \cos\left(\Delta - \frac{2\chi}{\delta}\right) - \cosh\left(\Delta - \frac{2\chi}{\delta}\right)\cos\Delta\right] d\chi \qquad \text{(H.5)}$$

$$I_8 = -2\beta \int_0^{h_{cu}} \left[\sinh\Delta \sin\left(\Delta - \frac{2\chi}{\delta}\right) - \sinh\left(\Delta - \frac{2\chi}{\delta}\right)\sin\Delta\right] d\chi \qquad \text{(H.6)}$$

The four integrals are now evaluated in sequence.

$$\begin{aligned} I_5 &= \int_0^{h_{cu}} \left[\cosh\left(\frac{2\chi}{\delta}\right) - \cos\left(\frac{2\chi}{\delta}\right)\right] d\chi \\ &= \frac{\delta}{2}\left[\sinh\left(\frac{2\chi}{\delta}\right) - \sin\left(\frac{2\chi}{\delta}\right)\right]_0^{h_{cu}} \\ &= \frac{\delta}{2}\left[\sinh\left(\frac{2h_{cu}}{\delta}\right) - \sin\left(\frac{2h_{cu}}{\delta}\right) - 0 + 0\right] \\ &= \frac{\delta}{2}\left[\sinh\left(\frac{2h_{cu}}{\delta}\right) - \sin\left(\frac{2h_{cu}}{\delta}\right)\right] \\ &= \frac{\delta}{2}\left[\sinh 2\Delta - \sin 2\Delta\right] \end{aligned} \qquad \text{(H.7)}$$

Evaluating I_6 gives

$$\begin{aligned} I_6 &= (\alpha^2+\beta^2)\int_0^{h_{cu}} \left[\cosh\left(2\Delta - \frac{2\chi}{\delta}\right) - \cos\left(2\Delta - \frac{2\chi}{\delta}\right)\right] d\chi \\ &= \frac{-\delta(\alpha^2+\beta^2)}{2}\left[\sinh\left(2\Delta - \frac{2\chi}{\delta}\right) - \sin\left(2\Delta - \frac{2\chi}{\delta}\right)\right]_0^{h_{cu}} \\ &= \frac{-\delta(\alpha^2+\beta^2)}{2}\left[\sinh\left(2\Delta - \frac{2h_{cu}}{\delta}\right) - \sin\left(2\Delta - \frac{2h_{cu}}{\delta}\right) - \sinh(2\Delta) + \sin(2\Delta)\right] \\ &= \frac{-\delta(\alpha^2+\beta^2)}{2}\left[0 - 0 - \sinh(2\Delta) + \sin(2\Delta)\right] \\ &= \frac{\delta(\alpha^2+\beta^2)}{2}\left(\sinh 2\Delta - \sin 2\Delta\right) \end{aligned} \qquad \text{(H.8)}$$

The evaluation of I_7 yields:

$$\begin{aligned}
I_7 &= 2\alpha \int_0^{h_{cu}} \left[\cosh\Delta\cos\left(\Delta - \frac{2\chi}{\delta}\right) - \cosh\left(\Delta - \frac{2\chi}{\delta}\right)\cos\Delta\right] d\chi \\
&= -\delta\alpha\left[\cosh\Delta\sin\left(\Delta - \frac{2\chi}{\delta}\right) - \sinh\left(\Delta - \frac{2\chi}{\delta}\right)\cos\Delta\right]_0^{h_{cu}} \\
&= -\delta\alpha\left[\cosh\Delta\sin\left(\Delta - \frac{2h_{cu}}{\delta}\right) - \sinh\left(\Delta - \frac{2h_{cu}}{\delta}\right)\cos\Delta\right. \\
&\qquad \left. - \cosh\Delta\sin\Delta + \sinh\Delta\cos\Delta\right] \\
&= -\delta\alpha\left[\cosh\Delta\sin(-\Delta) - \sinh(-\Delta)\cos\Delta - \cosh\Delta\sin\Delta + \sinh\Delta\cos\Delta\right] \\
&= -\delta\alpha\left[2\sinh\Delta\cos\Delta - 2\cosh\Delta\sin\Delta\right] \\
&= -\left(\frac{\delta}{2}\right)4\alpha\left[\sinh\Delta\cos\Delta - \cosh\Delta\sin\Delta\right] \qquad \text{(H.9)}
\end{aligned}$$

The evaluation of I_8 yields

$$\begin{aligned}
I_8 &= -2\beta \int_0^{h_{cu}} \left[\sinh\Delta\sin\left(\Delta - \frac{2\chi}{\delta}\right) - \sinh\left(\Delta - \frac{2\chi}{\delta}\right)\sin\Delta\right] d\chi \\
&= -\delta\beta\left[\sinh\Delta\cos\left(\Delta - \frac{2\chi}{\delta}\right) + \cosh\left(\Delta - \frac{2\chi}{\delta}\right)\sin\Delta\right]_0^{h_{cu}} \\
&= -\delta\beta\left[\sinh\Delta\cos\left(\Delta - \frac{2h_{cu}}{\delta}\right) + \cosh\left(\Delta - \frac{2h_{cu}}{\delta}\right)\sin\Delta\right. \\
&\qquad \left. - \sinh\Delta\cos\Delta - \cosh\Delta\sin\Delta\right] \\
&= -\delta\beta\left[\sinh\Delta\cos(-\Delta) + \cosh(-\Delta)\sin\Delta - \sinh\Delta\cos\Delta - \cosh\Delta\sin\Delta\right] \\
&= \delta\beta\left[\sinh\Delta\cos\Delta + \cosh\Delta\sin\Delta - \sinh\Delta\cos\Delta - \cosh\Delta\sin\Delta\right] \\
&= 0 \qquad \text{(H.10)}
\end{aligned}$$

Substituting (H.7), (H.8), (H.9), and (H.10) into (H.2) gives the desired result of

$$\int_0^{h_{cu}} \underline{H}_z(\chi)\underline{H}_z^*(\chi)\, d\chi = \frac{|\underline{H}_z(\chi = h_{cu})|^2\, \delta}{2\,(\cosh 2\Delta - \cos 2\Delta)} \times \Big\{ \Big(1 + \alpha^2 + \beta^2\Big)\Big(\sinh 2\Delta - \sin 2\Delta\Big) - 4\alpha\Big(\sinh\Delta\cos\Delta - \cosh\Delta\sin\Delta\Big) \Big\} \quad \text{(H.11)}$$

Appendix I

Description of Pot-Core Transformer Tested in Section 6.3

In this appendix, we describe the pot-core transformer that is shown in Fig. 6.10 and tested in Section 6.3. Figures 6.11 and 6.12 show comparisons between the measured and modeled short-circuit resistances and inductances for this core. The values of $\underline{I}_\ell/\underline{I}_{BASE}$, $\underline{H}_{z\text{-}N}$ and α for the pot-core transformer under the six short-circuit tests are identical to those given for the EE-core transformer in Table 6.5. As much as possible, data are presented in this appendix in the same format as in Tables 6.1 and 6.2. Since the transformer of interest is wound on a pot core, certain parameters such as X_{bob} and Y_{bob} have no meaning and have not been included in Tables I.1 and I.2.

The eight-layer four-winding transformer[1] was wound on a Ferroxcube 4229F1D bobbin which was placed inside a Ferroxcube 4229PL00-3C8 ferrite pot core. Each winding has twenty turns and is composed of two layers of ten turns each. Each layer contains twenty insulated conductors since two electrically paralleled wires were wound together. Five-mil paper insulation was put between windings to produce a winding cross-section similar to Fig. 6.1.

[1]Duke's internal reference number for this core is pc01b05

Table I.1: Initial Collection of Mechanical and Electrical Parameters

Parameter	*Value*	
N_ℓ	10	(all layers)
n_s	2	(all layers)
N_c	20	(all layers)
AWG	20	(all layers)
h_t	5 mil $= 1.27 \times 10^{-4}$ m	
b_{win}	2.07×10^{-2} m	
$\rho_{cu,20°C}$	1.7241×10^{-8} Ω-m	
K_T	3.93×10^{-11} Ω-m/C°	
T	60 °C	

Table I.2: Calculated Mechanical Parameters

Symbol	*Value*	
d_{cu}	8.12×10^{-4} m	(all layers)
d_o	8.84×10^{-4} m	(all layers)
h_{cu}	7.20×10^{-4} m	(all layers)
b_{cu}	7.20×10^{-4} m	(all conductors)
η	0.696	(all layers)

Symbol	*Layer Number*							
	1	2	3	4	5	6	7	8
ℓ_T	6.46×10^{-2}	7.01×10^{-2}	7.70×10^{-2}	8.25×10^{-2}	8.92×10^{-2}	9.42×10^{-2}	1.01×10^{-1}	1.06×10^{-1}

Symbol	*Gap Number*						
	1	2	3	4	5	6	7
g	1.6 e-4	3.7 e-4	1.6 e-4	3.5 e-4	0.7 e-4	3.1 e-4	0.8 e-4
ℓ_g	6.74×10^{-5}	7.36×10^{-2}	7.98×10^{-2}	8.59×10^{-2}	9.17×10^{-2}	9.76×10^{-2}	1.04×10^{-1}

APPENDIX J

Calculating the Short-Circuit Impedances of a Multiwinding Transformer from its Geometry

IEEE Power Electronics Specialists Conference Record, 89CH2721-9, June 1989

This page has been left blank intentionally.

CALCULATING THE SHORT-CIRCUIT IMPEDANCES OF A MULTIWINDING TRANSFORMER FROM ITS GEOMETRY

Van A. Niemela Glenn R. Skutt† Audrey M. Urling Yain-Nan Chang
Thomas G. Wilson Harry A. Owen, Jr. Ronald C. Wong

Department of Electrical Engineering
Duke University, Durham, NC 27706, USA

Abstract

From a simplified field analysis, expressions are derived to calculate the set of frequency-dependent leakage inductances of a multiwinding-transformer from the layout and dimensions of its windings. Experimental data are provided that illustrate the accuracy and the limitations of such leakage-inductance calculations, as well as the accuracy of ac-winding-resistance calculations carried out using a similar, previously-published method.

1 INTRODUCTION

As switching frequencies rise, the design of transformers for multiple-output dc-to-dc power converters becomes increasingly difficult because frequency-dependent stray effects can no longer be neglected. In the windings of a transformer, skin and proximity effects induce eddy currents in the conductors, increasing copper losses, and by opposing the penetration of magnetic flux into the conductors, decreasing leakage inductances. Often stray effects can be incorporated in transformer equivalent-circuit models for use in SPICE-like circuit simulations; the difficulty is that usually there is no easy way to determine *a priori* what parameter values to use in such circuit models to accurately predict the behavior of a proposed transformer design.

In the equivalent circuits proposed in the literature for low-frequency modeling of a multiwinding transformer under sinusoidal excitation, the parameters needed to characterize the model can be obtained from the measured low-frequency short-circuit inductances or impedances of the transformer [1,2]. With respect to the high-frequency operation of transformers, much of the work that has appeared in the last two decades has focused on calculating the ac-winding-resistance component of short-circuit impedance. A review of a portion of this literature is given in [3]. Although receiving considerably less attention and often ignored, the leakage-inductance component can be just as important, significantly affecting circuit operation at high frequencies. In certain types of circuits such as quasi-resonant switching converters, the leakage inductance of the transformer is a desirable and important element in the circuit. However, in other applications, the inductances in the windings cause undesirable component stresses and cross-regulation effects which influence the steady-state output voltages that appear on unregulated outputs.

Dowell presents a method in [4] for calculating the frequency dependence of winding resistance and leakage inductance. His method is useful for two-winding transformers, but since it cannot accommodate the open-circuited windings present during the short-circuit-impedance tests described in Section 4, it is unsuitable for transformers having multiple secondary windings. In this paper, a method that appears in [5] is presented for calculating the leakage inductances between pairs of windings in a multiwinding transformer, a method which is based on the layer-by-layer approach used in [6] for calculating winding losses at high frequencies. The present approach is more versatile than Dowell's, accounting for the magnetic-energy-storage variation and the losses due to eddy currents that are induced in open-circuited windings at high frequencies.

Considered in this paper are transformers having ungapped pot cores and EE cores of high-permeability material, and windings of round, strip, and foil conductors arranged in concentric cylindrical layers. The magnetizing current of the core and the capacitances of the windings are neglected.

This paper builds on a method that has evolved over the past two decades for successfully predicting the ac winding losses of a multilayer transformer from the magnetic-field-intensity distribution in its winding

This work was supported in part by a research contract with Digital Equipment Corporation, Maynard, MA.

†Now with Digital Equipment Corporation, Northboro, MA.

CH2721-9/89/0000-0607 $1.00 © 1989 IEEE

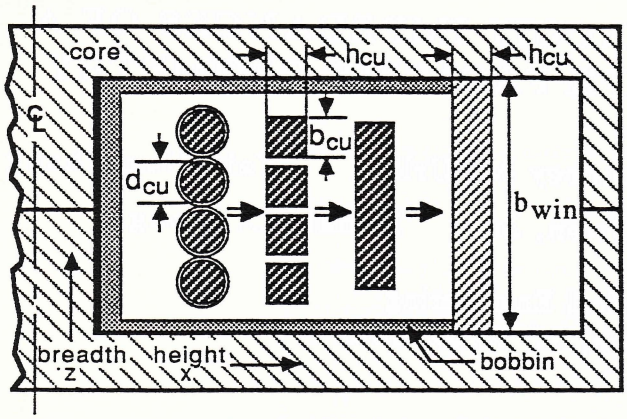


Figure 1: Steps in transforming a layer of round wires on a bobbin into an equivalent foil layer for analysis. The round wires are replaced by square conductors of the same cross-sectional area, with $h_{cu} = b_{cu}$, which are brought together into a single foil layer, then "stretched" to fill the entire window breadth b_{win} without changing the height of the layer h_{cu} or the position of the layer in the x-direction. Layers of strip and foil conductors are transformed similarly.

space [6–8]. Extending that pattern, an expression is derived by which the leakage inductances of a transformer may be calculated from its dimensions and the layout of its windings. Such leakage-inductance calculations, coupled with the earlier winding-resistance calculations, let us predict the short-circuit impedances which can be used to model a transformer. These predictions are shown to be in close agreement with laboratory measurements.

2 APPROXIMATIONS

Both the resistive and inductive components of short-circuit impedances can be calculated from the magnetic-field distribution inside the winding space of a transformer. To permit solving for this field distribution as a one-dimensional problem, the magnetic field in the winding space is assumed to be parallel to the center leg of the transformer. In practice, a high-permeability pot core surrounding the winding structure produces such a field pattern, and experimental results indicate that the assumption of parallel field lines is a valid one for a high-permeability EE core as well.

The actual winding layers of a transformer are commonly approximated by equivalent-foil windings which span the entire breadth of the core window as illustrated in Fig. 1 [4,6]. To compensate for the increase in the cross-sectional area of the conducting layer which occurs in the last step of the transformation, an effective conductivity $\eta\sigma_{cu}$ is used in the field equations

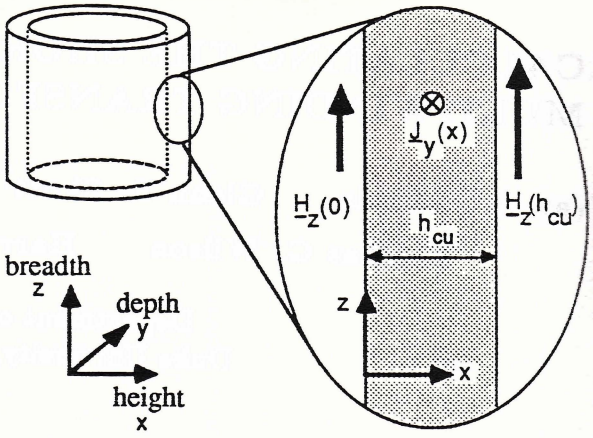


Figure 2: A cylindrical winding layer is approximated by an infinite current sheet, which is assumed mathematically to extend to infinity in the y (depth) and z (breadth) directions to obtain the field solution. The height of the sheet is h_{cu} in the x-direction.

for the layer. The effective conductivity is lower than the conductivity σ_{cu} of the conductors by a factor of the layer porosity η, defined as $\eta = N_c b_{cu}/b_{win}$, where N_c is the number of conductor cross sections appearing in a cross-sectional view of the winding layer. It is reasonable to expect that for η less than some limit, the equivalent-foil-layer approximation is no longer valid. However, fairly good test results have been obtained for η as low as approximately 0.5.

For the cylindrical equivalent-foil winding layer pictured in Fig. 2, a field solution is most accurately derived in cylindrical coordinates, but cumbersome Bessel functions appear in the solution [7]. Although it is possible to replace them by approximations [8], Bessel functions can be avoided altogether by using a flat current sheet, shown enlarged in Fig. 2, to approximate the layer. The error is small as long as the thickness h_{cu} of the layer is small with respect to its radius of curvature [7]. It is this infinite-current-sheet field solution which is derived in the next section.

3 FIELD SOLUTION

In this section, it is assumed that a transformer-winding layer may be modeled as a finite portion of an infinite current sheet. The complete boundary-value solution for the magnetic energy stored in such a current sheet for any frequency is then derived from Maxwell's equations, and the corresponding equation for power dissipation previously derived by Vandelac and Ziogas is repeated for use in Section 4. In that section, both results are applied to the winding layers of a transformer to calculate its short-circuit impedan-

ces, each consisting of an ac winding resistance and a leakage reactance. SI units are used in all equations.

3.1 Diffusion Equation for H

An equation that describes the magnetic-field-intensity distribution across an infinite current sheet is first derived from Maxwell's equations, then solved in Section 3.2. Beginning with the differential form of Ampere's law,

$$\nabla \times \mathbf{H} = \mathbf{J} + \frac{\partial \mathbf{D}}{\partial t} \tag{1}$$

the curl of both sides is taken and the vector identity $\nabla \times \nabla \times \mathbf{H} = \nabla(\nabla \bullet \mathbf{H}) - \nabla^2\mathbf{H}$ is used, along with the constitutive relations $\mathbf{B} = \mu\mathbf{H}$, $\mathbf{J} = (\eta\sigma_{cu})\mathbf{E}$, and $\mathbf{D} = \epsilon\mathbf{E}$, Gauss's law for magnetism $\nabla \bullet \mathbf{B} = 0$, and Faraday's law $\nabla \times \mathbf{E} = -\partial\mathbf{B}/\partial t$, to obtain the following result.

$$\nabla^2\mathbf{H} = \mu(\eta\sigma_{cu})\frac{\partial \mathbf{H}}{\partial t} + \mu\epsilon\frac{\partial^2\mathbf{H}}{\partial t^2} \tag{2}$$

The effective conductivity $\eta\sigma_{cu}$ is used in these equations for the reason given in Section 2.

If the magnetic field is varying sinusoidally in time, then the time-varying vector quantity $\mathbf{H}$ can be represented in the frequency domain by a vector phasor $\underline{\mathbf{H}}$, where the magnitude $|\underline{\mathbf{H}}|$ of the vector phasor is chosen to be the rms value of the field intensity.

$$\mathbf{H}(x,y,z,t) = \sqrt{2}\,\mathrm{Re}\left[\underline{\mathbf{H}}(x,y,z)e^{j\omega t}\right] \tag{3}$$

The vector phasor $\underline{\mathbf{H}}$ represents three phasors, one for each spatial component of the vector $\mathbf{H}$.

$$\underline{\mathbf{H}}(x,y,z) = \underline{H}_x\,\hat{\mathbf{a}}_\mathbf{x} + \underline{H}_y\,\hat{\mathbf{a}}_\mathbf{y} + \underline{H}_z\,\hat{\mathbf{a}}_\mathbf{z} \tag{4}$$

Substituting (3) into (2), and using the knowledge that, for sinusoidal waveforms, differentiating a vector with respect to time is equivalent to multiplying its vector phasor by $j\omega$, the standard three-dimensional diffusion equation results.

$$\nabla^2\underline{\mathbf{H}} = j\omega\mu(\eta\sigma_{cu})\underline{\mathbf{H}} - \omega^2\mu\epsilon\underline{\mathbf{H}} = \underline{k}^2\underline{\mathbf{H}} \tag{5}$$

where $\underline{k}$ is the complex wave number.

$$\underline{k} = \sqrt{j\omega\mu(\eta\sigma_{cu}) - \omega^2\mu\epsilon} \tag{6}$$

Note that underlines are used to denote all complex quantities, not just phasors.

For windings made of a good conductor, the permittivity ϵ and the permeability μ are given by their free-space values $\epsilon_0 = 8.854 \times 10^{-9}$ F/m and $\mu_0 = 4\pi \times 10^{-7}$ H/m, respectively. For any frequency of interest in our analysis, $(\eta\sigma_{cu}) \gg \omega\epsilon_0$, which allows the following approximation to be made.[1]

$$\underline{k} \approx \sqrt{j\omega\mu_0(\eta\sigma_{cu})} \tag{7}$$

The close relationship between the complex wave number $\underline{k}$ and the skin depth δ, defined as

$$\delta = \sqrt{\frac{2}{\omega\mu_0(\eta\sigma_{cu})}} \tag{8}$$

may be seen by substituting from Euler's identities

$$\sqrt{j} = \left(e^{j\frac{\pi}{2}}\right)^{\frac{1}{2}} = e^{j\frac{\pi}{4}} = \tfrac{1}{\sqrt{2}}(1+j) \tag{9}$$

into (7) to give

$$\underline{k} = \sqrt{\frac{\omega\mu_0(\eta\sigma_{cu})}{2}}\,(1+j) = \frac{1}{\delta}(1+j) \tag{10}$$

For the infinite-current-sheet problem under consideration, the spatial magnetic-field-intensity phasor $\underline{\mathbf{H}}(x,y,z)$ is assumed to be a function of x only and to be directed in the z-direction. Using this fact, the three-dimensional diffusion equation (5) becomes the one-dimensional diffusion equation which must be solved.

$$\frac{\partial^2\underline{H}_z(x)}{\partial x^2} = \underline{k}^2\underline{H}_z(x) \tag{11}$$

3.2 Magnetic-Field-Intensity Profile

The general solution of (11) has the form

$$\underline{H}_z(x) = \underline{H}_1 e^{\underline{k}x} + \underline{H}_2 e^{-\underline{k}x} \tag{12}$$

where $\underline{H}_1$ and $\underline{H}_2$ are arbitrary complex phasors which can be determined by applying the boundary conditions of magnetic field intensity at the surfaces of the current sheet, $\underline{H}_z(x=0)$ and $\underline{H}_z(x=h_{cu})$ shown in Fig. 2, which are obtained from the low-frequency field-intensity profile as described in Section 4. Using the definition $\sinh u = (e^u - e^{-u})/2$,

$$\underline{H}_z(x) = \frac{1}{\sinh \underline{k}h_{cu}}\left[\underline{H}_z(x=h_{cu})\sinh \underline{k}x + \underline{H}_z(x=0)\sinh \underline{k}(h_{cu}-x)\right] \tag{13}$$

A thorough discussion and graphical display of the field variations represented by this equation are contained in [9] for a range of frequencies and various conditions of excitation.

[1] For copper with $\sigma_{cu} = 5.315 \times 10^7$ S/m at 60°C, this assumption is good for frequencies below approximately 1×10^{12} hertz.

To prevent zeroes from appearing in the denominators of some of the equations to be derived, a new variable χ (chi) is defined to take the place of x in (13).

$$\chi = \begin{cases} x & \text{if } |\underline{H}_z(x=h_{cu})| \geq |\underline{H}_z(x=0)| \\ h_{cu} - x & \text{if } |\underline{H}_z(x=h_{cu})| < |\underline{H}_z(x=0)| \end{cases} \quad (14)$$

This definition causes $\chi = 0$ always to be at the surface which has the smaller of the two boundary magnetic fields, and $\chi = h_{cu}$ always to be at the surface with the larger field. By defining the boundary-condition ratio as

$$\alpha + j\beta = \frac{\underline{H}_z(\chi=0)}{\underline{H}_z(\chi=h_{cu})} \quad (15)$$

an alternate form of (13) is obtained in terms of χ.

$$\underline{H}_z(\chi) = \frac{\underline{H}_z(\chi=h_{cu})}{\sinh \underline{k} h_{cu}} \Big[\sinh \underline{k}\chi + (\alpha + j\beta) \sinh \underline{k}(h_{cu} - \chi) \Big] \quad (16)$$

If both boundary conditions of magnetic field intensity are equal to zero, (15) is undefined; but it is clear from (13) that the magnetic field intensity is zero everywhere inside the current sheet, thus no magnetic energy is stored and no power is dissipated in the current sheet.

3.3 Energy Storage

The magnetic energy stored in any winding layer of a transformer can now be derived from the profile given by (16) for the magnetic field intensity inside an infinite current sheet. In general, the instantaneous energy stored in a magnetic field per unit volume at a point in space is

$$w_m(t) = \frac{\mu}{2} |\mathbf{H}(t)|^2 \quad (17)$$

The time-average energy stored in the magnetic field in any layer of the transformer windings is obtained by integrating this expression over both the time for one cycle of the excitation current and the volume occupied by the layer. The time integral is performed first in the following derivation.

Because $\mathbf{H}(t)$ is assumed to have only a z-component inside the winding space of a transformer, (17) may be written in terms of the scalar quantity $H_z(t)$. Substituting a cosine expression for $H_z(t)$, written in terms of the rms phasor magnitude $|\underline{H}_z|$ and the phase angle θ_H, the time-average magnetic energy density $\langle w_m \rangle$ in a layer is derived from the integral of (17) over the excitation period T, where angle brackets $\langle\ \rangle$ denote the time average of the enclosed quantity.

$$\langle w_m \rangle = \frac{1}{T} \int_T \frac{\mu_0}{2} \left[\sqrt{2} |\underline{H}_z| \cos(\omega t + \theta_H) \right]^2 dt \quad (18)$$

After performing the integration,

$$\langle w_m \rangle = \frac{\mu_0}{2} |\underline{H}_z|^2 \quad (19)$$

where $|\underline{H}_z|^2$ can be expressed as the product of the phasor $\underline{H}_z$ and its complex conjugate $\underline{H}_z^*$. Therefore, the time-average magnetic energy density can be rewritten as

$$\langle w_m \rangle = \frac{\mu_0}{2} \underline{H}_z(\chi)\, \underline{H}_z^*(\chi) \quad (20)$$

where, as a reminder, the dependence of $\underline{H}_z$ on the height χ is indicated.

The time-average energy $\langle W_m \rangle$ stored in the magnetic field in a conducting layer is then obtained by integrating (20) over the volume occupied by the layer. To simplify the calculation, the winding layer is assumed to be flat instead of cylindrical, extending a distance equal to the length-of-turn ℓ_T in the y-direction. Using b_{win} and h_{cu} from Fig. 1,

$$\langle W_m \rangle = \int_0^{b_{win}} \int_0^{\ell_T} \int_0^{h_{cu}} \langle w_m \rangle \, d\chi \, dy \, dz \quad (21)$$

Because $\langle w_m \rangle$ does not depend on y or z, the integration with respect to those variables is a simple multiplication.

$$\langle W_m \rangle = b_{win}\, \ell_T \int_0^{h_{cu}} \langle w_m \rangle \, d\chi = b_{win}\, \ell_T \, \langle Q_H \rangle \quad (22)$$

where $\langle Q_H \rangle$ is defined as the time-average magnetic energy stored in the infinite current sheet per square meter in the y-z plane. The integration in (22) is carried out in the Appendix with the following result.

$$\langle Q_H \rangle = \frac{\mu_0 \delta |\underline{H}_z(\chi = h_{cu})|^2}{4} \times \left[(1 + \alpha^2 + \beta^2) F_3(\Delta) - 4\alpha F_4(\Delta) \right] \quad (23)$$

where

$$F_3(\Delta) = \frac{\sinh 2\Delta - \sin 2\Delta}{\cosh 2\Delta - \cos 2\Delta} \quad (24)$$

$$F_4(\Delta) = \frac{\sinh \Delta \cos \Delta - \cosh \Delta \sin \Delta}{\cosh 2\Delta - \cos 2\Delta} \quad (25)$$

The variable $\Delta = h_{cu}/\delta$ is defined as the height of the winding layer h_{cu} normalized to skin depth δ, α and β constitute the boundary-condition ratio in (15), and $|\underline{H}_z(\chi = h_{cu})|^2$ is the square of the rms value of the larger of the magnetic field intensities at the two surfaces of the current sheet.

These equations make clear that the ac effects of interest are dependent not on conductor size alone, but

on Δ, the conductor size relative to skin depth, which is a function of the excitation frequency as shown in (8). Furthermore, the limiting values of one and zero for F_3 and F_4, respectively, may be used for large Δ to greatly simplify the calculation. This approximation introduces an error in $\langle Q_H \rangle$ which is always less than 10% for $\Delta \geq 3.1$, and less than 5% for $\Delta \geq 3.4$.

3.4 Power Dissipation

A simple expression may be derived for the profile $\underline{J}_y(x)$ of the current-density phasor across an infinite current sheet in terms of the corresponding profile $\underline{H}_z(x)$ of the magnetic-field-intensity phasor given by (13). Applying the constitutive relations $\mathbf{J} = (\eta\sigma_{cu})\mathbf{E}$ and $\mathbf{D} = \epsilon_0\mathbf{E}$ to (1), and converting to vector phasors for sinusoidal steady-state,

$$\nabla \times \underline{\mathbf{H}} = (\eta\sigma_{cu})\underline{\mathbf{E}} + j\omega\epsilon_0\underline{\mathbf{E}} \approx (\eta\sigma_{cu})\underline{\mathbf{E}} = \underline{\mathbf{J}} \quad (26)$$

where the good-conductor approximation used to obtain (7) is used here also. For the conditions illustrated in Fig. 2, where $\underline{\mathbf{J}}$ is in the y-direction only, $\underline{\mathbf{H}}$ is in the z-direction only, and both are functions of only x, the following expression can be obtained from (26) by expanding the curl of $\underline{\mathbf{H}}$ in rectangular coordinates and eliminating all the terms which are equal to zero.

$$\underline{J}_y(x) = \frac{-\partial \underline{H}_z(x)}{\partial x} \quad (27)$$

From (27) and the fundamental expression for the power dissipated per unit volume at a point in space,

$$p_d(t) = \frac{|\mathbf{J}(t)|^2}{\sigma} \quad (28)$$

the power dissipation in a current sheet may be derived in a manner which parallels that in Section 3.3 for energy storage. The resulting expression for power dissipation per square meter of an infinite current sheet is given by Vandelac and Ziogas as (A-17) in [6], repeated here in terms of our symbols.

$$\langle Q_J \rangle = \frac{|\underline{H}_z(\chi = h_{cu})|^2}{(\eta\sigma_{cu})\delta} \times \left[(1 + \alpha^2 + \beta^2)F_1(\Delta) - 4\alpha F_2(\Delta)\right] \quad (29)$$

where

$$F_1(\Delta) = \frac{\sinh 2\Delta + \sin 2\Delta}{\cosh 2\Delta - \cos 2\Delta} \quad (30)$$

$$F_2(\Delta) = \frac{\sinh \Delta \cos \Delta + \cosh \Delta \sin \Delta}{\cosh 2\Delta - \cos 2\Delta} \quad (31)$$

Once again, the limiting values of one and zero for F_1 and F_2, respectively, may be used for large Δ to simplify the calculation. This approximation introduces an error in $\langle Q_J \rangle$ which is always less than 10% for $\Delta \geq 2.2$, and less than 5% for $\Delta \geq 4.1$.

The equations presented up to this point are quite general, applicable to any possible combination of sinusoidal winding currents, with a minor exception: Equations (23) and (29) cannot be applied to winding layers in regions of zero magnetic field intensity, but as mentioned in Section 3.2, there is no magnetic energy stored and no power dissipated in such layers. Not all of the generality of these equations is needed at present, however. It is seen in the next section that for the short-circuit tests considered in this paper, β is always equal to zero.

4 SHORT-CIRCUIT TESTS

In a multiwinding transformer, there is one short-circuit or leakage impedance for each possible pair of windings, totaling $K(K-1)/2$ impedances for a transformer having K windings. The short-circuit impedance

$$\underline{Z}_{(jk)} = R_{(jk)} + j\omega L_{(jk)} = \left(\frac{N_j}{N_k}\right)^2 \underline{Z}_{(kj)} \quad (32)$$

is the impedance seen at the terminals of winding j during short-circuit test (jk), where winding j is excited at an angular frequency ω, winding k is short-circuited, and the remaining windings are open-circuited. This impedance multiplied by the turn ratio squared would be seen at the terminals of winding k if winding k were excited and winding j were short-circuited. The core loss is assumed to be negligible, and the magnetizing inductance of the core is neglected because it is assumed to be much larger than the leakage inductance.

Each different short-circuit test has a characteristic low-frequency magnetic-field-intensity profile as illustrated in Fig. 3(c). A profile of this shape is produced when the exciting current is of low enough frequency that the skin depth δ is much larger than the height of the conductors h_{cu}, and under the assumption that the high-permeability core requires equal and opposite ampere-turns in the open-circuited and short-circuited windings. If the rms current flowing at the terminals of the excited winding is held constant as the frequency is varied, the magnetic-field-intensity in any interlayer space remains uniform and has a constant rms value, although the profile changes shape inside the layers. Therefore, the low-frequency magnetic-field-intensity profile can be used to obtain the *frequency-independent* boundary conditions of magnetic field intensity in the spaces between winding layers that are needed to calculate the *frequency-dependent* magnetic energy storage and power dissipation in each layer of conducting material.

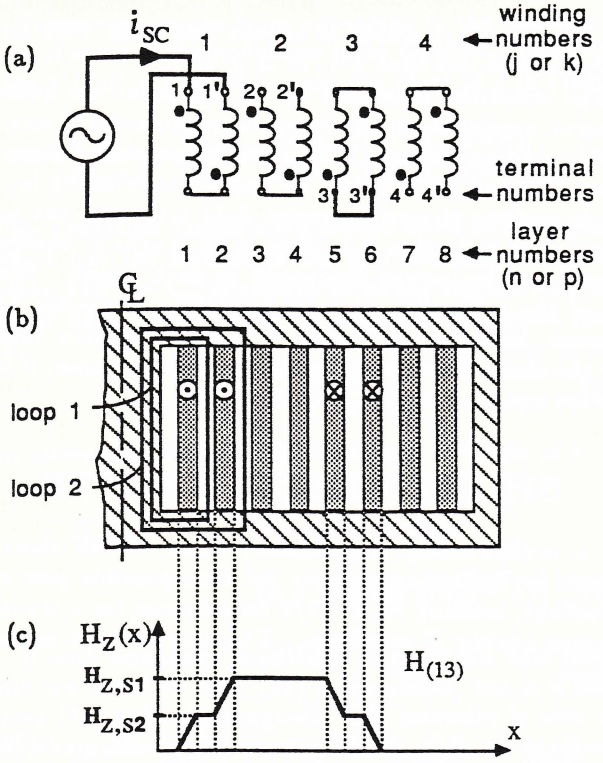


Figure 3: (a) Schematic diagram of short-circuit test (13) for a 4-winding 8-layer transformer. Dotted terminals of each winding are labeled with the corresponding winding number, and undotted terminals are labeled with the winding number primed. (b) Cross-section of the right half of the transformer, showing instantaneous current directions in the equivalent-foil layers during one half of an excitation cycle. (c) Low-frequency magnetic-field-intensity profile corresponding to the current directions shown in Part (b).

To obtain expressions for the field-intensity phasor $\underline{H}_z$ in the interlayer spaces, which become the boundary conditions for the layer calculations, the integral form of Ampere's law is applied to loops such as those shown in Fig. 3(b). If $N_{\ell p}$ is the number of turns in the p^{th} layer, and $\underline{I}_{\ell p}$ is the phasor of current flowing in each turn of the p^{th} layer, the expression obtained for the field intensity in interlayer space S_n to the right of the n^{th} layer in Fig. 3(b) is

$$\underline{H}_{z,Sn} = \frac{-1}{b_{win}} \sum_{p=1}^{n} N_{\ell p}\, \underline{I}_{\ell p} \tag{33}$$

Note that the magnetic field in the space to the inside of the innermost conducting layer, designated $\underline{H}_{z,S0}$, is equal to zero under the assumption of equal and opposite ampere-turns. If $\underline{I}_{SC}$ is the phasor representing the short-circuit current i_{SC} in Fig. 3(a), then $\underline{I}_{\ell p}$ can be expressed as $\underline{I}_{SC}$ for the layers in the excited winding j, and as $(-N_j/N_k)\underline{I}_{SC}$ for the layers in the short-circuited winding k, where and N_j and N_k are the numbers of turns in the corresponding *windings* rather than the layers. Then (33) can be reduced to a constant times $\underline{I}_{SC}$ for each short-circuit test. There is no need to substitute a particular value for $\underline{I}_{SC}$ in the intermediate results because $\underline{I}_{SC}$ is ultimately canceled in (37) and (39) to obtain the equivalent short-circuit inductance and resistance, which are independent of the short-circuit current $\underline{I}_{SC}$.

Once (33) has been used to obtain expressions for the interlayer magnetic-field-intensity phasors $\underline{H}_{z,Sn}$ in terms of $\underline{I}_{SC}$, the total time-average energy stored in the winding space can be calculated, from which the short-circuit or leakage inductance $L_{(jk)}$ can then be obtained. The total time-average energy $\langle W_T \rangle$ stored in the transformer winding structure is composed of two parts: the time-average energy $\langle W_\ell \rangle$ stored in the winding layers, and the time-average energy $\langle W_S \rangle$ stored in the interlayer spaces.

$$\langle W_T \rangle = \langle W_\ell \rangle + \langle W_S \rangle \tag{34}$$

$\langle W_\ell \rangle$ is calculated by summing the results of (22) for all N winding layers, using $\underline{H}_{z,S(n-1)}$ and $\underline{H}_{z,Sn}$ as the boundary conditions to evaluate $\langle Q_H \rangle$ for the n^{th} layer.

$$\langle W_\ell \rangle = b_{win} \sum_{n=1}^{N} \ell_{Tn}\, \langle Q_H \rangle_n \tag{35}$$

To calculate $\langle W_S \rangle$, use is made of the fact that the magnetic field intensity is uniform in each interlayer space. The magnetic energy stored in one interlayer space is thus the volume of the space times the energy density $\langle w_m \rangle$ from (19), with the field intensity given by (33). If s_n is the height of the n^{th} interlayer space in the x-direction, and ℓ_{Sn} is the "length-of-turn" of the interlayer space in the y-direction, $\langle W_S \rangle$ is the following sum of energies for all $(N-1)$ interlayer spaces.

$$\langle W_S \rangle = b_{win} \sum_{n=1}^{N-1} \ell_{Sn}\, s_n \left[\frac{\mu_0}{2} |\underline{H}_{z,Sn}|^2 \right] \tag{36}$$

After calculating the total time-average energy stored in the transformer winding space using (34), (35), and (36), the short-circuit or leakage inductance is obtained from

$$L_{(jk)} = \frac{2\langle W_T \rangle}{|\underline{I}_{SC}|^2} \tag{37}$$

This is the equivalent lumped inductance which, if carrying the sinusoidal current represented by $\underline{I}_{SC}$, stores the same amount of magnetic energy as the winding space of the short-circuited transformer, averaged over

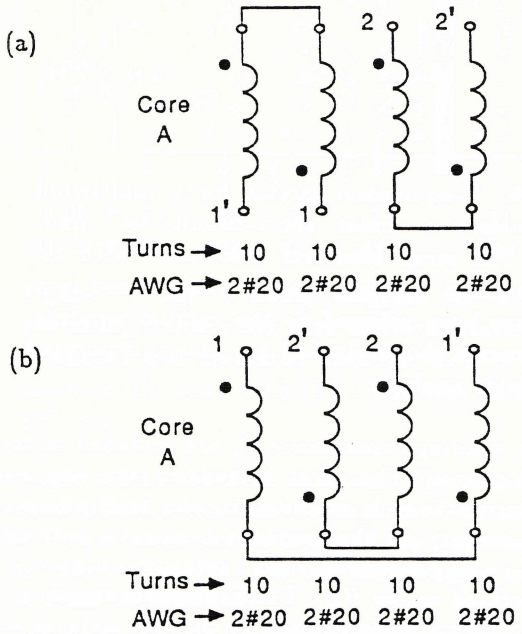


Figure 4: Winding diagrams for a 4-layer 2-winding transformer with (a) windings composed of adjacent winding layers and (b) a split winding.

one cycle of the current. The *instantaneous* magnetic energies typically are not equal, however. While the energy stored in the equivalent lumped inductance is zero at two instants in every cycle of the current, the instantaneous energy stored in the transformer winding space at high frequencies is never zero because the magnetic field intensity is never simultaneously equal to zero at all points in the conducting layers.

The resistance for a particular short-circuit test is calculated in a manner similar to the above calculation for inductance, except that only the winding layers need to be considered because there are no losses in the interlayer spaces. The equation for the total time-average power dissipated in the windings is analogous to (35).

$$\langle P_D \rangle = b_{win} \sum_{n=1}^{N} \ell_{Tn} \langle Q_J \rangle_n \qquad (38)$$

Then the short-circuit resistance is given by

$$R_{(jk)} = \frac{\langle P_D \rangle}{|\underline{I}_{SC}|^2} \qquad (39)$$

5 VERIFICATION

To compare calculated and measured values of short-circuit resistance and inductance over a frequency range of 100 Hz to 10 MHz, short-circuit tests were performed on several transformers using an HP 4192A impedance analyzer, with some of the results given in Figs. 5, 7, and 8. The impedance analyzer results were confirmed by repeating some of the same tests at higher current levels using an HP 3330B frequency synthesizer in conjunction with either a Crown DO-2000 2-kilowatt audio amplifier or an Amplifier Research 50A15 50-watt RF amplifier as the excitation source, and a Tektronix 7854 oscilloscope to record waveforms and calculate impedances. Great care was taken to minimize the inductances of the transformer leads by keeping them as short as possible and minimizing loop areas. All of the transformers tested have cores of ungapped ferrite and windings of round copper wire.

Core	Type	Magnetics, Inc. Part Number	A_L (mH @1000t)	ℓ_m (cm)	A_m (cm^2)
A	pot	P-44229-UG	≥7500	6.81	2.66
B	EE	F-44317-EC	5900	7.75	1.47
C	pot	F-43428-UG	7550	5.89	1.60

Table 1: Manufacturer's data for the magnetic cores used in the tests, including the inductance factor A_L, the magnetic path length ℓ_m, and the magnetic cross-section A_m.

Winding diagrams for the first test transformers are shown in Fig. 4. They are similar to the diagram of Fig. 3(a), where the leftmost layer in the diagram corresponds to the innermost layer of the actual transformer, except that the excitation source and the short circuit are omitted from the figures in this section. The source and the short circuit are connected to different windings for the different short-circuit tests as indicated by the numbers representing the test; for example, for short-circuit test (12), the excitation source is connected between terminals 1 and 1′ and the short circuit is connected between terminals 2 and 2′. The core for each transformer is identified by a letter on the left side of the winding diagram, with descriptive information provided in Table 1. The two different interconnections of the winding layers shown in Fig. 4 were tested to compare split- and non-split-winding arrangements. This was made possible by providing external leads at both ends of each layer so that any desired interconnection of the layers could be made. The wire size "2#20" stands for two strands of AWG#20 wire wound side-by-side and connected in parallel.

For the winding configurations in Fig. 4, the predicted and measured short-circuit inductances and resistances are plotted in Fig. 5. The curves of predicted data were calculated by computer using (37), (39), and the dimensions of the windings measured when each transformer was built. The offset between the predicted and measured curves of inductance is thought to be caused principally by the lead inductances not included in the calculations, which cannot be avoided in the measurements. The leakage inductance data con-

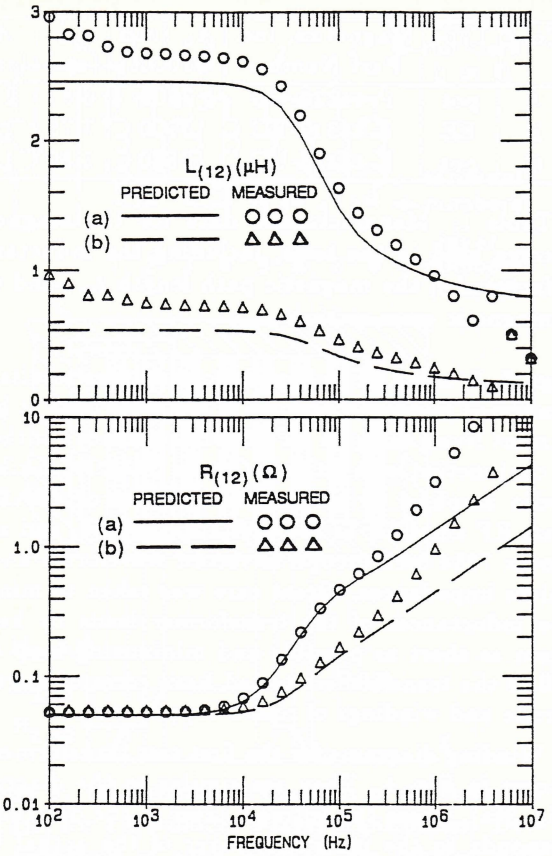


Figure 5: Predicted and measured short-circuit-test data for winding structures (a) and (b) in Fig. 4.

firm that a split winding, represented by case (b), produces a lower leakage inductance.

The two curves of predicted resistance in Fig. 5 match at low frequencies, but as expected, a split winding produces lower losses at high frequencies. The measured resistances agree well with the predicted curves, except for a rapid increase in the measured values as frequency rises above approximately 1 MHz. This effect can be understood by considering a T-equivalent circuit of the transformer.

A multiwinding transformer under short-circuit-test conditions can be represented by the T-equivalent circuit in Fig. 6, which shows only the two windings of the transformer that carry net currents. The short-circuit inductance $L_{(jk)}$ is the sum of the two series leakage inductances L_j and L'_k, and the short-circuit resistance $R_{(jk)}$ is likewise the sum of the two series winding resistances R_j and R'_k. The values of those four circuit elements are clearly frequency-dependent, but because they change at a slower rate than the frequency, they may be considered to be fixed for the following argument.

The faster-than-expected rise in the measured resistance in Fig. 5 can be explained if a core-loss resistor

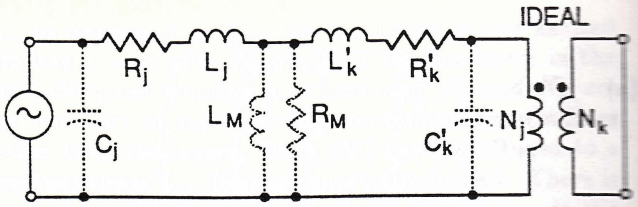


Figure 6: T-equivalent circuit for a multiwinding transformer under short-circuit-test conditions. The stray elements associated with the short-circuited winding, labeled with primed symbols, have been referred to the excited winding. The elements shown dashed are not incorporated in the fields analysis.

R_M and a winding capacitance C_j are included in the equivalent circuit. The effect of neither core loss nor winding capacitance is included in the field analysis presented earlier. As the resonant frequency between C_j and $(L_j + L'_k)$ is approached, a relatively high voltage is generated across R_M. This represents significant core loss, which manifests itself in the test data as an increase in the apparent winding resistance $R_{(jk)}$ that is not predicted by the field analysis.

The same resonance also explains the corresponding faster-than-expected decrease in the short-circuit inductance $L_{(jk)}$ as frequency rises. The "measured" leakage inductance is actually an *effective* leakage inductance, calculated from a measured reactance using (32). As frequency increases, the effective inductance $L_{(jk)}$ is reduced by the decreasing capacitive reactance $(-1/\omega C_j)$ that is not included in the field analysis.

Another test transformer is shown in Fig. 7. The windings contain an electrostatic shield of copper foil, which is treated as an open-circuited winding in the calculations since, at high frequencies, it dissipates power and affects leakage inductances just as any winding does. Data are shown for three of the six possible short-circuit tests, with the same bobbin placed in both a pot core and an EE core. The predicted curves are the same for the two cores, and the close match between the two sets of measured data demonstrates that the field analysis, which assumes parallel flux lines in the winding space, is accurate for EE cores as well as pot cores. For this winding structure, the resonant frequency between the winding capacitance and the leakage inductances is seen in the resistance plots of Fig. 7 to be approximately 2.5 MHz.

Another effect not accounted for in the analysis causes the equivalent inductances in Fig. 7 to increase dramatically as the frequency drops toward 100 Hz. If the frequency sweep were continued in the decreasing direction, it is expected that a second inductance plateau would be seen at a level approximately equal to the magnetizing inductance of the transformer, which

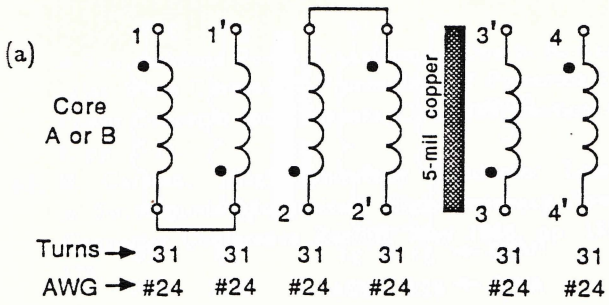


Figure 7: (a) Winding diagram for a 6-layer 4-winding transformer with an electrostatic shield. Predicted and measured data for three of the six short-circuit tests with (b) a pot core and (c) an EE core.

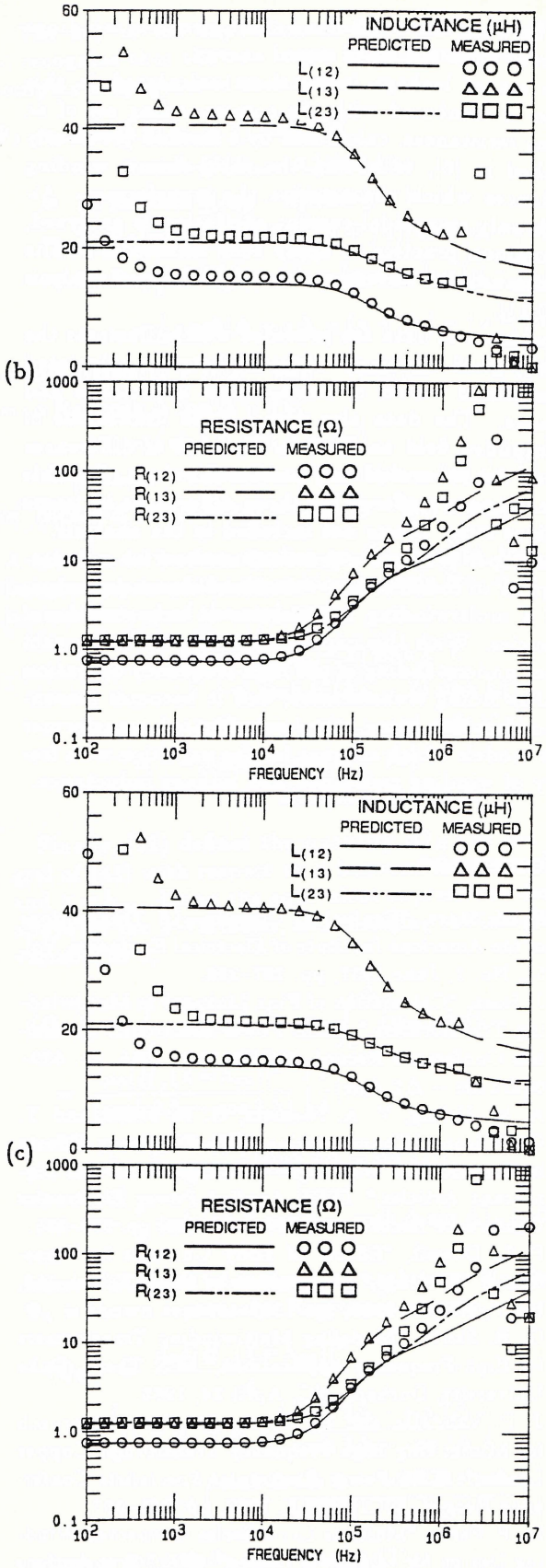
is neglected in the field analysis. The reason for the second plateau can also be explained by considering the T-equivalent circuit in Fig. 6. In this case, C_j and R_M may be ignored, but the magnetizing inductance L_M must be included.

As the excitation frequency decreases, the reactances of all the inductive elements in the T-equivalent circuit decrease proportionately, but the series combination of $j\omega L'_k$ and R'_k approaches a lower bound which is equal to R'_k. As frequency drops lower, the reactance ωL_M of the magnetizing inductance becomes much lower than R'_k; therefore, the short-circuit inductance $L_{(jk)}$ seen at the excited terminals reaches a maximum value which is the sum of L_M and L_j, with $L_M \gg L_j$.

Test results are given in Fig. 8 for one additional transformer, which has a mix of different wire sizes, an electrostatic shield, and a turn ratio greater than 3:1. Again, agreement is reasonably good between calculated and measured values of short-circuit inductance and resistance.

6 CONCLUSION

By considering the set of short-circuit tests which can be performed on a multiwinding transformer, analytical expressions are derived for the leakage inductances between all pairs of transformer windings, expressions which depend on only the winding geometry and the frequency of excitation. For each short-circuit test, a simplified field analysis gives the complete solution for the *frequency-independent* magnetic field intensity between winding layers, and the *frequency-dependent* distribution of magnetic field intensity within each layer. Then, for any frequency of interest, the magnetic energy stored in each winding layer and interlayer space is calculated, and the results are summed to give the total energy stored in the entire winding space of the transformer. Finally, the leakage induc-



tance between the excited and short-circuited windings is derived from the total stored energy.

The set of leakage inductances calculated in this manner is combined with the corresponding set of ac winding resistances, calculated by a method previously published in [6], to obtain the short-circuit winding impedances which characterize the transformer. Although only sinusoidal-current excitation is analyzed, it is common practice to apply such sinusoidal results to nonsinusoidal waveforms through Fourier analysis [6,8,10,11].

Experimental data are provided which illustrate the generally good agreement obtained between calculated and measured values of short-circuit inductance and resistance. The data also reveal some limitations of the simplified field analysis in the form of differences between the measured and predicted values. Possible explanations are offered for those differences in terms of various stray effects not included in the analysis.

This paper presents a practical method for calculating—prior to construction—the short-circuit impedances of a multiwinding transformer at any number of frequencies. With this capability, it is possible to gain a better understanding of the high-frequency operation of multiwinding transformers, and it becomes reasonable to consider using more complicated transformer circuit models which account for the variation with frequency of winding resistance and leakage inductance.

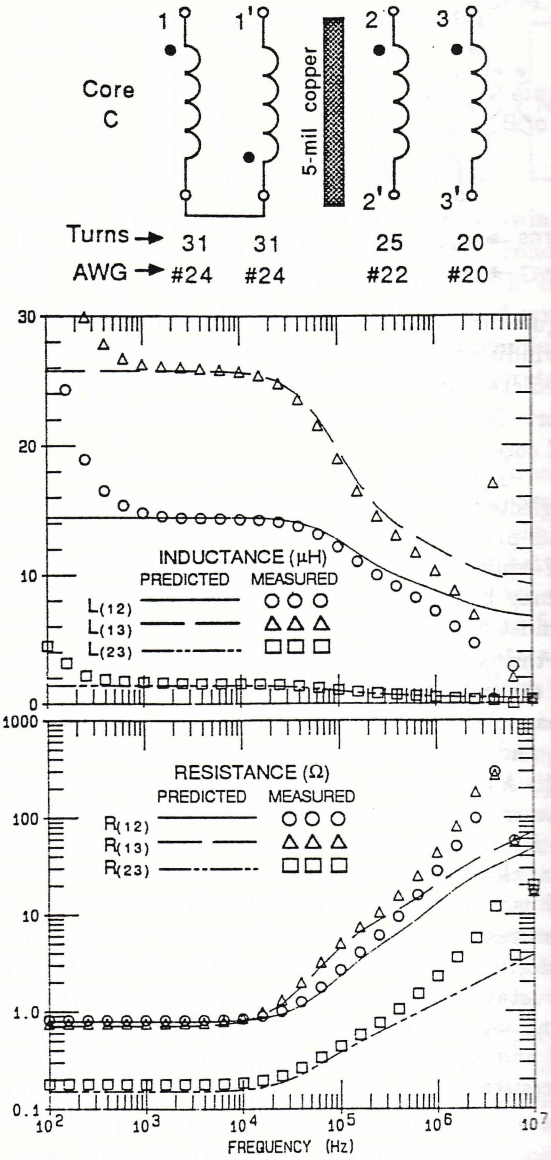


Figure 8: Winding diagram and short-circuit-test data for a 4-layer 3-winding transformer with a mix of wire sizes and an electrostatic shield.

References

[1] F. M. Starr, "Equivalent Circuits—I," *Transactions of the American Institute of Electrical Engineers*, Vol. 51, No. 2, June 1932, pp. 287–298.

[2] J. Rosa, "Calculation of Flux Linkages in Multiwinding Transformers," *IEEE Power Electronics Specialists Conference Record*, 86CH2310-1, 1986, pp. 639–644.

[3] A. M. Urling, V. A. Niemela, G. R. Skutt, and T. G. Wilson, "Characterizing High-Frequency Effects in Transformer Windings—A Guide to Several Significant Articles," *IEEE Applied Power Electronics Conference Record*, 89CH2719-3, 1989, pp. 373–385.

[4] P. L. Dowell, "Effects of Eddy Currents in Transformer Windings," *Proceedings of the IEE*, Vol. 113, No. 8, August 1966, pp. 1387–1394.

[5] G. R. Skutt, "Modeling Multiwinding Transformers for High-Frequency Applications," M.S. Thesis, Duke University, Durham, NC, April 24, 1988.

[6] J. P. Vandelac and P. Ziogas, "A Novel Approach for Minimizing High Frequency Transformer Copper Losses," *IEEE Power Electronics Specialists Conference Record*, 87CH2459-6, 1987, pp. 355–367.

[7] M. P. Perry, "Multiple Layer Series Connected Winding Design for Minimum Losses," *IEEE Transactions on Power Apparatus and Systems*, Vol. PAS-98, No. 1, Jan./Feb. 1979, pp. 116–123.

[8] S. D. Goad, "The Theory and Design of Switched-Mode Power Transformers for Minimum Conductor Loss," Ph.D. Dissertation, Virginia Polytechnic Institute and State University, Blacksburg, VA, December 1985.

[9] C. E. Hawkes, T. G. Wilson, and R. C. Wong, "Magnetic-Field-Intensity and Current-Density Distributions Within Transformer Windings," to be published in the *IEEE Power Electronics Specialists Conference Record*, 1989.

[10] P. S. Venkatraman, "Winding Eddy Current Losses

in Switch Mode Power Transformers Due to Rectangular Wave Currents," *Proceedings of Powercon 11*, Power Concepts Inc., Ventura, Ca., 1984, Section A-1, pp. 1–11.

[11] B. Carsten, "High Frequency Conductor Losses in Switchmode Magnetics," *High-Frequency Power Converter Conference Record*, May 1986, pp. 155–176.

Appendix: Derivation of Eq. (23)

To derive (23), (16) is first substituted into (20).

$$\langle w_m \rangle = \frac{\mu_0}{2} \underline{H}_z(\chi)\, \underline{H}_z^*(\chi) = \tag{40}$$

$$\frac{\mu_0}{2} \left\{ \frac{\underline{H}_z(\chi = h_{cu})}{\sinh \underline{k} h_{cu}} [\sinh \underline{k}\chi + (\alpha + j\beta)[\sinh \underline{k}(h_{cu} - \chi)] \right.$$

$$\left. \times \frac{\underline{H}_z^*(\chi = h_{cu})}{\sinh \underline{k}^* h_{cu}} [\sinh \underline{k}^*\chi + (\alpha - j\beta)[\sinh \underline{k}^*(h_{cu} - \chi)] \right\}$$

The multiplication is carried out, and the Ψ-variables defined in the following paragraphs are used to represent portions of the product.

$$\langle w_m \rangle = \frac{\mu_0}{2} \left[\frac{|\underline{H}_z(\chi = h_{cu})|^2}{\Psi_0} (\Psi_1 + \Psi_2 + \Psi_3 + \Psi_4) \right] \tag{41}$$

Equivalent expressions are derived below for each of the Ψ-variables by applying various hyperbolic and trigonometric identities.

Using (10) and the definition $\Delta = h_{cu}/\delta$,

$$\underline{k} h_{cu} = \frac{1}{\delta}(1 + j) h_{cu} = \Delta + j\Delta \tag{42}$$

To simplify expressions, a new variable $u = \chi/\delta$ is defined such that

$$\underline{k}\chi = \frac{1}{\delta}(1 + j)\chi = u + ju \tag{43}$$

Then

$$\begin{aligned} \Psi_0 &= \sinh \underline{k} h_{cu} \sinh \underline{k}^* h_{cu} \\ &= \tfrac{1}{2}\{\cosh[(\Delta + j\Delta) + (\Delta - j\Delta)] \\ &\quad - \cosh[(\Delta + j\Delta) - (\Delta - j\Delta)]\} \\ &= \tfrac{1}{2}(\cosh 2\Delta - \cos 2\Delta) \end{aligned} \tag{44}$$

$$\begin{aligned} \Psi_1 &= \sinh \underline{k}\chi \sinh \underline{k}^*\chi \\ &= \tfrac{1}{2}(\cosh 2u - \cos 2u) \end{aligned} \tag{45}$$

$$\begin{aligned} \Psi_2 &= (\alpha^2 + \beta^2)[\sinh \underline{k}(h_{cu} - \chi) \sinh \underline{k}^*(h_{cu} - \chi)] \\ &= \tfrac{1}{2}(\alpha^2 + \beta^2)[\cosh(2\Delta - 2u) - \cos(2\Delta - 2u)] \end{aligned} \tag{46}$$

The key to the expansion of Ψ_3 and Ψ_4 below is to recognize that the two terms in each expression are complex conjugates of each other.

$$\begin{aligned} \Psi_3 &= \alpha[\sinh \underline{k}(h_{cu} - \chi) \sinh \underline{k}^*\chi \\ &\quad + \sinh \underline{k}^*(h_{cu} - \chi) \sinh \underline{k}\chi] \\ &= 2\alpha \,\mathrm{Re}\{\sinh \underline{k}(h_{cu} - \chi) \sinh \underline{k}^*\chi\} \\ &= 2\alpha \,\mathrm{Re}\{\sinh[\Delta + j\Delta - (u + ju)] \sinh(u - ju)\} \\ &= 2\alpha \,\mathrm{Re}\{\tfrac{1}{2}\cosh[\Delta + j\Delta - (u + ju) + (u - ju)] \\ &\quad - \tfrac{1}{2}\cosh[\Delta + j\Delta - (u + ju) - (u - ju)]\} \\ &= \alpha \,\mathrm{Re}\{\cosh[\Delta + j(\Delta - 2u)] - \cosh[(\Delta - 2u) + j\Delta]\} \\ &= \alpha \,\mathrm{Re}\{\cosh\Delta\cos(\Delta - 2u) \\ &\quad + j\sinh\Delta\sin(\Delta - 2u) \\ &\quad - [\cosh(\Delta - 2u)\cos\Delta + j\sinh(\Delta - 2u)\sin\Delta]\} \end{aligned} \tag{47}$$

$$= \alpha[\cosh\Delta\cos(\Delta - 2u) - \cosh(\Delta - 2u)\cos\Delta] \tag{48}$$

A similar derivation applies to Ψ_4, except that the imaginary part of the expression in curly braces in (47) is used instead of the real part.

$$\begin{aligned} \Psi_4 &= j\beta[\sinh \underline{k}(h_{cu} - \chi) \sinh \underline{k}^*\chi \\ &\quad - \sinh \underline{k}^*(h_{cu} - \chi) \sinh \underline{k}\chi] \\ &= -2\beta \,\mathrm{Im}[\sinh \underline{k}(h_{cu} - \chi) \sinh \underline{k}^*\chi] \\ &= -\beta[\sinh\Delta\sin(\Delta - 2u) \\ &\quad - \sinh(\Delta - 2u)\sin\Delta] \end{aligned} \tag{49}$$

Finally, (22) defines the quantity $\langle Q_H \rangle$ as the integral of (41) with respect to χ between the limits $\chi = 0$ and $\chi = h_{cu}$. Using the equivalent expressions derived above for the Ψ-variables, and changing the integration variable to u,

$$\begin{aligned} \langle Q_H \rangle &= \int_0^{h_{cu}} \langle w_m \rangle \, d\chi = \int_0^{\Delta} \langle w_m \rangle \, \delta \, du \\ &= \frac{\mu_0 |\underline{H}_z(\chi = h_{cu})|^2}{(\cosh 2\Delta - \cos 2\Delta)} \left[\frac{\delta}{4}(\sinh 2\Delta - \sin 2\Delta) \right. \\ &\quad + \frac{\delta(\alpha^2 + \beta^2)}{4}(\sinh 2\Delta - \sin 2\Delta) \\ &\quad \left. - \frac{\delta}{4} 4\alpha(\sinh\Delta\cos\Delta - \cosh\Delta\sin\Delta) + 0 \right] \end{aligned} \tag{50}$$

where the result of integrating each term Ψ_1 through Ψ_4 is shown separately. Regrouping terms,

$$\begin{aligned} \langle Q_H \rangle &= \frac{\mu_0 \delta |\underline{H}_z(\chi = h_{cu})|^2}{4} \\ &\quad \times \left[(1 + \alpha^2 + \beta^2) \left(\frac{\sinh 2\Delta - \sin 2\Delta}{\cosh 2\Delta - \cos 2\Delta} \right) \right. \\ &\quad \left. - 4\alpha \left(\frac{\sinh\Delta\cos\Delta - \cosh\Delta\sin\Delta}{\cosh 2\Delta - \cos 2\Delta} \right) \right] \end{aligned} \tag{51}$$

which is essentially the same as (23).

This page has been left blank intentionally.

APPENDIX K

Magnetic-Field-Intensity and Current-Density Distributions in Transformer Windings

IEEE Power Electronics Specialists Conference

Record, 89CH2721-9, June 1989

This page has been left blank intentionally.

MAGNETIC-FIELD-INTENSITY AND CURRENT-DENSITY DISTRIBUTIONS IN TRANSFORMER WINDINGS

Charles E. Hawkes Thomas G. Wilson Ronald C. Wong

Department of Electrical Engineering
Duke University, Durham, NC 27706

Abstract

The well-established solutions for the approximate magnetic-field-intensity and current-density distributions within the windings of a transformer are extensively illustrated as phasors in a series of three-dimensional graphs. The results greatly enhance the understanding of eddy currents and their impact on the energy-storage and power-dissipation characteristics of transformer windings.

1 INTRODUCTION

As the switching frequencies of multiple-output dc-to-dc coverters continue to rise, it becomes increasingly important that the parasitic effects of various components are included as design parameters. In many cases, these "second order" effects can have a significant influence on the efficiency, stability, or regulation of a converter. Such is the case with eddy currents in the windings of a transformer. This phenomenon causes the fields and currents within a conductor to be concentrated in regions near the surface, resulting in an increase in copper loss and a decrease in leakage inductance.

The impact of eddy currents on the distribution of the magnetic field intensity and current density within the windings of a transformer has been discussed in the literature over the last two decades, and certain articles have been summarized in [1]. Consequently, it is now possible to calculate the ac resistance and the leakage inductance based upon transformer geometry [2]. However, the ability merely to *calculate* parametric values for such stray effects is not sufficient for the design engineer who must also make intelligent and effective design choices. Rather, it is important for the engineer to have some fundamental understanding of eddy currents.

Unfortunately, due to the complex nature of eddy currents, a thorough understanding normally requires a substantial investment of time in addition to a working knowledge of electromagnetic field theory. This paper provides a format in which the crucial elements of eddy currents are extensively illustrated. The goal is to make the basic properties of eddy currents understandable to the design engineer, without requiring a detailed knowledge of electromagnetic field theory.

After making a series of simplifying assumptions concerning the structure of a transformer winding, it is possible to apply Maxwell's equations and arrive at solutions for the magnetic field intensity and current density within the winding. These two quantities are the key elements in describing eddy currents, since they determine the energy-storage and power-dissipation characteristics of a transformer winding. Even though they are of primary importance, nevertheless, the magnetic-field-intensity and current-density distributions have received relatively little attention in terms of graphical illustrations. In fact, only one of the cited references provides plots of these solutions, namely, Reference 4 of [1].

This paper contributes to the existing literature by illustrating the phasor distributions of the magnetic field intensity and current density across the height of a winding in a series of isometric plots. In an extensive array of plots for both single-layer and multi-layer examples, this paper highlights some of the most important properties of eddy currents.

2 FIELD SOLUTIONS

The validity of the transformer model used in this paper and the domain of its application are established elsewhere in the literature, and are therefore not addressed here (see [2] and Reference 7 of [1]). The assumptions concerning transformer structure and their implications may be summarized as:

1. The windings are closely wrapped and fill most of the window breadth. *Implication:* a layer of discrete conductors may be modeled as a foil conductor.
2. The windings are enclosed by a pot core of infinite permeability. *Implication:* the foil windings may be modeled by infinite solenoids.

This work was supported in part by a research contract with Digital Equipment Corporation, Maynard, MA.

CH2721-9/89/0000-1021 $1.00 © 1989 IEEE

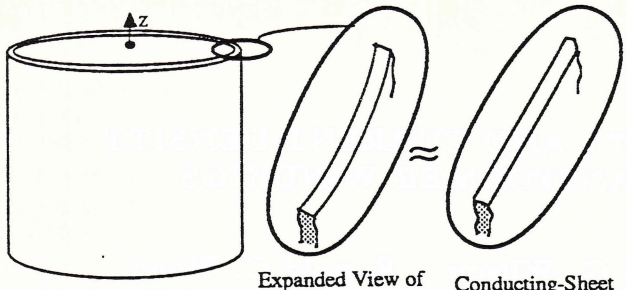


Figure 1: The approximation of a cylindrical winding by an infinite conducting sheet.

3. The diameter of each solenoid is large with respect to the conductor thickness. *Implication:* a small portion of each infinite solenoid may be treated as a portion of an infinite conducting sheet.

Figure 1 illustrates assumption 3, which reduces the field problem of an infinite solenoid to the simpler problem of an infinite conducting sheet. This conducting sheet, assumed to be made of copper, is shown in Fig. 2, together with a reference coordinate system.

The solutions for the magnetic-field-intensity and current-density distributions within an infinite conducting sheet may now be obtained through an application of Maxwell's equations. The derivation of these distributions has been well-documented (see References 1, 6 and 7 of [1]), and only the results are stated here. The three most significant assumptions used in the derivation are:

4. Sinusoidal steady-state current excitation.
5. The magnetic field intensity is directed along only the z-axis and the current density along only the y-axis.
6. Both the magnetic field intensity and the current density are functions of x only.

Because of these assumptions, we can write the magnetic field intensity and the current density as the phasors $\underline{H}_z(x)$ and $\underline{J}_y(x)$, respectively, where the underline signifies a complex number representing the phasor expression for a sinusoidal time function, the subscript indicates the axial direction of the field, and the symbol (x) indicates that the phasor quantity varies with position x across the height h_{cu} of the conducting (copper) sheet. The solutions for the magnetic field intensity and current density at any point x across the conducting sheet may be written as

$$\underline{H}_z(x) = \frac{1}{\sinh \underline{k} h_{cu}} \left[\underline{H}_z(h_{cu}) \sinh \underline{k} x + \underline{H}_z(0) \sinh \underline{k}(h_{cu} - x) \right] \quad (1)$$

and

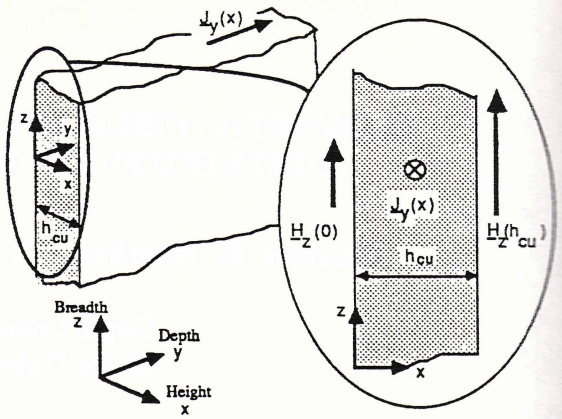


Figure 2: Model of infinite conducting sheet which is assumed to extend to infinity in both the y (*depth*) and the z (*breadth*) directions.

$$\underline{J}_y(x) = \frac{-\underline{k}}{\sinh \underline{k} h_{cu}} \left[\underline{H}_z(h_{cu}) \cosh \underline{k} x - \underline{H}_z(0) \cosh \underline{k}(h_{cu} - x) \right] \quad (2)$$

where $\underline{k}$ is the complex wave number, h_{cu} is the height of the copper sheet as shown in Fig. 2, and $\underline{H}_z(0)$ and $\underline{H}_z(h_{cu})$ are the phasors that represent the sinusoidally varying magnetic fields at the two surfaces of the sheet. The complex wave number $\underline{k}$ may by written as

$$\underline{k} = \sqrt{\frac{\omega \mu_o \sigma}{2}}(1 + j) = \frac{1}{\delta}(1 + j) \quad (3)$$

where $\delta = \sqrt{2/\omega \mu_0 \sigma}$ is defined as the *skin depth* for a conductor. Equation (1) is identical to an equation that appears in [2], and (2) is similar to equation (A-15) found in Reference 7 of [1]. Equations (1) and (2) are the solutions which we investigate in this paper. Note that for a multi-layer transformer winding structure, we model each layer with an infinite conducting sheet, so that the magnetic-field-intensity and current-density distributions for each layer can be calculated using (1) and (2). This enables us to explore the nature of the magnetic-field-intensity and current-density distributions for both single-layer and multi-layer example winding structures.

3 SINGLE-LAYER EXAMPLE

3.1 Plots of Phasor Magnitudes

The four curves plotted in Fig. 3 show the magnitude of the phasor in (1) at each of four excitation frequencies ranging from 1 kHz to 1 MHz. The data for these plots are generated from (1) for a particular example where $\underline{H}_z(0) = 1\angle 0°$, $\underline{H}_z(h_{cu}) = 2\angle 0°$, and $h_{cu} = 7 \times 10^{-4}$ m. The complex wave number $\underline{k}$ that appears in (1) is calculated using (3), where the permeability is taken as its free space value of $4\pi \times 10^{-7}$ H/m. Note that because of the modeling process of

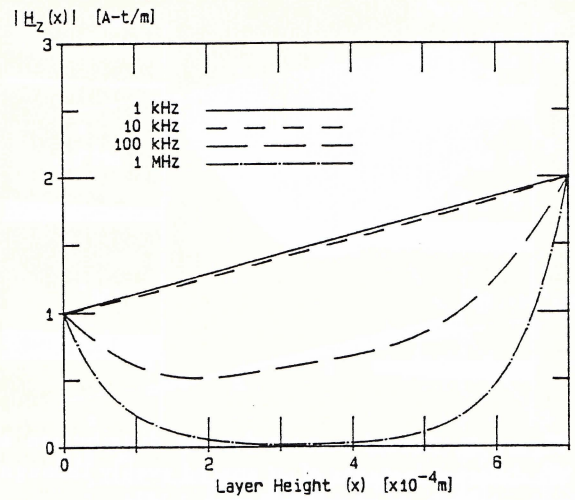


Figure 3: Magnitude of magnetic-field-intensity phasor $\underline{H}_z(x)$ in an infinite conducting sheet at 1 kHz, 10kHz, 100 kHz, and 1 MHz, with $\underline{H}_z(0) = 1\angle 0°$ and $\underline{H}_z(h_{cu}) = 2\angle 0°$.

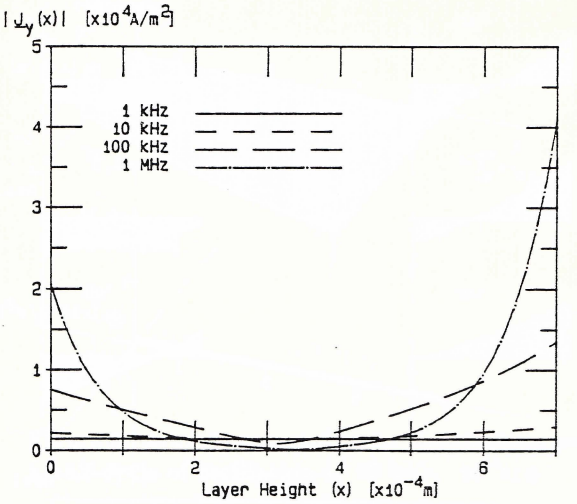


Figure 4: Magnitude of current-density phasor $\underline{J}_y(x)$ in an infinite conducting sheet at excitation frequencies of 1 kHz, 10kHz, 100 kHz, and 1 MHz, with $\underline{H}_z(0) = 1\angle 0°$ and $\underline{H}_z(h_{cu}) = 2\angle 0°$.

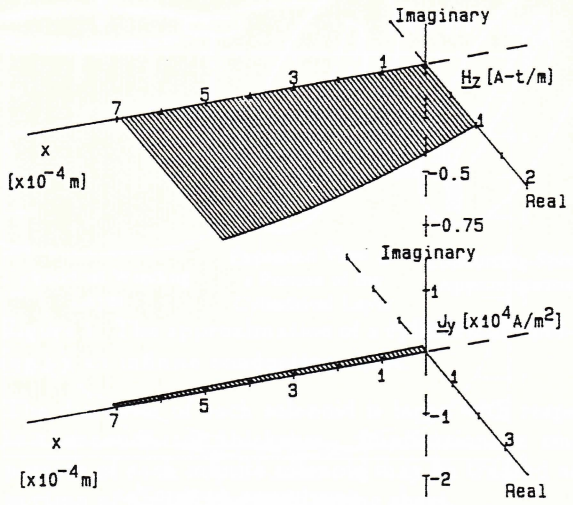
assumption 1 in Section 2, the *effective* conductivity of the conducting sheet would generally be lower than the actual value for copper [2]. Since this correction does not significantly influence the shape of the $\underline{H}_z(x)$ and $\underline{J}_y(x)$ distributions, however, we assume throughout this paper that the conductivity of the conducting sheet is the same as that of copper, which has a value of 5.315×10^7 S/m at 60°C. Figure 4 shows the corresponding variation in the magnitude of the phasor current density at each of the four same frequencies. The data for the plots of Fig. 4 are generated from (2) using the same example values as in Fig. 3.

The plots in Figs. 3 and 4 reveal the dramatic impact that excitation frequency can have on the distributions of the magnetic field intensity and the current density. At 1 kHz, the magnitude of the magnetic field intensity varies approximately linearly from one layer surface to the other, and the magnitude of the current density is approximately constant at a value of 1.43 kA/m^2 over the 0.7 mm height of the winding. At higher frequencies, the magnitude of the magnetic field intensity decreases substantially away from the layer boundaries, but remains constant over frequency at the two surfaces of the layer—as it must since the boundary conditions of the problem do not change with frequency. Furthermore, the magnitude of the current density increases near the surfaces of the winding layer and drops to approximately zero in the interior regions.

3.2 Plots of Phasors

In interpreting Figs. 3 and 4, we must be careful to remember that they are only *magnitude* plots, and therefore do not contain any information on the phase angles that are associated with $\underline{H}_z(x)$ and $\underline{J}_y(x)$. Although the magnitudes of the magnetic-field-intensity and current-density phasors are sufficient to determine the energy-storage and power-dissipation characteristics of transformer windings, we can gain additional insight by including the phase information as well. One way to incorporate this information is to accompany each of the magnitude plots with a corresponding phase plot, or similarly, with plots of the corresponding real and imaginary parts of the phasors. Magnitude plots such as those in Figs. 3 and 4, together with plots of the corresponding real and imaginary parts of the phasors are found in Reference 4 of [1]. Although this approach does illustrate all of the information contained in the phasors of (1) and (2), it is generally quite difficult to gain physical insight into these solutions when the magnitude and phase information appears in two or more separate plots. To remedy this, we show the phasors of (1) and (2) at equally spaced intervals across the layer. Such a representation, however, needs to be three-dimensional, since each phasor has two components (real and imaginary) and the position of each phasor across the layer height requires a third dimension. This information can be represented in a three-dimensional, isometric drawing.

For the same numerical example that is illustrated in Figs. 3 and 4, Fig. 5 contains plots of the magnetic-field-intensity and current-density phasors, together with a table of selected data points. The upper set of three-dimensional axes in Fig. 5 shows the variation of the magnetic-field-intensity phasors across the height of the layer calculated using (1). The coordinate system represented by this set of axes is different from the one introduced in Fig. 2 in that the Re-axis and Im-axis in Fig. 5 define, respectively, the real and imaginary parts of some phasor quantity, whereas the y-axis and z-axis in Fig. 2 define, respectively, the geometrical dimensions of layer depth and layer breadth.



x	$\underline{H}_z(x)$	$\underline{J}_y(x)$
$\times 10^{-4}$m	A − t/m	$\times 10^4$A/m^2
0	1.00 ∠0.00°	0.144∠172.18°
1	1.14 ∠−0.87°	0.143∠173.96°
2	1.29 ∠−1.34°	0.143∠175.99°
3	1.43 ∠−1.49°	0.143∠178.28°
4	1.57 ∠−1.40°	0.143∠180.80°
5	1.71 ∠−1.10°	0.143∠183.55°
6	1.86 ∠−0.63°	0.144∠186.53°
7	2.00 ∠0.00°	0.145∠189.70°

Figure 5: Magnetic-field-intensity phasor $\underline{H}_z(x)$ and current-density phasor $\underline{J}_y(x)$ at an excitation frequency of 1 kHz.

However, the x-axis of Fig. 5 *does* correspond to the x-axis of Figure 2 in that they both define the geometrical dimension of layer height. The real part of $\underline{H}_z(x)$ is plotted on the horizontal Re-axis, the imaginary part is plotted on the vertical Im-axis, and the distance through the layer is plotted on the horizontal x-axis that is coming out of the page to the left. Note that the positive half of each axis is drawn with a solid line, while the negative half is drawn with a dashed line. The magnetic-field-intensity phasors are drawn parallel to the Re versus Im-plane at evenly spaced points across the layer (x-axis). Each phasor has its tail on the x-axis, and its head at a point corresponding to the real and imaginary parts. Thus, a phasor with zero phase angle (no imaginary part) would be shown parallel to the positive Re-axis, and a phasor with a 90° phase angle would be shown parallel to the positive Im-axis. The arrow head usually drawn at the head of a phasor is omitted here to avoid unnecessary cluttering of subsequent drawings. Instead, the heads of the phasors are all connected with a single, solid line to enhance the appearance of a surface.

The plot and associated tabular values of $\underline{H}_z(x)$ in Fig. 5 reveal that the magnitude of the magnetic field at 1 kHz varies relatively linearly across the layer. Also, since none of the phasors differ by more than

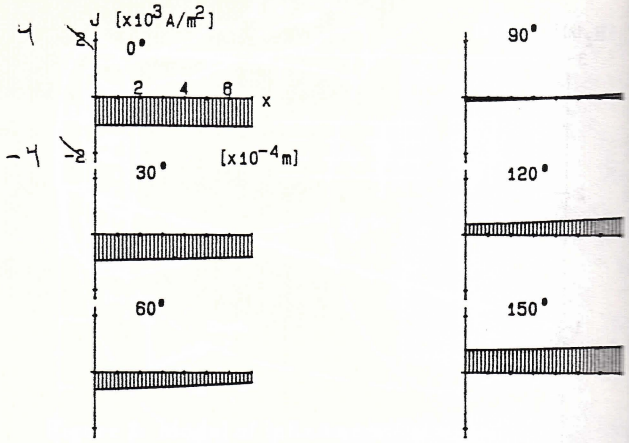
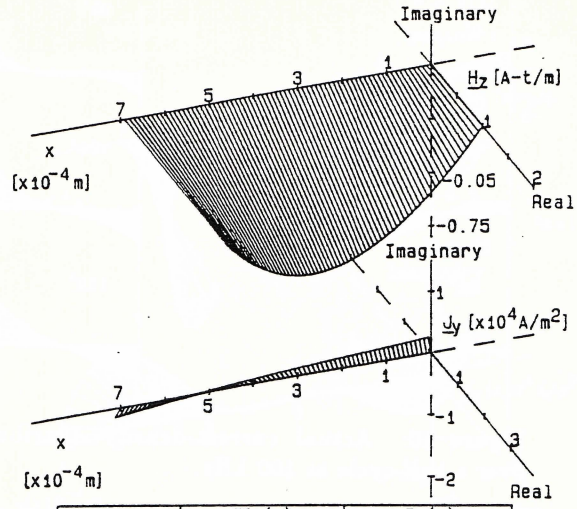


Figure 6: Actual current-density distribution at six different instants of ωt spaced evenly throughout a half-cycle of oscillation at 1 kHz.

2° from being parallel to the real axis, the magnetic field at every point across the layer must be oscillating very nearly in phase with the magnetic field at the surfaces. This simple, approximately linear distribution of magnetic-field-intensity phasors is similar to the result that is obtained by a direct application of Ampere's law to a conducting sheet that is carrying a uniform dc current. The low-frequency case of Fig. 5 is, of course, different from the dc-case since the actual magnetic-field-intensity distribution that is represented by Fig. 5 is varying sinusoidally in time at every point across the height of the layer.

The current-density phasors associated with these magnetic-field-intensity phasors have been calculated using (2) and the results are plotted on the lower set of axes in Fig. 5. Note that on this plot the scaling on the real and imaginary axes has been changed from the upper plot to accommodate the current-density phasors, while the scaling on the x-axis is the same as that on the upper set of axes. The plot of the current-density phasors and the table of values in Fig. 5 reveal that the magnitude of $\underline{J}_y(x)$ remains essentially constant across the layer while the phase angle varies by less than ±10°. Therefore, we conclude that the actual current density is almost uniform across the layer and varies sinusoidally with time.

We can obtain additional insight into how the current density across the height of the layer varies with time if we imagine all of the phasors on the lower set of axes in Fig. 5 to be rotating at an angular frequency $2\pi f$ in a counterclockwise direction around the x-axis. Thus, the actual time-varying distribution of the current density would be proportional to the projections of the phasors onto the plane of x versus Real. If the phasor magnitude is taken as the rms value of the actual sinusoid, the proportionality constant is $\sqrt{2}$. Figure 6, which is a companion piece to Fig. 5, shows the actual distribution of current density across the winding



x	$\underline{H}_z(x)$	$\underline{J}_y(x)$
$\times 10^{-4}$m	A − t/m	$\times 10^4$A/m^2
0	1.00 ∠0.00°	0.217∠119.70°
1	1.12 ∠−8.55°	0.182∠127.62°
2	1.26∠−13.19°	0.154∠141.74°
3	1.40∠−14.74°	0.141∠162.94°
4	1.54∠−13.82°	0.151∠186.99°
5	1.68∠−10.86°	0.185∠207.14°
6	1.83 ∠−6.16°	0.236∠221.84°
7	2.00 ∠0.00°	0.298∠232.84°

Figure 7: $\underline{H}_z(x)$ and $\underline{J}_y(x)$ at 10 kHz.

layer for an excitation frequency of 1 kHz at various points in time throughout one half-cycle. Each small plot is labeled with an angle measure, corresponding to the angular measure of time ωt. The plots divide a half-cycle of oscillation into six equal intervals, and they are ordered in time from top to bottom down the left column, and then down the right. Note that the six current-density distributions evenly spaced for ωt between 180° and 360°, which would complete the sequence of one time cycle for Fig 6, are simply mirror images about the x versus Im plane of the six distributions shown in Fig 6. From Fig. 6, we can see that the current density appears nearly uniform across the layer at every instant of time throughout a single cycle. At $\omega t = 90°$, the slight lack of uniformity manifests itself as a small negative current on the $x = 0$ side of the layer and a small positive current on the $x = h_{cu}$ side of the layer. These oppositely flowing currents have, however, an instantaneous value of zero when averaged over the height of the layer. Since we take the real, or cosinusoidal part of the phasor $\underline{J}_y(x)$ to be proportional to the actual, time-varying current density, we would expect that for a perfectly uniformly distributed current density there would be zero current at all points across the winding layer at times corresponding to $\omega t = 90°$ and $\omega t = 270°$. We conclude from Figs. 5 and 6 that skin effect does not have a significant influence on the distributions of magnetic field

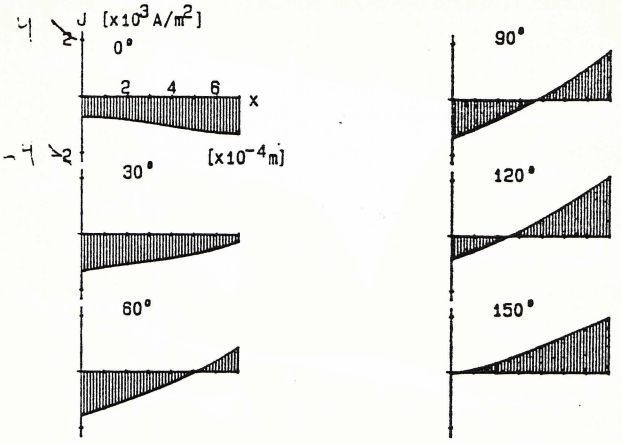
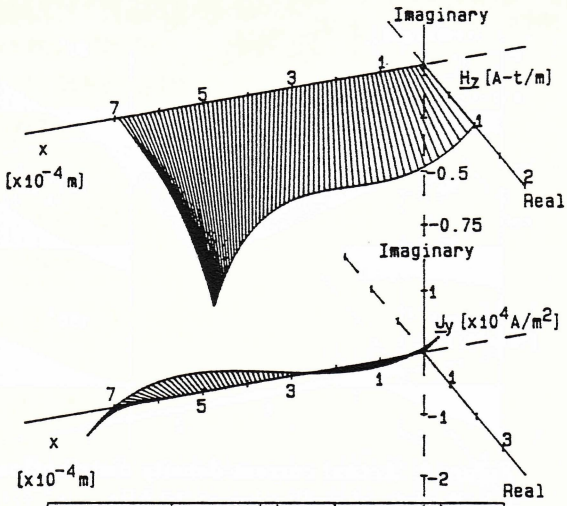


Figure 8: Actual current-density distribution over a half-cycle of oscillation at 10 kHz.

intensity and current density when the excitation frequency is low or, more precisely, when the skin depth is large with respect to the layer height.

Figure 7 contains plots of $\underline{H}_z(x)$ and $\underline{J}_y(x)$ for an excitation frequency of 10 kHz and Fig. 8 shows the corresponding time variation of the actual current density. The boundary conditions and layer height are the same as those used in Fig. 5. Throughout this section, we continue to use the example that is introduced in Section 3.1 and only the frequency is varied. The plot of the $\underline{H}_z(x)$ phasors and the table of values in Fig. 7 show that the magnitudes of the phasors no longer vary linearly across the layer, and that the phasors near the center of the layer are lagging by almost 15° behind those which have been established at the surfaces. Likewise, the current-density phasors plotted on the lower set of axes in Fig. 7 are also beginning to show the influence of skin effect. With respect to the 1 kHz example, there is now a noticeable increase in the magnitude of the current-density phasors near the surfaces of the layer, while the magnitude near the center has decreased slightly. More importantly, this plot reveals that there is now a substantial phase difference of 113° between the current-density phasors at $x = 0$ and those at $x = h_{cu}$. It appears as though the small ribbon of current density that is seen in the lower set of axes in Fig. 5 has been twisted and widened at the ends to give us the distribution of Fig. 7. As a result of this phase difference, there is now an appreciable portion of a cycle during which the actual current flows in opposite directions on the two surfaces of the conducting sheet. This can be seen more clearly in Fig. 8. This figure reveals, for example, that during the interval $60° \leq \omega t \leq 150°$ the current near the surface at $x = 0$ is flowing in the $-y$-direction, while the current near the surface at $x = h_{cu}$ is flowing in the $+y$-direction.

The $\underline{H}_z(x)$ and $\underline{J}_y(x)$ phasors for the case of 100-kHz excitation frequency are plotted in Fig. 9, and the corresponding variation of actual current density is plotted in Fig. 10. Corresponding plots of $\underline{H}_z(x)$



x	$\underline{H}_z(x)$	$\underline{J}_y(x)$
$\times 10^{-4}$m	A − t/m	$\times 10^4$A/m^2
0	1.00 ∠0.00°	0.755 ∠44.46°
1	0.61∠−35.90°	0.503 ∠25.76°
2	0.52∠−75.93°	0.286 ∠19.57°
3	0.59∠−93.22°	0.094 ∠63.88°
4	0.68∠−85.37°	0.240∠158.21°
5	0.85∠−59.89°	0.521∠180.11°
6	1.25∠−28.72°	0.868∠200.89°
7	2.00 ∠0.00°	1.352∠224.83°

Figure 9: $\underline{H}_z(x)$ and $\underline{J}_y(x)$ at 100 kHz.

and $\underline{J}_y(x)$ are shown for 1 MHz in Figs. 11 and 12. Due to the increase in peak current density, each of the two high-frequency plots of the actual current density in Figs. 10 and Fig. 12 is drawn to a different scale from the two low-frequency cases of Figs. 6 and 8. The variation of the magnetic-field-intensity phasors on the upper set of axes in Fig. 9 reveals the substantial impact of skin effect on this example layer at 100 kHz. The phasors near the center of the layer are now lagging in phase by more than 90° with respect to the phasors at the surfaces. There is also an attenuation in the magnitude of the $\underline{H}_z(x)$ phasors away from the surfaces of about 40% with respect to the two lower frequency cases. Based upon electromagnetic wave theory, we know that this attenuation in the magnetic field is a result of energy being transferred (via the electric field) into the medium in the form of increased current density. Accordingly, we see that the current-density phasors of Fig. 9 are, in fact, substantially larger in magnitude near the surfaces of the layer, more than 5 times that for 1 kHz at $x = 0$ and more than 9 times at $x = h_{cu}$. Moreover, since the phase angles of the current-density phasors at $x = 0$ and at $x = h_{cu}$ differ by 180°, Fig. 9 suggests that at every instant of time throughout a cycle the actual current will be flowing in opposite directions at $x = 0$ and at $x = h_{cu}$. This fact is evident from Fig. 10, which shows the time variation of the actual current-density distribution at 100 kHz.

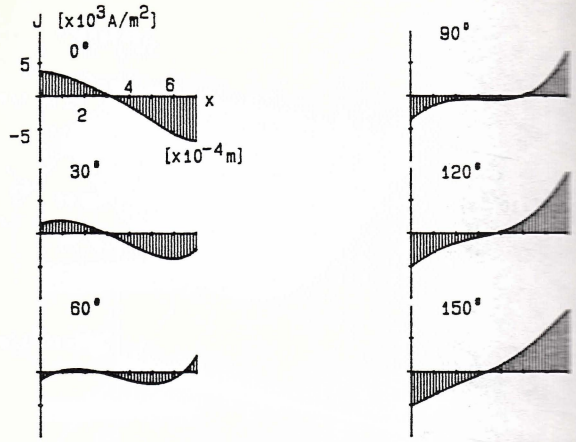
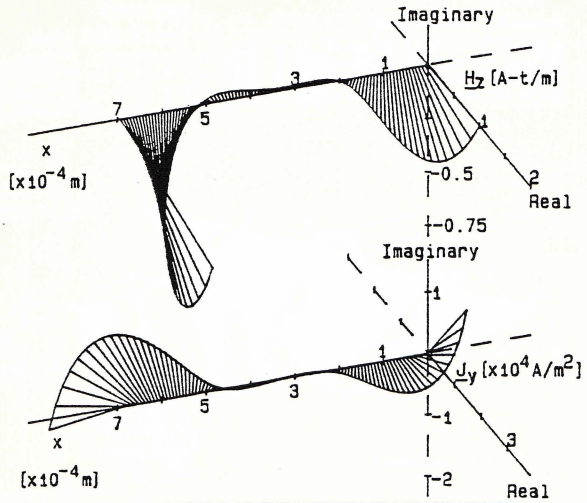


Figure 10: Actual current-density distribution over a half-cycle at 100 kHz.

Also, at $\omega t = 60°$ there are three reversals of current direction across the height of the layer.

Figure 11 shows the distribution of $\underline{H}_z(x)$ and $\underline{J}_y(x)$ at a 1-MHz excitation frequency, and Fig. 12 shows the corresponding time variation of the actual current-density distribution at this frequency. On the upper set of axes in Fig. 11, we see that the magnitude of the magnetic field intensity $|\underline{H}_z(x)|$ drops off rapidly away from the surfaces of the layer, and the phase angle of $\underline{H}_z(x)$ near the center of the layer is now lagging as much as 270° behind the phase angle of $\underline{H}_z(x)$ at the surfaces. Once again, this sharp attenuation of the magnetic field intensity is associated with an increase in surface current density. The plot of $\underline{J}_y(x)$ in Fig. 11 shows that the magnitude of the current-density phasors has now dramatically increased near the surfaces by more than 14 times the 1 kHz value at $x = 0$ and more than 28 times at $x = h_{cu}$. Near the center of the layer, the magnitude of the current-density phasors has attenuated substantially to as low as 20% of the 1 kHz value.

Figure 12 reveals the complicated manner in which the actual current-density distribution at 1 MHz evolves in time. Note that the actual current-density distribution at each point in time is nearly odd symmetric about the center of the layer and the imbalance in the symmetry corresponds to the net instantaneous current flowing in the layer. It is important to realize that, although the shapes of the J versus x plots in Figs. 6, 8, 10 and 12 are dramatically different, the net current, obtained by integrating the area under each curve, is identical for each frequency at corresponding instants of time. This fact is not at all evident from the plots of the magnitude of $\underline{J}_y(x)$ in Fig. 4. It is also interesting to observe in Fig. 12 that at any instant in time, as we move across the winding layer from $x = 0$ to $x = h_{cu}$, we see that the current flow undergoes several changes in direction. This dispels the notion that skin-effect currents are simply surface currents that travel in one direction on one side of the winding layer and



x	$\underline{H}_z(x)$	$\underline{J}_y(x)$
$\times 10^{-4}$m	A − t/m	$\times 10^4$A/m^2
0	1.00 ∠0.00°	2.049 ∠44.99°
1	0.24 ∠−83.07°	0.481 ∠−37.93°
2	0.05 ∠−164.59°	0.114 ∠−122.37°
3	0.01 ∠−272.79°	0.028 ∠−177.67°
4	0.03 ∠−255.54°	0.053 ∠−17.24°
5	0.11 ∠−165.64°	0.227 ∠58.66°
6	0.47 ∠−83.01°	0.962 ∠142.02°
7	2.00 ∠0.00°	4.097 ∠225.00°

Figure 11: $\underline{H}_z(x)$ and $\underline{J}_y(x)$ at 1 MHz.

in the opposite direction on the other side of the winding layer. At $\omega t = 60°$, for example, a current at each surface is flowing in one direction while just below this there is an even wider region with a current of larger instantaneous value flowing in the opposite direction.

4 FOUR-LAYER EXAMPLES

4.1 Plots of Phasor Magnitudes

Figure 13 shows the cross-section of a four-layer infinite solenoid and its associated low-frequency magnetic-field-intensity diagram. Currents have been established in this solenoid so that each of the inner three layers carries a net current whose magnitude is 1 unit, while the outermost layer caries a net current whose magnitude is 3 units. This condition closely models that of an ideal, four-layer transformer, in which the inner three layers comprise one winding and the outermost layer comprises a second winding. Each layer in this structure has a height h_{cu} of 0.7 mm, the same as that of the individual layer of Figs. 3 and 4, and each layer is separated by an air gap of 0.2 mm. The magnetic-field-intensity boundary conditions corresponding to the low-frequency magnetic-field-intensity diagram of Fig. 13 are given for the four layers by $\underline{H}_z(0) = 0\angle 0°$, $\underline{H}_z(0.7\text{ mm}) = \underline{H}_z(0.9\text{ mm}) = 1\angle 0°$, $\underline{H}_z(1.6\text{ mm}) = \underline{H}_z(1.8\text{ mm}) = 2\angle 0°$, $\underline{H}_z(2.5\text{ mm}) = \underline{H}_z(2.7\text{ mm}) = 3\angle 0°$, and $\underline{H}_z(3.6\text{ mm}) = 0\angle 0°$. Note that although

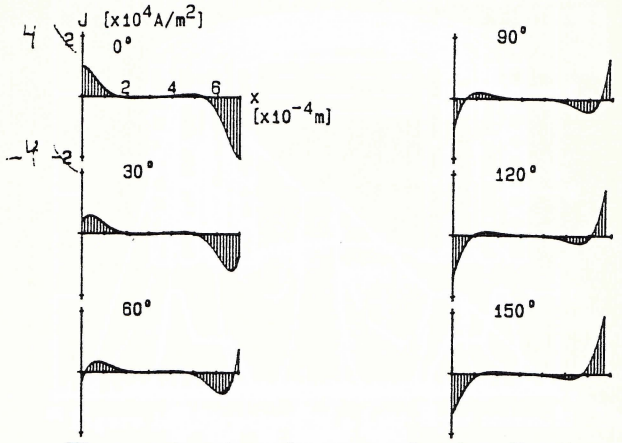


Figure 12: Actual current-density distribution over a half-cycle at 1 MHz.

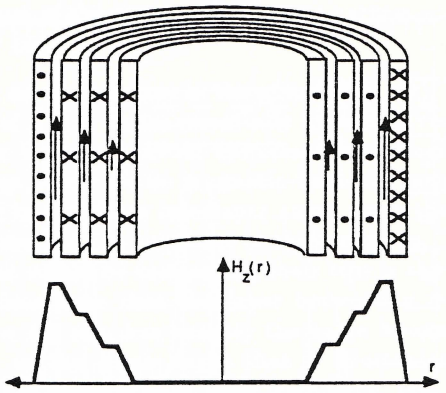


Figure 13: Structure of a four-layer solenoid. The three inner layers are all of one winding and the outer layer is of a second winding. The outer layer carries a current equal to the sum of the currents in the other layers.

the low-frequency magnetic-field-intensity diagram can be more completely represented in phasor form, the diagram of Fig. 13 is applicable to the examples in this paper since all magnetic-field-intensity boundary conditions are chosen to be in phase (see [2] and Reference 6 of [1]). It is important to realize that the four-layer infinite solenoid of Fig. 13 is not a transformer *per se*, since there is no magnetic core, and therefore places no constraints whatever on the magnetic fields in the air spaces. Thus, we *intentionally* choose the values of the magnetic fields in the air spaces so that the total number of ampere-turns across the four layers is zero.

Figures 14 and 15 show plots of the magnitude of the magnetic-field-intensity and current-density distributions, respectively, across all layers of this four-layer solenoid, at the same four excitation frequencies. The solid-line in each figure shows the distribution for the lowest-frequency of excitation. In Fig. 14, this solid line corresponds closely to the low-frequency magnetic-

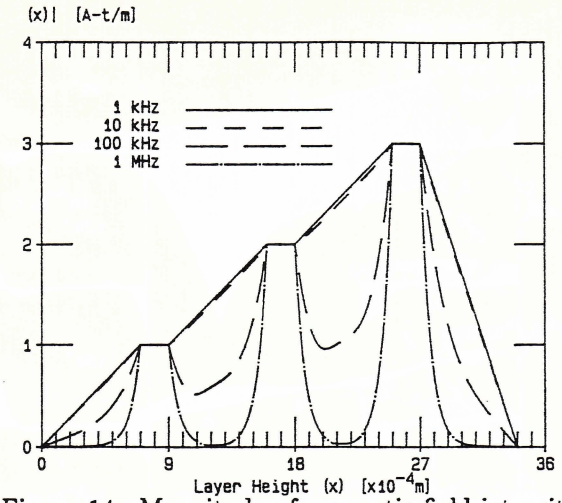


Figure 14: Magnitude of magnetic-field-intensity phasor distribution for solenoid of Fig. 13.

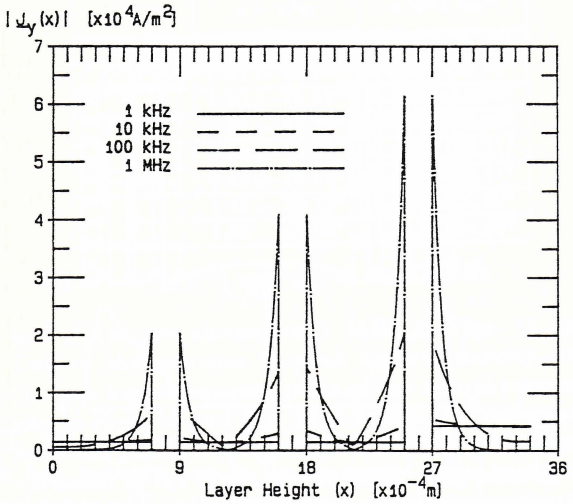
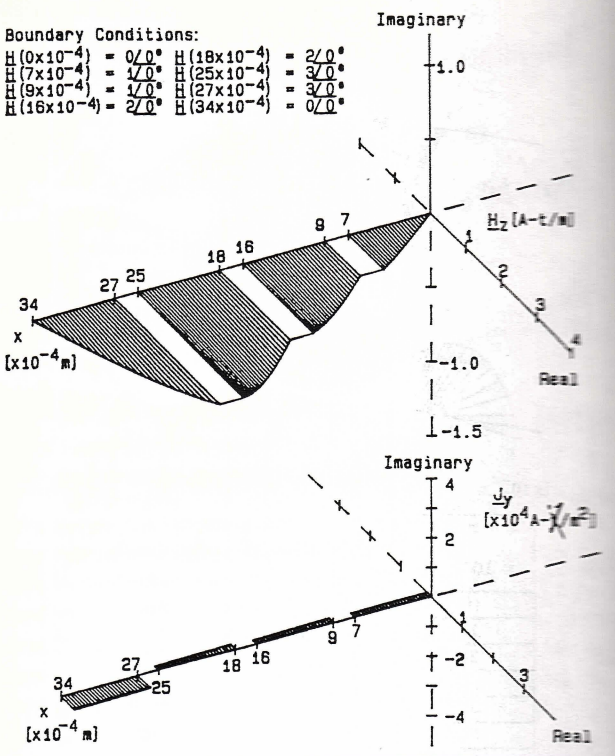


Figure 15: Magnitude of current-density phasor distribution for solenoid of Fig. 13.

field-intensity diagram of Fig. 13, while the solid line of Fig. 15 suggests that the current is almost uniformly distributed across the height of each layer. At higher frequencies, however, the magnitude of the magnetic field intensity and current density both decrease sharply near the center of each layer. Near the surfaces of each layer, the magnitude of the current density increases dramatically, while the magnitude of the magnetic field intensity, which we assume to be a sinusoid of constant magnitude and phase, remains constant.

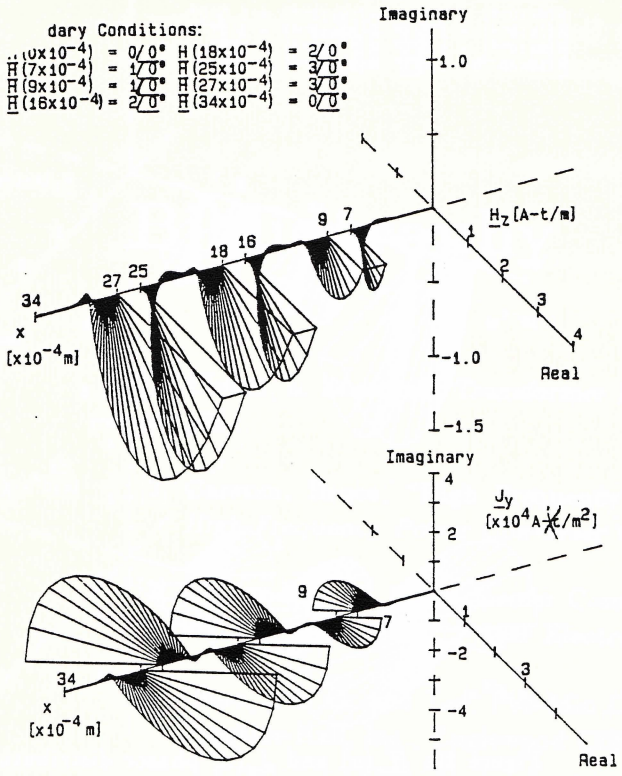
4.2 Plots of Phasors

Figure 16 shows the variation of the $\underline{H}_z(x)$ and the $\underline{J}_y(x)$ phasors across four layers at an excitation frequency of 1 kHz, together with an illustrative table of selected data points. The magnetic-field-intensity phasor distribution is plotted on the upper set of axes in Figure 16, while the current-density phasor distribution is plotted on the lower set of axes. The upper plot and the data table in Fig. 16 reveal that, although there



x m	$\lvert\underline{H}_z(x)\rvert$ A-t/m	$\angle\underline{H}_z(x)$ Degrees	$\lvert\underline{J}_y(x)\rvert$ A/m^2	$\angle\underline{J}_y(x)$ Degrees
0.000E+00	0.000E+00	0.00	1.428E+03	178.04
1.000E−04	1.428E−01	−1.92	1.428E+03	178.16
2.000E−04	2.856E−01	−1.80	1.428E+03	178.52
3.000E−04	4.284E−01	−1.60	1.428E+03	179.12
4.000E−04	5.713E−01	−1.32	1.428E+03	179.96
5.000E−04	7.141E−01	−0.96	1.429E+03	181.04
6.000E−04	8.570E−01	−0.52	1.430E+03	182.36
7.000E−04	1.000E+00	−0.00	1.433E+03	183.92
8.000E−04	1.000E+00	−0.00	0.000E+00	0.00
9.000E−04	1.000E+00	−0.00	1.438E+03	172.18
1.000E−03	1.142E+00	−0.87	1.433E+03	173.96
1.100E−03	1.285E+00	−1.34	1.429E+03	175.99
1.200E−03	1.428E+00	−1.49	1.428E+03	178.28
1.300E−03	1.571E+00	−1.40	1.429E+03	180.80
1.400E−03	1.713E+00	−1.10	1.433E+03	183.55
1.500E−03	1.856E+00	−0.63	1.441E+03	186.53
1.600E−03	2.000E+00	−0.00	1.453E+03	189.70
1.700E−03	2.000E+00	−0.00	0.000E+00	0.00
1.800E−03	2.000E+00	−0.00	1.463E+03	166.46
1.900E−03	2.142E+00	−0.80	1.445E+03	169.81
2.000E−03	2.285E+00	−1.28	1.434E+03	173.48
2.100E−03	2.428E+00	−1.47	1.428E+03	177.44
2.200E−03	2.570E+00	−1.42	1.430E+03	181.64
2.300E−03	2.713E+00	−1.14	1.440E+03	186.05
2.400E−03	2.856E+00	−0.66	1.459E+03	190.61
2.500E−03	3.000E+00	0.00	1.487E+03	195.26
2.600E−03	3.000E+00	−0.00	0.000E+00	0.00
2.700E−03	3.000E+00	−0.00	4.299E+03	3.92
2.800E−03	2.571E+00	−0.52	4.292E+03	2.36
2.900E−03	2.142E+00	−0.96	4.288E+03	1.04
3.000E−03	1.713E+00	−1.32	4.286E+03	−0.04
3.100E−03	1.285E+00	−1.60	4.285E+03	−0.88
3.200E−03	8.569E−01	−1.80	4.284E+03	−1.48
3.300E−03	4.284E−01	−1.92	4.284E+03	−1.84
3.400E−03	0.000E−00	−1.94	4.284E+03	−1.96

Figure 16: Magnetic-field-intensity and current-density phasor distributions across the four-layer solenoid of Fig. 13 at 1 kHz.



x m	$\lvert\underline{H}_z(x)\rvert$ A-t/m	$\angle\underline{H}_z(x)$ Degrees	$\lvert\underline{J}_y(x)\rvert$ A/m^2	$\angle\underline{J}_y(x)$ Degrees
0.000E+00	0.000E+00	0.00	1.617E+00	4.03
1.000E−04	1.770E−04	−137.25	3.258E+00	86.22
2.000E−04	7.134E−04	−55.06	1.469E+01	170.10
3.000E−04	3.045E−03	28.02	6.237E+01	253.01
4.000E−04	1.296E−02	111.01	2.655E+02	336.01
5.000E−04	5.518E−02	194.01	1.130E+03	419.01
6.000E−04	2.349E−01	277.00	4.812E+03	502.00
7.000E−04	1.000E+00	360.00	2.048E+04	585.00
8.000E−04	1.000E+00	−0.00	0.000E+00	0.00
9.000E−04	1.000E+00	−0.00	2.048E+04	44.99
1.000E−03	2.351E−01	−83.07	4.808E+03	−37.93
1.100E−03	5.469E−02	−164.59	1.141E+03	−122.37
1.200E−03	1.498E−02	−272.79	2.793E+02	−177.67
1.300E−03	2.647E−02	−255.54	5.271E+02	−17.24
1.400E−03	1.101E−01	−165.64	2.266E+03	58.66
1.500E−03	4.699E−01	−83.01	9.622E+03	142.02
1.600E−03	2.000E+00	−0.00	4.097E+04	225.00
1.700E−03	2.000E+00	−0.00	0.000E+00	0.00
1.800E−03	2.000E+00	−0.00	4.097E+04	45.00
1.900E−03	4.701E−01	−83.05	9.619E+03	−37.95
2.000E−03	1.096E−01	−164.95	2.277E+03	−122.03
2.100E−03	2.852E−02	−267.53	5.411E+02	−183.91
2.200E−03	4.009E−02	−257.66	7.912E+02	−14.98
2.300E−03	1.650E−01	−165.53	3.402E+03	58.55
2.400E−03	7.049E−01	−83.02	1.443E+04	142.03
2.500E−03	3.000E+00	0.00	6.145E+04	225.00
2.600E−03	3.000E+00	−0.00	0.000E+00	0.00
2.700E−03	3.000E+00	−0.00	6.145E+04	45.00
2.800E−03	7.047E−01	−83.00	1.443E+04	−38.00
2.900E−03	1.655E−01	−165.99	3.391E+03	−120.99
3.000E−03	3.888E−02	−248.99	7.966E+02	−203.99
3.100E−03	9.136E−03	−331.98	1.871E+02	−286.99
3.200E−03	2.140E−03	−415.06	4.408E+01	−369.90
3.300E−03	5.311E−04	−497.25	9.775E+00	−453.78
3.400E−03	0.000E−00	0.00	4.852E+00	−535.97

Figure 17: Magnetic-field-intensity and current-density phasor distributions across the four-layer solenoid of Fig. 13 at 1 MHz.

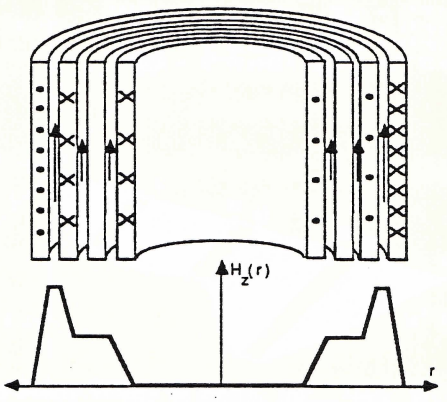


Figure 18: Structure of a four-layer solenoid. Two of the three inner layers are a part of the same winding while the other inner layer is left open circuited. The outer layer carries a current equal to the sum of the currents in the two current-carrying inner layers.

is some small variation in the phase of $\underline{H}_z(x)$, the magnitude of $\underline{H}_z(x)$ varies essentially linearly across each of the four layers. To avoid unnecessary cluttering of the drawings, there are no magnetic-field-intensity phasors plotted in the three interlayer gaps, since the phasors are assumed to be constant in these regions. The solid line that would be connecting their tips is shown, however. Also note that the layer between $x = 0.9$ mm and $x = 1.6$ mm has exactly the same boundary conditions as the single layer that is illustrated in Section 3.2. Therefore, at each frequency, the layer between $x = 0.9$ mm and $x = 1.6$ mm exhibits the exact same $\underline{H}_z(x)$ and $\underline{J}_y(x)$ distributions as is seen for the single-layer example of Section 3.2.

The plot of the current-density phasors on the lower set of axes and the values in the data table of Fig. 16 suggest that at 1 kHz the current in each of the four layers is almost uniformly distributed, since the magnitude and phase of $\underline{J}_y(x)$ across each layer is approximately constant. Also, we see from Fig. 16 that the current density in the outer layer is three times greater in magnitude, and 180° out of phase with respect to the current density in each of the three inner layers. Therefore, if we consider each of our layers to consist of a single turn of conductor, then the instantaneous sum of the ampere-turns across the four layers is, in fact, zero.

Figure 17 shows the magnetic-field-intensity and current-density phasor distributions at an excitation frequency of 1 MHz, together with a table of corresponding data points. Although the distributions for the 10 kHz and 100 kHz cases are not shown here, the changes in the phasor distributions across each of the four layers as frequency increases are similar to those of the single layer example discussed above in Section 3.2. In general, as the frequency increases, the magnitude

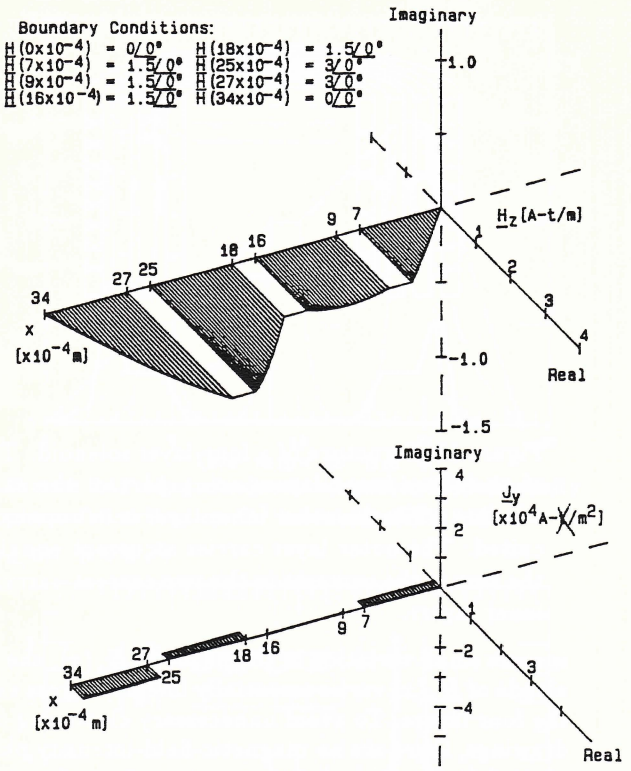


Figure 19: $\underline{H}_z(x)$ and $\underline{J}_y(x)$ phasor distributions across the four-layer solenoid of Fig. 18 at 1 kHz.

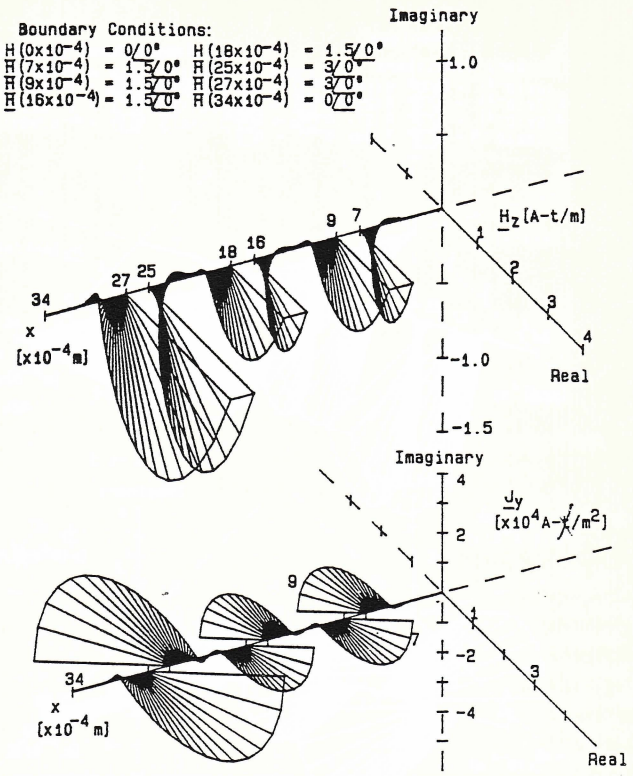


Figure 20: $\underline{H}_z(x)$ and $\underline{J}_y(x)$ phasor distributions across the four-layer solenoid of Fig. 18 at 1 MHz.

of both $\underline{H}_z(x)$ and $\underline{J}_y(x)$ becomes attenuated near the center of each layer, while the magnitude of $\underline{J}_y(x)$ becomes much greater near the surfaces of each layer. In other words, the diminishing ability of the alternating magnetic field to penetrate deep into each winding layer causes the current to be concentrated in regions near the surfaces of each layer.

A final example that we consider is illustrated in Fig. 18. Once again, this four-layer solenoid is modeled with four infinite conducting sheets, and a four-layer total of zero ampere-turns is intentionally established so that the solenoid resembles a real transformer with a high-permeability core. In this case, however, we choose two of the inner winding layers to carry 1.5 units of current each, and the outer winding to carry 3 units of current. Thus, one of the inner windings is left open-circuited, so that it has zero net current. Figures 19 and 20 show the distributions of $\underline{H}_z(x)$ and $\underline{J}_y(x)$ at excitation frequencies of 1 kHz and 1 MHz, respectively. These distributions look somewhat similar to those seen in Figs. 16 and 17. On the lower set of axes in Fig. 19, no current flows in the open-circuited winding layer which lies between $x = 0.9$ mm and $x = 1.6$ mm. However, as the frequency increases, we begin to see some current flow; for the 1 MHz case of Fig. 20, there are large current densities that appear in the open-circuited layer. Nevertheless, the net current density in this layer at any instant in time is still zero (as it must be) since there is an equal amount of current flowing in both the negative and the positive directions.

5 CONCLUSIONS

One single-layer and two four-layer example winding structures are used to illustrate the impact of excitation frequency on the magnetic-field-intensity and current-density distributions in transformer windings. By plotting the distributions as phasors in three-dimensional isometric plots, greater insight is gained into the origin and behavior of eddy currents. This insight enhances the design engineer's ability to understand and evaluate the available design options.

References

[1] A. M. Urling, V. A. Niemela, G. R. Skutt, and T. G. Wilson, "Characterizing High-Frequency Effects in Transformer Windings—A Guide to Several Significant Articles," *IEEE Applied Power Electronics Conference Record, 89CH2719-3, 1989, pp. 373-385.*

[2] V. A. Niemela, G. R. Skutt, A. M. Erling, Y. N. Chang, T. G. Wilson, H. A. Owen, Jr., and R. C. Wong, "Calculating the Short-Circuit Impedances of a Multiwinding Transformer from its Geometry," *IEEE Power Electronics Specialists Conference Record*, 1989.

Bibliography

[1] Blume, L. F. , et al., *Transformer Engineering*, John Wiley & Sons, Inc., New York, 1951.

[2] Carsten, Bruce, "High Frequency Conductor Losses in Switchmode Magnetics," *High-Frequency Power Converter Conference*, May 1986, pp. 155–176.

[3] Coonrod, N.R., "Transformer Computer Design Aid For Higher Frequency Switching Power Supplies," *Power Electronics Specialists Conference*, 1984, pp. 257–267.

[4] Chua, Leo O. and Lin, Pen-Min,*Computer-Aided Analysis of Electronic Circuits*, Prentice-Hall, Inc., Englewood Cliffs, New Jersey, 1975.

[5] Dahl, O.G.C., *Electric Circuits: Theory and Applications*, Volume 1, McGraw-Hill Book Company, Inc., New York, 1928.

[6] Dowell, P.L., "Effects of Eddy Currents in Transformer Windings," *PROC. IEE*, Vol. 113, No. 8, August 1966, pp. 1387–1394.

[7] Goad, S. D., "The Theory and Design of Switched-Mode Power Transformers for Minimum Conductor Loss," Ph.D. Dissertation, Virginia Polytechnic Institute and State University, Blacksburg, VA, December 1985.

[8] Griffiths, David J., *Introduction to Electrodynamics*, Prentice-Hall, Inc., Englewood Cliffs, New Jersey, 1981.

[9] Halliday, David and Resnick, Robert, *Fundamentals of Physics*, second edition, John Wiley & Sons, Inc., New York, 1981.

[10] *HP-15C Owner's Handbook*, January 1985 edition, Hewlett-Packard Company, Corvallis, Oregon, copyright 1982, pp. 164–166.

[11] Jongsma, J., "Minimum-Loss Transformer Windings for Ultrasonic Frequencies" "Part 1 – Background and Theory," E.A.B. 35, No. 3, pp. 146-163, "Part 2 – Design Methods and Aids," E.A.B. 35, No. 4, pp. 211–226.

[12] Jongsma, J., "High-Frequency Ferrite Power Transformer and Choke Design; Part 3: Transformer Winding Design," *Philips Electronic Components and Materials Technical Publication 207.*

[13] M.I.T. Staff, *Magnetic Circuits and Transformers*, John Wiley & Sons, Inc., New York, 1943.

[14] Perry, M.P., "Multiple Layer Series Connected Winding Design for Minimum Losses," *IEEE Transactions on Power Apparatus and Systems*, Vol. PAS-98, No. 1 Jan/Feb 1979, pp. 116–123.

[15] Rosa, John, "Calculation of Flux Linkages in Multiwinding Transformers," *PESC*, 1986, pp. 639–644.

[16] Skutt, G.R., *Modeling Multiwinding Transformers for High-Frequency Applications*, M.S. Thesis, Duke University, April 24, 1988.

[17] E. C. Snelling, *Soft Ferrites — Properties and Applications*, Iliffe Books Ltd., London, 1969.

[18] Starr, F.M., "Equivalent Circuits," *Transactions of the American Institute of Electrical Engineers*, June 1932, pp. 287–298.

[19] Vandelac, J.P., Ziogas, P., "A Novel Approach for Minimizing High Frequency Transformer Copper Losses," *PESC*, 1987, pp. 355–367.

[20] Venkatraman, P.S., "Winding Eddy Current Losses in Switch Mode Power Transformers Due to Rectangular Wave Currents," *Proceedings of Powercon 11*, Power Concepts Inc., Ventura Ca., 1984.

[21] Watson, J. K., *Applications of Magnetism*, Published by the author, Gainesville, Florida, 1985.

[22] Weast, Robert C., *Handbook of Chemistry and Physics*, 59th ed., CRC Press, Boca Raton, Florida, 1985.